



DEVELOPMENT OF NEW MATERIALS AND TECHNIQUES FOR LUMINESCENCE NANOTHERMOMETRY AND PHOTOTHERMAL CONVERSION

Oleksandr Savchuk

ADVERTIMENT. L'accés als continguts d'aquesta tesi doctoral i la seva utilització ha de respectar els drets de la persona autora. Pot ser utilitzada per a consulta o estudi personal, així com en activitats o materials d'investigació i docència en els termes establerts a l'art. 32 del Text Refós de la Llei de Propietat Intel·lectual (RDL 1/1996). Per altres utilitzacions es requereix l'autorització prèvia i expressa de la persona autora. En qualsevol cas, en la utilització dels seus continguts caldrà indicar de forma clara el nom i cognoms de la persona autora i el títol de la tesi doctoral. No s'autoritza la seva reproducció o altres formes d'explotació efectuades amb finalitats de lucre ni la seva comunicació pública des d'un lloc aliè al servei TDX. Tampoc s'autoritza la presentació del seu contingut en una finestra o marc aliè a TDX (framing). Aquesta reserva de drets afecta tant als continguts de la tesi com als seus resums i índexs.

ADVERTENCIA. El acceso a los contenidos de esta tesis doctoral y su utilización debe respetar los derechos de la persona autora. Puede ser utilizada para consulta o estudio personal, así como en actividades o materiales de investigación y docencia en los términos establecidos en el art. 32 del Texto Refundido de la Ley de Propiedad Intelectual (RDL 1/1996). Para otros usos se requiere la autorización previa y expresa de la persona autora. En cualquier caso, en la utilización de sus contenidos se deberá indicar de forma clara el nombre y apellidos de la persona autora y el título de la tesis doctoral. No se autoriza su reproducción u otras formas de explotación efectuadas con fines lucrativos ni su comunicación pública desde un sitio ajeno al servicio TDR. Tampoco se autoriza la presentación de su contenido en una ventana o marco ajeno a TDR (framing). Esta reserva de derechos afecta tanto al contenido de la tesis como a sus resúmenes e índices.

WARNING. Access to the contents of this doctoral thesis and its use must respect the rights of the author. It can be used for reference or private study, as well as research and learning activities or materials in the terms established by the 32nd article of the Spanish Consolidated Copyright Act (RDL 1/1996). Express and previous authorization of the author is required for any other uses. In any case, when using its content, full name of the author and title of the thesis must be clearly indicated. Reproduction or other forms of for profit use or public communication from outside TDX service is not allowed. Presentation of its content in a window or frame external to TDX (framing) is not authorized either. These rights affect both the content of the thesis and its abstracts and indexes.

Development of new materials and techniques for luminescence nanothermometry and photothermal conversion

Oleksandr Savchuk

Doctoral thesis

Supervised by:

Dr. Joan Josep Carvajal

Prof. Dr. Francesc Díaz

Departament de Química Física i Inorgànica
Física i Cristal·lografia de Materials i Nanomaterials (FiCMA-
FiCNA)



UNIVERSITAT ROVIRA I VIRGILI

Tarragona

2016

UNIVERSITAT ROVIRA I VIRGILI
DEVELOPMENT OF NEW MATERIALS AND TECHNIQUES FOR LUMINESCENCE NANOTHERMOMETRY AND PHOTOTHERMAL CONVERSION
Oleksandr Savchuk

Development of new materials and techniques for luminescence nanothermometry and photothermal conversion

Oleksandr Savchuk

Oleksandr Savchuk, 2016

Física i Cristal·lografia de Materials i Nanomaterials (FiCMA-FiCNA)

Departament de Química Física i Inorgànica

Universitat Rovira i Virgili

C/ Marcel·li Domingo 1

E-43007, Tarragona (Spain)

UNIVERSITAT ROVIRA I VIRGILI
DEVELOPMENT OF NEW MATERIALS AND TECHNIQUES FOR LUMINESCENCE NANOTHERMOMETRY AND PHOTOTHERMAL CONVERSION
Oleksandr Savchuk



UNIVERSITAT
ROVIRA I VIRGILI

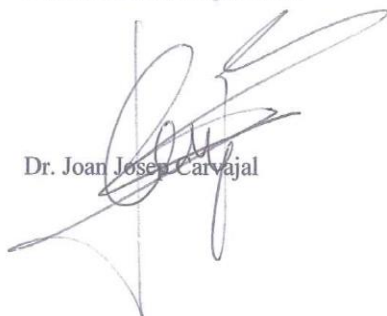
DEPARTAMENT DE QUÍMICA FÍSICA
I INORGÀNICA

Campus Sescelades
Marcel·lí Domingo, s/n
43007 Tarragona
Tel. +34 977 55 81 37
Fax +34 977 55 95 63
www.quimica.urv.es

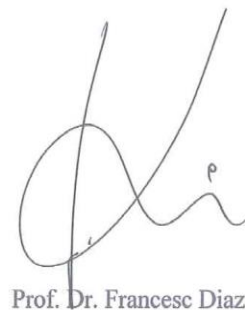
We STATE that the present study, entitled “**Development of new materials and techniques for luminescence nanothermometry and photothermal conversion**”, presented by Oleksandr Savchuk for the award of the degree Doctor, has been carried out under our supervision at the Department of Physical and Inorganic Chemistry of this university, and that it fulfils all the requirements to be eligible for the European Doctorate Award.

Tarragona, 8 April 2016

Doctoral Thesis Supervisors



Dr. Joan Josep Carvajal



Prof. Dr. Francesc Diaz

UNIVERSITAT ROVIRA I VIRGILI
DEVELOPMENT OF NEW MATERIALS AND TECHNIQUES FOR LUMINESCENCE NANOTHERMOMETRY AND PHOTOTHERMAL CONVERSION
Oleksandr Savchuk

Abstract

Development of new materials and techniques for luminescence nanothermometry and photothermal conversion

Temperature is today recognized as one of the basic variables in science. With the development of the nanotechnology, the temperature of a given system with submicrometric spatial resolution becomes possible to measure. This has led to the development of a new subfield of thermometry named nanothermometry, related to the temperature measurement at the nanoscale level. There are many areas where the temperature determination at the nanoscale is of great importance, for instance in microelectronics and medicine. Luminescence nanothermometry, as a non-contact technique is one of the most promising techniques for temperature determination at nanometer scale.

The main objective of this thesis is to study the temperature dependence of the luminescence properties of optically active lanthanide ions in different host matrices emitting in the visible and near infrared region of electromagnetic spectrum and to explore their luminescent nanothermometric potentialities. We also explored if these nanoparticles might present additional properties, especially if they can also be used as photothermal converters for photothermal therapy. Also in this field we studied the photothermal conversion efficiency of graphene and graphene oxide putting in context the results obtained by comparing them with those of the most common photothermal agent nowadays. Moreover, we developed a new method for determining the photothermal conversion efficiency by using an integrating sphere that simplifies the procedures applied up to now for these measurements. Furthermore, we analyzed the present detection technology for the luminescence of these nanothermometers and explored some modifications to develop compact and faster luminescence nanothermometer setups.

Keywords: nanothermometry, luminescence, photothermal conversion, upconversion.

UNIVERSITAT ROVIRA I VIRGILI
DEVELOPMENT OF NEW MATERIALS AND TECHNIQUES FOR LUMINESCENCE NANOTHERMOMETRY AND PHOTOTHERMAL CONVERSION
Oleksandr Savchuk

Preface

The research contained in this doctoral thesis was conducted in the laboratories of the *Física i Cristal·lografia de Materials i Nanomaterials (FiCMA-FiCNA)* group of the *Departament de Química Física i Inorganica* of the *Universitat Rovira i Virgili* in Tarragona, and was supervised by Dr. Joan Josep Carvajal and Prof. Dr. Francesc Diaz.

This research was financed by

Ministerio de Economía y Competitividad, Gobierno de España:

MAT 2011-29255-C02-02

MAT 2013-47395-C4-4-R

TEC 2010-21574-C02-02

TEC 2014-55948-R

Generalitat de Catalunya:

2009 SGR 235

2014 SGR 1358

2013 FI_B 01032

2014 FI_B1 00222

2015 FI_B 00136

2010 ICREA – 02

Oleksandr Savchuk

Tarragona, 2016

UNIVERSITAT ROVIRA I VIRGILI
DEVELOPMENT OF NEW MATERIALS AND TECHNIQUES FOR LUMINESCENCE NANOTHERMOMETRY AND PHOTOTHERMAL CONVERSION
Oleksandr Savchuk

Acknowledgements

This thesis would not be possible without the great support and assistance of many people. First of all, I would like to thank my thesis directors the FiCMA-FiCNA group leader Prof. Dr. Francesc Díaz for giving me the opportunity to carry out this research at his respective group and constant supervision and guidance throughout my stay and Dr. Joan Josep Carvajal for his enormous support, powerful motivation, strong patience, brilliant ideas, friendly attitude, non-stopping revision of the articles and shared knowledge.

I also would like to thank the other members of the FiCMA-FiCNA group Prof. Dr. Magdalena Aguiló, Dr. Jaume Massons, Dra Cinta Pujol, Dr. Airan Rodenas, Dr. Xavier Mateos, Dra Rosa Sole, Dra Josefina Gavalda and Dr. Xavier Rius. Special thank to Dr. Jaume Massons for his valuable assistance and outstanding ideas, Dra Cinta Pujol and Dr Airan Rodenas for all the help, support and valuable advices.

Also, I'm very grateful to technician members of the group. I would like to thank Agusti Montero, Nicolette Bakker, Laura Escorihuela and Gemma Marsal for their help in the laboratory.

I give my thanks to the technicians of the Servei de Recursos Científico-Tècnics of the University Rovira i Virgili (Mariana, Francesc, Rita, Merce, Nuria and Lucas), who helped me a lot in my research.

During my thesis I was lucky to spend time performing experiments abroad. I'm very grateful to Prof. L. D. Carlos for his help and hospitality and for giving me an opportunity to carry out the experiments in the laboratories of Department of Physics at University of Aveiro and CICECO. Also, my sincere thank to Dr. Carlos Brites for his help in laboratory.

Also, I want to thank Dr. Daniel Jaque for his ideas, great support and strong contribution in carrying out experiments with chicken breast, which were performed in the laboratories of Department of Physics of Materials at

Autonoma de Madrid. Special thank to Dr. Patricia Haro-González for her friendly attitude, positive mood and her help in performing HeLa cells and NIR imaging experiments.

I'm very grateful to Dr. Concepcion Cascales for her scientific discussions, fast answers and for providing some high quality luminescent nanoparticles.

Furthermore, I would like to extent my thanks to the members of our group (past and present). Venkatesan Jambunathan, Martha Segura, Jaume Cugat, Western Bolaños, William Barrera, Muhammad Usman Qadri, Oleksandr Bilousov, Ali Butt, Josue Mena, Marc Medina, Josep Maria Serres, Xavier Martinez, Eric Pedrol, Iryna Adell, Esrom Aschenaki and of course Dati Nguyen.

Last but not the least I would like to thank my family for their great support and encouragements.

To my family...

UNIVERSITAT ROVIRA I VIRGILI
DEVELOPMENT OF NEW MATERIALS AND TECHNIQUES FOR LUMINESCENCE NANOTHERMOMETRY AND PHOTOTHERMAL CONVERSION
Oleksandr Savchuk

List of publications

- Paper I:** Savchuk, Ol. A.; Haro-González, P.; Carvajal J. J.; Jaque, D.; Massons, J.; Aguiló, M.; and Díaz, F. *Er:Yb:NaY₂F₅O up-converting nanoparticles for sub-tissue fluorescence lifetime thermal sensing (2014)* *Nanoscale* 6, 9727-9733.
- Paper II:** Savchuk, Ol. A.; Carvajal, J. J.; Pujol, M. C.; Massons, J.; P.; Martínez, O.; Jiménez, J.; Aguiló, M.; Díaz, F. *New strategies involving upconverting nanoparticles for determining moderate temperatures by luminescence thermometry (2016)* *Journal of Luminescence* 169, 711–716.
- Paper III:** Savchuk, Ol. A.; J. J. Carvajal, M. C. Pujol, J. Massons, P. Haro-González, D. Jaque, M. Aguiló and F. Díaz. *New strategies for luminescence thermometry in the biological range using upconverting nanoparticles (2015)* *Proc. of SPIE* 9129, 91292-7.
- Paper IV:** Savchuk, Ol. A.; Carvajal, J. J.; Cascales, C.; Massons, J.; Aguiló, M.; Díaz, F. *Thermochromic upconversion nanoparticles for visual temperature sensors with high thermal, spatial and temporal resolution (2016)* To be submitted to *ACS Applied surfaces & interfaces*.
- Paper V:** Savchuk, Ol. A.; Carvajal, J. J.; Massons, J.; Cascales, C.; Aguiló, M.; Díaz, F. *A novel low-cost, compact and fast signal processing sensor for ratiometric luminescent nanothermometry (2016)* Submitted to *Sensors and Actuators A*.
- Paper VI:** Savchuk, Ol. A.; Carvajal, J. J.; Pujol, M. C.; Barrera, E. W.; Massons, J.; Aguiló, M.; and Diaz, F. *Ho,Yb:KLu(WO₄)₂ nanoparticles: A versatile material for multiple thermal sensing purposes by luminescent thermometry (2015)* *J. Phys. Chem. C* 119, 18546–18558.
- Paper VII:** Savchuk, Ol. A.; Carvajal, J. J.; Barrera, E.W.; Pujol, M.; Mateos, C. X.; Solé, R.; Massons, J.; Aguiló, M.; Díaz, F. *(Ho, Tm, Yb): KLuW nanoparticles, an efficient thermometry sensor in the biological range (2013)* *Proc. of SPIE* 8594, 859406-8.
- Paper VIII:** Savchuk, Ol. A.; Carvajal, J. J.; Cesteros, Y.; Salagre, P.; Nguyen, H. D.; Rodenas, A.; Massons, J.; Aguiló, M.; Díaz, F. *Microwave-assisted solvothermal synthesis of Er,Yb:NaYF₄ nanoparticles for luminescent thermometric applications (2016)* To be submitted to *Chemistry of materials*.
- Paper IX:** Savchuk, Ol. A.; Carvajal, J. J.; Cascales, C.; Aguiló, M.; Díaz, F. *Benefits of silica core-shell structures on the temperature sensing properties of Er,Yb:GdVO₄ up-conversion nanoparticles (2016)* *ACS Applied surfaces & interfaces* 8, 7266-7273.

- Paper X:** Savchuk, Ol. A.; Carvajal, J. J.; Cascales, C.; Haro-González, P.; Aguiló, M.; and Díaz, F. *NIR-to-NIR upconversion emissions of $Tm^{3+}, Yb^{3+}:GdVO_4@SiO_2$ core-shell nanoparticles for temperature sensing purposes and imaging in the first biological window (2016)* To be submitted to Advanced Functional Materials.
- Paper XI:** De la Cruz, L.G.; Savchuk, Ol.; Carvajal, J. J.; Haro-González, P.; Aguiló, M.; Díaz, F. *Luminescence thermometry and imaging in the second biological window with $Nd:KGd(WO_4)_2$ nanoparticles (2016)* Submitted to Chemistry of materials.
- Paper XII:** Savchuk, Ol. A.; Carvajal, J. J.; Haro-González, P.; Aguiló, M.; Díaz, F. *Luminescent nanothermometry using short-wavelength infrared light (2016)* To be submitted to Chem. Phys. Phys. Chem.
- Paper XIII:** Savchuk, Ol. A.; Carvajal, J. J.; Massons, J.; Aguiló, M.; Díaz, F. *Determination of photothermal conversion efficiency of graphene and graphene oxide through an integrating sphere method (2016)* Carbon 103, 134-141.
- Paper XIV:** Savchuk, Ol. A.; Carvajal, J. J.; Brites, C. D. S.; Carlos, L. D.; Aguiló, M.; and Díaz, F. *Multifunctional $Ho, Tm:KLuW$ nanoparticles for temperature sensing applications (2016)* To be submitted to Nanoscale.

CONTENTS

Chapter 1.	
1 Introduction	1
1.1 Historical development of the thermometry	3
1.2 From “classical” thermometry to nanothermometry.....	5
1.2.1 Methods of nanothermometry	9
1.3 Luminescence nanothermometry	11
1.3.1 Intensity- and band shape-based luminescence nanothermometry.....	13
1.3.2 Theory of the fluorescence intensity ratio (FIR) technique	15
1.3.3 Lifetime based nanothermometry	17
1.3.4 Nanothermometry based on the spectral position of the emission lines.....	19
1.3.5 Bandwidth-based nanothermometry	20
1.4 Materials used in luminescence nanothermometry	21
1.4.1 Quantum dots	22
1.4.2 Organic dyes	24
1.4.3 Gold nanoparticles	26
1.4.4 Polymer-based systems	28
1.4.5 Lanthanide-doped nanoparticles	30
1.4.5.1 Upconverting nanoparticles.....	33
1.4.5.2 Upconversion mechanism	34
1.4.5.3 Single-center Ln ³⁺ -UCNPs nanothermometry	35
1.4.5.4 Multi-center Ln ³⁺ -UCNPs nanothermometry	38
1.4.6 Complex systems	39
1.5 Aim of this thesis	42
1.6 Structure of the thesis	42
1.7 References	44
Chapter 2.	
2 Experimental techniques.....	59
2.1 Synthesis of luminescent nanoparticles	60
2.1.1 Sol-Gel synthesis: the Pechini method.....	60
2.1.2 Hydrothermal method	61
2.1.2.1 Preparation of core-shell Er ³⁺ , Yb ³⁺ and Tm ³⁺ , Yb ³⁺ co-doped GdVO ₄ nanoparticles.....	63
2.1.3 Synthesis of Er ³⁺ , Yb ³⁺ :NaYF ₄ nanoparticles by the microwave-assisted heating solvothermal method.....	63
2.2 Structural characterization	65
2.2.1 X-ray diffraction	65

2.2.2 Raman scattering.....	67
2.3 Microscopic characterization techniques.....	69
2.3.1 Transmission electron microscopy (TEM).....	69
2.3.2 Environmental scanning electron microscopy (ESEM).....	71
2.4 Spectroscopic techniques.....	72
2.4.1 Optical absorption.....	72
2.4.2 Photoluminescence emission measurements.....	74
2.4.3 NIR imaging using Ln ³⁺ -doped nanoparticles.....	77
2.4.4 Measurements of an absolute intensity.....	78
2.4.5 Lifetime measurements.....	79
2.5 Photothermal conversion efficiency.....	80
2.6 References.....	82
Chapter 3.	
3 Luminescence nanothermometry in the visible: I. New detection techniques.....	87
3.1 Paper I: Er,Yb:NaY ₂ F ₅ O up-converting nanoparticles for sub-tissue fluorescence lifetime thermal sensing.....	89
3.2 Paper II: New strategies involving upconverting nanoparticles for determining moderate temperatures by luminescence thermometry.....	99
3.3 Paper III: New strategies for luminescence thermometry in the biological range using upconverting nanoparticles.....	115
3.4 Paper IV: Thermochromic upconversion nanoparticles for visual temperature sensors with high thermal, spatial and temporal resolution.....	123
3.5 Paper V: A novel low-cost, compact and fast signal processing sensor for ratiometric luminescent nanothermometry.....	137
Chapter 4.	
4 Luminescence nanothermometry in the visible: II. New materials.....	157
4.1 Paper VI: Ho,Yb:KLu(WO ₄) ₂ nanoparticles: A versatile material for multiple thermal sensing purposes by luminescent thermometry.....	159
4.2 Paper VII: (Ho, Tm, Yb): KLuW nanoparticles, an efficient thermometry sensor in the biological range.....	195
4.3 Paper VIII: Microwave-assisted solvothermal synthesis of Er,Yb:NaYF ₄ nanoparticles for luminescent thermometric applications.....	205
4.4 Paper IX: Benefits of silica core-shell structures on the temperature sensing properties of Er,Yb:GdVO ₄ up-conversion nanoparticles.....	227
Chapter 5.	
5 Luminescence nanothermometry in the NIR.....	251
5.1 Paper X: NIR-to-NIR upconversion emissions of Tm ³⁺ ,Yb ³⁺ :GdVO ₄ @SiO ₂ core-shell nanoparticles for temperature sensing purposes and imaging in the first biological window.....	253
5.2 Paper XI: Luminescence thermometry and imaging in the second biological window with Nd:KGd(WO ₄) ₂ nanoparticles.....	271
5.3 Paper XII: Luminescent nanothermometry using short-wavelength infrared light.....	293
Chapter 6.	
6 Photothermal converter materials.....	319

6.1 Paper XIII: Determination of photothermal conversion efficiency of graphene and graphene oxide through an integrating sphere method	321
6.2 Paper XIV: Multifunctional Ho,Tm:KLuW nanoparticles for temperature sensing applications.....	343
Conclusions.....	365

Chapter 1

Introduction

What is temperature? According to Max Plank, the concept of temperature is our qualitative sense of touch about how hot or how cold a body is [1]. A body that is felt hot usually has a higher temperature than a similar body that is felt cold. But this definition is so undetermined that a perception of temperature based on the sense of touch can be deceivable. If we touch two different materials, for example wood and metal, both of which are at the same temperature, our senses tell us that the metal is much colder/hotter than the wood only because the metal conducts heat faster. So the heat transfer is a very important parameter in every temperature measuring situation [1].

Temperature is today recognized as one of the basic variables in science. Many industrial and scientific processes as well as processes in everyday life, from cooking the food to the production of complicated materials, depend on the temperature [2]. Extraction of metals from ores, refining, casting, shaping and heat treatment, for instance, all take place at high temperatures [3]. Glass, cement, brick and pottery manufacture involve high-temperature processing as well. Distillation columns and reactors in chemical industries involve also processes where temperature monitoring and control is critical [3]. Also temperature control is essential in biotechnology and medicine. The controlled growth of microorganisms in

fermentation processes, for instance, always requires maintaining a specified temperature to promote their optimum growth [3].

This chapter will start with a brief description of the historical evolution of thermometry and the appearance of a new sub-field of thermometry, named nanothermometry. We will explain the importance of the nanothermometry in medicine and electronics. We will focus our main attention on luminescence nanothermometry, the method of nanothermometry, which operates luminescence properties of particular material that change with temperature to achieve thermal sensing by temporal (rise and decay time) or spectral (intensity, band shape, spectral peak position, bandwidth and polarization) analysis of the emission. Finally, the chapter will end with the objectives of this thesis.

1.1 Historical development of the thermometry

The scientific principles and methods on which temperature measurements are based are part of the development of science. Here we will shortly review the main scientific discoveries and inventions that constitute the present thermometry.

The first mention to the measurements of the degree of heat and cold arose in the sixteen and seventeen centuries, and it is ascribed to Galileo Galilei and his pupils [4-6]. The instrument named thermoscope, consisted of a glass bulb with air and a long rod immersed in a liquid, and was based on the principles that certain substances such as air and liquids expand when heated. The device was not sealed, so it was affected by changes in pressure and to losses by evaporation [7]. A design of Galileo thermoscope is shown in Figure 1.1.



Figure 1.1. Galileo Galilei with thermoscope [8].

The word “thermometer” first appeared in the literature in 1624 in a book by the French priest and mathematician Jean Leurechon [9]. The author describes a thermometer as an instrument of glass which has a little bulb above and a long neck below, and it ends in a vessel full of water. According to the author, those who wished to determine the changes in temperature by numbers (degrees) could draw a line all along the tube and divide it into 8 degrees [9].

At about 1654, Ferdinand II of Medici (Grand Duke of Tuscany) made thermoscopes of the usual form (glass which has a little bulb above and a long neck below), filled them with

alcohol, hermetically sealed them and then marked off 360 divisions in the neck. Those were the first temperature sensing instruments to be independent of pressure and water losses by evaporation, and after which scientists began to call such divisions by the name of degrees [10].

In 1694, the Padua mathematician, Carlo Renaldi suggested taking the melting point of ice and the boiling point of water as two fixed points on a thermometer scale [11]. Then, in 1701 Newton labeled the melting point of ice as zero on his temperature scale [12].

The mercury thermometer, which was invented by the German physicist Daniel Gabriel Fahrenheit in 1714, can be considered to be the first modern thermometer. In 1724 he introduced the standard temperature scale that was used to record changes in temperature in an accurate way [13]. The Fahrenheit scale ($^{\circ}\text{F}$) divided the freezing and boiling points of water into 180 degrees. According to that, 0°F was based on the temperature of an equal mixture of ice and salt, 32°F was the freezing point of water and 212°F was the boiling point of water. Fahrenheit based his temperature scale on the temperature of the human body. Originally, the human body was 100°F on the Fahrenheit scale, but it has since then been adjusted to 98.6°F .

In 1740, the Swedish astronomer, physicist and mathematician Anders Celsius proposed the centigrade scale [13]. He proposed to divide the range of temperature between the melting point of ice and the steam point of water in 100 parts. He attributed the 100 value to the melting point of ice, and the 0 value to the steam point of water. The Swiss botanist Carl Linnaeus inverted the scale so that 0 was the melting point of ice and 100 was the steam point of water [14]. In 1948, at the 9th international conference on weight and measures, the centigrade scale was changed to the Celsius scale in honor to Anders Celcius.

The problem with early temperature scales is that all of them were empirical, and their reading often depended on the material (usually a liquid or a gas) used to indicate the temperature change. For instance, in a liquid-glass thermometer the difference between the thermal expansion coefficient of the liquid and the glass causes the liquid to change height when the temperature changes. If the thermal expansion coefficient changes with temperature then an accurate thermometer cannot be constructed [15].

In 1848, the Irish mathematician physicist and engineer William Thomson (later known as Lord Kelvin) proposed a thermodynamic absolute temperature scale that was independent of the measuring material. The idea for the Kelvin scale was sparked by a discovery in the 1800s of a relationship between the volume and the temperature of a gas. Scientists theorized that the volume of a gas should become zero at a temperature of -273.15°C [15]. He defined "absolute" as the temperature at which molecules would stop moving, or "infinite cold." From absolute zero, he used the same unit as Celsius to determine the increments. Because of this fact; it could

be constructed from a single fixed calibration point once the degree size had been chosen. The triple point of water (0.01 °C or 273.16 K) was selected as the fixed point.

The measurable temperature range of liquid glass thermometers was extended by the development of electrical thermometers. The dependence of the electrical resistance of pure metals on temperature was used by Sir William Siemens in 1871 for his platinum thermometer, but it was found to have defects [16]. In 1887 H. L. Callendar overcame these troubles by taking care to avoid strain or contamination of the platinum wire. He established that its resistance was always the same at a given temperature. In 1887 H. L. Callendar presented his research on the variation of the electrical resistance of platinum and pioneered the use of platinum resistance thermometers for accurate temperature measurement [17, 18].

An important extension of the measurable temperatures was made with the development of radiation thermometers. The first pyrometers were made by Le Chatelier in 1892 for measuring objects that were hot enough to glow [19]. This instrument used an oil lamp flame as a brightness comparison source, a viewing telescope with red filters and an iris diagram for adjusting brightness to achieve a photometric match. The user would adjust an iris diaphragm until the brightness of the object, seen through a viewing telescope, matched the flame of an oil lamp. The iris setting would then indicate the temperature. This technique was made more practical when an electric bulb replaced the oil lamp in the early 1900s. Few years later it was improved by Fery [20]. A limitation that Charles Fery overcame in 1901 with the first radiation thermometer using a lens to focus thermal energy onto a thermocouple. The temperature could then be read directly from a galvanometer driven by the thermocouple. After this invention, thermometry was divided into two categories: contact and non-contact. Contact thermometers measure temperature using the heat transfer. Thus, require physical contact with the measured object to bring the sensor body to the object temperature. While in non-contact measurements, no contact with the measurable object is needed. Temperature reading is done through different temperature dependent properties of an object.

1.2 From “classical” thermometry to nanothermometry

After the time of the invention of the thermoscope by Galileo, many other temperature measuring methods and equipments have been developed considering the field of application, measurement accuracy and measurement conditions [21]. With the development of the nanotechnology, the temperature of a given system with submicrometric spatial resolution

becomes possible to measure. This has led to the development of a new subfield of thermometry named nanothermometry, related to the temperature measurement at the nanoscale level [22].

There are many areas where the temperature determination at the nanoscale is of great importance. For example, in electronics the reduction in size of the electrical conduction channels leads to relevant resistances values, resulting in a heating of the systems caused by Joule effect and the appearance of well-localized temperature increments, called “hot-spots” [23]. These “hot-spots” can affect the performance of the electronic devices and could lead to the irreversible damages. Brites et al. [24] developed a luminescent molecular thermometer based on the Eu^{3+} , Tb^{3+} co-doped $\gamma\text{-Fe}_2\text{O}_3@$ TEOS/APTES nanoparticles that were used for temperature mapping of an integrated circuit. The scheme of the setup is shown in Figure 1.2a. The temperature profile along the A and B lines marked in the integrated circuit are shown in Figures 1.2b and c, respectively, with the blue points corresponding to the measurements performed with a infrared (IR) camera for comparison. A spatial resolution of $35\ \mu\text{m}$ was achieved, with a temperature uncertainty of $0.5\ \text{K}$.

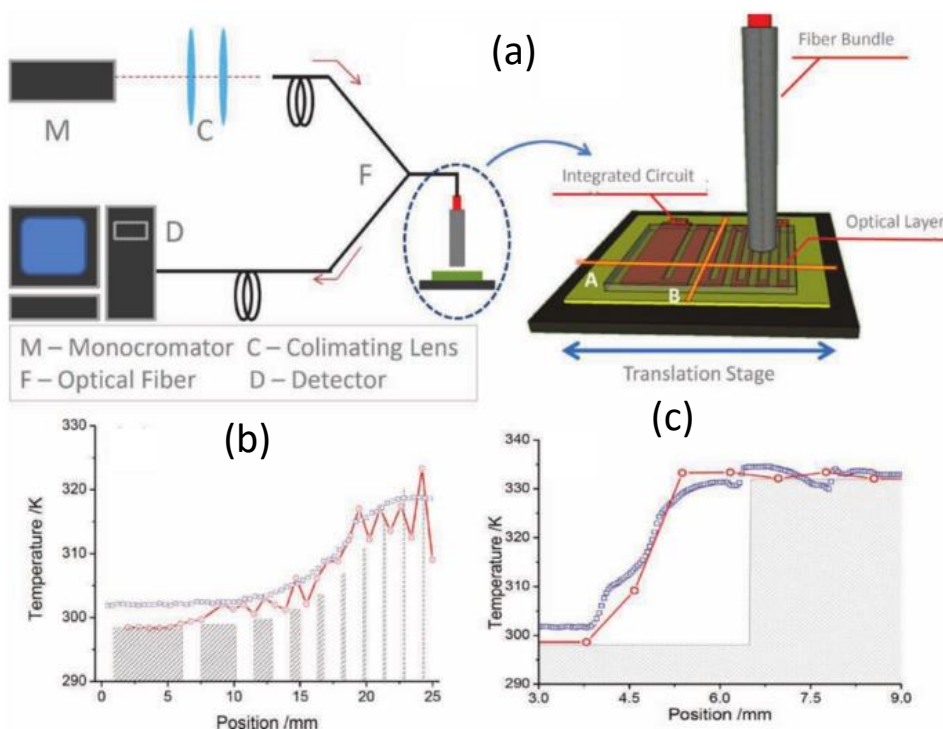


Figure 1.2. (a) Scheme of the setup used for the thermal mapping of an integrated circuit, whose tracks were covered with a layer of Eu^{3+} , Tb^{3+} co-doped $\gamma\text{-Fe}_2\text{O}_3@$ TEOS/APTES nanoparticles. Temperature profiles recorded along the A (b) and B (c) lines shown in (a), compared with the measurements performed with a IR camera (blue points) [24].

Aigouy and collaborators [25] developed a scanning thermal microscope able to map the temperature of electrically excited stripes with micro/nano sizes. It is based on gluing Er^{3+} , Yb^{3+} co-doped fluoride small particles on the scanning tip of an atomic force microscope. The particles were excited by a 975 nm laser, and the temperature dependent emission of Er^{3+} was used to determine the temperature using a ratiometric technique. The scheme of the setup is illustrated in Figure 1.3

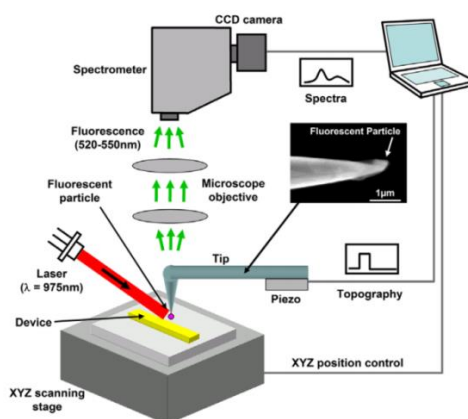


Figure 1.3. Scheme of the experimental setup developed by Aigouy [25].

Another area that could use the benefits offered by nanothermometry is biomedicine. For instance, metabolism and enzyme reactions in a biological cell are marked by temperature changes [26]. An accurate and noninvasive determination of temperature is, thus, of particular importance for the investigation of the dynamics of cellular heat production and propagation in the different intracellular compartments. It is also well known, that the pathogenesis of diseases like cancer is characterized by the increment of temperature [27]. Thus, temperature monitoring will provide not only the understanding of cellular activities, but also the possibility of detection of diseases in an early stage of development. Furthermore, heat can be used as an instrument to increase death rate in cells [28]. This becomes apparent as temperature goes over a definite threshold (312 K). Increasing the temperature of biological molecules above this limit induces new chemical reactions leading to denaturation [29, 30]. Those modifications (denaturation) damage cells and tissues in performing their functions, and finally at the temperature above 321 K necrosis is induced. Thus, if controlled, heat may be used to treat abnormal cells, such as cancer cells through hyperthermia treatment [31].

Heat would also affect negatively to healthy tissues. Thus, since the increase of the damage with temperature in biological tissues is critical, it is obvious that predicting and controlling the temperature distribution in a body region during hyperthermia treatment is

mandatory. Carrasco et al. [32] performed *in vivo* efficient temperature controlled photothermal therapy of cancer tumors by using Nd^{3+} doped LaF_3 nanoparticles. These nanoparticles have the ability to act at the same time as a heater and as a fluorescent thermal nanosensor. They demonstrated the intratumoral temperature sensing from the analysis of the fluorescence generated by the Nd^{3+} doped LaF_3 nanoparticles during the hyperthermia treatment. Figure 1.3a illustrates the two tumors, induced in the mouse, the one with the presence of Nd^{3+} doped LaF_3 nanoparticles and the other one used as control, with equivalent volume of phosphate-buffered saline (PBS). The presence of the luminescent nanoparticles can be seen in the bright fluorescence and the elevated temperature they produce. The temperature profiles in the tumor during the treatment are shown in Figure 1.3b, indicating the importance of monitoring the intratumoral temperature since its temperature is 20 % higher than the surface temperature.

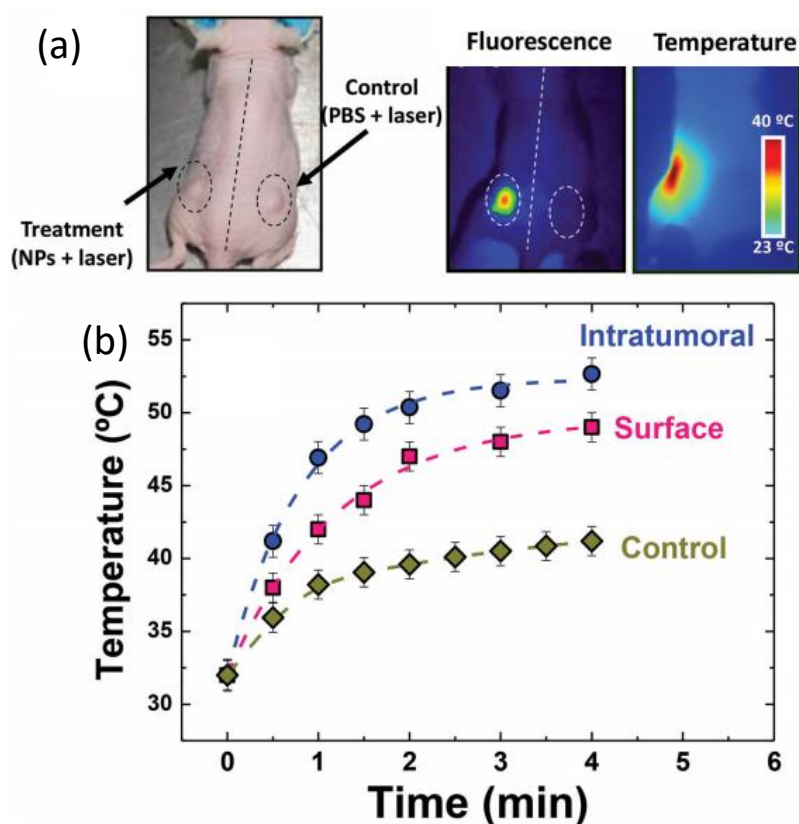


Figure 1.4. (a) Picture illustrating the photothermal therapy treatment in a mouse, in which two tumors have been induced. $\text{Nd}:\text{LaF}_3$ nanoparticles have been injected in one of the tumors as revealed by the bright fluorescence and high increment of the temperature; (b) temperature profile monitoring the treatment process in different regions of the mouse [32].

Another example of the temperature determination at the nanoscale also include microfluidics systems, that offer several advantages including efficiency, speed, portability, and reduced amount of reagent consumption [33]. The accurate and precise temperature control inside a microfluidic system is crucial, and has been demonstrated in variety of applications [34-39].

Samy et al. reported the temperature measurements in poly(dimethylsiloxane) (PDMS) thin film using Rhodamine B dye [35]. A thin PDMS/RhB film was used to measure the temperature distribution in a tapered PDMS microfluidic channel, where Joule heating was generated by an electrical field. As shown in Figure 1.5a, the chip was placed in a custom-made acrylic holder that suspended the microfluidic chip over the inverted microscope objective. The picture of the thermal map is shown in Figure 1.5b, illustrating a temperature gradient in the film. In that case, spatial resolutions in the order of hundreds of microns were obtained, with the relative temperature sensitivities between $1.3 \% K^{-1}$ and $2.3 \% K^{-1}$.

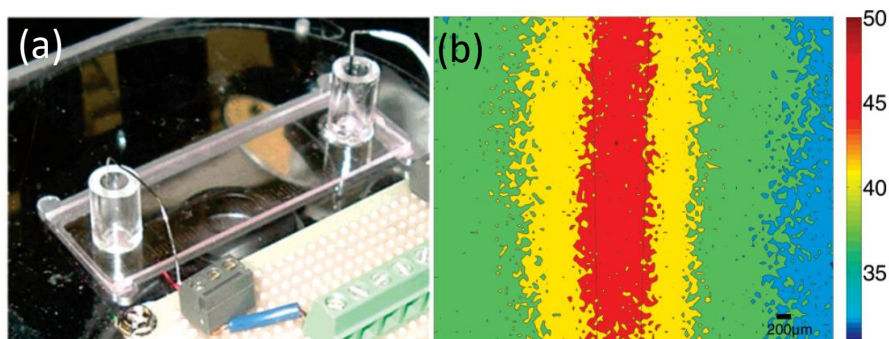


Figure 1.5. (a) Setup used to observe the PDMS microfluidic channel coated with a PDMS/RhB thin film on of the inverted microscope intensity measurements; (b) thermal map obtained, in which it can be seen the heating effect diffusing into the surrounding side walls [35].

1.2.1 Methods of nanothermometry

Basically, the present methods for temperature determination at the nanoscale level can be classified in contact and non-contact methods.

The contact methods include the use of thermistors and thermocouples, in which the thermal reading is achieved by the thermal variation of the resistance, conductivity, voltage or electrical capacity of the probe [40]. Nowadays, due to the intense development of micro/nano-fabrication techniques these systems can be fabricated with sub-micrometric sizes [41, 42]. Even more, when those temperature sensors are placed at the tip of an atomic force microscope,

scanning thermometry mapping can be performed at sub-500 nm scale providing a two-dimensional thermal image of the sample [43]. The same scanning thermal microscope can be made with a cantilever made of biomaterial instead of a thermocouple, and the temperature reading is performed by the deflection of the cantilever [44]. Scheme of the device is shown in Figure 1.6.

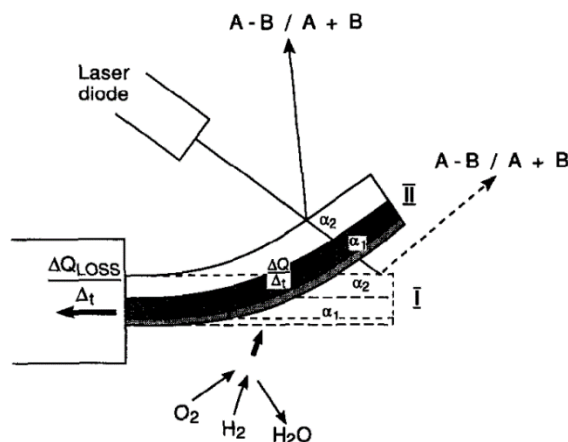


Figure 1.6. Scheme of the device based of deflection of the cantilever. The chemical reaction of H_2 with O_2 to form H_2O over a Pt catalytic layer releases heat which bends the bimorph structure comprised of two layers of differing thermal expansion coefficients (α_1 and α_2) from position I to II. This bending is detected by the deflection of a light beam from a laser diode reflected from the surface using a position-sensitive detector as the differences in the electrical signals from two opposite sensors A and B and normalized by the total signal $A+B$ [44].

This technique has resolution of 0.1 \AA and a temperature resolution of 10^{-5} K , better than that of a thermocouple. Also thin film nano-thermocouples have been developed, that show high spatial and thermal resolution (around 0.6 K) [42, 45]. However, they have serious drawbacks as the electrical wiring they can produce strong electromagnetic noise and cannot be applied in harsh environments. Since those thermal probes required the physical contact with the system under study, heat transfer between them can result in error in the temperature measurements. Also, and common to the rest of contact techniques, is that only surface measurements can be performed with these systems.

In order to overcome these problems, non-contact methods have been developed, such as infrared thermometry, thermoreflectance, Raman spectroscopy and luminescence thermometry [46]. The most commonly used of these non-contact methods is based on infrared thermometry, in which temperature is calculated from the amount of thermal radiation emitted by the target that is being measured [47]. By knowing the amount of infrared energy emitted by the object and its emissivity, the target temperature can be determined. This device can measure

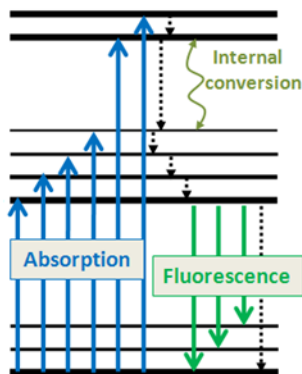
the temperature remotely and allow getting fast imaging. But it requires to know the emissivity of the target and its spatial resolution is in the micrometer range, limited by the size of the pixels of the sensor. Furthermore, it only allowed measuring temperature on the surface of the target [48].

Thermoreflectance thermometry, which is based on the temperature dependence of the refractive index of the materials, that constitutes the sample, requires the calibration of the reflectivity index of the material and its spatial resolution is limited by the light diffraction limit [48]. Moreover, the thermoreflectance coefficient of the materials depends on the excitation wavelength and the thickness of the optical layer [23]. Raman spectroscopy can be also classified as a non-contact temperature determination technique. It is based on the analysis of the properties of Raman modes in materials which are affected by changes in temperature [47]. Although Raman spectroscopy shows a very high spatial resolution (1 μm) and can measure temperature in small volumes of solids or even liquids, it has also significant disadvantages. It is very high time-consuming technique and can only be applied to materials showing a large Raman efficiency and it is thus restricted to a few numbers of systems [41, 49-53].

The development of new measurement techniques, which demonstrate high spatial, thermal and temporal resolution, high stability, a large measurement range, acceptable cost and size, is of great interest. Luminescence thermometry in the visible and near-infrared (NIR) has shown to meet all these criteria and is considered to be one of the most promising non-contact techniques for temperature determination, as will be detailed in the next section.

1.3 Luminescence nanothermometry

Luminescence is the process in which the emission of light from a given substance is occurs [54]. In general, the excitation (absorption of one or more photons in the case of photoluminescence) causes the energy of the luminescent molecule to jump to higher electronic states, from where, according to the conservation of the energy principle, it will be emitted in the form of light or heat, returning back to the ground state or to an intermediate state [54]. This process is schematically illustrated in the Jablonski energy level diagram in Figure 1.7. The properties of the emitted light depend on the properties of the electronic states involved in the emission process, which in turns depend on the local temperature of the system. Thus, luminescence nanothermometry operates in base to the luminescence properties that change with temperature to achieve thermal sensing by temporal or spectral analysis of the emission.



⋮ - Vibrational relaxation, quenching, or other non-radiative processes

Figure 1.7. Jablonski energy level diagram showing the luminescence process.

Temperature can affect the luminescence emission spectrum parameters in different ways, from which the temperature can be determined. Figure 1.8 illustrates schematically these variable parameters, including intensity, lifetime, bandwidth, polarization and spectral position of the peak [55]. The most studied parameters to determine temperature will be analyzed in detail in the following subsections.

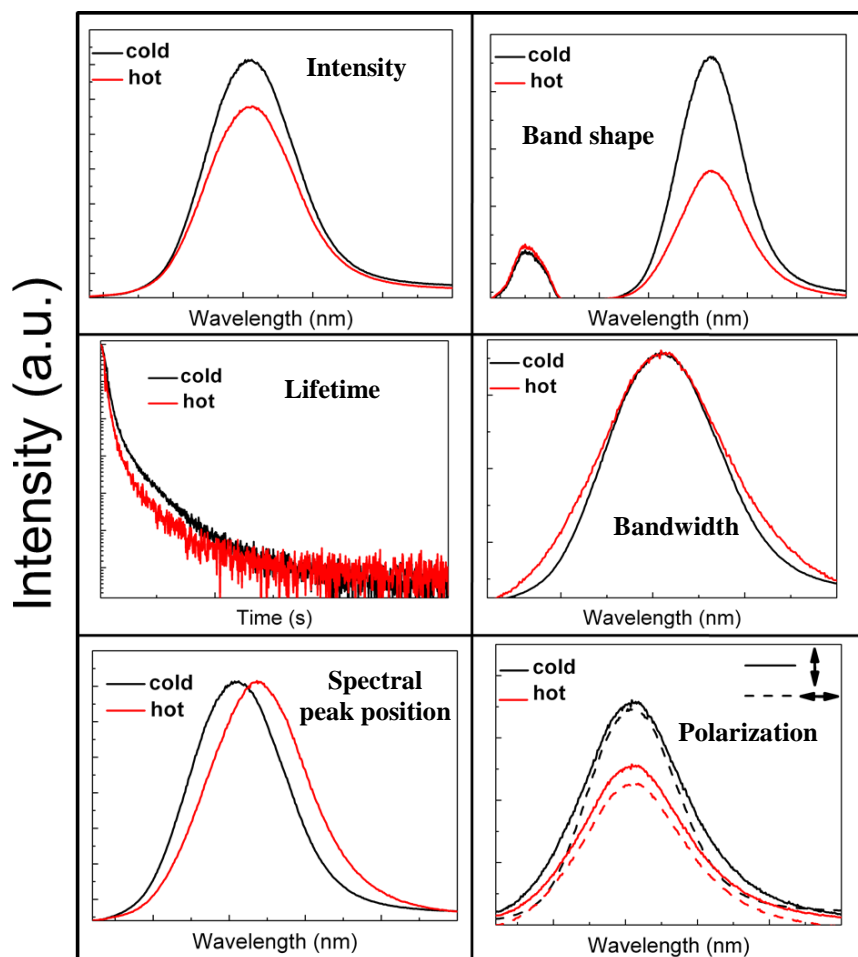


Figure 1.8. Schematic representation of the possible effects caused by an increase of the local temperature on the luminescence of given a material.

1.3.1 Intensity- and band shape-based luminescence nanothermometry

Temperature induced changes on the intensity of luminescence are caused by several factors, including: (i) quenching mechanisms – temperature increments would activate mechanisms of cross-relaxation while luminescent quenching centers would reduce the intensity; (ii) relaxation non-radiative processes – electrons in an excited state would relax to the ground state by generating heat instead of light; (iii) population redistribution due to Boltzmann statistics – the change of temperature would activate the population redistribution among the different energy states that follows the Boltzmann distribution, and (iv) phonon assisted Auger conversion processes – absence of temperature dependence [56].

Intensity-based nanothermometry has been reported in different systems, including quantum dots (QDs) [57-59], organic dyes [60, 61] lanthanide doped systems [62-64] and polymers [65, 66]. Relevant works of this kind of technique on lanthanide-doped materials will be discussed in the 1.4.5.1 subsection (Lanthanide doped nanoparticles) in the 1.4 section (Materials used in nanothermometry). In the case of QDs, the great advantage of using them in intensity-based nanothermometry is that in general they show linear dependence of intensity variation with temperature. As an example, the first work on intensity-based nanothermometry using QDs for bioapplications was done by Han et al [58]. They performed thermal imaging of human prostate cancer cells based on fluorescence intensity changes of internalized QDs. Two kinds of QDs were tested in the experiment, CdSe/ZnS core-shell QDs with an emission peak at 620 ± 10 nm and CdSe/ZnS core-shell QDs with an emission peak at 655 ± 10 nm. QDs emitting at 620 nm were more sensitive to temperature changes, as can be seen in Figure 1.9a. Additionally, metallic nanoparticles were mixed with the QDs to be used as nanoheaters to promote the temperature increase of the system. The authors used a double excitation source in experiment, which consisted on a near infrared laser emitting at 820 nm to excite the surface plasmons of the metallic nanoparticles and on halogen lamp provided excitation light via blue additive filter with transmission wavelength of ≤ 525 nm for excitation of the QDs. As can be seen in the micrograph in Figure 1.9b, the thermal heating generated by metallic nanoparticles is evident in the point where the laser was focused, where cells, where were killed. No cell death was observed outside of the laser-focused spot. The thermal sensitivity was determined by the temperature induced luminescence quenching rate and found to be close to $1\% \text{ K}^{-1}$.

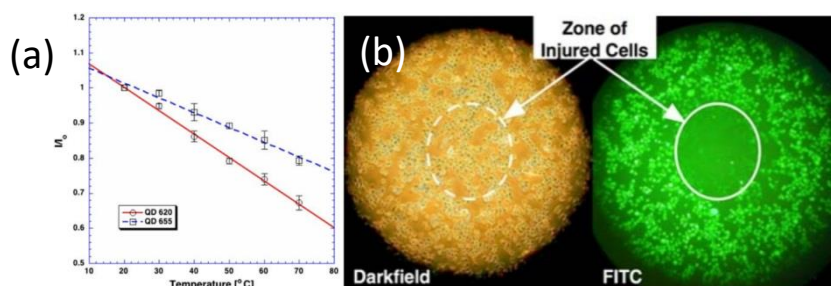


Figure 1.9. (a) QDs fluorescence intensity variation with temperature increase corresponds to the CdSe/ZnS and CdSe/ZnS core-shell QDs, respectively; (b) micrographs in dark and fluorescence fields, respectively, showing the damage induced by the heating of an infrared laser beam, on the human prostate cancer cells [58].

The band shape-based nanothermometry is referred to the luminescence of a system whose luminescence spectrum consists on several emission bands/lines, and the intensity of which is strongly temperature dependent [23, 55]. Basically, there are two models of operation

in band shape nanothermometry: (i) when the emission lines/bands are generated from a single luminescent center, and (ii) when the emission lines/bands are generated by different emitting centers. In the first model, the changes in the band shape of the system are generally caused by a thermally induced population re-distribution between the different energy levels of the emitting center [23, 55]. In the second model, the temperature induced changes in the band shape of the system arise from the different thermal quenching ratio of each center or from thermally induced changes in the energy transfer rate between these emitting centers [23, 55]. The main advantage of this technique over the intensity-based nanothermometry is that the thermal reading is not affected by fluctuations in the concentration of the luminescence centers. Band shape-based nanothermometry has been previously reported in a great variety of luminescent systems, including lanthanide doped systems [24, 67-69], quantum dots [70-72] and organic dyes [73, 74]. Some important examples of this kind of technique on QDs and lanthanides-doped materials will be discussed in the 1.4.1 subsection (Quantum dots) in the 1.4 section (Materials used in nanothermometry).

1.3.3.1 Theory of the fluorescence intensity ratio (FIR) technique

In band shape-based nanothermometry, the thermal sensing is achieved through the analysis of the changes in the emission intensity caused by temperature [75]. However, the main disadvantage of this technique is that the observed emission intensity is also a function of other variables, such as the power fluctuation of the excitation source, the variation of the concentration of luminescence nanoparticles in the target in which the temperature is going to be measured or the inhomogeneity on the distribution of the luminescent centers in the luminescent nanoparticles used as thermal probes [75].

Taking into account that the electronic population of the individual energy levels is directly proportional to the total electronic population of the system, one way to avoid the errors arising from such parameters that affect the emission intensity is to measure the emission intensity coming from two different energy levels. The ratio between the intensities of these two emission lines will provide an independent measurement from these parameters. The particular case of the fluorescence intensity ratio (FIR) technique involves the ratio of fluorescence from two very close energy levels that can be considered to be thermally coupled. The FIR from two thermally coupled energy levels follows a Boltzmann type population distribution and can be written as [75]:

$$FIR = \frac{I_1}{I_2} = \frac{g_1 v_1 \sigma_1}{g_2 v_2 \sigma_2} \exp\left(-\frac{\Delta E}{k_B T}\right) = B \exp\left(-\frac{\Delta E}{k_B T}\right) \quad (1)$$

where g_i , ν_i , and σ_i are the degeneracy of levels, the spontaneous emission, and the absorption rates, respectively, k_B is the Boltzmann constant, T is the absolute temperature, ΔE is the energy difference between the two energy states considered and $B = \frac{g_1\nu_1\sigma_1}{g_2\nu_2\sigma_2}$. An example of this particular situation is shown in Figure 1.10. As can be seen from the Figure 1.10 the terminal level of fluorescence can be the ground state or another excited state with energy less than the levels from which fluorescence originates.

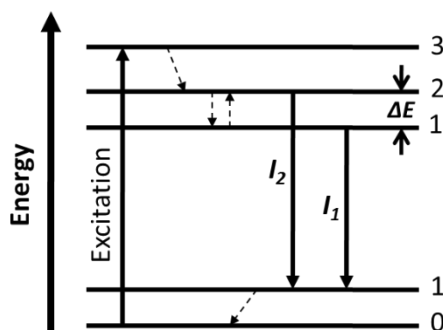


Figure 1.10. Simplified energy level diagram showing the energy levels and transitions of interest in a possible example in which the FIR technique can be used to sense temperature. The dashed lines correspond to non-radiative decay processes, while solid arrows correspond to the fluorescence transitions used to calculate the fluorescence intensity ratio.

If the emission peaks considered to calculate the FIR are located very close to each other, they might partially overlap. In order to take into account this effect, Wade et al. revised equation 1, taking the form [76]:

$$FIR = \left(\frac{n_2}{n_1}\right) B \exp\left[-\frac{\Delta E}{k_B T}\right] + \left(\frac{m_1}{n_1}\right) \quad (2)$$

where n_i defines the fraction of the total fluorescence intensity of the transition originating from level i (upper level $i = 2$, lower level $i = 1$) measured by the detector for the i level and m_i defines the fraction of the total intensity from level i which is measured by the detector for the other thermalizing level.

For temperature sensing applications it is important to know the rate at which the FIR changes for a small change in temperature. This quantity, known as the absolute sensitivity, can be calculated from the first derivative of FIR with respect to the temperature:

$$S_{abs} = \frac{dFIR}{dT} = FIR \left(\frac{\Delta E}{k_B T}\right) \quad (3)$$

To facilitate the quantitative comparison among the different ratiometric optical temperature sensors operating by different mechanisms, the use of the relative sensitivity has been proposed [23]:

$$S_{\text{rel}} = \frac{S_{\text{abs}}}{\text{FIR}} = \frac{\Delta E}{k_B T} \quad (4)$$

From these equations we can see that by using a pair of energy levels with a bigger energy difference the FIR sensitivity would increase. However, this is true to a finite limit, if the energy gap between them is too big, the thermalization would then not be observed [75].

Another important parameter that describes the quality of a temperature sensor is the thermal resolution (also called thermal uncertainty) and the temporal resolution. These parameters depend on the actual temperature resolvable by the material and on the detection setup used in the experiment. The thermal resolution (δT) can be calculated from the FIR and S_{rel} values as follows [77]:

$$\delta T = \frac{1}{S_{\text{rel}} \frac{\delta \text{FIR}}{\text{FIR}}} \quad (5)$$

where $\frac{\delta \text{FIR}}{\text{FIR}}$ is the relative error in the determination of the thermometric parameter which depends on the signal-to-noise ratio of the acquisition setup. The temporal resolution strongly depends on the integration time of the detector used. It increases when the signal arising from the luminescent materials is low. Thus, the use of highly efficient emission intensity materials is recommended to work with the smallest integration time of the detector in order to get a faster temporal response of the thermometric sensor.

1.3.2 Lifetime-based nanothermometry

Among the different luminescence thermometry techniques, lifetime-based nanothermometry is of great relevance. Lifetime nanothermometry is based on the estimation of the temperature of the nanoprobe from the analysis of its fluorescence lifetime [55]. Decay probabilities from electronic levels depend on a large number of parameters and many of them are related to temperature, such as phonon assisted energy transfer processes and multiphonon decays. This technique has several advantages when compared with the intensity based approaches. Lifetime thermometry eliminates problems related to non-controllable spatial fluctuations of the fluorescence intensity due to the non-homogeneous distribution of nanoprobe, the uncontrolled motion of nanoprobe or biocomponents and the shading and light distribution in the sample, among others [55]. Since, in a first order approximation, fluorescence

lifetime does not depend on the local concentration of luminescent probes, all these inconveniences can be overcome. Furthermore, lifetime thermometry avoids the necessity of acquisition of the whole luminescence spectra, a time consuming procedure. When this is associated with the requirement of high spatial resolution, which leads to low signal levels and long acquisition times in intensity- and band shape-based techniques, the short measuring times required by the lifetime technique minimizes the possibility of laser-induced local heating of the system under investigation. Moreover, temperature reading is not affected by the luminescence intensity and thus the signal from which the temperature will be deduced can be acquired at a time interval of the order of the luminescence lifetime, in the range of picoseconds to milliseconds, leading to a very fast temporal response of the sensor. Finally, it should also be mentioned that this technique can be used for high temperature measurements avoiding the undesired contributions of the black body radiation [48, 78-81].

However, this technique has a significant disadvantage, since it demands to use a pulsed-light excitation source with a frequency shorter than the lifetime to be measured that sometimes requires working in the femtosecond regime, which makes it costly and bulky. The sensitivity of a thermal sensor based on the lifetime technique is represented by a value called normalized lifetime thermal coefficient (α_τ) given by the following equation [78]:

$$\alpha_\tau = \left| \frac{d\tau^{norm}(T)}{dT} \right| \quad (6)$$

where $\tau^{norm}(T)$ is the luminescence decay time at temperature T normalized to the room temperature value. Large α_τ values are desirable so that small temperature variations would cause large lifetime changes.

One of the interesting works on lifetime based nanothermometry was done by Haro-Gonzalez et al. [78]. They reported a high lifetime thermal coefficient for ultra-small CdTe QDs, with a value of 1.7 % K⁻¹, much superior than that of other reported systems [82-86]. The fluorescence lifetime of 1 nm CdTe QDs at two different temperatures is presented in Figure 1.11a. They demonstrated the possibility of using these QDs for microfluidics applications. The scheme of the setup is shown in Figure 1.11c. The experiment consisted in using partially overlapped double laser beams which were focused on a microchannel containing QDs dispersed in aqueous solution. A laser with emission at 1090 nm was used to heat the water and a laser with emission at 532 nm was used for exciting the QDs. The magnitude of the temperature increment was determined from the analysis of the fluorescence decay curves of the QDs located at the spot of the laser. The increment of the temperature of the laser focus as a

function of the incident laser power is shown in Figure 1.11d, obtained after comparison with the calibration shown in Figure 1.11b.

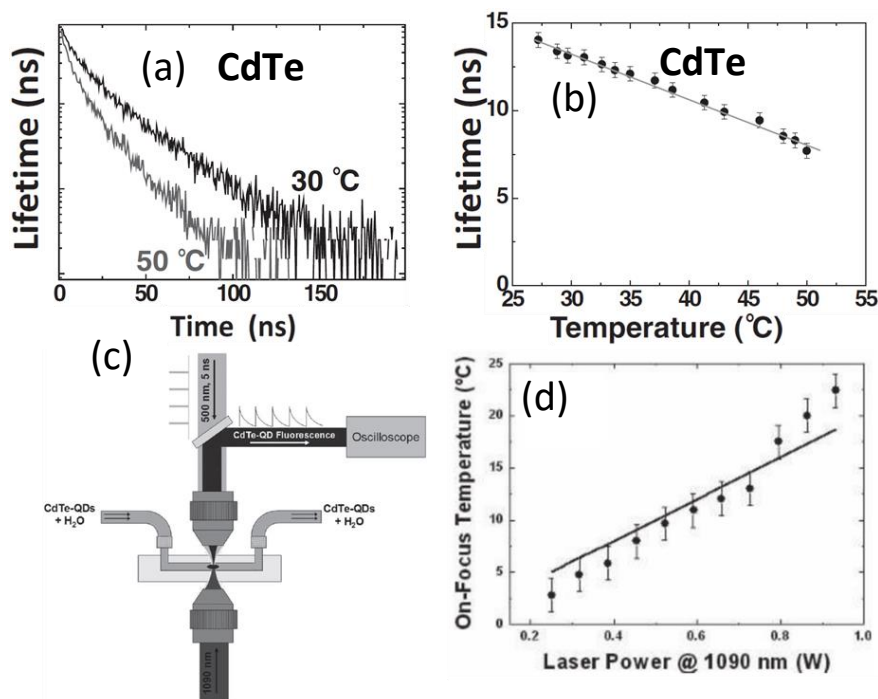


Figure 1.11. (a) Fluorescence decay curves for ultra-small CdTe QDs at two different temperatures; (b) variation of the lifetime value of CdTe QDs as a function of temperature; (c) scheme of the experimental setup used for the temperature measurements; (d) on focus temperature calculated from the analysis of QDs lifetime at different power of the 1090 nm heating laser [78].

1.3.3 Nanothermometry based on the spectral position of the emission lines

This technique is based on the analysis of the spectral position on the emission lines, assigned to the energy separation between the two electronic levels involved in the emission which in turns depends on a large number of temperature dependent parameters, such as the refractive index and the inter-atomic distances [87]. The main advantage of this technique is that temperature reading is not affected by luminescence intensity fluctuations caused by variations in the concentration of the emitting centers, fluctuations of the power of the excitation source, shading effects or movements. QDs have been used for spectral position nanothermometry [87]. However, due to a number of drawbacks of these materials, like high toxicity and poor biocompatibility, other kinds of nanomaterials have been intensively studied. Rocha and co-workers, for instance showed that the spectra generated by Nd:LaF₃ nanoparticles possess a

spectral shift at around 864 nm, as can be observed in Figure 1.12a, that can be used for spectral position-based nanothermometry, with an almost constant rate of $710^{-3} \text{ nmK}^{-1}$ (see Figure 1.12b) [88]. The temperature induced changes in the spectral shift is much lower than that reported for other systems, such as QDs [87, 89]. However, the band of Nd^{3+} at 864 nm is much narrower (3 nm), whereas in QDs is of order of several tens of nanometers, which difficult sometime spectral shift determination. Therefore, the final contrast of the temperature-induced spectral shift is similar in both systems [88, 89].

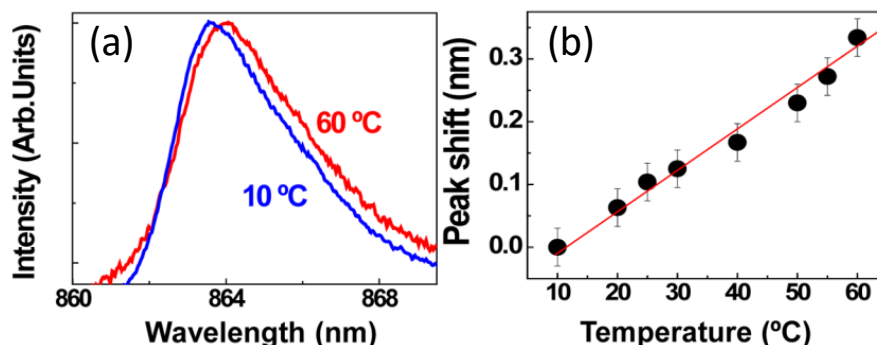


Figure 1.12. (a) Spectral shift on the emission generated by Nd^{3+} -doped LaF_3 nanoparticles at two different temperatures; (b) peak shift as a function of temperature [88].

1.3.4 Bandwidth-based nanothermometry

For any elevation of temperature above the absolute zero, higher energy phonon levels are populated. This effect leads to a broadening of the emission/absorption bands, since excited electronic sublevels are also populated and so they participate in the emission/absorption process. Henderson and Imbusch in 1989 showed how the bandwidth of emission/absorption bands W varies with temperature according to the following expression [90]:

$$W(T) = W_0 \sqrt{\coth\left(\frac{\hbar\Omega}{2kT}\right)} \quad (7)$$

where W_0 is the full width at half maximum (FWHM) of the emission/absorption band at 0 K, k is the Boltzmann constant and $\hbar\Omega$ is the energy of the lattice vibration that interacts with the electronic transitions. So, the higher the temperature, the wider the emission band because of the contribution of thermal vibrations of the luminescent center and its neighboring atoms/molecules

The change in bandwidth of the absorption/emission bands is used in the bandwidth luminescence nanothermometry to achieve a thermal reading. However, the main disadvantage of this technique is that the magnitude of the emission band broadening caused by temperature

increase is small, thus it can only be observed in systems showing narrow emission lines, like lanthanide-doped materials [91]. For example, Nd:YAG shows two hypersensitive luminescence lines located near 940 nm, assigned to transitions between the two Stark sublevels of the $^4F_{3/2}$ metastable state to the highest energy sublevel of the $^4I_{9/2}$ state. The bandwidths of these two transitions show a strong linear dependence with temperature [91]. The rate of the changes was determined to be close to $0.04 \text{ cm}^{-1} \text{ K}^{-1}$.

Another promising result was obtained by Park et al. on bandwidth nanothermometry [92]. They demonstrated how the bandwidth temperature dependent luminescence of Mn-doped CdS-ZnS core-shell nanocrystals can be used in a ratiometric temperature imaging. The normalized temperature dependent bandwidth of Mn:CdS@ZnS core shell nanocrystals is shown in Figure 1.13a. The FWHM as a function of temperature is shown in Figure 1.13b. However, they decided to use band shape-based nanothermometry by utilizing bandpass filters at 600 and 650 nm, which were used to cut the luminescence emission arising from the Mn-doped CdS-ZnS core-shell nanocrystals and create the ratiometric measurable values. The temperature sensitivity was found to be around $0.5 \% \text{ K}^{-1}$ [92].

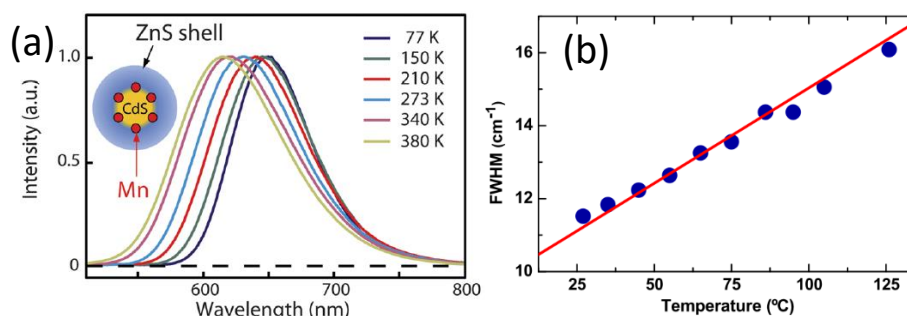


Figure 1.13. (a) Normalized intensity spectra of Mn:ZnS@CdS core-shell nanocrystals at different temperatures; (b) FWHM of the emission line at 620 nm as a function of temperature. The red line is the linear fitting of the experimental points [92].

1.4 Materials used in luminescence thermometry

With the fast development of nanotechnology it has become possible to synthesize nanometric biocompatible nanoparticles with the typical size below 100 nm. The small size of these nanoparticles and the chemical functionalization of their surfaces have given an opportunity to incorporate them easily in living cells and to have a good potentiality for luminescence mapping *in vitro* experiments. Consequently, since the luminescence of these

nanoparticles is sensitive to small changes of temperature this makes them potential candidates for nanothermometry, providing the possibility of intracellular thermal mapping [93].

There are several kinds of luminescent nanothermometers with great potentiality for practical applications including, QDs, gold nanoparticles, organic dyes, luminescent polymers and lanthanide-doped nanoparticles. Organic dyes and QDs have shown the highest sensitivity to changes of temperature [23], however, their main disadvantage consists in that they need to be excited using ultraviolet (UV) or visible light, thus leading to the background fluorescence arising from biological tissues and also with the possibility that the excitation light damages the surrounding biological tissues [94]. The use of lanthanide-doped (Ln^{3+} -doped) upconversion nanoparticles (UCNPs), which emit light at higher photon energies when absorbing two or more lower energy excitation photons through sequential absorption or energy transfer processes, has several advantages. It allows using near infrared (NIR) excitation, which causes negligible photodamage to living organisms and weak autofluorescence background. Also, it has a deeper penetration depth in biological tissues for biomedical thermometry purposes, when compared to visible radiation [95]. Moreover, NIR excitation sources are commercially available with high power and low cost. Furthermore, UCNPs are more optically stable and have lower toxicity than QDs [95].

In this section we will briefly review the most common materials that have been used for nanothermometry, including QDs, organic dyes, gold nanoparticles, polymers, Ln^{3+} -doped, Ln^{3+} -UCNPs and complex systems.

1.4.1 Quantum dots

A semiconductor or metal that shows quantum confinement effect due to the reduction in grain size is called a QD. In semiconductors it occurs when the grain size is equal to or less than the exciton Bohr radius, while in metals it occurs when grain size is equal to or less than the mean free path of charge carriers [96]. The quantum confinement effects in semiconductor QDs systems have attracted considerable attention. Especially interesting are the modified electronic and optical properties of these structures which are controllable to a certain degree through the flexibility in the structure design [96]. This feature makes QDs very promising for possible device applications in microelectronics, nonlinear optics and many other fields.

The fluorescence of QDs is strongly dependent on temperature [70, 97, 98]. With a temperature increase, the fluorescence intensity decreases, a phenomenon known as

fluorescence quenching, which is also accompanied by a spectral shift towards the red region of the electromagnetic spectrum. The fluorescence quenching is attributed to the activation of phonon-assisted processes as well as to the presence of thermally-assisted energy transfer processes from bulk (excitons) to surface states (traps).

An interesting feature of the fluorescence quenching and the spectral shift experienced by QDs is that they can be assumed to be linear in the physiological range of temperatures [97]. However, intensity-based QDs temperature sensors often induce to errors in temperature determination due to variations in the concentration of the material that constitutes the QDs, excitation or detection efficiency [98]. These problems were overcome by using dual emitting QDs systems and correlating the intensity of the two emission bands by a ratiometric technique [70]. Vlaskin et al. reported that the use of dual emitting QDs systems allowed avoiding problems associated with instabilities in the excitation source and in the photobleaching of the emission arising from the QDs [70]. Maestro and co-workers reported for the first time intracellular temperature measurements using the temperature induced spectral shift in QDs under two-photon excitation [89]. Moreover, they demonstrated that the two-photon excitation lead to a large spatial resolution due to its nonlinear nature. The spatial resolution was determined to be 400 nm, 6 times higher than for one-photon excitation. The experimental setup they used is shown in Figure 1.14a. The 800 nm excitation beam was focused inside the cell by means of a 100x microscope objective, giving a lateral spatial resolution close to 400 nm. The same objective was used to collect the emission from QDs. The cell temperature was externally varied by using a micro air-heater. Thus, they were able to measure the intracellular temperature by using CdSe QDs nanothermometers. The evolution of the intracellular temperature as a function of the heating time is shown in Figure 1.14b.

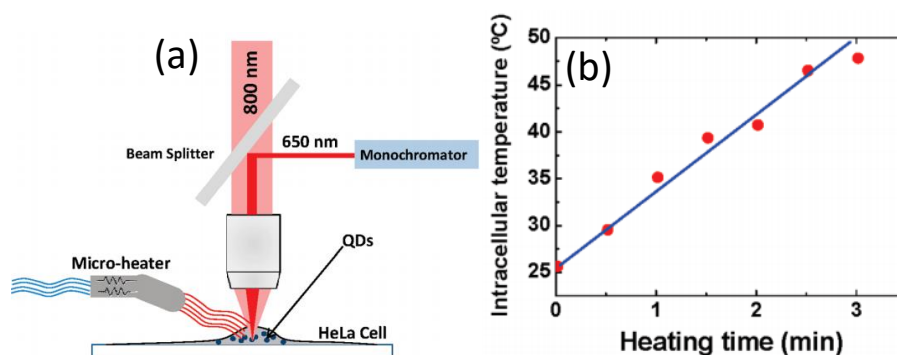


Figure 1.14. (a) Schematic diagram of the experimental setup used to monitor the of HeLa cells heating process by using a two-photon excitation CdSe QDs fluorescence thermometry; (b) intracellular temperature increase as calculated from the spectral shift of the emission of CdSe QDs as a function of heating time [89].

Yang and co-workers used QDs to map the intracellular heat generation in NIH/3T3 cells following Ca^{2+} -induced stress and cold shocks [99]. Ca^{2+} -induced shock was used to boost heat production, due to the promotion of activities of ion pumps in the cells and the acceleration of the respiration rate. They showed that different regions of the cells exhibited different temperature progressions, creating a subcellular temperature gradient. Position-dependent temperature variation is shown in Figure 1.15. It can be seen that the temperature inside the cell following the addition of Ca^{2+} and the different region of the cell exhibit the different temperature progressions. The spatial resolution in that case was only limited by the size of the QDs used (~ 20 nm).

Also QDs were used in the determination of the heat/absorption efficiency produced of gold nanoparticles of different geometries when excited at 488 nm [87]. The solution containing the Au nanoparticles and QDs was introduced in a microchamber and analyzed in a double beam fluorescence nanothermometry setup. The concentration of the QDs was small enough to be negligible in the optical absorption of the mixed solution. They demonstrated that the heating efficiency of gold nanoparticles strongly depends on the particular geometry of the nanoparticles. They found that the gold nanorods and long-edge gold nanostars to have an absorption efficiencies to close to unity, 95 ± 4 and 102 ± 3 %, respectively [87].

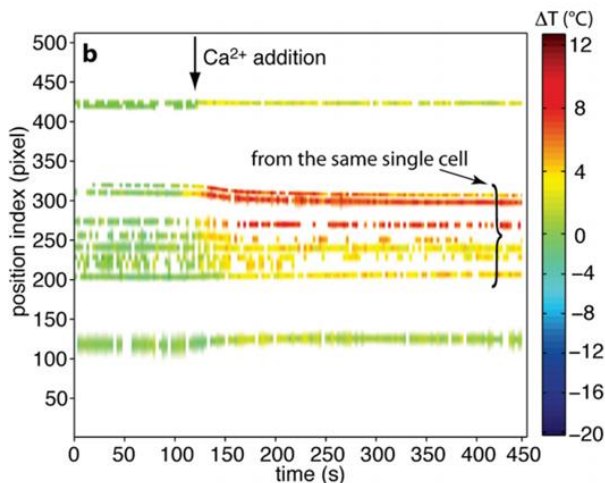


Figure 1.15. Position-dependent intracellular temperature variation as a function of time [99].

1.4.2 Organic dyes

Organic dyes are aromatic organic compounds which impart color to a substrate by selective absorption of light [100]. The first synthetic dye, Mauveine, derived from aniline, was

discovered by Perkin in 1856 [101], and since then the research on the synthesis of organic dyes has been intensively pursued. The main interest of organic dyes arises on their strong luminescence in the visible region when optically excited with ultraviolet or blue light [100]. The emission and absorption bands of the organic dyes strongly depend on their structure and chemical environment [102]. Moreover, in many organic dyes, their luminescence properties depend on temperature [103]. These facts make them excellent candidates for temperature sensing applications

In fact, the fluorescence intensity and lifetime of organic dyes are typical parameters that are modified when the temperature changes [104-106]. However, since the fluorescence intensity of organic dyes is seriously affected by fluctuations in the experimental conditions [104, 106], lifetime based thermometry in organic dyes is a more common and reliable technique for temperature measurements [105, 107, 108]. One of the most popular organic dyes is Rhodamine B (RhB) due to its good chemical stability and high luminescence efficiency and good chemical stability. Thus, its temperature dependent fluorescence response has been extensively studied [105]. However, the use of free organic dyes is limited by a number of factors like, adsorption onto surfaces, molecular interactions and contamination of the surrounding material [109]. As a result, there has been significant interest in using different encapsulation matrices for organic dyes in order to improve their temperature sensing properties [35, 110]. For instance, Jung and co-workers incorporated RhB in polydimethylsiloxane (PDMS) and SU8 polymer matrices to determine the temperature from an active layer covering a microfluidic device [110]. A similar work was done also by Samy et al., in mapping the temperature on microfluidics devices using organic dyes in encapsulated matrices, that has been described in the 1.2 section (From “classical” thermometry to nanothermometry) [35]. Other examples include the use of silica matrices together with organic dyes, since they are inert, optically transparent and temperature stable [111-113].

For instance, Ross et al. used the RhB for mapping the temperature inside the microfluidic systems [112]. The scheme of one of the microfluidic channel with T-shape they used is shown in Figure 1.16a. The pumping of the fluid containing RhB was done by applying the electrical field resulting in the temperature increase due to Joule effect. Fluorescence imaging of RhB was performed using fluorescence microscope equipped with mercury arc lamp with a filter at 500-550 nm for excitation and a CCD camera. The measurements were consisted on comparison of fluorescence intensity of RhB at a known, uniform temperature with that at an unknown. Temperature distribution is shown in Figure 1.16b. The direction of the

flow was from top to bottom, which is indicated with an arrow. The temperature variations that can be measured by this technique were between 2.4 and 3.5 K.

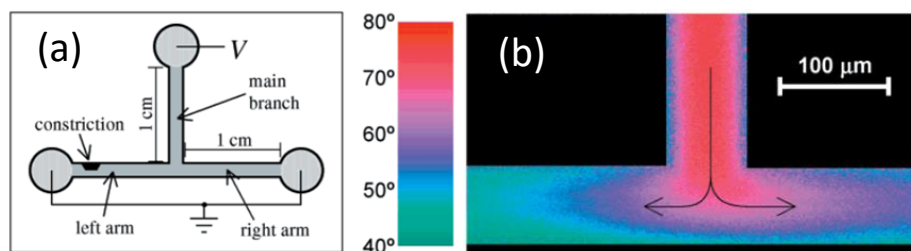


Figure 1.15. (a) Schematic diagram of the T-shaped microchannel used in experiment; (b) temperature distribution in T-shaped microchannel measured by the temperature-dependent fluorescence intensity of RhB [112].

1.4.3 Gold nanoparticles

Gold nanoparticles have attracted attentions for multiple applications due to its fascinating optical and electronic properties [114]. Because of their biocompatibility, facile conjugation to biomolecules and unique optical properties conferred by their localized surface plasmon resonance, they have been used as fluorescent probes for *in vitro* and *in vivo* imaging [115, 116]. Moreover, due to its very high light-to-heat conversion efficiency [117], Au nanoparticles are one of the most promising photothermal agents that have been already investigated for photothermal therapy [118]. On the other hand, Bomm et al. have shown that Au nanoparticles present a thermosensitive luminescence behavior that can be used for temperature determination purposes [119].

Following these properties Shang et al. sensed the intracellular temperature by using Au nanoparticles, by taking advantage of the temperature dependence of their luminescence lifetime and emission intensity, which change considerably over the physiological temperature range [120]. Gold nanoparticles were incorporated into the cells by simple endocytosis and then temperature was changed through a temperature controlled stage. The thermal resolution that can achieved in this case was estimated from the thermal response of the lifetime value of Au nanoclusters in HeLa cells, which is shown in Figure 1.16a, and to be around 0.3–0.5 K in the range of 287 – 316K. Another important fact is that under continuous excitation with intensities up to 2.8 kW cm⁻² for 2 h the lifetime values remain constant, with a little change of less than 5 % (see Figure 1.16b). Moreover, the good thermal resolution is accompanied by a long luminescence lifetime, which can be separated from the fluorescence background generated by

biological tissues. Authors also observed a complete reversibility, a long-term stability (see Figure 1.16c) and minimum cell toxicity for these Au nanoclusters (see Figure 1.16d).

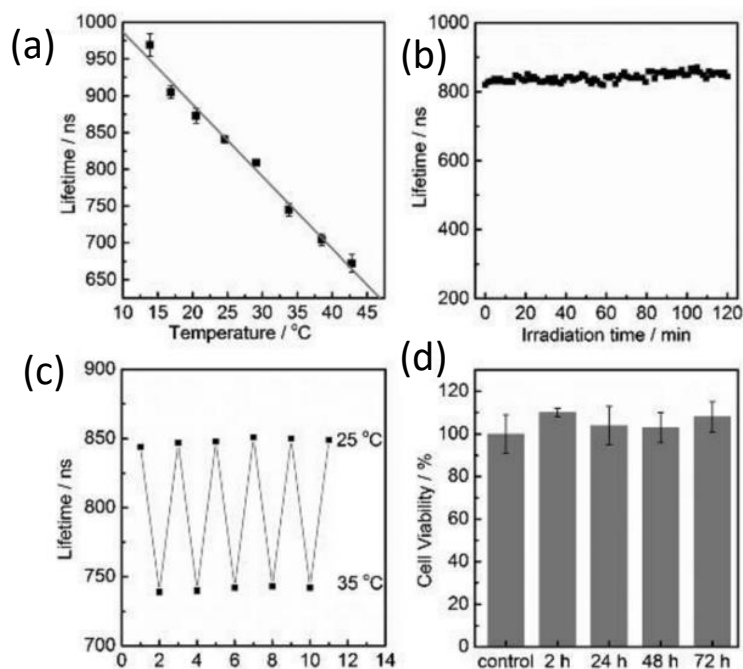


Figure 1.16. (a) Evolution of the fluorescence lifetime of Au nanoclusters with temperature incorporated in HeLa cells. Fluorescence lifetime of the Au nanoclusters; (b) as a function of irradiation time and (c) upon cycling the temperature five times between 298 and 308 K; (d) viability of HeLa cells with incorporated Au nanoclusters in cell medium as a function of time [120].

However, the temperature induced changes on the luminescence intensity arising from Au nanoparticles can be affected by the local environment, including oxygen content, pH, and concentration of material, which might result in accurate temperature measurements. In order to avoid these problems, Wang et al. developed novel dual-emitting microspheres containing the blue fluorescence of carbon dots and the red fluorescence of Au nanoclusters covered with a TiO₂ layer [121]. Figure 1.17a shows the fluorescence response of the carbon dots and Au nanoclusters towards the temperature increase. It can be clearly seen that the red emission arising from the Au nanoclusters was changing when the temperature increased, but the blue emission of the carbon dots remained almost constant. The intensity ratio of the two emission lines at 596 and 436 nm showed a linear evolution with temperature from 293 to 353 K (see Figure 1.17b). The system showed a temperature resolution of about 0.5 K, combined with the

high stability and good dispersion in aqueous solution of the microspheres, which suggests they have promising applications *in vivo* temperature sensing.

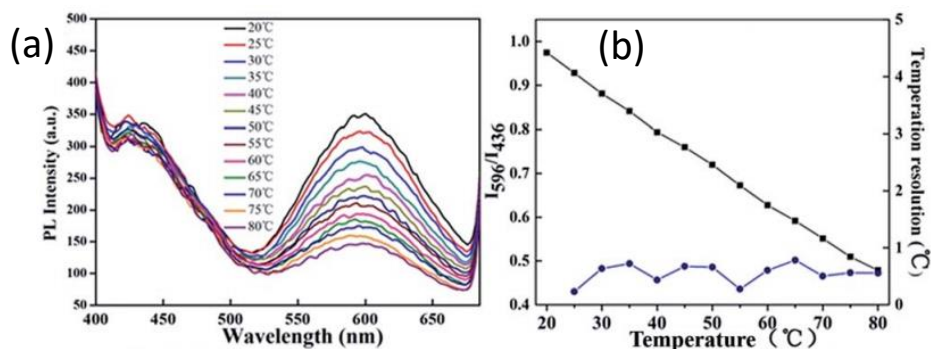


Figure 1.17. (a) Evolution of the photoluminescence spectra of the dual-emission fluorescent microspheres containing carbon dots and Au nanoclusters covered by a TiO_2 layer when temperature increased from 293 to 353 K; (b) intensity ratio of the 596 and 436 nm emission bands plotted against temperature and temperature resolution (blue line, right axis) [121].

1.4.4 Polymer-based systems

Polymers are chemical compound or a mixture of compounds formed by polymerization and consisting from essentially repeating structural units [122]. Polymers have very distinct characteristics, some of them being thermoplastic, others very resistant to chemicals and even can be both thermal and electrical insulators [122]. Another attractive feature of polymeric materials is the possibility to alter their electronic and spectral properties through the attachment of different functional groups in their polymeric backbone [123, 124]. Furthermore, polymers have been used for encapsulation of other luminescent materials for incorporating their properties [125-127].

It is not clear who observed first the variation of the fluorescence emission of polymers with temperature, but to the best of our knowledge, the earliest work was done by J. Yang and co-workers, who showed the temperature dependence of fluorescence of ladder-like polyphenylsilsesquioxane (LPPS) and ladder-like 1,4-phenylene-bridged polyvinylsiloxane (LPPVS) [128]. Excimers are excited-state complexes formed by a couple of chromophores in aromatic synthetic polymer placed face to face at short distance. Monomer is a compound whose molecules can join together to form a polymer. The excimer to monomer intensity ratio of a diluted LPPS solution shows a double linear Arrhenius plot with a break

point which is attributed to a transition induced by temperature involving the formation and dissociation of an excimer in the solution (see Figure 1.18a). In the case of LPPVS, the Arrhenius plot versus $1/T$ presented a simple linear variation with a positive slope that can be used in temperature sensing applications (see Figure 1.18b).

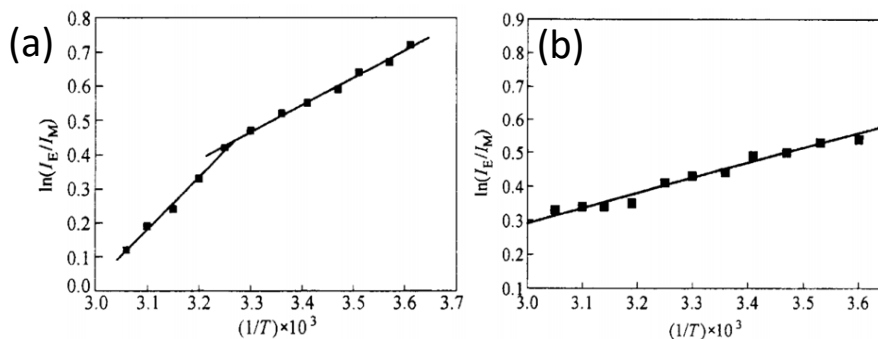


Figure 1.18. (a) Arrhenius plot of the intensity ratio between excimer and monomer for LPPS; (b) logarithm of the intensity ratio excimer and monomer versus inverse temperature for LPPVS [128].

Almeida et al. demonstrated that the fluorescence emission intensity of the 3-(N-pyrrolyl)propyl dansylglycinate (PyPDG) polymer is enhanced as the temperature increased, indicating that the fluorescence of this compound is due to a thermally activated process. Thus, it can also be considered to be a promising candidate for temperature sensing applications [129].

Besides the strong changes observed in the fluorescence emission intensity with temperature, the fluorescence lifetime of the polymers can also be an efficient parameter to monitor temperature [38, 130]. Graham et al. demonstrated an important variation of the fluorescence lifetime of 4-N-(2-acryloyloxyethyl)-N-methylamino-7-N,N-dimethylaminosulfonyl-2,1,3-benzoxadiazole (DBD-AE) with N-isopropylacrylamide (NIPAM) copolymer as the temperature increased [38]. The fluorescence lifetime value of this copolymer increased from 3 ns to 13 ns in the range of temperature 296 – 311.3 K (see Figure 1.19a). The strong temperature dependence was attributed to a phase transition that involved changes in the microenvironment of the copolymer. As a practical application of that copolymer for temperature sensing the authors recorded fluorescence lifetime microscopy images (see Figure 1.19b), mapping temperature changes in a microfluidic device (see Figure 1.19c). A thermal resolution of <0.1 K was estimated for this copolymer.

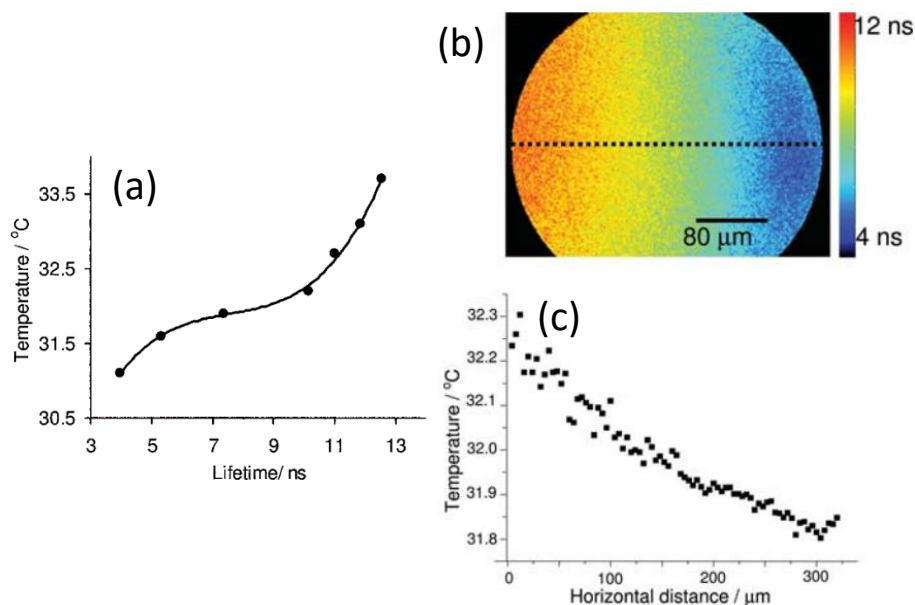


Figure 1.19. (a) Evolution of the fluorescence lifetime of poly(DBD-AE-co-NIPAM) with temperature; (b) fluorescence lifetime image of the microfluidic chip with incorporated copolymer; (c) temperature profile along the line indicated in (b) [38].

However, the main drawback of the polymer systems is the short operational temperature range limited to the phase transition and the hysteresis kind of response in the output for the same value of temperature depending on if the temperature is increasing or decreasing [23]. Although the phase transition can be extended to 334 K [131] and hysteretic response can be reduced by using PEG-based methacrylates [132, 133].

1.4.5 Lanthanide-doped nanoparticles

Lanthanide (Ln^{3+}) ions are characterized by an incomplete 4f shell that is shielded from the effects of the crystal lattice by their outer filled shells [90]. When incorporated in a material, their emissions appear as narrow spectral lines and their luminescence lifetime are relatively long (from μs to ms) [90]. The intensity of the luminescence lines of Ln^{3+} ions depends on many parameters, like pressure, pH, oxygen and, the most critical one, temperature [90]. The earlier Ln^{3+} -doped materials used for temperature sensing applications were also known as thermographic phosphors [134] and temperature-sensitive paints [135]. In those cases, the

excitation was usually performed by an ultraviolet or a visible light source. Basically, two methods of determination temperature were employed, the temporal and the spectral methods [136, 137]. Both methods allow punctual or two-dimensional measurements to be performed. As an example, thermal resolutions of 0.08 K and spatial resolutions of 0.7 μm were obtained using a metal stripe covered with a thin film of predeutero-PMMA polymer heavily doped with europium thenoyltrifluoroacetate complex whose photoluminescence intensity drops rapidly with temperature [138]. Another fascinating work was done by Suzuki et al. on measuring of thermogenesis in a single HeLa cell. The temperature was monitored by following the quenching of the emission of the Eu^{3+} thenoyltrifluoroacetate tetrahydrate (Eu-TTA) dissolved in dimethylsulfoxide (DMSO) and placed in a micropipette that was in physical contact with the HeLa cell [139]. A scheme of the experimental setup is shown in Figure 1.21a. It consists on an inverted microscope with an objective, mercury lamp and filter wheel with 480 and 365 nm bandpass filters for the excitation filters of Eu-TTA and Fluo-4, respectively and then were imaged by CCD camera. The recorded images were then digitized by a frame grabber and analyzed. Eu-TTA was gently pressing the cell to ensure good contact with the cell membrane, and Fluo-4 was separated at least 20 mm from the cell, served as a reference thermometer. Temperature change was estimated by the use of calibration curve illustrated in Figure 1.21b, indicated a strong dependence of the Eu-TTA fluorescence on temperature. The intensity reduction rate was found to be close to 3 % K^{-1} .

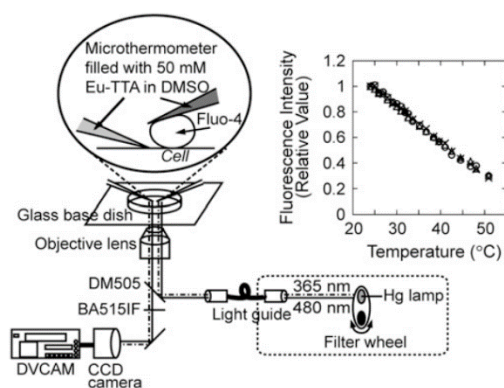


Figure 1.21. (a) Schematic illustration of the setup; (b) fluorescence intensity as a function of temperature for Eu-TTA fluorophor [139].

Another example of using Ln^{3+} -doped nanoparticles devoted to the luminescence nanothermometry is based on the NIR emission generated from the Nd^{3+} ion [32, 88, 140, 141]. The works of Carrasco [32] and Rocha [88] were already described in detailed in the section 1.2 and 1.3.3, respectively. Wawrzynczyk et al. reported a multifunctionality of the Nd^{3+} doped

NaYF₄ nanoparticles, acting as heaters and nanothermometer (at low excitation power) [140]. The heat generation was attributed to the cross-relaxation (CR) process: (⁴F_{3/2}; ⁴I_{9/2}) / (⁴I_{15/2}; ⁴I_{15/2}), followed by a non-radiative depopulation of ⁴I_J (J = 15/2, 13/2, 11/2) occurring between neighboring Nd³⁺ ions in heavily doped samples. The temperature sensing was done through the FIR of emissions from two closely spaced Stark components of ⁴F_{3/2} energy level and located at 863 and 870 nm. The maximum thermal sensitivity was found to be 0.12 % K⁻¹ at room temperature [140].

Depending on the criteria, whether the luminescence under analysis is generated by a single type of lanthanide ion or by a combination of different lanthanide ions, the Ln³⁺-based luminescence nanothermometry can be classified into two groups: single-center Ln³⁺- and multi-center Ln³⁺-based luminescence nanothermometry [142]. Brites et al. developed a multi-center molecular thermometer, which shows a high photostability and flexibility for thin film fabrication, based on the ratiometric emission intensities arising from Eu³⁺ and Tb³⁺, located at 612 and 545 nm, respectively [24]. The spatial resolution was limited by the size of the detector (1-10 μm) with a maximum thermal sensitivity of 4.9 % K⁻¹, being the highest value compared with other multi-centers Ln³⁺-doped systems. The application of such nanothermometer was described in section 1.2 as temperature mapping of electronic circuit for detecting “hot spots”.

Another example on efficient multi-center Ln³⁺-doped system was shown by Ishiwada and co-workers [143]. They developed a phosphor thermometer based on Tb³⁺, Tm³⁺ co-doped in Y₂O₃ particles that operated in a wide temperature range from 323 – 1123 K. The ratio between the intensities of the Tm³⁺ emission in the blue at 466 nm and the green emission of Tb³⁺ at 540 nm is strongly temperature dependent, as can be seen in Figure 1.22a, together with the ratio of other emissions analyzed by the authors. The emission of Tm³⁺ does not change when temperature increased while the emission of Tb³⁺ is fully quenched at 1123 K. Moreover, they noticed that the color of the emission arising from the particles also changed when the temperature increased, as can be seen in the Figure 1.22b. Thus, they suggested that it would be possible to measure the temperature not only by analyzing the intensity ratio but also by observing the color change visually. However, the authors did not provide information on thermal sensitivity of such system.

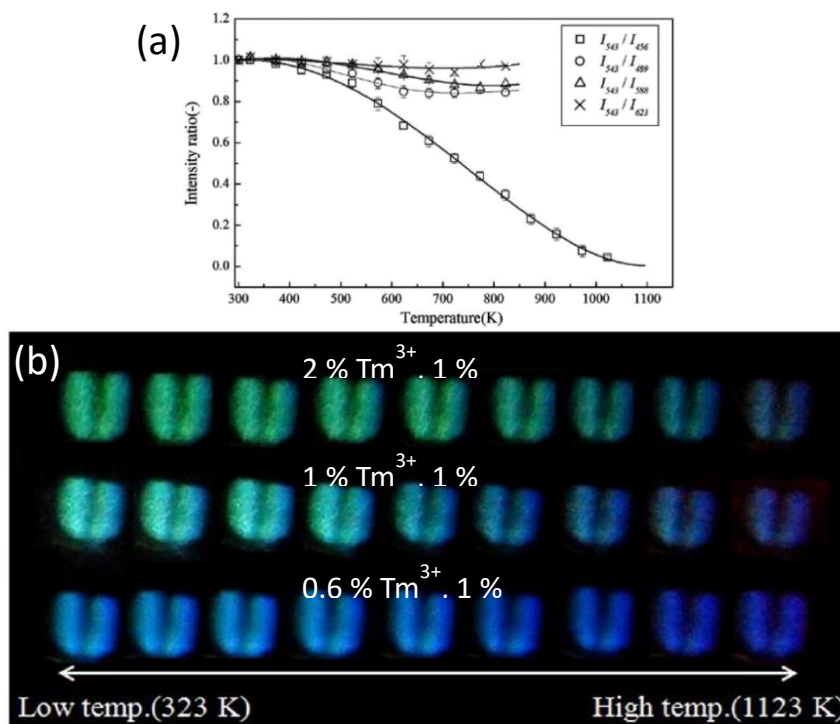


Figure 1.22. (a) Temperature dependence of the intensity ratios of different emissions in Tb³⁺, Tm³⁺-codoped Y₂O₃ particles; (b) images of temperature-sensitive visible photoluminescence of Tb³⁺, Tm³⁺-codoped Y₂O₃ particles as a function of the dopants concentrations [143].

1.4.5.1 Upconverting nanoparticles

Of particular interest are those Ln³⁺-doped luminescent thermometers based on upconversion nanoparticles. These nanoparticles absorb light in the NIR region of the electromagnetic spectrum, and emit light in the visible range [144]. As was pointed out before, pumping in the NIR allows overcoming problems related with the background fluorescence arising from biological tissues and the potential damage that UV light can generate in the surrounding tissues. Moreover, the NIR lasers used to excite those UCNPs are cheaper and more powerful than the UV lasers. Finally, the use of NIR radiation also preserves the operative lifetime of the phosphors used, in comparison with those illuminated with UV light that might be damaged by this radiation, shortening their operational lifetimes [145].

1.4.5.2 Upconversion mechanism

Upconversion refers to nonlinear optical processes in which the sequential absorption of two or more photons leads to the emission of light at shorter wavelength than the excitation wavelength (anti-Stokes type of emission). The upconversion process involves a number of different mechanisms, and roughly includes (see Figure 1.23): (i) ground state absorption (GSA) – results in the promotion of electrons in an ion from its ground state (G) to an excited state (E_1); (ii) excited state absorption (ESA) – results in the absorption of a photon by electrons of an ion that are already in an excited state, and their promotion to an even higher excited state (E_2); (iii) energy transfer upconversion (ETU) – in which one photon is absorbed by the sensitizer ion, but the energy is subsequently transferred to a neighboring emitting ion, whose electronic population is excited to a high energy state [146]. This, energy transfer mechanism between two ions, both in excited states, leading to an emission line at short wavelengths was first mentioned by Bloembergen in 1959 [147] and first experimentally demonstrated by Auzel in 1966 [148]. In the same year, he discovered that the upconversion emission originating from ESA was not easily observable, mainly owing to the fact that the second photon to be absorbed must be captured by an electron in an intermediate state, where the electronic population is usually rather low [149].

Important requirements to observe the phenomenon of upconversion are the existence of long lifetimes of the excited states and a ladder-like arrangement of the electronic energy levels with similar energy separation, which can be found in certain ions of the d and f elements [147]. The properties of the host matrix and its interaction with the dopant ions have also a strong influence on the upconversion process. The host matrices with the low phonon energy, good chemical stability and low lattice impurities would be a perfect choice for efficient upconversion processes [150].

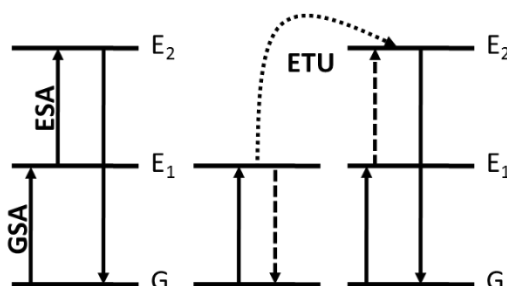


Figure 1.23. Upconversion mechanisms: ground state absorption (GSA) followed by the excited state absorption (ESA) and energy transfer upconversion (ETU). Upward arrows represent the excitation of an electron to the higher

energy level, downward arrows – radiative relaxation, dotted downward arrow – nonradiative relaxation, dotted upward
– indirect excitation of an electron. Dotted curved arrow – energy transfer

In contrast to other emission processes based on multiphoton absorption, upconversion can be efficiently excited even at low excitation densities [144]. The most efficient UC mechanisms are present in solid-state materials doped with rare-earth ions [151].

1.4.5.3 Single-center Ln^{3+} -UCNPs nanothermometry

There are plenty of examples in the literature of Ln^{3+} -based UCNPs luminescence nanothermometry. As in the case of Ln^{3+} -doped materials, UCNPs can be distinguished between single-center Ln^{3+} -UCNPs and multi-center Ln^{3+} -UCNPs.

Different Ln^{3+} ions have been used in single-center Ln^{3+} -UCNPs nanothermometry. Er^{3+} is the most used one because of its very intense green emission that consist of two luminescence bands centered at 520 and 540 nm, arising from two thermally coupled electronic levels ($^4\text{S}_{3/2}$ and $^2\text{H}_{11/2}$, respectively) and whose relative intensity is strongly temperature dependent [152-154]. Normally, the single-center systems for nanothermometry are sensitized by Yb^{3+} , because its absorption cross-section at 980 nm is larger than that of other Ln^{3+} ions in this region. Furthermore, Yb^{3+} can efficiently transfer the absorbed energy to other Ln^{3+} ions, such as Er^{3+} , Tm^{3+} and Ho^{3+} , because they have almost resonant energetic levels [155]. Furthermore, Yb^{3+} only presents one excited energy level in its electronic structure, reducing the possibility for non-radiative losses.

In 1990 Berthou and Jörgensen reported for the first time thermal measurements using the thermally coupled electronic levels $^4\text{S}_{3/2}$ and $^2\text{H}_{11/2}$ of Er^{3+} ion for temperature measurement with the FIR technique [156]. They compared the thermal response of different Er^{3+} -doped fluorides matrices (BIZYT and ZBLA) in the 293 – 473 K temperature range. Figure 1.24 shows the intensity ratio of the $^2\text{H}_{11/2}$ and $^4\text{S}_{3/2}$ emission lines as a function of temperature in one of these fluorides (ZBLA glass). However, they did not analyze the thermal sensitivity of those systems. Since then, new ideas on using temperature dependent transitions of Er^{3+} have been developed [152, 154, 25, 157]. One of the most remarkable works was done by Aigouy and co-workers that modified the scanning tip of an atomic force microscope by attaching Er^{3+} , Yb^{3+} nanoparticles to it as describe before in section 1.2 [25, 157].

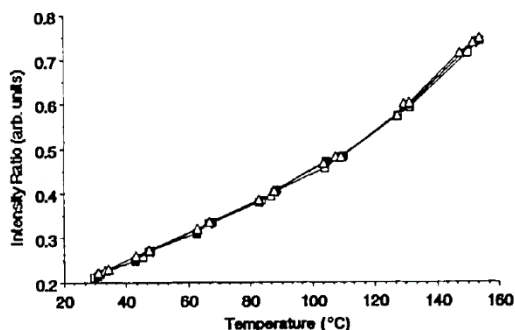


Figure 1.24. Intensity ratio versus temperature of the two green emissions of Er^{3+} in a 2 % Er^{3+} , 9 % Yb^{3+} ZBLA glassfluoride optical fiber after excitation at 972 nm [156].

Vetrone et al. used Er^{3+} , Yb^{3+} codoped NaYF_4 nanoparticles which is a material widely used in upconversion applications especially as an intracellular nanothermometer because of its outstanding luminescence brightness, low toxicity and good chemical and physical stability. The authors internalized Er^{3+} , Yb^{3+} codoped NaYF_4 upconversion nanoparticles in HeLa cells and monitored their death induced by heat using the ratio between the intensities of the 525 and 545 nm (I_{525}/I_{545}) emission bands of Er^{3+} [152]. The temperature of the cell was varied by means of a metallic platform connected to a resistor, by changing the applied voltage the cell temperature could be varied. Figure 1.25 shows the I_{525}/I_{545} intensity ratio of the nanothermometers changed with the applied voltage that permitted measurement of the internal temperature of the illuminated HeLa cell with internalized Er^{3+} , Yb^{3+} codoped NaYF_4 nanoparticles.

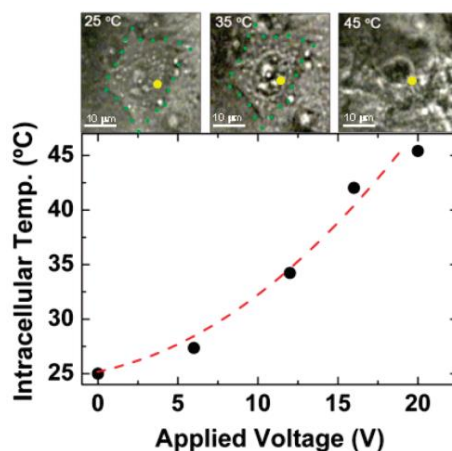


Figure 1.25. Optical transmission images of an individual HeLa cell at three different temperatures. Temperature of the HeLa cell determined using the ratio between the intensities of the 525 and 545 nm emission bands of Er^{3+} ion as a function of the applied voltage [152].

Besides Er^{3+} ion, Tm^{3+} has also the electronic levels that are thermally coupled and can be used in ratiometric thermal sensing purposes [158-160]. Wang and co-workers analyzed the thermal properties of the luminescence arising from $\text{Tm}^{3+}:\text{NaYbF}_4@\text{SiO}_2$ core-shell microparticles and they found that the $^1\text{D}_2$ and $^1\text{G}_4$ energy levels of Tm^{3+} are thermally coupled [149]. Dong et al. used $\text{Tm}^{3+}, \text{Yb}^{3+}:\text{CaF}_2$ nanoparticles to perform bioimaging in HeLa cells and demonstrated the potentiality of these nanoparticles as nanothermometers [158]. They found that the ratio between different luminescent lines, generated from thermally coupled sub-Stark levels belonging to the $^3\text{H}_4$ excited state of Tm^{3+} , follow an almost linear tendency with temperature. The emission spectra of the $\text{Tm}^{3+}, \text{Yb}^{3+}:\text{CaF}_2$ nanoparticles at two different temperature is shown in Figure 1.26a. It can be seen that the intensity of the peak located at 790 nm did not change, when the temperature increased, while the intensity of the peak located at 800 nm increases. The linear tendency of the ratio between the intensity of these two peaks with temperature is shown in Figure 1.26b.

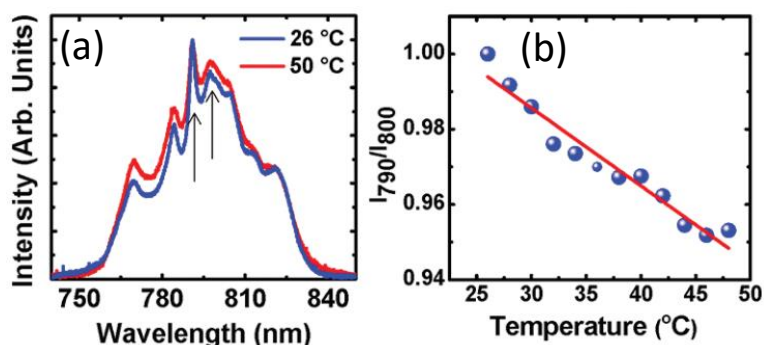


Figure 1.26. (a) Emission spectra of $\text{Tm}^{3+}, \text{Yb}^{3+}$ -codoped CaF_2 nanoparticles recorded at two different temperatures; (b) the ratio between the intensities of the fluorescence lines located at 790 and 800 nm with temperature. Solid lines are guides for the eyes [159].

Several works have explored the temperature sensing properties of Ho^{3+} -doped and $\text{Ho}^{3+}, \text{Yb}^{3+}$ co-doped systems [161-165]. Xu et al. analyzed the dependence of the luminescence generated from $\text{Ho}^{3+}, \text{Yb}^{3+}$ co-doped CaWO_4 nanoparticles with temperature. The ratio between the intensities of the upconversion emissions centered at 455 and 490 nm, arising from the $^5\text{F}_{2,3}/^3\text{K}_8$ and $^5\text{G}_6/^5\text{F}_1$ states of Ho^{3+} , respectively, follows an exponential dependence with temperature, that can be fitted with a Boltzmann type distribution equation. These energy levels have an appropriate energy separation considered to be thermally coupled [161]. The same kind of behavior was observed in $\text{Ho}^{3+}, \text{Yb}^{3+}, \text{Zn}^{2+}:\text{Y}_2\text{O}_3$ phosphors by Pandey and Rai [162]. The incorporation of Zn^{2+} in the host matrix in that case provided an enhancement of the intensity of

the emission. The maximum thermal sensitivity obtained in that case was about $0.3\% \text{ K}^{-1}$ at 673 K. Another interesting work was done by Lojpur and co-workers in analyzing the temperature dependence of the intensities of the emissions of $\text{Ho}^{3+}, \text{Yb}^{3+}:\text{Y}_2\text{O}_3$ and $\text{Tm}^{3+}, \text{Yb}^{3+}:\text{Y}_2\text{O}_3$ powders [165]. They found that the thermal sensitivity of the ratio of the intensities corresponding to the bands located at 536 and 772 nm in $\text{Ho}^{3+}, \text{Yb}^{3+}:\text{Y}_2\text{O}_3$ particles achieved a value of $9.7\% \text{ K}^{-1}$, which is the highest ever found in Ln^{3+} -doped systems. The ratio of intensities of the emission lines analyzed by these authors in $\text{Ho}^{3+}, \text{Yb}^{3+}:\text{Y}_2\text{O}_3$ powders is presented in Figure 1.27a and their thermal sensitivities in Figure 1.27b [165]. However, the authors did not provide any information on how they calculated this thermal sensitivity. Also it has to be taken into account if the emissions considered arise from two thermally coupled energy levels since they are separated by more than 200 nm. If not, the FIR technique cannot be used strictly speaking.

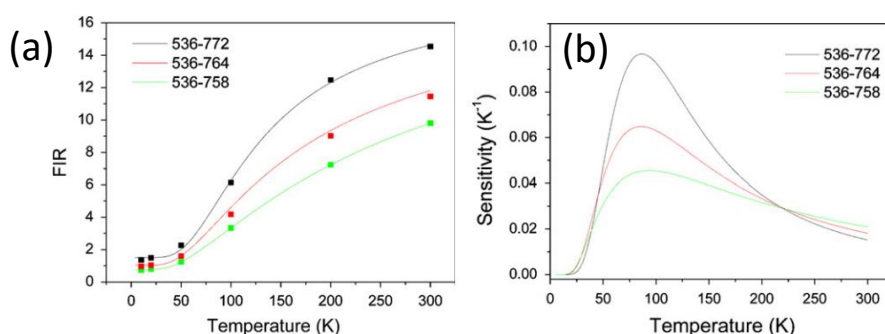


Figure 1.27. (a) Evolution of the intensity ratio between the emissions located at 536 nm relative to those located at 758 nm, 764 nm and 772 nm $\text{Ho}^{3+}, \text{Yb}^{3+}$ co-doped Y_2O_3 particles (black, red and green symbols, respectively); (b) thermal sensitivities of the intensity ratios considered in (a) [165].

1.4.5.4 Multi-center Ln^{3+} -UCNPs nanothermometry

The ratiometric systems for temperature determination based on the analysis of the emission intensity of thermally coupled energy levels proved their potentiality in various applications [152, 154, 25, 157]. However, those systems still suffer from a low thermal sensitivity. One of the ways to increase this sensitivity would be to use ions with pairs of thermally coupled energy levels located at a larger energy difference. However, if the distance between these levels is too large, then thermalization is no longer observed. Moreover, when the energy difference is very large, the electronic population, and hence the fluorescence intensity, of the upper level will decrease, which may introduce problems in detecting the emission arising from it [75].

Another way that has been explored to increase the thermal sensitivity is the use of multi-centered Ln^{3+} -UCNPs nanothermometry, which is based on the incorporation in a

luminescent compound of two different Ln^{3+} ions (both as emitters), whose luminescence intensities or at least that arising from one of the ions are strongly temperature dependent [55]. It has been shown that such systems are excellent candidates for noncontact temperature measurements with high sensitivities [166]. However, there are only few works on the multi-center UCNPs-based nanothermometry. Pandey and Rai were studied the temperature dependent blue upconversion emission generated from the Ho^{3+} , Yb^{3+} , $\text{Tm}^{3+}:\text{Y}_2\text{O}_3$ phosphors [167]. Intensity ratio of the two emission lines at 477 and 488 nm, arising from the radiative transition $^1\text{G}_4 \rightarrow ^3\text{H}_6$ of the Tm^{3+} ion and $^5\text{F}_3 \rightarrow ^5\text{I}_8$ of Ho^{3+} ion showed a linear tendency in 303–703 K temperature range. A thermal sensitivity in this case was found to be $0.7\% \text{ K}^{-1}$ [167].

Zheng and co-workers have designed a core-shell nanostructure ($\text{NaGd}:\text{Yb}^{3+}/\text{Tm}^{3+}@\text{Tb}^{3+}/\text{Eu}^{3+}$) for ratiometric multi-centered nanothermometry, which exhibit a high sensitivity of ($1.2\% \text{ K}^{-1}$) in the range of temperatures from 125 to 300 K based on the emissions of Tb^{3+} at 545 nm and Eu^{3+} at 615 nm [166]. Tm^{3+} and Yb^{3+} ions are present in the core of nanoparticles to harvest NIR photons and then promote the energy to the shell through two-step energy transfer via $\text{Yb}^{3+}-\text{Tm}^{3+}-\text{Gd}^{3+}$ [168]. Finally Gd^{3+} , present both in core and shell, transfers the energy to Tb^{3+} and Eu^{3+} that finally emit (see Figure 1.28a). The proposed energy transfer mechanism in Figure 1.28b.

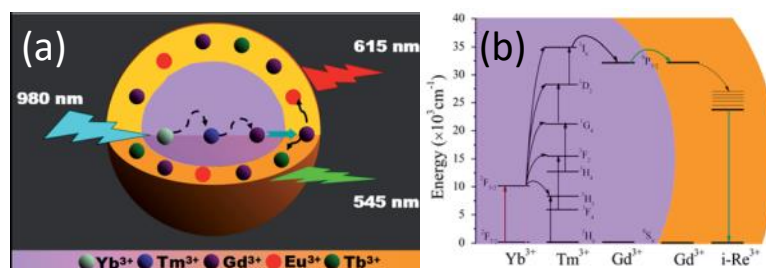


Figure 1.28. (a) Schematic design of a lanthanide-doped Yb^{3+} , $\text{Tm}^{3+}:\text{NaGd}@\text{Tb}^{3+}$, Eu^{3+} core-shell nanoparticles for energy migration-mediated upconversion; (b) proposed energy transfer mechanisms in the core-shell nanoparticles [166].

1.4.6 Complex systems

Sometimes simple systems may not meet the need for high thermal sensitivity and high thermal resolution nanothermometry. In order to improve the sensing properties, more complex systems have been designed [169-172]. A hybrid complex system based on Rhodamine 6G (R6G) and $\text{Er}^{3+}, \text{Yb}^{3+}:\text{NaYF}_4$ nanoparticles were developed by Chen et al [173]. The authors combined the Ln^{3+} -doped nanoparticles and Rhodamine 6G to create a hemispherical microstructure using the hydrophobic properties of distributed Bragg reflector substrate due to

Förster resonance energy transfer mechanism from the Ln^{3+} -doped nanoparticles (as the donor) to the dye (as the acceptor). An scheme of the experimental setup is shown in Figure 1.29. Continuous wave diode laser of 2.5 W at 980 nm was used as an excitation source. Upconversion emission from the microstructures were collected by a 50x microscope and delivered to a spectrometer via an optical fiber. Heater with controllable temperature and position was used to vary the temperature. The authors estimated a thermal sensitivity of $1\% \text{ K}^{-1}$ over the physiological temperature range (298 – 318 K) and $27\% \text{ K}^{-1}$ in the higher temperature region (320 – 330 K) [173].

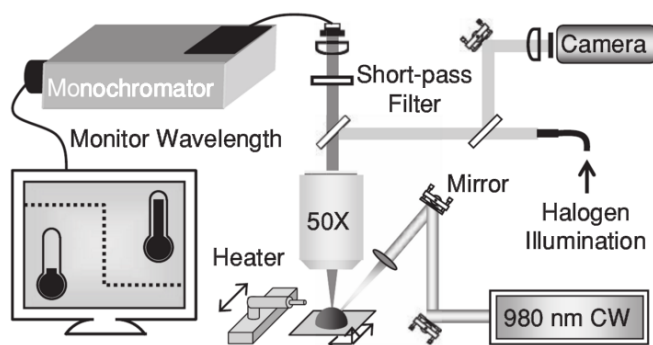


Figure 1.29. Scheme of the experimental setup for temperature sensing of individual microstructures [173].

Ceron and co-workers developed a system based on the combination of a Nd^{3+} -doped NaGdF_4 nanoparticles and semiconductors $\text{PbS}/\text{CdS}/\text{ZnS}$ quantum dots were encapsulated in poly(lactic-co-glycolic acid) (PLGA) polymer [174]. An scheme of the PLGA nanostructures encapsulated both Nd^{3+} -doped NaGdF_4 nanoparticles and semiconductors $\text{PbS}/\text{CdS}/\text{ZnS}$ QDs is shown in Figure 1.30a and their compositional analysis in the Figure 1.30b. The system was rationally design to emit in the range of the wavelengths from 1000 – 1350 nm, where the absorption and scattering of the biological tissues is minimized, so called second biological window [175-177]. The thermal sensitivity achieved ($2.5\% \text{ K}^{-1}$) is the highest reported up to now on luminescent nanothermometers operating in the first biological window [174].

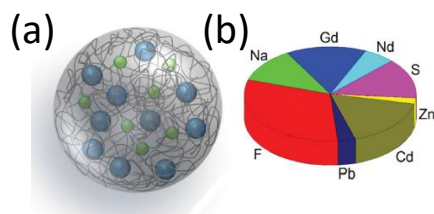


Figure 1.30. (a) Schematic view of the PLGA nanostructures encapsulated both Nd^{3+} -doped NaGdF_4 nanoparticles and semiconductors $\text{PbS}/\text{CdS}/\text{ZnS}$ quantum dots; (b) qualitative composition of nanostructure (atomic %) [174].

Xiao et al. also designed a hybrid complex based on the Förster resonance energy transfer (FRET) mechanism [178]. Red and NIR dual emitting Ln^{3+} , Mn^{2+} : NaLuF_4 upconversion nanoparticles acted as energy donors for Au nanoparticles as acceptor. Additionally they used poly(N-isopropylacrylamide) (PNIPAM) polymer to control the distance between the donor UCNPs and the acceptor Au nanoparticles. An scheme of the proposed nanocomposite is illustrated in Figure 1.31. The spectrometer was set to monitor the emission intensity from the transitions corresponding to ${}^4\text{F}_{9/2} \rightarrow {}^4\text{I}_{15/2}$ (Er^{3+}) at 660 nm and ${}^3\text{H}_4 \rightarrow {}^3\text{H}_6$ (Tm^{3+}) at 800 nm, respectively, in the temperature range of 298 – 328 K. The thermal resolution of the nanocomposite was found to be 0.9 K [178].

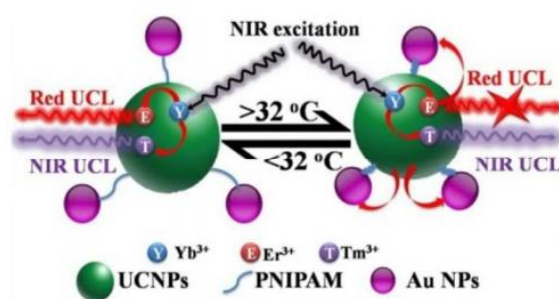


Figure 1.31. Schematic illustration of the switchable FRET made of donor Ln^{3+} , Mn^{2+} : NaLuF_4 UCNPs and Au nanoparticles as acceptor nanocomposites, spaced by PNIPAM polymer [178].

These complex systems can be modified to generate multifunctional systems. For example, Debasu et al. combined Ln^{3+} -doped nanoparticles and Au nanoparticles to form a multi-function nanoplatform that can be used as a heater and as a nanothermometer [179]. Ln^{3+} -doped nanoparticles served as nanothermometers and Au nanoparticles as nanoheaters. A transmission electron microscope image of the nanocomposite can be seen in Figure 1.32a. The local temperature was ascertained from a Boltzmann distribution in the range from room temperature to 1050 K with a thermal resolution of 0.3 – 2 K and a thermal sensitivity of 1.5 % K^{-1} . In the range 1200 – 2000 K, temperature was calculated using the Plank law with a thermal resolution of 4 – 13 K. Changing the concentration of the Au nanoparticles the authors could modulate the FIR of UCNPs and consequently the surface temperature induced by the Au nanoparticles (see Figure 1.32b) [179].

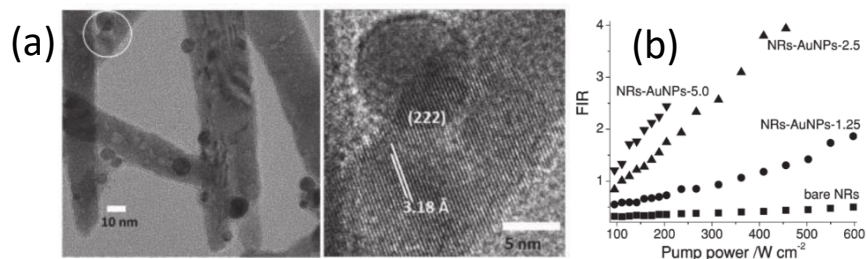


Figure 1.32. (a) Transmission electron micrograph of the $\text{Er}^{3+}, \text{Yb}^{3+}:\text{Gd}_2\text{O}_3$ UCNPs decorated with Au nanoparticles; (b) evolution of FIR with the pump power of UCNPs with different concentration of Au nanoparticles [179].

1.5 Aims of the thesis

After analyzing the literature, we detected some ways in which we could contribute to expand the field of luminescence nanothermometry to other materials, combination of ions, schemes of detection, etc. Our goal is to study the temperature dependence of the luminescence properties of optically active Ln^{3+} ions in different host matrices, including $\text{KLu}(\text{WO}_4)_2$ (KLuW), GdVO_4 , NaYF_4 and $\text{NaY}_2\text{F}_5\text{O}$ and to explore with them different techniques of luminescence nanothermometry that could be potentially improved by the use of these materials and identify potential applications for them.

But we did not limit our objectives here, we also explored if these nanoparticles might present additional properties, especially if they can also be used as photothermal converters for photothermal therapy. Also in this field we studied the photothermal conversion efficiency of grapheme and graphene oxide putting in context the results obtained by comparing them with those of the most common photothermal agent nowadays, Au nanorods. Moreover, we have developed a new method for determining the photothermal conversion efficiency by using an integrating sphere that would not only be valid for grapheme but for other photothermal agents.

Furthermore, we also analyzed the present detection technology for the luminescence of these nanothermometers and explored some modifications to develop compact and faster luminescence nanothermometer setups.

1.6 Structure of the thesis

Apart from this introduction, the thesis has been structured in the following way:

Chapter 2 will be focused on the experimental techniques used in this thesis.

Chapter 3 will be focused on the new detection techniques of luminescence nanothermometry. Here we present the potential use of $\text{Er}^{3+}, \text{Yb}^{3+}:\text{NaYF}_4$ and

$\text{Er}^{3+}, \text{Yb}^{3+}:\text{NaY}_2\text{F}_5\text{O}$ upconversion nanoparticles as thermal sensors by means of lifetime-based luminescent nanothermometry. In this chapter we also present a thermochromic temperature sensor based on the blue to deep red color change of the upconverted light from Yb^{3+} -sensitized Tm^{3+} -doped $\text{GdVO}_4@\text{SiO}_2$ core-shell nanoparticles.

Finally, we also present a novel low-cost non-invasive temperature sensor that uses a digital color sensor to capture simultaneously the emission in the blue, green and red region of electromagnetic spectrum. Two kinds of upconversion nanoparticles, including $\text{Er}^{3+}, \text{Yb}^{3+}:\text{NaYF}_4$ and Yb^{3+} -sensitized Tm^{3+} -doped GdVO_4 , were tested in order to prove the potentiality of this setup for temperature sensing.

Chapter 4 will be focused on the new materials we used in luminescence nanothermometry. We studied the temperature dependence of the upconversion emission in the green and the red regions of the electromagnetic spectrum of $\text{Ho}^{3+}, \text{Yb}^{3+}:\text{KLuW}$ nanocrystals after excitation at 980 nm. Also, we studied the upconversion emission of triply doped $\text{Ho}^{3+}, \text{Tm}^{3+}, \text{Yb}^{3+}:\text{KLuW}$ nanocrystals in the range of temperatures 296-673 K at different excitation wavelengths. Also, we report the synthesis of $\text{Er}^{3+}, \text{Yb}^{3+}:\text{NaYF}_4$ nanoparticles by a microwave-assisted solvothermal method and evolution of the upconversion emission spectra of these nanoparticles for their use in luminescence thermometry. Finally, we show the temperature dependent luminescence of $\text{Er}^{3+}, \text{Yb}^{3+}:\text{GdVO}_4@\text{SiO}_2$ core-shell nanoparticles and determined their thermal sensing properties through the fluorescence intensity ratio (FIR) technique.

Chapter 5 is focused on the nanothermometry in the first, second and third biological windows. Temperature dependent characterization of the upconversion emission arising from silica-coated $\text{Tm}^{3+}, \text{Yb}^{3+}:\text{GdVO}_4$ core-shell nanoparticles with different concentrations of Tm^{3+} are presented. Also Nd^{3+} -doped $\text{KGd}(\text{WO}_4)_2$ nanoparticles were investigated. Finally, we include infrared emission in the 1.4 – 2.1 μm range generated from Er^{3+} and Tm^{3+} ions sensitized by Yb^{3+} in the different host matrices after excitation at 980 nm, and analyzed their possibilities for temperature sensing purposes. Moreover, the excitation of Tm^{3+} at 808 nm was analyzed.

Chapter 6 is focused on the photothermal materials we analyzed that can efficiently convert the NIR light into heat. We developed a fast and effective method for determining the efficiency of the heat production after laser illumination for these materials based on the use of an integrating sphere. Moreover, we demonstrate the multifunctionality of the $\text{Ho}^{3+}, \text{Tm}^{3+}$ co-doped KLuW nanoparticles, which have ability to generate heat when illuminated at 808 nm, as result of as a consequence of the non-radiative processes between Ho^{3+} and Tm^{3+} ions.

Finally, we expose the conclusions of this thesis.

1.7 References

1. Young, H. D., Freedman, R. A. (2008). *Sears and Zemansky's university physics: with modern physics 12th ed.* (San-Francisco: Pearson Education).
2. Michalski, L., Eckersdorf, K., Kucharski, J., McGhee, J. (2001). *Temperature measurement., 2^{ed} ed.* (West Sussex: John Wiley & Sons).
3. Leigh, J. R. (1988). *Temperature measurements and control* (London: Peter Peregrinus).
4. McGee, T. D. (1988). *Principles and Methods of Temperature Measurement*, (New York: John Wiley and Sons).
5. Benedict, R. P. (1977). *Fundamentals of temperature, pressure, and flow measurements* (New York: John Wiley and Sons).
6. Encyclopaedia Britannica (1990). *The new Encyclopaedia britannica, macropaedia*. Vol. 23, 734-741.
7. Giambattista della Porta. *Nature Magic*. Naples (1558) (1589).
8. Ring, E. R. J. (2006). *The historical development of thermometry and thermal imaging in medicine*. J. Med. Eng. Technol. 30, 192-198.
9. Leurechon, J. (1653). *Recreation Mathematique* 110.
10. Bolton, H. C. (1900). *Evolution of thermometer, 1592-1743* (Easton: Chemical Publishing).
11. Fraden, J. (2010). *Handbook of Modern sensors: Physics, Designs and Applications* (New York: Spinger) .
12. published anonymously. (1701). *Scala graduum calorias. Calorum descriptiones & signa*. 824-829.
13. Shimek, W. J., Overlie, G. (1975). *The Celcius thermometer* (Washington: Lerner Publications).
14. Shachtam, T. (1999). *Absolute zero and the conquest of cold* (New York: Houghton Mifflin company).
15. Thomson, W. (1848). *On an absolute scale founded on Carnot's theory of the motive power of heat*. (Cambridge philosophical society proceedings).
16. Siemens, W. (1871). *The Bakerian lecture* (Royal Society).
17. Callender, H. L. (1887). *On the practical measurement of temperature. Experiments made at the Cavendish laboratory* (London: Cambridge Phil. Trans. Royal Society).
18. Hunt, L. B. (1980). *The origin of the platinum resistance thermometer*. Platinum metals Rev. 24, 104-112.

19. DeWitt, D. P., and Nutter, G. D. (1988). *Theory and practice of radiation thermometry* (New York: John Wiley & Sons).
20. Fery, C. (1901). *Thermoelektrisches pyrometer*. German Patent 135064.
21. Thyageswaran, S. (2012). *Developments in thermometry from 1984 to 2011: a review*. Recent patents on mechanical engineering 5, 4-44.
22. Lee, J., and Kotov, N. A. (2007). *Thermometer design at the nanoscale*. Nano today 2, 48-51.
23. Brites, C. D. S., Lima, P. P., Silva, N. J. O., Millan, A., Amaral, V. S., Palacio, F., and Carlos, L. D. (2012). *Thermometry at the nanoscale*. Nanoscale 4, 4799-4829.
24. Brites, C. D. S., Lima, P. P., Silva, N. J. O., Millan, A., Amaral, V. S., Palacio, F., Carlos, L. D. (2010). *A luminescent molecular thermometer for long-term absolute temperatura measurements at the nanoscale*. Adv. Mater. 22, 4499-4504.
25. L. Aigouy, G. Tessier, M. Mortier and B. Charlot, Appl. Phys. Lett., 2005, 87, 184105.
26. Hildebrandt, B., Wust, P., Ahlers, O., Dieing, A., Sreenivasa, G., Kerner, T., Riess, H. (2002). *The cellular and molecular basis of hyperthermia*. Critical Rev. Oncol./Hematol. 43, 33-56.
27. Kuruganti, P. T., Qi, H. (2002). *Asymmetry analysis in breast cancer detection using thermal infrared images*. Proceedings of the Second Joint EMBSiBMES Conference 2, 1155-1156.
28. Pustovalov, K., Astafyeva, L. G., and Fritzsche, W. (2013). *Selection of thermo-optical parameter of nanoparticles for achievement of their maximal thermal energy under optical irradiation*. Nano Energy 2, 1137-1141.
29. Lepock, J. R., Cheng, K. H., Al-qysi, H., Sim, I., Koch, C. J., and Kruuv, J. (1987). *Hyperthermia-induced inhibition of respiration and mitochondrial protein denaturation in CHL cells*. Int. J. Hyperthermia 3, 123-132.
30. Lepock, J. R., Frey, H. E., Rodahl, A. M. and Kruuv, J. (1988). *Thermal analysis of CHL V79 cells using differential scanning calorimetry: implications for hyperthermic cell killing and the heat shock response*. J. Cell. Physiol. 137, 14-24.
31. Roemer, R. B. (1989). *Engineering aspects of hyperthermia therapy*. Annu. Rev. Biomed. Eng. 1, 347-376.
32. Carrasco, E., del Rosal, B., Sanz-Rodriguez, F., de la Fuente, A. J., Haro-Gonzalez, P., Rocha, U., Kumar, K. U., Jacinto, C., Sole, J. G., and Jaque, D. (2015). *Intratumoral thermal reading during photo-thermal therapy by multifunctional fluorescent nanoparticles*. Adv. Funct. Mater. 25, 615-626.

33. Shields IV, C. W., Reyes, C. D., and Lopez, G. P. (2015). *Microfluidic cell sorting: a review of the advances in the separation of cells from debulking to rare cell isolation*. *Lab Chip* 15, 1230-1249.
34. Mao, H. B., Yang, T. L., and Cremer, P. S. (2002). *A microfluidic device with a linear temperature gradient for parallel and combinatorial measurements*. *J. Am. Chem. Soc.* 124, 4432-4435.
35. Samy, R., Glawdel, T., and Ren, C. L. (2008). *Method for microfluidic whole-chip temperature measurement using thin-film poly(dimethylsiloxane)/rhodamine B*. *Anal. Chem.* 80, 369-375.
36. Gosse, C., Bergaud, C., and Low, P. (2009). *Topics in advanced physics* (Berlin: Springer-Verlag).
37. Barilero, T., Le Saux, T., Gosse, C., and Jullien, L. (2009). *Fluorescent thermometers for dual-emission-wavelength measurements: molecular engineering and application to thermal imaging in a microsystem*. *Anal. Chem.* 81, 7988-8000.
38. Graham, E. M., Iwai, K., Uchiyama, S., de Silva, A. P., Magennis, S. W., and Jones, A. C. (2010). *Quantitative mapping of aqueous microfluidic temperature with sub-degree resolution using fluorescence lifetime imaging microscopy*. *Lab Chip* 10, 1267-1273.
39. Feng, J., Tian, K. J., Hu, D. H., Wang, S. Q., Li, S. Y., Zeng, Y., Li, Y., and Yang, G. Q. (2011). *A triarylboron-based fluorescent thermometer: sensitive over a wide temperature range*. *Angew. Chem. Int. Ed.* 50, 8072-8076.
40. Sadat, S., Tan, A., Chua, Y. J., and Reddy, P. (2010). *Nanoscale thermometry using point contact thermocouples*. *Nano Lett.* 10, 2613-2617
41. Childs, P. R. N., Greenwood, J. R., and Long, C. A. (2000). *Review of temperature measurement*. *Rev. Sci. Instrum.* 71, 2959-2978.
42. Shi, L., Kwon, O., Miner, A. C., and Majumdar, A. (2001). *Design and batch fabrication of probes for sub-100 nm scanning thermal microscopy*. *J. Microelectromechan. Syst.* 10, 370-378.
43. Majumbar, A. (1999). *Scanning thermal microscopy*. *Annu. Rev. Mater. Sci.* 29, 505-585.
44. Gimzewski, J. K., Gerber, C., Meyer, E., Schlittler, R. R. (1994). *Observation of a chemical reaction using a micromechanical sensor*. *Chem. Phys. Lett.* 217, 589-594.
45. Guthy, C. J., Zou, X., Pei, Z. J., Wang, X. (2013). *A review of temperature measurements methods for twist drilling processes*. *Int. J. Machin. Machinabil. Mater.* 13, 372-397.

46. Brites, C. D. S., Lima, P. P., Silva, N. J. O., Millan, A., Amaral, V. S., Palacio, F. and Carlos, L. D. (2011). *Lanthanide-based luminescent molecular thermometers*. *New J. Chem.* 35, 1177-1183.
47. Carlos, L. D., and Palacio, F. (2016). *Thermometry at the Nanoscale: Techniques and Selected Applications* (Cambridge: The Royal Society of Chemistry).
48. Khalid, A. H., Kontis, K. (2008). *Thermographic phosphors for high temperature measurements: principles, current state of the art and recent applications*. *Sensors*, 8, 5673-5744.
49. Baffou, G., Bon, P., Savatier, J., Polleux, J., Zhu, M., Merlin, M., Rigneult, H., Monneret, S. (2012). *Thermal imaging of nanostructures by quantitative optical phase analysis*. *ACS Nano* 6, 2452-2458.
50. Christofferson, J., Shakouri, A. (2005). *Thermoreflectance based thermal microscope*. *Rev. Sci. Instrum.* 76, 024903-024906.
51. Beechem, T., Graham, S., Kearney, S. P., Phinney, L. M., Serrano, J. R. (2007). *Simultaneous mapping of temperature and stress in microdevices using micro-Raman spectroscopy*. *Rev. Sci. Instrum.* 78, 061301-061309.
52. Kuball, M., Hayes, J. M., Uren, M. J., Martin, T., Birneck, J. C. H., Balmer, R. S., Hughes, B. T. (2002). *Measurement of temperature in active high-power AlGaIn/GaN HFETs using Raman spectroscopy*. *IEEE Electron Device Lett.* 23, 7-9.
53. Chenais, S., Forget, S., Druon, F., Balembois, F., Georges, P. (2004). *Direct and absolute temperature mapping and heat transfer measurements in diode-end-pumped Yb:YAG*. *Appl. Phys. B* 79, 221-224.
54. Sole, J. G., Bausa, L. E., and Jaque, D. (2005). *An introduction to the optical spectroscopy of inorganic solids* (West Sussex: John Wiley & Sons).
55. Jaque, D., Vetrone, F. (2012). *Luminescence nanothermometry*. *Nanoscale* 4, 4301-4326.
56. Wu, K., Cui, J., Kong, X., Wang, Y. (2011). *Temperature dependent upconversion luminescence of Yb/Er codoped NaYF₄ nanocrystals*. *J. Appl. Phys.* 110, 053510-053516.
57. Walker, G. W., Sundar, V. C., Rudzinski, C. M., Wun, A. W., Bawendi, M. G., and Nocera, D. G. (2003). *Quantum-dot optical temperature probes*. *Appl. Phys. Lett.* 83, 3555-3557.

58. Han, B., Hanson, W. L., Bensalah, K., Tuncel, A., Stern, J. M. and Cadeddu, J. A. (2009). *Development of quantum dot-mediated fluorescence thermometry for thermal therapies*. *Ann. Biomed. Eng.* 37, 1230-1239.
59. Lee, J., Govorov, A. O., and Kotov, N. A. (2005). *Nanoparticle assemblies with molecular springs: a nanoscale thermometer*. *Angew. Chem. Int. Ed.* 44, 7439-7442.
60. Ross, D., Gaitan, M., and Locascio, L. E. (2001). *Temperature measurement in microfluidic systems using a temperature-dependent fluorescent dye*. *Anal. Chem.* 73, 4117-4123.
61. Löw, P., Kim, B., Takama, N., and Bergaud, C. (2008). *High-spatial-resolution surface-temperature mapping using fluorescent thermometry*. *Small* 4, 908-914.
62. Allison, S. W., Gillies, G. T. (1997). *Remote thermometry with thermographic phosphors: instrumentation and applications*. *Rev. Sci. Instrum.* 68, 2615-2650.
63. Yap, S. V., Ranson, R. M., Cranton, W. M., Koutsogeorgis, D. C., and Hix, G. B. (2009). *Temperature dependent characteristics of La₂O₂S: Ln (Ln=Eu, Tb) with various Ln concentrations over 5-60 °C*. *J. Lumin.* 129, 416-422.
64. Fonger, H., and Struck, C. W. (1970). *Eu³⁺ ⁵D quenching to the charge-transfer states in Y₂O₂S, La₂O₂S, and LaOCl*. *J. Chem. Phys.* 52, 6364-6366.
65. Uchiyama, S., Kawai, N., de Silva, A. P., and Iwai, K. (2004). *Fluorescent polymeric AND logic gate with temperatura and pH as inputs*. *J. Am. Chem. Soc.* 126, 3032-3033.
66. Uchiyama, S., Matsumura, Y., de Silva, A. P., and Iwai, K. (2003). *Fluorescent molecular thermometers based on polymers showing temperature-induced phase transitions and labeled with polarity-responsive benzofurazans*. *Anal. Chem.* 75, 5926-5935.
67. Haro-Gonzalez, P., Martin, I. R., Martin, L. L., Leon-Luis, S. F., Perez-Rodriguez, C. and Lavin, V. (2011). *Characterization of Er³⁺ and Nd³⁺ doped strontium barium niobate glass ceramic as temperature sensors*. *Opt. Mater.* 33, 742-745.
68. Bizzak, D. J., Chyu, M. K. (1995). *Use of a laser-induced fluorescence thermal imaging system for local jet impingement heat transfer measurement*. *J. Heat Mass Trans.* 38, 267-274.
69. Rakov, N., Maciel, G. S. (2014). *Optical temperature sensing by use of band-shape method in Tb³⁺-doped oxide powders*. *Opt. Mater.* 37, 635-640.
70. Vlaskin, V. A., Janssen, N., van Rijssel, J., Beaulac, R., and Gamelin, D. R. (2010). *Tunable dual emission in doped semiconductor nanocrystals*. *Nano Lett.* 10, 3670-3674.

71. MacLaurin, E. J., Vlaskin, V. A., and Gamelin, D. R. (2011). *Water-soluble dual-emitting nanocrystals for ratiometric optical thermometry*. J. Am. Chem. Soc. *133*, 14978-14980.
72. Hsia, C. H., Wutting, A., and Yang, H. (2011). *An accessible approach to preparing water-soluble Mn²⁺-doped (CdSSe) ZnS (core) shell nanocrystals for ratiometric temperature sensing*. ACS Nano *5*, 9511-9522.
73. Ebert, S., Travis, K., Lincoln, B., and Guck, J. (2007). *Fluorescence ratio thermometry in a microfluidic dual-beam laser trap*. Opt. Express *15*, 15493-15499.
74. Peterman, E. J. G., Gittes, F., and Schmidt, C. F. (2003). *Laser-induced heating in optical traps*. Biophys. J. *84*, 1308-1316.
75. Wade, S. A., Collins, S. F., Baxter, G. W. (2003). *Fluorescence intensity ratio technique for optical fiber point temperature sensing*. J. Appl. Phys. *94*, 4743-4756.
76. Wade, S. A. (1999). *Temperature measurement using rare earth doped fiber fluorescence*. Ph.D. thesis, Victoria University, Melbourne, Australia,.
77. Wang, Z., Ananias, D., Carné-Sánchez, A., Brites, C. D. S., Imaz, I., MasPOCH, D., Rocha, J., and Carlos, L. D. (2015). *Lanthanide-organic framework nanothermometers prepared by spray-drying*. Adv. Funct. Mater. *25*, 2824-2830.
78. Haro-Gonzalez, P., Martinez-Maestro, L., Martin, I. R., Garcia-Sole, J. and Jaque, D. (2012). *High-sensitivity fluorescence lifetime thermal sensing based on CdTe quantum dots*. Small *8*, 2652-2658.
79. Sun, T., Zhang, Z. Y., and Grattan, K. T. V. (2000). *Erbium/ytterbium fluorescence based fiber optic temperature sensor system*. Rev. Sci. Instrum. *71*, 4017-4022.
80. Gota, C., Uchiyama, S., Yoshihara, T., Tobita, S. and Ohwada, T. (2008). *Temperature-dependent fluorescence lifetime of a fluorescent polymeric thermometer, poly(N-isopylacrylamide), labeled by polarity and hydrogen bonding sensitive 4-sulfamoyl-7-aminobenzofurazan*. J. Phys. Chem. B *112*, 2829-2836.
81. Chambers, M. D., and Clarke, D. R. (2009). *Doped oxides for high-temperature luminescence and lifetime thermometry*. Annu. Rev. Mater. Res. *39*, 325-359.
82. Bennet, M. A., Richardson, P. R., Arlt, J., McCarthy, A., Buller, G. S., Jones, A. C. (2011). *Optically trapped microsensors for microfluidic temperature measurement by fluorescence lifetime imaging microscopy*. Lab Chip *11*, 3821-3828.
83. Owen, D. M., Lanigan, P. M. P., Dunsby, C., Munro, I., Grant, D., Neil, M. A. A., French, P. M. W., Magee, A. I. (2006). *Fluorescence lifetime imaging provides*

- enhanced contrast when imaging the phase-sensitive dye di-4-ANEPPDHQ in model membranes and live cells.* Biophys. J. 90, 80-82.
84. Müller, C. B., Weiß, K., Loman, A., Enderlein, J., Richtering, W. (2009). *Remote temperature measurements in femto-liter volumes using dual-focus-fluorescence correlation spectroscopy.* Lab Chip 9, 1248-1253.
85. Mendels, D. A., Graham, E. M., Magennis, S. W., Jones, A. C., Mendels, F. (2008). *Quantitative comparison of thermal and solutal transport in a T-mixer by FLIM and CFD.* Microfluid. Nanofluid. 5, 603-617.
86. Jeon, S. M., Turner, J., Granick, S. (2003). *Noncontact temperature measurement in microliter-sized volumes using fluorescent labeled DNA oligomers.* J. Am. Chem. Soc. 33, 9908-9909.
87. Maestro, L. M., Haro-Gonzalez, P., Sanchez-Iglesias, A., Liz-Marzan, L. M., Sole, J. G., and Jaque, D. (2014). *Quantum dot thermometry evaluation of geometry dependent heating efficiency in gold nanoparticles.* Langmuir 30, 1650-1658.
88. Rocha, U., da Silva, C. J., Silva, W. F., Guedes, I., Benayas, A., Maestro, M. L. M., Bovero, E., van Veggel, F. C. J. M., Sole, J. A. G. S., Jaque, D. (2013). *Subtissue thermal sensing based on neodymium-doped LaF₃ nanoparticles.* ACS Nano 7, 1188-1199.
89. Maestro, L. M., Rodriguez, E. M., Cruz, M. C. I., Juarranz, A., Naccache, R., Vetrone, F.; Jaque, D., Capobianco, J. A., Sole, J. G. (2010). *CdSe Quantum Dots for Two-Photon Fluorescence Thermal Imaging.* Nano Lett. 10, 5109-5115.
90. Imbusch, G. F., and Henderson, B. (2006). *Optical Spectroscopy of Inorganic solids* (London: Oxford Science Publications).
91. Benayas, A., Escuder, E. and Jaque, D. (2012). *High-resolution confocal fluorescence thermal imaging of tightly pumped microchip Nd:YAG laser ceramics.* Appl. Phys. B 107, 697-701.
92. Park, Y., Ko, C., Chen, H. Y., Han, A., and Son, D. H. (2013). *Ratiometric temperature imaging using environment-insensitive luminescence of Mn-doped core-shell nanocrystals.* Nanoscale 5, 4944-4950.
93. Jaque, D., del Rosal, B, Rodríguez, E.M., Maestro, L. M., Haro-Gonzalez, P., Sole, J. G. (2014). *Fluorescent nanothermometers for intracellular thermal sensing.* Nanomedicine 9, 1743-1758

94. Sapsford, K. E., Algar, W. R., Berti, L., Gemmill, K. B., Casey, B. J., Oh, E., Stewart, M. H., Medintz, I. L. (2013). *Functionalizing nanoparticles with biological molecules: developing chemistries that facilitate nanotechnology*. Chem. Rev. 113, 1904-2074.
95. Cheng, L., Wang, C. and Liu, Z. (2013). *Upconversion nanoparticles and their composite nanostructures for biomedical imaging and cancer therapy*. Nanoscale 5, 23-37.
96. Banyai, L., and Koch, S. W. (1993). *Semiconductors quantum dots* (Singapore: World Scientific Publishing).
97. Li, S., Zhang, K., Yang, J. M., Lin, L., Yang, H. (2007). *Single quantum dots as local temperature markers*. Nano Lett. 7, 3102-3105.
98. McLaurin, E. J., Bradshaw, L. R., and Gamelin, D. R. (2013). *Dual-emitting nanoscale temperature sensors*. Chem. Mater. 25, 1283-1292.
99. Yang, J. M. (2011). *Quantum dot nano thermometers reveal heterogeneous local thermogenesis in living cells*. ACS Nano 5, 5067-5071.
100. Duarte, F. J. (2012). *Tunable organic dye lasers: physics and technology of high-performance liquid and solid-state narrow-linewidth oscillators*. Prog. Quant. Electron. 36, 29-50.
101. Garfield, S. (2002). *Mauve: how one man invented a color that changed the world* (New York: W. W. Norton & Company).
102. Zollinger, H. (2003). *Color chemistry: syntheses, properties and applications of organic dyes and pigments, 3rd edition* (Zürich: Verlag Helvetica Chimica Acta).
103. Sirohi, R. S. (2016). *Introduction to optical metrology* (New York: Taylor & Francis Group).
104. Ebert, S., Travis, K., Lincoln, B., and Guck, J. (2007). *Fluorescence ratio thermometry in a microfluidic dual-beam laser trap*. Opt. Express 15, 15493-15499.
105. Shah, J. J., Gaitan, M., and Geist, J. (2009). *Generalized temperature measurement equations for rhodamine B dye solution and its application to microfluidics*. Anal Chem. 81, 8260-8263.
106. Estrada-Perez, C. E., Hassan, Y. A., and Tan, S. (2011). *Experimental characterization of temperature sensitive dyes for laser induced fluorescence thermometry*. Rev. Sci. Instrum. 82, 074901-074907.
107. Hu, H., and Koochesfahani, M. M. (2003). *A novel technique for quantitative temperature mapping in liquid by measuring the lifetime of laser induced phosphorescence*. J. Visual. 16, 143-153.

108. Itoh, H., Arai, S., Sudhaharan, T., Lee, S. C., Chang, Y. T., Ishiwata, S., Suzuki, M., Lane, E. B. (2016). *Direct organelle thermometry with fluorescence lifetime imaging microscopy in single myotubes*. Chem. Commun. 52, 4458-4461.
109. Karstens, T., and Kobs, K. (1980). *Rhodamine B and rhodamine 101 as reference substances for fluorescence quantum yield measurements*. J. Phys. Chem. 84, 1871-1872.
110. Jung, W., Kim, Y. W., Yim, D., and Yoo, J. Y. (2011). *Microscale surface thermometry using SU8/Rhodamine-B thin layer*. Sensor. Actuat. A-Phys 171, 228-232.
111. Duong, H. D., Rhee, J. I. (2007). *Exploitation of thermo-effect of rhodamine B entrapped in sol-gel matrix and silica gel for temperature detection*. Sensor. Actuat. B-Chem. 124, 18-23.
112. Ross, D., Gaitan, M., Locascio, L. E. (2001). *Temperature measurement in microfluidic systems using a temperature-dependent fluorescent dye*. Anal. Chem. 73, 4117-4123.
113. Soraru, G. D., Suttor, D. (1999). *High temperature stability of sol-gel-derived SiOC glasses*. J. Sol-Gel Sci. Techn. 14, 69-74.
114. Louis, C., Pluchery, O. (2012). *Gold nanoparticles for physics, chemistry and biology* (London: Imperial college press).
115. Hutter, E., and Maysinger, D. (2011). *Gold nanoparticles and quantum dots for bioimaging*. Microsc. Res. Tech. 74, 592-604.
116. Lomenie, N., Racoceanu, D., Gouaillard, A. (2001). *Advances in bioimaging: from physics to signal understanding issues* (Berlin: Springer).
117. Cole, J. R., Mirin, N. A., Knight, M. W., Goodrich, G. P., and Halas, N. J. (2009). *Photothermal efficiencies of nanoshells and nanorods for clinical therapeutic applications*. J. Phys. Chem. C 113, 12090-12094.
118. Goodrich, G. P., Bao, L., Gill-Sharp, K., Sang, K. L., Wang, J., Payne, J. D. (2010). *Photothermal therapy in a murine colon cancer model using near-infrared absorbing gold nanorods*. J. Biomed. Opt. 15, 1-8.
119. Bomm, J., Günter, C., and Stumpe, J. (2012). *Synthesis and optical characterization of thermosensitive, luminescent gold nanodots*. J. Phys. Chem. C 116, 81-85.
120. Shang, L., Stockmar, F., Azadfar, N., Nienhaus, G. U. (2013). *Intracellular thermometry by using fluorescent gold nanoclusters*. Angew. Chem. Int. Ed. Eng. 52, 11154-11157.

121. Wang, C., Huang, Y., Lin, H., Xu, Z., Wu, J., Humphrey, M. G., and Zhang, C. (2015). *Gold nanoclusters based dual-emission hollow TiO₂ microsphere for ratiometric optical thermometry*. RSC Advances 5, 61586-61592.
122. Mark, J. E. (2007). *Physical properties of polymers handbook*. 2nd edition (New York: Springer).
123. Gerrard, M., Chaubey, A., Malhotra, B. D. (2002). *Application of conducting polymers to biosensors*. Biosens. Bioelectron. 17, 345-359.
124. Disney, M. D., Zheng, J., Swager, T. M., Seeberger, P. H. (2004). *Detection of bacteria with carbohydrate-functionalized fluorescent polymers*. J. Am. Chem. Soc. 126, 13343-13346.
125. Baleizão, C., Nagl, S., Borisov, S. M., Schäferling, M., Wolfbeis, O. S. and Berberan-Santos, M. N. (2007). *An optical thermometer based on the delayed fluorescence of C₇₀*. Chem. Eur. J. 13, 3643-3651.
126. Fan, Y., Liu, H., Han, R., Huang, L., Shi, H., Sha, Y., Jiang, Y. (2015). *Extremely high brightness from polymer-encapsulated quantum dots for two-photon cellular and deep-tissue imaging*. Scient. Report. 5, 9908-9915.
127. Pietsch, C., Schubert, U. S., and Hoogenboom, R. (2011). *Aqueous polymeric sensors based on temperature-induced polymer phase transitions and solvatochromic dyes*. Chem. Commun. 39, 8750-8765.
128. Yang, J., and Bai, F. (2002). *Temperature dependence of the fluorescence spectra of ladderlike polyphenylsilsesquioxane and ladderlike 1,4-phenylene-bridged polyvinylsiloxane*. Chin. J. Polym. Sci. 20, 15-23.
129. Almeida, A. K. A., Monteiro, M. P., Dias, J. M. M., Omena, L., da Silva, A. J. C., Tonholo, J., Mortimer, R. J., Navarro, M., Jacinto, C., Ribeiro, A. S., de Oliveira, I. N. (2014). *Synthesis and spectroscopic characterization of a fluorescent pyrrole derivative containing electron acceptor and donor groups*. Spectrochim. Acta Mol. Biomol. Spectrs. 128, 812-818.
130. Okabe, K., Inada, N., Gota, C., Harada, Y., Funatsu, T., and Uchiyama, S. (2012). *Intracellular temperature mapping with a fluorescent polymeric thermometer and fluorescence lifetime imaging microscopy*. Nat. Commun. 3, 705-714.
131. Yan, Q., Yuan, J. Y., Kang, Y., Cai, Z. N., Zhou, L. L., and Yin, Y. W. (2010). *Dual-sensing porphyrin-containing copolymer nanosensor as full-spectrum colorimeter and ultra-sensitive thermometer*. Chem. Commun. 46, 2781-2783.

132. Wu, W. T., Shen, J., Banerjee, P. and Zhou, S. Q. (2010). *Core-shell hybrid nanogels for integration of optical temperature-sensing, targeted tumor cell imaging, and combined chemo-photothermal treatment*. *Biomaterials* 31, 7555-7566.
133. Pietsch, C., Vollrath, A., Hoogenboom, R., and Schubert, U. S. (2010). *A fluorescence thermometer based on a pyrene-labeled thermoresponsive polymer*. *Sensors* 10, 7979-7990.
134. Alden, M., Omrane, A., Richter, M., Särner, G. (2011). *Thermographic phosphors for thermometry: a survey of combustion applications*. *Prog. Energ. Combust.* 37, 422-461.
135. Brübach, J., Pflitsch, C., Dreizler, A., Atakan, B. (2013). *On surface temperature measurements with thermographic phosphors: a review*. *Prog. Energ and Combust.* 39, 37-60.
136. Li, X., Jiang, G., Zhou, S., Wei, X., Chen, Y., Duan, C. K., Yin, M. (2014). *Luminescent properties of chromin(III)-doped lithium aluminate for temperature sensing*. *Sensor. Actuat B-Chem.* 202, 1065-1069.
137. Peng, H., Stich, M. I. J., Yu, J., Sun, L. -N., Fischer, L. H., and Wolfbeis, O. S. (2010). *Luminescent europium(III) nanoparticles for sensing and imaging of temperature in the physiological range*. *Adv. Mater.* 22, 716-719.
138. Kolodner, P., and Tyson, J. A. (1983). *Remote thermal imaging with 0.7- μ m spatial resolution using temperature-dependent fluorescent thin film*. *Appl. Phys. Lett.* 42, 117-119.
139. Suzuki, M., Tseeb, V., Oyama, K., and Ishiwata, S. (2007). *Microscopic detection of thermogenesis in a single HeLa cell*. *Biophys J.* 92, 46-48.
140. Wawrzynczyk, D., Bednarkiewicz, A., Nyk, M., Streck, W., and Samoc, M. (2012). *Neodymium(III) doped fluoride nanoparticles as non-contact optical temperature sensors*. *Nanoscale* 4, 6959-6961.
141. Benayas, A., del Rosal, B., Perez-Delgado, A., Santacruz-Gomez, K., Jauque, D., Hirata, G. A., and Vetrone, F. (2015). *Nd:YAG near-infrared luminescent nanothermometers*. *Adv. Opt. Mater.* 3, 687-694.
142. Marciniak, Ł., Bednarkiewicz, A., Stefanski, M., Tomala, R., Hreniak, D. and Streck, W. (2015). *Near infrared absorbing near infrared emitting highly-sensitive luminescent nanothermometer based on Nd³⁺ to Yb³⁺ energy transfer*. *Phys. Chem. Chem. Phys.* 17, 24315-24321.
143. Ishiwada, N., Fujioka, S., Ueda, T. and Yokomori, T. (2011). *Co-doped Y₂O₃:Tb³⁺/Tm³⁺ multicolor emitting phosphors for thermometry*. *Opt. Lett.* 36, 760-762.

144. Haase, M., and Schäfer, H. (2011). *Upconverting nanoparticles*. Angew. Chem. Int. Ed. 50, 5808-5829.
145. Rapaport, A., Milliez, J., Cassanho, A., Jenssen, H. J. (2006). *Review of the properties of upconversion phosphors for new emissive display*. J. Disp. Technol. 2, 68-78.
146. Atwood, D. A. (2012). *The rare earth elements: Fundamentals and Applications* (West Sussex: John Wiley & Sons).
147. Bloembergen, M. (1959). *Solid state infrared quantum counters*. Phys. Rev. Lett. 2, 84-85.
148. Auzel, F. (1966). *Compteur quantique par transfert d'énergie entre deux ions de terres rares dans un tungstate mixte et dans un verre*. C. R. Acad. Sci. Paris B 262, 1016-1019.
149. Auzel, F. (1966). *Compteur quantique par transfert d'énergie entre de Yb^{3+} a Tm^{3+} dans un tungstate mixte et dans verre germanate*. C. R. Acad. Sci. Paris B 263, 819-821.
150. Bünzli, J. C. G. and Pecharsky, V. K. (2015). *Handbook of the physics and chemistry of rare earths volume 47* (Amsterdam: Elsevier).
151. Jha, A. R. (2014). *Rare earth materials properties and applications* (Boca raton: CRC press).
152. Vetrone, F., Sole, J. G., Naccache, R., Sanz-Rodríguez, F., Capobianco, J. A. (2010). *Temperature sensing using fluorescent nanothermometers*. ACS Nano 4, 3254-3258
153. Li, C. R., Dong, B., Ming, C. G., Lei, M. (2007). *Application to temperature sensor based on green up-conversion of Er^{3+} doped silicate glass*. Sensors 7, 2652-2659.
154. Fischer, L. H., Harms, G. S., Wolfbeis, O. S. (2011). *Upconverting nanoparticles for nanoscale thermometry*. Angew. Chem. Int. Ed. 50, 4546-4551.
155. DeLoach, L. D., Payne, S. A., Chase, L. L., Smith, L. K., Kway, W. L., Krupke, W. F. (1993). *Evaluation of absorption and emission properties of Yb^{3+} doped crystals for laser applications*. IEEE J. Quantum Electron. 29, 1179
156. Berthou, H. and Jörgensen C. K., (1990). *Optical-fiber temperature sensor based on upconversion-excited fluorescence*. Opt. Lett. 15, 1100-1102.
157. Saïdi, E., Samson, B., Aigouy, L., Volz, S., Löw, P., Bergaud, C., and Mortier, M. (2009). *Scanning thermal imaging by near-field fluorescence spectroscopy*. Nanotechnology 20, 115703-115711.
158. Dong, N. N., Pedroni, M., Piccinelli, F., Conti, G., Sbarbati, A., Ramirez-Hernandez, J. E., Maestro, L. M., de la Cruz, M. C. I., Sanz-Rodríguez, F., Juarranz, A., Chen, F., Vetrone, F., Capobianco, J. A., Sole, J. G., Bettinelli, M., Jaque, D., Speghini, A.

- (2011). *NIR-to-NIR two-photon excited $\text{CaF}_2:\text{Tm}^{3+}$, Yb^{3+} nanoparticles: multifunctional nanoprobes for highly penetrating fluorescence bioimaging*. ACS Nano 5, 8665-8671.
159. Wang, X., Zheng, J., Xuan, Y., and Yan, X. (2013). *Optical temperature sensing of $\text{NaYbF}_4:\text{Tm}^{3+}@\text{SiO}_2$ core-shell micro-particles induced by infrared excitation*. Opt. Express 21, 21596-21606.
160. Xing, L., Xu, Y., Wang, R., Xu, W., Zhang, Z. (2014). *Highly sensitive optical thermometry based on upconversion emissions in $\text{Tm}^{3+}/\text{Yb}^{3+}$ codoped LiNbO_3 single crystal*. Opt. Lett. 39, 454-457.
161. Xu, W., Zhao, H., Li, Y., Zheng, L., Zhang, Z., Cao, W. (2013). *Optical temperature sensing through the upconversion luminescence from $\text{Ho}^{3+}/\text{Yb}^{3+}$ codoped CaWO_4* . Sensor. Actuat. B-Chem. 188, 1096-1100.
162. Pandey, A., Rai, V. K. (2013). *Improved luminescence and temperature sensing performance of $\text{Ho}^{3+}-\text{Yb}^{3+}-\text{Zn}^{2+}:\text{Y}_2\text{O}_3$ phosphor*. Dalton Trans. 42, 11005-11011.
163. Singh, A. K. (2007). *$\text{Ho}^{3+}:\text{TeO}_2$ glass, a probe for temperature measurements*. Sensor. Actuat. A-Phys. 136, 173-177.
164. Verma, R. K., Rai, S. B. (2012). *Laser induced optical heating from $\text{Yb}^{3+}/\text{Ho}^{3+}:\text{Ca}_{12}\text{Al}_{14}\text{O}_{33}$ and its applicability as a thermal probe*. J. Quant. Spectrosc Radiant. Transfer 113, 1594-1600.
165. Lojpur, V., Nikolic, M., Mancic, L., Milosevic, O., Dramicanin, M. D. (2013). *$\text{Y}_2\text{O}_3:\text{Yb}$, Tm and $\text{Y}_2\text{O}_3:\text{Yb}$, Ho powders for low-temperature thermometry based on upconversion fluorescence*. Ceram. Int. 39, 1129-1134.
166. Zheng, S., Chen, W., Tan, D., Zhou, J., Guo, Q., Jiang, W., Xu, C., Liu, X., and Qiu, J. (2014). *Lanthanide-doped NaGdF_4 core-shell nanoparticles for non-contact self-referencing temperature sensors*. Nanoscale 6, 5675-5679.
167. Pandey, A., Rai, V. K. (2013). *Optical thermometry using FIR of two close lying levels of different ions in $\text{Y}_2\text{O}_3:\text{Ho}^{3+}-\text{Tm}^{3+}-\text{Yb}^{3+}$ phosphor*. Appl. Phys. B 113, 221-225.
168. Wang, F., Deng, R., Wang, J., Wang, Q., Han, Y., Zhu, H., Chen, X., Liu, X. (2011). *Tuning upconversion through energy migration in core-shell nanoparticles*. Nat. Mater. 10, 1-6
169. Huang, J., He, B., Cheng, Z., Zhou, L. (2015). *Upconverting PAAm/PNIPAM/ $\text{NaYF}_4:\text{Yb}:\text{Er}$ hydrogel with enhanced luminescence temperature sensitivity*. J. Lumin. 160, 254-257.
170. Xu, X., Wang, Z., Lei, P., Yu, Y., Yao, S., Song, S., Liu, X., Su, Y., Dong, L., Feng, J., and Zhang, H. (2015). *$\alpha\text{-NaYb}(\text{Mn})\text{F}_4:\text{Er}^{3+}/\text{Tm}^{3+}@\text{NaYF}_4$ UCNPs as "band-shape"*

- luminescence nanothermometers over a wide temperature range.* ACS Appl. Mater. Interfaces 7, 20813-20819.
171. Wang, Z., Zhang, P., Yuan Q., Xu, X., Lei, P., Liu, X., Su, Y., Dong, L., Feng, J., and Zhang, H. (2015). *Nd³⁺-sensitized NaLuF₄ luminescent nanoparticles for multimodal imaging and temperature sensing under 808 nm excitation.* Nanoscale 7, 17861-17870.
172. Cui, Y., Zhu, F., Chen, B., and Qian, G. (2015). *Metal-organic frameworks for luminescence thermometry.* Chem. Commun. 51, 7420-7431.
173. Chen, R., Ta, V. D., Xiao, F., Zhang, Q., Sun, H. (2013). *Multicolor hybrid upconversion nanoparticles and their improved performance as luminescence temperature sensors due to energy transfer.* Small 9, 1052-1057.
174. Ceron, E. N., Ortgies, D. H., del Rosal, B., Ren, F., Benayas, A., Vetrone, F., Ma, D., Sanz-Rodriguez, F., Sole, J. G., Jaque, D. and Rodriguez, E. M. (2015). *Hybrid nanostructures for high-sensitivity luminescence nanothermometry in the second biological window.* Adv. Mater. 27, 4781-4787.
175. Smith, A. M., Mancini, M. C., Nie, S. (2009). *Bioimaging: second window for in vivo imaging.* Nat. Nanotechnol. 4, 710-711.
176. Weissleder, R. (2001). *A clearer vision for in vivo imaging.* Nat. Biotechnol. 19, 316-317.
177. Helmchen, F., and Denk, W. (2005). *Deep tissue two-photon microscopy.* Nat. Methods 2, 932-940.
178. Xiao, Q., Li, Y., Li, F., Zhang, M., Zhang, Z., Lin, H. (2014). *Rational design of a thermalresponsive-polymer-switchable FRET system for enhancing the temperature sensitivity of upconversion nanophosphors.* Nanoscale 6, 10179-10186.
179. Debasu, M. L., Ananias, D., Pastoriza-Santos, I., Liz-Marzan, L. M., Rocha, J., and Carlos, L. D. (2013). *All-in-one optical heater-thermometer nanoplatfom operative from 300 to 2000 K based on Er³⁺ emission and blackbody radiation.* Adv. Mater. 25, 4868-4874.

CHAPTER 2

Experimental techniques

In the following chapter, the different experimental techniques used in this thesis are described. First we start with the synthesis methods for luminescent nanoparticles used in this thesis, such as the Pechini, the conventional hydrothermal and the hydrothermal accompanied with microwave oven methods. Also the synthesis of the core-shell nanostructures by a hydrothermal method is commented. Later, some structural characterization techniques are presented, including X-ray diffraction and Raman scattering. After, the electron microscopy characterization techniques, which are fundamental in the area of nanomaterial science, such as transmission electron and environmental scanning electron microscopes are discussed. Finally, the chapter ends with the spectroscopy characterization techniques, including optical absorption, photoluminescence and lifetime measurements.

2.1 Synthesis of luminescent nanoparticles

2.1.1 Sol-Gel synthesis: the Pechini method.

The sol-gel synthesis method was developed in the 1960s, mainly due to the need of new synthesis methods in the nuclear industry to reduce dust and sintering temperatures [1]. Sol is the name of a colloidal solution made of solid particles, a few hundred nm in diameter, suspended in a liquid phase. A gel can be considered as a solid macromolecule immersed in a solvent. Thus, the sol-gel process consists in the chemical transformation of a liquid (the sol) into a gel state with a subsequent thermal post-treatment and the transition into a solid material [2]. The main benefits of the sol-gel processing are the high purity and uniform nanostructure of compounds achievable at low temperatures [1].

In 1967 Maggio P. Pechini proposed a modification of sol-gel method to prepare lead and alkaline earth titanates and niobates by using resin intermediates [3]. This method is a useful technique for the preparation of high purity dielectrics materials with a precise control of their stoichiometry, avoiding the high temperatures and high vacuum pressures required to vaporize oxides [3]. Since then, this modification of the sol-gel method is known as the Pechini method.

We used the Pechini method to synthesize monoclinic potassium rare-earth tungstates, $(K(RE)WO_4)_2$, following the procedure of Galceran et al. [4]. The main advantages of the monoclinic potassium lutetium double tungstates $KLu(WO_4)_2$ (KLuW) are the very high values of the absorption and emission cross-section of the rare-earth dopants, partly due to the strong anisotropy of these biaxial crystals and the possibility to dope them with high concentration of the active ions without substantial fluorescence quenching. The KLuW host matrix is very suitable for doping with Yb^{3+} because of the close ionic radii and masses of Yb^{3+} and Lu^{3+} and the close lattice parameters of the isostructural KLuW. KLuW are widely known as hosts for active ions to constitute a solid-state laser material [5]. The method is described below and a scheme of the synthesis process is presented in Figure 2.1.

- (i) Analytic grade oxides of the elements contained in the nanoparticles were dissolved in hot nitric acid in stoichiometric proportions to form the nitrate precursors. The excess of nitric acid was evaporated by slow heating.
- (ii) An aqueous solution of ethylenediaminetetraacetic acid (EDTA), as the chelating agent, was mixed with the tungstate precursor and added to the nitrate precipitates in a specific molar ratio (C_M) in order to prepare the metal complexes:

$$C_M = \frac{[EDTA]}{[METAL]} = 1$$

where $[EDTA]$ and $[METAL]$ corresponds to the concentration of EDTA and metals present in the solution.

- (iii) The solution was heated to 353 K under magnetic stirring until complete dissolution.
- (iv) Then, ethylene glycol (EG), as the esterification agent, was added to the mixture with a ratio:

$$C_E = \frac{[EDTA]}{[EG]} = 2$$

- (v) The solution was heated at 423 K in order to evaporate the water and generate the polymeric gel.
- (vi) After that, the polymeric gel was calcinated at 573 K for 3 h to obtain the precursor powders.
- (vii) A final annealing at 1023 K h was carried out for 2 h to eliminate the organic compounds and crystallize the desired nanoparticles.

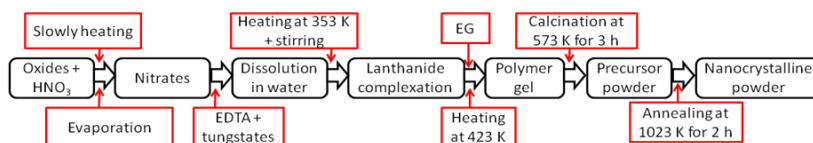


Figure 2.1. Scheme of the procedures followed in the modified Pechini method to produce monoclinic potassium rare-earth tungstates.

2.1.2 Hydrothermal method

The hydrothermal synthesis method uses the solubility in water of almost all inorganic substances at elevated temperatures and pressures and the subsequent crystallization of the dissolved material from the fluid [6]. Among the low temperature methods, the hydrothermal method is very versatile for the synthesis of nanomaterials [7]. Synthesis reactions can be carried out in a temperature range of 373 to 1273 K or more and in a pressure range of 1 atmosphere to several thousand atmospheres [7]. The reactions can be carried out in water or in any other solvent. When water is used as solvent, the process is called ‘hydrothermal’. When any solvent including water or organic solvents such as methanol, ethanol, polyol, etc. are used the process is called ‘solvothermal’. Two different operation modes can be distinguished. The

first one is the autogeneous pressure range mode, where the pressure of the closed system is given by the temperature applied to the system. However, the autogeneous pressure at a given temperature often is not sufficient for the necessities of hydrothermal processing. An alternative is the high pressure mode in which water at an external pressure, more elevated than the autogeneous equilibrium water vapor pressure, is used [6].

Temperature, the water pressure and the reaction time are the three principal physical parameters in the hydrothermal synthesis method. The autogeneous hydrothermal method at low temperature was used to synthesize Er^{3+} , Yb^{3+} and Tm^{3+} , Yb^{3+} co-doped GdVO_4 nanoparticles at the Instituto de Ciencia de Materiales de Madrid (ICMM) [8]. GdVO_4 is well established host possessing relevant characteristics related to crystal phase stability up to full Ln^{3+} replacement of Gd^{3+} . Moreover, like KLuW it possess a high optical absorption and emission cross-section values for the Ln doping ions, relatively high thermal conductivity, and moderated cut-off phonon energy [9]. An scheme of the synthesis procedure is presented in Figure 2.2. The steps involved in this preparation method are:

- (i) Preparation of an aqueous solution of the required amounts of the lanthanide nitrates and NH_4VO_3 with the pH adjusted to 7 by adding dilute NH_4OH under stirring during 1 h.
- (ii) Hydrothermal treatment of, the solution at 458 K during 24 h in sealed Teflon-lined autoclaves with a capacity of 75 ml.
- (iii) Separation of the obtained product by centrifugation, wash several times with distilled water and dry at 393 K in open air.
- (iv) Annealing of the samples at 875 K for 5 h to improve the emission efficiency of the nanoparticles.

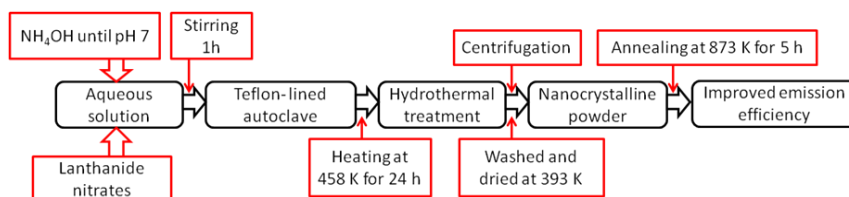


Figure 2.2. Scheme of the hydrothermal synthesis method of the GdVO_4 nanoparticles used in this thesis.

2.1.2.1 Preparation of core-shell Er^{3+} , Yb^{3+} and Tm^{3+} , Yb^{3+} co-doped GdVO_4 nanoparticles

Several methods have been reported to improve the emission quantum yields of Ln^{3+} -doped UCNPs, such as optimizing the dopant concentration [10], modifying the local chemical and structural environment [11, 12], controlling the distribution of active ions in the host materials as well as varying the composition [13], architecture and morphology of the UCNPs [15, 16]. The most spectacular improvement in emission intensity was observed, when the surface of nanoparticles was passivated with an undoped shell [17]. The enhancement of the luminescence intensity by this method can be attributed to the surface passivation in front surface defects, preventing quenching effects and solvent effects (ligand and solvent vibrational modes, ligand polarizability and effective refractive index of refraction).

The formation of silica-coated particles has been subject of extensive investigations for years because of their wide commercial applications and interesting structural properties [18]. One of the main advantages when using silica among other surface coatings is that silica coatings allow manipulation of the interaction potential and make it possible to disperse colloids in a wide range of solvents from very polar to a polar [19, 20].

Silica coating of the Er^{3+} , Yb^{3+} and Tm^{3+} , Yb^{3+} co-doped GdVO_4 nanoparticles with a layer of a controlled thickness in a core-shell structure was done at the Instituto de Ciencia de Materiales de Madrid by Dr. Concepcion Cascales. The formation of the silica coating requires a base-catalyzed hydrolysis of tetraethoxysilane ($\text{Si}(\text{OC}_2\text{H}_5)_4$, TEOS) and the subsequent condensation of silanol groups on the surface of the nanoparticles. This was carried out by dispersing the nanoparticles (1.5 mmol) in an ethanolic solution (40 ml) with the pH adjusted to 9 by adding 0.75 ml of NH_4OH and then adding slowly 2 ml of TEOS under stirring, which was maintained for 4 h. Finally, the obtained product was washed with ethanol, centrifuged and dried at 393 K.

2.1.3 Synthesis of Er^{3+} , Yb^{3+} : NaYF_4 nanoparticles by the microwave-assisted heating solvothermal method

One of the main drawbacks of the hydrothermal is the slow kinetics at any given temperature. Many energy sources have been used in a hydrothermal system, to increase the kinetics of crystallization, including microwaves, electric fields, and ultrasonic waves [21-23].

The main advantages of using a microwave oven in a hydrothermal system are the energy saving and the reduction of pollution towards the environment, because the reactions take place in closed isolated system conditions. In contrast to the conventional heating hydrothermal method, which requires a long time and high electric powers, microwave-assisted heating is a greener approach to synthesize materials in a shorter time and with a lower power [24-26].

In this thesis we used the microwave-assisted heating solvothermal method to synthesize Yb^{3+} (20 mol%), Er^{3+} (2 mol%) co-doped NaYF_4 nanoparticles. In general, fluoride based host matrices of whole categories of ABF_4 ($\text{A}=\text{Li}, \text{Na}, \text{K}$; $\text{B} = \text{Y}, \text{Gd}, \text{Lu}, \text{Sc}$), owing to their good chemical stability and low phonon energy, and is widely deployed as upconversion host materials [27]. It has been acknowledge that hexagonal (β -phase) NaYF_4 doped with Er^{3+} , Yb^{3+} and Yb^{3+} , Tm^{3+} are considered the most efficient NIR to green and blue upconversion materials, respectively [28, 29]. Crystal structure of the host matrix plays a critical role in the optical properties of material. For example, bulk β - NaYF_4 doped with Er^{3+} , Yb^{3+} has about 10 times higher upconversion efficiency than its cubic (α -phase) counterpart [30]. The phase-dependent optical properties can be ascribed directly to the different crystal field around Ln ions in matrices of various symmetries. However, special experimental conditions can lead to the formation of mixed phase (α - β) that may change optical properties in good manner.

The synthesis was done at the laboratories of Catalytic Materials in Green Chemistry (GreenCat) group of Rovira i Virgili University. A picture of the microwave hydrothermal processing equipment used in this thesis is shown in Figure 2.3a. High purity Y_2O_3 , Yb_2O_3 , Er_2O_3 , trisodium citrate ($\text{Na}_3\text{C}_6\text{H}_5\text{O}_7$), sodium fluoride (NaF) and ammonium fluoride (NH_4F) were used as precursor materials mixed in a stoichiometric proportion. The precursor nitrates $\text{RE}(\text{NO}_3)_3$ ($\text{RE} = \text{Y}, \text{Yb}, \text{Er}$) were prepared by dissolving the corresponding oxides in 10 ml of hot nitric acid (HNO_3). After, the evaporation of nitric acid, 50 ml of ethanol and the trisodium citrate were added to the nitrates and stirred during 30 – 60 min. In another vessel, NaF and NaH_2F were dissolved in 30 ml of hot water. Then, the two solutions were mix together. After a vigorous stirring for 1-2 h, the solution was transferred into a Teflon bottle and placed in the microwave autoclave, and maintained at a temperature ranging from 393 – 453 K during a period between 3 and 6 h. After the solution cooled down to room temperature, the precipitated nanoparticles were centrifuged at 40000 rates per minute during 30 min and washed with ethanol and deionized water three times in sequence. Finally, nanoparticles were placed in the oven at 353 K for drying. An scheme of the synthesis process is shown in Figure 2.3b.

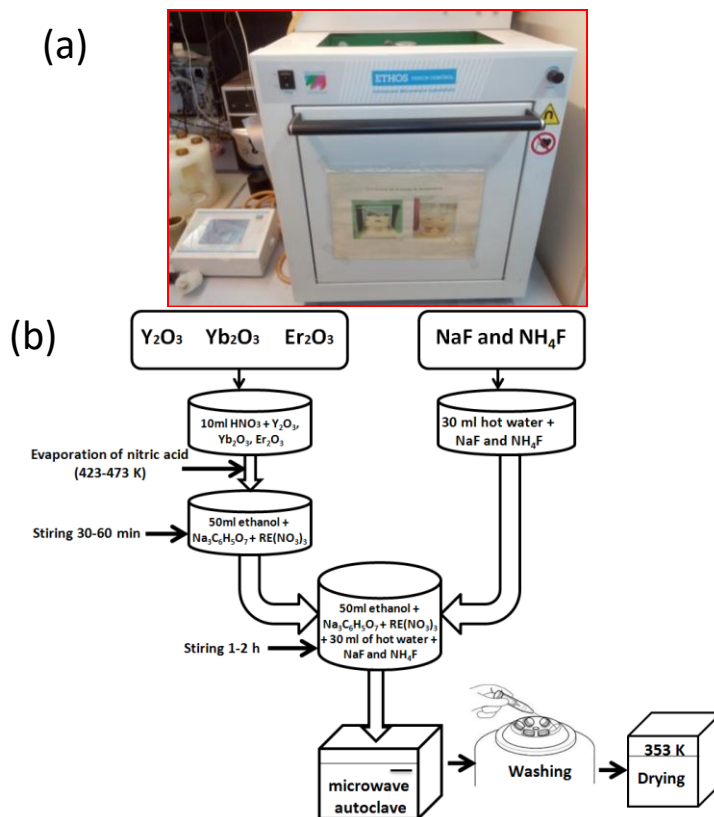


Figure 2.3. (a) Picture of the Ethos Touch Control Advanced Microwave Labstation oven used in this thesis in the synthesis of $\text{Er}^{3+}, \text{Yb}^{3+}:\text{NaYF}_4$ nanoparticles by the microwave-assisted heating solvothermal method; (b) scheme of the synthesis procedure.

2.2 Structural characterization

2.2.1 X-ray diffraction

The discovery of the X-rays in 1895 by Wilhelm Roentgen and the development of the fundamental X-ray diffraction law by W. H. Bragg and his son W. L. Bragg [31], explaining why the cleavage faces of crystals appear to reflect X-ray beams at certain angles of incidence, enabled scientists to probe the crystalline structure of materials at an atomic level. The crystalline material consists of an ordered number of planes that form a crystal lattice. When the X-ray beam falls on the planes of atoms, several processes may occur, including, transmission, absorption, scattering and diffraction. A simple example of diffraction of an X-ray beam produced on the planes of atoms is presented in Figure 2.4a, for which the conditions satisfying the Bragg's law are provided, written as:

$$n\lambda = 2d\sin\theta \quad (2.1)$$

where n is the order of the diffracted beam, λ is the wavelength of the incident X-ray beam, d is the distance between the atomic planes in a crystal, and θ is the angle of incidence of the X-ray beam.

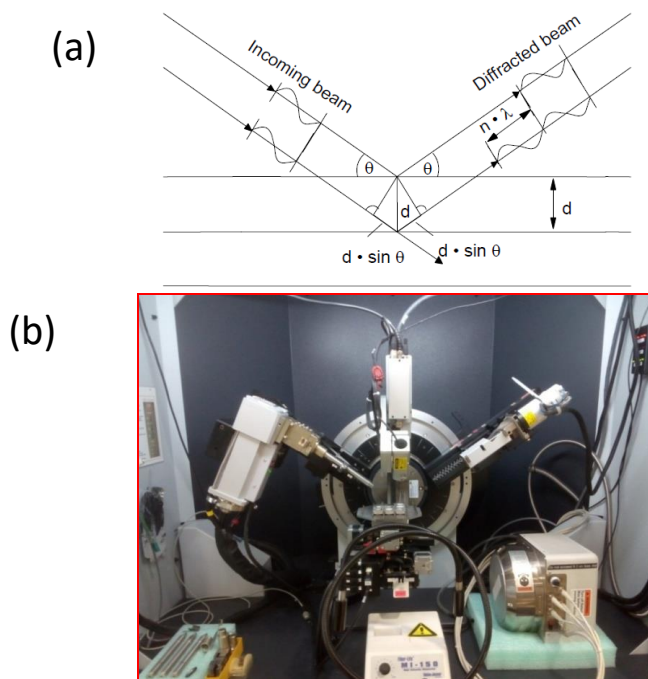


Figure 2.4. (a) Scheme showing the diffraction of X-rays by two consecutive atomic planes; (b) X-ray diffractometer Bruker-AXS D8-Discover diffractometer used in this thesis.

Thus, from the Bragg's law we can easily calculate the distance between the atomic planes, since we know λ (1.54056 Å in our case, corresponding to the $K\alpha$ of Cu) and the angle of incidence of the X-ray beam can be measured. An X-ray diffraction pattern records the X-ray intensity of the detected signal as a function of θ . The positions and numbers of the peaks appearing in this diffraction pattern give insight into the crystalline structure of the material analyzed. The intensities of the peaks are determined by the atoms present and their positions. The observed positions of the peaks obtained from an X-ray pattern provides information about the distance between crystal planes within a lattice [32].

$\text{Er}^{3+}, \text{Yb}^{3+}:\text{GdVO}_4$ and $\text{Tm}^{3+}, \text{Yb}^{3+}:\text{GdVO}_4$ nanoparticles were characterized by X-ray powder diffraction (XRD) using a Bruker AXS D8-Discover diffractometer with Cu $K\alpha$ radiation. This equipment is available at the Instituto de Ciencia de Materiales, Madrid.

$\text{Er}^{3+}, \text{Yb}^{3+}:\text{NaYF}_4$, $\text{Tm}^{3+}, \text{Ho}^{3+}:\text{KLu}(\text{WO}_4)_2$ and $\text{Ho}^{3+}, \text{Yb}^{3+}:\text{KLu}(\text{WO}_4)_2$ nanoparticles were characterized using the same equipment available at the Servei Recursos Científics i Tècnics of the Universitat Rovira i Virgili, Tarragona. A picture of this diffractometer is shown in Figure 2.4b.

2.2.2 Raman scattering

In 1928, the Indian scientist C. V. Raman demonstrated a type of inelastic scattering that gave rise to a new type of spectroscopy, in which the inelastic scattering of light from the sample is analyzed, called Raman spectroscopy in his honor. When light of frequency ν_i illuminates a sample, the output spectrum of the scattered light consists of a predominant line of the same frequency ν_i and much weaker side bands at frequencies $\nu_i \pm \nu_R$. The main line corresponds to the Rayleigh scattered light, while the side-bands spectra is the actual Raman spectrum.

When a monochromatic laser light strikes the sample, it excites molecules and transforms them into oscillating dipoles. These dipoles emit light of three different frequencies:

i) A molecule with no Raman-active modes absorbs a photon with the excitation frequency ν_i . The excited molecule returns back to the same basic vibrational state and emits light with the same frequency as the excitation source. This type of interaction is called an elastic Rayleigh scattering.

ii) A photon with frequency ν_i is absorbed by a Raman-active molecule which at the same time of interaction is in the basic vibrational state. Part of the photon's energy is transferred to the Raman-active mode with frequency ν_R and the resulting frequency of scattered light is reduced to $\nu_i - \nu_R$. This Raman frequency is called Stokes frequency.

iii) A photon with frequency ν_i is absorbed by a Raman-active molecule, which at the time of interaction is already in an excited vibrational state. The excessive energy of the excited Raman active mode is released, the molecule returns to the basic vibrational state and the resulting frequency of the scattered light goes up to $\nu_i + \nu_R$. This Raman frequency is called the Anti-Stokes frequency.

For a better understanding of the mentioned above processes, they are represented in an energy level diagram in Figure 2.5.

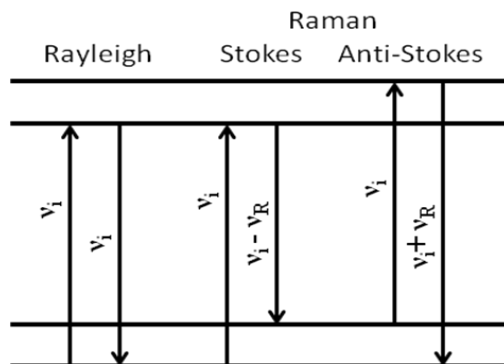


Figure 2.5. Schematic representation of an energy diagram of Rayleigh and Raman (Stokes and anti-Stokes) scattering.

The Raman spectrum has a set of properties: (i) the ν_R are the characteristic frequencies of the sample (in the case of solids they correspond to phonon frequencies); (ii) Stokes and anti-Stokes lines are found always at frequencies symmetrically located to both sides of the main line at ν_i ; (iii) the anti-Stokes lines are weaker than the Stokes lines; (iv) the intensity of the lines is proportional to ν_i^4 .

To record the Raman spectra, the photons from the excitation laser are absorbed by the sample and then reemitted. The frequency of the emitted photons is shifted up or down in comparison with original frequency, due to the Raman effect. This shift provides information about vibrational, rotational and other low frequency transitions in molecules. Raman spectroscopy can be used to study solid, liquid and gaseous samples [33].

About 99.999 % of all incident photons in spontaneous Raman undergo elastic Rayleigh scattering. This type of signal is useless for practical purposes of molecular characterization. Only the 0.001 % of the incident light produces inelastic Raman signal with frequencies $\nu_i \pm \nu_R$. Thus, spontaneous Raman scattering is very weak, and special measures should be taken to distinguish it from the predominant Rayleigh scattering. Instruments such as Notch filters, tunable filters, laser stop apertures, double and triple spectrometric systems are used to reduce the Rayleigh scattering and obtain high-quality Raman spectra. Also many different ways of sample preparation, sample illumination or scattered light detection have been used to enhance the intensity of the Raman signal. It was found that, if the sample is irradiated with a very strong laser pulse, a much larger portion of the incident light transforms into useful Raman scattering and can improve the signal-to-noise ratio.

Raman spectra in this thesis were obtained in the GdS-Optronlab of the Department of Condensed Matter Physics at the University of Valladolid, at room temperature using a Labram

HR800 UV Raman spectrometer from Horiba-Jobin-Yvon. It was attached to a metallographic microscope with confocal optics, and equipped with a LN₂-cooled charge-coupled device (CCD) detector. The excitation was carried out with a UV laser at 325 nm using a 40X UV microscope objective with 0.5 numerical aperture. The scattered light was collected by the same microscope objective, thus working in a nearly backscattering configuration.

2.3 Microscopic characterization techniques

2.3.1 Transmission electron microscopy (TEM)

Electron microscopes (EM) use the beam of highly charged electrons to examine object of interest at a very fine scale. The specimen interaction with an electron beam is what makes possible observe it. When the electron beam interacts with the atoms of the sample, electrons undergo two types of scattering: elastic and inelastic. Inelastic interactions include the generation of secondary electrons, backscattered electrons, characteristic X-rays, visible light, and Auger, that electrons are used when examining thick or bulk specimens. Other interactions include diffracted and transmitted electrons that are used when examining thin or foil specimens [34].

The transmission electron microscope (TEM) was the first type of EM to be developed. It was developed by Max Knoll and Ernst Ruska in Germany in 1931 [35]. TEM uses high energy electrons to penetrate through a thin sample. TEM exploits three different interactions of the electron beam with the sample: (i) unscattered electrons (transmitted beam); (ii) elastically scattered electrons (diffracted beam); (iii) and inelastically scattered electrons (absorbed beam). Thin samples are required to be used in this technique due to the important absorption of the electrons in the material. The formed image is shown either on a fluorescent screen or in a monitor or both.

It is convenient to divide a TEM system into three main components: the illumination system, the objective lenses, and the imaging system. The illumination system consists of an electron source (tungsten filaments) and the condenser lenses for focusing. It is necessary to use the electron beam in a vacuum environment, since electrons are very small and can be easily deflected by hydrocarbons or gas molecules present in the ambient. A series of pumps are used to accomplish an adequate vacuum for this purpose in the column. The electron beam is accelerated to an energy in the range 20-1000 keV, then the electron beam passes through a set of condenser lenses in order to produce a beam of electrons with the desired diameter. The objective lens and the specimen holder is where all the beam-specimen interactions take place.

The imaging system uses several lenses to magnify the image and to focus them on the fluorescent screen or computer display via a charge coupled detector (CCD) or a TV camera. A scheme of the TEM equipments used in this thesis is presented in Figure 2.6a (JEOL 1011 TEM). High-resolution transmission electron microscopy (HRTEM) is an imaging mode of the TEM system that allows for direct imaging of the atomic structure of the sample with a resolution in the 0.1 nm range [36]. In HRTEM the voltage at which electrons are accelerated is higher than in the TEM.

For sample preparation the nanocrystalline powders were dissolved in ethanol and sonicated for 10 min. Several drops of the resulting suspension were deposited on a 200 mesh copper grid coated with an amorphous thin carbon film.

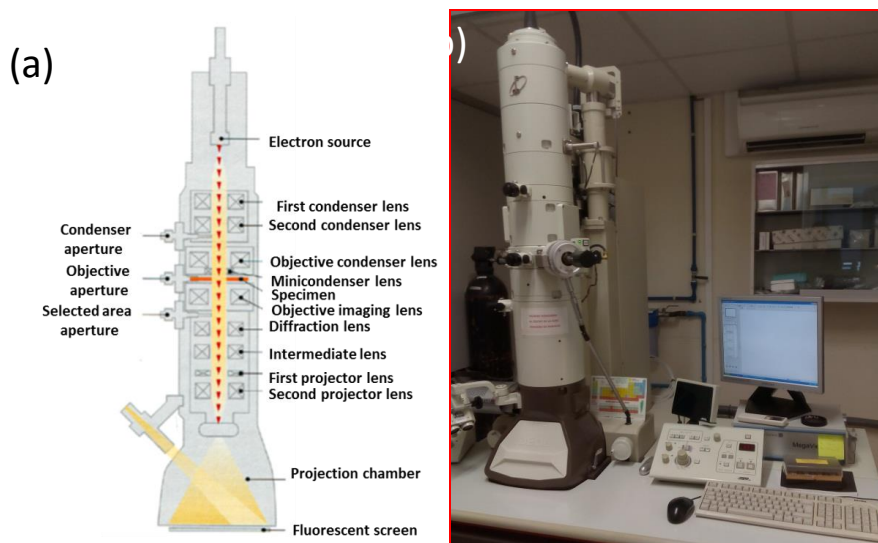


Figure 2.6. (a) Schematic representation of the JEOL 1011 transmission electron microscope system used in the thesis; (b) picture of this TEM system.

In this thesis we used a JEOL 1011 TEM equipment operating at an accelerating voltage of 100 kV. This equipment is available at the Servei de Recursos Científics i Tècnics, Universitat Rovira i Virgili, Tarragona (see Figure 2.6b). Also, TEM measurements were obtained with a JEOL 2000FXII microscope with an accelerating voltage of 200 kV, and high resolution HRTEM images were obtained with a JEOL model JEM-4000EX microscope, with an accelerating voltage of 400 kV available at the Centro Nacional de Microscopia Electronica, Universidad Complutense de Madrid.

2.3.2 Environmental scanning electron microscopy (ESEM)

To observe the surface of the sample, with high resolution, we can use the scanning electron microscopy (SEM) or environmental scanning electron microscopy (ESEM). SEM uses a focused beam of high-energy electrons to generate a variety of signals at the surface of solid specimens to reveal information about the sample, including external morphology and chemical composition. These signals include secondary electrons, backscattered electrons, characteristic X-rays, visible light photons, Auger electrons, and diffracted electrons. A schematic illustration of the electron beam interaction with the sample and the produced signals with the possible applications is presented in the Figure 2.6 [34].

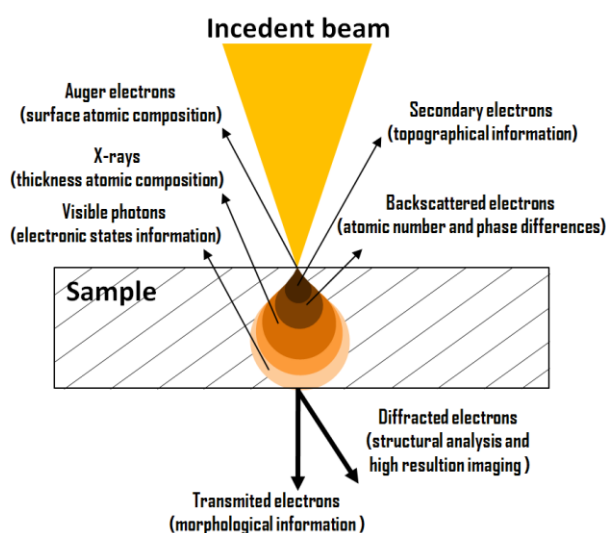


Figure 2.6. Electron beam interaction with the sample.

The incident electrons in SEM are generated by an electron gun using an emission from tungsten filaments. A positive electrical potential is applied to the anode and the filament (cathode) is heated by the beam of electrons produced. The positive potential accelerates electrons down the SEM column. Inside the column the electrons are focused by a series of lenses and coils and directed onto the desired point of the surface of the sample to visualize it. To get the final image, the electron beam scans the region of interest on the surface of the sample and the electrons of different kind emitted from the sample are detected for each position by an electron detector [34].

In this thesis we used an environmental scanning electron microscope (ESEM). It works under the same principle as SEM, but it uses multiple pressure limiting apertures (PLAs) that separate the sample chamber from the column. The sample chamber contains a low pressure

of gas. The primary electrons from the electron beam travel across the gas phase and interact with the surface of the sample, which release secondary electrons that interact with the gas phase producing additional secondary electrons. Also, the primary electrons interact with the gas molecules producing ions and additional electrons, which amplify the original secondary electron signal. In a non-conductive sample, the positive ions created are attracted to the sample surface, and effectively suppress charging effects. One of the main advantages is that the ESEM technique does not require sample preparation and allows to operate in “*wet mode*”, so it is not necessary to coat non-conductive samples with a conductive layer like in classical SEM. Thus, the original characteristics of the samples may be preserved for further testing or manipulation [37].

A FEI QUANTA 600 ESEM coupled to an Oxford Inca 3.0 microanalysis system from the Servei de Recursos Científics i Tècnics of the Universitat Rovira i Virgili was used to study the morphology of the obtained nanomaterials in this thesis. A schematic overview of the ESEM equipment and a picture of it are presented in Figure 2.7.

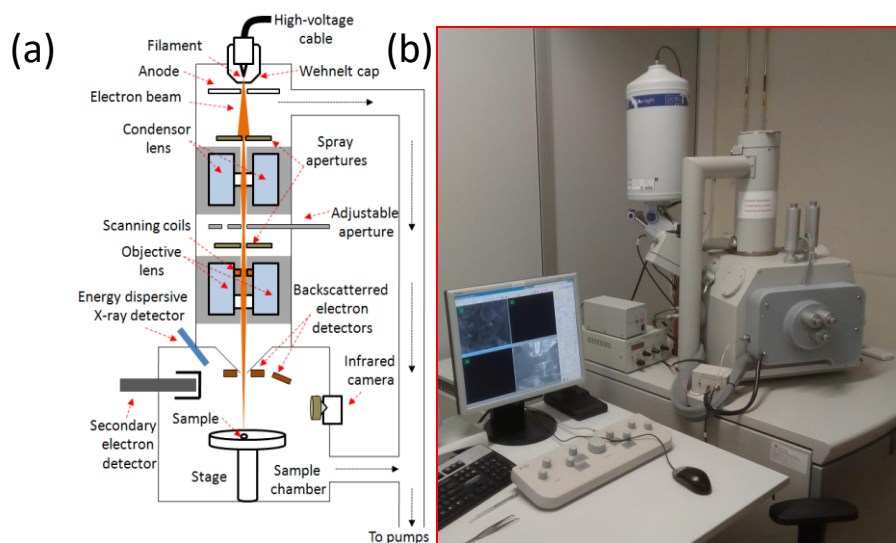


Figure 2.7. (a) Schematic representation of an ESEM system; (b) picture of the FEI Quanta 600 ESEM used in this thesis.

2.4 Spectroscopic techniques

2.4.1 Optical absorption

When light interacts with a material a number of events occur, including: (i) absorption; (ii) transmission; (iii) reflection and scattering. In the case of absorption, the

intensity of the light attenuation (dI) after passing a certain material with thickness (dx) can be written as:

$$dI = -\alpha I dx \quad (2.2)$$

where I is the light intensity at a distance x into the medium and α is called the absorption coefficient of the material. The integration of equation (2.2) gives us the Lambert-Beer law [38]:

$$I = I_0 e^{-\alpha x} \quad (2.3)$$

This law gives an exponential attenuation dependence correlating the intensity of the incoming light (I_0) to the thickness of the material (x).

Optical density (OD) is another important value that we can calculate experimentally using a spectrophotometer [39], and it can be written as:

$$OD = \log\left(\frac{I_0}{I}\right) \quad (2.4)$$

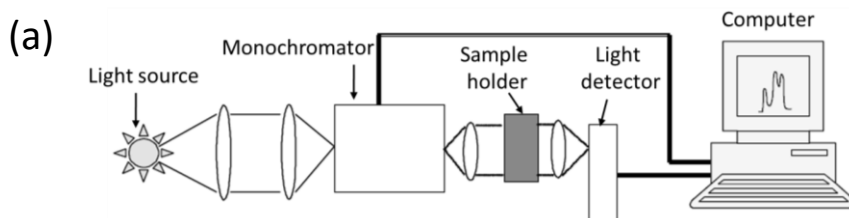
Correlating equations (2.3) and (2.4) the absorption coefficient can be estimated as:

$$\alpha = \frac{OD}{x \cdot \log(e)} = \frac{2.303 \cdot OD}{x} \quad (2.5)$$

Thus, by measuring the OD and knowing the sample thickness, the absorption coefficient can be determined.

A typical absorption measurement setup consists on the following elements (see Figure 2.8a.): (i) a light source; (ii) a monochromator; (iii) a sample holder; (iv) a light detector; (v) and finally a computer to display and record the absorption spectrum.

In this thesis the absorption measurements were carried out in a Varian Cary 500 Scan spectrometer (see Figure 2.8b), available at the laboratories of the FiCMA-FiCNA group at university Rovira i Virgili. It has two monochromators that can separate 1200 lines/mm in the UV-visible region and 300 lines/mm in the IR region of the electromagnetic spectrum. A deuterium lamp served as the light source in the UV region and a quartz halogen lamp for the visible-IR region. The light is detected by a photomultiplier in the UV-visible region and a PbS diode detector in the IR region.



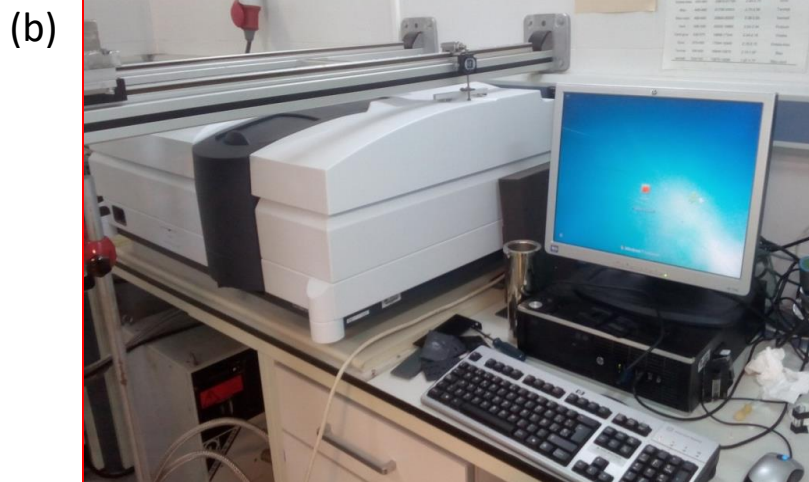


Figure 2.8. (a) Basic scheme of a typical setup for absorption measurements; (b) picture of the Varian Cary 500 Scan spectrometer used in this thesis.

2.4.2 Photoluminescence emission measurements

Luminescence can be considered as the inverse process of absorption. When light with an appropriate frequency is absorbed by a material, its electrons promote to excited states. After that, these electrons can return to the ground state or to a lower energy level existing in the energetic electronic diagram of the material. This de-excitation process produced by the spontaneous emission of photons is called luminescence. The excitation by photons, in general, and the later emission of radiation is called photoluminescence. Photoluminescence is divided into two categories: fluorescence and phosphorescence. Phosphorescence has longer emission lifetimes ($> 10^{-3}$ s) than fluorescence ($> 10^{-8}$ s) [39].

In a typical experiment, the sample of interest is excited with a lamp coupled to a monochromator for selecting the desired wavelength, or a laser beam. The emitted light is collected by a focusing lens and analyzed by means of a second monochromator coupled to a suitable detector connected to a computer.

Three kinds of setup were used in this thesis for photoluminescence emission measurements. In the first one, samples (luminescent nanoparticles) were placed in a heating stage Linkam THMS 600 to control the temperature of the samples, and there were excited with a laser with emission at 808 or 980 nm. The emission arising from the samples was collected by a set of optical lenses and dispersed in a JobinYvon HR 460 monochromator. A Hamamatsu PMTR 928 photomultiplier tube connected to a PerkinElmer DSP-7265 lock-in amplifier was used to detect and amplify the collected signal in the visible region of the electromagnetic

spectrum. The system was connected to a computer for recording the photoluminescence spectra. A scheme of this setup is shown in Figure 2.9.

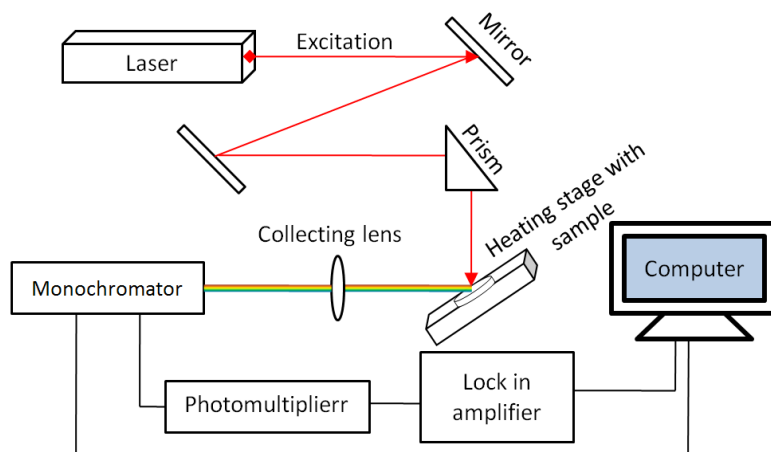


Figure 2.9. Scheme of the basic setup used for photoluminescence measurements.

The second setup, that we called luminescence microscope, consisted on the same heating stage Linkam THMS 600, where the samples were excited using the same lasers, but this time. The laser beam was focused on the sample by using a microscope objective. The emission was collected by the same microscope objective, and after passing a dichroic filter to eliminate the excitation wavelength, was sent either to a CCD camera for visualization of the emission generated by the sample or to an AVANTES AVS-USB2000 fiberoptic spectrometer or to an optical spectrum analyzer (OSA) Yokogawa AQ6373/AQ6375 for recording the emission spectra. The scheme of the setup is shown in Figure 2.10a. In this thesis we used two luminescence microscope setups, one available in the Fluorescence Imaging Group of the Universidad Autonoma de Madrid (Madrid) and another is available at the FiCMA-FiCNA laboratories of the Universidad Rovira i Virgili. A picture of these setups is shown in Figure 2.10 b and c, respectively.

The third kind of setup consisted on the homemade copper heating stage with attached thermocouples and connected to the temperature control. Nanoparticles were glued to the heating stage by means of conductive tape. Diode laser with emission at 800 nm was used as the excitation source. The laser beam was focused on the sample using a convex lens. The emission was collected by fiber at 45° with filter for complete elimination of the excitation wavelength. The signal was sent to Ocean Optics spectrometer connected to computer for recording of the spectrum. The scheme of this setup is shown in the Figure 2.10d. This kind of

setup is available in the laboratories of the physics department of Universidade de Aveiro and CICECO – Aveiro Institute of Materials, Portugal.

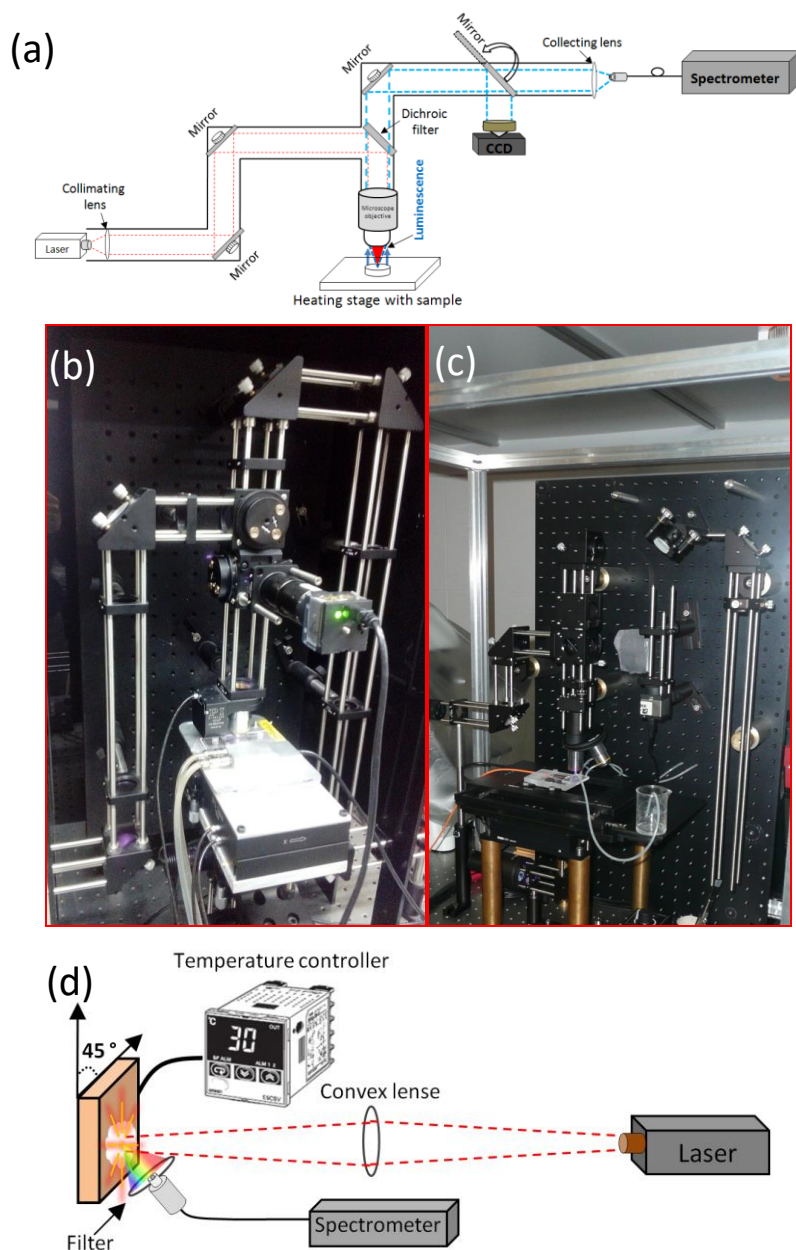


Figure 2.10. Scheme of the luminescence microscope setup used in this thesis. (b) picture of the luminescence microscope setups available (b) at the Fluorescence Imaging Group of the Universidad Autonoma de Madrid; and (c) at the FICMA-FICNA laboratories of the Universitat Rovira i Virgili. (d) Scheme of the setup available in the laboratories of the physics department of Universidade de Aveiro and CICECO, Portugal.

2.4.3 NIR imaging using Ln³⁺-doped nanoparticles

Optical imaging is emerging as promising noninvasive, real-time and high resolution modalities for the cancer detection [40]. The optical signals can provide molecular information of biological tissues and are related to the tumor anatomical structure as well as the tumor metabolism and biochemistry [41]. Among the optical imaging technologies, NIR fluorescence imaging has been attracted a lot of attention owing to its low absorption and autofluorescence from organisms and tissues in the NIR spectral range, which can minimize background interference, improve tissue depth penetration, image sensitively and noninvasively [42-44]. Also, much attention has been focused in recent years on the development of imaging agents with excitation and emission falling in the region of minimal tissue absorbance. Ln³⁺-doped nanoparticles have proved to be a potential tool for the NIR imaging in various *in vivo* and *ex vivo* experiments [45-47].

In this thesis we are using Nd³⁺-doped KGdW and Tm³⁺, Ho³⁺ co-doped KLuW nanoparticles as the agents for NIR imaging. The drop of dispersed nanoparticles in water with concentration of 0.5 mg/ml was placed between two microscopic slides. On top of the nanoparticles, chicken breast was placed as the materials to be imaged due to the comparable properties with human tissue [48]. The picture of the NIR imaging setup used in this thesis is illustrated in the Figure 2.11a, which is available in the Fluorescence Imaging Group of the Universidad Autonoma de Madrid (Madrid). It consists on the following pieces: continuous wave diode laser with 808 nm wavelength with variable power up to 10 W was used as an excitation source. The distance between laser to the sample was 5 cm producing the spot around ~ 3.5 cm. Signal was collected by Peltier cooled InGaAs infrared camera Xenics with attached filters wheel in order to collect emission of particular wavelength of interest and eliminate excitation laser. Finally, the recorded images were passed to computer. The scheme of the setup is presented in the Figure 2.11b.

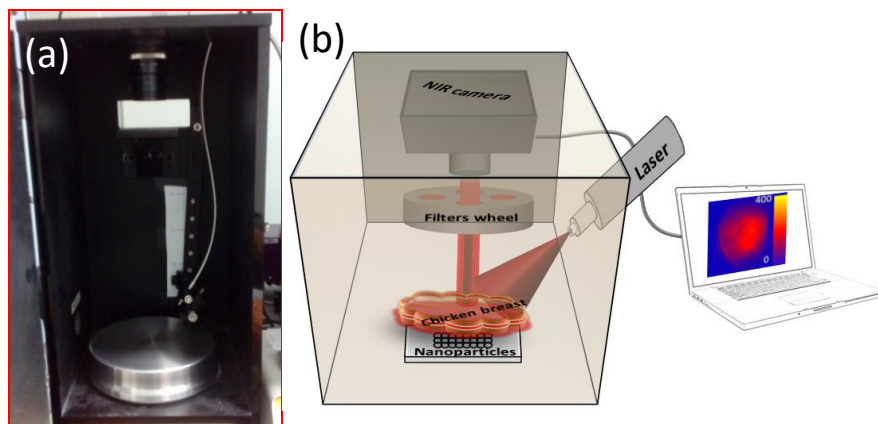


Figure 2.11. (a) Picture of the NIR imaging setup used in this thesis available at the Fluorescence Imaging Group of the Universidad Autonoma de Madrid; (b) scheme of the NIR imaging setup.

2.4.4 Measurements of an absolute intensity

To compare the absolute emission intensities of the samples in order to estimate their emission efficiencies the measurements were done using an integrating sphere. The scheme of the setup is shown in Figure 2.12a. The sphere is made from a diffusive reflection material, so the light generated inside the integrating sphere is spreaded evenly by multiple reflections over the entire sphere surface, ensuring that all the generated light is detected. This makes of the integrating sphere the ideal instrument for many applications to compare the emission properties of the samples including laser power, optical flux, radiance and reflectance measurements. The input and output ports of the integrating sphere can be equipped with fiber adapters. The detector port is equipped also with a baffle to avoid the direct exposure to the incident light.

To perform these measurements, powdered samples were placed in borosilicate bottom flat vials, slightly shaken to compact the powder, and placed inside a Labsphere 4GPS-020-SL integrating sphere (see Figure 2.12b). The samples were excited with a 200 μm core diameter fiber-coupled laser diode at 808 or 980 nm, depending on the type of samples to be analyzed. The laser beam was collimated to have the average spot size of 3 mm. The signal generated by the samples was collected using an AVANTES AVS-USB2000 fiberoptic spectrometer or an optical spectrum analyzer (OSA) Yokogawa AQ6373/AQ6375. This setup is available is available at the FicMA-FicNA laboratories of the Universidad Rovira i Virgili.

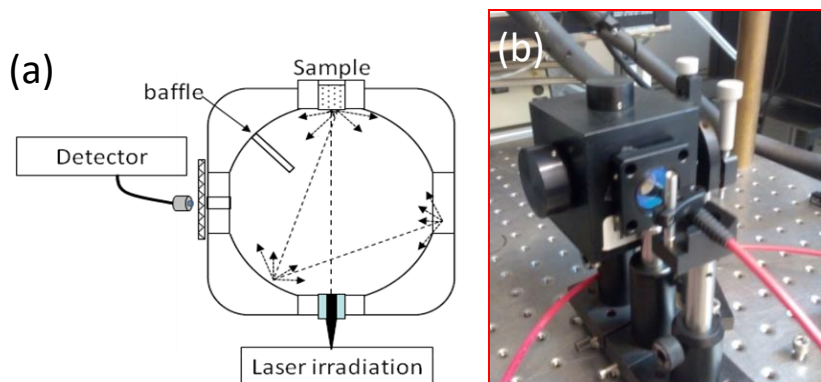


Figure 2.12. (a) Scheme of the integrating sphere setup and (b) picture of the Labsphere 4GPS-020-SL integrating sphere used in this thesis.

2.4.5 Lifetime measurements

When the material is excited by a pulsed excitation light source, relevant information on the kinetic behavior of luminescent excited states and intermediates [49]. The temporal evolution of the excited state follows a general rule of the form [50]:

$$\frac{dN(t)}{dt} = -A_T N(t) \quad (2.6)$$

where A_T is the total decay rate, which is written as: $A_T = A + A_{nr}$, where A and A_{nr} are being radiative and nonradiative rate, respectively. $N(t)$ is the density of excited centers at any time t [40]:

$$N(t) = N_0 e^{-A_T t} \quad (2.7)$$

where N_0 is the density of excited centers at $t=0$, just after the pulse of light has been absorbed. The emitted light intensity at a given time t , $I_{em}(t)$ is proportional to the density of centers de-excited per timeunit, and can be written as [39]:

$$I_{em}(t) = I_0 e^{-A_T t} \quad (2.8)$$

Here, the luminescence decay time, given as $\tau = 1/A_T$, represents the time in which the emitted intensity of the luminescence decays from its initial value to I_0/e and it can be obtained from the slope of the linear plot $\log I_{em}$ versus t [39].

In this thesis the measurements of the luminescence lifetime were performed as following, the samples were placed in the heating stage Linkam 600 and excited with a pulsed laser beam at 980 nm provided by an optical parametric oscillator (OPO) system Opotek Vibrant HE 355 II + UV with a pulse duration of 6 ns and a repetition frequency of 10 Hz. The

fluorescence light emitted by the samples was collected with a microscope objective, transferred to JobinYvon HR 460 monochromator and then detected using a Hamamatsu R928 photomultiplier. The decay curves were measured with a digital oscilloscope. An scheme of the setup used is shown in Figure 2.13, which is available at the FiCMA-FiCNA laboratories of the Universidad Rovira i Virgili.

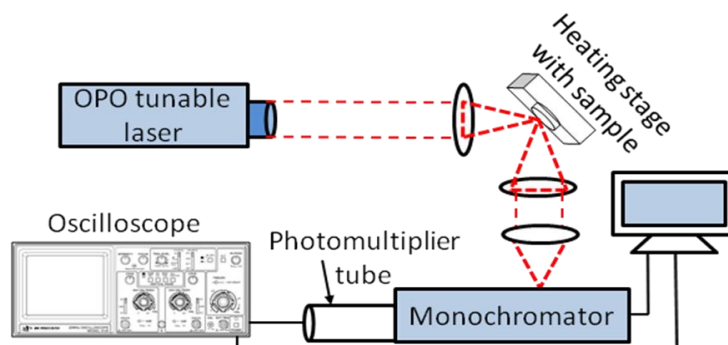


Figure 2.13. Scheme of the setup used for luminescence lifetime temperature dependent measurements.

2.5 Photothermal conversion efficiency

Heat can be used as an instrument to increase death rate in cells, useful to treat diseases as cancer [50]. However, heat can also affect negatively the health tissues as the above 321 K necrosis is induced. But if the amount of heat is controlled, it may be used to treat abnormal cells, known as hyperthermia treatment [51]. Thus, predicting and controlling the temperature distribution in a body region during hyperthermia treatment is mandatory [52]. Materials which are able to absorb the light energy and efficiently convert it into thermal energy called photothermal converters. Among the different type of the photothermal converters, graphene-based materials emerging as promising candidate with the good photothermal conversion properties [53-56].

In this thesis we study the photothermal conversion properties of graphene and graphene oxide and determined their efficiency using time-constant method. A scheme of the setup for the photothermal conversion efficiency measurements using time constant method is shown in Figure 2.14. The samples were placed in a glass cuvette with dimensions 2×1 cm and solutions were irradiated with fiber-coupled diode laser with 808 and 980 nm wavelength. The laser beam was focused on the cuvette with a collimating lens, allowing a beam diameter of 5 mm. The temperature evolution was recorded by a digital multimeter connected to a small Pt-100 thermo-resistor located inside of the cuvette, and finally the data were sent to computer. After around 10 min of irradiation, the samples reached the thermal equilibrium, and thus the

maximum temperature for a particular laser power irradiation. After that, laser irradiation was switched off for allowing the sample to cool down to the room temperature while data were recorded in the cooling cycle.

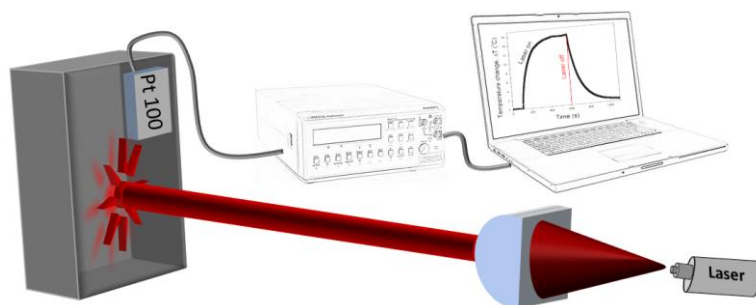


Figure 2.14. Scheme of the setup for photothermal conversion efficiency measurements using time constant method.

2.6 References

1. Levy, D., and Zayat, M. (2015). *The Sol-Gel Handbook* (Weinheim: Wiley-VCH Verlag GmbH & Co.).
2. Brinker, C. J., and Scherer, G. W. (1990). *Sol-Gel science the physics and chemistry of sol-gel processing* (London: Academic Press Inc.).
3. Pechini, M. P.(1967). *Method of preparing lead and alkaline earth titanates and niobates and coating method using the same to form a capacitor*. US patent 3330697.
4. Galceron, M., Pujol, M. C., Aguilo, M., Diaz, F. (2007). *Sol-gel modified Pechini method for obtaining nanocrystalline $KRE(WO_2)_4$ ($RE = Gd$ and Yb)*. J. Sol-Gel Sci. Techn. 42, 79–88.
5. Petrov, V., Pujol, M. C., Mateos, X., Silvestre, O., Rivier, S., Aguilo, M., Sole, R. M., Liu, J., Griebner, U., and Diaz, F. (2007). *Growth and properties of $KLu(WO_4)_2$, and novel ytterbium and thulium lasers based on this monoclinic crystalline host*. Laser & Photonics Reviews 1, 179-212.
6. Schäfer, O., Ghobarkar, H., and Knauth, P. (2004). *Hydrothermal synthesis of nanomaterials* (New York:Kluwer Academic Publishers).
7. Byrappa K., and Yoshimura, M. (2013). *Handbook of Hydrothermal technology 2nd edition* (Oxford: Elsevier Inc).
8. Calderon-Villajos, R., Zaldo, C. and Cascales, C. (2012). *Enhanced upconversion and white light luminescence in SiO_2 -coated lanthanide-doped $GdVO_4$ hydrothermal nanocrystals*. Nanotechnol. 23, 505205-505210.
9. Zagumennyi, A. I., Mikhailov, V. A., Vlasov, V. I., Sirotkin, A. A., Podreshetnikov, V. I., Kalachev, Yu. L., Zahartsev, Yu. D., Kutovoi, S. A., and Shcherbakov I. A. (2003). *Diode-pumped lasers based on $GdVO_4$ crystal*. Laser phys. 13, 311-318.
10. Misiak, M., Prorok, K., Cichy, B., Bednakiewicz, A., and Strek, W. (2013). *Thulium concentration quenching in the up-converting $\alpha-Tm^{3+}/Yb^{3+}$ $NaYF_4$ colloidal nanocrystals*. Opt. Mater. 35, 1124-1128.
11. Chen, G. Y., Liu, H. C., Liang, H. J., Somesfalean, G., Zhang, Z. G. (2008). *Upconversion emission enhancement in Yb^{3+}/Er^{3+} -codoped Y_2O_3 nanocrystals by tridoping with Li^{3+} ions*. J. Phys. Chem. C 112, 12030–12036.

12. Jiang, L., Xiao, S., Yang, X., Ding, J., Dong, K. (2012). *Enhancement of up-conversion luminescence in $Zn_2SiO_4:Yb^{3+}, Er^{3+}$ by co-doping with Li^{3+} or Bi^{3+}* . Appl. Phys. B: Laser Opt. 107, 477–481.
13. Chen, G., Yang, C., Prasad, P. N. (2013). *Nanophotonics and nanochemistry: controlling the excitation dynamics for frequency up- and down-conversion in lanthanide-doped nanoparticles*. Acc. Chem. Res. 46, 1474-1486.
14. Wang, F., Deng, R., Wang, J., Wang, Q., Han, Y., Zhu, H., Chen, X., and Liu, X. (2011). *Tuning upconversion through energy migration in core-shell nanoparticles*. Nat. Mater. 10, 968-973.
15. Wang, F., Wang, J., and Liu, X. (2010). *Direct evidence of surface quenching effect on size-dependent luminescence of upconversion nanoparticles*. Angew. Chem. Int. Ed. 49, 7456-7460.
16. Mai, H. X., Zhang, Y. W., Sun, L. D., and Yan, C. H. (2007). *Highly efficient multicolor up-conversion emissions and their mechanisms of monodisperse $NaYF_4$ core and core-shell-structured nanocrystals*. J. Phys. Chem. C 111, 13721-13729.
17. Cozzoli, P. D., Pellegrino, T., and Manna, L. (2006). *Synthesis, properties and perspectives of hybrid nanocrystal structures*. Chem. Soc. Rev. 35, 1195-1208.
18. Driver, M. (2012). *Coatings for biomedical applications* (Cambridge:Woodhead Publishing Limited).
19. Santra, S., Yang, H., Dutta, D., Stanley, J. T., Holloway, P. H., Tan, W., Moudgil, B. M., Mericle, R. A. (2004). *TAT conjugated, FITC doped silica nanoparticles for bioimaging applications*. Chem. Commun. 24, 2810-2811.
20. Qhobosheane, M., Santra, S., Zhang, P., Tan, W. (2001). *Biochemically functionalized silica nanoparticles*. Analyst 126, 1274-1278.
21. Komarneni, S., D'Arrigo, M. C., Leonelli, C., Pellacani, G. C., and Katsuki, H. (1998). *Microwave-hydrothermal synthesis of nanophase ferrites*. J. Am. Ceram. Soc. 81, 3041-3043.
22. Yoshimura, M., Yoo, S. E., Hayashi, M., and Ishizawa, N. (1989). *Preparation of $BaTiO_3$ thin film by hydrothermal electrochemical method*. J. Appl. Phys. 28, 2007-2009.
23. Wang, Y., Tang, X., Yin, L., Huang, W., and Gedanken, A. (2000). *Sonochemical synthesis of mesoporous titanium oxide with wormhole-like framework structures*. Adv. Mater. 12, 1183-1186.

24. Komarneni, S., Roy, R., Li, Q.H. (1992). *Microwave-hydrothermal synthesis of ceramic powders*. Mater. Res. Bull. 27, 1393-1405.
25. Komarneni, S., Li, Q., Stefansson, K. M., Roy, R. (1993). *Microwave-hydrothermal processing for synthesis of electroceramic powders*. J. Mater. Res. 8, 3176–3183.
26. Komarneni, S., Li, Q. H., Roy, R. (1994). *Microwave-hydrothermal processing for synthesis of layered and network phosphates*. J. Mater. Chem. 4, 1903-1906.
27. Chen, X., Liu, Y., Tu, D. (2014). *Lanthanide-doped luminescent nanomaterials from fundamentals to bioapplications* (Berlin:Springer-Verlag).
28. Page, R. H., Schaffers, K. I., Waide, P. A., Tassano, J. B., Payne, S. A., Krupke, W. F., and Bischel, W. K. (1998). *Upconversion-pumped luminescence efficiency of rare-earth-doped hosts sensitized with trivalent ytterbium*. J. Opt. Soc. Am. B 15, 996-1008.
29. Kramer, K. W., Biner, D., Frei, G., Güdel, H. U., Hehlen, M. P., and Luethi, S. R. (2004). *Hexagonal sodium yttrium fluoride based green and blue emitting upconversion phosphors*. Chem. Mater. 16, 1244-1251.
30. Wang, M., Abbineni, G., Clevenger, A., Mao, C., and Xu, S. (2011). *Upconversion nanoparticles: synthesis, surface modification and biological applications*. Nanomed. Nanotechnol. 7, 710-729.
31. Phillips, D. (1979). *William Lawrence Bragg. 31 March 1890 – 1 July 1971*. Biogr. Mems Fell. R. Soc. 25, 74-143.
32. Suryanarayana, C., and Norton, M. G. (1998). *X-Ray Diffraction: A Practical Approach* (New York: Springer).
33. Ferraro, J. R. (2003). *Introductory Raman Spectroscopy* (Elsevier).
34. Amelinckx, S., van Dyck, D., van Landuyt, J., van Tendeloo, G. (1997). *Electron microscopy: principles and fundamentals* (Weinheim: Wiley).
35. Hawkes, P. W. (1990). *Ernst Ruska*. Phys. Today 43, 84-85.
36. Klabunde, K. J. (2001). *Introduction to nanotechnology in nanoscale materials in chemistry* (New York: John Wiley & Sons).
37. Love, G., Nicholson, W. A. P., Armigliato, A. (1998). *Modern developments and applications in microbeam analysis* (New Delhi: Springer-Verlag).
38. Lambert, J. H. (1760). *On the measure and gradations of light, colors, and shade* (Augsburg: Augusta Vindelicorum).
39. Sole, J. G., Bausa, L. E., and Jaque, D. (2005). *An Introduction to the Optical Spectroscopy of Inorganic Solids* (West Sussex:John Wiley and Sons).

40. Kosaka, N., Ogawa, M., Choyke, P. L., Kobayashi, H. (2009). *Clinical implications of near-infrared fluorescence imaging in cancer*. *Future Oncol.* 5, 1501–1511.
41. Choy, G., Choyke, P., Libutti, S. K. (2003). *Current advances in molecular imaging: noninvasive in vivo bioluminescent and fluorescent optical imaging in cancer research*. *Mol. Imaging* 2, 303-312.
42. Hilderbrand, S. A., Weissleder, R. (2010). *Near-infrared fluorescence: application to in vivo molecular imaging*. *Curr. Opin. Chem. Biol.* 14, 71-79.
43. Pysz, M. A., Gambhir, S. S., Willmann, J. K. (2010). *Molecular imaging: current status and emerging strategies*. *Clin. Radiol.* 65, 500-516.
44. Frangioni, J. V. (2003). *In vivo near-infrared fluorescence imaging*. *Curr. Opin. Chem. Biol.* 7, 626-634.
45. Naccache, R., Rodriguez, E. M., Bogdan, N., Sanz-Rodriguez, F., de la Cruz, M. C. I., de la Fuente, Á. J., Vetrone, F., Jaque, D., Sole, J. G., and Capobianco, J. A. (2012). *High resolution fluorescence imaging of cancers using lanthanide ion-doped upconverting nanocrystals*. *Cancers* 4, 1067-1105.
46. Rocha, U., Kumar, K. U., Jacinto, C., Ramiro, J., Caamaño, A. J., Sole, J. G., and Jaque, D. (2014). *Nd³⁺ doped LaF₃ nanoparticles as self-monitored photo-thermal agents*. *Appl. Phys. Lett.* 104, 053703-053705.
47. Rocha, U., Kumar, K. U., Jacinto, C., Villa, I., Sanz-Rodriguez, F., de la Cruz, M. C. I., Juarranz, A., Carrasco, E., van Veggel, F. C. J. M., Bovero, E., Sole, J. G., and Jaque, D. (2014). *Neodymium-doped LaF₃ nanoparticles for fluorescence bioimaging in the second biological window*. *Small* 10, 1141-1154.
48. Marquez, G., Wang, L. V., Lin, S. P., Schwartz, J. A., and Thomsen, S. L. (1998). *Anisotropy in the absorption and scattering spectra of chicken breast tissue*. *Appl. Opt.* 37, 798-804.
49. Lakowicz, J. R. (2006). *Principles of Fluorescence Spectroscopy, 3rd ed.* (New York: Kluwer Academic/Plenum Publishers).
50. Pustovalov, V. K., Astafyeva, L. G., and Fritzsche, W. (2013). *Selection of thermo-optical parameter of nanoparticles for achievement of their maximal thermal energy under optical irradiation*. *Nano Energy* 2, 1137–1141.
51. Jaque, D., Maestro, L. M., del Rosal, B., Haro-Gonzalez, P., Benayas, A., Plaza, J. L., Rodriguez, E. M., and Sole, J. G. (2014). *Nanoparticles for photothermal therapy*. *Nanoscale* 6, 9494-9560.

52. Lepock, J.R., Frey, H. E., Rodahl, A. M., and Kruuv, J. (1988). *Thermal analysis of CHL V79 cells using differential scanning calorimetry: implications for hyperthermic cell killing and the heat shock response*. *J Cell Physiol*. 137, 14–24.
53. Wu, M. C., Deokar, A. R., Liao, J. H., Shih, P. Y., and Ling, Y. C. (2013). *Graphene-based photothermal agent for rapid and effective killing of bacteria*. *ACS Nano* 7, 1281–1290.
54. Yang, K., Zhang, S., Zhang, G., Sun, X., Lee, S. T., and Liu, Z. (2010). *Graphene in mice: ultrahigh in vivo tumor uptake and efficient photothermal therapy*. *Nano Lett.* 10, 3318–3323.
55. Shi, X., Gong, H., Li, Y., Wang, C., Cheng, L., Liu, Z. (2013). *Graphene-based magnetic plasmonic nanocomposite for dual bioimaging and photothermal therapy*. *Biomaterials* 34, 4786-4793.
56. Wang, Y., Wang, H., Liu, D., Song, S., Wang, X., Zhang, H. (2013). *Graphene oxide covalently grafted upconversion nanoparticles for combined NIR mediated imaging and photothermal/photodynamic cancer therapy*. *Biomaterials* 34, 7715-7724.

CHAPTER 3

Luminescence nanothermometry in the visible:

I. New detection techniques

By analyzing the available detection techniques for luminescence nanothermometry, which were described in Chapter 1, we tried to make a substantial contribution in using new modes of detection that can diversify the techniques used in luminescence nanothermometry, specially concerning upconversion nanoparticles. In this chapter we present a new possibility of temperature determination in biological systems by using lifetime-based nanothermometry in upconversion nanoparticles. We demonstrate how $\text{Er}^{3+}, \text{Yb}^{3+}:\text{NaY}_2\text{F}_5\text{O}$ nanocrystals present a higher thermal sensitivity than the $\text{Er}^{3+}, \text{Yb}^{3+}:\text{NaYF}_4$ ones and that their lifetime thermal coefficient is comparable to those corresponding to other nano-sized luminescent systems already used for high resolution lifetime fluorescence thermal sensing. We also evaluated the potential use of $\text{Er}^{3+}, \text{Yb}^{3+}:\text{NaY}_2\text{F}_5\text{O}$ nanoparticles as lifetime-based thermal probes by providing the first experimental evidence on sub-tissue lifetime fluorescence thermal sensing by using up-conversion nanoparticles in an *ex vivo* experiment. Also, we present a thermochromic phosphor $\text{Tm}^{3+}, \text{Yb}^{3+}\text{Co}$ -doped $\text{GdVO}_4@\text{SiO}_2$ core-shell nanoparticles, that has the ability to change the color of the upconversion emission arising from nanoparticles, from blue to deep red as a function of temperature. Thus, by using these nanoparticles, temperature measurements can be done through the detection of the change of color of the emission. To show the potentiality of our nanothermometer, we monitored the heating process produced by the Joule effect in a

Chapter 3 Luminescence nanothermometry in the visible: I. New detection techniques

Pt wire, 50 μm in diameter, with thermal and temporal resolutions of ± 0.1 K and < 16 ms, respectively.

Finally, we observed that the systems used up to now to measure the spectra from which the luminescence intensity ratio as a function of temperature is calculated demand to use bulky and relatively costly equipment such as monochromators, luminescence detectors (photomultiplier tubes, CCD cameras, etc.), lock-amplifiers, oscilloscopes, etc. Furthermore, also observed that recording an emission spectrum requires some time, during which the temperature of the sample might change. Taking this in mind we developed a low-cost, compact and non-invasive thermometric setup that would overcome these limitations. Our setup uses a digital color sensor able to capture simultaneously the emission in the blue, green and red region of electromagnetic spectrum, coupled to an optical system that focused the excitation light onto the luminescent nanoparticles and collects their emission. The potentiality of such non-invasive thermometer was proved in two kinds of upconversion nanoparticles, $\text{Er}^{3+}, \text{Yb}^{3+}:\text{NaYF}_4$ and Yb^{3+} -sensitized Tm^{3+} -doped GdVO_4 that operate in two different temperature ranges. Also, we developed PDMS/luminescent nanoparticles composites that together with this setup might allow temperature sensing in microfluidic devices.

Paper I

Savchuk, Ol. A.; Haro-González, P.; Carvajal J. J.; Jaque, D.; Massons, J.; Aguiló, M.; and Díaz, F. *Er:Yb:NaY₂F₅O up-converting nanoparticles for sub-tissue fluorescence lifetime thermal sensing* (2014) *Nanoscale* 6, 9727-9733.

Chapter 3 **Luminescence nanothermometry in the visible: I. New detection techniques**

Er:Yb:NaY₂F₅O up-converting nanoparticles for sub-tissue fluorescence lifetime thermal sensing

Ol.A. Savchuk,^a P. Haro-González,^b J.J. Carvajal,^{a,*} D. Jaque^b, J. Massons,^a M. Aguiló^a and F. Díaz^a

Non-contact thermometry is essential in biomedical studies requiring thermal sensing and imaging with high thermal and spatial resolutions. In this work we report on the potential use of Er:Yb:NaYF₄ and Er:Yb:NaY₂F₅O up-conversion nanoparticles as thermal sensors by means of lifetime based luminescent thermometry. We demonstrate how Er:Yb:NaY₂F₅O nanocrystals present a higher thermal sensitivity than Er:Yb:NaYF₄ ones and that their lifetime thermal coefficient is comparable to those corresponding to other nano-sized luminescent systems already used for high resolution lifetime fluorescence thermal sensing. We evaluate the potential use of Er:Yb:NaY₂F₅O nanoparticles as lifetime based thermal probes by providing the first experimental evidence on sub-tissue lifetime fluorescence thermal sensing by using up-conversion nanoparticles in an *ex vivo* experiment.

Chapter 3 Luminescence nanothermometry in the visible: I. New detection techniques

A. Introduction

Almost all physical, chemical and biological processes are temperature dependent, making accurate temperature knowledge essential for their control and understanding. There are many areas of industry where the temperature measurements are essential, such as metallurgical, glass manufacturing, material modeling, dairy products and, in general, food manipulation and testing. In most of these applications contact-based temperature measurements (using thermocouples, thermistors or resistance thermometers) are not applicable.¹ Non-contact thermometry becomes even more critical in biomedical studies at cellular level that simultaneously require thermal sensing and imaging with high thermal and spatial resolutions (below 1 °C and 1 μm, respectively). The simultaneous requirement of high resolution non-contact thermal sensing is, in this case, required due to the fact that a large variety of cellular events, such as cell division and dynamics, are marked by intracellular temperature changes of few degrees that occur at around 37 °C.² In addition, cellular pathogenesis of cancer and other diseases are characterized by heat production, so that high resolution thermal sensing could, in principle, be used as a diagnosis tool for early detection. Furthermore, heating of biological systems (including malignant tumors) above 45 °C lead, among many other processes, to denaturation of biological molecules causing the necrosis of cells and tissues.³ This effect can be used to develop thermal treatments in which dynamical temperature monitoring is essential to keep collateral damage at minimum. High resolution intracellular thermal sensing would, therefore, provide understanding and control over a great variety of cellular events also opening new opportunities for the development of novel diagnostic and therapeutic techniques.

As commented above, temperature sensing at cellular level or inside biosystems (sub-tissue thermal sensing), implies the complete absence of physical contact so that the original dynamics of the system are not modified by the measuring procedure itself. One of the most used non-contact thermal sensing methods is infrared thermometry (based on the estimation of temperature from an appropriate calibration of the black-body radiation). Despite the good results obtained with this technique, it has some drawbacks such as their low spatial resolution for *in vitro* applications (it works with wavelength radiations close to 10 μm) and the ability of measuring only “surface” temperatures. An excellent alternative is that given by luminescent nanothermometry (LNT), which takes advantage of the sensitivity of the temperature-dependent emission of luminescent nanomaterials.^{4, 5} Recent works have demonstrated how LNT can be efficiently used for thermal sensing in the biological temperature range (10 and 60 °C) by using a great variety of nanostructured luminescent materials ranging from semiconductor quantum dots to organic compounds.⁴⁻⁸ LNT could, depending on the material, offer relatively high sensitivities and spatial resolutions with short acquisition times, even in biological fluids, strong electromagnetic fields and fast-moving objects.⁹⁻¹³ Among the different systems proposed up to now for LNT, nanomaterials doped with lanthanide ions play an important role, due to their intrinsic advantages such as relatively large fluorescence lifetimes, good chemical and physical stabilities, narrow emission lines and so on.¹⁴⁻¹⁹

Among the different LNT modalities, lifetime based LNT (hereafter LT-LNT) is of spectral relevance. LT-LNT is said to be used when the temperature of the nanoprobe is estimated from the analysis of its fluorescence lifetime that, consequently, should be strongly temperature dependent. This approach has several advantages when compared with intensity based approaches (those in which temperature is

estimated from changes in fluorescence intensity emitted by nanoprobes). LT-LNT eliminates problems related with non-controllable spatial fluctuations of the fluorescence intensity that could be due to a large number of causes including non-homogeneous distribution of nanoprobes, uncontrolled motion of nanoprobes or bio-components, shading and light distribution of the sample, among others. Since, in a first order approximation, fluorescence lifetime does not depend on the local concentration of luminescent probes all these inconveniences are overcome by using the LT-LNT approach. Furthermore, LT-LNT avoids the necessity of acquisition of the whole luminescence spectra (a time consuming procedure). When this is associated to the requirement of high spatial resolution, which lead to low signal levels and long acquisition times in intensity based techniques, the short measuring times required by LT-LNT minimizes the possibility of laser-induced local heating in the system under investigation. In LT-LNT measurements, the signal from which the temperature will be deduced can be acquired at a time interval on the order of the luminescence lifetime, typically in the range of nanoseconds to milliseconds. Finally, it should also be mentioned that this technique can be used for high temperature measurements avoiding the undesired contributions of the black body radiation.²⁰⁻²⁴

Most of lanthanide-based luminescent nano-materials emits through the so-called down-conversion processes, in which UV or high energy visible radiations are used as the excitation source to obtain emissions at longer wavelengths. The use of short wavelength excitation sources is due the presence of autofluorescence, due to partial absorption by tissues.^{25, 26} Autofluorescence leads to a fluorescence background that can mask the signal emitted by luminescent nanoparticles and can also damage the biological tissues.²⁷⁻²⁹ The alternative use of up-conversion nanoparticles (UCNPs), which exhibit efficient visible emission after excitation with near infrared light, can overcome these problems and also can provide a dual function of imaging and temperature sensing at the nanoscale.³⁰⁻³⁵

Up to now, there are in the literature a large number of lanthanide doped nanomaterials capable of efficient two-photon emission.^{15, 36-39} Among all of them, Er:Yb doped biocompatible nanocrystals are of special relevance due, principally, to the very efficient energy transfer process between Yb³⁺ and Er³⁺ ions that in combination with the high absorption cross-section at the pumping wavelength (980 nm) result in a strong up-conversion visible emission obtained under infrared excitation.^{30, 36, 40} Due to all these properties Er:Yb doped NPs have been successfully used as UCNPs with outstanding properties in bioimaging experiments.^{33, 37-39} In addition, the potentiality of Er:Yb UCNPs for LNT in the biological range has been recently demonstrated by Vetrone et al. who measured the internal temperature of living HeLa cells incubated with Er:Yb:NaYF₄ UCNPs by extracting the intracellular temperature from an appropriate spectral analysis of their two photon emission.¹⁴ In addition, Fischer et al. sensed temperatures in human embryo kidney cells using the same nanoparticles at 18 °C and 33 °C through confocal fluorescence microscopy images of the green and red emissions of Er³⁺ in these NPs and comparing their intensities.⁴¹

However, up to now thermal sensing by using UCNPs has been only obtained from the spectral analysis of their fluorescence spectrum. In particular ratiometric fluorescent thermal sensing in Er:Yb doped nanoparticles are based on the suitable energy gap between the ²H_{11/2} and ⁴S_{3/2} energy levels of Er³⁺ that are thermally coupled leading to two fluorescence bands at around 530 nm where relative intensity has a marked temperature dependence around 37°C.⁴² In this work we demonstrate, for the first time up to

Chapter 3 Luminescence nanothermometry in the visible: I. New detection techniques

the best of our knowledge, on the use of Er:Yb UCNPs as LT-LNT thermal probes (i.e. by using their fluorescence lifetime instead of the spectral properties of their visible emission bands). Proof of concept has been demonstrated in both Er:Yb:NaYF₄ and Er:Yb:NaY₂F₅O UCNPs. We demonstrate how Er:Yb:NaY₂F₅O nanocrystals present a larger thermal sensitivity than Er:Yb:NaYF₄ nanoparticles, due to the marked temperature dependence of their fluorescence lifetime. The potential use of Er:Yb UCNPs for lifetime based fluorescent thermal sensing is evaluated by performing *ex vivo* experiments. We provide the first experimental evidence on sub-tissue lifetime fluorescence thermal sensing by using UCNPs.

B. Experimental

Hexagonal Er:Yb:NaYF₄ and Er:Yb:NaY₂F₅O nanoparticles were provided by Boston Applied Technology. The size and morphology of Er:Yb:NaYF₄, Er:Yb:NaY₂F₅O nanoparticles were determined by using a Transmission electron microscope (TEM) JEOL JEM-1011 operating with an accelerating voltage of 100 kV. In addition, and for the sake of comparison we have also investigated the temperature dependence of the fluorescence lifetime of Er:Yb:NaYF₄ nanoparticles synthesized by ourselves through the hydrothermal method.⁴³ The TEM images of these nanoparticles have been also included in Figure 1. As can be observed the size distribution and homogeneity, and their dispersion in the solvent, have been improved to respect those provided by Boston Applied Technology.

For luminescence decay-time experiments, Er:Yb:NaYF₄ and Er:Yb:NaY₂F₅O nanoparticles were excited at 980 nm with an optical parametric oscillator from Opotek (Vibrant HE 355 II+UV) with a pulse duration of 6 ns and a repetition frequency of 10 Hz. The fluorescence light emitted by the sample was collected with a microscope objective (10X), transferred to the monochromator for the selection of specific wavelengths, and then detected using a Hamamatsu R928 photomultiplier. The decay curves of the 545 nm and 660 nm emitted signals (generated from the ⁴S_{3/2} and ⁴F_{9/2} excited states, respectively) were measured with a digital oscilloscope.

For lifetime thermal sensing experiments, Er:Yb:NaYF₄, Er:Yb:NaY₂F₅O nanoparticles were introduced into a Linkam THMS 600 heating stage, with temperature controlled by thermocouples connected to the heating stage. After calibration, Er:Yb:NaY₂F₅O nanoparticles were dispersed in distilled water and injected into a fresh chicken breast. A 1090 nm continuous wave laser (pump laser) was used for heating the chicken breast with a spot size of 1 cm². Due to the non-vanishing absorption coefficient of tissue at this wavelength, the 1090 nm focused beam is expected to produce a relevant local heating. A 980 nm pulsed diode laser (probe laser) was focused in the injection, spatially overlapping with the heating spot. This probe beam is used as excitation source for the NPs. The generated fluorescence by the nanoparticles was collected by the same objective and after passing the selected filters was focused into the photomultiplier tube connected to the digital oscilloscope.

C. Results and discussion

Transmission electron microscope (TEM) images of the Er:Yb:NaYF₄ and Er:Yb:NaY₂F₅O NPs used in this work are shown in **Figure 1**. Er:Yb:NaYF₄ nanoparticles have a more spherical shape with a mean diameter of ~20 nm (see inset in **Figure 1a**). Instead, Er:Yb:NaY₂F₅O nanocrystals have rod like morphologies (see inset in **Figure 1b**) ~250 nm in length and ~70-80 nm in diameter, as can be seen from the histograms provided, in which we analyzed

statistically the distribution of sizes of those nanoparticles (see **Figures 1d** and **e**). However, as can be seen in the low magnification TEM images in **Figures 1a** and **b**, these particles tend to be agglomerated, especially in the case of Er:Yb:NaYF₄, with mean sizes for these agglomerates of ~350 nm (see histogram provided in **Figure 1c**). At this point it should be noted that the morphological characteristics of the samples used in this work can be improvable but we state that their quality is good enough to provide the scientific community with a trustable “proof on concept”.

The potential use of Er:Yb UCNPs as lifetime thermal sensors has been firstly evaluated by measuring the temperature induced variation, in the 25-60 °C biological range, of the ⁴S_{3/2} fluorescence lifetime. **Figures 2 (a,b)** show the decay curves of both Er:Yb:NaYF₄ and Er:Yb:NaY₂F₅O nanoparticles as obtained at room temperature and at 60 °C. In both cases, it is observed how the ⁴S_{3/2} fluorescence lifetime decreases with temperature. However, the ⁴S_{3/2} temperature induced lifetime reduction in Er:Yb:NaY₂F₅O UCNPs is more evident (see **Figure 2(b)**). The origin of the observed temperature induced lifetime reduction is not clear at this point but it is very likely due to consequence of the activation of phonon-assisted processes and of multiphonon decays driven by temperature increments.¹⁷ Both effects cause an increase in the net de-excitation probability of the emitting levels and, thus, to a decrease in its luminescence lifetime.^{44, 45}

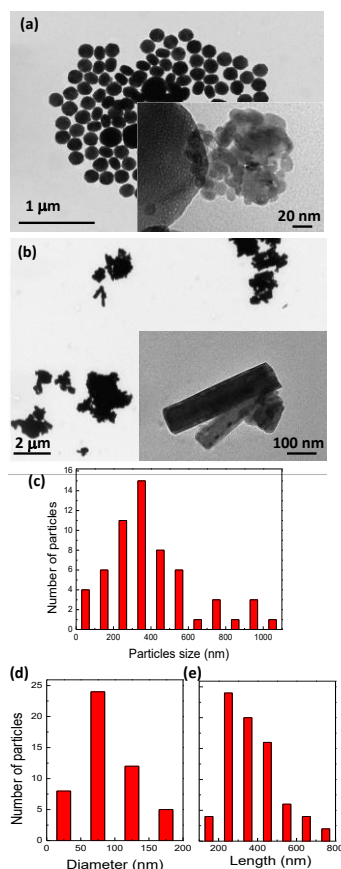


Fig 1. TEM images of (a) Er:Yb:NaYF₄ and (b) Er:Yb:NaY₂F₅O nanoparticles. Histograms showing (c) the mean sizes of the

Chapter 3 Luminescence nanothermometry in the visible: I. New detection techniques

aggregates of Er:Yb:NaYF₄ nanoparticles and (d,e) the diameter and lengths of the Er:Yb:NaY₂F₅O nanorods.

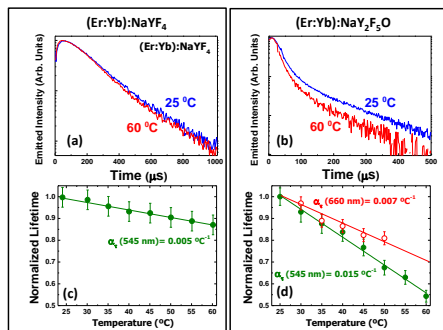


Fig 2 Fluorescence decay curves of the 545 nm emission line of (a) Er:Yb:NaYF₄ and (b) Er:Yb:NaY₂F₅O nanoparticles at 25 and 60 °C; and calculated lifetime values as a function of temperature for (c) Er:Yb:NaYF₄ and (d) Er:Yb:NaY₂F₅O nanoparticles. The temperature dependence of the normalized lifetime of the red emission generated by erbium ions in the Er:Yb:NaY₂F₅O nanoparticles has been also included in (d) as open circles. In all the cases dots are experimental data and solid lines are the best linear fits.

The temperature evolution of the normalized lifetimes ($\tau_{nor}(T)$), defined as $\tau_{nor}(T) = \tau(T)/\tau(25\text{ }^\circ\text{C})$, where $\tau(T)$ is the fluorescence lifetime measured at a temperature T and $\tau(25\text{ }^\circ\text{C})$ is the fluorescence lifetime measured at room temperature) of Er:Yb:NaYF₄ and Er:Yb:NaY₂F₅O nanoparticles are shown in **Figures 2 (c, d)**, as obtained for the 545 nm emission. At this point we should emphasize that, all along this work, the fluorescence lifetime has been estimated from the fluorescence decay curves ($I(t)$) by: $\tau = \frac{\int I(t) \cdot t \cdot dt}{\int I(t) \cdot dt}$. For the two nanomaterials studied in this work we found that the fluorescence lifetime decreases almost linearly with temperature in the biophysical temperature range. This is, indeed, an outstanding feature for the final purpose of lifetime based thermal sensing since it does not only simplifies the calibration of the measurement, also gives place to a temperature independent thermal sensitivity.^{5,6} From data included in **Figure 2**, it is clear that Er:Yb:NaY₂F₅O UCNPs postulate as lifetime based nanothermometer with a larger sensitivity than Er:Yb:NaYF₄ UCNPs. From the experimental data shown in **Figures 2 (c,d)**, it is possible now to estimate the thermal sensitivity of the probes by calculating the so-called lifetime thermal coefficient (α_τ) here defined as the slope of the normalized lifetime vs. temperature linear curve (best fit used in each case is included together with the experimental data). From the linear fits we have calculated the lifetime thermal coefficients of both types of NPs; $5.4 \times 10^{-3}\text{ }^\circ\text{C}^{-1}$ for Er:Yb:NaYF₄ and $15 \times 10^{-3}\text{ }^\circ\text{C}^{-1}$ for Er:Yb:NaY₂F₅O nanoparticles. So, $\alpha_\tau(\text{Er:Yb:NaY}_2\text{F}_5\text{O}) \approx 3 \alpha_\tau(\text{Er:Yb:NaYF}_4)$. At this point it should be noted that the temperature dependence of the fluorescence lifetime of the Er:Yb:NaYF₄ nanoparticles synthesized by the solvothermal method was also investigated in detail resulting also in a reduced lifetime thermal coefficient (below $2 \times 10^{-3}\text{ }^\circ\text{C}^{-1}$). The more pronounced temperature dependence of fluorescence lifetime in Er:Yb:NaY₂F₅O UCNPs can be tentatively associated to the fact that non-radiative relaxation and multiphonon phenomena, responsible for the shortening of fluorescence lifetime decays, are more significant in oxide materials than in fluoride ones.⁴⁶

At this point it should be mentioned that we have also investigated the temperature dependence of the fluorescence lifetime of the characteristic red emission of

Erbium ions at around 660 nm that corresponds to the $^4\text{F}_{9/2} \rightarrow ^4\text{I}_{15/2}$ transition. Results obtained in the Er:Yb:NaY₂F₅O system are included in **Figure 2 (d)** as open circles. As can be observed, the fluorescence lifetime of the $^4\text{F}_{9/2} \rightarrow ^4\text{I}_{15/2}$ red emission also decreases monotonously with temperature, although with a reduced lifetime thermal coefficient in respect to that found for the green emission (α_τ of the 660 nm emission was found to be close to $0.007\text{ }^\circ\text{C}^{-1}$). This reduced value of α_τ is found to be in agreement with previous works also studying the temperature dependence of the fluorescence lifetimes of both red and green emissions of erbium ions.⁴⁷ This reduced thermal dependence is explained in terms of the fact that the number of phonons involved in the non-radiative de-excitations from the $^4\text{F}_{9/2}$ state is larger than that of the $^4\text{S}_{3/2}$ state. This, in turn, is due to the fact that the energy separation between the $^4\text{F}_{9/2}$ state and the next lower energy state is larger than that of the $^4\text{S}_{3/2}$.^{44, 47} Due to the larger thermal sensitivity found for the green emission of Erbium ions in the following we will focus on this transition.

To put in context the values obtained in this work for the lifetime thermal coefficients of UCNPs, it is necessary to point out that the lifetime thermal sensitivity found for Er:Yb:NaY₂F₅O UCNPs is of the order of that previously obtained for other lanthanide doped systems (see **Table 1**), such as Ce:YAG nanocrystals ($10 \times 10^{-3}\text{ }^\circ\text{C}^{-1}$),⁴⁸ or Tb³⁺- and Eu³⁺- complexes ($12 \times 10^{-3}\text{ }^\circ\text{C}^{-1}$ and $20 \times 10^{-3}\text{ }^\circ\text{C}^{-1}$, respectively),⁴⁹ although in that case the systems had to be excited in the UV. Er³⁺ doped nano-materials have been also used as a thermal probes through lifetime measurements in microspheres composed of a heavy-metal fluoride glass (ZBLaLiF) pumped at 488 nm, although in that case, apart from the size of the probes, the relation between lifetime and temperature was not linear, and in the vicinity of room temperature, the lifetime was almost temperature independent.⁴⁵ Er:Yb:NaY₂F₅O UCNPs also show a superior performance, as lifetime based thermal sensors, than gold nanoclusters ($\sim 13 \times 10^{-3}\text{ }^\circ\text{C}^{-1}$), these operating under visible (580 nm) laser excitation.⁵⁰ The thermal sensitivity measured in our Er:Yb:NaY₂F₅O nanoparticles is also comparable to that obtained in CdTe quantum dots ($17 \times 10^{-3}\text{ }^\circ\text{C}^{-1}$).²⁰ Compared with other lifetime luminescence nanothermometric systems, such as dye-based systems, the thermal coefficient of our nanoparticles is smaller to that obtained in Rhodamine B ($30 \times 10^{-3}\text{ }^\circ\text{C}^{-1}$).⁵¹ However, this system has some serious drawbacks for lifetime thermal sensing, such as its low solubility in water and the very likely existence of toxic effects.⁵² Finally, we should compare the thermal coefficients of our nanoparticles with those of luminescent polymers, that show the highest sensitivity reported up to now ($60 \times 10^{-3}\text{ }^\circ\text{C}^{-1}$), although these values can only be achieved during phase transitions (32.5 °C for poly(DBD-AE-co-NOPAM), for instance).⁵³ Since the lifetime thermal coefficients of our Er:Yb NPs are similar to those reported for already used systems, the achievable thermal resolution for Er:Yb:NaY₂F₅O is expected to be close to those already achieved for the other systems reported here: 0.1 °C, making of our NPs a new valuable lifetime based thermal probe for biomedical applications in which temperature control is critical. Another advantage of UCNPs for LF-LNT is the long lifetimes of the green emission of Er³⁺, of the order of hundreds of microseconds, which reduces significantly the cost of the detectors to be used.

To probe the potentiality of Er:Yb:NaY₂F₅O nanoparticles for sub-tissue lifetime thermal sensing, we have tested them in an *ex vivo* experiment by using a chicken breast that was heated externally by a partially absorbed laser beam of wavelength 1090 nm.⁵⁴ Er:Yb:NaY₂F₅O nanoparticles were dispersed in water, and injected into a fresh chicken breast at a depth of 1 mm. Measurements of the luminescence decay curves were recorded in a double beam confocal

Chapter 3 Luminescence nanothermometry in the visible: I. New detection techniques

microscope. Optical excitation was achieved by using a 980 nm diode laser (300 mW power). The luminescence generated by the injection was first collected and collimated by using a low numerical aperture microscope objective and later it was focused into a photomultiplier by using a single lens. A set of absorptive filters was used to ensure that non laser radiation was reaching the photomultiplier. A 1090 nm continuous laser beam was slightly focused into the injection's area and used as the heating beam due to the non-vanishing absorption coefficient of tissues at this wavelength (due to the presence of water).²⁶

Table 1. Excitation and detection wavelengths, and normalized lifetime thermal coefficient (α_t) of some luminescent systems previously used for Fluorescence Lifetime Thermal Imaging.

	Excitation wavelength (nm)	Detection wavelength (nm)	α_t (%)	Ref
Rhodamine B	840	580	0.030	51
Ce:YAG nanocrystals	337	700	0.010	48
Tb doped complex	405	545	0.012	49
Tb doped complex	405	612	0.020	49
Au nanostar	580	710	0.013	50
CdTe Quantum Dots	405	510	0.017	20
Poly (DBD-AL-co-NDPAM)	430	590	0.060	51
Er:Yb:NaYF ₄	980	545	0.005	This work
Er:Yb:NaY ₂ F ₅ O	980	545	0.015	This work

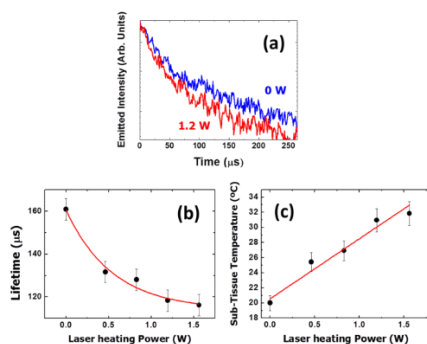


Fig 3 (a) Fluorescent lifetime for the 545 nm emission line of Er:Yb:NaY₂F₅O nanoparticles injected 1 mm below the surface of the chicken breast when the heating laser was on (1.2 W) or off (0 W). (b) Change of lifetime values when the power of the heating laser was increased. The continuous line is a guide for the eye. (c) Sub-tissue temperature increment measured through lifetime variations in the 545 nm emission line of Er:Yb:NaY₂F₅O nanoparticles as a function of the increase of the laser heating power.

Figure 3(a) shows the injection fluorescence decay curves as obtained when the 1090 nm heating laser was on (with a power of 1.2 W) or off (0 W). The faster decay curve obtained when the heating laser was on revealed the presence of tissue laser-induced heating due to residual absorption at 1090 nm. **Figure 3(b)** shows the reduction of the lifetime measured inside the chicken breast as a function of the 1090 nm laser power. As can be observed, the lifetime is substantially reduced from ~160 μ s when the laser was off, to less than 120 μ s for heating laser power close to 1.5 W. This lifetime reduction evidences the progressive heating of the tissue surrounding the UCNP's injection. The actual injection's temperature (sub-tissue temperature) can be calculated from the experimental data of **Figure 3(b)** and the calibration curves of **Figure 2**. Results (sub-tissue temperature as a function of heating laser power) are shown in **Figure 3(c)**. As can be observed 1090 nm laser powers of 1.5 W (corresponding to a laser intensity of 1.5 W/cm²) lead to temperature increments in the tissue close to 10 °C, in reasonable agreement with the magnitude of 1090 nm laser induced tissue heating observed in recent *in vivo* experiments by using infrared thermometry.⁵⁴

It is important to note that we have verified that the presence of the 1090 nm radiation had no influence on the fluorescence dynamics of Erbium ions as absorption measurements revealed no absorption of the Er:Yb doped particles at 1090 nm. Therefore, the lifetime changes reported in **Figure 3** can be unequivocally attributed to the laser induced heating of tissue.

Finally, it is important to note that sub-tissue thermal sensing experiments reported in **Figure 3** have been obtained at a reduced depth of 1 mm. This is because when using the two photon excited visible emission of rare earth doped nanoparticles, penetration depths into tissues has been reported to be limited to few millimeters.⁵⁵ Sub-tissue thermal measurements at longer penetration depths would be possible, although a detection system with an improved sensitivity than that used in this work would be required. In our experimental conditions, reliable lifetime measurements can be done for maximum injection depths of 1-2 mm. Larger penetration depths led to a low signal-to-noise ratios in the fluorescence decay curves and hence to a large uncertainty in the sub-tissue thermal measurements. Results included in this work constitute a proof-of-concept that lanthanide doped nanoparticles could be also used for lifetime fluorescence thermal sensing. For the purpose of sub-tissue thermal sensing at larger penetration depths the use of lanthanide doped infrared emitting nanoparticles emerge as an interesting alternative.

D. Conclusions

In summary, we provide experimental evidence demonstrating how the ubiquitous Er:Yb up-converting fluorescent nanoparticles can be used not only as fluorescent nanoprobes for *in vivo* and *in vitro* imaging but also as fluorescent thermal nano-sensors based on their strongly temperature dependent visible fluorescence lifetime. It has been demonstrated that the lifetime based thermal sensitivities of Er:Yb:NaY₂F₅O up-converting nanoparticles in the biological range are comparable to those reported for other fluorescent nanoparticles. We not only report on this possibility but we have demonstrated real sub-tissue thermal sensing in *ex-vivo* experiments. We have been able to measure laser induced tissue heating by the sub-tissue injection of Er:Yb:NaY₂F₅O up-converting nanoparticles and by the subsequent analysis of their fluorescence lifetime.

Results presented in this work introduce to the scientific community Er:Yb:NaY₂F₅O up-converting nanoparticles as a novel nanosized fluorescent system capable of lifetime based thermal sensing with improved sensitivity in the biological range of temperatures, and that might constitute an interesting alternative to the widely used Er:Yb:NaYF₄ nano particles in applications requiring fast and accurate thermal sensing.

Acknowledgements

This work was supported by the Spanish Government under projects No. MAT2011-29255-C02-02, MAT2010-16161 and TEC2010-21574-C02-02, the Catalan Government under project No. 2009SGR235, the European Commission within the Seventh Framework Program under project No. FP7-SPA-2010-263044, and by the Universidad Autónoma de Madrid and Comunidad Autónoma de Madrid (Project S2009/ MAT- 1756) O.A. Savchuk is supported by Catalan Government through the fellowship 2013FL_B 01032. P.H.G thanks Fundación Doctor Manuel Morales and Ministerio de Economía y Competitividad (subprograma Juan de la Cierva) for financial support.

Chapter 3 Luminescence nanothermometry in the visible: I. New detection techniques

Notes and references

**Física i Cristal·lografia de Materials i Nanomaterials (FiCMA-FiCNA)-EMaS, Universitat Rovira i Virgili (URV), Campus Sescelades, C/ Marcel·li Domingo s/n, E-43007, Tarragona, Spain, E-mail: joanosep.carvajal@urv.cat.*

- C. D. Geddes and J. R. Lakowicz, *Reviews in fluorescence 2004*, Kluwer Academic/Plenum Publishers, New York, 2004.
- K. Okabe, N. Inada, C. Gota, Y. Harada, T. Funatsu and S. Uchiyama, *Nat Commun*, 2012, 3, 705.
- B. Hildebrandt, P. Wust, O. Ahlers, A. Dieing, G. Sreenivasa, T. Kerner, R. Felix and H. Riess, *Critical Reviews in Oncology/Hematology*, 2002, 43, 33-56.
- D. Jaque and F. Vetrone, *Nanoscale*, 2012, 4, 4301-4326.
- C. D. Brites, P. P. Lima, N. J. Silva, A. Millan, V. S. Amaral, F. Palacio and L. D. Carlos, *Nanoscale*, 2012, 4, 4799-4829.
- C. D. S. Brites, P. P. Lima, N. J. O. Silva, A. Millán, V. S. Amaral, F. Palacio and L. D. Carlos, *Journal of Luminescence*, 2013, 133, 230-232.
- C. D. Brites, P. P. Lima, N. J. Silva, A. Millan, V. S. Amaral, F. Palacio and L. D. Carlos, *Nanoscale*, 2013, 5, 7572-7580.
- C. D. Brites, P. P. Lima, N. J. Silva, A. Millan, V. S. Amaral, F. Palacio and L. D. Carlos, *Adv Mater*, 2010, 22, 4499-4504.
- T. Barilero, T. Le Saux, C. Gosse and L. Jullien, *Anal Chem*, 2009, 81, 7988-8000.
- O. S. Wolfbeis, *Advanced Materials*, 2008, 20, 3759-3763.
- S. W. Allison and G. T. Gillies, *Review of Scientific Instruments*, 1997, 68, 2615-2650.
- S. Uchiyama, Y. Matsumura, A. P. de Silva and K. Iwai, *Anal Chem*, 2003, 75, 5926-5935.
- A. L. Heyes, *Journal of Luminescence*, 2009, 129, 2004-2009.
- F. Vetrone, R. Naccache, A. Zamarron, A. Juarranz de la Fuente, F. Sanz-Rodríguez, L. Martínez Maestro, E. Martín Rodríguez, D. Jaque, J. García Sole and J. A. Capobianco, *ACS Nano*, 2010, 4, 3254-3258.
- F. Vetrone, R. Naccache, A. J. d. I. Fuente, F. Sanz-Rodríguez, A. Blazquez-Castro, E. M. Rodríguez, D. Jaque, J. G. Solé and J. A. Capobianco, *Nanoscale*, 2010, 2, 495-498.
- P. Haro-Gonzalez, L. M. Maestro, M. Trevisani, S. Polizzi, D. Jaque, J. G. Sole and M. Bettinelli, *Journal of Applied Physics*, 2012, 112.
- B. H. a. G. F. Imbusch, *Optical Spectroscopy of Inorganic Solids*, Oxford Science, New York, 1989.
- D. Wawrzynczyk, A. Bednarkiewicz, M. Nyk, W. Strek and M. Samoc, *Nanoscale*, 2012, 4, 6959-6961.
- A. Bednarkiewicz, D. Wawrzynczyk, M. Nyk and W. Strek, *Applied Physics B*, 2010, 103, 847-852.
- P. Haro-González, L. Martínez-Maestro, I. R. Martín, J. García-Solé and D. Jaque, *Small*, 2012, DOI: 10.1002/smll.201102736, n/a-n/a.
- A. H. Khalid and K. Kontis, *Sensors*, 2008, 8, 5673-5744.
- T. Sun, Z. Y. Zhang and K. T. V. Grattan, *Review of Scientific Instruments*, 2000, 71, 4017-4022.
- C. Gota, S. Uchiyama, T. Yoshihara, S. Tobita and T. Ohwada, *J Phys Chem B*, 2008, 112, 2829-2836.
- M. D. Chambers and D. R. Clarke, in *Annual Review of Materials Research*, 2009, vol. 39, pp. 325-359.
- L. O. Svaasand, T. Boerslid and M. Oeveraasen, *Lasers in surgery and medicine*, 1985, 5, 589-602.
- W.-F. Cheong, S. A. Prah and A. J. Welch, *IEEE J. Quantum Electron.*, 1991, 26, 2166-2185.
- X. H. Huang, P. K. Jain, I. H. El-Sayed and M. A. El-Sayed, *Lasers in Medical Science*, 2008, 23, 217-228.
- X. Huang, I. H. El-Sayed, W. Qian and M. A. El-Sayed, *Journal of the American Chemical Society*, 2006, 128, 2115-2120.
- A. M. Smith, M. C. Mancini and S. Nie, *Nature Nanotechnology*, 2009, 4, 710-711.
- A. Gnach and A. Bednarkiewicz, *Nano Today*, 2012, 7, 532-563.
- D. K. Chatterjee, M. K. Gnanasammandhan and Y. Zhang, *Small*, 2010, 6, 2781-2795.
- N. Dong, M. Pedroni, F. Piccinelli, G. Conti, A. Sbarbati, J. R. Hernandez, L. M. Maestro, M. C. Iglesias de la Cruz, F. Sanz-Rodríguez and A. Juarranz, *Acs Nano*, 2011.
- U. Rocha, K. U. Kumar, C. Jacinto, I. Villa, F. Sanz-Rodríguez, M. del Carmen Iglesias de la Cruz, A. Juarranz, E. Carrasco, F. C. J. M. van Veggel, E. Bovero, J. G. Solé and D. Jaque, *Small*, 2013, DOI: 10.1002/smll.201301716.
- O. A. Savchuk, J. J. Carvajal, E. W. Barrera, M. C. Pujol, X. Mateos, R. Sole, J. Massons, M. Aguilo and F. Diaz, in *Nanoscale Imaging, Sensing, and Actuation for Biomedical Applications X*, eds. A. N. Cartwright and D. V. Nicolau, 2013, vol. 8594.
- D. K. Chatterjee, A. J. Ruffalbah and Y. Zhang, *Biomaterials*, 2008, 29, 937-943.

Chapter 3 Luminescence nanothermometry in the visible: I. New detection techniques

36. J. C. Boyer, F. Vetrone, L. A. Cuccia and J. A. Capobianco, *J Am Chem Soc*, 2006, 128, 7444-7445.
37. L. M. Maestro, E. M. Rodriguez, F. Vetrone, R. Naccache, H. L. Ramirez, D. Jaque, J. A. Capobianco and J. G. Sole, *Optics Express*, 2010, 18, 23544-23553.
38. R. Abdul Jalil and Y. Zhang, *Biomaterials*, 2008, 29, 4122-4128.
39. S. A. Hilderbrand, F. W. Shao, C. Salthouse, U. Mahmood and R. Weissleder, *Chemical Communications*, 2009, DOI: 10.1039/b905927j, 4188-4190.
40. F. Wang, D. Banerjee, Y. S. Liu, X. Y. Chen and X. G. Liu, *Analyst*, 2010, 135, 1839-1854.
41. L. H. Fischer, G. S. Harms and O. S. Wolfbeis, *Angewandte Chemie-International Edition*, 2011, 50, 4546-4551.
42. M. Quintanilla, E. Cantelar, F. Cusso, M. Villegas and A. C. Caballero, *Applied Physics Express*, 2011, 4.
43. C. Li, Z. Quan, J. Yang, P. Yang and J. Lin, *Inorganic Chemistry*, 2007, 46, 6329-6337.
44. X. Shen, Q. Nie, T. Xu, S. Dai and X. Wang, *Journal of Luminescence*, 2010, 130, 1353-1356.
45. Z. P. Cai, L. Xiao, H. Y. Xu and M. Mortier, *Journal of Luminescence*, 2009, 129, 1994-1996.
46. C. Brecher, L. A. Riseberg and M. J. Weber, *Physical Review B*, 1978, 18, 5799-5811.
47. S. K. Ghoshal, M. R. Sahar, M. S. Rohani and S. Sharma, *Indian Journal of Pure & Applied Physics*, 2011, 49, 509-515.
48. S. W. Allison, G. T. Gillies, A. J. Rondinone and M. R. Cates, *Nanotechnology*, 2003, 14, 859-863.
49. J. Yu, L. Sun, H. Peng and M. I. J. Stich, *Journal of Materials Chemistry*, 2010, 20, 6975-6981.
50. L. Shang, F. Stockmar, N. Azadfar and G. U. Nienhaus, *Angewandte Chemie International Edition*, 2013, 52, 11154-11157.
51. R. K. Benninger, Y. Koc, O. Hofmann, J. Requejo-Isidro, M. A. Neil, P. M. French and A. J. DeMello, *Anal Chem*, 2006, 78, 2272-2278.
52. U. Resch-Genger, M. Grabolle, S. Cavaliere-Jaricot, R. Nitschke and T. Nann, *Nature Methods*, 2008, 5, 763-775.
53. E. M. Graham, K. Iwai, S. Uchiyama, A. P. de Silva, S. W. Magennis and A. C. Jones, *Lab Chip*, 2010, 10, 1267-1273.
54. L. M. Maestro, P. Haro-Gonzalez, B. del Rosal, J. Ramiro, A. J. Caamano, E. Carrasco, A. Juarraz, F. Sanz-Rodriguez, J. G. Sole and D. Jaque, *Nanoscale*, 2013, 5, 7882-7889.
55. N.-N. Dong, M. Pedroni, F. Piccinelli, G. Conti, A. Sbarbati, J. E. Ramirez-Hernández, L. M. Maestro, M. C. I.-d. I. Cruz, F. Sanz-Rodriguez, A. Juarraz, F. Chen, F. Vetrone, J. A. Capobianco, J. G. Solé, M. Bettinelli, D. Jaque and A. Speghini, *ACS Nano*, 2011, 11, 8665-8671.

Chapter 3 **Luminescence nanothermometry in the visible: I. New detection techniques**

Paper II

Savchuk, Ol. A.; Carvajal, J. J.; Pujol, M. C.; Massons, J.; c, P.; Martínez, O.; Jiménez, J.; Aguiló, M.; Díaz, F. *New strategies involving upconverting nanoparticles for determining moderate temperatures by luminescence thermometry* (2016) Journal of Luminescence 169, 711–716.

Chapter 3 **Luminescence nanothermometry in the visible: I. New detection techniques**

NEW STRATEGIES INVOLVING UPCONVERTING NANOPARTICLES FOR DETERMINING MODERATE TEMPERATURES BY LUMINESCENCE THERMOMETRY

O.I.A. Savchuk,¹J.J. Carvajal,^{1,*} M.C. Pujol,¹ J. Massons,¹P. Haro-González,²O. Martínez,³ J. Jiménez,³M. Aguiló,¹ F. Díaz¹

¹*Física i Cristal·lografia de Materials i Nanomaterials (FiCMA-FiCNA) and EMaS, Universitat Rovira i Virgili (URV), c/Marcel·lí Domingo s/n E-43007, Tarragona, Spain*

²*Fluorescence Imaging Group, Departamento de Física de Materiales, Facultad de Ciencias, Universidad Autónoma de Madrid, C/Francisco Tomás y Valiente 7, E-28049, Madrid, Spain*

³*GdS-Optronlab, Departamento Física Materia Condensada, Univ. de Valladolid, Edificio I+D, Paseo de Belén, 11, 47011, Valladolid, Spain*

*Corresponding author: joanjosep.carvajal@urv.cat

Keywords: Luminescent nanothermometry, intensity ratio, lifetime measurements, ex-vivo temperature determination, $\text{KLu}(\text{WO}_4)_2$, $\text{NaY}_2\text{F}_5\text{O}$, lanthanide ions.

Abstract

Here we analyze alternative luminescence thermometry techniques to FIR, such as intensity ratio luminescence thermometry between the emission arising from two electronic levels that are not necessarily thermally coupled, but that show different evolutions with temperature, and lifetime luminescence nanothermometry in $(\text{Ho},\text{Tm},\text{Yb}):\text{KLu}(\text{WO}_4)_2$ and $(\text{Er},\text{Yb}):\text{NaY}_2\text{F}_5\text{O}$ nanoparticles. $(\text{Ho},\text{Tm},\text{Yb}):\text{KLu}(\text{WO}_4)_2$ nanoparticles exhibited a maximum relative sensitivity of 0.61 % K^{-1} , similar to that achievable in Er-doped systems, which are the upconverting systems presenting the highest sensitivity. From another side, $(\text{Er},\text{Yb}):\text{NaY}_2\text{F}_5\text{O}$ nanocrystals show great potentiality as thermal sensors at the nanoscale for moderate temperatures due to the incorporation of additional non-radiative relaxation mechanisms that shorten the emission lifetime generated by the oxygen present in the structure when compared to $(\text{Er},\text{Yb}):\text{NaYF}_4$ nanoparticles exhibiting the highest upconversion efficiency. We used those nanoparticles for ex-vivo temperature determination by laser induced heating in chicken breast using lifetime-based thermometry. The results obtained indicate that these techniques might constitute alternatives to FIR with potential applications for the determination of moderate temperatures, with sensitivities comparable to those that can be achieved by FIR or even higher.

1. Introduction

Heat is produced in several processes, which generates an increase of temperature that in general is interesting to know and be measured. Examples include monitoring the evolution of temperature in chemical reactors [1], detection of “hot spots” in microelectronic devices [2], detection of local temperatures within integrated photonic devices to prevent irreversible damages [3], monitoring heat dissipation during optical trapping [4], monitor temperature changes in microfluidic systems [5] and monitoring metabolic processes in living organisms [6], to name a few.

Typical systems used to control the temperature increment require contact, which generates technological challenges when spatial resolution decreases to the submicron scale. Fortunately, there are various types of non-contact nanothermometry approaches, one of the most attractive of which is luminescence thermometry, based on the temperature-dependent emission intensity, lifetime value, band shape or position of emission bands of luminescent nanoparticles [7, 8]. These methods offer relatively high detection sensitivity and spatial resolution in short acquisition time, even in fluids, strong electromagnetic fields and fast moving objects [9-11].

The use of upconversion nanoparticles, which exhibit efficient visible emission properties after excitation in the near infrared, can provide simultaneously the dual function of imaging and temperature sensing at the nanoscale [12].

The potentiality of Er^{3+} , Yb^{3+} codoped upconversion nanoparticles for nanothermometry in the range of moderate temperatures has been especially highlighted [13,14], especially due to the suitable energy gap between the $^2\text{H}_{11/2}$ and $^4\text{S}_{3/2}$ energy levels of Er^{3+} , which are thermally coupled, using, for instance, (Er,Yb): NaYF_4 nanoparticles.

However, there exist other alternative materials and thermometry techniques with potential use for the determination of moderate temperatures that can offer a similar or even higher sensitivity with respect to those offered by Er^{3+} -doped systems. Here, we analyze the possibilities offered by two dielectric phosphors, (Ho,Tm,Yb): $\text{KLu}(\text{WO}_4)_2$ and (Er,Yb): $\text{NaY}_2\text{F}_5\text{O}$, by measuring the luminescence thermometry intensity ratio between the emission arising from two electronic levels that are not necessarily thermally coupled, but that show different evolutions with temperature in the former, with sensitivities comparable to those obtained in Er^{3+} -doped systems, and by measuring lifetimes in the second.

2. Experimental section

Synthesis of luminescent nanoparticles. 1.5 at. % Ho, 1 at.% Tm, and 1 at. % Yb doped KLu(WO₄)₂ nanocrystals were synthesized by the sol-gel modified Pechini method [20] Analytic grade purity reagents of Ho₂O₃ (99.9999%), Tm₂O₃ (99.9999%), Yb₂O₃ (99.9%), and Lu₂O₃ (99.9999%), were dissolved in hot nitric acid in the specific proportions to form the nitrate precursors. Citric acid (CA) was used as the chelating agent while ethylenglycol (EG) was used as the esterification agent in the synthesis process. The nitrate precursors were dissolved in distilled water with citric acid in a molar ratio of CA to metal cations equal to 1. Ammonium tungstate (NH₄)₂WO₄ (99.99%) and potassium carbonate K₂CO₃ (99.99%) were added to the aqueous solution and we heated it at 353 K under magnetic stirring during 24 h until complete dissolution. Further, EG was added to the mixture in a molar ratio [EG]/[CA]=2. The solution was heated at 373 K in order to evaporate water and generate the polymeric gel. After that, the polymeric gel was calcinated at 573 K for 3 hours, and later at 1023 K for 2 hours to eliminate the organic compounds and crystallize the desired nanoparticles. The raw (Er,Yb):NaY₂F₅O nanoparticles were purchased to Boston Applied Technology.

Raman scattering measurements. Micro-Raman spectra were obtained at room temperature with a Labram HR800 UV Raman spectrometer from Horiba-Jobin-Yvon attached to a metallographic microscope with confocal optics, and equipped with a LN₂-cooled charge-coupled-device (CCD) detector. The excitation was carried out with a UV laser at 325 nm using a 40 X UV microscope objective with 0.5 numerical aperture (NA). The scattered light was also collected by the objective, thus working in a nearly backscattering configuration.

Temperature-dependent luminescent experiments. For upconversion emission measurements, (Ho,Tm,Yb):KLuW nanoparticles were introduced in a Linkam THMS 600 heating stage. The sample was excited with a diode laser emitting at 808 nm, which corresponds to the maximum absorption wavelength of Tm³⁺. The beam from the laser source was focused on the sample and the emission was collected in 90° geometry in order to eliminate the residual laser pump. Emission radiated from the sample was collected and dispersed on a JobinYvon HR 460 monochromator. For detection, a Hamamatsu PMTR 928 photomultiplier tube, connected to a Perkin Elmer DSP-7265 lock-in amplifier was used.

Lifetime thermometry. For luminescence decay-time experiments as a function of temperature, (Er,Yb):NaY₂F₅O nanoparticles were introduced in a Linkam THMS 600 heating stage and excited at 980 nm with an optical parametric oscillator (OPO) from Opotek (Vibrant HE 355 II+UV) with a pulse duration of 6 ns and a repetition frequency of 10 Hz. The fluorescence light emitted by the sample was collected with a microscope objective, transferred to the monochromator for the selection of specific wavelengths, and then detected using a Hamamatsu R928 photomultiplier. The decay of the signal was measured as a function of time with a digital oscilloscope, averaging the signal from 3000 laser pulses.

Lifetime thermal sensing experiments. After calibration, (Er,Yb):NaY₂F₅O nanoparticles were dispersed in distilled water and injected in a fresh chicken breast. A heating laser with emission at 1090 nm and a pumping laser with emission at 980 nm, spatially overlapping, were simultaneously focused in the chicken breast using a microscope objective. The fluorescence arising from the nanoparticles was collected by the same objective, and after passing the selected filters, was focused into the photomultiplier tube connected to the digital oscilloscope.

3. Results and Discussion

3.1. (Ho,Tm,Yb):KLu(WO₄)₂ nanoparticles

We studied the upconversion emission of Ho³⁺, Tm³⁺, and Yb³⁺-codoped KLu(WO₄)₂ nanoparticles, and analyzed the possibilities of their emissions for temperature sensing applications. As a host material the KLu(WO₄)₂ monoclinic matrix has several advantages. For instance, the Yb³⁺ absorption cross-section in KLu(WO₄)₂ single crystals has been measured to be 11.8×10^{20} cm² [15], which is around 15 times bigger than that on Yb³⁺ in YAG crystals [16]. Furthermore, this host allows for large doping concentrations, up to 100%, without emission quenching effects [17]. (Ho,Tm,Yb):KLu(WO₄)₂ single crystals [18] and nanocrystals [19] have been used, for instance, for the generation of white light through the combination of the blue, green and red light emitted by this material when excited with 980 nm light by tuning the concentrations of the doping ions to equilibrate the intensity of the RGB emissions. Thus, they show a rich emission structure with possibilities to be used in thermal sensing. Its quantum yield in comparison to that reported for (Er,Yb):NaYF₄ nanoparticles [20], the most efficient up-converting system presented up to date, is around one order of magnitude lower [21]; however, it is comparable to other up-

Chapter 3 Luminescence nanothermometry in the visible: I. New detection techniques

converting oxide nanoparticles currently used for nanothermometry applications [22-27]. Furthermore, halide-based materials tend to be hygroscopic, showing relatively poor chemical and photophysical stabilities compared to oxide matrices; on the other hand, most of the preparative routes for halide-based nanoparticles are complex and environmentally harmful.

(Ho,Tm,Yb):KLu(WO₄)₂ nanoparticles have been synthesized by the sol-gel modified Pechini method. Figure 1 shows a TEM image in which the aspect of these nanoparticles can be seen. Particles show irregular shapes, with sizes below 50 nm, as can be seen in the histogram, in which we statistically analyzed the nanoparticles size distribution, furthermore, a relatively low degree of agglomeration is observed. (Ho,Tm,Yb):KLu(WO₄)₂ nanoparticles crystallize in the monoclinic system, with spatial group C2/c, as it was reported for single crystals with the same chemical composition [18].

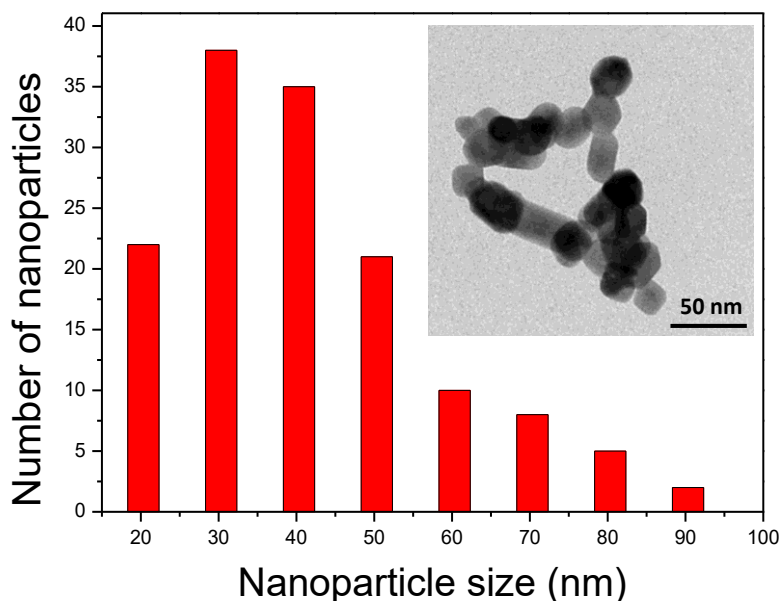


Figure 1. TEM image of (Ho,Tm,Yb):KLu(WO₄)₂ nanoparticles and histogram showing the mean sizes of these nanoparticles.

Chapter 3 Luminescence nanothermometry in the visible: I. New detection techniques

Figure 2(a) shows the evolution of the upconversion emission spectra of (Ho,Tm,Yb):KLu(WO₄)₂ nanocrystals excited at 808 nm in the range of temperatures 22 – 250 °C, which exhibits three emission bands in the blue, green and red region of the electromagnetic spectrum. In order to understand the origin of the different emission lines, we have studied the upconversion mechanism in detail by pumping at specific wavelengths in the visible to excite specific energy levels of the different emitting ions. Figure 2(b) summarizes the different excitation and emission mechanisms deduced for this material. From this analysis, it is clear that the green and red emissions arise from different ions of the system, and occurred due to energy transfer processes that are temperature dependent. In fact, we observed that while the green emission generated by Ho³⁺ decreases in intensity when the temperature increased, the red emission intensity generated by Tm³⁺ increased, showing that, despite we cannot consider, strictly speaking, that those levels are thermally coupled, they are somehow thermally linked through phononic processes associated with energy transfer processes. In fact, by increasing the temperature, the multiphonon nonradiative depopulation rate of the ⁵S₂ and ⁵F₄ energy levels of Ho³⁺ (from which the green emission originated) will become faster, populating the ⁵F₆ energy level of this ion. From here, an energy transfer process occurs to the ³F₂ and ³F₃ energy levels of Tm³⁺ from which the red emission occurs. Thus, although we cannot apply the FIR technique as defined by Wade et al. [28] in that case for temperature sensing purposes, this allows us to apply the intensity ratio technique to analyze the thermal evolution of the emission from these ions, and use these nanoparticles as luminescent nanothermometers.

In order to explore the possibilities of using these nanoparticles as a nanothermometer suitable for moderate temperatures, we have focused on the range of temperature between 22 and 50 °C. The ratio between the integrated intensities of the two emission bands, located in the red and the green spectral windows, as a function of temperature is plotted in Figure 2(c). The experimental data could be fitted to a linear equation: $I_{\text{red}}/I_{\text{green}} = -0.8 + 0.0061T$. The relative sensitivity, calculated as the first derivative of the intensity ratio divided by the intensity ratio is plotted in Figure 2(d). This parameter allows us to compare the performance of our system with respect to other luminescent thermometers reported before. The maximum relative sensitivity was found to be 0.61 % °C⁻¹, similar to those previously reported for Er³⁺ based systems, which up to date were the highest ones reported in

the literature [29, 30]. Thus, Tm^{3+} and Ho^{3+} ions in the $\text{KLu}(\text{WO}_4)_2$ host might become a competing technology with Er^{3+} for thermometry applications.

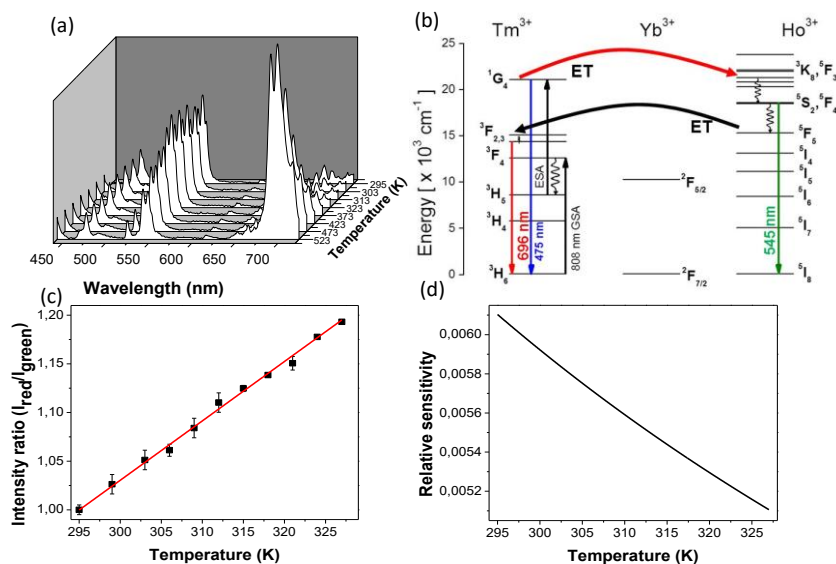


Figure 2. (a) Evolution of the emission spectra of (Ho,Tm,Yb):KLu(WO₄)₂ nanoparticles with temperature in the range 22 – 250 °C after excitation at 808 nm. (b) Energy level diagram and emission generated by upconversion after excitation at 808 nm for Ho³⁺, Tm³⁺, and Yb³⁺ in KLu(WO₄)₂nanoparticles. (c) I_{red}/I_{green} in the range of temperatures 22-50 °C. (d) Temperature dependence of the relative sensitivity for the (Ho,Tm,Yb):KLu(WO₄)₂ nanoparticles.

3.2. (Er,Yb):NaY₂F₅O nanoparticles

The entity to which the temperature wants to be determined may be in movement, or in a environment where others parameters, such as pH and oxygen concentration, can affect the luminescent intensity of the emission lines of the nanoparticles. An alternative means of temperature sensing that overcomes these limitations is lifetime thermometry, although it has been scarcely used with up-converting materials [31,32]. An additional advantage of this technique for thermometry consists of the temperature estimation from the measurement of a single parameter (lifetime), therefore it is to a first approximation calibration-free. The use of systems that incorporate non-radiative relaxation and multiphonon phenomena, responsible for the shortening of fluorescence lifetime decays, such as oxides instead of fluorides, might allow considering this technique as an alternative to the more conventionally used fluorescence intensity ratio technique. (Er,Yb):NaY₂F₅O nanoparticles are promising candidates for this approach [31], since their phononic response is extended to longer

wavenumbers with respect to pure fluorides, (Er,Yb):NaYF₄ for instance, see the Raman spectra in Figure 3. This extended phononic response allows for a more easy activation of the non-radiative relaxation and multiphonon phenomena, similar to what is happening with oxides [33]. This is due to the fact that the smaller the number of phonons required to cover the energy gap between two levels, the higher the non-radiative multiphonon rate to depopulate an excited energy level to another one, as described by the phenomenological model of Riserberg and Moos [34]. Therefore, by increasing the phonon energy values in oxifluorides when compared to fluorides, induces the enhancement of the non-radiative processes, which shorten the experimental decay times.

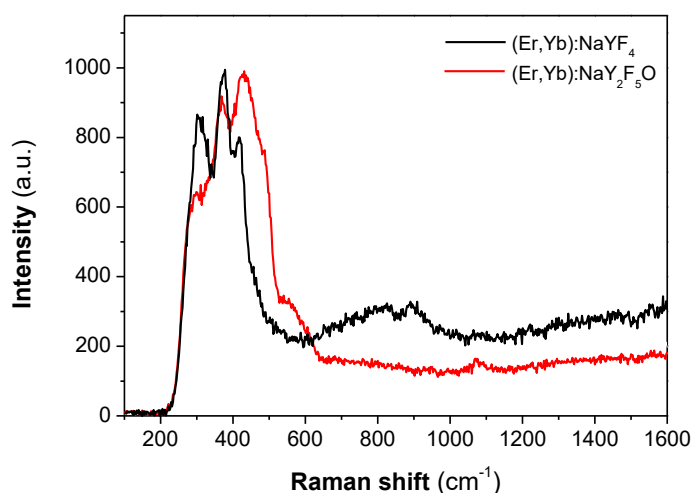


Figure 3. Raman spectra of (Er,Yb):NaYF₄ and (Er,Yb):NaY₂F₅O nanoparticles.

Figure 4(a) shows a TEM image of the (Er,Yb):NaY₂F₅O nanoparticles used in this work. They exhibit rod like morphologies, with diameters around 70-80 nm and lengths around 250 nm, as can be seen in the histograms provided in Figures 4 (b) and (c). However, these particles tend to be densely agglomerated. It is clear, thus, that for real applications, the morphological characteristics of the samples used in this work must be improved, but their quality is good enough to provide a trustable “proof of concept” of the potentiality of lifetime thermometry in the range of moderate temperatures.

Chapter 3 Luminescence nanothermometry in the visible: I. New detection techniques

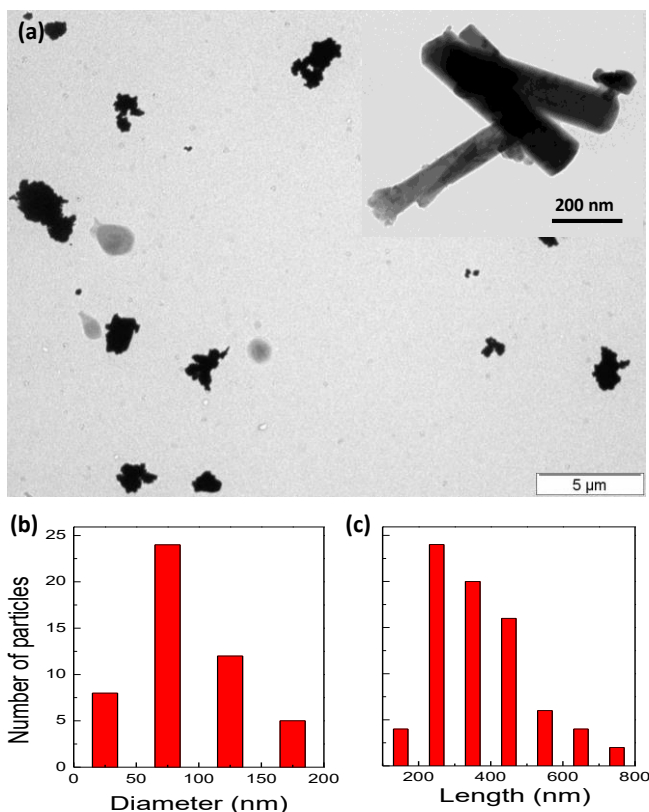


Figure 4. (a) TEM image of (Er,Yb):NaY₂F₅O nanoparticles. Histograms showing (b) the diameter and (c) lengths of the nanoparticles.

Figure 4(a) shows the emission spectrum of (Er,Yb):NaY₂F₅O nanoparticles after excitation at 980 nm. It consists mainly in two emission bands: a weak emission band in the green associated to the ²H_{11/2}, ⁴S_{3/2}→⁴I_{15/2} transitions of Er³⁺ and another more intense emission band in the red associated to the ⁴F_{9/2}→⁴I_{15/2} transition of Er³⁺. The temperature dependent normalized lifetime, defined as $\tau_{\text{nor}}(T) = \tau(T) / \tau(\text{RT})$, where $\tau(T)$ is the fluorescence lifetime measured at a temperature T, and $\tau(\text{RT})$ is the fluorescence lifetime measured at room temperature, of the 545 nm and 660 nm emission lines in the range of RT to 60°C are shown in Figure 4 (b). For that we analyzed only the decay part of the luminescent lifetimes, thus avoiding the rise time inherent in the energy transfer upconversion process, using the following expression:

$$\tau = \frac{\int I(t) \cdot t \cdot dt}{\int I(t) \cdot dt}$$

. In both cases we observed a linear decrease of the lifetime values

Chapter 3 Luminescence nanothermometry in the visible: I. New detection techniques

when the temperature increased. However, the slope of the evolution of the lifetime associated with the 545 nm emission line is higher, which will provide better temperature estimation sensitivity. In fact, the lifetime thermal coefficients (α_T), defined as the slope of the normalized lifetime vs. temperature, are $0.015\text{ }^\circ\text{C}^{-1}$ and $0.007\text{ }^\circ\text{C}^{-1}$, thus we can consider that $\alpha_T(545\text{ nm}) \approx 2\alpha_T(660\text{ nm})$. This reduced thermal quenching value for the red emission is not surprising, since it has been previously reported for Er^{3+} -doped glasses in the range of temperatures between 10 K and room temperature [35]. It should be noted here that the high sensitivity observed for the green emission lays in the order of that previously obtained for other lanthanide doped systems [36-38] and quantum dots [39] pumped in the UV and blue regions of the electromagnetic spectrum, furthermore, it shows a better performance than gold nanoclusters pumped in the green [40].

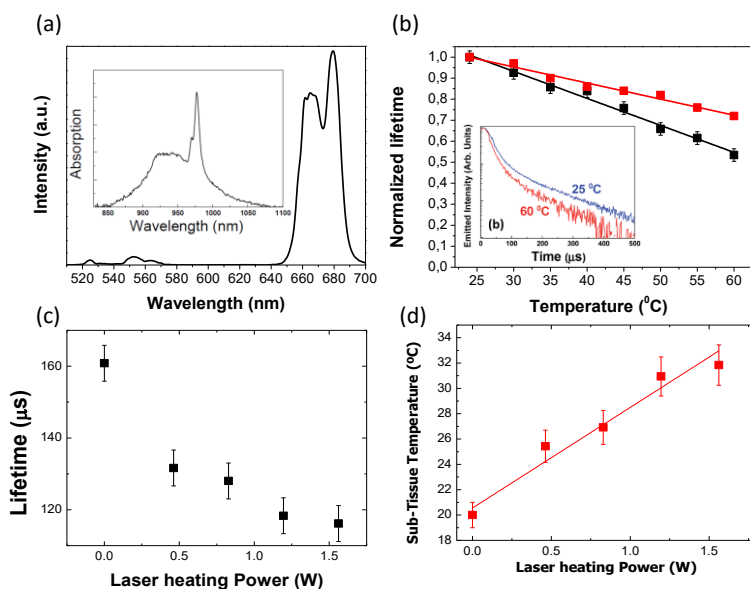


Figure 4. (a) Emission spectra of (Er,Yb):NaY₂F₅O nanoparticles after pumping at 980 nm. Inset shows the absorption spectrum of these nanoparticles in the 825-1100 nm region. (b) Normalized lifetime values as a function of temperature for the 545 nm and 660 nm emission lines. Inset shows the fluorescence decay curves of the 545 nm emission line at 25 and 60 °C (c) Effect of the heating laser emitting at 1090 nm on the lifetime values of the 545 nm emission line on the nanoparticles introduced in chicken breast. (d) Ex-vivo temperature increment measured through lifetime variations in the 545 nm emission line of (Er,Yb):NaY₂F₅O nanoparticles as a function of the increase of the laser heating power.

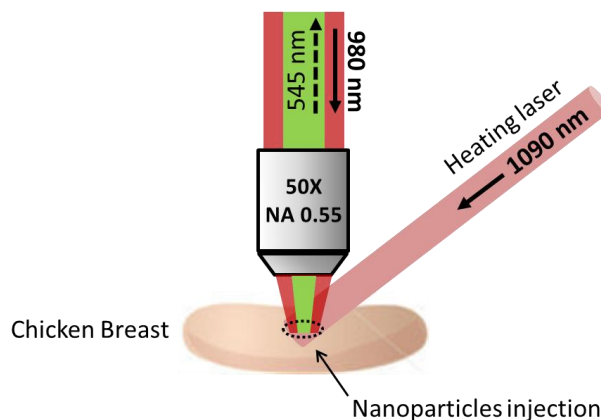


Figure 5. Scheme of the experimental set-up used in the ex-vivo thermal sensing experiment of sub-tissue temperature determination in chicken breast.

In order to show the potentiality of the $(\text{Er},\text{Yb}):\text{NaY}_2\text{F}_5\text{O}$ nanoparticles as a practical nano-thermometer for moderate temperatures, ex-vivo thermal sensing experiment of sub-tissue temperature determination in chicken breast were carried out as a function of the power of a heating laser emitting at 1090 nm. Figure 5 shows a scheme of the experimental set-up used. $(\text{Er},\text{Yb}):\text{NaY}_2\text{F}_5\text{O}$ were dispersed in water, and injected into a fresh chicken breast at a depth of 1 mm. A 1090 nm continuous laser beam was slightly focused into the injection's area and used as the heating beam due to the non-vanishing absorption coefficient of tissues at this wavelength (because of the presence of water). Optical excitation was achieved by using a 980 nm diode laser and the luminescence generated was first collected and collimated by using a low numerical aperture microscope objective and later it was focused into a photomultiplier by using a single lens. Figure 4(c) shows the decrease of the lifetime of the 545 nm emission line when we increased the power of the heating laser focused inside the chicken breast. Since $(\text{Er},\text{Yb}):\text{NaY}_2\text{F}_5\text{O}$ nanoparticles do not absorb energy at 1090 nm (see inset in Figure 4(a)), the reduction of the lifetime is due to the heating of the chicken breast tissues induced by the laser. By combining these data with those of the calibration previously performed (see Figure 4(b)), we can determine the temperature inside the chicken breast, and we show it as a function of the laser heating power in Figure 4(d).

4. Conclusions

In conclusion, we have shown alternative luminescence thermometry techniques to the most commonly used fluorescence intensity ratio technique for moderate temperature sensing purposes. (Ho,Tm,Yb):KLu(WO₄)₂ nanoparticles can be used as an efficient luminescence temperature sensor using the temperature-dependent ratio of two emission lines. From another side, (Er,Yb):NaY₂F₅O nanoparticles show a great potentiality in moderate temperature sensing purposes using the lifetime thermometry technique, demonstrated by the ex-vivo sub-tissue temperature determination experiment in chicken breast.

Acknowledgement

This work was supported by the Spanish Government under projects No. MAT2013-47395-C4-1-4-R, and by the Catalan Government under project No. 2014SGR1358. O.A. Savchuk is supported by Catalan Government through the fellowship 2013FI_B 01032.P.H.G. thanks the Spanish Ministerio de Economía y Competitividad (MINECO) for the Juan de la Cierva program.

References

- [1] S. Wang, S. Westcott, W. Chen, *J. Phys. Chem. B* 106 (2002) 11203.
- [2] L.D. Carlos
- [3] G. Nenna, G. Flaminio, T. Fasolino, C. Miaroni, R. Miscioscia, D. Palumbo, M. Pellegrino, *Macromol. Symp.* 247 (2007) 326.
- [4] A. Ashkin, J.M. Dziedzic, T. Yamane, *Nature* 330 (1987) 769.
- [5] H.B. Mao, T.L. Yang, P.S. Cremer, *J. Am. Chem. Soc.* 124 (2002) 4432.
- [6] M. Jang, S.S. Kim, J. Lee, *Exp. Mol. Med.* 45 (2013) e45.
- [7] D. Jaque, F. Vetrone, *Nanoscale* 4 (2012) 4301.
- [8] C.D. Brites, P.P. Lima, N.J. Silva, A. Millan, V.S. Amaral, F. Palacio, L.D. Carlos, *Nanoscale* 4 (2012) 4799.
- [9] S.W. Allison, G.T. Gillies, *Rev. Sci. Instrum.* 68 (1997) 2615.
- [10] S. Uchiyama, Y. Matsumura, A. P. de Silva, K. Iwai, *Anal. Chem.* 75 (2003) 5926.
- [11] A.L. Heyes, *J. Lumin.* 129 (2009) 2004.
- [12] N.N. Dong, M. Pedroni, F. Piccinelli, G. Conti, A. Sbarbati, J.E. Ramirez-Hernandez, L.M. Maestro, M.C. Iglesias-de la Cruz, F. Capobianco, J.G. Sole, M. Bettinelli, D. Joque, and A. Speghini, *ACS Nano* 5 (2011) 8665.
- [13] F. Vetrone, R. Naccache, A. Zamarron, A. Juarranz de la Fuente, F. Sanz-Rodriguez, L. M. Maestro, E. M. Rodriguez, D. Jaque, J.G. Sole, J.A. Capobianco, *ACS Nano* 4 (2010) 3254.
- [14] L.H. Fischer, G.S. Harmns, O.S. Wolfbeis, *Chem. Int. Ed.* 50 (2011) 4546.

Chapter 3 Luminescence nanothermometry in the visible: I. New detection techniques

- [15] V. Petrov, M.C. Pujol, X. Mateos, O. Silvestre, S. Rivier, M. Aguiló, R.M. Solé, J. Liu, U. Griebner, F. Díaz, *Laser Photon. Rev.* 1 (2007) 179.
- [16] L.D. Deloach, S.A. Payne, L.L. Chase, L.K. Smith, W.L. Kway, W.F. Krupke, *IEEE J. Quantum Electron.* 29 (1993) 1179.
- [17] M. Galceran, M. Pujol, M. C. Aguilo, M. Diaz, F. J. Sol-Gel Sci. Techn. 42(2007) 79.
- [18] V. Petrov, M.C. Pujol, X. Mateos, O. Silvestre, S. Rivier, M. Aguilo, R.M. Sole, J. Lin, U. Griebner, F. Diaz, *Laser and Photon. Rev.* 1 (2007) 179.
- [19] V. Jambunathan, X. Mateos, M.C. Pujol, J.J. Carvajal, F. Diaz and M. Aguilo, *J. Lumin.* 131 (2011) 2212.
- [20] R.H. Page, K.I. Schaffers, P.A. Waide, J.B. Tassano, S.A. Payne, W.F. Krupke, W.K. Bischel, *J. Opt. Soc. Am. B* 15 (1998) 996.
- [21] E.W. Barrera, Lanthanide-based Dielectric Nanoparticles for Upconversion Luminescence, PhD Thesis, Universitat Rovira i Virgili, Tarragona, 2013.
- [22] B. Dong, B. Cao, Y. He, Z. Liu, Z. Li, Z. Feng, *Adv. Mater.* 24 (2012) 1987.
- [23] M.L. Debasu, D. Ananias, I. Pastoriza-Santos, L.M. Liz-Marzán, J. Rocha, L.D. Carlos, *Adv. Mater.* 25 (2013) 4868.
- [24] L. Xing, Y. Xu, R. Wang, W. Xu, Z. Zhang, *Opt. Lett.* 39 (2014) 454.
- [25] S.K. Singh, K. Kumar, S.B. Rai, *Sens. Actuators A* 149 (2009) 16.
- [26] D. Li, Y. Wang, X. Zhang, K. Yang, L. Liu, Y. Song, *Opt. Comm.* 285 (2012) 1925.
- [27] A. Pandey, V.K. Rai, *Appl. Phys. B* 113 (2013) 221.
- [28] S.A. Wade, S.F. Collins, G.W. Baxter, *J. Appl. Phys.* 94 (2003) 4742.
- [29] E.W. Barrera, M.C. Pujol, C. Cascales, J.J. Carvajal, X. Mateos, M. Aguilo, F. Diaz, *Phys. Status Solidi C* 8 (2011) 2676.
- [30] B.S. Cao, Y.Y. He, Z.Q. Feng, Y. S. Li, B. Dong, *Sensor Actuat. B* 159 (2007) 8.
- [31] O.I.A. Savchuk, P. Haro-Gonzalez, J.J. Carvajal, D. Jaque, J. Massons, M. Aguilo, F. Diaz, *Nanoscale*, 6 (2014) 9727.
- [32] R.K. Benninger, Y. Koc, O. Hofmann, J. Requejo-Isidro, M.A. Neil, P.M. French, A.J. DeMello, *Anal. Chem.* 78 (2006) 2272.
- [33] H.U. Güdel, M. Pollnau, *J. Alloys Compd.* 303-304 (2000) 307.
- [34] L.A. Riseberg, H.W. Moss, *Phys. Rev.* 174 (1968) 429.
- [35] S.K. Ghoshal, M.R. Sahar, M.S. Rohani, S. Sharma, *Indian J. Pure Appl. Phys.* 49 (2011) 509.
- [36] K. Singh, K. Kumar, S.B. Rai, *Sensors and Actuators A* 149(2009) 16.
- [37] S.W. Allison, G.T. Gillies, A.J. Rondinone, M.R. Cates, *Nanotechnology* 14 (2003) 859.
- [38] J. Yu, L. Sun, H. Peng and M.I.J. Stich, *J. Mater. Chem.* 20 (2010) 6975.
- [39] Z.P. Cai, L. Xiao, H.Y. Xu, M. Mortier, *J. Lumin.* 129 (2009) 1994.
- [40] P. Haro-González, L. Martínez-Maestro, I.R. Martín, J. García-Solé, D. Jaque, *Small* 8 (2012) 2652.

Chapter 3 **Luminescence nanothermometry in the visible: I. New detection techniques**

Paper III

Savchuk, Ol. A.; J. J. Carvajal, M.C. Pujol, J. Massons, P. Haro-González, D. Jaque, M. Aguiló and F. Díaz. *New strategies for luminescence thermometry in the biological range using upconverting nanoparticles* (2015) Proc. of SPIE 9129, 91292-7.

Chapter 3 **Luminescence nanothermometry in the visible: I. New detection techniques**

New strategies for luminescence thermometry in the biological range using upconverting nanoparticles

Ol. A. Savchuk^a, J. J. Carvajal^{a*}, M.C. Pujol^a, J. Massons^a, P. Haro-González^b, D. Jaque^b, M. Aguiló^a and F. Díaz^a.

^aFísica i Cristal·lografia de Materials i Nanomaterials (FiCMA-FiCNA)- EMaS, Universitat Rovira i Virgili (URV), Campus Sescelades, C/ Marcel·li Domingo s/n, E-43007, Tarragona, Spain; ^bFluorescence Imagin Group, Departamento de Física de Materiales C-04 – Instituto Nicolás Cabrera, Universidad Autónoma de Madrid, C/ Francisco Tomás y Valiente 7, E-28049, Madrid, Spain

*corresponding autor: joanjosep.carvajal@urv.cat

ABSTRACT

We have studied different strategies of use of luminescence thermometry with upconverting nanoparticles in the biological range of temperatures, among them, the thermal sensing ability of fluorescent lifetime of Er,Yb:NaY₂F₅ nanoparticles. Er,Yb:NaY₂F₅O nanocrystals show great potentiality as thermal sensors at the nanoscale for biomedical applications due to the incorporation of additional non-radiative relaxation mechanisms that shorten the emission lifetime generated by the oxygen present in the structure. Here we report ex-vivo temperature determination by laser induced heating in chicken breast using lifetime-based thermometry in these up-conversion nanoparticles.

Keywords: Lifetime, thermometry, thermal sensing, temperature sensor.

INTRODUCTION

Non contact temperature measurements are of particular interest in most spheres of scientific activities and indeed in daily life. Almost all physical and chemical processes are temperature dependent. There are many areas of industry where the temperature measurements are essential, such as metallurgy, glass manufacture, moulding, dairy products and many other aspects of the food industries, where the contact conventional methods of temperature determination (thermocouples, thermistors or resistance thermometers) are not applicable due to altering of electrical signals and/or corrosion of the thermocouple junction [1]. Moreover, the importance of non contact thermometry in biomedical areas is enormous. For instance, a variety of cellular events, such as cell division and metabolism, are marked by temperature changes, cellular pathogenesis of cancer and other diseases is characterized by heat production, and increasing temperature beyond 45 °C leads to denaturation of biological molecules causing the necrosis of cells and tissues [2]. Consequently, regular monitoring of the temperature distribution in body regions of patients would be mandatory in the near future.

There are various types of non-contact nanothermometry approaches. The most studied is the luminescent nanothermometry based on temperature-dependent emission intensity, lifetime values, band shape or position of emission bands. These methods offer relatively high detection sensitivity and spatial resolution in short acquisition time, even in biological fluids, strong electromagnetic fields and fast-moving objects [3-9]. Lifetime-based thermometry has a lot of advantages when compared with intensity based approaches, since it can eliminate problems related with movement, shading and light distribution of the sample. Also this technique is much faster and can be used for high temperature measurements avoiding the black body radiation [10-13].

Many systems emit light through downconversion mechanisms of the excited wavelength, in which UV or high energy visible light are used as the excitation source to obtain emissions at longer wavelengths. The main limitation is that light in this range of wavelengths is absorbed by the surrounding biological tissues. This leads to background fluorescence, that can mask the signal emitted by luminescent nanoparticles used

Chapter 3 Luminescence nanothermometry in the visible: I. New detection techniques

to determine temperature and can also damage the biological tissue [14,15]. The use of upconversion nanoparticles, which exhibit efficient visible emission properties after being excited with near infrared (NIR) energy, can obviously overcome these problems and also provide a dual function of imaging and temperature sensing at the nanoscale [16].

Er³⁺ doped and Yb³⁺, Er³⁺ co-doped upconversion systems have received increasing interest in recent years in applications comprising bioimaging [17-19], displays [20] and nanothermometry [21-27]. The potentiality of Er³⁺, Yb³⁺ co-doped upconversion nanoparticles for nanothermometry in the biological range of temperatures has been recently demonstrated. Vetrone et al. have measured the internal temperature of living HeLa cells incubated with Er,Yb:NaYF₄ nanoparticles from 25 °C to its thermally induced death at 45 °C [27]. Fischer et al. sensed temperatures in human embryo kidney cells using the same nanoparticles at 18 °C and 33 °C through confocal fluorescence microscopy images of the green and red emissions of Er³⁺ in these nanoparticles and comparing their intensities [28].

However, up to now these upconversion systems have been used as nanothermometers through emission intensity based approaches, due especially to the suitable energy gap between the ²H_{11/2} and ⁴S_{3/2} energy levels of Er³⁺ that are thermally coupled. In this work we present the potentiality of temperature dependent fluorescent lifetimes in the biological range of Er,Yb:NaY₂F₅O nanoparticles. Er,Yb:NaY₂F₅O nanocrystals present a higher thermal coefficient than Er,Yb:NaYF₄ nanoparticles, with interesting possibilities as thermal sensors at the nanoscale for biomedical applications, as we demonstrate for sub-tissue temperature determination in chicken breast.

EXPERIMENTAL SECTION

Er,Yb:NaY₂F₅O nanoparticles were provided by Boston Applied Technology. The size and morphology of Er,Yb:NaY₂F₅O nanoparticles were determined by using a Transmission electron microscope (TEM) JEOL JEM-1011 operating with an accelerating voltage of 100 kV.

For luminescence decay-time experiments, Er,Yb:NaY₂F₅O nanoparticles were excited at 980 nm with an optical parametric oscillator from Opotek (Vibrant HE 355 II+UV) with a pulse duration of 6 ns and a repetition frequency of 10 Hz. The fluorescence light emitted by the sample was collected with a microscope objective, transferred to the monochromator for the selection of specific wavelengths, and then detected using a Hamamatsu R928 photomultiplier. The decay of the signal was measured as a function of time with a digital oscilloscope.

For lifetime thermal sensing experiments, Er,Yb:NaY₂F₅O nanoparticles were introduced into a Linkam THMS 600 heating stage, with temperature controlled by thermocouples connected to the heating stage. After calibration, Er,Yb:NaY₂F₅O nanoparticles were dispersed in distilled water and injected into a fresh chicken breast. A heating laser with emission at 1090 nm was focused in the chicken breast using a microscope objective. A second laser with emission at 980 nm was focused in the sample, spatially overlapping with the heating spot, to pump the luminescent nanoparticles. The generated fluorescence by the nanoparticles was collected by the same objective and after passing the selected filters was focused into the photomultiplier tube connected to the digital oscilloscope. Figure 1 shows a schematic representation of the setup used in the ex-vivo sub-tissue temperature determination.

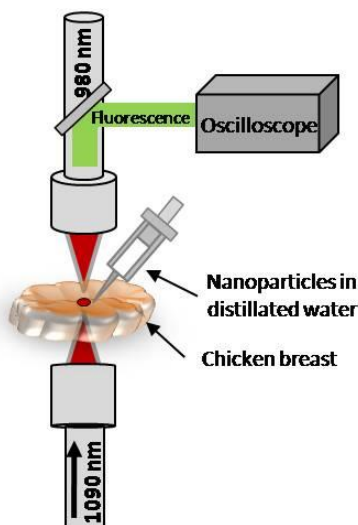


Figure 1. Scheme of the setup used in the experiment of ex-vivo sub-tissue temperature determination in chicken breast using a heating laser emitting at 1090 nm and a pumping laser for the luminescent nanoparticles emitting at 980 nm.

RESULTS AND DISCUSSION

We studied the temperature dependent fluorescence lifetime of the 545 nm emission line of Er,Yb:NaY₂F₅O nanoparticles in the biological range of temperatures from 25 to 60 °C. Temperature-dependent normalized lifetimes of Er,Yb:NaYF₄ and Er,Yb:NaY₂F₅O nanoparticles for the 545 nm emission line at the biological range of temperatures are shown in Figures 2 (a, b), defined as $\tau^{norm}(T) = \tau(T)/\tau(25\text{ °C})$, where $\tau(T)$ is the lifetime measured at a determined temperature and $\tau(25\text{ °C})$ is the lifetime measured at room temperature. In both cases, lifetime decreases almost linearly with temperature. In order to have a practical indicator of temperature using lifetime measurements, it is highly desirable to have a linear dependence with temperature since it simplifies the calibration of the system. Thus, in this case we have excellent temperature sensors, especially in the case of Er,Yb:NaY₂F₅O nanoparticles where the slope of the linear fit is higher.

For all kind of temperature sensors it is important to know the sensitivity of the measured parameter, i.e. the magnitude of the change of this parameter for every degree of temperature increased. Here, the sensitivity is represented by the thermal coefficient, that is defined as the first derivative of the normalized fluorescence lifetime at a given temperature to respect the temperature, and estimates the ability to measure small temperature changes associated to large changes in the measured fluorescence lifetimes. From the experimental data shown in Figures 2 (a,b) we calculated the thermal coefficient as the derivative of the linear fitting, as it is shown in the graphs. Thus, in our case, the thermal coefficients can be associated to the slopes of these linear fittings. They have values of $5.4 \times 10^{-3}\text{ °C}^{-1}$ for Er,Yb:NaYF₄ and $15 \times 10^{-3}\text{ °C}^{-1}$ for Er,Yb:NaY₂F₅O nanoparticles. This represents that $\alpha_T(\text{Er,Yb:NaY}_2\text{F}_5\text{O}) \approx 3 \cdot \alpha_T(\text{Er,Yb:NaYF}_4)$. The more pronounced change in lifetime in Er,Yb:NaY₂F₅O is associated to the nature of these nanoparticles. It is well known that non-radiative relaxation and multiphonon phenomena, responsible for the shortening of fluorescence lifetime decays, are more significant in oxide materials than in fluoride ones [12].

Chapter 3 Luminescence nanothermometry in the visible: I. New detection techniques

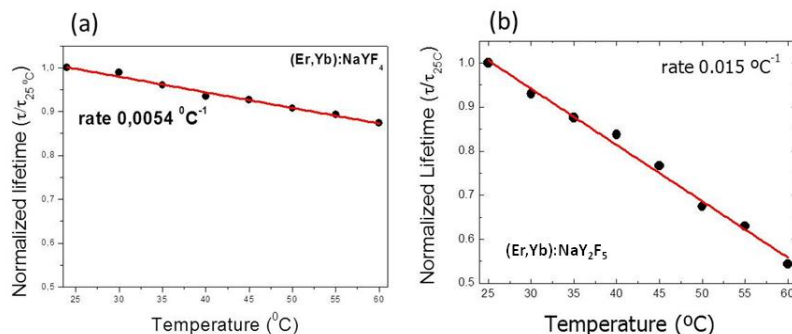


Figure 2. Calculated normalized lifetime values as a function of temperature for (a) Er,Yb:NaYF₄ and (b) Er,Yb:NaY₂F₅O nanoparticles.

In order to demonstrate the potential application of the lifetime thermometry of the green up-conversion emission obtained in Er,Yb:NaY₂F₅O nanoparticles, we have performed an ex vivo temperature determination experiment in chicken breast that was heated by an additional laser beam. Er,Yb:NaY₂F₅O nanoparticles were dispersed in water, and injected into a fresh chicken breast within a depth of 1 mm. Measurements of the lifetime of the emission at 545 nm in the chicken breast were recorded in a double beam confocal microscope, by pumping the luminescent nanoparticles at 980 nm through a microscope objective, while a 1090 nm continuous laser beam was spatially overlapped and used as the heating beam due to the non vanishing absorption coefficient of water at this wavelength. The fluorescence generated from the sample was collected by the same objective, and after passing selected filters and lenses was focused into the photomultiplier tube connected to a digital oscilloscope.

Figure 3(a) shows the reduction of the lifetime measured inside the chicken breast as the power of the heating laser was increased from 0 to above 1.5 W. As can be seen in the graph, the lifetime is substantially reduced from ~160 μs when the laser was off, to less than 120 μs for a power of the heating laser slightly above 1.5 W. Since Er,Yb:NaY₂F₅O nanoparticles do not absorb energy at 1090 nm, the reduction in the lifetime of the green emission of these particles is only due to the heat induced in the chicken breast tissue surrounding the nanoparticles by the heating laser beam. Thus, this evolution of the lifetime indicates the progressive heating of the tissue surrounding the nanoparticles by the effect of the increasing power of the 1090 nm laser. These data were used to determine the temperature inside the chicken breast, the sub-tissue temperature, as a function of the laser heating power, as can be seen in Figure 3(b). When the heating laser was off, the chicken breast was at room temperature, at around 20 °C. By switching the heating laser on, the temperature of the chicken breast could be increased to 25 °C, for a power of the laser of 0.5 W, and to above 30 °C for a power of the laser slightly higher than 1.5 W. Furthermore, the heating capacity of the laser seems to have a linear tendency with its power, as can be seen in this figure.

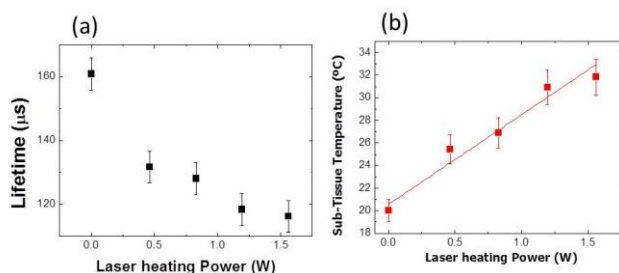


Figure 3. (a) Change of lifetime values when the power of the heating laser was increased; (b) Sub-tissue temperature increment measured through lifetime variations in the 545 nm emission line of Er,Yb:NaY₂F₅O nanoparticles as a function of the increase of the laser heating power.

CONCLUSION

Here we present how lifetime measured for the green emission produced by an upconversion process in Er,Yb-co-doped luminescent nanoparticles has been used as a thermal nanoprobe. The demonstrated capacity to determine sub-tissue temperatures in the biological range, together with the high thermal

coefficient obtained for Er,Yb:NaY₂F₅O nanoparticles, indicate the potentiality of this technique for future temperature determination in living organisms.

ACKNOWLEDGEMENTS

This work was supported by the Spanish Government under projects No. MAT2011-29255-C02-02, MAT2010-16161 and TEC2010-21574-C02-02, the Catalan Government under project No. 2009SGR235, the European Commission within the Seventh Framework Program under project No. FP7-SPA-2010-263044, and by the Universidad Autónoma de Madrid and Comunidad Autónoma de Madrid (Project S2009/MAT-1756). O.A. Savchuk is supported by Catalan Government through the fellowship 2013FI_B 01032. P.H.G. thanks Fundación Doctor Manuel Morales and Ministerio de Economía y Competitividad (subprograma Juan de la Cierva) for financial support.

REFERENCES

- [1]. Chris D. Geddes, Joseph R. Lakowicz, [Reviews in Fluorescence V.1], Kluwer Academic/Plenum Publishers, New York, 21-26 (2004).
- [2]. B. Hildebrandt, P. Wust, O. Ahlers, A. Dieing, G. Sreenivasa, T. Kerner, R. Felix, H. Riess, "The cellular and molecular basis of hyperthermia," *Crit. Rev. Oncol. Hemat.* 43, 33-56 (2002).
- [3]. T. Barilero, T. Le Saux, C. Gosse and L. Jullien, "Fluorescent thermometers for dual-emission-wavelength measurements: molecular engineering and application to thermal imaging in a microsystem," *Anal. Chem.* 81, 7988-8000 (2009).
- [4]. O. S. Wolfbeis, "Sensor paints," *Adv. Mater.* 20, 3759-3763 (2008).
- [5]. S. Allison and G. Gillies, "Remote thermometry with thermographic phosphors: instrumentations and applications," *Rev. Sci. Instrum.* 68, 2615-2650 (1997).
- [6]. P. R. N. Childs, J. R. Greenwood and C. A. Long, "Review of temperature measurement," *Rev. Sci. Instrum.* 71, 2959-2978 (2000).
- [7]. S. Uchiyama, A. P. de Silva and K. Iwai J., "Luminescent molecular thermometers," *Chem. Educ.* 83, 720-727 (2006).
- [8]. A. L. Heyes, J. Lumin., "On the design of phosphors for high-temperature thermometry," 129, 2004-2009 (2009).
- [9]. Ashiq Hussain Khalid and Konstantinos Kontis, "Thermographic phosphors for high temperature measurements: principles, current state of art and recent applications," *Sensors* 8, 5673-5744 (2008).
- [10]. T. Sun, Z. Y. Zhang, and K. T. V. Grattan, "Erbium/ytterbium fluorescence fiber optic temperature sensor system," *Rev. of Sci. Instrum.* 71, 11 (2000).
- [11]. Chie Gota, Seiichi Uchiyama, Toshitada Yoshihara, Seiji Tobita, and Tomohiko Ohwada, "Temperature-dependent fluorescence lifetime of a fluorescent polymeric thermometer, poly(*n*-isopropylacrylamide), labeled by polarity and hydrogen bonding sensitive 4-sulfamoyl-7-aminobenzofurazan," *J. Phys. Chem. B* 112, 2829-2836 (2008).
- [12]. M. D. Chambers and D. R. Clarke, "Doped oxides for high-temperature luminescence and lifetime thermometry" *Annu. Rev. Mater. Res.*, 325-359 (2009).
- [13]. P. Haro-Gonzalez, L. Martinez-Maestro, I. R. Martin, J. Garcia-Sole, and D. Jaque, "High sensitivity fluorescence lifetime thermal sensing based on CdTe quantum dots," *small*, 8 (17) 2652-2658 (2012).
- [14]. Y. T. Lim, S. Kim, A. Nakayama, N. E. Stott, M. G. Bawendi, and J. V. Frangioni, "Selection of quantum dot wavelengths for biomedical assays and imaging," *Molecular Imaging* 2 (1) 50-64 (2003).
- [15]. Stephen P. Jackson and Jiri Bartek, "The DNA-damage response in human biology and disease," *Nature* 461, 1071-1078 (2009).
- [16]. N. N. Dong, M. Pedroni, F. Piccinelli, G. Conti, A. Sbarbati, J. E. Ramirez-Hernandez, L. M. Maestro, M. C. Iglesias-de la Cruz, F. Capobianco, J. G. Sole, M. Bettinelli, D. Joque, and A. Speghini, "NIR-to-NIR Two-Photon Excited CaF₂:Tm³⁺, Yb³⁺ Nanoparticles: Multifunctional Nanoprobes for Highly Penetrating Fluorescence Bio-Imaging," *ACS Nano*, 5, 8665-8671 (2011).
- [17]. G. Jiang, J. Pinchaandi, N. J. J. Johnson, R. D. Burke, F. C. J. M. Van Veggel, "An effective polymer cross-linking strategy to obtain stable dispersion of upconverting NaYF₄ nanoparticles in buffers and biological growth media for biolabeling applications," *Langmuir* 28, 3239-3247, (2012)
- [18]. Z. Li, Y. Zhang, S. Jiang, "Multicolor Core/Shell-Structured Upconversion Fluorescent Nanoparticles," *Adv. Mater.* 20 4765-4769, (2008)
- [19]. G. S. Yi, H. C. Lu, S. Y. Zhao, G. Yue, W. J. Yang, D. P. Chen, L. H. Guo, "Synthesis, characterization and biological application of size-controlled nanocrystalline NaYF₄ : Yb,Er infrared-to-visible up-conversion phosphors," *Nano Letters* 4 2191 (2004).

Chapter 3 Luminescence nanothermometry in the visible: I. New detection techniques

- [20]. A. Rapaport, J. Milliez, M. Bass, A. Cassanho and H. Jenssen, "Review of the Properties of Up-Conversion Phosphors for New Emissive Displays," *Journal of display technology*, V. 2, 1, 68-78 (2006).
- [21]. Riya Dey, Anurag Pandey, Vineet Kumar Rai, "Er³⁺-Yb³⁺ and Eu³⁺-Er³⁺-Yb³⁺ codoped Y₂O₃ as a optical heater" *Sensors and Actuators B* 190, 512-515 (2014).
- [22]. Lu Liu, Yujin Chen, Xinlu Zhang, Zhengno Zhang, Yuxiao Wang, "Improved optical thermometry in Er³⁺:Y₂O₃ nanocrystals by re-calcination," *Optics Comm.* 309, 90-94 (2013).
- [23]. Nikifor Rakov, Glaucio S. Maciel, "Three-photon upconversion and optical thermometry characterization of Er³⁺:Yb³⁺ co-doped yttrium silicate powders," *Sensors and Actuators B* 164, 96-100 (2012).
- [24]. B. S. Cao, Y. Y. He, Z. Q. Feng, Y. S. Li, B. Dong, "Optical temperature sensing behavior of enhanced green upconversion emissions from Er-Mo:Yb₂Ti₂O₇ nanophosphor," *Sensors and Actuators B* 159, 8-11 (2011).
- [25]. K. Wu, J. Cui, X. Kong, and Y. Wang, "Temperature dependent upconversion luminescence of Yb/Er codoped NaYF₄ nanocrystals," *J. of Appl. Phys.* 110, 053510 (2011).
- [26]. Shaoshuai Zhou, Kaimo Deng, Xiantao Wei, Guicheng Jiang, Changkui Duan, Yonghu Chen, Mi Yin, "Upconversion luminescence of NaYF₄: Yb³⁺, Er³⁺ for temperature sensing," *Optics Comm.* 291, 138-142 (2013).
- [27]. F. Vetrone, R. Naccache, A. Zamarron, A. Juarranz de la Fuente, F. Sanz-Rodriguez, L. M. Maestro, E. M. Rodriguez, D. Jaque, J. G. Sole, and J. A. Capobianco, "Temperature Sensing Using Fluorescent Nanothermometers," *ACS Nano* 4, 3254-3258 (2010).
- [28]. L.H. Fischer, G.S. Harmns, O.S. Wolfbeis, "Upconverting Nanoparticles for Nanoscale Thermometry," *Chem. Int. Ed.* 50, 4546-4551 (2011).

Paper IV

Savchuk, Ol. A.; Carvajal, J. J.; Cascales, C.; Massons, J.; Aguiló, M.; Díaz, F. *Thermochromic upconversion nanoparticles for visual temperature sensors with high thermal, spatial and temporal resolution* (2016) To be submitted to ACS Applied surfaces & interfaces.

Chapter 3 **Luminescence nanothermometry in the visible: I. New detection techniques**

Thermochromic upconversion nanoparticles for visual temperature sensors with high thermal, spatial and temporal resolution

Ol. A. Savchuk, J. J. Carvajal,* C. Cascales, J. Massons, M. Aguiló, F. Díaz

Luminescence thermometry is one of the most currently studied approaches among the non-contact and non-invasive thermometry techniques working at the micro- and nanoscale, useful in situations where conventional thermometry is not able to make measurements, such as in temperature mapping of microcircuits and microfluidics. Here we present the first, to the best of our knowledge, thermochromic temperature small scale sensor based on the blue to deep red color change of the upconverted light from Yb³⁺-sensitized Tm³⁺-doped GdVO₄@SiO₂ core-shell nanoparticles under near infrared (NIR) excitation ($\lambda_{exc} = 980$ nm). The electronic coupling of corresponding ¹G₄ (blue) and ³F₂ (deep red) Tm³⁺ emitting levels has been experimentally evidenced. Furthermore, we propose energy transfer schemes accounting for the thermal evolution of the electronic populations of these energy levels that support the temperature dependent ratiometric relationship between the intensities of the visible signals, and thus provide the internal calibration to the temperature sensing system. To show the potentiality of our nanothermometer, we monitored the heating process produced by Joule effect in a Pt wire, 50 μ m in diameter, with thermal and temporal resolutions of ± 0.1 K and < 16 ms, respectively. The results matched very well with the theoretical modeling for this system.

A. Introduction

The knowledge of temperature at low-sized micro- and sub-micrometer scales, with adequate high spatial resolution and high sensitivity is essential in several industrial processes and scientific research. At these size scales heat transfer and related thermodynamic phenomena are drastically altered, and the dynamics and performances of micrometric and nanostructured systems are strongly determined by temperature. Thus, sensing temperature in an accurate way with high spatial resolution is critical in micro- and nanoelectronics, micro- and nanophotonics, microfluidics and nanomedicine.¹ In micro- and nanoelectronics it is necessary to take into account the non-negligible Joule heating effect arising from the reduced dimensions of electrical conduction channels, in which small variations in the local resistance could generate localized temperature increments (hot-spots) that can cause performance deterioration or even failure of the electronic systems.² Light control and manipulation in integrated photonic devices are achieved by small scale controlled variations of local refractive indexes. Thus, variations in the local temperature might strongly affect their performances.³ In optofluidics, where light is used to manipulate micron sized objects (including living specimens) moving within micro-fluidic channels through the use of optical forces, residual absorption of fluids at laser radiation wavelengths can cause heat loading and malfunctions of the devices,⁴ thus temperature determination at this scale is also of paramount importance in this field. Also, thermal sensing of biological systems might allow early detection of many diseases, including cancer, which are primarily manifested by the appearance of thermal singularities due to the incremented metabolic activity of the living cells,² and additionally the temperature control is crucial in hyperthermal tumor treatment and photodynamic therapies, in order to minimize thermally induced damage in surrounding tissues. The limitations of contact thermometers when they reach small size scales (shot noise, tunnel junction effects, etc) had led to the development of non-contact temperature sensing techniques, among which optical thermometers based on temperature-dependent emission lifetimes and intensity of dye-sensitized polymer dots, semiconducting quantum dots, and lanthanide (Ln^{3+})-doped materials, are arising as a strong alternative.^{5,6} Optical-fiber temperature sensing devices making use of the temperature dependence of the fluorescence decay time,⁷ or the emission intensity,⁸ built in the latter three decades, constitute preceding approaches of these current development.

Of particular interest are those luminescent thermometers based on upconversion nanoparticles containing Ln^{3+} ions,⁹ (Ln-UCNPs), that absorb light in the near-infrared (NIR) region of the electromagnetic spectrum, and emit light in the visible range. Upconversion is a nonlinear photoexcitation process where two or more photons, with low energy, typically in the NIR, are sequentially absorbed by a Ln^{3+} ion, followed by the emission from low-lying higher energy electronic states of the same or a different Ln^{3+} ion with which the initial one experiences a resonant energy transfer process.¹⁰ In that case, temperature determination is usually based on the measurement of the intensity ratio between two fluorescence transitions (FIR) arising from two closely spaced, thus in thermal equilibrium ("thermally-coupled") electronic energy levels, being the FIR an intrinsic function of the temperature alone. The main advantage of the ratiometric FIR methodology for temperature sensing is its independency of signal losses and possible fluctuations in the excitation intensity. A further crucial benefit for intended applications of Ln^{3+} -doped upconversion nanothermometers is associated to the NIR light used for exciting them, which extends the operating lifetime of the luminescent nanoparticles, avoiding the degradation problems generated, for instance, if the nanoparticles are pumped with UV light. Furthermore, when used in biological applications, NIR light can

deeply penetrate the biological tissue, while it does not cause background luminescence in the visible.¹¹ However, the use of visible emitted wavelengths restricts their real application in this field due to their short tissue penetration depths, caused by tissue scattering and specific absorptions of tissue components.¹¹ Also, illumination of biocompatible fluids like PBS with tightly focused femtosecond NIR lasers generates white light that can mask the emission arising from the thermal probes emitting in the visible.¹²

Unfortunately, some limitations to the efficiency of upconverted light from Ln-UCNPs arise from their inherently large surface area, which contains defects and a variety of luminescence quenchers, thus favoring non-radiative relaxations.¹³ By choosing low-phonon matrices such as halides, multiphonon de-excitation probabilities are minimized, overcoming this problem to some extent. However, halide-based materials are usually hygroscopic and show relatively poor chemical and photophysical stabilities compared with oxide matrices. Also, most of the preparative routes for halide-based Ln-UCNPs are complex and environmentally harmful.

Among potential Ln-UCNPs alternative to halide-based materials, nanocrystalline tetragonal zircon-type Ln^{3+} -doped GdVO_4 prepared by a low temperature cost-effective hydrothermal method offers an opportunity to develop a satisfactory optical nanothermometer. The GdVO_4 host is characterized by high optical absorption and emission cross-section values for the Ln^{3+} -doping ions, relatively high thermal conductivity and moderate cut-off phonon energy. When coated with SiO_2 , Yb^{3+} sensitized, Ln^{3+} -doped GdVO_4 nanocrystals (here after Ln, Yb:GdVO₄@SiO₂) show improved intensity of the upconverted visible emitted light following NIR diode laser excitation.¹⁴ Ladder-like energy levels of Tm^{3+} offers the possibility of simultaneous blue, red and deep red visible emissions under NIR excitation. In this work we demonstrate a new thermochromic nanosensor involving the temperature dependent blue to deep red light color change in $\text{Tm,Yb:GdVO}_4@\text{SiO}_2$ UCNPs whose Tm^{3+} concentration has been optimized, with high thermal, spatial and temporal resolutions. We proved the potentiality of our detector to monitor the heating process generated in a Pt microwire by the Joule effect. Furthermore, we also experimentally establish that blue and deep red lights are emitted from electronically coupled¹⁵ $^3\text{F}_{2,3}$ and $^1\text{G}_4$ Tm^{3+} energy levels, and we propose the electronic energy transfer schemes that support the temperature dependent ratiometric relationship between the intensities of these visible signals for a fixed Tm^{3+} concentration, thus providing an internal calibration to this temperature sensing system. Up to date, only deep red to NIR ratiometric thermal sensing through thermally coupled $^3\text{F}_{2,3}$ and $^3\text{H}_4$ energy levels has been demonstrated in Tm^{3+} -doped CaF_2 nanoparticles,¹¹ Tm^{3+} -doped LiNbO_3 nanocrystals,¹⁶ mixed hexagonal and cubic Tm^{3+} -NaYbF₄@SiO₂ microparticles,¹⁷ and other sub-micrometric systems.^{18,19}

B. Materials and Methods

Crystalline nanoparticles of GdVO_4 doped with Tm^{3+} (0.2 – 5.0 mol%), and sensitized with Yb^{3+} (15 mol%), whose single excited $^2\text{F}_{5/2}$ state provides a large absorption cross-section for the diode laser excitation at ~980 nm as well as efficient energy transfer to Tm^{3+} , have been prepared (2 mmol) using NH_4VO_3 (Cerac, 99.5 %) and lanthanide nitrates ($\text{Gd}(\text{NO}_3)_3 \cdot 6\text{H}_2\text{O}$, $\text{Yb}(\text{NO}_3)_3 \cdot 6\text{H}_2\text{O}$, $\text{Tm}(\text{NO}_3)_3 \cdot 6\text{H}_2\text{O}$, Strem Chemicals, 99.99%) as reactants. The first step involves the preparation of the solution (distilled water, 40 ml) of the required amounts of lanthanide nitrates and NH_4VO_3 , with the pH adjusted to 7 by adding dilute NH_4OH under stirring during 1 h. In each case, the yellow dispersion was afterwards hydrothermally treated at 458 K during 24 h in sealed Teflon-lined autoclaves of 75 ml capacity. The product obtained was separated by centrifugation, several times washed with distilled water and overnight dried at 393 K in open air. To achieve improved emission efficiency, the hydrothermal prepared samples were annealed to 873 K for 5 h. Further coating of the

nanoparticles surface with a layer of controlled thickness of silica SiO_2 was also carried out. The formation of the SiO_2 coating requires the base-catalyzed hydrolysis of tetraethoxysilane ($\text{Si}(\text{OC}_2\text{H}_5)_4$, TEOS, liquid, Alfa Aesar 99%) and subsequent condensation of silanol (Si-OH) groups onto the surface of $\text{Tm}_2\text{Yb}_2\text{GdVO}_4$ nanoparticles. A half of the prepared amount of above samples was dispersed in an ethanolic (40 ml ethanol absolute 99.5% Emplura Merck + 4 ml distilled water) solution with the pH adjusted to 9 with diluted NH_4OH , and then 2 ml of TEOS were added and kept under stirring for 4 h. The product was finally washed with ethanol, centrifuged and dried to 393 K.

The crystalline phase of the different $\text{Tm}_2\text{Yb}_2\text{GdVO}_4$ samples was characterized at room temperature by powder X-ray diffraction (XRD) using a Bruker AXS D-8 Advance diffractometer with $\text{Cu K}\alpha$ radiation. Hydrodynamic particle size distributions were measured by dynamic light scattering (DLS) using a Vasco 2-Cordouan equipment, with samples dispersed in distilled water. Transmission electron microscopy (TEM) images were obtained with a JEOL 2000FXII microscope with an accelerating voltage of 200 kV, and high resolution TEM (HRTEM) images were obtained with a JEOL model JEM-4000EX microscope, with an accelerating voltage of 400 kV.

The emission spectra of $\text{Tm}_2\text{Yb}_2\text{GdVO}_4@ \text{SiO}_2$ nanoparticles from room temperature up to 673 K were recorded by pumping at 980 nm with an Apollo Instruments, Inc. cw diode laser. The power of the laser was changed between 200 and 600 mW to pump samples with 1 and 2% Tm^{3+} , and the rest of the samples, respectively. The diameter of the laser spot after focusing was 5 mm^2 . However, it transformed to an ellipsoid with an area of 9 mm^2 when projected onto the sample since the incident laser illuminated the sample at 45°. In these conditions the laser power density in the surface of the samples was 24 mW cm^{-2} . The samples were illuminated with the laser only during the time needed to record each spectrum, to avoid any thermal heating of the samples induced by the excitation laser. Temperature of the samples was controlled by fixing them in a modified heating stage Linkam THMS 600 that incorporates a boron nitride disk to improve the homogeneity of temperature distribution along the sample and with a thermocouple placed below the sample to have an approximation of the real temperature on the sample on the temperature controller. The emission from the samples was dispersed in a JobinYvon HR 460 monochromator. A Hamamatsu PMTR 928 photomultiplier tube connected to a Perkin Elmer DSP-7265 lock in amplifier was used to detect and amplify the collected signal. Finally, pictures illustrating the color of the emission generated by the samples were recorded using a CCD camera Thorlabs DCU224C, and the emission spectra were recorded with a AVANTES AVS-USB2000 fiberoptic spectrometer.

C. Results and Discussion

All prepared $\text{Tm}_2\text{Yb}_2\text{GdVO}_4$ and $\text{Tm}_2\text{Yb}_2\text{GdVO}_4@ \text{SiO}_2$ core-shell nanoparticles are yellow in color, and present the pure tetragonal $I4_1/amd$ zircon-type phase (JCPDS File 86-0996). The described procedure to synthesize $\text{Tm}_2\text{Yb}_2\text{GdVO}_4$ nanoparticles involves considerably softer temperatures than those usually required in solid-state reactions (~1473 K)²⁰ to achieve polycrystalline tetragonal vanadates, commonly used as starting materials for Czochralski crystal growth of corresponding laser crystals (~2273 K).²¹ Figure 1 depicts the powder X-ray diffraction (XRD) patterns of raw hydrothermal $\text{Tm}_2\text{Yb}_2\text{GdVO}_4$ nanoparticles annealed at 873 K for 5 h, and the corresponding core-shell structures. By using Scherrer's equation the mean particle size of raw hydrothermal nanoparticles (i.e., individual crystalline domains or 'primary crystalline nanoparticles') calculated from the full width at half maximum (FWHM) of the observed Bragg peak at $\sim 25^\circ$ (2θ) is ~ 27 nm (see Fig. 1(a)). After thermal annealing at 873 K the observed narrowing of diffraction peaks indicates that the mean particle size increases to ~ 35 nm, Figure 1(b). No

additional reflections have been detected for SiO_2 -coated samples, the rougher background reflecting the presence of amorphous SiO_2 .

Figure 1(d) displays a characteristic TEM image of the annealed vanadate nanoparticles, with polygonal sections. Figures 1(e)-1(g) correspond to $\text{Tm}_2\text{Yb}_2\text{GdVO}_4@ \text{SiO}_2$ core-shell nanoparticles, with darker and lighter parts being the $\text{Tm}_2\text{Yb}_2\text{GdVO}_4$ core and their amorphous silica coating, respectively. It is observed that the coating layer has a thickness of ~ 5 nm, uniformly around all nanoparticles, which mostly retain their initial polygonal shape. HRTEM images of discrete nanoparticles reveal in all cases a well-defined single crystal structure characteristic of the tetragonal $I4_1/amd$ symmetry of GdVO_4 . From the lattice fringes in Figure 1(g) the resolved interplanar spacing are found to be about 0.473 nm, consistent with the d -spacing between (101) planes of GdVO_4 (JCPDS File 86-0996). Characteristic results from DLS measurements on the particle size distribution of $\text{Tm}_2\text{Yb}_2\text{GdVO}_4$ annealed at 873 K and silica-coated $\text{Tm}_2\text{Yb}_2\text{GdVO}_4@ \text{SiO}_2$ samples are included in the Supplementary Information, Figures S1(a) and S1(b), respectively. Their corresponding XRD patterns are those shown in Figures 1(b) and 1(c). The DLS histogram in Figure S1(a) indicates a narrow size distribution, with around 80% of nanoparticles having sizes in the range of 30-45 nm, in agreement with the calculated average size from XRD data, the difference being mainly due to the effect of the double layer thickness around the nanoparticles on the measurement of hydrodynamic radius carried out by DLS. For $\text{Tm}_2\text{Yb}_2\text{GdVO}_4@ \text{SiO}_2$ the histogram in Figure S1(b) indicates that around 65% of nanoparticles have sizes between 90 and 135 nm, and the difference with the calculated average size from XRD data arises from the presence of aggregates of the primary nanoparticles, i.e., aggregates of the individual crystalline domains measured by XRD.

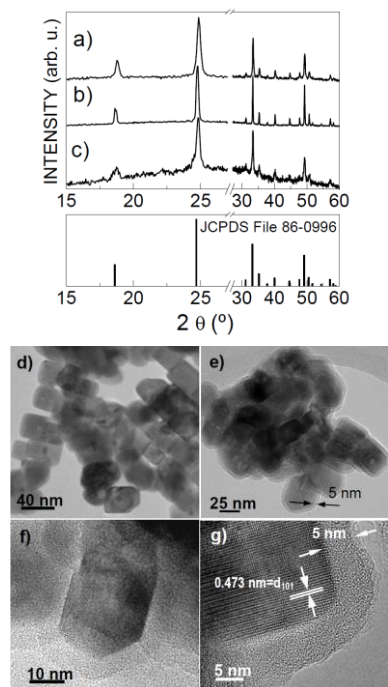


Fig. 1 X-ray diffraction (XRD) patterns of $\text{Tm}_2\text{Yb}_2\text{GdVO}_4$ samples: (a) The raw sample prepared by 24 h of hydrothermal synthesis at 458 K with pH

7; (b) The sample after thermal annealing at 873 K during 5 h; (c) The annealed sample with further coating with a layer of ~ 5 nm of SiO₂. For comparison the XRD pattern scheme of tetragonal I4₁/amd GdVO₄, JCPDS File 86-0996 has been also included; (d) TEM image of hydrothermal nanoparticles annealed at 873 K showing polygonal sections; (e), (f) and (g) HRTEM images of nanoparticles coated with a 5 nm-shell of SiO₂.

Figure 2(a) depicts a schematic representation of the distribution of energy levels of Yb³⁺ and Tm³⁺ as well as the energy transfer mechanisms proposed for visible upconversion emissions in GdVO₄ under NIR excitation at 980 nm. Figure 2(b) shows the upconversion spectra of the 1%Tm³⁺, 15%Yb³⁺:GdVO₄@SiO₂ sample, from room temperature up to 673 K under NIR (980 nm) diode laser excitation. Typically three emission bands are observed in the visible range, at ~473 nm (blue), corresponding to the ¹G₄→³H₆ Tm³⁺ transition, at ~642 nm (red), attributed to the ¹G₄→³F₄ Tm³⁺ transition, and at ~700 nm (deep-red), assigned to the ³F₃→³H₆ Tm³⁺ transition. The relative intensity of these transitions changes by increasing the temperature of the sample, being especially noteworthy the observed evolution of the blue and deep-red upconverted bands intensities. At room temperature the blue emission at ~475 nm is dominant, and the intensity of the deep-red band at ~700 nm is small, however, by rising the sample temperature the intensity of the blue band decreases while the intensity of the deep-red one increases, becoming significant at temperatures above 473 K. Finally, at the higher temperature measured, 673 K, the blue emission is severely quenched while the deep red one is enhanced by a factor of 3.1 with regards to its intensity at room temperature.

Thus, a temperature sensor can be built based on thermally induced changes in the intensity ratio of deep red and blue upconversion emissions (I_{700/475}) of 1% Tm³⁺, 15% Yb³⁺:GdVO₄@SiO₂ nanoparticles. Such ratiometric approach derives from the different temperature dependencies of radiative and non-radiative relaxation rates of blue and deep red emitting levels, as well as of the temperature dependent energy transfer rate from the first to the latter,^{22,23} and provides an internally calibrated signal to the sensing system. The mechanism for thermal sensing using current vanadate nanoparticles under diode laser excitation at 980 nm is proposed in Figure 2(a). For 1% Tm³⁺, 15% Yb³⁺:GdVO₄ nanoparticles kept at room temperature, the population of the blue emitting ¹G₄ Tm³⁺ level can be explained by sequential three-photon absorption and energy transfer processes from excited Yb³⁺. In a first step, the excited Yb³⁺ ²F_{5/2} level transfer part of its energy to the ³H₅ level of Tm³⁺, from which electrons relax very fast to the ³F₄ energy level. Then a second energy transfer from Yb³⁺ promotes Tm³⁺ to the ³F₂ energy level, which relaxes populating the ³F₃ and ³H₄ energy levels. Finally, the third electronic energy transfer promotes Tm³⁺ in ³H₄ to the ¹G₄ level. The blue and red emissions centered at 475 and 642 nm arise from radiative ¹G₄→³H₆ and ¹G₄→³F₄ electronic transitions, respectively. The progressive quenching of the blue emission from ¹G₄ and the simultaneous development of the deep-red emission from ³F₃ when the temperature increases point to the efficiency enhancement of some cross-relaxation (CR) processes, from which both ¹G₄ depopulation and (³F₂)³F₃ population take place: i) [¹G₄, ³H₆]→[³F₂)³F₃, ³F₄], see the scheme CR1 in Figure 2(a); additionally in this step the enhanced population of ³F₄ can also contribute to feed (³F₂)³F₃ levels via energy transfer from Yb³⁺ to Tm³⁺. ii) [¹G₄, ³H₆]→[³H₄, ³H₅], and iii) [¹G₄, ³H₆]→[³H₅, ³H₄], see the schemes CR2 and CR3, respectively, in Figure 2(a). (³F₂)³F₃ energy levels are separated of the ³H₄ level by an energy difference of ~1900 cm⁻¹,²⁴ and they have demonstrate to constitute thermally coupled states. Thus, the upper (³F₂)³F₃ levels can be populated from the ³H₄ level when the temperature increases,^{15,16} see

orange circular arrows (in the digital version) drawn between ³H₄ and (³F₂)³F₃ in Figure 2(a).

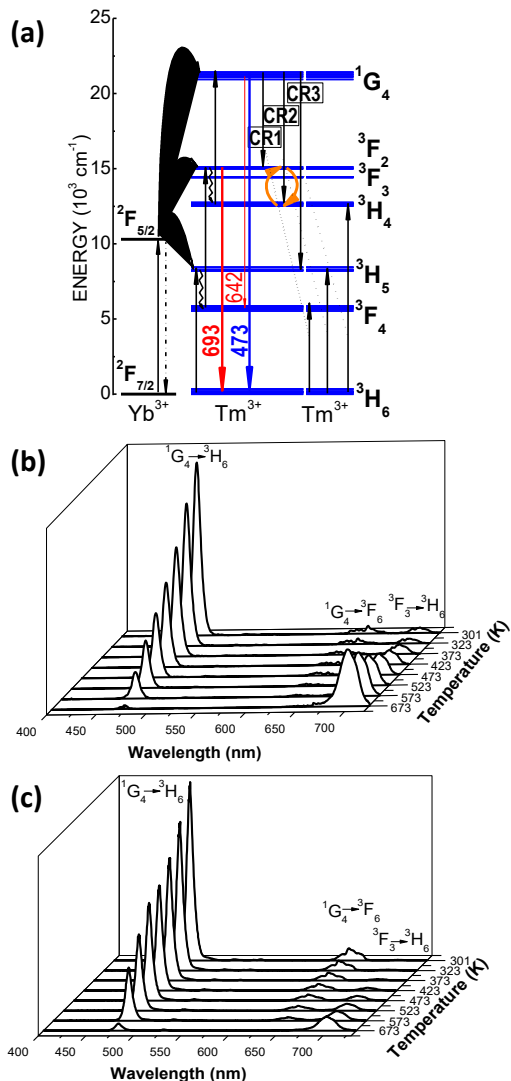


Fig. 2(a) Schemes of Yb³⁺ and Tm³⁺ energy levels and proposed mechanisms responsible for populating Tm³⁺ levels involved in observed blue, red and deep red emissions. Evolution from room temperature up to 673 K of upconversion spectra under 980 nm excitation: (b) Sample doped with 1% Tm³⁺. (c) Sample doped with 0.2% Tm³⁺.

The above CR processes for depopulating ¹G₄ and, directly (CR1) or indirectly (CR2, CR3), feeding (³F₂)³F₃ levels turn out to be important for concentrated samples, as for the measured 1% Tm-doped sample, and in fact, samples with lower Tm³⁺ content do not show such strong deep-red emission from ³F₃, as will be seen afterwards. To illustrate this point, the evolution with the temperature of the emission spectrum corresponding to a sample doped with low Tm³⁺ concentration (0.2%) can be seen in Figure 2(c), in which the small development of the deep-red band indicates that the Tm³⁺ concentration threshold for efficient CR has not been achieved. Proposed CR1, CR2 and CR3

processes have been previously described, and satisfactorily confirmed by an analytical model based on the luminescence decay curves and Judd-Ofelt theory, as responsible for the quenching of the blue emission from 1G_4 excited state and the strong development of the deep-red emission from 3F_3 state in a Tm,Yb-doped glass system.²⁵ In this last system, the indicated CR processes result strengthened due to the decrease of Tm³⁺ distances induced by the crystallization of the glass. In 1% Tm, 15% Yb:GdVO₄@SiO₂ nanoparticles, where the Tm³⁺ concentration has been optimized, the efficiency of the same CR energy transfers, which leads to near complete quenching of the blue emission from 1G_4 and the related enhancement of the deep-red emission from 3F_3 , is associated to the increasing temperature in the crystalline environment. Additionally, the specific distribution of the involved Tm³⁺ energy levels in the GdVO₄ host,²⁴ supports near-resonant CR2 and CR3 energy transfers.

To assess the temperature sensing performance of 1% Tm, 15% Yb:GdVO₄@SiO₂ nanoparticles based in the evolution of deep red and blue upconverted emissions, Figure 3(a) shows the plot representing their intensity ratio $R = I_{700}/I_{475}$ as function of the absolute temperature. It can be seen that the plot follows an increasing exponential function. The experimental data can be fitted to an exponential equation:

$$R(T) = \frac{I_{700}}{I_{475}} = A + B \exp[CT] \quad (1)$$

with $A = 0.44 \pm 0.01$, $B = 0.0020 \pm 0.0003$ and $C = 0.0146 \pm 0.0002$. From Figure 3(a) it is clear that the I_{700}/I_{475} intensity luminescence ratio is strongly temperature dependent, varying more than 5 times from 573 K and 673 K, thus it can ensure a very precise temperature measurement in this range. Error bars in Figure 3(a) reflect the reproducibility of the calibration curve after analyses of several spectra for each measured temperature. Following the usual definition, the intrinsic sensitivity is the main value that indicates the ability of the sensor to detect small changes in temperature, which in general terms is expressed as $S(T) = \partial P / \partial T$, where P is the measured temperature-sensitive parameter. For ratiometric optical thermometry P is the ratio R between intensities of the two emission bands, I_{700}/I_{475} in the currently proposed sensor:

$$S(T) = \frac{\partial (I_{700}/I_{475})}{\partial T} \quad (2)$$

From equation (2) the sensitivity S as a function of absolute temperature was calculated, see Figure 3(b). It can be seen that the sensitivity S sharply increases with the temperature up to 0.6 K^{-1} at 673 K, the higher measured temperature in this work.

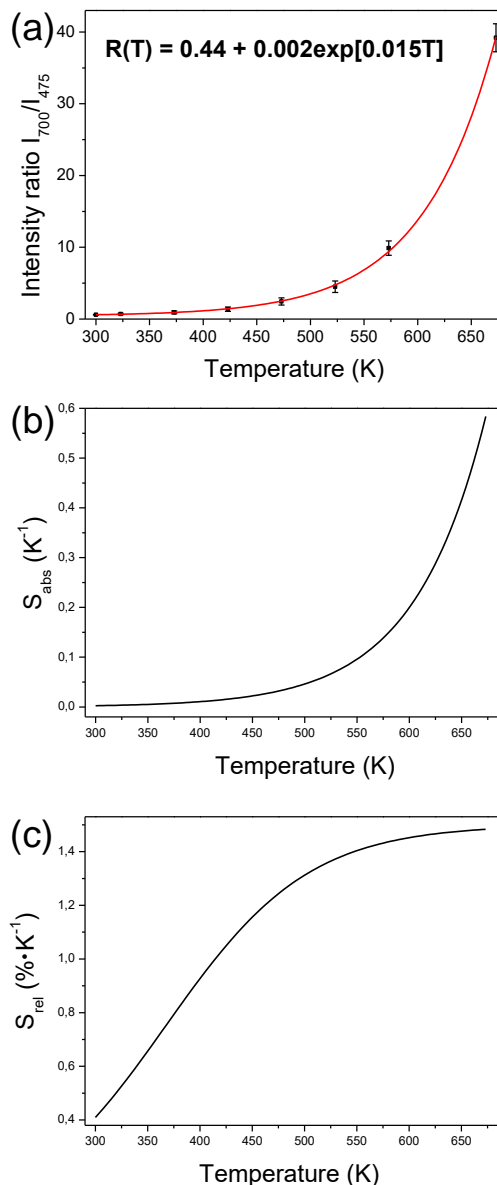


Fig. 3 (a) Calibration curve of the intensity ratio between the emission peaks located at 475 and 700 nm (I_{700}/I_{475}) as a function of temperature. Error bars reflect the reproducibility of the calibration curve after analyses of several spectra for each measured temperature; (b) Absolute sensitivity as a function of temperature calculated from Equation (2); (c) Relative sensitivity as a function of temperature calculated from Equation 5.

Sensitivity data found in the literature for temperature sensors based in Ln-UCNPs are specifically related to the intensity ratio of two closely spaced luminescent states of the active Ln³⁺ whose populations are in thermal equilibrium, i.e., thermally coupled electronic levels, typically excited $^4S_{3/2}$ and $^2H_{11/2}$ levels in Er³⁺-doped²⁶ and Yb³⁺, Er³⁺-codoped systems^{9,27} and $^2F_{2,3}$ and 3H_4 excited states in Yb³⁺, Tm³⁺-codoped systems.^{16,18,23} In these thermal sensing systems, the population exchange between the two involved luminescent excited states is orders of magnitude

faster than the luminescence decay from each excited state. Accordingly, the relative population of thermally coupled states follows a Boltzmann-type distribution, and their fluorescence intensity ratio (FIR) $FIR = I_1(T)/I_2(T)$ can be given by:

$$FIR = C \exp \left[-\frac{\Delta E}{k_B T} \right] \quad (3)$$

with C a constant depending on the degeneracy, the emission cross-sections and the angular frequency of the electronic transitions from the two excited thermally linked states to the terminal level, ΔE the energy difference between these two states, k_B the Boltzmann constant, and T the absolute temperature. Following the expression in Equation (2) the absolute sensitivity (S_{abs}) of this kind of temperature sensor is usually given as:²⁸

$$S_{abs}(T) = \frac{\partial R}{\partial T} = R \left[-\frac{\Delta E}{k_B T^2} \right] \quad (4)$$

However, for current 1% Tm, 15% Yb:GdVO₄@SiO₂ nanoparticles the regulation of the electronic population distribution over emitting ¹G₄ and ³F₂ states is quite different. Since the luminescence from ¹G₄, populated by photon absorption, occurs at the same time scale that energy transfers to ³F₂, directly by thermally enhanced CR1, or indirectly after thermal equilibrium from ³H₄ by CR2 and CR3, see mechanisms in Figure 2(a), the blue and deep-red emissions result to be competitive, and ¹G₄ and ³F₂ can be considered as electronically coupled states.²³ In fact, the expression of this electronic coupling is the plot of the thermal evolution of I_{700}/I_{475} depicted in Figure 3(a). Expressions for R(T) and then S(T) in plots of Figure 3(a) and 3(b) are empirical developments, and obviously do not include the ΔE value between ¹G₄ and ³F₂ states.

To facilitate quantitative comparison of ratiometric optical temperature sensors operating by different mechanisms, the use of the relative sensitivity (S_{rel}) has been proposed:¹

$$S_{rel}(T) = \frac{1}{R} \frac{\partial R}{\partial T} \quad (5)$$

Hence, for a reliable comparison S_{rel} was also calculated following Eq. (5) for 1% Tm, 15% Yb:GdVO₄@SiO₂ nanoparticles, and the result is plotted in Figure 3(c). The maximum $S_{rel} = 1.54\% K^{-1}$ was observed at the upper range of measured temperatures. When compared to the other "conventional" upconverting nanothermometers based in ratiometric signals from thermally coupled excited states, the S_{rel} of our system is the highest reported for Tm³⁺-doped materials operating above room temperature, and in the upper range when compared to other systems doped with Er³⁺,^{11,27a} and comparable to the achieved one with some organic dyes and Ln³⁺-doped phosphors pumped in the UV,²⁹ and higher than those for temperature sensors built with quantum dots.¹

The temperature resolution of luminescent thermal sensors ∂T can be determined from the ratio of the resolution calculated from the standard deviation of the residuals in the interpolation fit of experimental data (Fig. 3(a)) and the absolute sensitivity defined in equation 4.³⁰ The temperature resolution can also be deduced from the sensitivity of the detection system and the sensitivity calculated from the experimental data,³⁰ Figure 3(a) shows that the intensity ratio calculated for our luminescent nanoparticles increases by more than 350% upon raising the temperature from 300 to 473 K and by more than 2195% in the range of temperatures from 473 – 673 K. This means an increase of around 2% per degree in the first range and 11% per degree in the second range. The precision of our system is 0.5% (signal-to-noise ratio of AVANTES spectrometer is 500/1), thus, the thermal resolution we can obtain from our nanoparticles would be about ± 0.5 K in the 300 – 473 K range, and ± 0.1 K in the 473 – 673 K range. This would constitute the highest thermal resolution reported for luminescent thermometers based on upconversion nanoparticles operating in the upper range of temperatures.

But besides the above demonstrated high sensitivity ratiometric temperature detection and thermal resolution of our thermometer, it also allows for fast visualization of temperature changes just observing the evolution of the color of the emitted light under NIR 980 nm excitation.

To visualize the color change of the emission with temperature, Figure 4(a) shows the evolution from room temperature up to 723 K of the color of the upconverted light under 980 nm excitation arising from prepared x% Tm³⁺, 15% Yb³⁺:GdVO₄@SiO₂ nanoparticles (0.2 ≤ x ≤ 5.0 at%). No deep-red light is observed for samples with x < 1% Tm³⁺ in the measured temperature range, even though the excitation power of the laser had to be increased to 600 mW to be able to observe with the CCD camera the emission generated by these samples, suggesting the importance of the concentration of Tm³⁺ to achieve simultaneous depopulation of ¹G₄ and feeding of ³F₂ by efficient CR energy transfer, and further validating previous proposed energy transfer mechanisms. For samples with x > 2% Tm³⁺, although the change of color of the emission can still be observed, the power of the excitation laser had to be significantly increased to record the pictures of the emission, indicating that the emission process of these particles was less efficient than that generated by samples with 1 and 2% Tm³⁺. From this Figure it can be clearly seen that the most visual change of the color emission is produced by nanoparticles doped with 1% Tm³⁺.

From the recorded upconversion spectra of the 1% Tm³⁺, 15% Yb³⁺:GdVO₄@SiO₂ sample we calculated the CIE³¹ coordinates as a function of temperature. The CIE chromatic diagram with the results is shown in Figure 4(b). In fact, this CIE coordinates calculation supposes a new visual method to estimate the thermal resolution of the thermometer. We performed measurements in 5 K steps within the upper temperature range from 623 to 673 K. Results are shown in the inset of Figure 4. From the graph is clear that CIE coordinates corresponding to different temperature spectra appear as well resolved points even in this narrow temperature range.

In order to demonstrate the potential practical use of the studied Yb³⁺, Tm³⁺-GdVO₄@SiO₂ thermochromic nanoparticles for direct visualization of temperature, we have performed an experiment to visualize the temperature distribution on a platinum plate coated with these nanoparticles. Nanoparticles were dispersed in ethanol and deposited on the platinum plate. After evaporation of ethanol a uniform layer of nanoparticles coating the Pt plate was formed. To generate a gradient of temperature high enough to allow visualization of the change of color of the emission arising from the nanoparticles, one end of the platinum plate was placed in a cooled copper sink while the other end was put in a small oven, as can be seen in the scheme shown in Figure 5(a). The temperature was also monitored during the heating process using an infrared camera FLIR E40. The thermographic image recorded with the infrared camera in Figure 5(b) shows the big gradient of temperature generated in the sample with maximum at 843 K and minimum at 296 K. The arrow indicates the temperature in the cold part and the dash line corresponds to the visible emission from nanoparticles. A diode laser with emission at 980 nm was used for exciting the thermochromic nanoparticles. The laser beam was focused by a cylindrical lens to obtain a line spot. A CCD camera was mounted perpendicular to the platinum plate to record top view pictures of visible changes in the color of the emission during the heating process. Figure 5(c) shows four images recorded on the platinum plate at approximately 3 min intervals. The first image was recorded at room temperature just before the heating process. At room temperature the blue emission generated from the ¹G₄ energy level to the ground state of Tm³⁺ can be seen, that is the dominant emission at this temperature (see Figure 2(b)). Just after the platinum plate

become hot enough (3 min from the beginning of the experiment) other pictures have been taken, showing the visible changes in the color of the emission, tuning from the red in the hot part to the blue in the cool part of the platinum plate. In the figure it can also be seen how the distribution of temperatures evolves with time.

Filevich et al. used the decrease of intensity of red fluorescence of the $[\text{Ru}(\text{bpy})_3]^{2+}$ complex, after excitation in the blue, to observe the temperature gradient of a 10 mM solution of $[\text{Ru}(\text{bpy})_3]\text{Cl}_2$ confined between two cover glasses immersed in distilled water while being heated by a thermostated cell culture chamber.³² The luminescent thermometer was able to work between 293 K and 333 K. Under these conditions, they were able to map temperature gradients $\sim 1\text{K}$, with a thermal resolution of 0.05 K. However, the solutions had to be degassed to reach such high resolution. The authors used the same procedure to map the temperature gradient generated in a FIA reactor. Also, a dipyrren-1-yl (2,4,6-trisopropyl(phenyl)borane molecule was designed and synthesized to develop a visual thermometer operating in the range 223–373 K with a color change from green to blue with an accuracy better than 1 K, and was used to visualize the temperature gradient in a fluid contained in a quartz tube heated from the top and cooled from the bottom.³³ However, the broad emission band of this compound made difficult to accurately identify its maximum of intensity. Thus, the authors transformed the spectra to CIE coordinates, which reduced the accuracy to 2 K. Zhou et al. also visualized a temperature gradient in an aqueous solution of per-6-thio- α -cyclodextrin and per-7-thio- β -cyclodextrin decorated CdTe quantum dots (QDs), exhibiting a color change from yellow to salmon pink.³⁴ However, this luminescent thermometer could not be used above 333 K because QDs tend to grow spontaneously generating a red shift of the luminescence properties. Furthermore, long thermal equilibration times (10–20 min) are required which limits the temporal response of this thermometer. When compared to these previous approaches, the main advantages of our thermometer is that it can be used directly as a solid deposited directly on the surface to map, that the thermal gradient that can be visualized is larger (more than 500 K), and that no equilibration times are required to visualize the gradient generated in the sample.

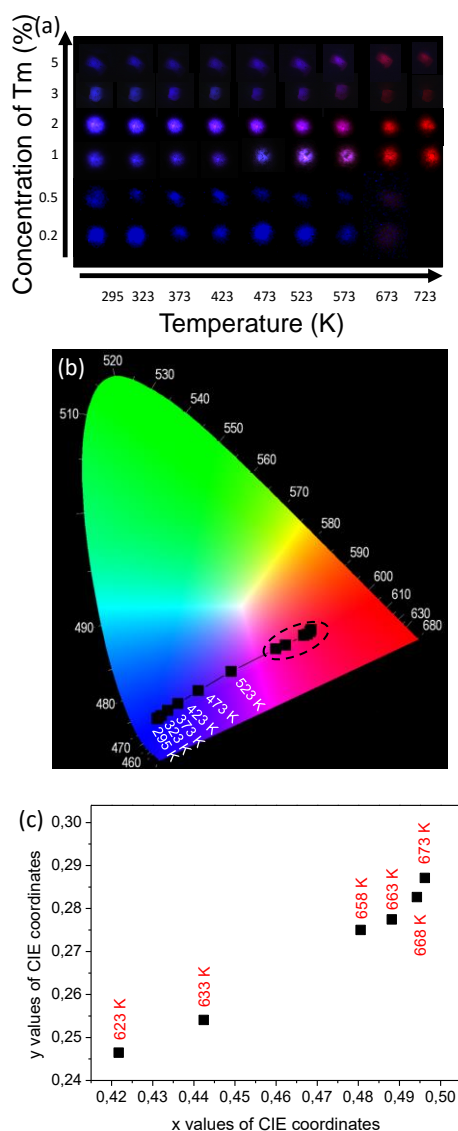


Fig. 4 (a) Color evolution images of the upconverted light using $x\% \text{Tm}^{3+}$, 15% $\text{Yb}^{3+}:\text{GdVO}_4@\text{SiO}_2$ ($0.2 \leq x \leq 5.0$ mol%) nanoparticles from room temperature up to 723 K. The NIR diode laser excitation was at 980 nm, the power of the laser was 600 mW for samples containing 0.2 and 0.5 % Tm^{3+} and 200 mW for the rest of the samples, and the images were captured with a CCD camera; (b) Fine-tuning of the temperature light color evolution from upconversion spectra of 1% Tm^{3+} , 15% $\text{Yb}^{3+}:\text{GdVO}_4@\text{SiO}_2$ nanoparticles plotted on a CIE chromatic diagram. (c) Thermal resolution achieved for measurements taken in 5 K steps in the high temperature range (623–673 K) circled in (b).

In order to demonstrate the sensing capability and spatial resolution of $\text{Tm,YbGdVO}_4@\text{SiO}_2$ core-shell nanoparticles, an experiment for evaluating the Joule heating effect in a Pt wire 50 μm in diameter was carried out. The luminescent nanoparticles (1 % wt.) were dispersed in ethanol and deposited on the top of the Pt wire by spreading some drops of this dispersion. Then, the Pt wire was attached to a piece of glass and introduced on a muffle in order to accelerate the evaporation of ethanol and fix the $\text{Tm,Yb:GdVO}_4@\text{SiO}_2$

nanoparticles on the wire. Finally, the platinum wire decorated with $\text{Tm}_2\text{Yb}_2\text{GdVO}_4@\text{SiO}_2$ nanoparticles was detached from the glass to reduce heat dissipation and was soldered between two electric contacts connected to the DC power supply with the maximum input of 30 V. Thermal reading was performed using an optical microscope setup (see Figure 6(a)), through which a fiber coupled diode laser with emission at 980 nm was focused on the Pt wire by using a 40X microscope objective and 0.6 numerical aperture, that produced a laser spot of $\sim 10 \mu\text{m}$. The luminescent signal arising from the $\text{Tm}_2\text{Yb}_2\text{GdVO}_4@\text{SiO}_2$ nanoparticles was collected through the same objective, and after passing a dichroic filter to eliminate the residual excitation wavelength reflected by the sample, was sent to a CCD Thorlabs camera to visualize the change of the color of the emission generated and to a AVANTES AVS-USB2000 fiberoptic spectrometer (fiber diameter = 200 μm) to record the spectra and determine the temperature.

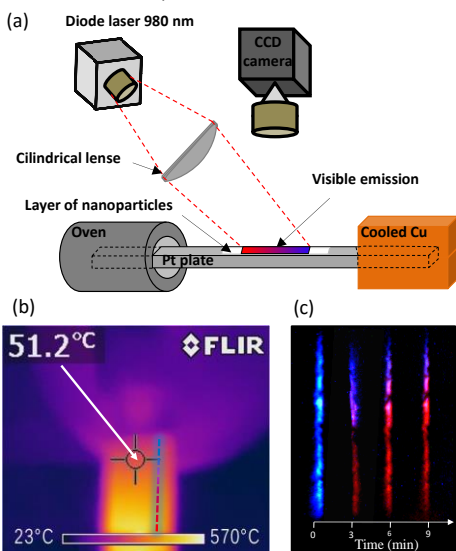


Fig. 5 (a) Scheme of the set up for real-time experiment of temperature distribution visualization; (b) Thermal image corresponding to the Pt plate showing the big gradient of temperature generated; (c) Images of the emission generated by the layer of 1% Tm, 15% $\text{Yb}_2\text{GdVO}_4@\text{SiO}_2$ nanoparticles coating the Pt plate during the heating process.

Figure 6(b) shows the room temperature blue luminescence generated by the $\text{Tm}_2\text{Yb}_2\text{GdVO}_4@\text{SiO}_2$ nanoparticles. After applying a current of 0.66 A to the Pt wire, the color of the emission changed to red, due to the high temperature (653 K) induced in the wire (see Fig. 6(c)). The nanoparticles, aggregated due to the evaporation of the ethanol and with sizes 10-20 μm , can be clearly seen in the images. This would limit the spatial resolution that we can achieve. This spatial resolution, however, could be improved by avoiding aggregation of nanoparticles.

The intensity ratio between the 700 nm and 475 nm emission lines was determined for different values of the electrical current applied to the Pt wire, as can be seen in Figure 6(d). Figure 6(e) shows the temperature of the Pt wire as a function of the intensity flowing through the wire. The experimental temperature corresponding to each intensity was obtained from the calibration shown in Figure 3(a). These experimental data are compared with the temperature values computed

using a heat transfer model that takes into account the convective and radiative flow under Joule heating:

$$hS(T_{\text{Pt}} - T_{\text{amb}}) + \varepsilon\sigma(T_{\text{Pt}}^4 - T_{\text{amb}}^4) = I^2R \quad (6)$$

where h and ε are the convective heat transfer coefficient and the emissivity of the Pt wire, S is its lateral area, T_{Pt} and T_{amb} are the wire and ambient temperature, respectively, σ is the Stefan-Boltzmann constant and I and R are the intensity and the resistance of the Pt wire, respectively. The resistance was computed considering the dilatation and the thermal dependence of the resistivity. The emissivity of Pt was assumed to be 0.1. The convective heat transfer coefficient that better matches the experimental result was found to be $h = 700 \text{ W m}^{-2}\text{K}^{-1}$. This high value of h can be explained due to the strong convective flow that develops in the hot surrounding of the wire. The calculations are little sensitive to changes in the emissivity of the wire, because the radiative term represents only around 2% of the total heat flow. The dominant role of the convective term is consistent with the quasi-parabolic behavior of the intensity-temperature graph shown in Figure 6(d). As can be seen in Figure 6(e), the theoretical calculations describing the evolution of the temperature of the wire as a function of the intensity flowing on it perfectly matches with the experimental thermal characterization of the wire using our luminescent nanoparticles.

Thermal maps of metallic wires and electronic components have previously reported in the literature. Rhodamine B films deposited on micro- and nanowires (1-4 μm width, 40-80 μm length, 40 nm thickness) were used to map temperature distribution in the wires when heated resistively, achieving a temperature resolution between 5-10 K with submicrometer spatial resolution.³⁵ $\text{Er}_2\text{Yb}_2\text{PbF}_2$ nanoparticles, 250 nm in diameter, glued at the end of a sharp atomic force microscope tip were used to determine the temperature of electrically heated micro- and nanowires through the changes of the intensity ratio between the emissions arising from the $^2\text{H}_{11/2} \rightarrow ^4\text{I}_{15/2}$ and the $^4\text{S}_{3/2} \rightarrow ^4\text{I}_{15/2}$ transitions of Er^{3+} , with a resolution smaller than 500 nm and a temperature sensitivity $\sim 1\% \text{ K}^{-1}$.^{29f,36} However, the scanning speed was very low, which impeded to observe transient phenomena in the wires. Benayas et al. used the thermal sensing capability of luminescent Nd:YAG nanoparticles pumped at 808 nm and with emission at around 940 nm to evaluate the Joule-heating in a 100 μm width copper wire, inducing a temperature increment of 43 K following the expected parabolic dependence.³⁷ Polyacetylene (PDA) vesicles embedded in polyvinyl alcohol (PVA) films were used to monitor temperature gradients in a resistance random access memory (RRAM) device structure and to uncover submicrometer size filamentary defects.³⁸ However, this thermometer operated only from 313 to 363 K because of the saturation of the fluorescence signal, and the results depended highly on the thickness of the film, with fluctuations exceeding 5%. Brites et al. used a di-ureasil thin-film co-doped with Eu^{3+} and Tb^{3+} tris(β -diketonate) chelates, excited in the UV, to obtain the temperature map of a FR4 printed wiring board, estimating an spatial and temporal resolutions of 420 nm and 4.8 ms, respectively, and a thermal resolution of 0.15 K.³⁹ The operation range of this thermometer was limited to 297-328 K. Thus, compared to the previous examples shown, our luminescent thermometer is able to work in a larger range of temperatures, and the change of temperature of the wire could be followed visually, while in the rest of examples instrumentation is required to observe changes in temperature. This makes of our luminescent nanothermometer a valuable potential tool for the visual detection of thermal anomalies in electronic components.

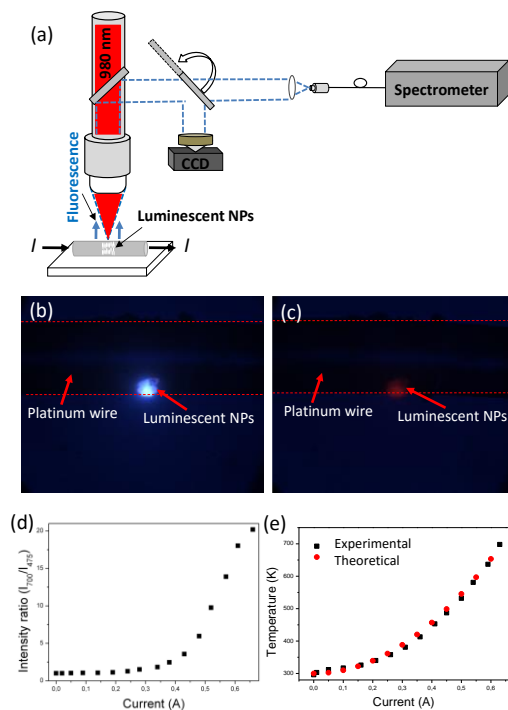


Fig. 6 (a) Scheme of the set-up used for the experiment; (b) Images of the room temperature blue luminescence of the $\text{Tm,Yb:GdVO}_4\text{@SiO}_2$ core-shell nanoparticles deposited on the surface of the Pt wire; (c) Image of the high temperature deep-red luminescence of the nanoparticles on the surface of the wire after applying a current of 0.66 A; (d) Intensity ratio of emissions at 700 and 475 nm of the $\text{Tm,Yb:GdVO}_4\text{@SiO}_2$ nanoparticles as a function of the applied current to the Pt wire; (e) Temperature determined from the analysis of the intensity ratio of emissions shown in panel (d) using the calibration shown in Figure 3(a) as a function of the applied current, and temperature determined theoretically from the a simple heat transfer model taking into account convective and radiative flow under Joule heating of the Pt wire.

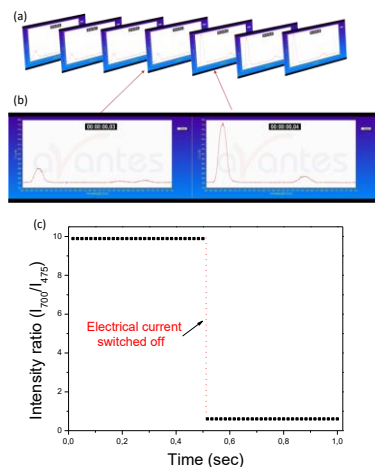


Fig. 7 (a) Temporal evolution of the emission spectra of the $\text{Tm,Yb:GdVO}_4\text{@SiO}_2$ nanoparticles deposited on the Pt wire collected

during the cooling process of the wire recorded at a frequency of 60 spectra per second. (b) Detail of two spectra taken consecutively just after and just before switching on of the electrical current through the Pt wire showing the changes experimented in the spectra. (c) Temporal evolution of the intensity ratio of emissions at 700 and 475 nm of the $\text{Tm,Yb:GdVO}_4\text{@SiO}_2$ UCNPs just before and just after switching on the electrical current through the Pt wire, showing in which timeframe the heating is produced and how the temperature evolved after.

Another important parameter for a thermometer is the response time. Contact thermometers usually show a response time too slow to follow the rapid changes occurring in many technological applications. However, in the case of luminescent thermometry this process is much faster, of the order of milliseconds⁴⁰ and in fact, the change of color of the emitted light by $\text{Tm,Yb:GdVO}_4\text{@SiO}_2$ UCNPs present on the Pt wire surface was perceived immediately by the naked eye. This last experiment of monitoring the Joule heating effect on a Pt wire also provides a tool to evaluate the response time of our temperature sensor. We used the fiberoptic spectrophotometer to capture the temporal evolution of the emission spectra when we pass an electrical current through the Pt wire. We chose an integration time of 16 ms which represents a compromise between a reasonable high cadence (60 spectra per second) and an integration time long enough to maintain the quality of the spectra. In order to visualize the results, we used a screen cam recorder software to record a video file showing the changes produced in the intensity of the luminescent spectra, since this process is much faster than recording the spectral data by the software of the fiberoptic spectrophotometer. In the experiment, we started to record the video while the Pt wire was at room temperature, and at a particular moment, we allowed the electrical current to pass through the Pt wire, heating it by the Joule effect, and recording time evolution of the emission spectra of the $\text{Tm,Yb:GdVO}_4\text{@SiO}_2$ UCNPs present on the Pt wire surface.

Figure 7(a) shows a sequence of the video frames recorded just before and just after the electrical current passed through the Pt wire. We selected the last frame recorded before switching the electrical current and the first frame recorded after this event to show the changes in temperature produced in the wire (see Figure 7(b)). As can be seen in this figure, the heating process of the Pt wire happened in a time shorter than our integration time (16 ms), and while the current is passing through the wire, its temperature is stable. To visualize better this sudden change of temperature and the later maintenance, we included in Figure 7(c) a representation of the evolution of the R parameter calculated according to Eq. (1). It can be clearly seen that the change of temperature happened in the timeframe of 16 ms and that after this event, it was maintained constant for at least 0.5 s. In fact, taking into account the diameter of the wire we estimate that this change of temperature would be of the order of 150-200 μs . The response time we found in this study is one order of magnitude higher than the one previously reported by C. D. S. Brites for Eu^{3+} , Tb^{3+} codoped metallic-organic frameworks,⁴⁰ and apparently it can be improved if a detector with a faster response is used.

D. Conclusions

In summary, we demonstrated that $\text{Tm,Yb:GdVO}_4\text{@SiO}_2$ core-shell nanoparticles can be used as visual thermochromic thermometers in the 300-673 K temperature range, with high spatial resolution, but more importantly, with a high thermal sensitivity (1.54% K^{-1}), the highest reported up to now for Tm^{3+} -doped UCNPs, a high thermal

resolution (± 0.1 K), the highest reported up to now for upconverting luminescent thermometers, and a high temporal resolution (16 ms), the highest reported up to now for any luminescent thermometer. We showed the potentiality of our sensor by monitoring the heating process of a Pt wire with a small diameter (50 μm) decorated with our nanoparticles, generated by the Joule effect when circulating an electrical current through it. The results obtained matched well with the theoretical calculations we performed using a heat transfer model that takes into account the convective and radiative flow under Joule heating. Although additional work is needed to avoid the aggregation of the nanoparticles, the results obtained indicate that these nanoparticles might be used to detect hot spots in microelectronic chips.

Acknowledgements

This work was supported by the Spanish Government under Projects No. MAT2013-47395-C4-4-R, TEC2014-55948-Rand MAT2014-56607-R, and by Catalan Authority under Project No. 2014SGR1358.OI. A. Savchuk is supported by Catalan Government through the fellowship 2013FI_B 01032. F. D. acknowledges additional support through the ICREA Academia awards 2010ICREA-02 for excellence in research. Dr. E. Urones is acknowledged for HRTEM experiments at the Centro Nacional de Microscopía Electrónica, Universidad Complutense de Madrid, and Dr. R. Calderón (ICMM-CSIC) is acknowledged by her contribution at the early stage of this work.

Notes and references

- 1 C. D. S. Brites, P. P. Lima, N. J. O. Silva, A. Millán, V. S. Amaral, F. Palacio, L. D. Carlos, *Nanoscale*, 2012, **4**, 4799.
- 2 D. Jaque, F. Vetrone, *Nanoscale*, 2012, **4**, 4301.
- 3 D. H. Jundt, *Opt. Lett.*, 1997, **22**, 1553.
- 4 S. Ebert, K. Travis, B. Lincoln, J. Guck, *Opt. Exp.*, 2007, **15**, 14493.
- 5 L. H. Fischer, G. S. Harms, O. S. Wolfbeis, *Angew. Chem. Int. Ed.*, 2011, **50**, 4546.
- 6 P. Haro-González, L. Martínez-Maestro, I. R. Martín, J. García-Solé, D. Jaque, *Small*, 2012, **8**, 2652.
- 7 K. T. V. Grattan, A. W. Palmer, C. A. Willson, *J. Phys. E: Sci. Instrum.*, 1987, **20**, 1201.
- 8 H. Berthou, C. K. Jörgensen, *Opt. Lett.*, 1990, **15**, 1100.
- 9 M. L. Debasu, D. Ananias, I. Pastoriza-Santos, L. M. Liz-Marzán, J. Rocha, L. D. Carlos, *Adv. Mater.*, 2013, **25**, 4868.
- 10 F. Auzel, *Chem. Rev.*, 2004, **104**, 139.
- 11 N. N. Dong, M. Pedroni, F. Piccinelli, G. Conti, A. Sbarbati, J. R. Hernandez, L. M. Maestro, M. C. Iglesias de la Cruz, F. Sanz-Rodríguez, A. Juarranz, F. Chen, F. Vetrone, J. A. Capobianco, J. G. Solé, M. Bettinelli, D. Jaque, and A. Speghini, *ACS Nano*, 2011, **5**, 8665.
- 12 C. M. Lemon, E. Karnas, X. Han, O. T. Bruns, T. J. Kempa, D. Fukumura, M.G. Bawendi, R. K. Jain, D. G. Duda, D. G. Nocera, *J. Am. Chem. Soc.*, 2015, **137**, 9832.
- 13 F. Esteban-Betegón, C. Zaldo, C. Cascales, *Chem. Mater.*, 2010, **22**, 2315.
- 14 R. Calderón-Villajos, C. Zaldo, C. Cascales, *Nanotechnology*, 2012, **23**, 505205.
- 15 E. J. McLaurin, L. R. Bradshaw, D. R. Gamelin, *Chem. Mater.* 2013, **25**, 1283.
- 16 L. Xing, Y. Xu, R. Wang, W. Xu, Z. Zhang, *Opt. Lett.*, 2014, **39**, 454.
- 17 X. Wang, J. Zheng, Y. Xuan, X. Yan, *Opt. Exp.*, 2013, **21**, 21956.
- 18 X. J. Xue, W. Qin, D. S. Zhang, D. Zhao, G. D. Wei, K. Z. Zheng, L. L. Wang, G. F. Wang, *J. Nanosci. Nanotechnol.*, 2010, **10**, 2028.
- 19 F. Vetrone, V. Mahalingam, J. A. Capobianco, *Chem. Mater.*, 2009, **21**, 1847.
- 20 (a) L. G. Van Uitert, R. C. Linares, R. R. Soden, A. A. Ballman, *J. Chem. Phys.*, 1962, **36**, 702; (b) H. J. Zhang, X. L. Meng, L. Zhu, H. Z. Zhang, P. Wang, J. Dawes, Q. C. Wang, Y. T. Chow, *Cryst. Res. Technol.*, 1998, **33**, 801; (c) R. Lisiecki, P. Solarz, G. Dominiak-Dzik, W. Ryba-Romanowski, and T. Lukasiewicz, *Laser Phys.*, 2006, **16**, 303.
- 21 (a) J. J. Rubin, L.G. Van Uitert, *J. Appl. Phys.*, 1966, **37**, 2920; (b) A. I. Zagumennyi, V. G. Ostroumov, I. A. Shcherbakov, T. Jensen, J. P. Meyen, G. Huben, *Sov. J. Quantum Electron.*, 1992, **22**, 1071; (c) H. H. Yu, H. J. Zhang, and J. Y. Wang, *Acta Phys. Polon.*, 2013, **124**, 301.
- 22 S. A. Wade, S. F. Collins, G. W. Baxter, *J. Appl. Phys.*, 2003, **94**, 4743.
- 23 N. Ishiwada, S. Fujioka, T. Ueda, T. Yokomori, *Opt. Lett.*, 2011, **36**, 760.
- 24 R. Lisiecki, P. Solarz, G. Dominiak-Dzik, W. Ryba-Romanowski, M. Sobchuk, P. Cerny, J. Sulc, *Phys. Rev. B*, 2006, **74**, 035103.
- 25 W. Xu, J. Chen, P. Wang, Z. Zhang, and W. Cao, *Opt. Lett.*, 2012, **37**, 205.
- 26 (a) M. A. R. C. Alencar, G. S. Maciel, C. B. Araújo, A. Patra, *Appl. Phys. Lett.*, 2004, **84**, 4753; (b) Z. P. Cai, H. Y. Xu, *Sens. Actuat. A*, 2003, **108**, 187.
- 27 (a) F. Vetrone, R. Naccache, A. Zamarron, A. J. de la Fuente, F. Sanz-Rodríguez, L. M. Maestro, E. M. Rodriguez, D. Jaque, J. G. Sole, J. A. Capobianco, *ACS Nano*, 2010, **4**, 3254; (b) S. P. Wang, S. Westcott, W. Chen, *J. Phys. Chem. B*, 2002, **106**, 11203.
- 28 S. Jiang, P. Zeng, L. Liao, S. Tian, H. Guo, Y. Chen, C. Duan, M. Yin, *J. Alloys and Compd.*, 2014, **617**, 538.
- 29 (a) C. F. Chapman, Y. Liu, G. J. Sonek, B. J. Tromberg, *Photochem. Photobiol.*, 1995, **62**, 416; (b) W. Jung, Y. W. Kim, D. Yim, J. Y. Yoo, *Sens. Actuat. A*, 2011, **171**, 228; (c) N. Chandrasekharan, L. A. Kelly, *J. Am. Chem. Soc.*, 2001, **123**, 9898; (d) G. A. Baker, S. N. Baker, T. M. McCleskey, *Chem. Commun.*, 2003, 2932; (e) L. Aigouy, G. Tessier, M. Mortier, B. Charlot, *Appl. Phys. Lett.*, 2005, **87**, 184105; (f) L. Aigouy, E. Saïdi, L. Lalouat, J. Labéguerie-Egéa, M. Mortier, P. Löw, *J. Appl. Phys.*, 2009, **106**, 074301; (g) E. Saïdi, B. Samson, L. Aigouy, S. Volz, P. Löw, C. Bergaud, M. Mortier, *Nanotechnology*, 2009, **20**, 115703; (h) A. H. Khalid, K. Kontis, *Meas. Sci. Technol.*, 2009, **20**, 025305.
- 30 Z. Wang, D. Ananias, A. Carne-Sanchez, C. D. S. Brites, I. Imaz, D. Maspoch, J. Rocha, and L. D. Carlos, *Adv. Mater.*, 2015, **25**, 2824.
- 31 T. Smith, J. Guild, *Trans. Opt. Soc.*, 1931, **33**, 73.
- 32 O. Filevich, R. Etchenique, *Anal. Chem.*, 2006, **78**, 7499.

- 33 J. Feng, K. Tian, D. Hu, S. Wang, S. Li, Y. Zeng, Y. Li, G. Yang, *Angew. Chem. Int. Ed.*, 2011, **50**, 8072.
- 34 D. Zhou, M. Lin, X. Liu, J. Li, Z. Chen, D. Yao, H. Sun, H. Zhang, B. Yang, *ACS Nano*, 2013, **7**, 2273.
- 35 P. Löw, B. Kim, N. Takama, C. Bergaud, *Small*, 2008, **4**, 908.
- 36 E. Saïdi, J. Labéguerie-Egéa, L. Billot, J. Lesueur, M. Mortier, L. Aigouy, *Int. J. Thermophys.*, 2013, **34**, 1405.
- 37 A. Benayas, B. del Rosal, A. Pérez-Delgado, K. Santacruz-Gómez, D. Jaque, G.A. Hirata, F. Vetrone, *Adv. Opt. Mater.*, 2015, **3**, 687.
- 38 O. Yarimanga, S. Lee, D.Y. Ham, J.M. Choi, S.G. Kwon, M. Inn, S. Kim, J.M. Kim, Y.K. Choi, *Macromol. Chem. Phys.*, 2011, **212**, 1211.
- 39 C. D. S. Brites, P. P. Lima, N. J. O. Silva, A. Millán, V. S. Amaral, F. Palacio, L. D. Carlos, *Front. Chem.*, 2013, **1**, 9.

Paper V

Savchuk, Ol. A.; Carvajal, J. J.; Massons, J.; Cascales, C.; Aguiló, M.; Díaz, F. *A novel low-cost, compact and fast signal processing sensor for ratiometric luminescent nanothermometry (2016)* Submitted to Sensors and Actuators A.

Novel low-cost, compact and fast signal processing sensor for ratiometric luminescent nanothermometry

Ol.A. Savchuk,¹ J.J. Carvajal,^{1,*} J. Massons,¹ C. Cascales,² M. Aguiló,¹ F. Díaz¹

¹*Física i Cristal·lografia de Materials i Nanomaterials (FiCMA-FiCNA) and EMaS, Universitat Rovira i Virgili (URV),
c/Marcel·lí Domingo 1, E-43007, Tarragona, Spain*

²*Instituto de Ciencia de Materiales de Madrid, c/ Sor Juana Inés de la Cruz, Cantoblanco, Madrid, 28049, Spain*

*Corresponding author: joanjosep.carvajal@urv.cat

Keywords: temperature sensor, non-invasive, luminescence, up-conversion, nanoparticles.

Abstract

We developed a compact, low-cost and non-invasive temperature sensor based on a ratiometric luminescence technique. The setup included a digital color sensor, which collects simultaneously signals in the blue, green and red regions of the electromagnetic spectrum, coupled to an optical system that focuses an excitation laser beam onto luminescent nanoparticles emitting at least in two of these electromagnetic regions. The same optical system collects the emission arising from the luminescent nanoparticles and directs it towards the digital color sensor through a dichroic mirror. We probed the potentiality of this setup for luminescence thermometry in the biological range of temperatures using Er,Yb:NaYF₄, and up to 673 K for microelectronic applications using Tm,Yb:GdVO₄ up-converting nanoparticles. The thermal sensitivity obtained in both cases is similar to that previously reported for the same kinds of nanoparticles using conventional systems. This validates our setup for temperature measurements. Also, we developed luminescent nanoparticles/PDMS composites that allow fabricating thermometric microfluidic chips in which temperature can be determined using our setup. The thermal sensitivity for these composites is slightly smaller than that of the bare nanoparticles, but still allowing for precise and fast temperature measurements.

1. Introduction

There are many areas of industry, where temperature measurements are essential, such as metallurgical industries, glass manufacturing, material modeling or dairy products, among others. There are other fields like biomedical sciences, where temperature provides basic diagnostic criteria [1, 2] and its control is essential during hyperthermia treatments [3, 4], for instance. Despite modern temperature measurement instruments at the nanoscale are in general

complex in nature and at the same time fascinating in operation [5], there are situations -because of hostile environments, presence of vibrations, electrical noise, strong electromagnetic fields, or other factors- where temperature measurements are difficult or even impossible with this kind of instruments. To overcome these difficulties and achieve temperature sensing in hardly accessible locations, optical non-contact thermometry methods have been developed since they provide electromagnetic immunity and possibilities for remote measurements [6, 7]. Most of the optical non-contact temperature sensors are based on reflection, absorption, scattering, fluorescence or interference phenomena of light [8, 9]. Among these optical non-contact thermometry methods, fluorescence thermometry is among the most versatile methods. It is based on fluorescence intensity, band-shift or lifetime changes produced by temperature [10]. Among these three techniques, it is difficult to select the optimal one, as each of them shows special features of interest. The lifetime-based technique allows performing measurements in objects in movement and at high temperature, for instance, avoiding the blackbody radiation effect [10, 11]. However, the signal used in this technique is not always reliable, due to fluctuations in the power of the excitation source, imperfections in the optical setup or changes in the sensitivity of the detector. Moreover, changes in the luminescent material concentration or the environmental parameters can also affect to the quality of the fluorescence signal. From another side, the band-shift technique can be very sensitive to temperature changes, but it can be only applied to a relatively narrow range of temperatures. Furthermore, since this technique has mainly used quantum dots and luminescent nanoparticles, it suffers from their signal bleaching. By using ratiometric measurements these problems can be avoided [6, 7]. Ratiometric measurements are based on systems with different luminescence emission bands whose relative intensities strongly depend on temperature. This thermal dependency is caused by a thermally induced electronic population re-distribution among the corresponding emitting energy levels of the optical center. An additional advantage is that the relative intensity of the luminescence bands depends only on temperature but not on the local concentration of the emitting center. Also, effects derived from fluctuations in the excitation source are avoided since the different luminescence lines will be affected in an equal manner.

In these techniques, the choice of a particular luminescent material determines the temperature range, thermal sensitivity and stability of the nanothermometer. The most used materials for luminescent nanothermometry are quantum dots [12-14], organic dyes [15-17] and lanthanide-doped materials [18-21]. Although, organic dyes and quantum dots show a high thermal sensitivity, their main disadvantage is that they need to be excited using ultraviolet (UV) or visible light. This may lead to the degradation of the fluorescent material. Furthermore,

when used in biological applications, the excitation with UV or visible light might induce the appearance of background fluorescence, and even the damage of biological tissues. From another side, the use of lanthanide-doped up-converting nanoparticles (Ln-UCNPs), which absorb photons sequentially in the near-infrared (NIR) and emit radiation in the visible, has several advantages, such as the negligible photodamage to living organisms, a weak autofluorescence background, and a deeper penetration in biological tissues for biomedical thermometry purposes. Moreover, NIR excitation can be achieved with high power, and low cost laser sources. Finally, it is also important to note that Ln-UCNPs are more optically stable and have lower toxicity than quantum dots, for instance.

However, the setups used up to now to determine changes in luminescence intensity with temperature in these ratiometric techniques require bulky and relatively costly equipment, such as monochromators, luminescence detectors (photomultiplier tubes, CCD cameras, etc.), lock-in amplifiers, oscilloscopes, sophisticated aligning mechanical systems, etc. The size of these devices also limits the practical applications of these thermometric techniques and their transfer to real industrial or medical environments, where the measurement conditions change continuously. Furthermore, recording an emission spectrum with these devices requires some seconds, or even minutes, a timeframe during which the temperature of the sample might change, which represents an additional disadvantage of this technology.

Here, we report a low-cost, compact, fast signal processing, and non-invasive temperature sensor using a ratiometric fluorescence thermometry technique. Our setup uses a digital color sensor coupled to an optical system that allows simultaneously the excitation of the Ln-UCNPs and the collection of their emission. The emission from the Ln-UCNPs is separated from the excitation radiation, and diverted towards the detector. The detector is build in a mosaic structure, and containing different filters that allows it detecting simultaneously signals in the red, green and blue channels. With a microprocessor we calculated the fluorescence intensity ratio corresponding to the signals of two of these channels, and after comparing it to a previously determined calibration curve, temperature is visualized in a LCD display [22]. We used different Ln-UCNPs to demonstrate the potentiality of this thermometer to operate in different temperature ranges. We also reported the fabrication of transparent polydimethylsiloxane (PDMS)/luminescent Ln-UCNPs composites, from which microfluidic microchips can be fabricated since PDMS is one of most used polymers for this purpose [23,24]. These composites would allow to determine temperature directly in the internal walls of the microchips.

2. Experimental section

2.1 Temperature measurements setup

The setup we propose for temperature measurements comprises a diode laser that can be adapted to emitting at a wavelength that can be absorbed by the Ln-UCNPs, a focusing system (a microscope objective in the particular applications we are showing here, but that can be substituted easily by an optical lens) to focus the laser beam onto the sample and, that at the same time, collects the light emitted by the nanoparticles, a mirror that deviates the visible light generated by the nanoparticles towards the digital color sensor and at the same time filters the excitation radiation, and a S9706 Hamamatsu digital color sensor. A schematic representation of this setup is shown in Figure 1(a). The S9706 Hamamatsu digital color sensor consists on 9×9 arrayed photodiode elements arranged in a mosaic pattern integrated on a chip (see Figure 1(b)) with a photosensitive area of 1.2×1.2 mm. Each element has an on-chip filter that is sensitive to a particular range of wavelengths corresponding to different colors: red (590-720 nm), green (480-600 nm) and blue (400-540 nm), as shown in Figure 1(c). This sensor allows the RGB components of the incident light to be simultaneously measured with high accuracy. This digital color sensor is connected to a microchip that converts and amplifies the light signals into 12-bit digital signals, with independent reading for the blue, green and red channels, which allows us to analyze the intensity ratios between these signals, and to compare these data with a previous calibration curve to determine the temperature of a particular measurement. The integration time of this kind of sensor depends on the illuminance conditions, ranging from 100 s for low illuminance conditions to 10 μ s for high illuminance conditions [25].

To establish the calibration curve, the Ln-UCNPs were introduced in a Linkam THMS 600 heating stage, taking measurements every 5 °C when we analyzed the biological range of temperatures (25-60 °C) and every 50 °C for higher temperature applications. An Apollo Instruments Inc. diode laser with emission at 980 nm and 100 mW was used as the excitation source. The laser beam was focused on the sample using a 40X microscope objective and a N.A. of 0.6, producing a laser spot ~ 10 μ m on the sample. The emission was collected by the same microscope objective, and after passing a dichroic filter for elimination of the excitation wavelength, was sent to the Hamamatsu S9706 sensor.

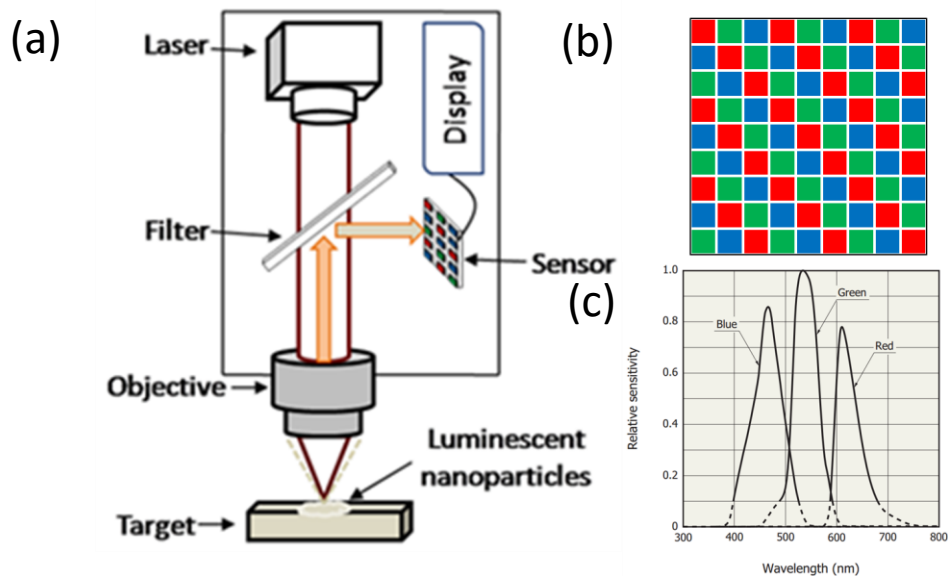


Figure 1. (a) Scheme of the temperature sensor we propose to use. (b) Structure of the Hamamatsu S9706 digital color sensor. (c) Relative sensitivity curve of the on-chip filters of the digital color sensor.

2.2 Ln-UCNPs synthesis and characterization

To demonstrate the operation of the sensor, we used different kinds of nanoparticles, with the only requirement that they emit light in two of the different ranges of the visible spectrum that can be detected by the Hamamatsu S9706 digital color sensor. An additional requirement we introduced was that the particles could be excited in the NIR, so we used Ln-UCNPs, given their previously indicated advantages as well as the possibility of providing simultaneous imaging and temperature sensing at nanoscale [21]. We selected different Ln-UCNPs to show the potentiality of our setup to be used in different temperature ranges.

Hexagonal β -Er,Yb:NaYF₄ nanoparticles, that have been extensively used to determine the temperature by optical methods in the biological range of temperatures [26], were provided by Boston Applied Technologies, Inc. From another side, we also used hydrothermally prepared Tm,Yb:GdVO₄@SiO₂ core-shell nanoparticles [27], which allow temperature determination up to 673 K with high sensitivity [28], and that can be used in microelectronics, for instance, to detect hot spots in microcircuits.

We recorded the emission spectra generated by the Ln-UCNPs by focusing the 980 nm diode laser beam through a 40X magnification microscope objective onto the sample, collecting

the emission arising from the sample by the same objective, and sending the signal to an AVANTES AVS-USB 2000 fiberoptic spectrometer that recorded it.

2.3 Preparation and characterization of Ln-UCNPs embedded PDMS composites

To prepare Er,Yb:NaYF₄/PDMS composites, the silicon elastomer was firstly mixed with the curing agent, followed by ultrasonication at room temperature for 10 min. Then, different quantities of Er,Yb:NaYF₄ nanoparticles were added to the above mixture under mechanical stirring for 30 min at room temperature. In order to remove the bubbles formed after the mechanical stirring, the composite was placed in a desiccator for 1 h. Finally, the Er,Yb:NaYF₄/PDMS composite was placed in an oven at 353 K during 40 min for polymerization.

The emission spectra of these composites were collected as described in the previous section. Images of these luminescent composites were recorded with a charge coupled device (CCD) Thorlabs camera to determine the distribution of Ln-UCNPs in the silicone.

3. Results and discussion

3.1 Luminescent thermometry with Ln-UCNPs

The potentiality of our setup was demonstrated by using two different kinds of Ln-UCNPs, Er³⁺-doped β-NaYF₄ and Tm³⁺-doped GdVO₄, both of them sensitized with Yb³⁺, which provide emission lines that overlap with the sensitivity curves of the on-chip filters of the digital color sensor in two different ways. Both kind of nanoparticles were excited at 980 nm, coinciding with the absorption band associated to the ²F_{7/2}→²F_{5/2} transition of Yb³⁺, that transfers its energy in a very efficient way to Er³⁺ and Tm³⁺ [29]. Yb³⁺ was used as the sensitizer since its absorption cross-section at 980 nm is higher than that of Er³⁺ or Tm³⁺ at the same wavelength, allowing for a more brilliant emission from these ions [29]. Figure 2 shows the emission spectra of Er,Yb:NaYF₄ and Tm,Yb:GdVO₄ UCNPs after excitation at 980 nm, and the overlap with the detection ranges of the digital color sensor. In the case of Er,Yb:NaYF₄ nanoparticles the emission bands are located in the green and red regions of the electromagnetic spectrum, corresponding to the ²H_{11/2}, ⁴S_{3/2} →⁴I_{15/2} and ⁴F_{9/2}→⁴I_{15/2} transitions of Er³⁺. In the case of Tm,Yb:GdVO₄ UCNPs the emission bands are located in the blue and red, corresponding to the ¹G₄ →³H₆ and ³F₃→³H₆ transitions of Tm³⁺, that provide another example to calibrate the temperature by changes in the luminescence intensities.

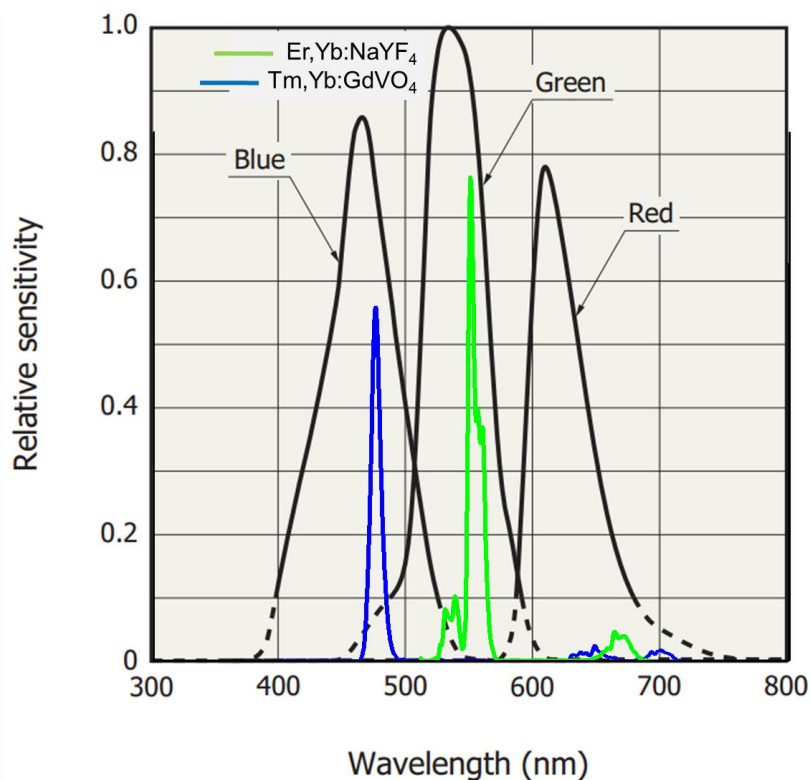


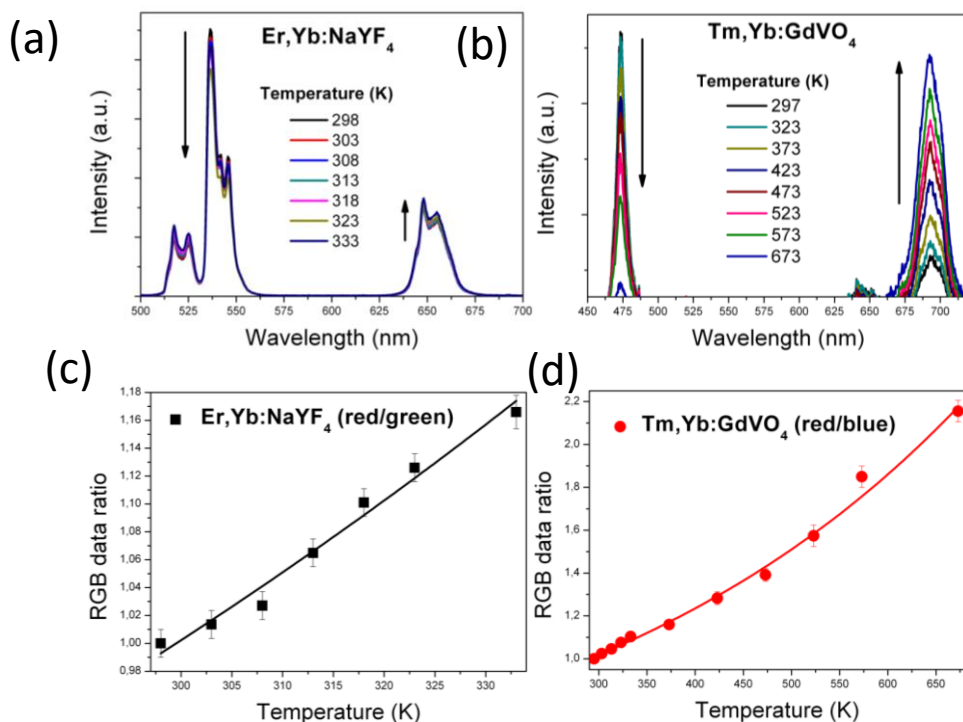
Figure 2. Overlap of the emission spectrum of Er,Yb:NaYF₄ and Tm,Yb:GdVO₄UCNPs with the detection ranges of the digital color sensor. Adapted from Digital Color Sensor S9706 datasheet, Hamamatsu.

Despite we cannot consider that the electronic levels from which the green and red emissions in the case of Er,Yb:NaYF₄UCNPs, or the blue and red emissions in the case of Tm,Yb:GdVO₄UCNPs are thermally coupled, since the electronic energy levels from which they arise lie too far apart, we observed that the intensity of these emission lines follows different tendencies as the temperature increased, as can be seen in Figures 3(a) and (b). As can be seen, in the case of Er,Yb:NaYF₄ nanoparticles (Figure 3(a)), the intensity of the green band decreases slightly when the temperature increases, while the intensity of the red band increases slightly. The same trend can be observed even magnified Tm,Yb:GdVO₄ nanoparticles: the intensity of the blue emission drops substantially when the temperature increases, while the intensity of the red band increases substantially. Thus, although we cannot consider that these systems are in thermal equilibrium governed by a Boltzmann distribution, we can observe how the intensity ratio between these two groups of lines evolves with temperature, since at the end, the two electronic levels from which each group of emissions are generated, are electronically linked. In fact, the evolution of the intensity ratio calculated from the values obtained for the integration of the green and red, and blue and red channels, respectively, of the digital color sensor with

temperature for the two kinds of nanoparticles is also presented in Figure 3, in the biological range of temperatures for Er,Yb:NaYF₄ UCNPs (see Figure 3 (c)), and in the range from room temperature to 673 K for Tm,Yb:GdVO₄ UCNPs (see Figure 3 (d)). It can be seen that the intensity ratio integrated from the two different channels in the case of Er,Yb:NaYF₄ nanoparticles follows almost a linear dependence, while in the case of Tm,Yb:GdVO₄ nanoparticles it follows an exponential dependence. The dispersion in the intensity ratios determined from the measurements performed with the digital color sensor is small and does not interfere in the determination of temperature, as can be seen in the figure. The fitting of the experimental points was done using an exponential equation of the form:

$$RGB \text{ data ratio} = A + B \cdot \exp(CT) \quad (1)$$

with the following parameters: $A = 0.16$, $B = 0.16$ and $C = 0.0056$ for Er,Yb:NaYF₄ UCNPs, and $A' = 0.23$, $B' = 0.38$ and $C' = 0.0024$ for Tm,Yb:GdVO₄ UCNPs.



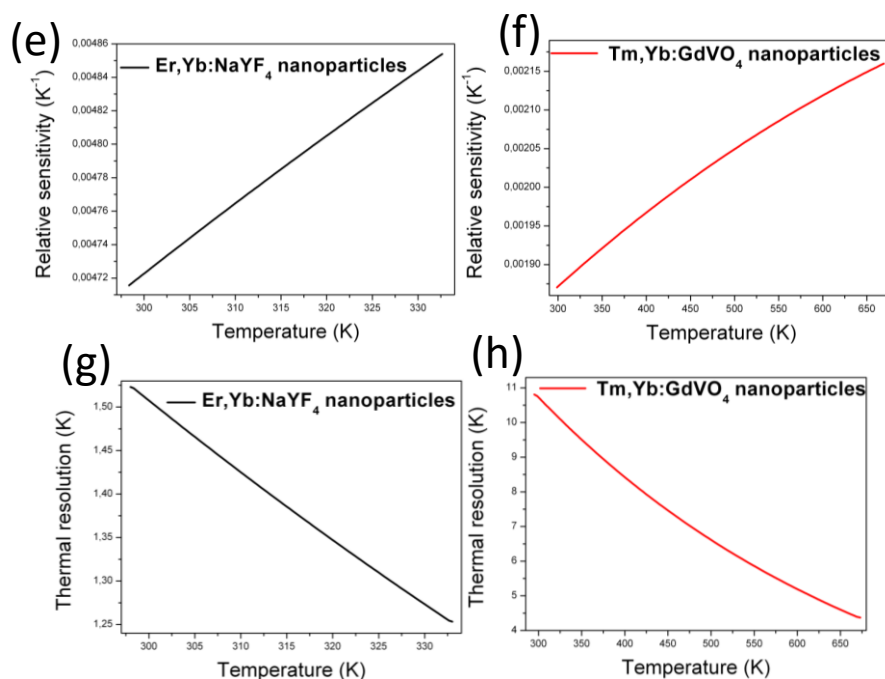


Figure 3. Evolution of the emission spectra with temperature for the (a) Er,Yb:NaYF₄ and (b) Tm,Yb:GdVO₄ nanoparticles. Evolution of the ratio between the signals of the blue, green and red channels recorded by the sensor with temperature for the (c) Er,Yb:NaYF₄ and (d) Tm,Yb:GdVO₄ nanoparticles. Relative thermal sensitivity for (e) Er,Yb:NaYF₄ and (f) Tm,Yb:GdVO₄ nanoparticles. Thermal resolution for the (g) Er,Yb:NaYF₄ and (h) Tm,Yb:GdVO₄ nanoparticles.

In order to compare the capacity for temperature determination of our sensor with that of other systems reported in the literature, we calculated the relative thermal sensitivity through the following equation [6]:

$$S_{rel}(T) = \frac{1}{RGB \text{ data ratio}} \cdot \frac{\partial RGB \text{ data ratio}}{\partial T} \quad (2)$$

The maximum relative thermal sensitivity for Er,Yb:NaYF₄ and Tm,Yb:GdVO₄ UCNPs was found to be 0.5 and 0.2% K⁻¹, respectively. The sensitivity value reported here for Tm,Yb:GdVO₄ nanoparticles, although smaller than that reported previously using a conventional system (1.54 % K⁻¹) [28], is similar to the one reported for other up-converting nanoparticles used for luminescence thermometry [30-32]. In the case of Er,Yb:NaYF₄ nanoparticles the relative thermal sensitivity reported in the literature varies from 0.21 to 1.24 % K⁻¹ [20,33]. Thus, the relative thermal sensitivity value we obtained lies in this range of sensitivities, indicating that we can use our system, avoiding using expensive and bulky equipment. From equation (2), the thermal resolution (∂T) can be estimated as:

$$\partial T = \frac{1}{RGB} \cdot \frac{\partial RGB}{S_{rel}(T)} \quad (3)$$

where ∂RGB is the standard deviation of the residuals in the fitting of the experimental points. Figures 3 (e) and (f) show the thermal resolutions of both kinds of nanoparticles as a function of temperature. The better thermal resolution was obtained at high temperature in both cases. Er,Yb:NaYF₄ nanoparticles show a thermal resolution of around 1.25K. Since the thermal resolution has not been reported for these nanoparticles using a conventional system, we cannot extract any conclusion about the influence of our system in this parameter. In the case of Tm,Yb:GdVO₄ nanoparticles, despite showing a higher thermal resolution, between 4 - 11 K, it is still valid to detect hot spots in microelectronic applications, for instance.

3.2 Luminescent thermometry in polymer composites for microfluidics applications

Microfluidics systems offer several advantages in many aspects of analytical chemistry and biochemistry, including efficiency, speed, portability, and reduced amount of reagent consumption [34]. However, the accurate and precise temperature control inside a microfluidic system is crucial, and has been demonstrated in a variety of applications [35-37]. When thermometry contact methods have been used for this purpose, problems associated to the size probe that these devices present [38]. Alternatively, non-contact methods for temperature determination in microfluidics have been reported, including thermo-reflectance methods [39], Raman spectroscopy [40], nuclear magnetic resonance [41], or luminescent thermometry by mixing organic dyes with the fluid circuiting in the microchip [42]. However, both Raman spectroscopy and nuclear magnetic resonance are based on the measurements of properties of water molecules, so they can only be used for aqueous solutions. In the case of thermo-reflectance methods, despite they offer a high thermal and spatial resolution, the use of expensive and complicated equipment is needed. Finally, in the cases where luminescence thermometry has been used, the organic dyes included are usually toxic, furthermore, they should be soluble or miscible with the fluid circulating through the microchip, which also limit their range of applications in microfluidics. Additionally, if the fluorescent dye is mixed with the fluid, it gives only information about the fluid and not about the platform on which the microfluidics chip is fabricated. Thus, there is a need to develop a cheap and accurate temperature determination technique in microfluidic systems that can be integrated in the same microfluidic chip.

PDMS is one of the most common silicon-based polymers used in microfluidics, exhibiting a high flexibility, a high optical transparency, a low surface tension, a high hydrophobicity, high thermal and chemical resistances, and biocompatibility [43-45]. Because of its excellent properties this material has been used in a wide range of applications including the fabrication

of microfluidic devices by soft-lithography systems [23], among others, and becoming one of the most popular polymers for lab-on-a-chip devices [24]. By generating organic / inorganic composites with this polymer, its properties have been complemented with additional ones introduced by the inorganic compounds. For instance, Fang and co-workers embedded Au nanocrystals in PDMS to generate plasmonic heating in a single device for microfluidic applications [46]. The mixing of magnetic nanoparticles with PDMS allowed producing magnetic and conductive composites for biological sensing purposes [47]. Also, by mixing luminescence nanoparticles with PDMS an enhanced luminescence has been reported [48].

Inspired by these works, we prepared Er,Yb:NaYF₄/PDMS composites as a new material that allows the fabrication of microfluidic chips for biological applications and at the same time allows temperature determination, namely thermal sensing on the surface and the internal part of a microfluidic chip based on our composite, through a non-contact and non-invasive method. Furthermore, by combining it with the experimental setup we designed, it might allow for the temperature determination in a compact device, perfect for the miniaturization of the whole system, and avoiding the use of bulk equipment for the same purpose.

Figure 4(a) depicts photographs of the Er,Yb:NaYF₄/PDMS composites containing different concentrations of luminescent nanoparticles. In the images, the optical transparency of these composites can be observed. Up to a nanoparticles concentration of 2 g/l could be embedded in the PDMS while keeping its transparency. Above this concentration the transparency decreased considerably (see for instance the image corresponding to the composite containing a nanoparticles concentration of 5 g/l). To verify that the nanoparticles were embedded uniformly in the polymer, we collected up-conversion emission maps of the composites (see Figure 4(b)), coupling the excitation and focusing parts of our setup to a CCD camera that substituted the digital color sensor. The images presented here are a composition of multiple images collected with this setup to show an enlarged area of the composites. As can be seen in these images, for concentrations above 2 g/l, the background luminescence of the composite dominates over the luminescence arising from the discrete nanoparticles, due to the high quantity of Ln-UCNPs that are excited at the same time by the diode laser, even if they are out of focus. This would affect the thermal measurement parameters of a device based on this material. Thus, composites containing a lower nanoparticles concentration will be used for further characterizations. An image of the luminescence that can be obtained in a Er,Yb:NaYF₄/PDMS composite with a concentration of 0.5 g/l is shown in Figure 4(c). In the image it can be appreciated the high transparency of the Er,Yb:NaYF₄/PDMS composite and the bright green luminescence that can be achieved after pumping at 980 nm with a power of 100

mW. In the inset, the luminescence map corresponding to a cross-section of this composite is shown, indicating a similar dispersion degree of the UCNPs in the polymer than that observed in the top-view images. This would ensure accuracy enough for the determination of temperature by luminescence measurements using a microchip based on this composite.

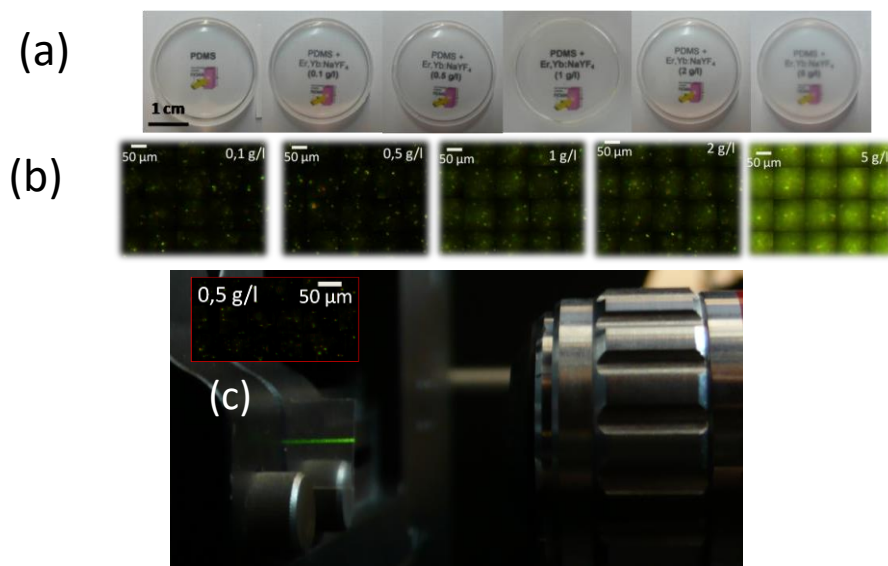


Figure 4. (a) Images of the Er,Yb:NaYF₄/PDMS composites containing different concentration of nanoparticles; (b) Up-conversion emission maps of selected composites; (c) Cross-section image of the 0,5 g/l Er,Yb:NaYF₄/PDMS composite showing the bright green emission that can be generated by the Er,Yb:NaYF₄ nanoparticles embedded in the polymer after pumping at 980 nm with a power of 100mW. The inset shows the corresponding luminescence map, indicating the homogeneity of the distribution of the nanoparticles.

To demonstrate the potential of these composites as luminescent thermometers we introduced a piece of them in a Linkam THMS 600 heating stage, to stabilize their temperature, and recorded their emission signals using the digital color sensor, from which we determined the RGB data ratio. Figure 5 (a) shows the temperature dependence of the intensity ratio corresponding to the signals recorded in the red and green channels of the digital color sensor for the Er,Yb:NaYF₄/PDMS composites with different concentrations of nanoparticles in the biological range of temperatures. The graph shows that for the samples containing a higher concentration of Ln-UCNPs the slope of these curves is smaller or even negative when the temperature increased, an effect that can be attributed to the background fluorescence arising from the nanoparticles which are out of focus, but that are still excited by the laser. The sample containing a particles concentration of 0.5 g/l shows an almost linear evolution of the red/green ratio. From its side, the sample containing 0.1 g/l of Ln-UCNPs shows an exponential increase of the red/green ratio as the temperature increased, following a tendency similar to that of the bare nanoparticles. Thus, this sample would be the most appropriate to develop a microfluidic

device in which we can monitor the temperature evolution in the whole chip, since it would provide the highest thermal sensitivity and thermal resolution. When we compare the relative thermal sensitivity of the 0.1 g/l Er,Yb:NaYF₄/PDMS composite with that of the bare nanoparticles, we observe that it is a little lower, maybe related to the interaction of light with the PDMS media [48], or the change of refractive index contrast between the two materials, but it is still similar to that reported in some publications for bare Er,Yb:NaYF₄ nanoparticles [20], indicating that we still can use this composite to determine the temperature by luminescence means.

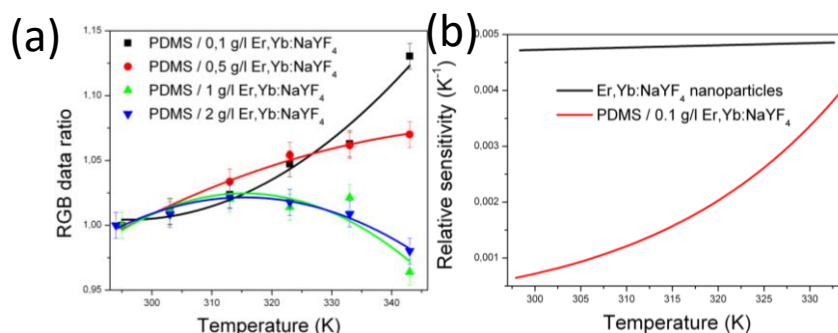


Figure 5. (a) RGB data ratio corresponding to different Er,Yb:NaYF₄/PDMS composites, containing different concentrations of Ln-UCNPs, as a function of temperature in the biological range. (b) Comparison of the relative thermal sensitivity of the 0.1 g/l Er,Yb:NaYF₄/PDMS composite and that of the bare Er,Yb:NaYF₄ nanoparticles.

4. Conclusions

We developed a novel non-contact and non-invasive luminescence thermometer by using a digital color sensor that allows collecting signals simultaneously in the blue, green and red channels of the electromagnetic spectrum, coupled to an excitation and an optical focusing system, together with luminescent up-conversion nanoparticles with emission in at least two of the detection channels of the digital color sensor. We demonstrated the potentiality of this setup for temperature sensing, by using Er,Yb:NaYF₄ nanoparticles emitting in the green and the red, with interest to explore temperatures in the biological range, and Tm,Yb:GdVO₄ nanoparticles emitting in the blue and the red, able to work up to 673 K, and thus, with interest in the microelectronic area to detect hot spots in microchips, for instance. The relative thermal sensitivity achieved with our setup is similar to that reported for the same kind of nanoparticles using conventional configurations in the fluorescence intensity ratio technique for temperature determination, which validates our new setup for temperature measurements. Furthermore, we have also shown that by embedding Er,Yb:NaYF₄ nanoparticles in PDMS, we can generate transparent composites that might allow the fabrication of thermometric microfluidic chips, in

which the same chip can be used as a luminescent thermometer for temperature determination in the walls of the microchannels.

Acknowledgements

This work was supported by the Spanish Government under Projects No. MAT2013-47395-C4-4-R, TEC2014-55948-R and MAT2014-56607-R, and by Catalan Authority under Project No. 2014SGR1358. Ol. A. Savchuk is supported by Catalan Government through the fellowship 2015FI_B2 00136. F. D. acknowledges additional support through the ICREA Academia awards 2010ICREA-02 for excellence in research.

References

- [1] B. Hildebrandt, P. Wust, O. Ahlers, A. Dieing, G. Sreenivasa, T. Kerner, R. Felix, H. Riess, The cellular and molecular basis of hyperthermia, *Crit. Rev. Oncol. Hematol.* 43 (2002) 33–56.
- [2] J. L. Roti Roti, Cellular responses to hyperthermia (40-46 degrees C): cell killing and molecular events, *Int. J. Hyperther.* 24 (2008) 3–15.
- [3] A.Y. Cheung, A. Neyzari, Deep local hyperthermia for cancer therapy, *Cancer Res.* 44 (1984) 4736-4744.
- [4] R.B. Roemer, Engineering aspects of hyperthermia therapy, *Annu. Rev. Biomed. Eng.* 1 (1989) 347-476.
- [5] M. P. Groover, *Fundamentals of modern manufacturing: materials, processes and systems*, fourth ed., John Wiley & Sons Inc., Hoboken, 2010.
- [6] D. Jaque, F. Vetrone, Luminescencenanothermometry, *Nanoscale* 4 (2012) 4301–4326.
- [7] C.D. Brites, P.P. Lima, N.J. Silva, A. Millan, V.S. Amaral, F. Palacio, L.D. Carlos, Thermometry at the nanoscale, *Nanoscale* 4 (2012) 4799–4829.
- [8] M. Asheghi, Y. Yang, Micro- and nano-scale diagnostic techniques for thermometry and thermal imaging of microelectronic and data storage devices, in *microscale diagnostic techniques*, in: K. S. Breuer (ed.), Springer-Verlag, Berlin, 2005, pp. 155–196.
- [9] J. Christofferson, K. Maize, Y. Ezzahri, J. Shabani, X. Wang, A. Shakouri, Microscale and nanoscale thermal characterization techniques, *J. Electron. Packaging*, 130 (2008) 041101–041106.
- [10] A. H. Khalid, K. Kontis, Thermographic phosphors for high temperature measurements: principles, current state of the art and recent applications, *Sensors* 8 (2008) 5673–5744.

- [11] P. Haro-González, L. Martínez-Maestro, I. R. Martín, J. García-Solé, D. Jaque, High-sensitivity fluorescence lifetime thermal sensing based on CdTe quantum dots, *Small* 8 (2012) 2652–2658.
- [12] L.M. Maestro, E.M. Rodríguez, F.S. Rodríguez, M.C. Iglesias-de la Cruz, A. Juarranz, R. Naccache, F. Vetrone, D. Jaque, J.A. Capobianco, J. García Solé, CdSe quantum dots for two-photon fluorescence thermal imaging, *Nano Lett.* 10 (2010) 5109–5115.
- [13] P.A.S. Jorge, M.A. Martins, T. Trindade, J.L. Santos, F. Farahi, Optical fiber sensing using quantum dots, *Sensors-Basel* 7 (2007) 3489–3534.
- [14] G. Walker, V. Sundar, C. Rudzinski, A. Wun, M. Bawendi, D. Nocera, Quantum-dot optical temperature probes, *Appl. Phys. Lett.* 83 (2003) 3555–3557.
- [15] W. Jung, Y.W. Kim, D. Yim, J. Y. Yoo, Microscale surface thermometry using SU8/Rhodamine-B thin layer, *Sens. Actuators A* 171 (2011) 228–232.
- [16] T. Barilero, T. Le Saux, C. Gosse, L. Jullien, Fluorescent thermometers for dual-emission-wavelength measurements: molecular engineering and application to thermal imaging in a microsystem, *Anal. Chem.* 81 (2009) 7988–8000.
- [17] Y. Shiraishi, R. Miyamoto, T. Hirai, A hemicyanine-conjugated copolymer as a highly sensitive fluorescent thermometer, *Langmuir* 24 (2008) 4273–4279.
- [18] E. Saïdi, B. Samson, L. Aigouy, S. Volz, P. Low, C. Bergaud, M. Mortier, Scanning thermal imaging by near-field fluorescence spectroscopy, *Nanotechnology* 20 (2009) 115703.
- [19] S.K. Singh, K. Kumar, S.B. Rai, Er³⁺/Yb³⁺-codoped Gd₂O₃ nano-phosphor for optical thermometry, *Sens. Actuators A* 149 (2009) 16–20.
- [20] F. Vetrone, R. Naccache, A. Zamarron, A. J. de la Fuente, F. Sanz-Rodríguez, L. M. Maestro, E.M. Rodríguez, D. Jaque, J. García Solé, J.A. Capobianco, Temperature sensing using fluorescent nanothermometers, *ACS Nano* 4 (2010) 3254–3258.
- [21] N.N. Dong, M. Pedroni, F. Piccinelli, G. Conti, A. Sbarbati, J.E. Ramirez-Hernandez, L.M. Maestro, M.C. Iglesias-de la Cruz, F. Sanz-Rodríguez, A. Juarranz, F. Chen, F. Vetrone, J.A. Capobianco, J. García Solé, M. Bettinelli, D. Jaque, A. Speghini, NIR-to-NIR two-photon excited CaF₂:Tm³⁺, Yb³⁺ nanoparticles: multifunctional nano probes for highly penetrating fluorescence bioimaging, *ACS Nano* 5 (2011) 8665–8671.
- [22] Ol. A. Savchuk, J. J. Carvajal, J. Massons, M. Aguilo, F. Diaz, “Dispositivo y metodo para medida remota de temperature,” Spain, P3110ES00, August 5, 2014.
- [23] A.J. Downard, D.J. Garret, E.S.Q. Tan, Microscale patterning of organic films on carbon surfaces using electrochemistry and soft lithography, *Langmuir* 22 (2006) 10739–10746.

- [24] J. Zhou, A.V. Ellis, N.H. Voelcker, Recent developments in PDMS surface modification for microfluidic devices, *Electrophoresis* 31 (2010) 2–16.
- [25] http://www.hamamatsu.com/resources/pdf/ssd/s9706_kpic1060e.pdf
- [26] L.H. Fischer, G.S. Harms, O.S. Wolfbeis, Upconverting nanoparticles for nanoscale thermometry, *Angew. Chem. Int. Ed.* 50 (2011) 4546-4551.
- [27] R. Calderon-Villajos, C.Zaldo, C. Cascales, Enhanced upconversion multicolor and white light luminescence in SiO₂-coated lanthanide-doped GdVO₄ hydrothermal nanocrystals, *Nanotechnology* 23 (2012) 505205.
- [28] O.A. Savchuk, J.J. Carvajal, C. Cascales, J. Massons, M. Aguiló, F. Díaz, Thermochromic upconversion nanoparticles for visual temperature sensors with high thermal, spatial and temporal resolution, *Nanoscale* (submitted).
- [29] M. Haase, H. Schäfer, Upconverting nanoparticles, *Angew. Chem. Int. Ed.* 50 (2011) 5808-5829.
- [30] B. Dong, B. Cao, Y. He, Z. Liu, Z. Li, Z. Feng, Temperature sensing and in vivo imaging by molybdenum sensitized visible upconversion luminescence of rare-earth oxides, *Adv. Mater.* 24 (2012) 1987-1993.
- [31] S. Zhou, K. Deng, X. Wei, G. Jiang, C. Duan, Y. Chen, M. Yin, Upconversion luminescence of NaYF₄:Yb³⁺, Er³⁺ for temperature sensing, *Optics Commun.* 291 (2013) 138-142.
- [32] OI. A. Savchuk, P. Haro-Gonzalez, J.J. Carvajal, D. Jaque, J. Massons, M. Aguiló, F. Díaz, Er:Yb:NaY₂F₅O up-converting nanoparticles for sub-tissue fluorescence lifetime thermal sensing, *Nanoscale* 6 (2014) 9727-9733.
- [33] S. Jiang, P. Zeng, L. Liao, S. Tian, H. Guo, Y. Chen, C. Duan, M. Yin, Optical thermometry based on upconverted luminescence in transparent glass ceramics containing NaYF₄:Yb³⁺/Er³⁺ nanocrystals, *J. Alloys Comp.* 617 (2014) 538–541.
- [34] C. W. Shields IV, C. D. Reyes, G. P. Lopez, Microfluidic cell sorting: a review of the advances in the separation of cells from debulking to rare cell isolation, *Lab Chip* 15 (2015) 1230-1249.
- [35] S. Köster, F. E. Angilè, H. Duan, J. J. Agresti, A. Wintner, C. Schmitz, A.C. Rowat, C.A. Merten, D. Pisignano, A.D. Griffiths, Drop-based microfluidic devices for encapsulation of single cells, *Lab Chip* 8 (2008) 1110-1115.
- [36] F. M. Weinert, J.A. Kraus, T. Franosch, D. Braun, Microscale fluid flow induced by thermoviscous expansion along a traveling wave, *Phys. Rev. Lett.* 100(2008) 164501.

- [37] M. U. Kopp, A. J. de Mello, A. Manz, Chemical amplification: continuous-flow PCR on a chip, *Science* 280 (1998) 1046-1048.
- [38] P.R.N. Childs, J.R. Greenwood, C.A. Long, Review of temperature measurement, *Rev. Sci. Instrum.* 71 (2000) 2959-2978.
- [39] L. J. Davis, M. Deutsch, Surface plasmon based thermo-optic and temperature sensor for microfluidic thermometry, *Review of Sci Inst.* 81(2010) 114905.
- [40] K. L. K. Liu, K. L. Davis, M. D. Morris, Raman spectroscopic measurement of spatial and temporal temperature gradients in operating electrophoresis capillaries, *Anal. Chem.* 66 (1994) 3744-3750.
- [41] M. E. Lacey, A. G. Webb, J. V. Sweedler, Monitoring temperature changes in capillary electrophoresis with nanoliter-volume NMR thermometry, *Anal. Chem.* 2000, 72, 4991-4998.
- [42] N. Ishiwada, S. Fujioka, T. Ueda, T. Yokomori, Co-doped $Y_2O_3:Tb^{3+} / Tm^{3+}$ multicolor emitting phosphors for thermometry, *Opt. Lett.* 36 (2011) 760-762.
- [43] R.A. Mendels, E.M. Graham, S.W. Magennis, A.C. Jones, F. Mendels, Quantitative comparison of thermal and solutal transport in a T-mixer by FLIM and CFD, *Microfluid. Nanofluid.* 5 (2008) 603-617.
- [44] X. Deng, B. Liu, S. Cao, R. Luo, H.Chen, A novel approach for the preparation of PMMA-PDMS core-shell particles with PDMS in the shell, *Appl. Surf. Sci.* 253 (2007) 4823-4829.
- [45] M. George, R. G. Weiss, Molecular organogels. Soft matter comprised of low-molecular-mass organic gelators and organic liquids, *Acc. Chem. Res.* 39 (2006) 489-497.
- [46] C. Fang, L. Shao, Y. Zhao, J. Wang, H. Wu. A gold nanocrystal/poly(dimethylsiloxane) composite for plasmonic heating on microfluidic chips, *Adv. Mater.* 24 (2012) 94-98.
- [47] Y. Jiang, H. Wang, S. Li, W. Wen, Applications of micro/nanoparticles in microfluidic sensors: a review, *Sensors* 14 (2014) 6952-6964.
- [48] H. Fu, G. Yang, S. Gai, N. Niu, F. He, J. Xu, P. Yang, Color-tunable and enhanced luminescence of well-defined sodium scandium fluoride nanocrystals, *Dalton Trans.* 42 (2013) 7863-7870.

CHAPTER 4

Luminescence nanothermometry in the visible: II.

New materials

In this chapter we included the new materials we investigated for luminescence nanothermometry. Ho^{3+} , $\text{Yb}^{3+}:\text{KLu}(\text{WO}_4)_2$ nanoparticles as a versatile materials for multiple thermal sensing by luminescence nanothermometry is presented. Different luminescence thermometric techniques have been used to evaluate the potentiality of this material, such as the fluorescence intensity ratio technique of two thermally coupled Stark sublevels, the intensity ratio between the red and green luminescence bands generated by two electronically and thermally linked manifolds of these nanoparticles, lifetime measurements, or by observing the change of the color of the emitted light arising from the sample. We have also shown how by adding an additional active ion to the host matrix we can generate a totally new and potential system. The change in the upconversion emission spectra of the triply doped Ho^{3+} , Yb^{3+} , $\text{Tm}^{3+}:\text{KLu}(\text{WO}_4)_2$ nanoparticles in range of the temperatures from 296 to 673 K were investigated. The intensity ratio between two emission lines at 648 and 661 nm, arising from the Tm^{3+} transition ${}^1\text{G}_4 \rightarrow {}^3\text{F}_4$ and the Ho^{3+} transition ${}^5\text{F}_3 \rightarrow {}^5\text{I}_7$, respectively, and between 539 and 549 nm, arising from two Stark sublevels of the Ho^{3+} transition ${}^5\text{F}_4$, ${}^5\text{S}_2 \rightarrow {}^5\text{I}_8$ were used for monitoring the temperature. Moreover, these nanoparticles have an alternative scheme of excitation at 808 nm, providing a linear evolution of the intensity ratio between the 687 nm (${}^1\text{G}_4 \rightarrow {}^3\text{F}_4$ Tm^{3+} transition) and the 545 nm (${}^5\text{S}_2$, ${}^5\text{F}_4 \rightarrow {}^5\text{I}_8$ Ho^{3+} transitions) emission bands in the biological range of the temperatures. Thus, with the same material we have shown that by pumping Yb^{3+} at 980 nm we obtain a good thermal sensitivity at relatively high temperatures,

while pumping Tm^{3+} at 808 nm we obtain an excellent thermal sensitivity in the biological range of temperatures.

Moreover, we report the synthesis of Er^{3+} , $\text{Yb}^{3+}:\text{NaYF}_4$ nanoparticles by a microwave-assisted solvothermal method. By tuning the basic parameters of the synthesis procedure, such as the time and temperature of reaction and the concentration of ethanol and water, the size and the crystalline phase of the nanoparticles could be controlled. We analysed the evolution of the upconversion emission spectra of the synthesized nanoparticles for their use in luminescence thermometry. We observed that the thermal sensitivity that can be achieved is a function of the size of the nanoparticles and the crystalline phase in which they crystallize. Finally, we proved their practical application by mapping the temperature distribution in a glass slide cover generated by graphene flakes illuminated by a 808 nm diode laser, achieving a thermal resolution of 0.1 K.

Finally, we analyzed the evolution of the upconversion emission spectra generated by Er^{3+} , $\text{Yb}^{3+}:\text{GdVO}_4@\text{SiO}_2$ core-shell nanoparticles in the physiological range of temperatures. We observed how the silica coating, in the core-shell structure, affects positively the temperature sensing characteristics of this material. The absolute thermal sensitivity calculated for the core-shell nanoparticles was double than that achieved in bare nanoparticles, allowing for an experimental thermal resolution of 0.4 K. Moreover, the silica-coated nanoparticles showed a good dispersibility in different solvents, such as water, DMSO and methanol, and good luminescence stability without any interaction with the solvent molecules. Furthermore, we also observed that the silica coating prevents the nanoparticles from a progressive heating during prolonged periods of excitation with the laser at 980 nm, which would affect their thermometric applications. To demonstrate the potentiality of these new nanothermometers, we performed a temperature sensing experiment in chicken breast heated externally by hot air.

Paper VI

Savchuk, Ol. A.; Carvajal, J. J.; Pujol, M. C.; Barrera, E. W.; Massons, J.; Aguilo, M.; and Diaz *Ho,Yb:KLu(WO₄)₂ nanoparticles: a versatile material for multiple thermal sensing purposes by luminescent thermometry (2015) J. Phys. Chem. C* 119, 18546–18558.

Ho,Yb:KLu(WO₄)₂ Nanoparticles, A Versatile Material for Multiple Thermal Sensing Purposes by Luminescent Thermometry

Oleksandr Savchuk, Joan J. Carvajal, Maria C. Pujol, William E. Barrera, Jaume Massons,
Magdalena Aguilo, Francesc Diaz.*

Física i Cristal·lografia de Materials i Nanomaterials (FiCMA-FiCNA) – EMaS, Universitat
Rovira i Virgili (URV), Campus Sescelades, Marcel·li Domingo 1, E-43007, Tarragona, Spain.

Corresponding Author

Joan J. Carvajal

joanjosep.carvajal@urv.cat

Física i Cristal·lografia de Materials i Nanomaterials (FiCMA-FiCNA) – EMaS, Universitat
Rovira i Virgili (URV), Campus Sescelades, Marcel·lí Domingo 1, E-43007, Tarragona, Spain
Tel. +34 977 558628

Abstract

We studied the temperature dependence of the up-conversion emission in the green and the red regions of the electromagnetic spectrum of Ho,Yb:KLu(WO₄)₂ nanocrystals after excitation at 980 nm, and analyzed their possible applications as thermal sensors in luminescence thermometry in the RT to 673 K range, by using different techniques. The different thermometric techniques used are the fluorescence intensity ratio technique of two thermally coupled Stark sublevels, the intensity ratio between the red and green luminescence bands

generated by two electronically and thermally linked manifolds of these nanoparticles, lifetime measurements, or by observing the change of the color of the emitted light arising from the sample. In all cases, thermal sensitivities comparable to those previously reported in the literature are obtained, but offering different thermal sensing approaches using a single material, providing a way to corroborate the temperature measurements.

1. Introduction

Contact thermometry has several limitations at the submicrometer scale, including stability, accuracy and the location of the sensor tip for a temperature measurement.¹ This promoted the development of different non-contact thermometry technologies,² from which those that use different properties of light constitute promising methods for temperature determination with high spatial resolution.¹ Among these techniques, however, there are some of them that's how serious drawbacks. The main one is that most of these techniques allow measuring the temperature in the surface of the sample.³ Furthermore, infrared (IR) and thermorefectance thermometers show a restricted spatial resolution. From another side, Raman spectroscopy can only be applied to materials showing a large Raman efficiency and thus it is restricted to a few numbers of systems.⁴⁻⁹

Luminescence thermometry has emerged as an alternative to overcome these problems, as it can increase the spatial resolution, can measure temperatures in the body when the luminescent nanoparticles are internalized in the sample, can be used to measure high temperatures, or to characterize moving surfaces and even it allows measuring the temperature in the presence of strong electromagnetic fields without interferences.^{1,10} Luminescence thermometry is based on the temperature dependence of the fluorescence features (intensity and peak position of the absorption and excitation bands, lifetime, etc.) of luminescence nanoparticles to determine the temperature of a sample in contact with them.³

Lanthanide-doped (Ln-doped) materials have often been used as temperature sensors in the luminescent thermometry techniques since those ions show several narrow emission and absorption lines, some of them even thermally coupled, that can be used for this purpose, apart from relatively long emission lifetimes (in the range of microseconds to milliseconds), and good chemical and physical stability they present.¹¹⁻¹³ Furthermore, Ln-doped materials have the capability to generate efficient up-conversion visible emissions through absorbing near-infrared (NIR) light, allowing to overcome problems related with background fluorescence and damaging of the surrounding tissues in biological applications when excited with ultraviolet light, as it happens with the usual luminescence process where the emitting ion is excited at a shorter wavelength to respect the light emitted.. Furthermore, the NIR lasers used to excite those up-conversion nanoparticles are much cheaper and more powerful than the UV lasers. Finally, the use of NIR radiation also preserves the operative lifetime of the phosphors used, in comparison with those illuminated with UV light, that are damaged usually by this radiation, shortening their operational lifetimes.¹⁴The most studied lanthanide element for this specific application is Er^{3+} which is usually coupled to Yb^{3+} , since it has a larger absorption cross section in the NIR region and provides an efficient energy transfer to Er^{3+} due to the large spectral overlap between these two ions.¹⁵⁻²¹

However, there exist other possible lanthanide candidates that can be efficiently used in luminescent thermometry, such as Ho^{3+} . It is known that Ho^{3+} sensitized by Yb^{3+} can generate a strong visible up-conversion emission under NIR excitation.²²⁻²⁷ Using Ho^{3+} as activator and Yb^{3+} as sensitizer, blue, green and red emission bands can be obtained after pumping with NIR light at 980 nm by up-conversion processes. However, so far, just a very few works have been devoted to the temperature sensing capabilities of Ho^{3+} or $\text{Ho}^{3+}, \text{Yb}^{3+}$ co-doped systems, that are mainly focused on the emission on the blue region of the spectrum, that has a low penetration depth in biological tissues and it suffers from the lower sensitivity of detection systems when compared to those operating in the green and/or red regions.²²⁻²⁷ In this context, the blue

emission of Ho^{3+} , $\text{Yb}^{3+}:\text{Y}_2\text{O}_3$ nanoparticles have been used to determine the temperature in the 10-300 K range,²⁷ and the blue emission of the $\text{Ho}^{3+},\text{Yb}^{3+}:\text{CaWO}_4$ phosphor was used to determine the temperature in the 303 – 923 K.²⁵

Here we propose to use the $\text{KLu}(\text{WO}_4)_2$ as a host for Ho and Yb ions,²⁸⁻³⁰ and explore their possibilities in luminescent thermometry applications. KLuW is a member of the family of monoclinic potassium double tungstate materials that crystallize in the $C2/c$ spatial group of symmetry,³¹ with laser applications,²⁸⁻³⁰ and more recently with interest for the fabrication of waveguides,³² since it allows for a high lanthanide ion doping concentration without quenching effects and lanthanides show high absorption and emission cross-sections when embedded in it.³¹

We report the temperature sensing capabilities of Ho^{3+} , Yb^{3+} co-doped KLuW nanoparticles using different techniques, such as the FIR technique applied to the red emission generated by these nanoparticles, with a higher penetration depth in the biological tissues when compared to the blue emission. We also explored the lifetime measurements technique on the green and red emissions arising from these nanoparticles upon NIR diode laser excitation at 980 nm. Both techniques show significant sensitivity and provide a great potentiality of using Ho^{3+} , Yb^{3+} co-doped KLuW nanoparticles as thermal probes. Moreover, we observed a temperature dependent change in the color perception of the emission arising from these nanoparticles that provides additional possibilities for visual, real-time temperature determination. Finally, we explored the possibilities of using the intensity ratio between the red and green emissions that are generated from linked electronic states, increasing still the possibilities of using this material for thermometric purposes.

2. Experimental Details

Synthesis of Ho,Yb:KLuW nanoparticles. 1at. % Ho and 10 at. % Yb doped KLuW nanocrystals were synthesized by the modified Pechini sol-gel method.³³ Analytic grade purity reagents of Ho_2O_3 (99.9999%) Yb_2O_3 (99.9%), and Lu_2O_3 (99.9999%), were dissolved in hot nitric acid in stoichiometric proportions to form the nitrate precursors. Citric acid (CA), as the chelating agent and ethylenglycol (EG), as the esterification agent, were used also in this reaction. The nitrate precursors were dissolved in distilled water with citric acid in a molar ratio of CA to metal cations $\text{CM} = [\text{CA}]/[\text{METAL}] = 1$. Ammonium tungstate $(\text{NH}_4)_2\text{WO}_4$ (99.99%) and potassium carbonate K_2CO_3 (99.99%) were added to the aqueous solution, that was heated at 353 K under magnetic stirring during 24 h until complete dissolution. Then, EG was added to the mixture in a molar ratio $\text{CE} = [\text{EG}]/[\text{CA}] = 2$. The solution was heated at 373 K in order to evaporate water and generate the polymeric gel. After that, the polymeric gel was calcinated at 573 K for 3 hours to obtain the precursor powders that were then calcinated at 1023 K for 2 hours to eliminate the organic compounds and crystallize the desired nanoparticles.

Spectroscopic characterization. The emission spectra of Ho,Yb:KLuW nanoparticles from room temperature up to 673 K were recorded after pumping at 980 nm with an Apollo Instruments, Inc. cw diode laser. The emission from the samples was dispersed in a JobinYvon HR 460 monochromator. A Hamamatsu PMTR 928 photomultiplier tube connected to a Perkin Elmer DSP-7265 lock in amplifier was used to detect and amplify the collected signal.

For thermal sensing experiments, Ho,Yb:KLuW nanoparticles were introduced into a Linkam THMS 600 heating stage, with thermocouples connected to the heating stage for temperature control, and with a boron nitride disk that homogenizes the temperature distribution along the sample.

Pictures illustrating the color of the emission generated by the samples were recorded using a CCD camera Thorlabs DCU224C.

For luminescence decay-time experiments, Ho,Yb:KLuW nanoparticles were excited at 980 nm with an optical parametric oscillator from Oportek (Vibrant HE 355 II + UV) with a pulse duration of 6 ns and a repetition frequency of 10 Hz. The fluorescence light emitted by the sample was collected with a microscope objective (10×), transferred to the monochromator for the selection of specific wavelengths, and then detected using a Hamamatsu R928 photomultiplier. The decay curves of the 540 nm and 650 nm emitted signals were measured with a digital oscilloscope. To analyze the changes in lifetime at different temperatures, Ho,Yb:KLuW nanoparticles were introduced into the Linkam THMS 600 heating stage described above.

3. Results and Discussion

A transmission electron microscopy (TEM) image of the Ho,Yb:KLuW nanoparticles synthesized by the Pechini method is shown in Figure 1a. It can be seen that the nanoparticles have an irregular shape with the presence of agglomerates, typical in nanoparticles synthesized by this method.³⁴ The average size was found to be 40 – 60 nm, as can be seen in the size distribution histogram depicted in Figure 1b, after analyzing over 1000 nanoparticles. Figure 1c shows the XRD pattern recorded for these nanoparticles, showing that they crystallize in the monoclinic system with $C2/c$ spatial group. The reference XRD pattern, corresponding to $KLu(WO_4)_2$ (JCPDS file 54-1204) was included for comparison. From the XRD pattern it was possible to estimate a crystallite size of 35 nm, using the Scherrer equation.³⁵ This is in agreement with the mean size of these nanoparticles determined by TEM.

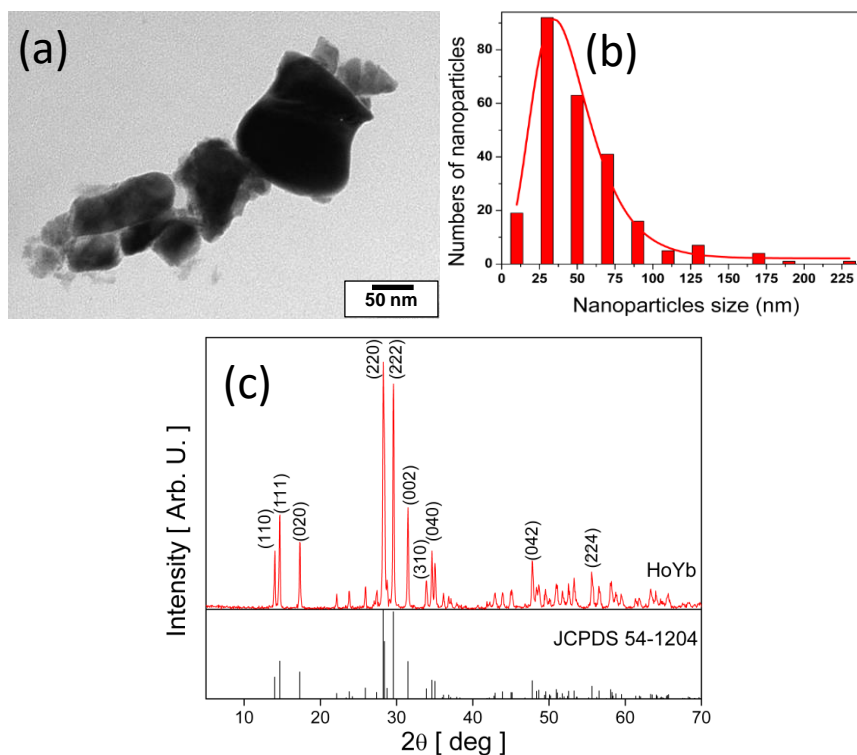


Figure 1. (a) TEM image and (b) size distribution histogram of Ho,Yb:KLuW nanoparticles synthesized by the Pechini method. (c) XRD pattern of these nanoparticles together with the KLuW reference pattern, JPDS file 54-1204.

The up-conversion emission spectra of 1 at. % Ho, 10 at. % Yb:KLuW nanoparticles in the range of temperatures from 297 – 673 K are shown in Figure 2a. Each spectrum consists of two separated emission bands located in the green and the red regions of the visible spectrum. In this material, we did not observe the blue emission as previously reported for $\text{Ho}^{3+}:\text{TeO}_2$ glasses or $\text{Ho}^{3+}, \text{Yb}^{3+}:\text{Ca}_{12}\text{Al}_{14}\text{O}_{33}$, $\text{Ho}^{3+}, \text{Yb}^{3+}:\text{CaWO}_4$, $\text{Ho}^{3+}, \text{Yb}^{3+}:\text{Y}_2\text{O}_3$ and $\text{Ho}^{3+}, \text{Yb}^{3+}, \text{Tm}^{3+}:\text{Y}_2\text{O}_3$ phosphors.²²⁻²⁷ The up-conversion mechanism can be explained as follows. The electronic population of the $^5\text{S}_2$, $^5\text{F}_4$ energy levels of Ho^{3+} under the 980 nm laser excitation is accomplished through the sequential energy transfer from two different electrons that have been promoted to the $^2\text{F}_{5/2}$ level of Yb^{3+} from the $^2\text{F}_{7/2}$ level, by means of ground state absorption (GSA) after pumping at 980 nm. First, energy transfer (ET) process from the excited $^2\text{F}_{7/2}$

energy level of Yb^{3+} promotes electrons in Ho^{3+} to the $^5\text{I}_6$ energy level. Then, a second ET from Yb^{3+} promotes electrons in Ho^{3+} from the $^5\text{I}_6$ to the $^5\text{S}_2$, $^5\text{F}_4$ multiplets. From these $^5\text{S}_2$, $^5\text{F}_4$ energy levels, the radiative relaxation to the ground state generates the green emission at 540 nm. A nonradiative relaxation from the $^5\text{S}_2$, $^5\text{F}_4$ energy levels populates the $^5\text{F}_5$ multiplet, from which the radiative process generates the red emission with two main peaks centered at 650 and 660 nm (see Figure 2b). A second path to explain the population of the $^5\text{F}_5$ energy level can also be postulated from a nonradiative process after the first ET transfer process, populating the $^5\text{I}_7$ energy level of Ho^{3+} ion. The ET from a second electron in the $^2\text{F}_{7/2}$ energy level of Yb^{3+} promotes these electrons to the $^5\text{F}_5$ energy level of Ho^{3+} .

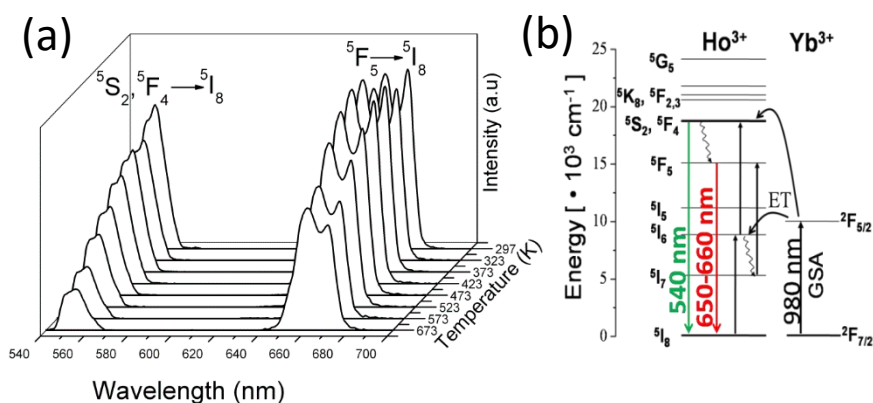


Figure 2. (a) Evolution of the up-conversion emission spectra of Ho,Yb:KLuW nanoparticles with temperature in the range 297-673 K after excitation at 980 nm.(b) Energy level diagram for Ho,Yb:KLuW nanoparticles indicating the transitions involved in the absorption and emission processes.

As can be seen in the spectra depicted in Figure 2a, when the temperature increased both up-conversion emission bands drop in intensity due to the thermal quenching effect.^{36, 37} However, the red emission band that consists of two peaks assigned to the radiative transition from different Stark sublevels of the $^5\text{F}_5$ energy level of Ho^{3+} to the ground state, shows a different

thermal evolution in the intensity of these two peaks (see Figure 3a). The energy gap between these Stark sublevels is small, so the upper sublevel can be thermally populated from the lower sublevel when the temperature increased indicating that these two levels are thermally coupled, which allowed to use the relative intensity between these two peaks to determine the temperature by using the Fluorescence Intensity Ratio (FIR) technique. The FIR technique consists in measuring the thermal dependence of the intensity of fluorescence arising from two different electronic levels that are thermally coupled and calculate their ratio.³⁸ The FIR from two thermally coupled energy levels is usually given as:

$$FIR = \frac{I_1}{I_2} = \frac{g_1\nu_1\sigma_1}{g_2\nu_2\sigma_2} \exp\left(-\frac{\Delta E}{k_B T}\right) = B \exp\left(-\frac{\Delta E}{k_B T}\right) \quad (1)$$

where I_1 and I_2 are the intensities of emission from the upper and the lower thermally coupled energy levels; g_i , ν_i , and σ_i , are the degeneracy of levels, the spontaneous emission, and the absorption rates, respectively, k_B is the Boltzmann constant, T is the absolute temperature, and ΔE is the energy difference between the two energy states considered. However, if the emission peaks are located very close to each other, they usually partially overlap. In order to modelize for this effect, Wade *et al.*³⁹ proposed some modification on the FIR in equation 1, taking the form:

$$FIR = \left(\frac{n_2}{n_1}\right) B \exp\left(-\frac{\Delta E}{k_B T}\right) + \left(\frac{m_1}{n_1}\right) \quad (2)$$

where n_i defines the fraction of the total fluorescence intensity of the transition originating from level i (upper level $i = 2$, lower level $i = 1$), and m_1 defines the fraction of the total intensity from level 1.

The experimental data were fitted to equation 2 giving the following expression: $FIR = 0,66\exp(-337/T) + 0,79$, as can be seen Figure 3b. This method was previously reported in Er-doped fibers using the Stark sublevels of the $^4I_{13/2}$ manifold³⁸ and in Yb-doped fibers using the Stark sublevels of the $^2F_{5/2}$ manifold.⁴⁰ However, in the case of Er-doped fibers, despite resolutions of 0.36 K were achieved, the lengths of the fibers used in the tests (6-7 m), made impractical this system for use as a point sensor.³⁸ In the case of Yb-doped fibers, the value of the energy level difference obtained from the fit was larger than the predicted value between the Stark sublevels of the $^2F_{5/2}$ manifold, similar to what is happening in our case with the 5F_5 Stark sublevels of Ho^{3+} , due to temperature dependent changes in reabsorption and fluorescence from the different Stark sublevels arising from changes in the population distribution of the ground state.³⁸ In order to compare the capacity for temperature determination of our nanoparticles with other systems reported in the literature for the same purpose, we calculated the absolute sensitivity through the derivative of this expression to respect temperature. The maximum sensitivity was found at room temperature, with a value of 0.00385 K^{-1} (see Figure 3c).

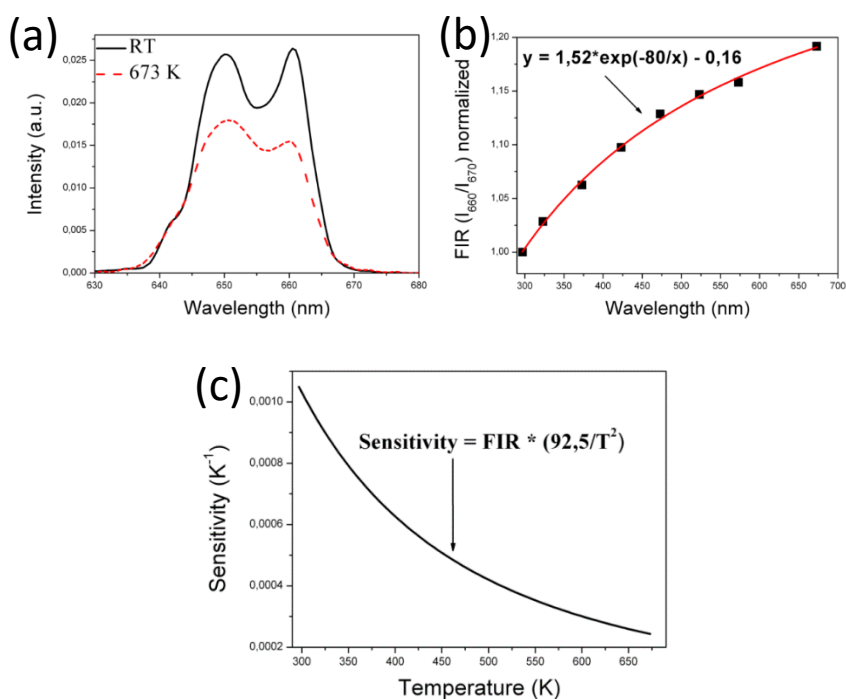


Figure 3. (a) Comparison of the spectra of the red emission at room temperature and 673 K. (b) FIR of the I_{650}/I_{660} in the range of the temperature 297 – 673 K. (c) Sensitivity graph for the ratio I_{650}/I_{660} .

Table 1 summarizes the results reported in the literature for ratiometric luminescent thermometric techniques, in which we highlighted the relative sensitivity reported, the temperature resolution and the temperature range analyzed. We also included in the table the excitation wavelength for the different systems, and the emission wavelengths used to calculate the intensity ratio, together with the electronic transitions involved, in the case of lanthanide ions, or the origin of the emission lines considered in the case of other systems. The table has been structured in five different blocks. The first block contains the information related to lanthanide-containing systems that have been pumped at wavelengths shorter than the emission recorded. The second block contains the information related to lanthanide-containing up-conversion systems. The third block contains the information related to quantum dot systems. The fourth block contains the information related to organic-dye containing systems. Finally, in the fifth block we included the information related to other systems that could not be classified in the other four blocks, like polymer compounds, or transition metal complexes.

Table 1. Comparison of Ln-doped systems used for luminescence thermometry based on the ratiometric techniques.

Material	Temperature range (K)	Excitation wavelength (nm)	Electronic transitions involved (ion) Wavelengths ratio	Relative sensitivity %K ⁻¹ (temperature, K)	Temperature resolution (K)	Ref.
<i>Lanthanide-containing systems, pumped at shorter wavelengths than the emission recorded</i>						
Eu-EDTA(H ₂ O) ₂ / Eu-EDTA(H ₂ O) ₃	274-343	579	⁷ F ₀ → ⁵ D ₀ (Eu ³⁺) 579.4 / 579.9 nm	8	1	41
Eu:P(VD C-co-AN) / BBS	273-323	365	⁵ D ₀ → ⁷ F ₂ (Eu ³⁺) / BBS 611/412 nm	7.2 (323 K)	-	42
Eu-DT / OASN in silica NPs	283-323	400	⁵ D ₀ → ⁷ F ₂ (Eu ³⁺) / OASN 614/498 nm	7.2 (323 K)	-	43
Eu:SiO ₂	298-348	405	⁵ D ₀ → ⁷ F ₄ (Eu ³⁺) / ⁵ D ₀ → ⁷ F ₄ (Eu ³⁺) 686 / 698 nm	5	-	13
Tb,Eu metal	10-350	365	⁵ D ₄ → ⁷ F ₅ (Tb ³⁺) / ⁵ D ₀ → ⁷ F ₂ (Eu ³⁺)	4.9 (150)	0.5	44

organic complex			545 / 612 nm			
Eu,Tb:Fe ₂ O ₃	10-350	365	⁵ D ₀ → ⁷ F ₂ (Eu ³⁺) / ³ D ₄ → ⁷ F ₅ (Tb ³⁺) 610 / 547 nm	4.7 (134)	0.5	45
Eu:TiO ₂	307-533	360	⁴ T ₁ → ⁶ A ₁ (Mn ²⁺) / ³ D ₀ → ⁷ F ₂ (Eu ³⁺) 613 / 438nm	2.7 (533)	0.46 (400 K)	46
Eu, Tb complexes	273-343	405	⁵ D ₄ → ⁷ F ₅ (Tb ³⁺) / ³ D ₀ → ⁷ F ₂ (Eu ³⁺) 545 / 615 nm	1.2	0.1	47
Er:SBN glass ceramic	300-700	532	² H _{11/2} → ⁴ I _{13/2} (Er ³⁺) / ⁴ S _{3/2} → ⁴ I _{13/2} (Er ³⁺) 800 / 850 nm	0.17 (600 K)	-	48
Nd:SBN glass ceramic	300-700	532	⁴ F _{5/2} → ⁴ I _{9/2} (Z ₄)(Nd ³⁺) / ⁴ F _{3/2} → ⁴ I _{9/2} (Z ₄)(Nd ³⁺) 820 / 880 nm	0.15 (600 K)	-	48
Mn, Eu: ZnS	293-423	394	⁵ D ₀ → ⁷ F ₂ (Eu ³⁺) / Trap states → Ground state (TiO ₂) / 595 / 612 nm	0.034 (353)	-	49
Eu, Tb: DMBDC	10-300	381	⁵ D ₄ → ⁷ F ₅ (Tb ³⁺) / ³ D ₀ → ⁷ F ₂ (Eu ³⁺) 545 / 613nm	-	-	50
Eu: Y ₂ O ₃	323-1273	365	³ D ₀ → ⁷ F ₂ (Eu ³⁺) / ⁵ D ₀ → ⁷ F ₂ (Eu ³⁺) 624 / 631 nm	-	-	51
Dy: YAG	300-1500	355	⁴ I _{15/2} → ⁶ H _{15/2} (Dy ³⁺) / ⁴ F _{9/2} → ⁶ H _{15/2} (Dy ³⁺) 467 / 497 nm	-	9	52
Dy: YAG	295-1350	355	⁴ I _{15/2} → ⁶ H _{15/2} (Dy ³⁺) / ⁴ F _{9/2} → ⁶ H _{15/2} (Dy ³⁺) 456 / 496 nm	-	2.5	53
Dy: YAG	300-800	355	⁴ I _{15/2} → ⁶ H _{15/2} (Dy ³⁺) / ⁴ F _{9/2} → ⁶ H _{15/2} (Dy ³⁺) 458 / 490 nm	-	0.2%	54
Dy: YSZ	300-900	355	⁴ I _{15/2} → ⁶ H _{15/2} (Dy ³⁺) / ⁴ F _{9/2} → ⁶ H _{15/2} (Dy ³⁺) 458 / 490 nm	-	0.4%	54
Er, Yb: Y ₂ O ₃	202-572	488	² H _{11/2} → ⁴ I _{15/2} (Er ³⁺) / ⁴ S _{3/2} → ⁴ I _{15/2} (Er ³⁺) -	-	-	55
Nd: LaF ₃	303-333	808	⁴ F _{3/2} (R ₂) → ⁴ I _{9/2} (Z ₄)(Nd ³⁺) / ⁴ F _{3/2} (R ₁) → ⁴ I _{9/2} (Z ₄)(Nd ³⁺) 885 / 863 nm	-	2	56
<i>Lanthanide-containing up-conversion systems</i>						
Ho, Yb: Y ₂ O ₃	10-300	978	⁵ F ₄ , ⁵ S ₂ → ⁵ I ₈ (Ho ³⁺) / ⁵ F ₄ , ⁵ S ₂ → ⁵ F ₇ (Ho ³⁺) 536 / 772 nm 536 / 764 nm 536 / 758 nm	9.7 (85 K) 6.5 (84 K) 4.6 (90 K)	-	27
Tm, Yb: Y ₂ O ₃	10-300	978	³ H ₄ → ³ H ₆ (Tm ³⁺) / ¹ D ₂ → ³ F ₄ (Tm ³⁺) 815 / 454 nm 815 / 460 nm	7.8 (270 K) 6.7 (178 K)	-	27
Tm, Yb: Y ₂ O ₃	10-300	978	³ H ₄ → ³ H ₆ (Tm ³⁺) / ¹ G ₄ → ³ H ₆ (Tm ³⁺) 815 / 656 nm	6.4 (290 K)	-	27
Er, Yb: CaF ₂	298-323	920	² H _{11/2} → ⁴ I _{15/2} (Er ³⁺) / ⁴ S _{3/2} → ⁴ I _{15/2} (Er ³⁺) 538 / 552 nm	2.3 (318 K)	-	57
Er, Yb: Gd ₂ O ₃ /Au NPs	300-1050	980	² H _{11/2} → ⁴ I _{15/2} (Er ³⁺) / ⁴ S _{3/2} → ⁴ I _{15/2} (Er ³⁺) 510-565 nm	1.51	1	58
Er, Mn: ZnS	293-318	450	Emission intensity 590 nm	1.2 (423 K)	-	59
Tm, Yb: NaGdF ₄ @Eu, Tb: NaGdF ₄ core-shell nanoparticles	50-300	980	³ D ₄ → ⁷ F ₅ (Tb ³⁺) / ³ D ₀ → ⁷ F ₂ (Eu ³⁺) 545 / 615 nm	1.2	-	60
Er, Yb: PbF ₂	290-325	975	² H _{11/2} → ⁴ I _{15/2} (Er ³⁺) / ⁴ S _{3/2} → ⁴ I _{15/2} (Er ³⁺)	1.1 (310)	-	61

Er,Yb: Fluoride Glass	335-375	975	523 / 548 nm $^2H_{11/2} \rightarrow ^4I_{15/2}$ (Er ³⁺) / $^4S_{3/2} \rightarrow ^4I_{15/2}$ (Er ³⁺)	1.1 (342 K)	0.8	62
Ho, Tm, Yb: Y ₂ O ₃	303-703	980	$^1G_4 \rightarrow ^3H_6$ (Tm ³⁺) / $^3F_3 \rightarrow ^5I_8$ (Ho ³⁺) 477 / 488 nm	0.69 (303 K)	6	26
Er: ZnO	273-573	978	$^2H_{11/2} \rightarrow ^4I_{15/2}$ (Er ³⁺) / $^4S_{3/2} \rightarrow ^4I_{15/2}$ (Er ³⁺) 536 / 553 nm	0.62 (443 K)	-	63
Ho, Yb: K LuW	297-673	980	$^5F_5 \rightarrow ^5I_8$ (Ho ³⁺) / $^5S_2, ^5F_4 \rightarrow ^5I_8$ (Ho ³⁺) 540 / 650 nm	0.54	1	This work
Er: BaTiO ₃	322-466	980	$^4S_{3/2} \rightarrow ^4I_{15/2}$ (Er ³⁺) / $^2H_{11/2} \rightarrow ^4I_{15/2}$ (Er ³⁺) 547 / 526 nm	0.52 (333 K)	-	15
Er, Yb: Al ₂ O ₃	295-973	978	$^4S_{3/2} \rightarrow ^4I_{15/2}$ (Er ³⁺) / $^2H_{11/2} \rightarrow ^4I_{15/2}$ (Er ³⁺) 534 / 549 nm	0.52 (476 K)	0.3	64
Er / Er, Yb: Chalcofenide Glass	293-498	1540 / 1060	$^4S_{3/2} \rightarrow ^4I_{15/2}$ (Er ³⁺) / $^2H_{11/2} \rightarrow ^4I_{15/2}$ (Er ³⁺) 530 / 555 nm	1.02 / 0.52	0.3 / 0.5	65
Tm, Yb: LiNbO ₃	323-773	980	$^3F_{2,3} \rightarrow ^3H_6$ (Tm ³⁺) / $^3H_4 \rightarrow ^3H_6$ (Tm ³⁺) 700 / 800 nm	0.52 (773 K)	-	66
Er, Mo: Yb ₃ Al ₅ O ₁₂	395-973	976	$^2H_{11/2} \rightarrow ^4I_{15/2}$ (Er ³⁺) / $^4S_{3/2} \rightarrow ^4I_{15/2}$ (Er ³⁺) 522 / 546 nm	0.48 (467 K)	0.3	19
Er, Yb: Fluoride Glass	296-448	1480	$^2H_{11/2} \rightarrow ^4I_{15/2}$ (Er ³⁺) / $^4S_{3/2} \rightarrow ^4I_{15/2}$ (Er ³⁺) 522 / 543 nm	0.4	1	67
Er, Yb: Gd ₂ O ₃	300-900	980	$^2H_{11/2} \rightarrow ^4I_{15/2}$ (Er ³⁺) / $^4S_{3/2} \rightarrow ^4I_{15/2}$ (Er ³⁺) 523 / 548 nm	0.39 (300 K)	-	16
Ho, Yb: K LuW	297-673	980	5F_5 sub-Stark energy levels of Ho³⁺ 650/660 nm	0.385 (297)	1	This work
Tm, Yb: Y ₂ O ₃	303-753	976	$^1G_{4(0)} \rightarrow ^3H_6$ (Tm ³⁺) / $^1G_{4(0)} \rightarrow ^3H_6$ (Tm ³⁺) 476 / 488 nm	0.35 (303 K)	-	68
Er, Yb: Silica Glass	296-723	978	$^2H_{11/2} \rightarrow ^4I_{15/2}$ (Er ³⁺) / $^4S_{3/2} \rightarrow ^4I_{15/2}$ (Er ³⁺) 526 / 549 nm'	0.33 (296 K)	0.2	69
Ho, Yb, Zn: Y ₂ O ₃	299-673	980	$^3K_8 \rightarrow ^5I_8$ (Ho ³⁺) / $^2F_3 \rightarrow ^5I_8$ (Ho ³⁺) 465 / 491 nm	0.3 (673)	-	23
Er, Yb, Li: ZrO ₂	323-673	976	$^4F_{9/2} \rightarrow ^4I_{15/2}$ (Er ³⁺) / $^4F_{9/2} \rightarrow ^4I_{15/2}$ (Er ³⁺) 646 / 678 nm	0.22 (110 K)	-	70
Er, Yb: NaYF ₄	299-336	920	$^2H_{11/2} \rightarrow ^4I_{15/2}$ (Er ³⁺) / $^4S_{3/2} \rightarrow ^4I_{15/2}$ (Er ³⁺) 525 / 545 nm	0.21	-	11
Tm, Yb: CaF ₂	298-323	920	$^3H_4 \rightarrow ^3H_6$ (Tm ³⁺) / $^3H_4 \rightarrow ^3H_6$ (Tm ³⁺) 790 / 800 nm	0.2 (315 K)	-	57
Er: SiO ₂	295-873	800	-	0.1	1.3	71
Er, Yb: Gd ₂ O ₃ nanorwires	293-600	978	$^2H_{11/2} \rightarrow ^4I_{15/2}$ (Er ³⁺) / $^4S_{3/2} \rightarrow ^4I_{15/2}$ (Er ³⁺) -	-	-	72
Er, Yb: NaYF ₄	293-333	980	$^4S_{3/2} \rightarrow ^4I_{15/2}$ (Er ³⁺) / $^2H_{11/2} \rightarrow ^4I_{15/2}$ (Er ³⁺) 541 / 523 nm	-	3.4	18
Er, Yb: NaYF ₄	293-333	980	$^4F_{9/2} \rightarrow ^4I_{15/2}$ (Er ³⁺) / $^4S_{3/2} \rightarrow ^4I_{15/2}$ (Er ³⁺) 656 / 541 nm	-	2.1	18
Er, Yb: NaYF ₄	291-306	980	$^2H_{11/2}, ^4S_{3/2} \rightarrow ^4I_{15/2}$ (Er ³⁺) / $^4F_{9/2} \rightarrow ^4I_{15/2}$ (Er ³⁺) 520-540 / 630-660 nm	-	-	17
Er, Yb: NaYF ₄	10-295	980	$^2H_{11/2} \rightarrow ^4I_{15/2}$ (Er ³⁺) / $^4S_{3/2} \rightarrow ^4I_{15/2}$ (Er ³⁺) -	-	-	73

Er,Yb:Na YF ₄ @ NaYF ₄	293-333	980	523 / 548 nm ⁴ S _{3/2} → ⁴ I _{15/2} (Er ³⁺) / ² H _{11/2} → ⁴ I _{15/2} (Er ³⁺) 541 / 523 nm	-	0.45	18
Ho,Yb:Na YF ₄	293-333	980	² F ₅ → ² I ₈ (Ho ³⁺) / ³ S ₂ → ³ I ₈ (Ho ³⁺) 656 / 541 nm	-	7.3	18
Tm,Yb:Na YF ₄	293-333	980	³ F ₃ → ³ H ₆ (Tm ³⁺) / ¹ G ₄ → ³ H ₆ (Tm ³⁺) 695 / 475 nm	-	>20.0	18
<i>Quantum dot systems</i>						
ZnMnSe / ZnCdSe NPs	293-373	380	Excitonic intensity ratio	1.3 (318 K)	0.2	74
CdSe/ZnS / CdTe/ZnS	287-320	470	CdSe/ZnS / CdTe/ZnS -	0.9 (320 K)	0.3	75
CdSe Nanocryst als / CdS Nanor ods with Alexa-647 dye	293-298	400	CdSe-CdS / Alexa-647 630-640 / 664-674 nm	0.66	-	76
<i>Organic dyes-containing systems</i>						
Fluorescei n D / Texas Red-A in DNA	278-318	495	Fluorescein / Texas Red 518 / 610 nm	4.5 (295 K)	-	77
Rhodamin e B / Rhodamin e 110	20-50	1064	Rhodamine B / Rhodamine 110 -	1.3	-	78
Rhodamin e B in SU8	293-353	Mercury lamp	SU8 / Rhodamine-B -	1.3 (338 K)	0.1	79
Di-4- ANEPPD HQ dye	293-310	473	530 / 570 nm	0.5 (N.A.)	-	80
PFBT polymer dots / Rhodamin e B	283-343	450	Rodhamine B / PFBT polymer dot 573 / 510 nm	0.23	-	81
<i>Othersystems</i>						
PNIPAM containing 3HF-AM	293-325	355	ESIPT / ECIST 436-423 / 508-538 nm	6.7 (314 K)	-	82
PtOEP	290-320	380	Emission of triplet T(0,0) level 540 / 650 nm	4.6 (305 K)	-	83
Pyrene- labeled poly(DEG MA-stat- PyMMA)	278-303	342	Excimer / Monomer 467 / 395	3.5 (294 K)	-	84
C ₇₀ in PtBMA	293-363	420	C70 / perylene 470 / 700 nm	1.8 (330 K)	-	85
1,3-Bis(1- pyrenyl)pr opane in [C ₄ mpy][Tf ₂ N]	303-413	325	Excimer/ Monomer 376/476 nm	1.4 (355 K)	0.16	86
Perylene / N-allyl-N- methylanil ine in PS	327-357	386	Exciplex / Monomer 475/543 nm	1.3 (350 K)	2	87
GFP	293-333	473	Polarization anisotropy	0.5 (333 K)	0.4	88
[Pt ^{II} (Br- thq)(acac)] / PtTFPP	278-323	405	PtTFPP / [Pt ^{II} (Br- thq)(acac)] Red / Blue	-	4.3	89

In a first sight to the table, we can see that the maximum thermal sensitivities were obtained for Eu-doped systems (in the form of complexes⁴¹ or combined with other luminescent systems^{42,43})

or for up-conversion lanthanide-doped materials working at temperatures below room temperature.²⁷ Other systems showing high sensitivities are luminescent polymer systems, like PNIPAM, but working in a very narrow temperature ranges.⁸² It is also evident in Table 1 that in several cases, the thermal sensitivity of a particular system was not provided, and those especially correspond to pioneer works in this field. This is why, despite this thermal sensitivity is not provided in the publication, we decided to include the rest of the data available to pay tribute to those that opened this field of research.

If we consider the systems listed in the table for which the ratiometric technique used is based on emissions exclusively lying in the red region of the electromagnetic spectrum, we can see that the sensitivity of the Ho,Yb:KLuW nanoparticles we report in this paper compared to that of others Ln-doped systems reported in the literature is among the highest in this spectral region, and only when a mixture of CdSe nanocrystals and CdSnanorods with Alexa-647 dye were used as thermometers, the sensitivity was one order of magnitude higher than that we can obtain with our nanoparticles. However, in the latter case, the synthesis procedure was complex, the temperature range explored was very narrow, and it was not indicated at which wavelength the quantum dots/organic dye system was pumped.⁷⁶ Also Eu-doped SiO₂ submicrometric spheres exhibit a higher sensitivity in a shorter temperature range,¹³ but those particles were excited with near ultraviolet light that can damage the luminescent nanoparticles, shortening their operating lifetimes.¹⁴ In the case of Eu:Y₂O₃ nanoparticles,⁵¹ no information about the sensitivity value is given, even though the ratio between the two peaks in the red region looks higher than that obtained in our case. However, again those particles are excited with UV light. Note also, that our Ho,Yb:KLuW nanoparticles show the maximum absolute sensitivity at room temperature, while Er,Yb,Li:ZrO₂ phosphors show the maximum absolute sensitivity at 110 K, obtained through and extrapolation of the data measured.

When compared to other up-conversion systems, here the sensitivity of our nanoparticles show a relatively low sensitivity, since sensitivities up to 6 times higher have been reported for Er-doped systems⁵⁷ (if the systems that have been explored only for temperatures below room temperature are excluded and for which even higher sensitivities have been reported.²⁷ However, most of these systems operated in the green region of the electromagnetic spectrum. Thus, our nanoparticles offer an alternative luminescence range that can be used for thermometric applications when interferences arise in the green range of wavelengths. The versatility of this material offer different strategies to determine temperature using the up-conversion emission spectra. In this context, the ratio of the integrated areas between the red and green bands emitted by the nanoparticles shown in Figure 2 is depicted in Figure 4. The main feature that can be observed in that graph is that this ratio follows a linear dependence with temperature that would simplify the calibration procedure.

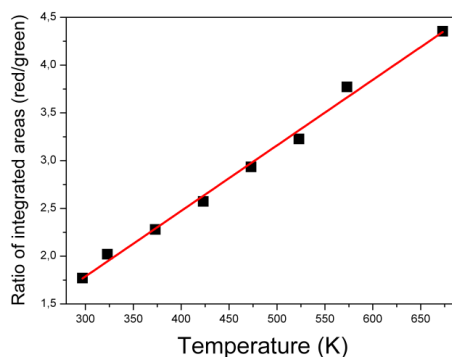


Figure 4. Ratio of integrated areas between the red and green emission bands as the function of temperature for Ho,Yb:KLuW nanoparticles.

Linearity is an outstanding feature for thermal sensing, since it ensures a constant thermal sensitivity in the whole working temperature range of the thermal probe.¹⁰ In this case, we cannot consider that the electronic populations of the excited states follow a Boltzmann-type distribution, since they are located far from each other.³⁸ Thus, we cannot use the FIR technique

in that case. However, since the population of the 5F_5 electronic level of Ho^{3+} is achieved mainly from the nonradiative relaxation from the 5S_2 and 5F_4 levels of the same ion, and this process is temperature dependent, as evidenced by the faster decrease of the intensity of the green band arising from the last electronic levels, in front of the intensity of the red band arising from the former, we can consider that all these levels are electronically coupled. The expression of this electronic coupling is the plot of the thermal evolution of $I_{\text{red}}/I_{\text{green}}$ depicted in Figure 4, and from which a linear dependence, as mentioned before, can be fitted. Then, to facilitate quantitative comparison with other ratiometric luminescence temperature sensors operating by different mechanisms we used the relative sensitivity, calculated taking the first derivative of the intensity ratio between the two emission bands with respect to the temperature divided by its ratio. The relative sensitivity was found to be $5.4 \cdot 10^{-3} \text{ K}^{-1}$, constant all over the range of temperatures analyzed. When compared to other systems for which this red/green or green/red ratio has been used to quantify the thermometric properties, and listed in Table 1, one can see that most of them are based on Tb^{3+} and Eu^{3+} co-doped systems,^{44,45,47} that although show high sensitivities (up to $4.9 \cdot 10^{-2} \text{ K}^{-1}$), are all pumped in the UV. Zheng et al. also reported temperature measurements by determining the intensity ratio of green and red emissions of $\text{Tb,Eu:NaGdF}_4@ \text{Tm,Yb:NaGdF}_4$ core-shell nanoparticles pumped at 980 nm,⁶⁰ which again showed a relative sensitivity one order of magnitude higher ($1.2 \cdot 10^{-2} \text{ K}^{-1}$) than the one reported for our nanoparticles, although in that case the range of temperatures analyzed was below room temperature (50-300 K). The Wolfbeis group also explored the possibility to use the green/red or green/red ratios in up-converting Er,Yb:NaYF_4 and Ho,Yb:NaYF_4 nanoparticles,^{17,18} but they did not report the sensitivity for their measurements.

We have also observed that the up-conversion emission of the Ho,Yb:KLuW nanoparticles shows still another attractive temperature dependent property. As the temperature increases the color perception of the emission arising from the sample changes from yellow to dark orange. The tunability of the color emission as a function of temperature is shown in Figure 5a. At room

temperature the green emission arising from the $^5S_2, ^5F_4 \rightarrow ^5I_8$ transition has a similar intensity than the red emission arising from the $^5F_5 \rightarrow ^5I_8$ transition. Thus, the emission is perceived as yellow. When the temperature rises up to 473 K the emission is perceived as orange, since the red emission dominates over the green emission. Finally, at 673 K the color is perceived as deep orange or red, since the intensity of this band is significantly higher than that of the green emission. Thus, this change of the color perception of the emission arising from the nanoparticles might constitute a new possibility for visual temperature determination, although the thermal resolution would be very wide, of the order of 50 K, if it is intended to be visualized by naked eye. We believe that this thermal resolution might be improved if a colorimeter is used instead, although no measurements have been made in this direction. A similar feature has been reported previously in Tb,Tm:Y₂O₃ particles pumped in the UV, and in which emission evolves from blue to green, with a similar visual thermal resolution.⁹⁰

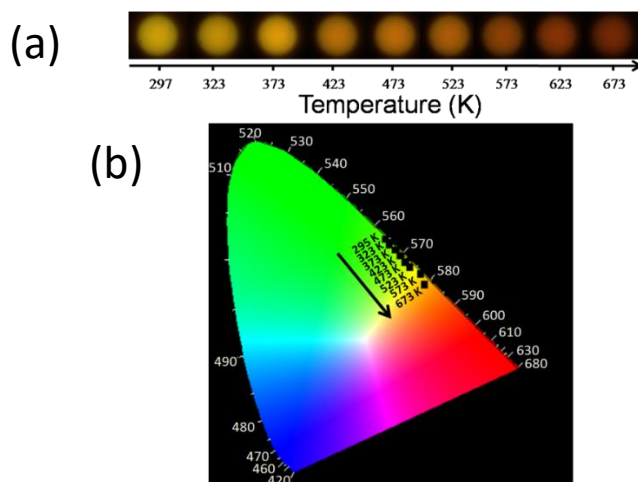


Figure 5. (a) Tunability of the color perception of the emission of the Ho,Yb:KLuW nanoparticles with temperature; (b) Change of the color emission according to the CIE 1931 chromatic diagram.

From the recorded spectra we calculated the CIE 1931 coordinates in the range of temperatures 297 – 673 K (see Figure 5b).⁹¹ The tuning of the CIE coordinates shows a linear dependence with temperature, starting from the border between the green and yellow regions and ending up at the border between the yellow and red regions of the CIE 1931 coordinates diagram.

Finally, we have measured the temperature dependent fluorescence lifetime corresponding to the 540 nm emission line of Ho,Yb:KLuW nanoparticles associated to the 5S_2 , 5F_4 radiative transitions. Figure 6a shows the decay curves recorded in the 296 – 673 K temperature range plot in a log scale. In these curves it is evident the presence of a rising time that denotes the energy transfer process occurring in our system. Also, in all cases we observed a non-single exponential component due to the existence of nonradiative processes, which are responsible for the reduction of the lifetime when the temperature increased, as can be observed in the graph. The temperature dependent normalized lifetimes of Ho,Yb:KLuW nanoparticles, defined as $\tau_{\text{norm}}(T) = \tau(T)/\tau(296)$, for the emission lines centered at 540 and 650 nm are shown in Figure 6b. To calculate τ_{norm} we took only into account the decay part of the luminescent lifetimes. In this way we avoided the rise time inherent in the energy transfer process. Furthermore, if $\tau = \frac{\int I(t) \cdot t \cdot dt}{\int I(t) \cdot dt}$, then by using this integration method, all the non-linear processes in the system occurring at a particular temperature are taken into account. As can be seen in the graph the lifetime decreases almost linearly in both cases, although the slope for the 540 nm is a little bit higher indicating that it will have a higher sensitivity than the red emission. The sensitivity of the temperature dependent fluorescence lifetime is associated to the thermal coefficient, that is defined as the first derivative of the normalized lifetime at a given temperature respect to the temperature. In the case of the emission line centered at 540 nm the thermal coefficient is $2.3 \cdot 10^{-3} \text{K}^{-1}$.

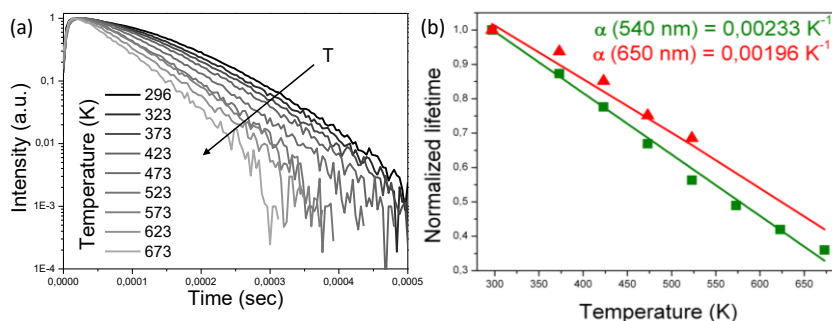


Figure 6. (a) Fluorescence decay curves, and (b) normalized lifetime values as a function of temperature of Ho,Yb:KLuW nanoparticles in the 296 - 673 K temperature range.

Table 2. Luminescent thermal data for different luminescent system used for fluorescence lifetime thermometry.

Material	Temperature range (K)	Excitation wavelength (nm)	Detection wavelength (nm)	Thermal sensitivity (%*K ⁻¹)	Ref.
Nanodiamond	296-298,5	532	650	9 mK/Hz ^{-1/2}	92
Poly(DBD-AE-co-NOPAM)	295,9-311,3	430	590	6	93
Rhodamine B	295-368	840	580	2.7	94
Euhybrid NPs	298-318	400	616	2.2	95
CdTe quantum dots	300-323	405	510	1.7	96
Er:Yb:NaY ₂ F ₅ O NPs	298-333	980	545	1.5	97
Au nanoclusters	287-316	580	710	1.3	98
Tb complexes	295-335	405	545	1.23	47
Ce:YAG NPs	283-350	337	700	1	99
Er:Yb:NaYF ₄ NPs	298-333	980	545	0.5	100
Di-4-ANEPDQH dye	293-310	473	530 and 570	0.5	86
Eu:TiO ₂ NPs	307-533	360	613	0.24	46
Ho:Yb:KLuW	296-673	980	540, 650	0.23, 0.19	This work

Table 2 compares the thermal sensitivity obtained in different luminescent systems used in nanothermometry by measuring luminescence lifetimes. The majority of the systems listed show a higher thermal sensitivity than the nanoparticles reported here, but in all these cases, with the exception of Rhodamine B, Er:Yb:NaY₂F₅O, and Er:Yb:NaYF₄ nanoparticles, they are pumped

with shorter wavelengths than the emission line measured. Some of these systems are pumped in UV, like Ce:YAG nanocrystals,⁹⁹ Eu hybrid nanoparticles,⁹⁵ and Eu:TiO₂ nanoparticles,⁴⁶ which would limit the potential applications of these luminescent nanothermometers for instance in biological applications, since the autofluorescence generated by the biological tissue when illuminated with UV light, might difficult the detection of the signal arising from the nanothermometer. Furthermore, UV pumping might also affect to the operational durability of the materials, especially in the case of organic dyes and polymers.

In other cases, the evolution of lifetime with temperature does not follow a linear tendency,⁴⁷ which makes the calibration procedures more complex, or the range of temperatures that can be measured by the system is very limited, as it happens with luminescent polymers⁹³ or nanodiamonds.⁹² Other systems, like quantum dots, display remarkable temperature-dependent spectral shifts, and the thermal sensitivity changes with their sizes.⁹⁶ Still other luminescent thermometers, like the Di-4-ANEPPDHQ dye,⁸⁰ or Au nanoclusters,⁹⁸ requires time-correlated single photon counters for the temperature measurements, incrementing in this way the complexity of the measurement set-up.

When compared with the three other up-converting systems used also for luminescence thermometry using lifetime measurements, we can conclude that the thermal sensitivity of Ho,Yb:KLuW nanoparticles is similar to that reported for Er,Yb:NaYF₄ nanoparticles,⁹⁷ although smaller than that of Er,Yb:NaY₂F₅O nanoparticles⁹⁷ and Rhodamine B.⁹⁴ However, in this last case, the very likely existence of toxic effects has been reported this system,⁹⁴ which again limits the potential applications of this luminescent system.

Despite that exist other systems that show a higher thermal sensitivity by using lifetime measurements as a luminescent thermometric technique, in the case of Ho,Yb:KLuW nanoparticles we explored the widest temperature range in which a linear evolution has been observed. This implies a constant thermal sensitivity over all this range of temperatures,

simplifying the calibration procedures, and allowing those particles to be used in a wide range of applications without introducing any change in the measurement procedures.

4. Conclusions

In summary, we analyzed the temperature dependence of the up-conversion emission of Ho,Yb:KLuW nanocrystals under excitation at 980 nm using different luminescence thermometry techniques. The FIR of the two thermally coupled Stark sublevels of the 5F_5 manifold, with emissions at 650 and 660 nm, shows a great potentiality. The absolute sensitivity determined in that case is among the highest of the previously reported in the literature for systems with emission in the red region of the electromagnetic spectrum. Another luminescence thermometry technique based on the ratio between the intensity of the red and green bands, electronically coupled, shows a linear dependence with temperature, which ensures a constant thermal sensitivity over the whole working temperature range of the nanoparticles, simplifying then the calibration procedure. We also demonstrated that the temperature dependent fluorescence lifetime of Ho,Yb:KLuW nanoparticles can be used for temperature determination with a thermal coefficient similar to that of the Er,Yb:NaYF₄ nanoparticles, the most efficient up-conversion system reported up to now. Thus, we demonstrated that we can use a single material to determine temperature by different luminescence thermometry techniques, and although the thermal operation range is the same in all cases, it provides a tool to corroborate the temperature measurements by different techniques. In fact, while the FIR method shows the highest sensitivity at room temperature, the intensity ratio technique comparing the green and red emission intensities and the lifetime technique show a constant thermal sensitivity over the thermal range tested, which would allow having more precise measurements at high temperatures. Finally, we have also shown that Ho,Yb:KLuW nanoparticles have the ability to change the color perception of the emitted light by the influence of temperature. Thus,

visualization of temperature changes can be done just by observing the evolution of the color of the emitted light under NIR 980 nm excitation. Briefly, Ho,Yb:KLuW nanoparticles are proved to be a versatile material for multiple thermal sensing purposes.

For future and real applications of these nanoparticles as nanothermometers, that might comprise monitoring temperature in chemical reactors and microfluidic systems, or the detection of “hot spots” in microelectronic devices and local temperatures within integrated photonic devices according to the range of temperatures analyzed, their degree of agglomeration needs to be addressed by functionalizing chemically their surfaces to prevent it. Furthermore, if the synthesis process is optimized to reduce the size and size dispersion of these nanoparticles, and if the appropriate chemical moieties are chosen to make them water dispersible, they might also be used with biological purposes.

Acknowledgment

This work was supported by the Spanish Government under projects No. MAT2011-29255-C02-02 and MAT2013-47395-C4-4-R, the Catalan Government under project No. 2014SGR1358. O.A. Savchuk is supported by Catalan Government through the fellowship 2015FI_B2 00136. F.D. acknowledges additional support through the ICREA Academia Award for Excellence in Research.

References

- (1) Brites, C. D. S.; Lima, P. P.; Silva, N. J. O.; Millan, A.; Amaral, V. S; Palacio, F.; and Carlos, L. D. Thermometry at the Nanoscale. *Nanoscale* **2012**, *4*, 4799-4829.
- (2) Geddes, C. D.; Lakowicz, J. R. *Reviews in Fluorescence 2004*; Kluwer Academic/Plenum Publishers: New York, 2004.

- (3) Khalid, A. H.; Kontis, K. Thermographic Phosphors for High Temperature Measurements: Principles, Current State of the Art and Recent Applications. *Sensors* **2008**, *8*, 5673-5744.
- (4) Childs, P. R. N.; Greenwood, J. R.; Long, C. A. Review of Temperature Measurement. *Rev. Sci. Instrum.* **2000**, *71*, 2959-2978.
- (5) Baffou, G.; Bon, P.; Savatier, J.; Polleux, J.; Zhu, M.; Merlin, M.; Rigneult, H.; Monneret, S. Thermal Imaging of Nanostructures by Quantitative Optical Phase Analysis. *ACS Nano* **2012**, *6*, 2452-2458.
- (6) Christofferson, J.; Shakouri, A. Thermorefectance Based Thermal Microscope. *Rev. Sci. Instrum.* **2005**, *76*, 024903.
- (7) Beechem, T.; Graham, S.; Kearney, S. P.; Phinney, L. M.; Serrano, J. R. Simultaneous Mapping of Temperature and Stress in Microdevices using Micro-Raman Spectroscopy. *Rev. Sci. Instrum.* **2007**, *78*, 061301.
- (8) Kuball, M.; Hayes, J. M.; Uren, M. J.; Martin, T.; Birneck, J. C. H.; Balmer, R. S.; Hughes, B. T. Measurement of Temperature in Active High-Power AlGaIn/GaN HFETs Using Raman Spectroscopy. *IEEE Electron Device Lett.* **2002**, *23*, 7-9.
- (9) Chenais, S.; Forget, S.; Druon, F.; Balembois, F.; Georges, P. Direct and Absolute Temperature Mapping and Heat Transfer Measurements in Diode-End-Pumped Yb:YAG. *Appl. Phys. B* **2004**, *79*, 221-224.
- (10) Jaque, D.; Vetrone, F. Luminescence Nanothermometry. *Nanoscale* **2012**, *4*, 4301-4326.
- (11) Vetrone, F.; Naccache, R.; Zamarron, A.; de la Fuente, A. J.; Sanz-Rodriguez, F.; Maestro, L. M.; Rodriguez, E. M.; Jaque, D.; Sole, J. G.; Capobianco, J. A. Temperature Sensing at the Nanoscale Using Fluorescent Nanothermometers. *ACS Nano* **2010**, *4*, 3254-3258.
- (12) Vetrone, F.; Naccache, R.; de la Fuente, A. J.; Sanz-Rodriguez, F.; Blazquez-Castro, A.; Rodriguez, E. M.; Jaque, D.; Sole, J. G.; Capobianco, J. A. Intracellular Imaging of

- HeLaCellsby Non-Functionalized NaYF₄:Er³⁺,Yb³⁺UpconvertingNanoparticles. *Nanoscale* **2010**, *2*, 495–498.
- (13) Haro-Gonzalez, P.; Maestro, L. M.; Trevisani, M.; Polizzi, S.; Jaque, D.; Sole, J. G.; Bettinelli, M. Evolution of Rare Earth Doped Silica Sub-Micrometric Spheres as Optically Controlled Temperature Sensors. *J. Appl. Phys.* **2012**, *112*, 054702.
- (14) Rapaport, A.; Milliez, J.; Cassanho, A.;Jensen, H. J. Review of the Properties of Up-Conversion Phosphors for New Emissive Display. *J. Displ. Technol.* **2006**, *2*, 68-78.
- (15) Alencar, M. A. R.; Maciel, G. S.; de Araújo, C. B.; Patra, A. Er³⁺-Doped BaTiO₃Nanocrystals for Thermometry: Influence of Nanoenviroment on the Sensitivity of a Fluorescence Based Temperature Sensor. *Appl. Phys. Lett.* **2004**, *84*, 4753-4755.
- (16) Singh, S. K.; Kumar, K.; Rai, S. B. Er³⁺/Yb³⁺Codoped Gd₂O₃ Nano-Phosphor for Optical Thermometry. *Sens. Actuators A* **2009**, *149*, 16-20.
- (17) Fischer, L. H.; Harms, G. S.; Wolfbeis, O. S. Upconverting Nanoparticles for Nanoscale Thermometry. *Angew. Chem. Int. Ed. Engl.* **2011**, *50*, 4546-4551.
- (18) Sedlmeier, A.; Achatz, D. E.; Fischer, L. H.; Gorris, H. H.; Wolfbeis, O. S. Photon Upconverting Nanoparticles for Luminescent Sensing of Temperature. *Nanoscale* **2012**, *4*, 7090-7096.
- (19) Dong, B.; Cao, B.; He, Y.; Liu, Z.; Li, Z.; Feng, Z. Temperature Sensing and In Vivo Imaging by Molybdenum Sensitized Visible Upconversion Luminescence of Rare-Earth Oxides. *Adv. Mater.* **2012**, *24*, 1987-1993.
- (20) MacLaurin, E. J.; Bradshaw, L. R.; Gamelin, D. R. Dual-Emitting Nanoscale Temperature Sensors. *Chem. Mater.* **2013**, *25*, 1283-1292.
- (21) Bebasu, M. L.; Ananias, D.; Pastoriza-Santos, I.; Liz-Marzán, L. M.; Rocha, J.; Carlos, L. D. All-in-One Optical Heater-Thermometer Nanoplatform Operative from 300 to 2000 K Based on Er³⁺ emission and blackbody radiation. *Adv. Mater.* **2013**, *25*, 4868-4874.

- (22) Singh, A. K. Ho³⁺:TeO₂ Glass, a Probe for Temperature Measurements. *Sens.Actuat. A* **2007**, *136*, 173-177.
- (23) Pandey, A.; Rai, V. K. Improved Luminescence and Temperature Sensing Performance of Ho³⁺, Yb³⁺, Zn²⁺:Y₂O₃ Phosphor. *Dalton Trans.* **2013**, *42*, 11005-11011.
- (24) Verma, R. K.; Rai, S. B. Laser Induced Optical Heating from Yb³⁺/Ho³⁺:Ca₁₂Al₁₄O₃₃ and its Applicability as the Thermal Probe. *J. Quant. Spectrosc. Ra.* **2012**, *113*, 1594-1600.
- (25) Xu, W.; Zhao, H.; Li, Y.; Zheng, L.; Zhang, Z.; Cao, W. Optical Temperature Sensing Through the Upconversion Luminescence from Ho³⁺/Yb³⁺ Codoped CaWO₄. *Sens.Actuat. B* **2013**, *188*, 1096-1100.
- (26) Pandey, A.; Rai, V. K. Optical Thermometry Using FIR of Two Close Lying Levels of Different Ions in Y₂O₃:Ho³⁺, Tm³⁺, Yb³⁺ Phosphor. *Appl. Phys B* **2013**, *113*, 221-225.
- (27) Lojpur, V.; Nikolic, M.; Mancic, L.; Milosevic, O.; Dramicanin, M. D. Y₂O₃:Yb, Tm and Y₂O₃:Yb, Ho Powders for Low Temperature Thermometry Based on the Up-Conversion Fluorescence. *Ceram. Int.* **2013**, *39*, 1129-1134.
- (28) Jambunathan, V.; Mateos, X.; Pujol, M. C.; Carvajal, J. J.; Diaz, F.; Aguilo, M.; Griebner, U.; Petrov, V. CW Lasing of Ho in KLu(WO₄)₂ In-Band Pumped by a Diode Pumped Tm:KLu(WO₄)₂ Laser. *Opt. Express* **2010**, *18*(20), 20793-20798.
- (29) Jambunathan, V.; Mateos, X.; Pujol, M. C.; Carvajal, J. J.; Zaldo, C.; Griebner, U.; Petrov, V.; Aguilo, M.; Diaz, F. Crystal Growth, Optical Spectroscopy and Continuous-Wave Laser Operation of Ho:KLu(WO₄)₂ Crystals. *Appl. Phys. B* **2014**, *116*, 455-466.
- (30) Jambunathan, V.; Mateos, X.; Pujol, M. C.; Carvajal, J. J.; Aguilo, M.; Diaz, F. Growth and Spectroscopy of (Ho, Yb):KLu(WO₄)₂ Crystals. *Phys. Proc.* **2010**, *8*, 162-167.
- (31) Petrov, V.; Pujol, M. C.; Mateos, X.; Silvestre, O.; Rivier, S.; Aguilo, M.; Sole, R. M.; Lin, J.; Griebner, U.; Diaz, F. Growth and Properties of KLu(WO₄)₂, and Novel Ytterbium and Thulium Lasers Based on This Monoclinic Crystalline Host. *Laser and Photon. Rev.* **2007**, *1*, 179-212.

- (32) Bolaños, W.; Carvajal, J. J.; Mateos, X.; Aguiló, M.; Díaz, F. Exploring Waveguiding Properties of Heavily Doped Yb^{3+} : $\text{KLu}(\text{WO}_4)_2$ Epitaxial Layers. *IEEE Photonics Journal* **2010**, *2*, 482-489.
- (33) Pechini M.P. Method of Preparing Lead and Alkaline Earth Titanates and Niobates and Coating Methods Using the Same to Form a Capacitor; US Patent No.3.330.697, 1967.
- (34) Galceran, M.; Pujol, M. C.; Aguiló, M.; Díaz, F. Sol-Gel Modified Pechini Method for Obtaining Nanocrystalline $\text{KRE}(\text{WO}_4)_2$ ($\text{RE} = \text{Gd}$ and Yb). *J. Sol-Gel Sci. Techn.* **2007**, *42*, 79-88.
- (35) Cullity, B. D. *Element of X-ray Diffraction*; Addison-Wesley: New York, 1978.
- (36) Van der Ziel, J. P.; Ostermayer, F. W.; Van Uitert, L. G.; Infrared Excitation of the Visible Luminescence in $\text{Y}_{1-x}\text{Er}_x\text{F}_3$ Via Resonant Energy Transfer. *Phys. Rev. B* **1970**, *2(11)*, 4432-4441.
- (37) Yu, W.; Xu, W.; Song, H.; Zhang, S. Temperature Dependent Upconversion Luminescence and Dynamics of $\text{NaYF}_4:\text{Yb}^{3+}/\text{Er}^{3+}$ Nanocrystals: Influence of Particle Size and Crystalline Phase. *Dalton Trans.* **2014**, *43*, 6139-6147.
- (38) Wade, S. A.; Collins, S. F.; Baxter, G. W. The Fluorescence Intensity Ratio Technique for Optical Fiber Point Temperature Sensing. *J. Appl. Phys.* **2003**, *94*, 4743-4756.
- (39) Wade, S.A. Temperature Measurement Using Rare Earth Doped Fiber Fluorescence. Ph.D. thesis, Victoria University, Melbourne, Australia, 1999.
- (40) Baxter, G. W.; Maurice, E.; Monnom, G. Thermal Variation of Absorption in Yb^{3+} -Doped Silica Fiber for High-Temperature Sensor Applications. *Proc. SPIE* **1995**, *2510*, 293-296.
- (41) Seaver, M.; Peele, P. R. Noncontact Fluorescence Thermometry of Acoustically Levitated Waterdrops. *Appl. Opt.* **1990**, *29*, 4956-4961.

- (42) Wang, X. D.; Song, X. H.; He, C. Y.; Yang, C. J.; Chen, G. N.; Chen, X. Preparation of Reversible Colorimetric Temperature Nanosensors and Their Application in Quantitative Two-Dimensional Thermo-Imaging. *Anal. Chem.* **2011**, *83*, 2434-2437.
- (43) Peng, H. S.; Huang, S. H.; Wolfbeis, O. S. Ratiometric Fluorescent Nanoparticles for Sensing Temperature. *J. Nanopart. Res.* **2010**, *12*, 2729-2733.
- (44) Brites, C. D. S.; Lima, P. P.; Silva, N. J. O.; Millán, A.; Amaral, V. S.; Palacio, F.; Carlos, L. D. A Luminescent Molecular Thermometer for Long-Term Absolute Temperature Measurements at the Nanoscale. *Adv. Mater.* **2010**, *22*, 4499-4504.
- (45) Brites, C. D. S.; Lima, P. P.; Silva, N. J. O.; Millán, A.; Amaral, V. S.; Palacio, F.; Carlos, L. D. A Luminescent Molecular Thermometer for Long-Term Absolute Temperature Measurements at the Nanoscale. *Adv. Mater.* **2010**, *22*, 4499-4504.
- (46) Nikolic, M. G.; Antic, Z.; Culubrk, S.; Nedeljkovic, J. M.; Dramicanin, M. D. Temperature Sensing with Eu³⁺ Doped TiO₂ Nanoparticles. *Sens. Actuators B* **2014**, *201*, 46-50.
- (47) Yu, J. B.; Sun, L. N.; Peng, H. S.; Stich, M. I. J. Luminescent Terbium and Europium Probes for Lifetime Based Sensing of Temperature Between 0 and 70 °C. *J. Mater. Chem.* **2010**, *20*, 6975-6981.
- (48) Haro-González, P.; Martín, IR.; Martín, L. L.; León-Luis, S. F.; Pérez-Rodríguez, C.; Lavín, V. Characterization of Er³⁺ and Nd³⁺ Doped Strontium Barium Niobate Glass Ceramic as Temperature Sensors. *Opt. Mater.* **2011**, *33*, 742-745.
- (49) Wang, S.; Westcott, S.; Chen, W. Nanoparticle Luminescence Thermometry. *J. Phys. Chem. B* **2002**, *106*, 11203-11209.
- (50) Cui, Y.; Xu, H.; Yue, Y.; Guo, Z.; Yu, Y.; Chen, Z.; Gao, J.; Yang, Y.; Qian, G.; Chen, B. A Luminescent Mixed-Lanthanide Metal-Organic Framework Thermometer. *J. Am. Chem. Soc.* **2012**, *134*, 3979-3982.

- (51) Ishiwada, N.; Ueda, T.; Yokomori, T. Characteristics of Rare Earth (RE = Eu, Tb, Tm)-Doped Y_2O_3 Phosphor for Thermometry. *Lumin.* **2011**, *26*, 381-389.
- (52) Goss, L. P.; Smith, A. A.; Post, M. E. Surface Thermometry by Laser-Induced Fluorescence. *Rev. Sci. Instrum.* **1989**, *60*, 3702-3706.
- (53) Kontis, K.; Syogenji, Y.; Yoshikawa, N. Surface Thermometry by Laser-Induced Fluorescence of Dy^{3+} : YAG. *N. Aeronaut. J.* **2002**, *106*, 453-457.
- (54) Heyes, A. L.; Seefeldt, S.; Feist, J. P. Two-Colour Phosphor Thermometry for Surface Temperature Measurement. *Opt. Laser Technol.* **2006**, *38*, 257-265.
- (55) Bai, X.; Song, H.; Pan, G.; Lei, Y.; Wang, T., Rn, X.; Lu, S.; Dong, B.; Dai, Q.; Fan, L. Size-Dependent Upconversion Luminescence in Er^{3+}/Yb^{3+} -Codoped Nanocrystalline Ytria: Saturation and Thermal Effects. *J. Phys Chem.* **2007**, *111*, 13611-13617.
- (56) Rocha, U.; da Silva, C. J.; Ferreira Silva, W.; Guedes, I.; Benayas, A.; Martínez Maestro, L.; Acosta Elias, M.; Bovero, E.; van Veggel, F. C. J. M.; García Solé, J. A.; Jaque, D. Subtissue Thermal Sensing Based on Neodymium-Doped LaF_3 Nanoparticles. *ACS Nano* **2013**, *7*, 1188-1199.
- (57) Dong, N. N.; Pedroni, M.; Piccinelli, F.; Conti, G.; Sbarbati, A.; Ramírez-Hernández, J.E.; Martínez Maestro, L.; Iglesias-de la Cruz, M. C.; Sanz-Rodríguez, F.; Juarranz, A.; Chen, F.; Vetrone, F.; Capobianco, J. A.; García Solé, J.; Bettinelli, M.; Jaque, D.; Speghini, A. NIR-to-NIR Two-Photon Excited $CaF_2: Tm^{3+}, Yb^{3+}$ Nanoparticles: Multifunctional Nanoprobes for Highly Penetrating Fluorescence Bio-Imaging. *ACS Nano* **2011**, *5*, 8665-8671.
- (58) Debasu, M. L.; Ananias, D.; Pastoriza-Santos, I.; Liz-Marzán, L. M.; Rocha, J.; Carlos, L. D. All-in-One Optical Heater-Thermometry Nanoplatform Operative From 300 to 2000 K Based in Er^{3+} Emission and Blackbody Radiation. *Adv. Mater.* **2013**, *25*, 4868-4874.

- (59) Herrera, A. P.; Rodríguez, M.; Torres-Lugo, M.; Rinaldi, C. Multifunctional Magnetite Nanoparticles Coated with Fluorescent Thermo-Responsive Polymeric Shells. *J. Mater. Chem.* **2008**, *18*, 855-858.
- (60) Zheng, S.; Chen, W.; Tan, D.; Zhou, J.; Guo, Q.; Jiang, W.; Xu, C.; Liu, X.; Qiu, J. Lanthanide-Doped NaGdF₄ Core-Shell Nanoparticles for Non-Contact Self-Referencing Temperature Sensors. *Nanoscale*, **2014**, *6*, 5675-5679.
- (61) Aigouy, L.; Saidi, E.; Lalouat, L.; Labeguerie-Egea, J.; Mortier, M.; Low, P.; Bergaud, C. AC Thermal Imaging of a Microwire with a Fluorescent Nanocrystal: Influence of the Near Field on the Thermal Contrast. *J. Appl. Phys.* **2009**, *106*, 074301.
- (62) Saïdi, E.; Samson, B.; Aigouy, L.; Volz, S.; Low, P.; Bergaud, C.; Mortier, M. Scanning Thermal Imaging by Near-Field Fluorescence Spectroscopy. *Nanotechnology* **2009**, *20*, 115703.
- (63) Wang, X.; Kong, X. G.; Yu, Y.; Sun, Y. J.; Zhang, H. Effect of Annealing on Upconversion Luminescence of ZnO:Er³⁺ Nanocrystals and High Thermal Sensitivity. *J. Phys. Chem. C* **2007**, *111*, 15119-15124.
- (64) Li, C. R.; Dong, B.; Ming, C. G.; Lei, M. Application to Temperature Sensor Based on Green Up-Conversion of Er³⁺ Doped Silicate Glass. *Sensors* **2007**, *7*, 2652-2659.
- (65) dos Santos, P.V.; de Araujo, M.T.; Gouveia-Neto, A.S.; Medeiros Neto, J.A.; Sombra, S.B. Optical Thermometry Through Infrared Excited Upconversion Fluorescence Emission in Er³⁺ and Er³⁺-Yb³⁺-doped Chalcogenide Glasses. *IEEE J. Quantum Electron.* **1999**, *35*, 395-399.
- (66) Xing, L.; Xu, Y.; Wang, R.; Xu, W.; Zhang, Z. Highly Sensitive Optical Thermometry Based on Upconversion Emissions in Tm³⁺/Yb³⁺ Codoped LiNbO₃ Single Crystal. *Opt. Lett.* **2014**, *39*, 454-457.

- (67) Maciel, G.S.; de S. Menezes, L.; Gomes, A.S.L.; de Araujo, C.B.; Messaddeq, Y.; Florez, A.; Aegerter, M.A. Temperature Sensor Based on Frequency Upconversion in Er³⁺-Doped Fluoroindate Glass. *IEEE Photonic Tech. Lett.* **1995**, *7*, 1474-1476.
- (68) Liu, D.; Wang, Y.; Zhang, X.; Yang, K.; Liu, L.; Song, Y. Optical Thermometry Through Green and Red Upconversion Emission in Er³⁺/Yb³⁺Li⁺:ZrO₂. *Opt. Comm.* **2012**, *285*, 1925-1928.
- (69) Li, C. R.; Dong, B.; Li, S. F.; Song, C. Er³⁺-Yb³⁺ Co-Doped Silicate Glass for Optical Temperature Sensor. *Chem. Phys. Lett.* **2007**, *443*, 426-429.
- (70) Liu, L.; Wang, Y.; Zhang, X.; Yang, K.; Bai, Y.; Huang, C.; Song, Y. Optical Thermometry Through Green and Red Upconversion Emission in Er³⁺/Yb³⁺Li⁺:ZrO₂. *Opt. Commun.* **2011**, *284*, 1876-1879.
- (71) Maurice, E.; Monnom, G.; Dussardier, B.; Saissy, A.; Ostrowsky, D.B.; Baxter, G.W. Erbium-Doped Silica Fibres for Intrinsic Fibre-Optic Temperature Sensors. *Appl. Opt.* **1995**, *34*, 8019-8025.
- (72) Lei, Y.; Song, H.; Yang, L.; Yu, L.; Liu, Z.; Pan, G.; Bai, X.; Fan, L. Upconversion Luminescence, Intensity Saturation Effect, and Thermal Effect in Gd₂O₃:Er³⁺,Yb³⁺ Nanowires. *J. Chem. Phys.* **2005**, *123*, 174710.
- (73) Wu, K.; Cui, J.; Kong, X.; Wang, Y. Temperature Dependent Upconversion of Er/YbCodoped NaYF₄ Nanocrystals. *J. Appl. Phys.* **2011**, *110*, 053510.
- (74) Vlaskin, V. A.; Janssen, N.; van Rijssel, J.; Beaulac, R.; Gamelin, D. R. Tunable Dual Emission in Doped Semiconductor Nanocrystals. *Nano Lett.* **2010**, *10*, 3670-3674.
- (75) Jorge, P. A. S.; Martins, M. A.; Trindade, T.; Santos, J. L.; Farahi, F. Optical Fiber Sensing Using Quantum Dots. *Sensors* **2007**, *7*, 3489-3534.
- (76) Albers, A. E.; Chan, E. M.; McBride, P. M.; Ajo-Franklin, C. M.; Cohen, B. E.; Helms, B. A. Dual-Emitting Quantum Dot/Quantum Rod-Based Nanothermometers with

- Enhanced Response and Sensitivity in Live Cells. *J. Am. Chem. Soc.* **2012**, *134*, 9565-9568.
- (77) Barilero, T.; Le Saux, T.; Gosse, C.; Jullien, L. Fluorescent Thermometers for Dual-Emission Wavelength Measurements: Molecular Engineering and Application to Thermal Imaging in a Microsystem. *Anal. Chem.* **2009**, *81*, 7988-8000.
- (78) Petermann, E. J. G.; Gittes, G.; Schmidt, C. F. Laser-Induced Heating in Optical Traps. *Biophys. J.* **2003**, *84*, 1308-1316.
- (79) Jung, W.; Kim, Y. W.; Yim, D.; Yoo, J. Y. Microscale Surface Thermometry Using SU8/Rhodamine-B Thin Layer. *Sens. Actuators A* **2011**, *171*, 228-232.
- (80) Owen, D. M.; Lanigan, P. M. P.; Dunsby, C.; Munro, I.; Grant, D.; Neil, M. A. A.; French, P. M. W.; Magee, A. I. Fluorescence Lifetime Imaging Provides Enhanced Contrast when Imaging the Phase-Sensitive Dye di-4-ANEPPDHQ in Model Membranes and Live Cells. *Biophys. J.* **2006**, *90*, 80-82.
- (81) Ye, F.; Wu, C.; Jin, Y.; Chan, Y.H.; Zhang, X.; Chiu, D. T. Ratiometric Temperature Sensing with Semiconducting Polymer Dots. *J. Am. Chem. Soc.* **2011**, *133*, 8146-8149.
- (82) Chen, C. T.; Chen, C. Y. A PNIPAM-Based Fluorescent Nanothermometer with Ratiometric Readout. *Chem. Commun.* **2011**, *47*, 994-996.
- (83) Lupton, J. M. A Molecular Thermometer Based on Long-Lived Emission From Platinum OctaethylPorphyrin. *Appl. Phys. Lett.* **2002**, *81*, 2478-2480.
- (84) Pietsch, C.; Vollrath, A.; Hoogenboom, R.; Schubert, U. S. A Fluorescent Thermometer Based on a Pyrene-Labeled Thermoresponsive Polymer. *Sensor* **2010**, *10*, 7979-7990.
- (85) Baleizao, C.; Nagl, S.; Borisov, S. M.; Schaferling, M.; Wolfbeis, O. S.; Berberan-Santos, M. N. An Optical Thermometer Based on the Delayed Fluorescence of C₇₀. *Chem. Eur. J.* **2007**, *13*, 3643-3651.

- (86) Baker, G. A.; Baker, S. N.; McCleskey, T. M. Noncontact Two-Color Luminescence Thermometry Based on Intramolecular Luminophore Cyclization Within an Ionic Liquid. *Chem. Commun.* **2003**, 2932-2933.
- (87) Chandrasekharan, N.; Kelly, L. A. A Dual Fluorescence Temperature Sensor Based on Perylene/Exciplex Interconversion. *J. Am. Chem. Soc.* **2001**, *123*, 9898-9899.
- (88) Donner, J. S.; Thompson, S. A.; Kreuzer, M. P.; Baffou, G.; Quidant, R. Mapping Intracellular Using Green Fluorescent Protein. *Nano Lett.* **2012**, *12*, 2107-2111.
- (89) Fischer, L. H.; Karakus, C.; Meier, R. J.; Risch, N.; Wolfbeis, O. S.; Holder, E.; Schäferling, M. Referenced Dual Pressure- and Temperature-Sensitive Paint for Digital Color Camera Read Out. *Chem. Eur. J.* **2012**, *18*, 15706-15713.
- (90) Ishiwada, N.; Fujioka, S.; Ueda, T.; Yokomori, T. Co-Doped $Y_2O_3:Tb^{3+}/Tm^{3+}$ Multicolor Emitting Phosphor for Thermometry. *Opt. Lett.* **2011**, *36*, 760-762.
- (91) Smith, T.; Guild, J. The CIE Colorimetric Standards and Their Use. *Trans. Opt. Soc.* **1931**, *33*, 73-134.
- (92) Kucsko, G.; Maurer, P. C.; Yao, N. Y.; Kubo, M.; Noh, H. J.; Lo, P. K.; Park, H.; Lukin, M. D. Nanometre-Scale Thermometry in a Living Cell. *Nature*, **2013**, *500*, 54-58
- (93) Graham, E. M.; Iwai, K.; Uchiyama, S.; de Silva, A. P.; Magennis S. W.; Jones, A. C. Quantitative Mapping of Aqueous Microfluidic Temperature with Sub-Degree Resolution Using Fluorescence Lifetime Imaging Microscopy. *Lab Chip*, **2010**, *10*, 1267-1273.
- (94) Benninger, R. K.; Koc, Y.; Hofmann, O.; Requejo-Isidro, J.; Neil, M. A.; French, P. M.; DeMello, A. J. Quantitative 3D Mapping of Fluidic Temperatures within Microchannel Networks Using Fluorescence Lifetime Imaging. *Anal. Chem.*, **2006**, *78*, 2272-2278.
- (95) Peng, H.; Stich, M. I. J.; Yu, J.; Sun, L.; Fischer, L. H.; Wolfbeis, O. S. Luminescent Europium Nanoparticles for Sensing and Imaging of Temperature in the Physiological Range. *Adv. Mater.* **2010**, *22*, 716-719.

- (96) Haro-Gonzalez, P.; Martinez-Maestro, L.; Mart'ın, I. R.; Garcia-Sole, J. Jaque, D. High-Sensitivity Fluorescence Lifetime Thermal Sensing Based on CdTe Quantum Dots. *Small*, **2012**, *8*, 2652–2658.
- (97) Savchuk, O. A.; Haro-Gonzalez, P.; Carvajal, J.J.; Jaque, D.; Massons, J.; Aguiló, M.; Diaz, F. Er:Yb:NaY₂F₅O Up-Converting Nanoparticles for Sub-Tissue Fluorescence Lifetime Thermal Sensing. *Nanoscale* **2014**, *6*, 9727-9733.
- (98) Shang, L.; Stockmar, F.; Azadfar, N.; Nienhaus, G. U. Intracellular Thermometry by Using Fluorescent Gold Nanoclusters. *Angew. Chem. Int. Ed.* **2013**, *52*, 11154 –11157.
- (99) Allison, S. W.; Gillies, G. T.; Rondinone, A. J.; Cates, M. R. Nanoscale Thermometry Via the Fluorescence of YAG:Ce Phosphor Particles: Measurements from 7 to 77 °C. *Nanotechnol.*, **2003**, *14*, 859–863.
- (100) Yi, G.; Lu, H.; Zhao, S.; Ge, Y.; Yang, W.; Chen, D.; Guo, L. H. Synthesis, Characterization, and Biological Application of Size-Controlled Nanocrystalline NaYF₄:Yb,Er Infrared-to-Visible Up-Conversion Phosphors. *Nano Lett.* **2004**, *4*, 2191-2196.

Paper VII

Savchuk, Ol. A.; Carvajal, J. J.; Barrera, E.W.; Pujol, M.; Mateos, C. X.; Solé, R.; Massons, J.; Aguiló, M.; Díaz, F. *(Ho, Tm, Yb):KLuW nanoparticles, an efficient thermometry sensor in the biological range (2013)* Proc. of SPIE 8594, 859406-8

(Ho, Tm, Yb): KLuW nanoparticles, an efficient thermometry sensor in the biological range

O.I.A. Savchuk, J.J. Carvajal*, E.W. Barrera, M.C. Pujol, X. Mateos, R. Solé, J. Massons, M. Aguiló, F. Díaz

Física i cristal·lografia de Materials i Nanomaterials (FiCMA-FiCNA)-EMaS, Universitat Rovira i Virgili (URV), Campus Sescelades, C/Marcel·li Domingo s/n E-43007 Tarragona, Spain

*joanjosep.carvajal@urv.cat; phone (+34)977558628; fax (+34)977559563

ABSTRACT

We studied up-conversion emission of triply doped (Ho,Tm,Yb):KLu(WO₄)₂ (KLuW) nanocrystals at the range of temperature 296-673 K at different excitation wavelengths. The intensity ratio between two emission lines was used for monitoring the temperature. Pumping Yb³⁺ at 980 nm provides a good response at relatively high temperatures, while pumping Tm³⁺ at 802 nm provides an excellent sensitivity in the biological range of temperatures., which make the material also attractive for biological temperature sensors.

Keywords: up-conversion emission, lanthanides, thermometry, nanoparticles.

1. INTRODUCTION

Temperature is one of the fundamental and important parameters for all the processes and phenomena. In many applications, knowledge about temperature plays a substantial role. Accurate temperature measurements with high spatial resolution is a challenging research topic nowadays [1-6]. Advances in nanotechnology demand precise thermometry down to the nanoscale regime, where conventional methods are not able to make measurements. The development of a nanoscale thermometer is not only a matter of size, but also requires materials with novel physical properties.

In this context, the fact that pathological cells are warmer than healthy ones due to their enhanced metabolic activity shows a great possibility for the use of nanoscale thermometers to biological applications.

Various types of luminescent nanoparticles have been developed for their use as a temperature sensors in biomedical applications. Many systems exhibit light emission through usual down-conversion of the excitation wavelength. The main limitation is that light in this range of wavelengths is absorbed by surrounding biological tissues. This leads to background fluorescence and damage of the biological environment. The use of up-conversion nanoparticles, which exhibit efficient visible emission properties through near-infrared excitation can overcome these problems and also provide a dual function of imaging and temperature sensing at the nanoscale. Luminescent nanothermometers are based on the temperature dependence of the fluorescence features (intensity and peak position of the absorption and excitation bands, lifetime, etc.). In this context, the intensity ratio between two different emission lines has attracted much attention [7]. This simple non-contact method is applicable over a wide temperature range (from 10 K to 2000 K) and involves the comparison of intensities of two emission lines in photoluminescent spectrum.

The rare earth elements, divided into the lanthanides and actinides, are a group of elements that display remarkably similar chemical and physical properties and were discovered in the late 18th century. Almost 100 years later, the luminescence obtained from them was observed for the first time, and applications based on these elements were developed. Rare earth ions, and specially lanthanides are characterized by their distinct spectra and spectral lines. When doped in a crystal, the lanthanide ion emissions appear as sharp spectral lines, due to the transitions in the 4f shell being unaffected by perturbations of the crystal.

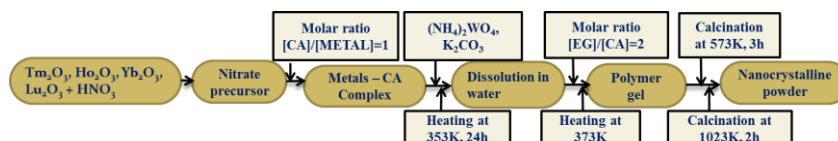
In recently years, lanthanide doped materials are widely used as temperature sensors as they have the capability to generate efficient up-conversion emission through absorbing near-infrared light. The most studied lanthanide element for this specific application is Er³⁺ which is usually coupled to Yb³⁺ that has a larger absorption cross section in the near-infrared region and provides an efficient energy transfer to Er³⁺ due to the large spectral overlap between these two ions. Er³⁺/Yb³⁺ codoped Gd₂O₃ nanocrystalline phosphors have been used for optical thermometry using the green up-

conversion emission centered at 523 and 548 nm in the 300–900K temperature range. A maximum sensitivity of about 0.0039K^{-1} was observed (at room temperature) [8-9]. More recently also $\text{Tm}^{3+}/\text{Yb}^{3+}$ co-doped materials have been used for the same purpose, with a much deeper penetration imaging power using the ${}^3\text{H}_4 \rightarrow {}^3\text{H}_6$ transition of Tm^{3+} ions [10].

We studied a novel lanthanide doped KLuW nanoparticles, using different excitation wavelengths for applications in thermometry. The use of monoclinic KLuW as the host material has several advantages: (i) large absorption and emission cross sections; (ii) possibility of large doping concentrations without concentration quenching; and (iii) good mechanical properties [11]. Ho^{3+} , Yb^{3+} , Tm^{3+} are promising dopants for this host material as they are closer to Lu^{3+} in the lanthanide series of the periodic table of elements, which implies similar ionic radius, and thus a small distortion of the crystallographic structure after doping. Furthermore, Ho^{3+} and Tm^{3+} present several emission lines in the blue, green and red region of the emission spectra that can generated by up-conversion processes after excitation of Yb^{3+} and Tm^{3+} in the near-infrared region of the electromagnetic spectrum and efficient energy transfer to Tm^{3+} and Ho^{3+} , depending on the ion excited. These emission lines can be used to determine the temperature by the FIR technique.

2. EXPERIMENTAL SECTION

1.5 at. % Ho, 1 at. % Yb, 1 at. % Tm doped KLuW nanocrystals were synthesized by the modified Pechini sol-gel method [12]. Analytic grade purity reagents of Tm_2O_3 (99.9999%), Ho_2O_3 (99.9999%), Yb_2O_3 (99.9%), and Lu_2O_3 (99.9999%), were dissolved in hot nitric acid in the specific proportions to form the nitrate precursor. Citric acid (CA) as the chelating agent and ethylenglycol (EG) were used as the esterification agent. The nitrate precursors were dissolved in distilled water with citric acid in a molar ratio of CA to metal cations $\text{CM}=[\text{CA}]/[\text{METAL}] = 1$. Ammonium tungstate $(\text{NH}_4)_2\text{WO}_4$ (99.99%) and potassium carbonate K_2CO_3 (99.99%) were added to the aqueous solution and we heated it at 353 K under magnetic stirring during 24 h until complete dissolution. Further, EG was added to the mixture in a molar ratio $\text{CE}=[\text{EG}]/[\text{CA}]=2$. The solution was heated at 373 K in order to evaporate water and generate the polymeric gel. After that, the polymeric gel was calcinated at 573 K for 3 hours, and 1023 K for 2 hours to eliminate the organic compounds and crystallize the required nanoparticles. A summary of this process can be seen in Scheme 1.



Scheme 1. Modified Pechini method for nanoparticles synthesis.

For up-conversion emission measurements, doped KLuW nanoparticles were introduced in a Linkam THMS 600 microscope heating stage. The sample was excited with diode lasers emitting at 980 and 808 nm, which correspond to the maximum absorption wavelengths of Yb^{3+} and Tm^{3+} ions, respectively. The beam from the laser source was focused on the sample and the emission was collected in 90° geometry in order to eliminate the residual laser pump. Emission radiated from the sample was collected and dispersed on a Jobin Yvon HR 460 monochromator. For detection a Hamamatsu PMTR 928 photomultiplier tube, connected to a Perkin Elmer DSP-7265 lock in amplifier was used to detect and amplify the collected signal.

The intensity ratio from two energy levels can be defined as,

$$\text{Intensity} \cdot \text{ratio} = \frac{I_1}{I_2} = B \exp\left(-\frac{A}{T}\right) \quad (1)$$

where B and A are coefficients that include the degeneracy of levels, the spontaneous emission angular frequency, the emission cross section, and the energy transfer parameters between ions, and T is the absolute temperature. For temperature sensing applications it is important to know the rate at which the intensity ratio changes for a small change in temperature. This quantity, known as the sensitivity, can be calculated by:

$$S = \frac{d(\text{Intensity} \cdot \text{ratio})}{dT} = \text{Intensity} \cdot \text{ratio} \left(-\frac{A}{T^2}\right) \quad (2)$$

3. RESULTS AND DISCUSSION

The stoichiometric composition the doped KLuW nanocrystals was determined by electron probe microanalysis (EPMA). The obtained stoichiometric formula was $\text{KLu}_{0.96(2)}\text{Ho}_{0.02(1)}\text{Tm}_{0.01(5)}\text{Yb}_{0.01(4)}(\text{WO}_4)_2$.

Figure 1 shows the X-ray powder diffraction pattern obtained after calcination of the nanocrystals at 1023 K for 2 hours. All peaks were indexed according to the monoclinic phase with space group $C2/c$ of KLuW by comparison with the JCPDS 54-1204 card, indicating that the nanocrystals are formed by a single crystalline phase and the doping cations have been incorporated into the host lattice, replacing Lu^{3+} ions in the C_2 sites.

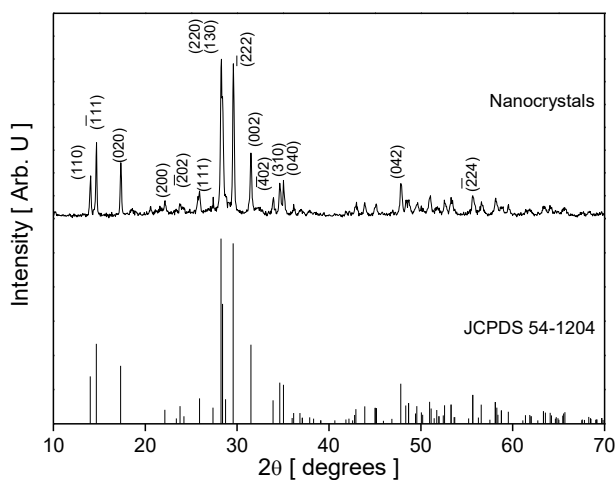


Figure 1. X-ray diffraction pattern of (1.5%Ho, 1%Tm, 1%Yb):KLuW nanocrystals compared with the JCPDS 54-1204 pattern.

The morphology of doped KLuW nanocrystals was analyzed with transmission electron microscopy (TEM) (see Figure 2). The images obtained indicated that the average size of the nanoparticles was around 100 nm and they have an irregular shape. It can also be observed a small degree of agglomeration among the nanoparticles.

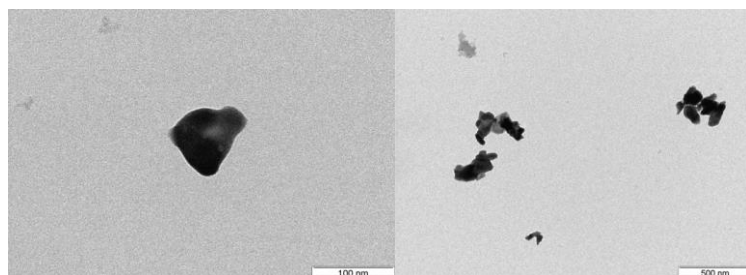


Figure 2. TEM images of the synthesized nanoparticles.

Up-conversion emission spectra of doped KLuW nanocrystals recorded after excitation at the maximum absorption of Yb^{3+} ions at 980 nm in the range of temperatures from 296 to 573 K are shown in Figure 3. Three emission bands are observed for these samples: a blue emission at 460 – 500 nm that arises from the $^1\text{G}_4 \rightarrow ^3\text{H}_6$ Tm^{3+} transition and the $^5\text{F}_3 \rightarrow ^5\text{I}_8$ Ho^{3+} transition, a green emission at 532 – 566nm the arises from the $^5\text{S}_2, ^5\text{F}_4, \rightarrow ^5\text{I}_8$ transitions of Ho^{3+} , and a red emission at 625 -675nm that arises from the $^1\text{G}_4 \rightarrow ^3\text{F}_4$ Tm^{3+} transition and the $^5\text{F}_3 \rightarrow ^5\text{I}_7$ Ho^{3+} transition. The intensity of all up-conversion bands is changing when increasing the temperature.

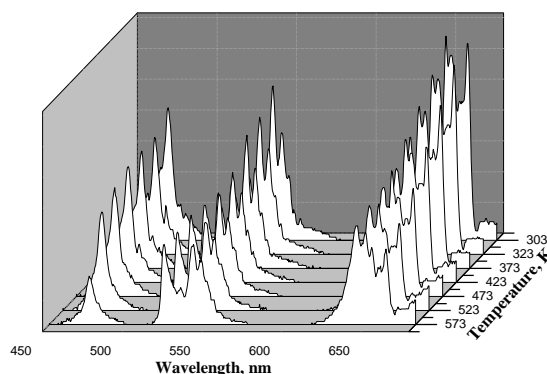


Figure 3. Up-conversion emission spectra of 1.5 at. % Ho, 1 at. % Yb, 1 at. % doped KLuW nanocrystals at the range of temperature 303-573 K, excited with 980 nm.

It is well known that for an ensemble of ions doped in a host material, the fluorescence levels depend on a number of parameters, such as the host material, the particular energy level of interest, the dimensions of the doped material and the excitation method employed. Thermally induced changes in the emission intensity usually arise from the temperature dependence of the non-radiative rates of the ions. The temperature dependent ratio of emissions from different energy levels may provide a method for measuring the temperature.

We focused on the up-conversion emission which results from the thermally coupled energy levels, and that involve the $^1G_4 \rightarrow ^3F_4$ transition at 648 nm from Tm^{3+} and the $^3F_3 \rightarrow ^5I_7$ transition at 661 nm from Ho^{3+} . The intensity ratio as a function of temperature for these transitions can be seen in Figure 4(a).

We also focused on the $^5S_2, ^5F_4 \rightarrow ^5I_8$ transitions of Ho^{3+} , located at 539 and 549 nm, respectively that are also coupled thermally. The intensity ratio as a function of absolute temperature for these transitions is plotted in Figure 4(b).

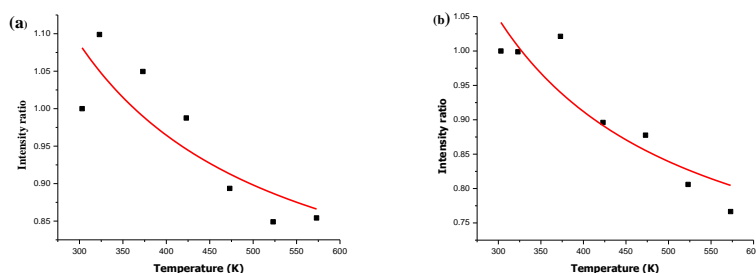


Figure 4. Intensity ratio as a function of absolute temperature of (a) $Tm^{3+} \ ^1G_4 \rightarrow ^3F_4$ (648 nm) and Ho^{3+} transition $^3F_3 \rightarrow ^5I_7$ (661 nm); and (b) Ho^{3+} transitions $^5F_4, ^5S_2 \rightarrow ^5I_8$ (539 and 549 nm).

It can be clearly seen in Figure 4 that the intensity ratio decreases when the temperature increased. Experimental data from fluorescence ratio between the 661 nm peak and the 648 nm peak could be fitted to the exponential equation like:

$$Intensity \cdot ratio = 0.67 \cdot \exp(142/T) \quad (3)$$

For the 539 and 549 nm peaks, FIR could be fitted to an exponential equation like:

$$Intensity \cdot ratio = 0.6 \cdot \exp(165/T) \quad (4)$$

With these equations sensitivity as a function of absolute temperature was calculated and it is presented in Figure 5. The maximum of sensitivity in both cases was observed at room temperature, and corresponded to a value of 0.0017 and 0.0019 K^{-1} , respectively. These values, although being of the same order of those reported for Er^{3+} [8-9], are almost half of the values that can be obtained in the $Er^{3+}-Yb^{3+}$ systems.

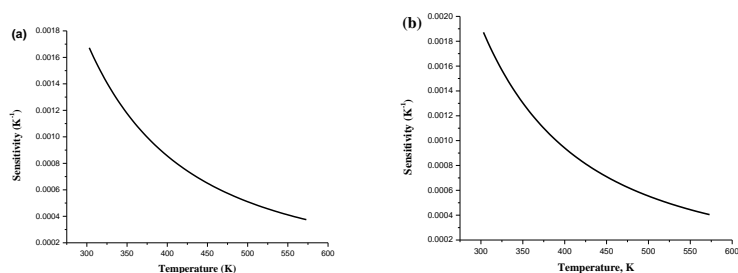


Figure 5. Sensitivity of the intensity ratio calculated for (a) I_{661}/I_{648} and (b) I_{539}/I_{549} as a function of temperature.

However, the doped KLuW nanocrystals present an alternative scheme of excitation, that is pumping directly to Tm^{3+} at 808 nm. Luminescence spectra of these nanoparticles in the range of the temperatures 295-523 K after excitation at 808 nm are shown in Figure 6. We observed again three principal luminescence bands, which can be identified again as those corresponding to the ${}^1G_4 \rightarrow {}^5H_6$ Tm^{3+} transition and the ${}^5F_3 \rightarrow {}^5I_8$ Ho^{3+} transition (460 – 500 nm); the ${}^5S_2, {}^5F_4 \rightarrow {}^5I_8$ Ho^{3+} transitions (518 – 557 nm); and the ${}^5S_2, {}^5F_4$ levels could be excited thermally into upper level of the 1G_4 level, giving rise to the thermal population of the 1G_4 level. The change of intensity of the green emission (518 – 557 nm) with temperature is rather small compared to that of the red emission (645 – 720 nm), that is observed to increase when the temperature increased. Thus, we used the variation of intensity of these two bands to calculate the intensity ratio for temperature determination.

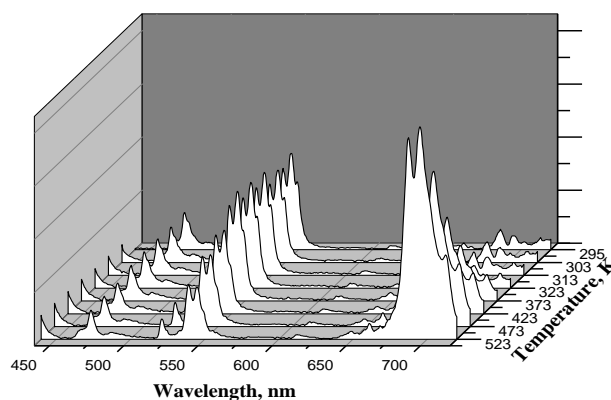


Figure 6. Up-conversion emission spectra of (Ho, Tm, Yb):KLuW nanocrystals in the range of temperatures 295-523 K after excitation at 808 nm.

Figure 7 shows the intensity ratio obtained by comparing the intensity of the green and red emission bands, using the peaks located at 545 and 687 nm, respectively. As opposite to the previous case, the ratio between the intensity of these peaks increase exponentially with temperature. However, and more interestingly, the data included in Figure 7(b) indicate that the doped KLuW nanocrystals can be used as nanothermometers for biological applications since they present an almost linear response in biological range of temperatures.

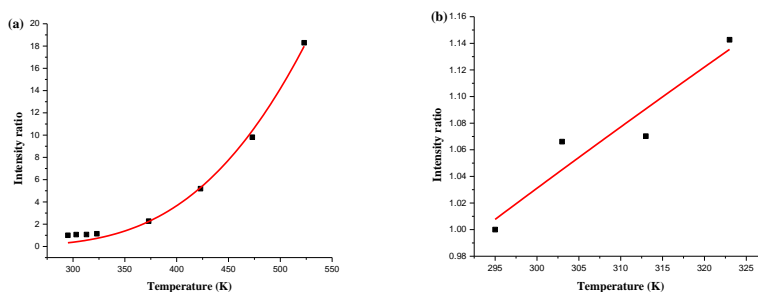


Figure 7. Intensity ratio of I_{687}/I_{545} as a function of absolute temperature in the (a) 295 – 523 K range and (b) in the biological range of temperatures 295 – 323 K.

The sensitivity of the intensity ratio for the doped KLuW nanocrystals after excitation at 808 nm is shown in Figure 8. In that case the maximum sensitivity is three orders of magnitude higher when compared to the nanoparticles excited at 980 nm excitation.

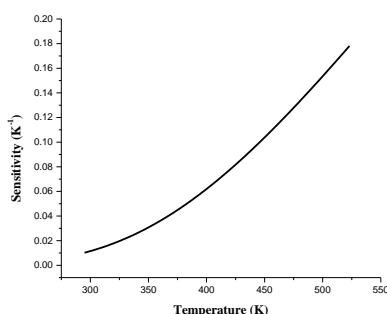


Figure 8. Sensitivity of the intensity ratio calculated for I_{687}/I_{545} as a function of temperature.

4. CONCLUSION

In conclusion, triply doped (Ho, Tm, Yb):KLuW nanocrystals have been prepared and their up-conversion emission dependence with temperature have been studied for two different excitation wavelengths. The intensity ratio between two emission lines was used for analyzing optical thermometry. In the case of excitation at 808 nm, the nanoparticles exhibited a higher temperature sensitivity as compared with excitation at 980 nm. The results indicates that (Ho, Tm, Yb):KLuW nanocrystals are promising candidate for applications as biological temperature sensors after excitation at 808 nm.

ACKNOWLEDGEMENTS

This work was supported by the European Union under Project Num. FP7-SPA-2010-263044, by the Spanish government under Project Num. MAT2011-29255-C02-02, TEC2010-21574-C02-02 and PI09/90527, and by the Catalan Authority under Project Num. 2009SGR235.

REFERENCES

- [1] Suzuki, M., Tseeb, V., Oyama, K., Ishiwata, S., “Microscopic Detection of Thermogenesis in a Single HeLa Cell”, *Biophys.J.* 92, 46 – 48 (2007).
- [2] Zohar, O., Ikeda, M., Shinagawa, H., Inoue, H., Nakamura, H., Elbaum, D., Alkon, D. L., Yoshioka, T., “Thermal Imaging of Receptor-Activated Heat Production in Single Cells”, *Biophys.J.* 74, 82 – 89 (1998).
- [3] Muller, C. B., Weiss, K., Loman, A., Enderlein, J., Richtering, W., “Remote temperature measurements in femto-liter volumes using dual-focus-Fluorescence Correlation Spectroscopy”, *Lab Chip* 9, 1248 – 1253 (2009).

- [4] Stich, M. I. J., Nagl, S., Wolfbeis, O. S., Henne, U., Schaeferling, M., "A Dual Luminescent Sensor Material for Simultaneous Imaging of Pressure and Temperature on Surfaces", *Adv. Funct. Mat.* 9, 1399 – 1406 (2008).
- [5] Bennet, M. A., Richardson, P. R., Arlt, J., McCarthy, A., Buller, G. S., Jones, A. C., "Optically trapped microsensors for microfluidic temperature measurement by fluorescence lifetime imaging microscopy", *Lab Chip* 11, 3821 (2011).
- [6] Owen, D. M., Lanigan, P. M. P., Dunsby, C., Munro, I., Grant, D., Neil, M. A. A., French, P. M. W., Magee, A. I., "Fluorescence Lifetime Imaging Provides Enhanced Contrast when Imaging the Phase-Sensitive Dye di-4-ANEPPDHQ in Model Membranes and Live Cells", *Biophys.J.* 90, 80 – 82 (2006).
- [7] Wade, S. A., Collins, S. F., and Baxter, G. W., "Fluorescence intensity ratio technique for optical fiber point temperature sensing", *Journal of Applied physics* 94, 4743 (2003).
- [8] Singh, S. K., Kumar, K., Rai, S. B., "Er³⁺/Yb³⁺ codoped Gd₂O₃ nano-phosphor for optical thermometry", *Sensors and Actuators A* 149, 16-20 (2009).
- [9] Cao, B. S., He, Y. Y., Feng, Z. Q., Li, Y. S., Dong, B., "Optical temperature sensing behavior of enhanced green upconversion emissions from Er–Mo:Yb₂Ti₂O₇ nanophosphor", *Sensors and Actuators B* 159, 8-11 (2011).
- [10] Dong, N. N., Pedroni, M., Piccinelli, F., Conti, G., Sbarbati, A., Ramirez-Hernandez, J. E., Maestro, L. M., Iglesias-de la Cruz, M. C., Capobianco, F., Sole, J. G., Bettinelli, M., Joque, D., and Speghini, A., "NIR-to-NIR Two-Photon Excited CaF₂:Tm³⁺, Yb³⁺ Nanoparticles: Multifunctional Nanoprobes for Highly Penetrating Fluorescence Bio-Imaging", *ACS Nano* 5, 8665-8671 (2011).
- [11] Petrov, V., Pujol, M. C., Mateos, X., Silvestre, O., Rivier, S., Aguilo, M., Sole, R. M., Lin, J., Griebner, U., and Diaz, F., "Growth and properties of KLu(WO₄)₂, and novel ytterbium and thulium lasers based on this monoclinic crystalline host", *Laser and Photon. Rev.* 1, 179-272 (2007).
- [12] Galceran, M., Pujol, M. C., Aguilo, M., Diaz, F., "Sol-gel modified Pechini method for obtaining nanocrystalline KRE(WO₄)₂ (RE = Gd and Yb)", *J. Sol-Gel Sci. Techn.* 42, 79–88 (2007).

Paper VIII

Savchuk, Ol. A.; Carvajal, J. J.; Cesteros, Y.; Salagre, P.; Nguyen, H. D.; Rodenas, A.; Massons, J.; Aguiló, M.; Díaz, F. *Microwave-assisted solvothermal synthesis of Er,Yb:NaYF₄ nanoparticles for luminescent thermometric applications* (2016) Submitted to Inorganic chemistry.

Microwave-assisted solvothermal synthesis of Er,Yb:NaYF₄ nanoparticles for luminescent thermometric applications with high thermal resolution

Ol. A. Savchuk,^a J.J. Carvajal,^{a} Y. Cesteros,^b P. Salagre,^b H. D. Nguyen,^a A. Rodenas,^a J.*

Massons,^a M. Aguiló,^a F. Díaz^a

^aPhysics and Crystallography of Materials and Nanomaterials (FiCMA-FiCNA) and EMaS, Universitat Rovira i Virgili (URV), Marcel·lí Domingo 1, E-43007 Tarragona, Spain.

^bCatalytic Materials in Green Chemistry (GreenCat), Department of Physical and Inorganic Chemistry, Universitat Rovira i Virgili (URV), Marcel·lí Domingo 1, E-43007 Tarragona, Spain.

*Corresponding author: joan josep.carvajal@urv.cat

ABSTRACT

We report the synthesis of Er,Yb:NaYF₄ nanoparticles by a microwave-assisted solvothermal method. By tuning the basic parameters of the synthesis procedure, such as the time and temperature of reaction and the concentration of ethanol and water, the size and the crystalline phase of the nanoparticles could be controlled, getting the right conditions to obtain 100 % of the β hexagonal phase, the most efficient spectroscopically. Moreover, we analysed the evolution of the upconversion emission spectra of the synthesized nanoparticles for their use in luminescence thermometry. We observed that the thermal sensitivity that can be achieved is a function of the size of the nanoparticles and the crystalline phase in which they crystallize. Finally, we proved their practical application by mapping the temperature distribution generated by graphene in a glass slide cover after illumination at 808 nm, achieving a thermal resolution of 0.1 K, the highest reported up to now for these luminescent nanoparticles. We believe that, with the suitable changes, these nanoparticles might be used to map temperature gradients in living cells in the future with the same thermal resolution.

1. Introduction

Temperature is today recognized as one of the basic variables in science. Many industrial and scientific processes as well as others in everyday life, from cooking food to producing complicated materials, depend on temperature.¹ With the development of nanotechnology, determination of the temperature of a given system with submicrometric spatial resolution became possible. This has led to the development of a new subfield of thermometry, named nanothermometry, which concerned with the science of temperature measurement at the nanoscale level.²

Luminescence thermometry is considered to be one of the most promising non-contact techniques for temperature determination at the sub-micrometer and nanometer scale due to its very high spatial, thermal and temporal resolutions, large measurement ranges and acceptable costs.^{3, 4} A large number of materials have been studied for luminescence nanothermometry

applications, including quantum dots,⁵⁻⁸ organic dyes,⁹⁻¹² gold nanoparticles,^{13, 14} polymers¹⁵⁻¹⁷ and lanthanide doped materials.¹⁸⁻²⁴

Also, the different measurement techniques used in luminescence nanothermometry, and based on the changes in radiative lifetimes, intensity variations, spectral position shifting and broadening of emission lines induced by temperature have been proved to be potential tools for temperature determination even in biosystems.²⁵⁻²⁷

However, a kind of materials emerged among others for their interesting advantages for luminescent nanothermometry, as are the Ln³⁺-doped upconversion nanoparticles (Ln³⁺-UCNPs). These kind of materials absorb light in the near-infrared (NIR) region of the electromagnetic spectrum, while emit light in the visible range.²⁸ Pumping in the NIR allows overcoming problems related to background fluorescence arising from biological tissues and the potential damage that ultraviolet (UV) light can generate in them.²⁹ Moreover, the NIR lasers used to excite those UCNPs are cheaper and more powerful than UV lasers. Finally, the use of NIR radiation also preserves the operative lifetime of the phosphors used, in comparison with those illuminated with UV light, that are damaged usually by this radiation, shortening their operational lifetimes.³⁰

Er³⁺ is the most used lanthanide ion for luminescence thermometry purposes in UCNPs because of its intense green emission that consist of two luminescence bands centered at 520 and 540 nm and assigned to the ${}^2\text{H}_{11/2} \rightarrow {}^4\text{I}_{15/2}$, ${}^4\text{S}_{3/2} \rightarrow {}^4\text{I}_{15/2}$ radiative transitions, respectively. These two energy levels, from which the emission arises (${}^2\text{H}_{11/2}$ and ${}^4\text{S}_{3/2}$), are thermally coupled and, thus, the relative emissions of these two luminescence bands show strong temperature dependence.²⁵⁻²⁷ Among the potential crystalline matrices that can host this ion hexagonal β -NaYF₄, with space group P6₃/m, emerges as the most promising one, since it is considered the most efficient material for NIR to green upconversion.^{31, 32} Vetrone et al. have shown that Er³⁺, Yb³⁺ co-doped NaYF₄ nanoparticles can be successfully used as an intracellular nanothermometer. They internalized Er³⁺, Yb³⁺ co-doped NaYF₄ nanoparticles in the HeLa cells and measured the temperature change induced by a heating plate on an individual cell through the temperature dependence of the fluorescence intensity ratio of the emission lines centered at 525 and 545 nm, up to its thermally induced death.²⁶ Fischer et al. also used these nanoparticles in their studies to sense temperature in human embryo kidney cells. In that case, they determined temperature from the ratiometric temperature dependence of the red to green bands generated by these nanoparticles.²⁵

NaYF₄ can crystallize in two polymorphic phases: α -NaYF₄ with $Fm\bar{3}m$ space group and hexagonal β -NaYF₄ with $P6_3/m$ space group.³¹ High reaction temperatures and long

reaction times can induce the phase transformation from the metastable α phase to the thermodynamically stable β phase.³³ Thus, the synthesis of NaYF₄ phosphors has been extensively studied, especially to explore the best conditions to obtain pure β phase with a high production yield. The most common synthesis procedures to synthesize NaYF₄ are the hydro/solvothermal methods using a conventional autoclave, which allow obtaining highly crystalline material at relatively low temperatures.^{26, 34, 35} Also, the thermal decomposition method was successfully developed to synthesize hexagonal Er,Yb:NaYF₄ nanoparticles with different morphologies and sizes.^{36, 37} However, the main drawbacks of this method are the use of expensive precursors and the complex synthesis procedure. The co-precipitation method has been also used for the synthesis of NaYF₄ nanoparticles with a narrow size distribution.^{38, 39} However, it requires performing a post-growth annealing process to obtain the hexagonal phase.

Microwave-assisted hydrothermal synthesis emerged as an efficient method for the synthesis of monodispersed and highly luminescent NaYF₄ nanoparticles,⁴⁰ since it allows for a fast and uniform heating in a eco-friendly and energy-efficient way. However, up to now poor yields,⁴⁰ mixtures of α and β phases,⁴¹ microtubes,^{42,43} nanowires,⁴⁴ and micron-size particles,⁴⁵ have been obtained using microwave assisted procedures.

Here, we report the synthesis of Er,Yb:NaYF₄ nanoparticles by a microwave-assisted solvothermal method which allowed us to obtain these nanoparticles in short times and at low temperatures. Furthermore, by tuning the basic parameters of the synthesis process such as temperature and time of the reaction, we succeeded in obtaining nanoparticles with different sizes and also to isolate different crystalline phases, getting the right conditions to obtain 100 % pure β -NaYF₄ phase with a production yield ranging from 64 to 98 %. We also analyzed the temperature dependence of the luminescence of these nanoparticles. Nanoparticles with bigger sizes belonging to the hexagonal β phase showed higher relative sensitivity than those with smaller sizes or those belonging to the cubic α phase. Finally, we showed that these nanoparticles can be used to map the temperature distribution generated by the laser-induced heating in graphene through a glass cover slide, with a thermal resolution of 0.1 K.

2. Experimental techniques

2.1 Synthesis of Er,Yb:NaYF₄ nanoparticles

Yb (20 mol. %), Er (2 mol. %) co-doped NaYF₄ nanoparticles were synthesized by a microwave-assisted solvothermal method. High purity Y₂O₃, Yb₂O₃, and Er₂O₃, analytical reagents, trisodium citrate (Na₃C₆H₅O₇), sodium fluoride (NaF) and ammonium fluoride

(NH₄F) were used as raw materials. RE(NO₃)₃ (RE = Y, Yb, Er) were prepared by dissolving the corresponding RE₂O₃ in 10 ml of hot nitric acid (HNO₃). After the evaporation of nitric acid, 15-65.5 ml of ethanol (depending on the experiment) in which 8.1 – 24.7 g of trisodium citrate (depending on the experiment) were dissolved, were added and stirred during 60 min. In another vessel, 0.08 – 0.36 g of NaF and 0.45 – 3.62 g of NaH₄F were dissolved in 7.5-60 ml of hot water, depending on the experiment. Then, the two solutions were mixed together. After vigorous stirring for 2 h, the solution was transferred to a Teflon reactor with a volume of 75 ml, and placed into a Milestone ETHOS-TOUCH CONTROL laboratory microwave autoclave equipped with a temperature controller, where it was maintained at a temperature between 393 and 453 K under stirring during a period of time ranging from 3 to 6 h, depending on the experiment. Finally, the solution was cooled down naturally, and the precipitated nanoparticles were washed with ethanol and deionized water three times. Table 1 summarizes the synthesis conditions for the different experiments we performed.

Table 1. Synthesis conditions and main characteristics of the Er,Yb:NaYF₄ nanoparticles obtained by the microwave-assisted solvothermal method.

Temperature (K)	Time (h)	[Ethanol]/[Water] (Volume %)	Crystalline phase	Crystallite size (nm)	Shape	Production yield (%)
453	6	70/30	β	63	long rods	77
		60/40		74	long rods	67
		50/50		55	long rods	67
		40/60	α + β	68	long rods	67
		30/70		48	long rods	65
		20/80		42	short rods	64
453	3	90/10	β	52	spheres	98
		80/20		58	spheres	97
		70/30		29	irregular	97
		60/40	40	spheres + short rods	96	
		50/50	26	irregular	86	
		40/60	28	irregular	71	
423	3	90/10	α	22	spheres	98
		80/20	β	128	spheres	97
		70/30		60	short rods	98
		60/40		57	short rods	98
		50/50	37	short rods	75	
		40/60	65	short rods	69	
393	3	80/20	β	62	short rods	98
		70/30		55	short rods	98
		60/40		72	short rods	97
		50/50		72	short rods	81
		40/60		58	short rods	64

2.2 Structural and morphological characterization

The crystalline structure of the obtained Er,Yb:NaYF₄ nanoparticles was investigated by means of X-ray powder diffraction analysis using a Bruker-AXS D8-Discover diffractometer using Cu Kα radiation. Crystallite size was calculated with the data corresponding to the all the reflections in the diffraction pattern using the Scherrer equation.

The morphology of the Er,Yb:NaYF₄ nanoparticles obtained by the microwave-assisted solvothermal method was investigated by using an environmental scanning electron microscope (ESEM) FEI Quanta 600 and a transmission electron microscope (TEM) JEOL 1011.

2.3 Temperature-dependent luminescence measurements

For temperature dependent luminescence measurements, the Er,Yb:NaYF₄ nanoparticles were placed in a Linkam THMS 600 heating stage equipped with a BN disk that allowed an improved temperature distribution in the chamber. The nanoparticles were excited by a fiber-coupled diode laser at 980 nm wavelength with a power of 50 mW. The laser beam was focused on the sample by a 40 X microscope objective with numerical aperture N.A. = 0.6 providing a spot size of around 20 μm on the sample. The NPs visible emission was collected by the same microscope objective, and after passing a dichroic filter to eliminate the excitation radiation was fiber coupled to an AVANTES AVS-USB2000 spectrometer for analyzing the emission spectra. Spectra were recorded at temperatures between RT and 333 K.

2.4 Thermal mapping of heat transfer through a graphene-coated glass

100 μl of a graphene solution in dimethylformamide (DMF) with a concentration of 1 mg ml⁻¹ were deposited on a microscope slide cover glass with a thickness of 100 μm. The solvent was evaporated letting it dry at 353 K. On the other side of the same microscope slide cover glass 100 μl of a dispersion of the Er,Yb:NaYF₄ nanoparticles in ethanol with a concentration of 10 mg ml⁻¹ was deposited. A fiber-coupled diode laser emitting at 808 nm was focused on the graphene-coated cover glass using a 60 X microscope objective (N. A. = 0.7), generating a beam with a diameter of 9 μm on the sample. Graphene efficiently absorbs the 808 nm laser light and converts it into heat.⁴⁶ Temperature then was determined through the analysis of the upconversion emission spectra of Er,Yb:NaYF₄ nanoparticles.

3. Results and discussion

3.1 Microwave-assisted solvothermal synthesis of Er,Yb:NaYF₄ nanoparticles

Er,Yb:NaYF₄ nanoparticles were synthesized by the microwave-assisted solvothermal method. Compared to the conventional heating hydrothermal methods, microwave heating is a greener approach to synthesize materials, since it allows shortening the reaction time, reducing

the reaction temperature or time and thus, lowering the energy consumption.⁴⁷⁻⁴⁹ By changing the reaction temperature, the reaction time and the ethanol and water volumes we obtained nanoparticles with different sizes and crystallizing in different crystalline phases, as observed in Table 1, getting the conditions to obtain pure α - and β -NaYF₄ nanoparticles.

In the case of nanoparticles synthesized at 453 K for 6 h, the pure β -NaYF₄ phase was obtained for solutions containing ethanol concentrations between 40-70 %, while a mixture of α and β phases (α phase with lower concentration than β phase) were obtained in solutions containing lower ethanol concentrations. These solutions containing lower ethanol concentrations were avoided in the rest of the experiments. When the reaction time was reduced to 3 h, while keeping the reaction temperature at 453 K, the pure β phase was obtained for the solutions analyzed. However, when the temperature was reduced to 423 K, the pure α phase was obtained for the solution containing 90 % ethanol and 10 % water, while for the rest of the solutions, the pure β phase was obtained. Thus, this solution composition was avoided in the last experiment, in which the temperature was still reduced to 393 K, while the reaction time was kept at 3 h. Under these conditions, again the pure β phase was obtained for all the solutions analyzed. Thus, by controlling the synthesis parameters, we have been able to obtain pure α - and β -NaYF₄ nanoparticles, avoiding the presence of mixtures of both phases. Also, since the β phase is more interesting for spectroscopic applications due to the higher emission intensity that can be achieved with nanoparticles crystallizing in this phase for up-conversion applications, we focused our efforts in maximizing the production of this β phase.

The yields of production in all cases were high in all cases, of the order of 76%, which allowed us obtaining 0.76 g of Er,Yb:NaYF₄ nanoparticles in each batch.

The crystallite size of these nanoparticles was calculated using the Scherrer equation.⁵⁰ The results are listed in Table 1. Comparing the crystallite size of the nanoparticles obtained from solutions containing the same ethanol concentrations at different temperatures and reaction times, we observed that the smallest crystallite sizes were obtained for the nanoparticles synthesized at 453 K for 3 h, while, even when the temperature was reduced to 423 or 393 K, the crystallite size increased again. By comparing the crystallite size of nanoparticles obtained at the same temperature and reaction time but in solutions containing different ethanol concentrations, it seems that there is a tendency to obtain smaller crystallite sizes as the ethanol content is reduced, although there exist several exceptions. Thus, a clear conclusion about this point could not be extracted.

If we take a look at the shape of the nanoparticles obtained, we observed that at low synthesis temperatures we obtained short rods, but as the temperature increases these rods tend to transform towards more irregular or spherical shapes. However, the surfaces of these nanoparticles are not smooth, indicating that probably they are formed by the agglomeration of the smaller short rod units. Also, when the reaction time was increased from 3 h to 6 h, sub-micrometric size particles were obtained exhibiting a long rod shape. Finally, comparing the shape of the nanoparticles obtained using different ethanol concentrations, we observed that as the ethanol concentration increased, the nanoparticles tend to show more irregular, spherical or long rod shapes, depending on the synthesis temperature and reaction time used.

As explained in the Introduction to this article, microwave-assisted hydrothermal methods have been previously used for the synthesis of NaYF₄ phosphors. Wang and Nann used sodium trifluoroacetate (TFA), yttrium-TFA, ytterbium-TFA and erbium-TFA as initial reagents dissolved in oleic acid and 1-octadecene to obtain NaYF₄ nanocrystals through a microwave-assisted process at 563 K for 5 min at 300 W, and they obtained cubic α -NaYF₄ with very small sizes (11 nm in diameter) with a poor yield.⁴⁰ Chen et al.⁴² used NaF, NH₄HF₂, and Y, Yb and Tm nitrates as initial reagents dissolved in water to obtain NaYF₄, adjusting the pH with HF, and heating the solution at 453 K for 4 h in a microwave synthesizer. They obtained β -NaYF₄ microtubes, 0.5 μ m in diameter and 2-3 μ m long. Similar microtubes were obtained by Ling et al.⁴³ using a similar methodology. Later, Mi et al.⁴¹ used rare earth acetates as rare earth precursors and NH₄F and NaCl as the fluorine and sodium sources, respectively, dissolved in a mixture of water and ethylene glycol, and treated thermally in a microwave autoclave at 433 K for 1 h. Under these conditions they obtained a mixture of α and β phases with average sizes about 40 nm. More recently, Wawrzynczyk et al.⁴⁴ using a microwave flash-heating method obtained NaYF₄ nanowires 1.5 μ m long and 100 nm wide. From another side, Som et al.⁴⁵ prepared Er,Yb:NaYF₄ phosphors using rare earth nitrates, NaF dissolved in water and adding ethylenediamine tetra acetic acid (EDTA) as chelating agent, adjusting the pH of the solution with NaOH in a microwave digestion unit at 453 K for different time periods extending from 10 min to 2 h, operating at a frequency of 2.45 GHz and a power of 400 W. The samples obtained at shorter times crystallized in the α metastable phase with small amounts of YF₃, indicating the incompleteness of the reaction. For intermediate time they obtained mixtures of the α and β phases, while the samples obtained at longer times exhibited pure β -NaYF₄ phase with a hexagonal prism shape with a mean diameter of 1.0 μ m and a length of 5.5 μ m.

Thus, comparing these results previously reported with the ones we obtained and that are presented in this article, we can conclude that the developed microwave-assisted

solvothermal method allows obtaining pure β -NaYF₄ nanoparticles with smaller size and at lower temperatures and time than other microwave-assisted hydrothermal methods reported in the literature. Also, we avoided the appearance of microtubes or nanowires, the production of which have been also reported using microwave-assisted hydrothermal methods.^{42, 44} Furthermore, the synthesis procedure we presented here avoid the use of organic ligands like oleic acid⁴⁰ or EDTA,⁴⁵ which are difficult to eliminate at the end of the reaction. Regarding to the production yields, with our new synthesis procedure, the production yields obtained ranged from 64 % to 98 %, as can be seen in Table 1. The production yields are higher for the samples prepared in solutions containing a higher ethanol concentration, and they do not seem to depend on the synthesis temperature. However, as the reaction time increased, the production yields decreased, which would indicate that the products formed tend to dissolve again with a long exposure to the solution. Thus, the methodology presented here shows several advantages over the technologies previously reported in the literature, such as the use of lower temperatures, the production of pure α and β phases, avoiding mixtures of both phases, or the use of cheaper solvents avoiding organic ligands that have to be removed at the end of the synthesis process. Furthermore, the nanoparticles obtained are dispersible in water and biological compatible fluids as synthesized, without any post-growth treatment.

From all the experiments, we selected three representative sets of nanoparticles: NP1, synthesized at 453 K during 6 h with an ethanol/water volume ratio 70/30; NP2, synthesized at 453 K during 3 h with an ethanol/water volume ratio 80/20 and NP3, synthesized at 423 K during 3 h with an ethanol/water volume ratio 90/10. An ESEM image of NP1 nanoparticles is shown in Figure 1a. They have a prismatic shape with a hexagonal base with average sizes 300 nm in diameter and 600 nm long. This is the morphology we labelled as long rods in Table 1. Instead, samples NP2 and NP3 show nanoparticles with an almost circular shape with average sizes of 50-70 and 20 nm, respectively, as observed from the TEM pictures shown Figures 1b and c. They correspond to the morphologies labeled as irregular and spherical, respectively, in Table 1. The sizes of the nanoparticles corresponding to NP2 and NP3 samples, determined from the TEM pictures, matches well with the crystallite sizes determined using the Scherrer equation. In the case of NP1 sample, however, a large discrepancy was observed. This can be due to the fact that the size of these sub-micrometer particles is at the limit of the validity range for size determination using this equation, established at around 500 nm.⁵¹ Figure 1d shows the X-ray diffraction (XRD) patterns recorded for these samples. We observed that samples NP1 and NP2 crystallize in the hexagonal system, with space group P6₃/m corresponding to the β -NaYF₄ phase, as confirmed by comparison with the JCPDS reference pattern 16-334, also

included in the figure. In contrast, nanoparticles in sample NP3, which were synthesized at a lower temperature and a shorter time, crystallize in the cubic system, with space group $Fm\bar{3}m$ corresponding to the α - NaYF_4 phase, as confirmed by comparison with the JCPDS reference pattern 39-723, included also in the figure. Additionally, we confirmed that the β - NaYF_4 nanoparticles obtained by this procedure were highly crystalline, as confirmed by the SAED pattern obtained by electron diffraction of one of these nanoparticles included in the inset of Figure 1 b.

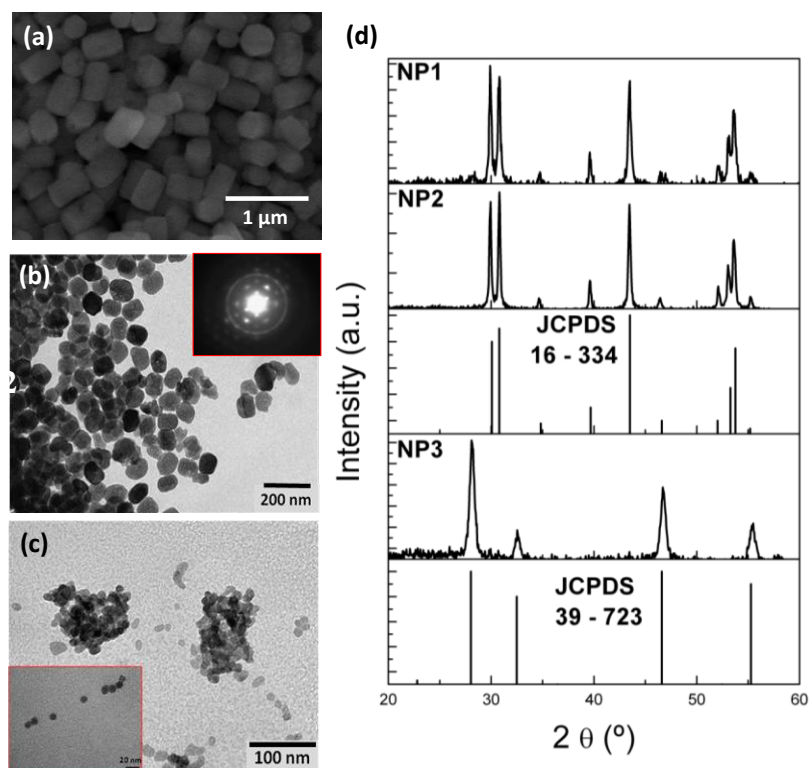


Figure 1. (a) ESEM image of the NP1 sample. TEM images of (b) NP2 and (c) NP3 samples. (d) X-ray diffraction patterns of the samples, together with the reference diffraction patterns for α - and β - NaYF_4 crystalline phases.

3.2 Temperature-dependent luminescence measurements

The emission spectra of these nanoparticles after excitation at 980 nm are shown in Figure 2, at room temperature and at 333 K. These spectra consist of two green bands centered at 520 and 540 nm, assigned to the ${}^2\text{H}_{11/2} \rightarrow {}^4\text{I}_{15/2}$ and ${}^4\text{S}_{3/2} \rightarrow {}^4\text{I}_{15/2}$ transitions of the Er^{3+} ion, respectively. An additional red band was observed at 630-670 nm, assigned to the ${}^4\text{F}_{9/2} \rightarrow {}^4\text{I}_{15/2}$ transition of Er^{3+} . While this red band shows a lower intensity than the green bands in samples

NP1 and NP2, it is the main band in sample NP3, associated to the different crystalline phases of these nanoparticles.

The pathways for generation of these emission lines through an upconversion process are well known and have been previously used for luminescence thermometric applications.^{26, 52, 53} Excitation at 980 nm promotes electrons of Yb^{3+} from the $^2\text{F}_{7/2}$ fundamental state to the $^2\text{F}_{5/2}$ excited state, from where an energy transfer process to Er^{3+} occurs populating the $^4\text{I}_{11/2}$ energy level of Er^{3+} . A second energy transfer process from Yb^{3+} promotes the electrons of Er^{3+} from the $^4\text{I}_{11/2}$ to the $^4\text{F}_{7/2}$ level. Then, the nonradiative relaxation populates the $^2\text{H}_{11/2}$ and $^4\text{S}_{3/2}$ states, which results in the $^2\text{H}_{11/2} \rightarrow ^4\text{I}_{15/2}$ and $^4\text{S}_{3/2} \rightarrow ^4\text{I}_{15/2}$ radiative decays emitting photons centered at 520 and 540 nm, respectively. The red band observed at 630-680 nm, can be assigned to the $^4\text{F}_{9/2} \rightarrow ^4\text{I}_{15/2}$ transition of Er^{3+} ion. The $^4\text{F}_{9/2}$ energy level is populated from a second energy transfer process from Yb^{3+} to Er^{3+} that occurs after a non-radiative relaxation from the $^4\text{I}_{11/2}$ to the $^4\text{I}_{13/2}$ energy level.

As observed in Figure 2(a), the intensity of the visible emissions decreased when the temperature increased for all samples.

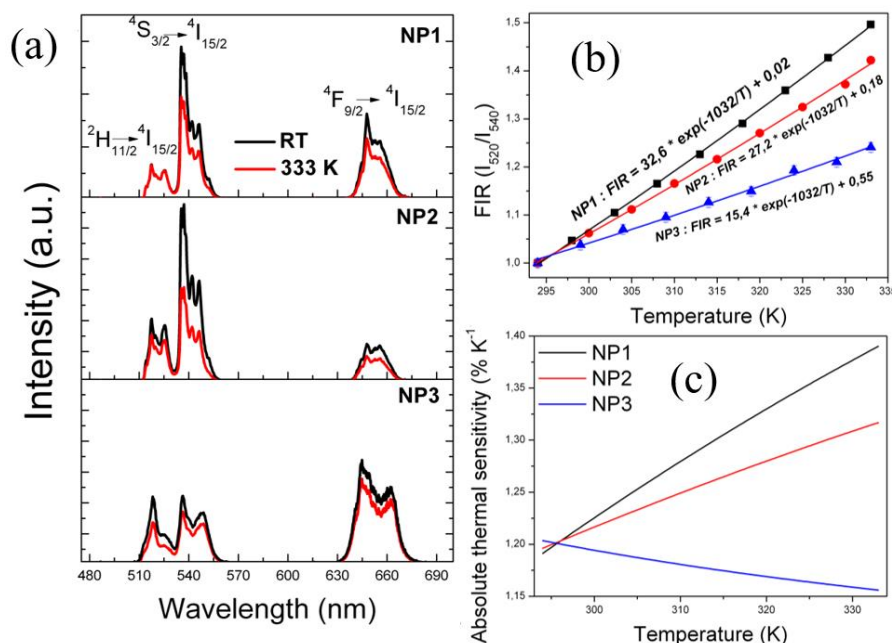


Figure 2. (a) Upconversion emission spectra at room and 333 K temperature for NP1, NP2 and NP3 Er,Yb:NaYF₄ samples. (b) Normalized FIR as a function of temperature for NP1, NP2 and NP3 samples with the fitting following a Boltzmann thermal distribution. (c) Absolute thermal sensitivity curve for the NP1, NP2 and NP3 samples.

The fluorescence intensity ratio (FIR) technique has proven to be an efficient tool to evaluate the luminescence thermometry properties of the green emissions generated by Er^{3+} in several materials, including Er,Yb:NaYF_4 nanoparticles.^{26, 52, 53} This technique is based on the comparison of the intensities of two emission bands arising from two closely spaced energy levels, the $^4\text{S}_{3/2}$ and $^2\text{H}_{11/2}$ levels of Er^{3+} in this case, whose populations are in thermal equilibrium governed by a Boltzmann distribution. Figure 2b shows the evolution of the FIR with temperature. Since the emission peaks considered to calculate the FIR are located very close to each other and may overlap, we added an offset to the Boltzmann distribution equation that takes into account this effect, defined as:⁵³

$$FIR \left(I_{520} / I_{540} \right) = \frac{n_2 g_1 \gamma_1 \sigma_1}{n_1 g_2 \gamma_2 \sigma_2} \exp \frac{\Delta E}{kT} + \frac{m_1}{n_1} = A \exp \frac{B}{T} + C \quad (1)$$

where I_{520} and I_{540} are the intensities of the emission bands located at 520 and 540 nm, respectively, n_i defines the fraction of the total fluorescence intensity of the transition originating from level i (upper level $i = 2$, lower level $i = 1$) measured by the detector for the i level, m_1 defines the fraction of the total intensity from level i which is measured by the detector for the other thermalizing level, g_i are the degeneracy of levels, γ_i are the spontaneous emission rates, σ_i are the absorption rates, ΔE is the energy difference between the two thermally coupled energy levels involved in the radiative transitions, k is the Boltzmann constant, T is the temperature, and A , B and C are the fitting parameters.

Experimental points for the different samples were fitted to eq. 1, and the obtained expressions are included in Figure 2b. The nanoparticles that show the highest slope are those corresponding to sample NP1, indicating that the luminescence intensity showed the maximum change with temperature for these nanoparticles.

The qualitative performance of these nanoparticles to sense small changes in temperature was obtained by the calculation of the absolute thermal sensitivity as the first derivative of FIR with respect to temperature.⁴ The absolute thermal sensitivities of the analyzed samples are included in Figure 2c. Sample NP1, with nanoparticles showing bigger sizes, possesses the highest thermal sensitivity with a maximum of 1.39 % K^{-1} at 333 K. The thermal sensitivity for the NP2 sample is smaller than that of NP1. This might seem controversial with the data reported by Dong et al.⁵² since they reported that $\beta\text{-Er,Yb:NaYF}_4$ particles with smaller sizes present a higher thermal sensitivity. However, they analyzed micron-size particles, while the nanoparticles here presented lay in the sub-micron and nanoscale. Thus, based on the presented results we can conclude that at the sub-micron and nanoscale, smaller $\beta\text{-Er,Yb:NaYF}_4$

nanoparticles would show smaller thermal sensitivities. The thermal sensitivity of the β -Er,Yb:NaYF₄ nanoparticles synthesized by this microwave-assisted solvothermal is similar, or even slightly higher, than that reported for the same nanoparticles synthesized by other methods, in the range 0.21-1.24 % K⁻¹.^{25, 26, 52, 56, 57} Finally, α -Er,Yb:NaYF₄ nanoparticles in sample NP3 showed the smallest thermal sensitivity. This is not surprising since the luminescence efficiency of this phase has been reported to be smaller than that of the β phase,⁵⁵ however, the thermal efficiency of this phase for luminescence thermometry had not been reported before.

3.3 Temperature distribution mapping by luminescence thermometry

In order to prove the potentiality of the Er,Yb:NaYF₄ nanoparticles synthesized through the microwave-assisted solvothermal method, we used them to map the temperature distribution generated on a glass coated with graphene when illuminated with a laser beam. Graphene has been reported to be an excellent photothermal converter.⁴⁶ To do that, we took a 100 μ m thick microscope slide cover glass and we coated it with graphene flakes on one side, and Er,Yb:NaYF₄ nanoparticles (corresponding to sample NP1) on the other side. Two spatially overlapped lasers were focused on both sides of the slide cover glass. A fiber-coupled diode laser emitting at 808 nm with a beam diameter of 9 μ m was focused on the face of the cover glass coated with graphene. Graphene efficiently absorbs the 808 nm laser light and converts it into heat.⁴⁶ The propagation of the heat generated by graphene to the opposite side of the cover glass was measured through the spectra generated by the Er,Yb:NaYF₄ nanoparticles when excited with a fiber-coupled diode laser emitting at 980 nm with a beam diameter of 10 μ m and converted to temperature by using the calibration curve shown in Figure 2b. The details are explained in the experimental techniques section. The scheme of this experimental setup is shown in Figure 3a.

First, we measured the temperature that can be achieved in the system when the power of the 808 nm laser focused on graphene is increased. The results are shown in Figure 3b. We observed that the temperature increased linearly with the power of the laser. Based on these results, we decided to fix the power of the laser at 100 mW, which allow achieving a temperature \sim 312 K on the opposite side of the glass in order to get a constant heating and generate a thermal gradient on the surface of the cover glass coated with the Er,Yb:NaYF₄ nanoparticles. The 980 nm excitation laser was fixed to a motorized stage that allowed to scan the sample below microscope setup, and we recorded the spectra of the Er,Yb:NaYF₄ nanoparticles every 50 μ m. Each spectrum recording took around 60 s, and the total scan duration was of 1 h. Figure 3c shows the temperature profile achieved on the opposite side of

the glass cover slide from the heating spot (corresponding to the 0 position) to the external part of the glass along the horizontal direction. The temperature decreased slowly from the center of the heating spot to the external part of the cover glass, dropping down from 313.0 K to 300.5 K. We were able to detect temperature changes as small as 0.1 K, the smallest reported up to now, to the best of our knowledge, for this kind of nanoparticles.

To contrast these results, the temperature distribution on the glass substrate was numerically analyzed by a finite element method (FEM) based on the commercial software COMSOL Multiphysics. The simulation was performed in a three-dimensional (3D) geometry using the heat transfer model for a steady-state study.⁵⁸ To model the experiment, computational domains were defined with two attached blocks which represent the glass substrate and the deposited graphene layer. The glass block used had an area of $10 \times 10 \text{ mm}^2$, and a height of 100 μm . The graphene block was constructed with an area of $10 \times 10 \text{ mm}^2$, and a height of 1 μm , based on the estimations of the deposition technique. In order to assign the laser beam as a heat source, a cylindrical domain (9 μm diameter, 1 μm height) was additionally created in the middle of the graphene domain corresponding to the waist of the pumping laser.

A triangular mesh was defined with a well-refined size (minimum 1 μm) within the small domain (the cylindrical heat source domain) and coarse size (maximum 1 mm) within the big domains (glass and graphene domain).

To solve the heat transfer problem in the stationary state, the following thermal conductivity values of the materials were assigned to the corresponding domains: $k = 3100 \text{ W m}^{-1} \text{ K}^{-1}$ for graphene,⁵⁹ and $k = 1.38 \text{ W m}^{-1} \text{ K}^{-1}$ for the silica glass.⁶⁰ The heat source was introduced to the cylindrical graphene domain with an overall heat transfer rate of 100 mW. The boundary condition was specified with a convective heat flux in all the boundaries in which a convection coefficient (h) was determined from the best fit to the measured temperature distribution. The value of h obtained was $80 \text{ W/m}^2\text{K}$, which is reasonable for the natural convection conditions taking place in the experiment.

Figure 3 (c) shows the heat gradient on the glass within the approximate range of 300 K and 314 K, which is closely matched with the experimental result. However, the exponential decay of the heat gradient shown in the simulated graph was not clearly observed in the experiment. This could be due to the non-homogeneity of the deposited graphene layer and its poor bonding quality with the glass slide which are critical in the heat transfer problem, while these factors were idealized in the simulation. Additionally, the material coefficients taken from the literature might not precisely correspond to those of the real sample. In the model, the

thermal conductivity of graphene was assumed to be isotropic whereas this might have an anisotropic behavior, for instance.

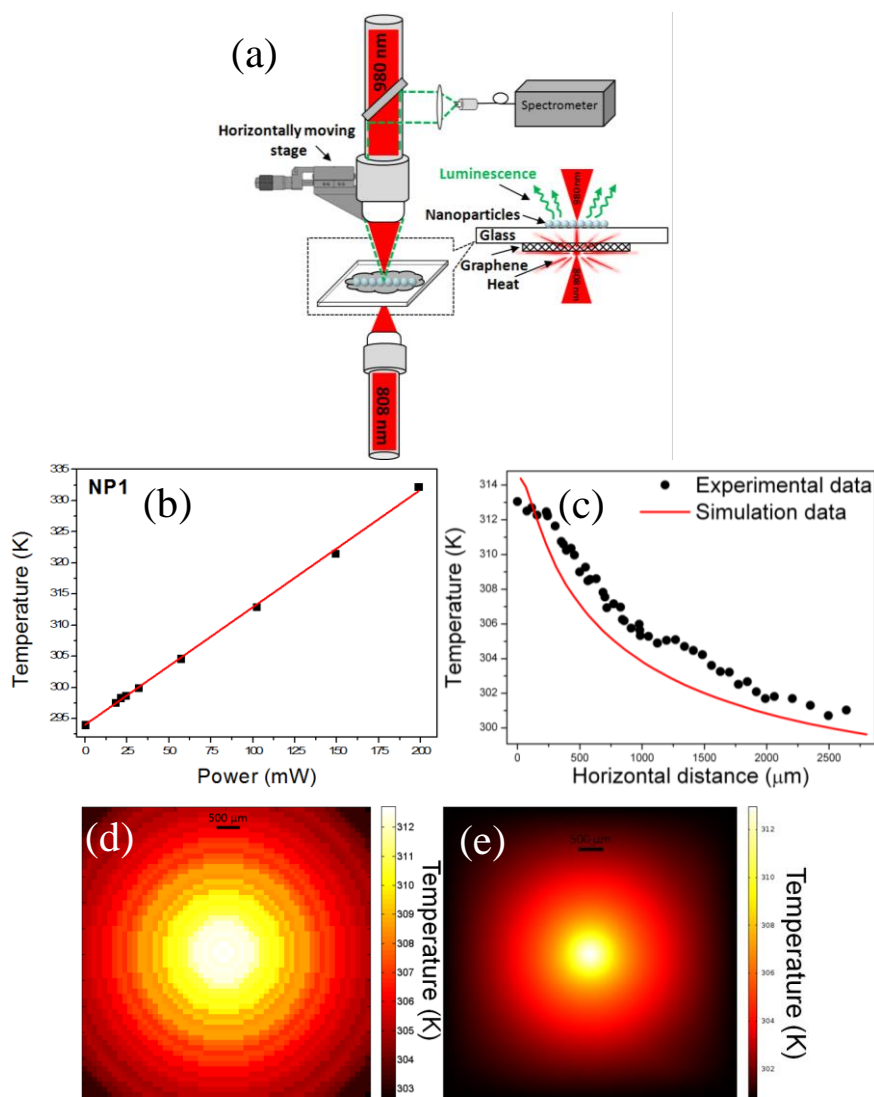


Figure 3. (a) Scheme of the setup used to map the temperature distribution generated by graphene when illuminated with a 808 nm laser on a microscope slide cover glass. (b) Temperature achieved on the surface of the graphene-coated glass as a function of the power of the irradiating laser at 808 nm. (c) Temperature distribution generated by graphene on the slide cover glass determined from the luminescence spectra of the Er,Yb:NaYF₄ nanoparticles and comparison with the temperature distribution calculated from a heat transfer model in a 3D geometry. 2D contour map generated from the heat transfer of (d) experimental (e) simulation data.

We believe that, by internalizing these luminescent nanoparticles on living cells as previously reported in the literature,²⁵⁻²⁷ with the required suitable chemical functionalization of

their surfaces as prior steps, thermal contour maps would also be obtained by *in vitro* procedures with the same thermal sensitivity, illustrating the internal temperature gradients in the cells.

4. Conclusion

In summary, we synthesized Er,Yb:NaYF₄ nanoparticles by a microwave-assisted solvothermal method at lower temperatures and reaction times than previously reported methods using conventional heating devices or even microwave-assisted hydrothermal methods. Furthermore, this synthesis method allowed to produce α - and β -Er,Yb:NaYF₄ separately, avoiding the production of mixtures and avoiding also the use of organic solvents and ligands not miscible with water or difficult to eliminate after the reaction. An additional advantage of this synthesis method is that the produced nanoparticles are hydrophilic and can be dispersed in water or other biological compatible fluids without requiring any post-growth chemical functionalization procedure.

We analyzed the temperature dependent upconversion emission of these nanoparticles for their use as luminescent nanothermometers. We observed that nanoparticles with bigger sizes possess higher thermal sensitivity. Their thermal sensing capabilities were proved to determine the temperature distribution induced by the heating generated by a graphene layer deposited on a microscope slide cover glass when illuminated with a laser emitting at 808 nm, obtaining a thermal resolution of 0.1 K. With this experiment we wanted to show that these nanoparticles can be used to monitor the temperature increase generated by graphene and derivatives when illuminated with a laser, one of the most promising techniques now a days for tumor treatment by hyperthermia. We believe that by using the suitable chemical functionalization steps, these nanoparticles can be internalized in living cells to visualize internal temperature distribution maps in them through *in vitro* procedures with the same thermal resolution.

Acknowledgements

This work was supported by the Spanish Government under Projects No. MAT2013-47395-C4-4-R, and TEC2014-55948-R, and by Catalan Authority under Project No. 2014SGR1358. Ol. A. Savchuk is supported by Catalan Government through the

fellowship 2015FI_B2 00136. F. D. acknowledges additional support through the ICREA Academia awards 2010ICREA-02 for excellence in research.

References

1. Michalski, L.; Eckersdorf, K.; Kucharski, J.; McGhee, J. *Temperature Measurement*, 2^{ed}, John Wiley & Sons: West Sussex, 2001.
2. Lee, J.; Kotov, N. A. Thermometer Design at the Nanoscale. *Nano today* **2007**, *2*, 48-51.
3. Jaque, D.; Vetrone, F. Luminescence Nanothermometry. *Nanoscale* **2012**, *4*, 4301-4326.
4. Brites, C. D. S.; Lima, P. P.; Silva, N. J. O.; Millan, A.; Amaral, V. S.; Palacio, F.; and Carlos, L. D. Thermometry at the Nanoscale. *Nanoscale* **2012**, *4*, 4799-4829.
5. Maestro, L. M.; Rodriguez, E. M.; Cruz, M. C. I.; Juarranz, A.; Naccache, R.; Vetrone, F.; Jaque, D.; Capobianco, J. A.; Solé, J. G. CdSe Quantum Dots for Two-Photon Fluorescence Thermal Imaging. *Nano Lett.* **2010**, *10*, 5109-5115.
6. Vlaskin, V. A.; Janßen, N.; van Rijssel, J.; Beaulac, R.; Gamelin, D. R. Tunable Dual Emission in Doped Semiconductor Nanocrystals. *Nano Lett.* **2010**, *10*, 3670-3674.
7. Li, S.; Zhang, K.; Yang, J. M.; Lin, L.; Yang, H. Single Quantum Dots as Local Temperature Markers. *Nano Lett.* **2007**, *7*, 3102-3105.
8. McLaurin, E. J.; Bradshaw, L. R. and Gamelin, D. R. Dual-Emitting Nanoscale Temperature Sensors. *Chem. Mater.* **2013**, *25*, 1283-1292.
9. Ebert, S.; Travis, K.; Lincoln, B. and Guck, J. Fluorescence Ratio Thermometry in a Microfluidic Dual-Beam Laser Trap. *Opt. Express* **2007**, *15*, 15493-15499.
10. Peterman, E. J. G.; Gittes, F. and Schmidt, C. F. Laser-Induced Heating in Optical Traps. *Biophys. J.* **2003**, *84*, 1308-1316.
11. Mendels, D. A.; Graham, E. M.; Magennis, S. W.; Jones, A. C. and Mendels, F. Quantitative Comparison of Thermal and Solutal Transport in a T-Mixer by FLIM and CFD. *Microfluid. Nanofluid.* **2008**, *5*, 603-617.
12. Karstens, T. and Kobs, K. Rhodamine B and Rhodamine 101 as Reference Substances for Fluorescence Quantum Yield Measurements. *J. Phys. Chem.* **1980**, *84*, 1871-1872.
13. Bomm, J.; Günter, C. and Stumpe, J. Synthesis and Optical Characterization of Thermosensitive, Luminescent Gold Nanodots. *Phys Chem. C* **2012**, *116*, 81-85.
14. Shang, L.; Stockmar, F.; Azadfar, N.; Nienhaus, G. U. Intracellular Thermometry by Using Fluorescent Gold Nanoclusters. *Angew. Chem. Int. Ed. Engl.* **2013**, *52*, 11154-11157.

15. Almeida, A. K. A.; Monteiro, M. P.; Dias, J. M. M.; Omena, L.; da Silva, A. J. C.; Tonholo, J.; Mortimer, R. J.; Navarro, M.; Jacinto, C.; Ribeiro, A. S.; de Oliveira, I. N. Synthesis and Spectroscopic Characterization of a Fluorescent Pyrrole Derivative Containing Electron Acceptor and Donor Groups. *Spectrochimica Acta A* **2014**, *128*, 812-818.
16. Graham, E. M.; Iwai, K.; Ischiyama, S.; de Silva, A. P.; Magennis, S. W. and Jones, A. C. Quantitative Mapping of Aqueous Microfluidic Temperature with Sub-Degree Resolution Using Fluorescence Lifetime Imaging Microscopy. *Lab Chip* **2010**, *10*, 1267-1273.
17. Okabe, K.; Inada, N.; Gota, C.; Harada, Y.; Funatsu, T. and Uchiyama, S. Intracellular Temperature Mapping with a Fluorescent Polymeric Thermometer and Fluorescence Lifetime Imaging Microscopy. *Nat. Commun.* **2012**, *3*, 705-714.
18. Alden, M.; Omrane, A.; Richter, M.; Särner, G. Thermographic Phosphors for Thermometry: a Survey of Combustion. *Prog. Energ. Combust.* **2011**, *37*, 422-461.
19. Brübach, J.; Pflitsch, C.; Dreizler, A.; Atakan, B. On Surface Temperature Measurements with Thermographic Phosphors: A Review. *Prog. Energ. Combust.* **2013**, *39*, 37-60.
20. Wang, F.; Deng, R.; Wang, J.; Wang, Q.; Han, Y.; Zhu, H.; Chen, X.; Liu, X. Tuning Upconversion Through Energy Migration Incore-Shell Nanoparticles. *Nat. Mater.* **2011**, *10*, 1-6.
21. Zheng, S.; Chen, W.; Tan, D.; Zhou, J.; Guo, Q.; Jiang, W.; Xu, C.; Liu, X. and Qiu, J. Lanthanide-Doped NaGdF₄ Core-Shell Nanoparticles for Non-Contact Self-Referencing Temperature Sensors. *Nanoscale* **2014**, *6*, 5675-5679.
22. Chen, R.; Ta, V. D.; Xiao, F.; Zhang, Q.; Sun, H. Multicolor Hybrid Upconversion Nanoparticles and Their Improved Performance as Luminescence Temperature Sensors Due to Energy Transfer. *Small* **2013**, *9*, 1052-1057.
23. Ceron, E. N.; Ortgies, D. H.; del Rosal, B.; Ren, F.; Benayas, A.; Vetrone, F.; Ma, D.; Sanz-Rodriguez, F.; Sole, J. G.; Jaque, D. and Rodriguez, E. M. Hybrid Nanostructures for High-Sensitivity Luminescence Nanothermometry in the Second Biological Window. *Adv. Mater.* **2015**, *27*, 4781-4787.
24. Xiao, Q.; Li, Y.; Li, F.; Zhang, M.; Zhang, Z.; Lin, H. Rational Design of a Thermalresponsive-Polymer-Switchable FRET System for Enhancing the Temperature Sensitivity of Upconversion Nanophosphors. *Nanoscale* **2014**, *6*, 10179-10186.
25. Fischer, L. H.; Harms, G. S.; Wolfbeis, O. S. Upconverting Nanoparticles for Nanoscale Thermometry. *Angew. Chem. Int. Ed.* **2011**, *50*, 4546-4551.
26. Vetrone, F.; Sole, J. G.; Naccache, R.; Sanz-Rodriguez, F.; Capobianco, J. A. Temperature Sensing Using Fluorescent Nanothermometers. *ACS Nano* **2010**, *4*, 3254-3258.

27. Li, C. R.; Dong, B.; Ming, C. G.; Lei, M. Application to Temperature Sensor Based on Green Up-Conversion of Er³⁺ Doped Silicate Glass. *Sensors* **2007**, *7*, 2652-2659
28. Haase, M.; Schäfer, H. Upconverting Nanoparticles. *Angew. Chem. Int. Ed.* **2011**, *50*, 5808-5829
29. Diao, S.; Hong, G.; Antaris, A. L.; Blackburn, J. L.; Cheng, K.; Cheng, Z. and Dai, H. Biological Imaging Without Autofluorescence in the Second Near-Infrared Region. *Nano Research* **2015**, *8*, 3027–3034
30. Rapaport, A.; Milliez, J.; Cassanho, A.; Jenssen, H. J. Review of the Properties of Upconversion Phosphors for New Emissive Display. *J. Disp. Technol.* **2006**, *2*, 68-78.
31. Page, R. H.; Schaffers, K. I.; Waide, J. P.; Tassano, A. B.; Payne, S. A.; Krupke, W. F. and Bischel, W. K. Upconversion-Pumped Luminescence Efficiency of Rare-Earth-Doped Hosts Sensitized with Trivalent Ytterbium. *J. Opt. Soc. Am. B* **1998**, *15*, 996-1008.
32. Krämer, K. W.; Biner, D.; Frei, G.; Güdel, H. U.; Hehlen, M. P. and Luethi, S. R. Hexagonal Sodium Yttrium Fluoride Based Green and Blue Emitting Upconversion Phosphors. *Chem. Mater.* **2004**, *16*, 1244-1251.
33. Zhou, J.; Chen, G.; Wu, E.; Bi, G.; Wu, B.; Teng, Y.; Zhou, S.; Qiu, J. Ultrasensitive Polarized Up-Conversion of Tm³⁺-Yb³⁺ Doped β-NaYF₄ Single Nanorod. *Nano Lett.* **2013**, *13*, 2241-2246.
34. Ma, Y.; Chen, M.; Li, M. Hydrothermal Synthesis of Hydrophilic NaYF₄:Yb,Er Nanoparticles with Bright Upconversion Luminescence as Biological Label. *Mater. Lett.* **2015**, *139*, 22-25.
35. Li, Z.; Zhang, Y. An Efficient and User-Friendly Method for the Synthesis of Hexagonal-Phase NaYF₄:Yb, Er/Tm Nanocrystals with Controllable Shape and Upconversion Fluorescence. *Nanotechnology* **2008**, *19*, 345606-345611.
36. Yu, S. Y.; Gao, X. C.; Jing, H.; Zhao, J. and Su, H. A Synthesis and Up-Conversion Photoluminescence Study of Hexagonal Phase NaYF₄:Yb,Er Nanoparticles. *Cryst. Eng. Comm.* **2013**, *15*, 10100-10106.
37. Kumar, R.; Nyk, M.; Ohulchanskyy, T. Y.; Flask, C. A.; Prasad, P. N. Combined Optical and MR Bioimaging Using Rare Earth Ion Doped NaYF₄ Nanocrystals. *Adv. Funct. Mater.* **2009**, *19*, 853-859.
38. Yi, G.; Lu, H.; Zhao, S.; Ge, Y.; Yang, W.; Chen, D.; Guo, L. H. Synthesis, Characterization, and Biological Application of Size-Controlled Nanocrystalline NaYF₄:Yb,Er Infrared-to-Visible Upconversion Phosphors. *Nano Lett.* **2004**, *4*, 2191-2196.

39. Wang, L.; Yan, R.; Huo, Z.; Wang, L.; Zeng, J.; Bao, J.; Wang, X.; Peng, Q.; Li, Y. Fluorescence Resonant Energy Transfer Biosensor Based on Upconversion-Luminescent Nanoparticles. *Angew. Chem. Int. Ed.* **2005**, *44*, 6054-6057.
40. Wang, H.-Q. and Nann, T. Monodisperse Upconverting Nanocrystals by Microwave-Assisted Synthesis. *ACS Nano* **2009**, *3*, 3804-3808.
41. Mi, C.; Tian, Z.; Cao, C.; Wang, Z.; Mao, C.; Xu, S. Novel Microwave-Assisted Solvothermal Synthesis of NaYF₄:Yb,Er Upconversion Nanoparticles and Their Application in Cancer Cell Imaging. *Langmuir* **2011**, *27*, 14632-14637.
42. Chen, X.; Wang, W.; Chen, X.; Bi, J.; Wu, L.; Li, Z.; Fu, X. Microwave Hydrothermal Synthesis and Upconversion properties of NaYF₄:Yb³⁺, Tm³⁺ with Microtube Morphology. *Mater. Lett.* **2009**, *63*, 1023-1026.
43. Ling, Z.; Jie, Z. Microwave Hydrothermal Synthesis of Hexagonal NaYF₄ and Yb³⁺, Er³⁺-Doped NaYF₄ Microtubes. *J. Inorg. Mater.* **2009**, *24*, 553-558.
44. Wawrzynczyk, D.; Piatkiwski, D.; Mackowski, S.; Samoc, M.; Nyj, M. Microwave-Assisted and Single Particle Spectroscopy of Infrared Down- and Visible Up-Conversion in Er³⁺ and Yb³⁺ Co-Doped Fluoride Nanowires. *J. Mater. Chem. C* **2015**, *3*, 5332-5338.
45. Som, S.; Das, S.; Yang, C. Y.; Lu, C. H. Enhanced Upconversion of NaYF₄:Er³⁺/Yb³⁺ Phosphors Prepared via the Rapid Microwave-Assisted Hydrothermal Route at Low Temperature: Phase and Morphology Control. *Opt. Lett.* **2016**, *41*, 464-467.
46. Savchuk, O. A.; Carvajal, J. J.; Massons, J.; Aguilo, M.; Diaz, F. Determination of Photothermal Conversion Efficiency of Graphene and Graphene Oxide Through an Integrating Sphere Method. *Carbon* **2016**, *103*, 134-141.
47. Komarneni, S.; Roy, R.; Li, Q. H. Microwave-Hydrothermal Synthesis of Ceramic Powders. *Mater. Res. Bull.* **1992**, *27*, 1393-1405.
48. Granados-Reyes, J.; Salagre, P.; Cesteros, Y. Effect of microwaves, ultrasounds and interlayer anion on the hydrocalumnites synthesis. *Micropor. Mesopor. Mater.* **2014**, *199*, 117-124.
49. Sánchez, T.; Salagre, P.; Cesteros, Y. Ultrasounds and microwave-assisted synthesis of mesoporous hectorites. *Micropor. Mesopor. Mater.* **2013**, *171*, 24-34.
50. Patterson, A. L. The Scherrer Formula for X-Ray Particles Size Determination. *Phys. Rev.* **1939**, *56*, 978-982.
51. Langford, J. I. and Wilson, A. J. C. Scherrer After Sixty Years: A Survey and Some New Results in the Determination of Crystallite Size. *J. Appl. Cryst.* **1978**, *11*, 102-113.

52. Dong, B.; Hua, R. N.; Cao, B. S.; Li, Z. P.; He, Y. Y.; Zhang, Z. Y. and Wolfbeis, O. S. Size Dependence of the Upconverted Luminescence of NaYF₄:Er,Yb Microspheres for Use in Ratiometric Thermometry. *Phys. Chem. Chem. Phys.* **2014**, *16*, 20009-20012.
53. Jiang, S.; Zeng, P.; Liao, L.; Tian, S.; Guo, H.; Chen, Y.; Duan, C.; Yin, M. Optical Thermometry Based on Upconverted Luminescence in Transparent Glass Ceramics Containing NaYF₄:Yb³⁺/Er³⁺ Nanocrystals. *J. Alloy. Compd.* **2014**, *617*, 538-541.
54. Wade, S. A.; Collins, S. F.; Baxter, G. W. The Fluorescence Intensity Ratio Technique for Optical Fiber Point Temperature Sensing. *J. Appl. Phys.* **2003**, *94*, 4743-4756
55. Wang, M.; Abbineni, G.; Clevenger, A.; Mao, C. and Xu, S. Upconversion Nanoparticles: Synthesis, Surface Modification and Biological Applications. *Nanomed. Nanotechnol.* **2011**, *7*, 710-729.
56. Wu, K.; Cui, J.; Kong, X.; Wang, Y. Temperature Dependent Upconversion of Yb/Er Codoped NaYF₄ Nanocrystals. *J. Appl. Phys.* **2011**, *110*, 053510-053516.
57. Sedlmeier, A.; Achatz, D. E.; Fischer, L. H.; Gorris, H. H.; Wolfbeis, O. S. Photon Upconverting Nanoparticles for Luminescent Sensing of Temperature. *Nanoscale* **2012**, *4*, 7090-7096.
58. Incropera, F. P. and DeWitt, D. P. *Fundamentals of Heat and Mass Transfer, 4th ed.*, John Wiley & Sons: Hoboken, 1996.
59. Pop, E.; Varshney, V. and Roy, A. K. Thermal Properties of Graphene: Fundamentals and Applications. *MRS Bulletin* **2012**, *37*, 1273-1281.
60. Bansal, N. P. and Doremus, R. H. *Handbook of glass properties*, Academic Press: Orlando, 1986.

Paper IX

Savchuk, Ol. A.; Carvajal, J. J.; Cascales, C.; Aguiló, M.; Díaz, F. *Benefits of silica core-shell structures on the temperature sensing properties of Er,Yb:GdVO₄ up-conversion nanoparticles (2016)* ACS Applied surfaces & interfaces 8, 7266-7273.

Benefits of Silica Core-Shell Structures on the Temperature Sensing Properties of Er,Yb:GdVO₄ Up-Conversion Nanoparticles

Oleksandr A. Savchuk,¹ Joan J. Carvajal,^{1} C. Cascales,² M. Aguiló,¹ F. Díaz¹*

¹Physics and Crystallography of Materials and Nanomaterials (FiCMA-FiCNA) and EMaS,
Universitat Rovira i Virgili (URV), Marcel·lí Domingo 1, Tarragona, 43007, Spain

²Instituto de Ciencia de Materiales de Madrid, c/ Sor Juana Inés de la Cruz, Cantoblanco,
Madrid, 28049, Spain

Corresponding Author

*joanjosep.carvajal@urv.cat

Abstract

We studied the temperature dependent luminescence of GdVO₄ nanoparticles co-doped with Er³⁺ (1 mol%) and Yb³⁺ (20 mol%) and determined their thermal sensing properties through the fluorescence intensity ratio (FIR) technique. We also analyzed how a silica coating, in a core-shell structure, affects the temperature sensing properties of this material. Spectra were recorded in the range of biological temperatures (298–343 K). The absolute sensitivity for temperature determination calculated for the core-shell nanoparticles is double than the one calculated for bare nanoparticles, achieving a thermal resolution of 0.4 K. Moreover, silica-coated nanoparticles show good dispersibility in different solvents, such as water, DMSO and

methanol. Also, they show good luminescence stability without interactions with solvent molecules. Furthermore, we also observed that the silica coating shell prevents from a progressive heating of the nanoparticles during prolonged excitations periods with the 980 nm laser, preventing effects on their thermometric applications.

KEYWORDS: luminescence, thermometry, core-shell, up-conversion, nanosensors.

1. Introduction

Temperature is the most frequently measured physical property in science, industries and life. Many properties of matter depend on temperature, thus, it is important to monitor it during material processing for controlling the quality of the final products as well as in biomedical areas, where temperature provides basic diagnostic criteria.^{1,2}

To overcome the problems evidenced in conventional contact thermometry methods (invasiveness and big sizes), non-contact thermometry methods have been developed.^{3,4} Among these methods, luminescence nanothermometry, and particularly luminescence nanothermometry based on measurements of the fluorescence intensity ratio (FIR) is particularly interesting, since it can prevent errors in measurements arising from power fluctuations of the excitation source, variations on the concentration of luminescent nanoparticles and inhomogeneities of the material.⁵ The FIR method is based in the Boltzmann distribution of electrons between two adjacent emitting energy levels, that depends on temperature, and is manifested as a temperature-dependent intensity ratio between the emissions arising from two distinct lines in the spectrum. Furthermore, the FIR technique constitutes a self-referencing method to compute the absolute temperature, since one spectrum contains all the information needed, avoiding the use of an internal reference.³

Trivalent lanthanide (Ln)-doped nanoparticles (NPs) are among the most promising candidates for temperature determination through luminescence thermometry. Optically active Ln cations show several narrow absorption and emission lines, some of them from excited states lying very close in energy that can be considered to be thermally coupled. They also show relatively long emission lifetimes, and good chemical and physical stability.⁶⁻⁸

Most of the work developed up to now on ratiometric luminescence nanothermometry by the FIR technique was performed using Er³⁺ doped⁹⁻¹¹ and Er³⁺/Yb³⁺ co-doped materials.^{6,11-18} Er³⁺ shows an efficient green up-conversion emission from two thermally coupled excited states, ²H_{11/2} and ⁴S_{3/2}, upon NIR excitation at 980 nm. Yb³⁺ is used as a sensitizer since it shows a higher absorption cross-section at this wavelength. Furthermore, the energy transfer between Yb³⁺ and Er³⁺ is very efficient. This allows generating a bright emission in the visible, especially in the green. Er³⁺/Yb³⁺ co-doped NPs have been used, for instance, to show the temperature evolution of cancer HeLa cells up to its thermally induced death⁷ or to determine the temperature in human embryo kidney cells.¹⁹

Despite the significant progress achieved in recent years on luminescence thermometry using Ln-doped NPs, there are still several aspects that need to be improved, such as sensitivity to determine smaller temperature changes. For instance, it was demonstrated that the combination of Ln-doped NPs with a thermosensitive polymer can enhance this thermal sensitivity.²⁰ Also, the sensitivity and the temperature sensing range can be tuned in organic-inorganic complexes based on Ln ions just by changing the chelate ligands on the Ln-complexes or the host in which the luminescent centers were embedded.²¹

The benefits of core-shell structures to enhance the emission properties of up-conversion nanoparticles has already been reported.²² Here, we report the enhancement of the luminescence temperature sensitivity in Er,Yb:GdVO₄ nanoparticles coated with a silica shell that allowed to get a thermal resolution of 0.4 K. Furthermore, we probed that the as-synthesized Er,Yb:GdVO₄@SiO₂ core-shell nanoparticles are dispersible in biological compatible fluids that

facilitate their potential biological applications. Finally, we also observed that the silica shell prevents the heating of the luminescent nanoparticles when excited for prolonged periods at 980 nm.

2. Experimental Section

2.1 Synthesis of luminescent nanoparticles.

Crystalline NPs of GdVO_4 codoped with Er^{3+} (1 mol%) and Yb^{3+} (20 mol%) were prepared by a hydrothermal process. Details of the synthesis can be found elsewhere.²³ Shortly, NH_4VO_3 and lanthanide nitrates ($\text{Gd}(\text{NO}_3)_3 \cdot 6\text{H}_2\text{O}$, $\text{Yb}(\text{NO}_3)_3 \cdot 6\text{H}_2\text{O}$, $\text{Er}(\text{NO}_3)_3 \cdot 6\text{H}_2\text{O}$ (Strem Chemicals 99.99%) were used as reactants. The first step involved the preparation of a solution with the required amounts of lanthanide nitrates and NH_4VO_3 in distilled water (40 ml), in which the pH was adjusted to 7 by adding diluted NH_4OH under stirring during 1 h. The yellow dispersion was afterwards hydrothermally treated at 458 K during 24 h in a sealed Teflon-lined autoclave with a capacity of 75 ml. The product obtained was separated by centrifugation, washed several times with distilled water and overnight dried at 393 K in open air.

To improve their emission efficiency, the samples were then annealed to 873 K for 5 h. Further coating of the NPs surface with a layer of silica (SiO_2) ($\text{Er,Yb:GdVO}_4 @ \text{SiO}_2$) was carried out through the base-catalyzed hydrolysis of tetraethoxysilane ($\text{Si}(\text{OC}_2\text{H}_5)_4$, TEOS, Alfa Aesar 99%) and the subsequent condensation of silanol (Si-OH) groups onto the surface of the Er,Yb:GdVO_4 NPs. To do that, a half of the prepared amount of NPs was dispersed in an ethanolic solution (40 ml ethanol absolute 99.5% Emplura Merck + 4 ml distilled water) in which the pH was adjusted to 9 with diluted NH_4OH , and then 2 ml of TEOS were added and kept under stirring for 4 h. The product was finally washed with ethanol, centrifuged and dried to 393 K.

2.2 Structural characterization and particle size determination.

1 mol% Er, 20 mol% Yb:GdVO₄ and 1 mol% Er, 20 mol% Yb:GdVO₄@SiO₂ NPs were characterized by powder X-ray diffraction (XRD) using a Bruker AXS D-8 Advance diffractometer with Cu K α radiation. Transmission electron microscopy (TEM) images were obtained with a JEOL 2000FXII microscope with an accelerating voltage of 200 kV. High resolution TEM (HRTEM) and selected area electron diffraction (SAED) images were obtained with a JEOL model JEM-4000EX microscope, with an accelerating voltage of 400 kV. Hydrodynamic particle size distributions were measured by dynamic light scattering (DLS) using a Vasco 2-Cordouan equipment, with samples dispersed in distilled water. Fourier transform infrared absorption (FT-IR) data were collected on a Nicolet 20SXC spectrophotometer in the range 4000 – 400 cm⁻¹, using KBr to prepare pellets of the analyzed materials.

2.3 Spectroscopic characterization

For the analysis of the temperature dependent up-conversion emission, Er,Yb:GdVO₄ and Er,Yb:GdVO₄@SiO₂ NPs were introduced in a heating stage Linkam THMS 600 that was placed in a homemade microscope setup. An Apollo Instruments Inc diode laser with emission at 980 nm and a power of 100 mW was used as the excitation source. The laser beam was focused on the sample using a microscope objective with 40X magnification and N.A. of 0.6 that produced a laser spot of around 10 μ m on the sample. The emission was collected by the same microscope objective, and after passing a dichroic filter to eliminate the excitation radiation, was collected by an AVANTES AVS-USB2000 fiberoptic spectrometer connected to a computer to record the spectra.

Spectra were also collected using a Labsphere 4GPS-020-SL integrating sphere to compare the intensity of the spectra generated by the different samples, using the same fiberoptic spectrometer described above to record the spectra.

3. Results and Discussion

3.1 Structural characterization

The XRD pattern of the raw 1% Er, 20% Yb:GdVO₄ nanoparticles corresponds to the pure tetragonal *I4₁/amd* zircon-type phase (see Figure 1). By using the Scherrer's equation, the mean individual crystalline domains (also called 'crystallites') calculated from the full width at half maximum (FWHM) of the Bragg peak located at $\sim 25^\circ 2\theta$ is ~ 25 nm, see Figure 1(b). No additional reflections were detected for 1% Er, 20% Yb:GdVO₄@SiO₂ core-shell nanoparticles, see Figure 1(c), although the somewhat rougher background reflects the presence of amorphous SiO₂. The XRD pattern of NPs coated with thicker silica shells (not included in the current study) revealed that the roughness of the background at $18\text{-}32^\circ 2\theta$ was, as expected, considerably accentuated, see Figures S1(a-c) included in the Supplementary Information.

Figures 1(d) and 1(f) display typical TEM images of Er,Yb:GdVO₄ and Er,Yb:GdVO₄@SiO₂ NPs, respectively, mainly with square and rounded sections, and Figures 1(e) and 1(g) display HRTEM images of these samples. Darker interiors and surrounding lighter shells in the TEM and HRTEM images of NPs in Figures 1 (f) and 1(g) correspond to Er,Yb:GdVO₄ cores and their amorphous silica coating, respectively. It is observed that the coating layer has a thickness of ~ 7 nm around the NPs, which mostly retain their initial polygonal or rounded shape. A characteristic TEM image of a sample in which the vanadate NPs were coated with a thicker silica shell can be seen in the Supplementary Information, Figure S2. HRTEM images of discrete NPs reveal in all cases a well-defined single crystal structure, characteristic of the tetragonal *I4₁/amd* symmetry of GdVO₄ (see further images in Figures S3a-d). From the lattice

fringes in Figure S3(a), as well as the corresponding selected area electron diffraction (SAED) pattern in Figure S3(b), the resolved interplanar spacings are found to be about 0.359 nm, consistent with the d -spacing between (200) planes of GdVO_4 (JCPDS File 86-0996).

FT-IR spectra for the raw hydrothermal, 873 K annealed, and annealed and further silica coated 1%Er, 20% Yb:GdVO₄ samples, whose XRD patterns are shown in Figures 1(a-c), are provided in Figures S4(a-c) of the Supplementary Information, along with the discussion for vibronic assignments accounting for the formation of the Ln:GdVO₄@SiO₂ entity, which further probe the silica shell formation on the nanoparticles.

Figures S5(a),(b) included in the Supplementary Information show characteristic results from DLS measurements on the particle size (hydrodynamic size) distribution for both 873 K annealed and ~ 7 nm silica-coated Er, Yb:GdVO₄ samples.

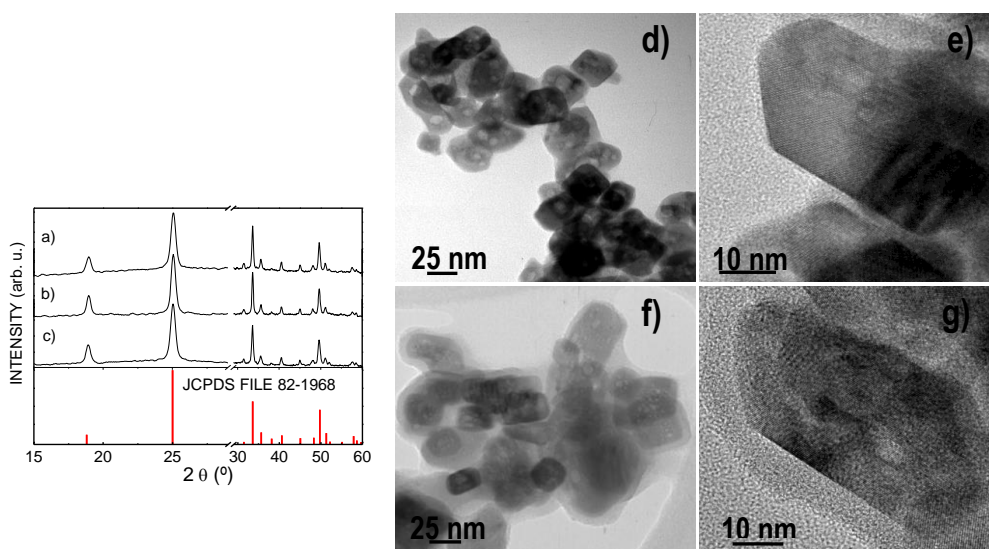


Figure 1. X ray diffraction patterns of (a) raw hydrothermal 1 % Er, 20 % Yb:GdVO₄, (b) 1 % Er, 20 % Yb:GdVO₄ after 873 K thermal annealing during 5 h, and (c) the annealed sample in (b) with further SiO₂ coating, 1 % Er, 20 % Yb:GdVO₄@SiO₂. For comparison, the XRD pattern scheme of tetragonal $I4_1/amd$ YVO₄, JCPDS File 82-1968 has been also included. TEM images of (d) Er, Yb:GdVO₄ and (f) Er, Yb:GdVO₄@SiO₂ nanoparticles. HRTEM images of (e) Er, Yb:GdVO₄ and (g) Er, Yb:GdVO₄@SiO₂ nanoparticles.

3.2 Spectroscopic characterization

Nanoparticles were placed in a borosilicate bottom flat vial and compacted to ensure that they fill the bottom of the vial. This vial was introduced in a sample holder that was placed inside a Labsphere 4GPS-020-SL integrating sphere. Then, the samples were excited with a 200 μm core diameter fiber-coupled laser diode from Apollo Instruments, Inc. emitting at 980 nm. The laser was collimated to a spot size of 3 mm on the sample, and a power of 100 mW. The emission arising from the NPs was collected using an AVANTES AVS-USB2000 fiberoptic spectrometer. The inner part of the integrating sphere is made from a diffusive material that facilitates the luminescence generated by the NPs to spread evenly by multiple reflections over the entire sphere surface before being collected by the detectors. In this way, all the light emitted by the sample is collected by the detector, allowing us to compare the intensity of the emission generated by the different samples.

Figure 2 shows the up-conversion photoluminescence emission spectra of Er,Yb:GdVO_4 and $\text{Er,Yb:GdVO}_4@\text{SiO}_2$ core-shell NPs after excitation at NIR 980 nm collected in the integrating sphere. The up-conversion emission spectra of these samples consist on two main bands centered at 520 and 550 nm, which correspond to the ${}^2\text{H}_{11/2} \rightarrow {}^4\text{I}_{15/2}$ and ${}^4\text{S}_{3/2} \rightarrow {}^4\text{I}_{15/2}$ transitions of the Er^{3+} ion, respectively. Also a weak red band was observed at 640-670 nm, assigned to the ${}^4\text{F}_{9/2} \rightarrow {}^4\text{I}_{15/2}$ transition of Er^{3+} . Splittings of all optical transitions in the Figure 2 are similar to those reported for Er-doped single crystal, indicating that the crystal site for Er^{3+} is kept in the prepared nanoparticles.²³ In Figure 2, however, the emission bands presented are broad, due to the conditions of detection we had to use because of the low intensity of the emissions in the integrating sphere. Since the concentration of doping ions in both cases was identical, Figure 2 represents the comparison of the corresponding fluorescence efficiencies. It can be seen that the emission intensity is higher for $\text{Er,Yb:GdVO}_4@\text{SiO}_2$ core-shell NPs. This enhancement might

be due to the reduction of surface defects on the core-shell NPs due to the presence of the inert SiO₂ coating.²⁴

To further confirm this enhancement of the emission intensity generated by the silica coating, Figures S6(a),(b) in the Supporting Information display the evolution of the integrated intensity of the visible upconverted emissions for Ln, Yb:GdVO₄ NPs as a function of the surface treatment (annealing and silica coating) after the hydrothermal synthesis. As can be seen in the figure, 1% Er, 20%Yb:GdVO₄ NPs coated with a ~7 nm silica shell show the highest upconversion efficiency.

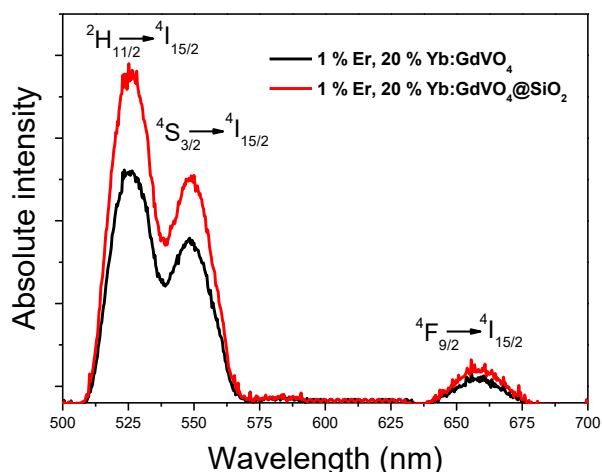


Figure 2. Up-conversion emission spectra of the 1%Er, 20%Yb:GdVO₄ nanoparticles and 1%Er, 20%Yb:GdVO₄@SiO₂ core-shell nanoparticles after excitation at 980 nm.

3.3 Luminescence thermometry

In order to find out the effect of the silica coating on the temperature sensing capabilities of our NPs, we measured the dependence of the up-conversion emission spectra with temperature for both samples in the biological range. This thermal characterization was made using the FIR technique, using the following equation:⁵

$$FIR = \frac{I_1}{I_2} = \frac{g_1 v_1 \sigma_1}{g_2 v_2 \sigma_2} = B \exp\left(-\frac{\Delta E}{k_B T}\right) \quad (1)$$

where g_i , v_i , and σ_i , are the level degeneracy, the spontaneous emission, and the absorption rates, respectively, k_B is the Boltzmann constant, T is the absolute temperature, and ΔE is the energy difference between the two energy states considered.

Figure 3(a) shows the changes in the normalized intensity of the spectra in the green region recorded for the Er,Yb:GdVO₄@SiO₂ core-shell NPs at room temperature and at the maximum temperature analyzed in this work (343 K). As can be seen, while the intensity of the emission arising from the ²H_{11/2} level increases substantially when the temperature increased. Figure 3(b) shows the evolution of the FIR with temperature of both kinds of NPs. In the two cases they follow a linear tendency with regression coefficients of 0.992 and 0.987 for Er,Yb:GdVO₄ and Er,Yb:GdVO₄@SiO₂ core-shell NPs, respectively. The slope is higher for core-shell NPs. This results in a higher absolute sensitivity, calculated as the first derivative of the FIR to respect temperature, as shown in Figure 3(c). The maximum absolute sensitivity of Er,Yb:GdVO₄@SiO₂ core-shell NPs was found to be 1.01 % K⁻¹, almost double than the one obtained for the bare nanoparticles (0.69 % K⁻¹). In order to compare the sensitivity of the Er,Yb:GdVO₄@SiO₂ core-shell NPs with other Er-doped materials for which the FIR technique was applied to determine temperature using the same electronic transitions we used in this work, we calculated the relative sensitivity, as the first derivative of the FIR to respect temperature divided by the FIR. The comparison is presented in Table 1.

Table 1. Comparison of Er-doped materials used for luminescence nanothermometry using the FIR technique in the green region of the electromagnetic spectrum.

Material	Temperature range (K)	Excitation wavelength (nm)	Wavelength ratio	Relative sensitivity %K ⁻¹ (temperature, K)	Thermal resolution (K)	Ref.
Er,Yb:CaF ₂	298-323	920	538/522	2.3	-	25
Er,Yb:Gd ₂ O ₃ /Au NPs	300-1050	980	510-565	1.51	1	12
Er,Yb:PbF ₂	290-325	975	523/548	1.1(310)	-	13

Er,Yb:Fluoride glass	335-375	975	523/548	1.1(342)	0.8	14
Er/Er,Yb:Chalcogenide glass	293-498	1540/1060	530/555	1.05/0.52	0.3/0.5	11
Er,Yb:NaYF ₄	299-336	920	525/545	1.0	-	6
Er,Yb:GdVO ₄ @SiO ₂	297-343	980	520/550	0.94 (343)	0.4	this work
Er:ZnO	273-573	978	536/553	0.62 (443)	-	9
Er:BaTiO ₃	322-466	980	547/526	0.52(333)	-	10
Er,Yb:Al ₂ O ₃	295-973	978	534/549	0.52(476)	0.3	15
Er,Mo:Yb ₃ Al ₅ O ₁₂	395-973	976	522/546	0.48(467)	0.3	25
Er,Yb:Fluoride glass	296-448	1480	522/543	0.4	1	16
Er,Yb:Gd ₂ O ₃	300-900	980	523/548	0.39(300)		17
Er,Yb:silica glass	296-723	978	526/549	0.33(296)	0.2	18

In comparison with other Er-doped materials our results lie in the upper relative sensitive range, with values around 1 % K⁻¹ or higher. Er,Yb:CaF₂²⁵ and Er,Yb:Gd₂O₃/Au¹² NPs show higher relative sensitivities, with values of 2.3 and 1.51 % K⁻¹, respectively, while Er,Yb:PbF₂,¹³ Er,Yb:fluoride¹⁴ and Er:chalcogenide¹¹ glasses, and Er,Yb:NaYF₄⁶ nanoparticles show similar values than Er,Yb:GdVO₄@SiO₂ core-shell nanoparticles. In the case of Er,Yb:PbF₂, despite its high sensitivity, its spatial resolution is limited by the size of the NPs (<500 nm). Thus, the main application proposed for this material is the thermal characterizations of devices.¹³ For the rest of the materials listed in the table, the reported relative sensitivities are lower than that of Er,Yb:GdVO₄@SiO₂ core-shell NPs. In terms of thermal resolution, the 0.4 K that can be achieved with our NPs are only surpassed by the values reported for Er,Yb:silica glass¹⁸, Er,Mo:Yb₃Al₅O₁₂,²⁶ Er,Yb:Al₂O₃¹⁵ and Er/Er,Yb:chalcogenide glass.¹¹ However, in all these cases the thermal resolution was estimated from the sensitivity values, and not measured experimentally. Thus, our results are the first ones to confirm the thermal resolution that can be achieved with Er³⁺-based up-conversion nanoparticles.

Apart from the data included in the table, it is also worthy to note that Sedlmeier et al. analyzed the luminescent thermometric properties of Er,Yb:NaYF₄@NaYF₄ core-shell nanoparticles, capped with citric acid (CA), and compared them with those of bare

Er,Yb:NaYF₄ nanoparticles capped with ethylene diamine tetraacetic acid (EDTA) and CA.²⁷ The slope of the FIR ratio in the three cases was similar, being a little smaller for Er,Yb:NaYF₄ NPs capped with CA, but no difference was found between Er,Yb:NaYF₄@NaYF₄ core-shell CA-capped NPs and Er,Yb:NaYF₄ EDTA-capped NPs. Only the thermal resolution was improved by 5 times when the NaYF₄ shell was used, although again, the thermal resolution was estimated from the FIR adjusted curves.

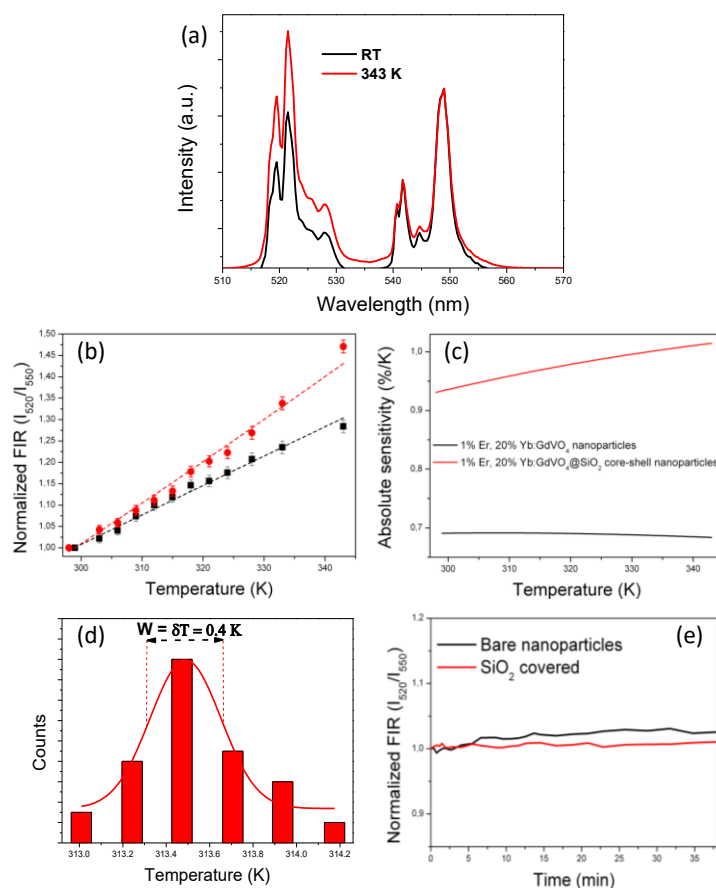


Figure 3. (a) Evolution of the intensity of the emission spectra of Er³⁺ in the green region obtained from Er,Yb:GdVO₄@SiO₂ NPs; (b) $I[{}^2\text{H}_{11/2}]/I[{}^4\text{S}_{3/2}]$ FIR as the function of temperature for Er,Yb:GdVO₄ and Er,Yb:GdVO₄@SiO₂ NPs; (c) Comparison of absolute sensitivity values for both kind of NPs; (d) Thermal resolution measured for Er,Yb:GdVO₄@SiO₂ NPs; (e) Time evolution of the intensity ratio for Er,Yb:GdVO₄ and Er,Yb:GdVO₄@SiO₂ NPs.

To know the minimum temperature change that Er,Yb:GdVO₄@SiO₂ NPs can discriminate, we collected 60 consecutive emission spectra at a fixed temperature (313 K) in the Linkam 600 heating stage, controlled with its embedded thermocouple. In this way we were able to determine the range of variability in the measurements.²⁸ Then, we calculated the temperature corresponding to each spectra using the calibration curve shown in Figure 3(b). This results in a Gaussian distribution of temperatures centered at 313.5 K with a FWHM of 0.4 K, as can be seen in Figure 3(d). This gives an estimation of the thermal resolution that can be achieved in a measurement with these NPs.

We also analysed the effect of the illumination during a prolonged time with the 980 nm laser. For this, we introduced the NPs in the Linkam 6000 heating stage, although we kept the nanoparticles at room temperature, and recorded the luminescent spectra at intervals of 10 s during 40 min. By calculating the FIR for each spectra and comparing it with the calibration curve displayed in Figure 3(b), we could plot the temporal evolution of the FIR, as can be seen in Figure 3(e). It can be seen in this graph that the FIR corresponding to the core-shell NPs remains constant under the pumping laser at 980 nm over an extended illumination period, while for the bare NPs the FIR increases, slightly but continuously, with time. This would indicate that the population of the ²H_{11/2} electronic level would increase when the exposure to the excitation laser is prolonged, and thus that the Er,Yb:GdVO₄ NPs increase their own temperature, introducing an incorrect temperature determination. In the graph it can also be observed that these effects are evident after 7 min of continuous excitation. We repeated this experiment several times to confirm this effect, observing always similar results. Also, since the NPs were located in the heating stage during the experiment, we could also use the screen of the controller of this device to monitor the temperature evolution, measured in that case by the internal thermocouple of the heating stage, observing the same tendency. So, an additional benefit of the silica shell with which we coated our Er,Yb:GdVO₄ nanoparticles is that it dissipates more

effectively the heat generated in the body of NPs by the excitation laser, avoiding their heating, and providing a more stable thermal probe.

3.4 Dispersibility in different solvents

An additional advantage of the SiO₂ coating in our nanoparticles is that it allows stabilising H bridge bonds with protic polar solvents, like H₂O or methanol (CH₃OH), or van der Waals weak interactions with aprotic polar solvents, like dimethyl sulfoxide (DMSO, CH₃SOCH₃). This would allow the dispersion of the Er,Yb:GdVO₄@SiO₂ core-shell NPs in these kinds of solvents. We tested the possibility of dispersing our core-shell nanoparticles in these three solvents. For that, 10 mg of Er,Yb:GdVO₄@SiO₂ nanoparticles were dispersed in 10 ml of H₂O, methanol and DMSO, respectively, with the aid of an ultrasonic bath, and observed their sedimentation as a function of time. The results are shown in Figure 4(a). In general, the nanoparticles show a good stability in the three solvents analyzed, although after 24 h, it was reduced significantly in DMSO. These results indicate that Er,Yb:GdVO₄@SiO₂ NPs might be dispersed, if required in biological compatible fluids for temperature determination in biomedical applications.

We also analyzed how the different solvents affected to the up-conversion emission properties of Er,Yb:GdVO₄@SiO₂ NPs, and thus, to the FIR calculated from their spectra. Figure 4(b) shows the emission spectra corresponding to the NPs dispersed in water, methanol and DMSO, normalized to the intensity of the ⁴S_{3/2} → ⁴I_{15/2} band. The emission spectrum corresponding to the dry NPs, measured under the same experimental conditions, is also included for comparison. As can be seen in this graph, the emission intensity of the band located at 520 nm decreases when the NPs are dispersed in a solvent. This might be attributed to more efficient non-radiative relaxation processes in that case that depopulate the ⁴S_{3/2} level of Er³⁺ towards lower energy emitting levels because of the interactions established with the solvation molecules. This also

affects to the I_{520} / I_{550} FIR, as can be seen in Figure 4(c), which is reduced by 20 % when compared to that of the powder not dispersed in any solvent. This reduction seems to be similar for NPs dispersed in any of the three solvents analysed in this study, with the smallest values attained in water and DMSO that have a higher dipolar moment.

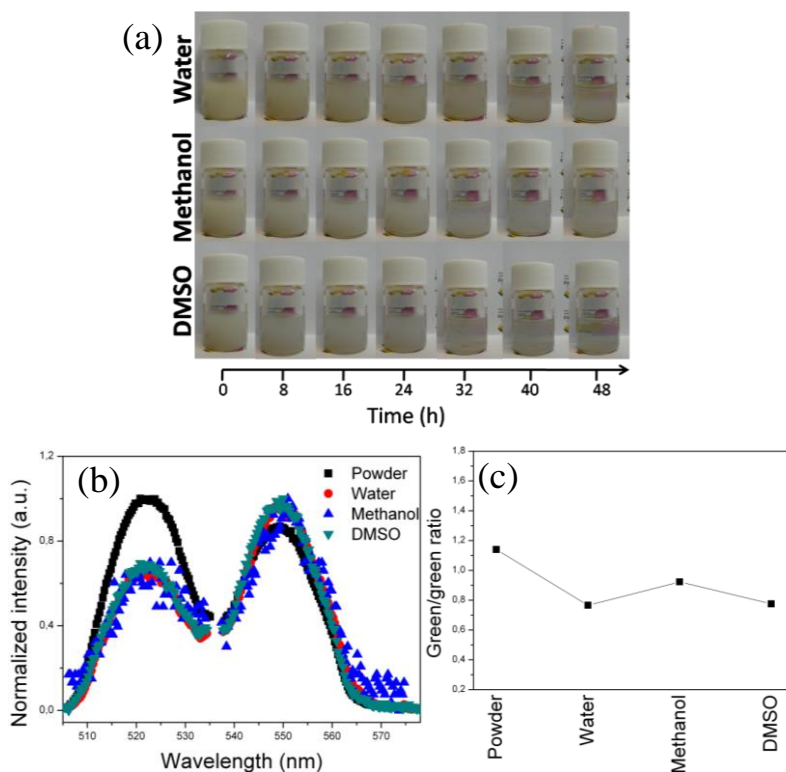


Figure 4.(a) Time evolution of the sedimentation of Er,Yb:GdVO₄@SiO₂ nanoparticles dispersed in water, methanol and DMSO; (b) Up-conversion emission spectra of Er,Yb:GdVO₄@SiO₂ nanoparticles in different solvents normalized in intensity to the $^4S_{3/2} \rightarrow ^4I_{15/2}$ band; (c) Green-to-green ($^2H_{4/2} \rightarrow ^4I_{15/2}$ to $^4S_{3/2} \rightarrow ^4I_{15/2}$) emission intensity ratios calculated for the core-shell nanoparticles dispersed in the different solvents.

3.5 Ex-vivo experiment to monitor temperature evolution

To probe the potentiality of the use of Er,Yb:GdVO₄@SiO₂ core-shell nanoparticles for temperature changes investigation in biological systems, we injected an aqueous dispersion of the nanoparticles (1 wt %) in fresh chicken breast at the depth of around 1-2 mm. A heating gun was used to heat the chicken breast. We monitored the temperature change induced in the

chicken breast by observing the luminescence emitted by the injected nanoparticles after excitation with an Apollo Instruments Inc diode laser with emission at 980 nm and a power of 100 mW. The laser was focused on the chicken breast by means of a microscope objective with 40X magnification and N.A. of 0.6. The emission arising from the nanoparticles was collected by the same objective, and after passing a dichroic filter for elimination of the excitation wavelength, was sent to an AVANTES AVS-USB2000 fiberoptic spectrometer connected to a computer to record the spectra. The analysis of the emission spectra and their comparison with the calibration line (see Figure 3b), the temperature was deduced. Moreover, in order to verify the data, the temperature evolution of the chicken breast was also recorded by a digital multimeter connected to the small thermo-resistor Pt-100 located inside the chicken breast, close to the injected nanoparticles. The scheme of the setup is shown in Figure 5a.

The evolution of the temperature with time, during the induced heating process, monitored by using the luminescent nanoparticles and the thermo-resistor Pt-100 are shown in Figure 5b. A fast increase of temperature was clearly observed in both cases. Despite a time delay can be observed in the monitoring process between the thermos-resistor and the luminescent nanoparticles, it is smaller than 1 min, and when the thermal equilibrium is reached, both systems show the same temperature (313 K, with an error of 0.03 K). This experiment demonstrates the potentiality of using Er,Yb:GdVO₄@SiO₂ core-shell nanoparticles for temperature determination purposes in *ex-vivo* biomedical applications with a good thermal resolution.

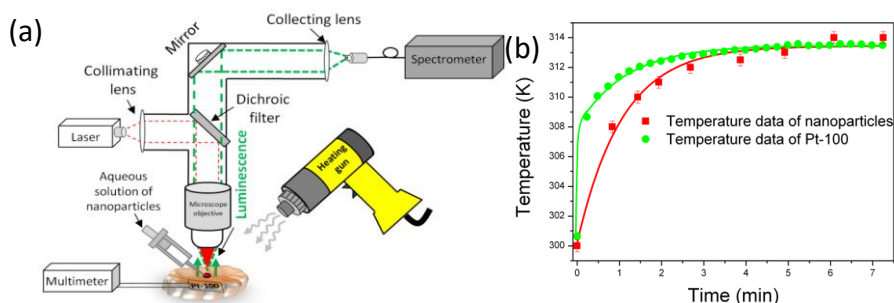


Figure 5. (a) Scheme of the setup for the *ex-vivo* temperature determination experiment; (b) temporal evolution of temperature during the induced heating process in the chicken breast monitored by the Er,Yb:GdVO₄@SiO₂ core-shell nanoparticles and a thermo-resistor Pt-100. Lines were plotted to help the reader to follow the temperature evolution.

4. Conclusions

In conclusion, Er,Yb:GdVO₄@SiO₂ core-shell NPs can be used as an efficient luminescence temperature sensor. To the best of our knowledge, we have demonstrated for the first time the benefits of a SiO₂ coating on the luminescent thermometric properties. By using a SiO₂ coating, we achieved a ×2 enhancement of the thermal sensitivity. Moreover, the SiO₂ shell protects the NPs from overheating during the excitation process. Also, we demonstrated that a high thermal resolution can be achieved using these core-shell NPs. The spatial resolution is estimated to be of the order of the size of the core-shell NPs. Good stability in different solvents, like water, methanol and DMSO, make possible to use them as a temperature sensor in biological applications, as the one we reported to monitor an induced heating process in an *ex-vivo* experiment.

ASSOCIATED CONTENT

SUPPORTING INFORMATION:

Figure S1. X-ray powder diffraction patterns of 1%Tm, 15%Yb:GdVO₄ nanoparticles: a) raw sample prepared by 24 h of hydrothermal synthesis at 185 °C; b) sample after thermal annealing at 873 K during 5 h; c) annealed sample with further coating with a layer of 15-20 nm of silica. For comparison, the X-ray pattern scheme of tetragonal *I4₁/amd* GdVO₄, JCPDS File 86-0996 has been also included in d).

Figure S2. TEM image of hydrothermal Tm, Yb:GdVO₄ sample prepared as for the title samples, annealed at 873 K during 5 h and then coated with a thick shell of SiO₂

Figure S3. a) HRTEM image of a polygonal nanoparticle prepared by hydrothermal treatment at 185°C during 24 h and then annealed at 873 K; b) The corresponding SAED pattern along the [004] zone axis; c) and d) HRTEM images of nanoparticles annealed and coated with a silica shell (light amorphous area around the polygonal nanoparticle).

Figure S4. Comparison of room temperature FT-IR spectra of nanocrystalline tetragonal vanadate samples: a) bare hydrothermal (24h at 185 °C) prepared sample, b) hydrothermal sample annealed at 873 K during 5 h, c) sample as in b) with further surface coating with a ~7 nm shell of SiO₂.

Figure S5. Distribution by number of the hydrodynamic size of particles in hydrothermal Er, Yb:GdVO₄: a) after annealing at 873 K for 5 h, and b) after annealing at 873 K for 5 h and coating with a ~7 nm shell of SiO₂.

Figure S6. Evolution of integrated upconverted luminescence in nanocrystalline 1%Ln, x%Yb:GdVO₄ with processing for surface treatments after the hydrothermal synthesis: a) green bands corresponding to ²H_{11/2}, ⁴S_{3/2}→⁴I_{15/2} Er³⁺ transitions, b) blue band corresponding to ¹G₄→³H₆ Tm³⁺ transition. NA = bare non annealed hydrothermal sample, A = annealed at 873 K during 5 h, A+@7 nm SiO₂ = annealed and 7 nm-SiO₂ coated sample, A+@15-20 nm SiO₂ = annealed and 15-20 nm-SiO₂ coated sample.

AUTHOR INFORMATION

Corresponding Author: joanjosep.carvajal@urv.cat

Authors Contributions

The manuscript was written through contributions of all authors. All authors have given approval to the final version of the manuscript

Notes

The authors declare no competing financial interests.

ACKNOWLEDGMENTS

This work was supported by the Spanish Government under Projects No. MAT2013-47395-C4-4-R, TEC2014-55948-R and MAT2014-56607-R, and by Catalan Authority under Project No. 2014SGR1358. Ol. A. Savchuk is supported by Catalan Government through the fellowship

2015FI B2 00136. F.D. acknowledges additional support through the ICREA Academia award 2010ICREA-02 for excellence in research.

REFERENCES

- (1) Hildebrandt, B.; Wust, P.; Ahlers, O.; Dieing, A.; Sreenivasa, G.; Kerner, T.; Felix R.; and Riess, H. The Cellular and Molecular Basis of Hyperthermia. *Crit. Rev. Oncol. Hematol.* **2002**, *43*, 33–56.
- (2) Roti Roti, J. L. Cellular Responses to Hyperthermia (40-46 degrees C): Cell Killing and Molecular Events. *Int. J. Hyperthermia* **2008**, *24*, 3–15.
- (3) Brites, C. D. S.; Lima, P. P.; Silva, N. J. O.; Millan, A.; Amaral, V. S; Palacio, F.; and Carlos, L. D. Thermometry at the Nanoscale. *Nanoscale* **2012**, *4*, 4799-4829.
- (4) Jaque, D.; Vetrone, F. Luminescence Nanothermometry. *Nanoscale* **2012**, *4*, 4301–4326.
- (5) Wade, S. A.; Collins, S. F.; Baxter, G. W. The Fluorescence Intensity Ratio Technique for Optical Fiber Point Temperature Sensing. *J. Appl. Phys.* **2003**, *94*, 4743-4756.
- (6) Vetrone, F.; Naccache, R.; Zamarron, A.; de la Fuente, A. J.; Sanz-Rodriguez, F.; Maestro, L. M.; Rodriguez, E. M.; Jaque, D.; Sole, J. G.; Capobianco, J. A. Temperature Sensing at the Nanoscale using Fluorescent Nanothermometers. *ACS Nano* **2010**, *4*, 3254–3258.
- (7) Vetrone, F.; Naccache, R.; de la Fuente, A. J.; Sanz-Rodriguez, F.; Blazquez-Castro, A.; Rodriguez, E. M.; Jaque, D.; Sole, J. G.; Capobianco, J. A. Intracellular Imaging of HeLa Cells by Non-Functionalized NaYF₄:Er³⁺,Yb³⁺ Upconverting Nanoparticles. *Nanoscale* **2010**, *2*, 495–498.
- (8) Haro-Gonzalez, P.; Maestro, L. M.; Trevisani, M.; Polizzi, S.; Jaque, D.; Sole, J. G.; Bettinelli, M. Evolution of Rare Earth Doped Silica Sub-Micrometric Spheres as Optically Controlled Temperature Sensors. *J. Appl. Phys.* **2012**, *112*, 054702-054709.

- (9) Wang, X.; Kong, X. G.; Yu, Y.; Sun, Y. J.; Zhang, H. Effect of Annealing on Upconversion Luminescence of ZnO:Er³⁺ Nanocrystals and High Thermal Sensitivity. *J. Phys. Chem. C* **2007**, *111*, 15119–15124.
- (10) Alencar, M. A. R.; Maciel, G. S.; de Araújo, C. B.; Patra, A. Er³⁺-Doped BaTiO₃ Nanocrystals for Thermometry: Influence of Nanoenvironment on the Sensitivity of a Fluorescence Based Temperature Sensor. *Appl. Phys. Lett.* **2004**, *84*, 4753–4755.
- (11) dos Santos, P. V.; de Araujo, M. T.; Gouveia-Neto, A. S.; Neto, J. A. M.; Sombra, S. B. Optical Thermometry Through Infrared-Excited Upconversion Fluorescence Emission in Er³⁺ and Er³⁺-Yb³⁺-doped Chalcogenide Glasses. *IEEE J. Quantum Electron.* **1999**, *35*, 395–399.
- (12) Debasu, M. L.; Ananias, D.; Pastoriza-Santos, I.; Liz-Marzán, L. M.; Rocha, J.; Carlos, L. D. All-in-One Optical Heater-Thermometry Nanoplatfom Operative From 300 to 2000 K Based in Er³⁺ Emission and Blackbody Radiation. *Adv. Mater.* **2013**, *25*, 4868–4874.
- (13) Aigouy, L.; Saidi, E.; Lalouat, L.; Labeguerie-Egea, J.; Mortier, M.; Low, P.; Bergaud, C. AC Thermal Imaging of a Microwire with a Fluorescent Nanocrystal: Influence of the Near Field on the Thermal Contrast. *J. Appl. Phys.* **2009**, *106*, 074301-074310.
- (14) Saïdi, E.; Samson, B.; Aigouy, L.; Volz, S.; Low, P.; Bergaud, C.; Mortier, M. Scanning Thermal Imaging by Near-Field Fluorescence Spectroscopy. *Nanotechnology* **2009**, *20*, 115703.
- (15) Li, C. R.; Dong, B.; Ming, C. G.; Lei, M. Application to Temperature Sensor Based on Green Up-Conversion of Er³⁺ Doped Silicate Glass. *Sensors* **2007**, *7*, 2652–2659.
- (16) Maciel, G. S.; Menezes, L. d. S.; Gomes, A. S. L.; de Araujo, C. B.; Messaddeq, Y.; Florez, A.; Aegerter, M. A. Temperature Sensor Based on Frequency Upconversion in Er³⁺-Doped Fluoroindate Glass. *IEEE Photonics Technol. Lett.* **1995**, *7*, 1474–1476.

- (17) Singh, S. K.; Kumar, K.; Rai, S. B. Er³⁺/Yb³⁺Codoped Gd₂O₃Nano-Phosphor for Optical Thermometry. *Sens. Actuators A* **2009**, *149*, 16–20.
- (18) Li, C. R.; Dong, B.; Li, S. F.; Song, C. Er³⁺-Yb³⁺ Co-Doped Silicate Glass for Optical Temperature Sensor. *Chem. Phys. Lett.* **2007**, *443*, 426–429.
- (19) Fischer, L. H.; Harms, G. S.; Wolfbeis, O. S. Upconverting Nanoparticles for Nanoscale Thermometry. *Angew. Chem. Int. Ed.* **2011**, *50*, 4546–4551.
- (20) Huang, J.; He, B.; Cheng, Z.; Zhou, L. *J. Lumin.* **2015**, *160*, 254–257.
- (21) Brites, C. D. S.; Lima, P. P.; Carlos, L. D. *J. Lumin* **2015**
<http://dx.doi.org/10.1016/j.jlumin.2015.01.025>.
- (22) Prorok, K.; Bednarkiewicz, A.; Cichy, B.; Gnach, A.; Misiak, M.; Sobczyk, M.; Streck, W.; The Impact of Shell Host (NaYF₄/CaF₂) and Shell Deposition Methods on the Up-Conversion Enhancement in Tb³⁺, Yb³⁺Codoped Colloidal α-NaYF₄ Core-Shell Nanoparticles. *Nanoscale* **2014**, *6*, 1855–1864.
- (23) Bertini, C.; Toncelli, A.; Tonelli, M.; Cavalla, E.; and Magnani, N. *J. Lumin.* **2004**, *106*, 235–242.
- (24) Calderon-Villajos, R.; Zaldo, C.; and Cascales, C. Enhanced Upconversion Multicolor and White Light Luminescence in SiO₂-Coated Lanthanide-Doped GdVO₄ Hydrothermal Nanocrystals. *Nanotechnology* **2012**, *23*, 505205–505215.
- (25) Dong, N. N.; Pedroni, M.; Piccinelli, F.; Conti, G.; Sbarbati, A.; Ramírez-Hernández, J. E.; Martínez Maestro, L.; Iglesias-de la Cruz, M.C.; Sanz-Rodriguez, F.; Juarranz, A.; Chen, F.; Vetrone, F.; Capobianco, J. A.; García Solé, J.; Bettinelli, M.; Jaque, D.; and Speghini, A. *ACS Nano* **2011**, *5*, 8665–8671.
- (26) Dong, B.; Cao, B.; He, Y.; Liu, Z.; Li, Z.; Feng, Z. Temperature Sensing and In Vivo Imaging by Molybdenum Sensitized Visible Upconversion Luminescence of Rare-Earth Oxides. *Adv. Mater.* **2012**, *24* 1987–1993.

- (27) Sedlmeier, A.; Achatz, D.E.; Fischer, L.H.; Gorris, H.H.; Wolfbeis, O.S. *Nanoscale* **2012**, *4*, 7090-7096.
- (28) Wang, Z.; Ananias, D.; Carne-Sanchez, A.; Brites, C. D. S.; Imaz, I.; Maspoch, D.; Rocha, J.; and Carlos, L. D. *Adv. Func. Mater.* **2015**, *25* 2824-283.

CHAPTER 5

Luminescence nanothermometry in the NIR

The near infrared region of the electromagnetic spectrum, with wavelengths from 650 – 980 nm, is known as the first biological window (I-BW), and is of interest for luminescence nanothermometry due to the reduced scattering and minimal absorption of biological tissues in this spectral region, achieving a deeper penetration depth when compared to visible radiation. The range of wavelengths from 1000 – 1400 nm is known as the second biological window (II-BW). At this spectral window, the absorption of water is larger than in the I-BW, but optical scattering is minimized because of the longer wavelengths. Thus, even a deeper penetration in biological tissues can be achieved when compared to the I-BW. The range of wavelengths from 1400 – 2300 nm is known as the short wavelength infrared (SWIR) region. This region has not explored for luminescence nanothermometry, but bioimaging tests performed at 1-5 mm indicate that brighter images and deeper penetrations can be achieved specially in melanin-containing tissues due to reduced absorbance and scattering within this region.

In this chapter we present the use of the upconversion emission generated by Tm^{3+} , $\text{Yb}^{3+}:\text{GdVO}_4$ core-shell nanoparticles and located at the I-BW for thermal sensing purposes. We investigated the evolution of the intensity of the emission lines located at 700 and 800 nm, arising from two thermally coupled energy levels of Tm^{3+} , with temperature. Due to the silica coating, these nanoparticles are dispersible in water for long periods. This allowed us to internalize these $\text{Tm}^{3+}, \text{Yb}^{3+}:\text{GdVO}_4$ core-shell nanoparticles in the HeLa cells. The obtained results prove the potentiality of the use of these $\text{Tm}^{3+}, \text{Yb}^{3+}:\text{GdVO}_4@\text{SiO}_2$ core-shell nanoparticles in temperature sensing applications and bioimaging.

Also, we investigated the photoluminescence properties of $\text{Nd}^{3+}:\text{KGd}(\text{WO}_4)_2$ nanoparticles for temperature sensing purposes. Under excitation at 808 nm, they exhibited strong emission bands at 883 nm and 1067 nm in the NIR region lying in the I- and II-BWs, respectively. The temperature dependence of the intensity of luminescence of these nanoparticles showed a linear increase of the fluorescence intensity ratio in both cases, which simplifies the calibration procedures to use them as luminescent nanothermometers. Finally, the surface of these nanoparticles was functionalized using 3-Aminopropyltriethoxysilane, which allowed their deagglomerating and their dispersion in aqueous solutions for future applications in biological systems. A penetration depth up to 1 cm was achieved with these nanoparticles at 1075 nm. We believe that such deep penetration depth might be related to the high absorption cross-section of lanthanide ions in the $\text{KGd}(\text{WO}_4)_2$ host. Hence, $\text{Nd}^{3+}:\text{KGd}(\text{WO}_4)_2$ nanoparticles are promising new material for nanothermometry applications operating in the II-BW.

Finally, we have studied the infrared emissions lying in the SWIR region generated by Er^{3+} and Tm^{3+} ions sensitized by Yb^{3+} in different host matrices after excitation at 980 and 808 nm (only in the case of Tm^{3+}) for luminescence nanothermometry purposes. The excitation of Tm^{3+} at 808 nm provides an additional advantage for biological applications, since it lies in the I-BW. The 1.55 μm emission band generated by Er^{3+} ion presents different Stark sub-levels that are thermally coupled and that can be used in the temperature sensing purposes. This emission can be also used to detect temperature changes in telecommunications system. $\text{Er}^{3+}, \text{Yb}^{3+}:\text{NaY}_2\text{F}_5\text{O}$ nanoparticles show the highest thermal sensitivity ($0.15\% \text{ K}^{-1}$). In the case of $\text{Tm}^{3+}, \text{Yb}^{3+}$ co-doped systems, the $\text{Tm}^{3+} {}^3\text{F}_4$ and ${}^3\text{H}_4$ energy levels are electronically coupled and the intensity ratio between the emission bands arising from them and located at 1.45 and 1.8 μm can be used for luminescence nanothermometry purposes, showing a linear increase with temperature. $\text{Tm}^{3+}, \text{Yb}^{3+}:\text{NaYF}_4$ nanoparticles were found to have the highest thermal sensitivity among other $\text{Tm}^{3+}, \text{Yb}^{3+}$ co-doped systems. Adding Ho^{3+} to the system generates an efficient energy transfer between Tm^{3+} and Ho^{3+} , resulting in the generation of a new emission band centered at 1.96 μm . The intensity ratio between the Tm^{3+} emission at 1.45 μm and the Ho^{3+} emission at 1.96 μm provides a new a channel for luminescence thermometry with a good thermal sensitivity.

Paper X

Savchuk, Ol. A.; Carvajal, J. J.; Cascales, C.; Haro-González, P.; Aguiló, M.; and Díaz, F. *NIR-to-NIR upconversion emissions of $Tm^{3+}, Yb^{3+}:GdVO_4@SiO_2$ core-shell nanoparticles for temperature sensing purposes and imaging in the first biological window* (2016) To be submitted to *Advanced Functional Materials*.

NIR-to-NIR upconversion emissions of $Tm^{3+}, Yb^{3+}:GdVO_4@SiO_2$ core-shell nanoparticles for temperature sensing purposes and imaging in the first biological window

Ol. A. Savchuk,¹ J. J. Carvajal,^{1} C. Cascales² P. Haro-Gonzalez,³ F. Sanz-Rodriguez,^{3,4} M. Aguilo,¹ and F. Diaz¹*

¹Física i Cristal·lografia de Materials i Nanomaterials (FiCMA-FiCNA) –EMaS, Universitat Rovira i Virgili (URV),
Campus Sescelades, Marcel·li Domingo 1, E-43007 Tarragona, Spain

²Instituto de Ciencia de Materiales de Madrid, c/ Sor Juana Ines de la Cruz, Cantoblanco, Madrid, 28049, Spain

³Fluorescence Imaging Group, Departamento de Física de Materiales, Facultad de Ciencias, Universidad Autónoma de
Madrid, 28049 Madrid, Spain

⁴Departamento de Biología, Facultad de Ciencias. Campus de Cantoblanco. Universidad Autónoma de Madrid. Madrid
28049, Spain

*corresponding author: joanjosep.carvajal@urv.cat

Abstract

We investigated the possibilities of using the upconversion emissions generated in the first biological window by $Tm, Yb:GdVO_4@SiO_2$ core-shell nanoparticles for temperature sensing purposes in the physiological range of temperatures. The two emission lines located at 700 and 800 nm, that lie in the first biological window, and arising from the thermally coupled $^3F_{2,3}$ and 3H_4 energy levels of Tm^{3+} , respectively, were identified to have potential to develop a luminescent thermometer operating by the FIR technique, with a very high thermal sensitivity of $2.26 \% K^{-1}$. Since the inert silica shell surrounding the luminescent active core allowed dispersing these nanoparticles in water and biological compatible fluids, we investigated the penetration depth that can be achieved with the emissions in the NIR arising from these core-shell nanoparticles in biological tissues, achieving a value of 1.6 mm, and internalized them in HeLa cells, proving their potentiality for biolabelling applications.

1. Introduction

Accurate temperature measurements at the nanoscale are important in many industrial processes as well as in medicine.^[1,2] Sometimes, the area in which the temperature has to be measured is difficult or even impossible to reach. In this context, noncontact thermometry can be used. Among the different noncontact thermometry techniques, luminescent thermometry offers high spatial and thermal resolutions.^[3,4] By using luminescent thermometry, for instance,

it would be possible to detect cancer cells at an early stage of development just monitoring the temperature increase in the body due to the enhanced metabolic activities in abnormal cells.^[2] Moreover, luminescent thermometry has been used to control the temperature reached during the photothermal therapy of a tumor, avoiding the potential damage caused by overheating.^[5] All this has become possible with the development of materials whose luminescent properties strongly depend on small changes of the local temperature and whose luminescence emission bands lie in the so called biological windows (BW).^[6]

There are two BW that are mostly used for bioimaging^[7-9] and temperature control of photothermal therapy.^[5] The first BW (I-BW) lays in the range 650 – 950 nm, where the optical absorption of biological tissues, and especially the optical absorption of water, is minimized.^[10] The second BW (II-BW) lays in the range 1000 - 1350 nm, where the Rayleigh and Mie scatterings are reduced.^[11]

Lanthanide-doped upconversion nanoparticles, that emit light at shorter wavelengths than the light they absorbed, emerged as potential candidates for luminescence thermometry since they possess a long range of emissions from the ultraviolet (UV) to the near infrared (NIR).^[12] Moreover, they do not exhibit photobleaching effects,^[13] they can be excited with low cost NIR laser diodes with emission also lying in the BWs, they offer an enhanced penetration depth in biological tissues when operating in the BWs, and also they allow avoiding the autofluorescence from biological tissues generated by UV light, as it happens with conventional quantum dots or organic dyes.^[14] It has been reported the potentiality of using NIR-to-NIR upconversion transitions in Tm^{3+} and Yb^{3+} doped fluoride nanophosphors, which enables high cellular contrast and tissue imaging.^[15] Also, Dong and co-workers have performed cellular imaging and temperature sensing experiments using $Tm,Yb:CaF_2$ nanoparticles, demonstrating that the NIR emissions from Tm^{3+} lead to a deeper penetration.^[16] However, for temperature calibration, they used thermally coupled sub-Stark energy levels, with low energy gaps that reduces sensitivity to temperature changes.

One of the main problems of upconversion nanoparticles is their low quantum efficiency, which in addition suffer from the large surface area containing defects and luminescence quenchers. One of the ways to reduce these energy losses is to coat them with an appropriate inert shell material.^[17] Furthermore, the inert shell can increase the hydrophilic properties of nanoparticles, facilitating their dispersion in biological compatible fluids, and protect them from the quenching caused by differences in pH and calcium levels in biological tissues and living cells.^[18]

Here, we present a study of the temperature dependent upconversion emissions of $\text{Tm,Yb:GdVO}_4@\text{SiO}_2$ core-shell nanoparticles lying in the I-BW. Different concentrations of Tm^{3+} as the active ion were studied in order to optimize the thermal sensing capabilities. The silica coating of the nanoparticles increases the intensity of their upconversion emissions and makes them dispersible in biological compatible fluids like PBS. The results presented prove the potentiality of the use $\text{Tm,Yb:GdVO}_4@\text{SiO}_2$ core-shell nanoparticles in NIR-to-NIR temperature sensing applications and bioimaging.

2. Experimental techniques

Synthesis of $\text{Tm,Yb:GdVO}_4@\text{SiO}_2$ core-shell nanoparticles

Samples (2 mmol) with composition $\text{Gd}_{0.85-x}\text{Yb}_{0.15}\text{Tm}_x\text{VO}_4$ ($x = 0.5 - 3$ mol %) have been prepared by soft hydrothermal synthesis. Rare earth sesquioxides (Gd_2O_3 , Yb_2O_3 , Tm_2O_3 , Strem Chemicals, 99.9%) and ammonium metavanadate NH_4VO_3 (Sigma Aldrich 99%) were used as starting reagents. Ln^{3+} -nitrates were firstly prepared by dissolving together the required stoichiometric amounts of corresponding sesquioxides in a solution of nitric acid (10 ml of distilled water and 10 ml of 69% HNO_3), which was heated until complete dryness. Then, the Ln^{3+} -nitrates were dissolved in 10 ml of distilled water and added to a solution of NH_4VO_3 in 20 ml of distilled water, the pH adjusted to 7 with diluted NH_4OH , and after 15 min of magnetic stirring the pale yellow dispersion was in each case heated at 458 K for 24 h in a Teflon-lined autoclave. The product resulting from the hydrothermal reaction was collected by centrifugation, washed with distilled water several times, and dried overnight at 393 K. With the aim of removing surface defects associated with wet low-temperature synthesis as well as to promote a better crystallization, the prepared samples were annealed to 873 K for 5 h. To achieve a further improvement of the optical emission efficiency, the obtained nanoparticles (NPs) were coated with a SiO_2 layer of controlled thickness. In brief, the process was carried out by dispersing the above NPs (1.5 mmol) in an ethanolic (40 ml ethanol absolute 99.5% Emplura Merck + 4 ml distilled water) solution with the pH adjusted to 9 with 0.75 ml of NH_4OH , and then 2 ml of tetraethoxysilane ($\text{Si}(\text{OC}_2\text{H}_5)_4$, TEOS, Alfa Aesar 99%) were slowly added under stirring, which was maintained for 4 h, and finally the product was washed with ethanol, centrifuged and dried to 423 K.

Structural and morphological characterization

The characterization of the crystalline phase for each prepared Tm,Yb:GdVO_4 composition and then for corresponding $\text{Tm,Yb:GdVO}_4@\text{SiO}_2$ core-shell structures was carried

out at room temperature by powder X-ray diffraction (XRD) performed on a Bruker AXS D-8 Advance diffractometer using Cu K α radiation.

Transmission electron microscopy (TEM) images were obtained with a JEOL JEM2100 microscope, with an accelerating voltage of 200 kV, and high resolution TEM (HRTEM) images with a JEOL JEM3000F microscope operating at 300 kV.

Further characterization data of hydrodynamic particle size distributions measured by dynamic light scattering (DLS), and Fourier transform infrared absorption (FT-IR) spectra to determine the possible presence of adsorbed species at the NPs surface as well as to account for the formation of the Tm,Yb:GdVO $_4$ @SiO $_2$ entity, can be consulted elsewhere.

Temperature-dependent photoluminescence measurements

For temperature dependent photoluminescence measurements the Tm,Yb:GdVO $_4$ @SiO $_2$ core-shell nanoparticles were placed in a Linkam THMS 600 heating stage and excited by a fiber-coupled laser diode with emission at 980 nm and a power of 50 mW. The laser beam was focused on the sample by a 40X microscope objective with N.A. = 0.6 providing a spot size of around 10 μ m on the sample. The emission was collected by the same microscope objective, and after passing a dichroic filter to eliminate the excitation wavelength, was sent to an AVANTES AVS-USB2000 fiberoptic spectrometer for recording the emission spectra.

Subtissue spectroscopic Measurements

The subtissue penetration depths achievable by using Tm,Yb:GdVO $_4$ @SiO $_2$ core-shell nanoparticles were investigated by using a double beam fluorescence microscope. This double beam experimental arrangement allowed us to place a phantom tissue of variable thickness between the Tm,Yb:GdVO $_4$ @SiO $_2$ core-shell nanoparticles and the detection optics. The penetration depths achievable by using the emission bands of Tm $^{3+}$ ions were obtained by monitoring the infrared luminescence generated for different tissue thicknesses. Mock tissue phantom depth penetration studies were performed by using Intralipid as the phantom tissue. Intralipid is an absorbing and scattering medium that has been extensively used in the past to mimic the optical properties of human skin in the first and second biological windows. In this work we used Intralipid 10%, diluted in a concentration of 2%. At this concentration, the wavelength dependence is similar to that previously reported for several human tissues.^[19]

In vitro experiments

HeLa (Human cervical cancer cell line) cells were grown as a monolayer employing Dulbecco's Modified Eagle Medium (DMEM) containing 10% fetal calf serum (FCS) and 50 units ml⁻¹ penicillin and 50 µg ml⁻¹ streptomycin (Sigma). The cells were incubated at 310 K in a humidified 5% CO₂ atmosphere and the medium was changed daily. For the fluorescence observation, cells were plated onto round coverslips placed into 24-wells plates.

For evaluation of Tm,Yb:GdVO₄@SiO₂ core-shell nanoparticles on *in vitro* thermal scanning experiment, the cells were seeded in 24-well plates containing sterile round coverslips and were kept in a sterile environment in the incubator for 24 h until the experiment start. After 2h of incubations with Tm,Yb:GdVO₄@SiO₂, cells were washed with PBS, and used in luminescence experiments.

In vitro cell cytotoxicity/viability studies

To determine cell cytotoxicity/viability, the cells were plated in a 24 well plate at 310 K in 5% CO₂ atmosphere. After 48 h of culture, the medium in the well was replaced with the fresh medium containing the Tm,Yb:GdVO₄@SiO₂ particles in a volume ratio ranging from 1:50 to 1:500, and cells were incubated for 2 hours. After incubation, the medium was removed and added completed medium without particles. After 24 h, 0.5 ml of 3-[4,5-dimethylthiazol-2-yl]-2,5-diphenyltetrazolium-bromide (MTT) dye solution (0.05 mg ml⁻¹ of MTT, Sigma) was added to each well. After 2-3 h of incubation at 310 K and 5% CO₂, the medium was removed and formazan crystals were solubilized with 0.5 ml of dimethylsulphoxide (DMSO) and the solution was vigorously mixed to dissolve the reacted dye. The absorbance of each well was read at 540 nm on a Spectra Fluor4 (TECAN) microplate reader. The spectrophotometer was calibrated to zero absorbance-using culture medium without cells. The relative cell viability (%) related to control wells containing cell culture medium without nanoparticles was calculated by $[A]_{\text{test}}/[A]_{\text{control}} \times 100$, where $[A]_{\text{test}}$ is the absorbance of the test sample and $[A]_{\text{control}}$ is the absorbance of the control sample. The MTT assay is a simple non-radioactive colorimetric assay to measure cell cytotoxicity, proliferation or viability. MTT is yellow, water soluble, tetrazolium salt. Metabolically active cells are able to convert this dye into a water-insoluble dark blue formazan by reductive cleavage of the tetrazolium ring.^[20] Formazan crystals, then, can be dissolved in an organic solvent such as DMSO and quantified by measuring the absorbance of the solution at 540 nm, and the resultant value is related to the number of living cells.

3. Results and Discussion

All pale yellow products obtained after the hydrothermal reaction result to be isostructural to the tetragonal $I4_1/amd$ zircon-type phase of $GdVO_4$ (JCPDS File 86-0996), and the crystal phase is maintained after the 5 h annealing at 873 K, although with narrower Bragg peaks, an indication of the increase of the average size of individual crystalline domains constituting vanadate NPs. No additional reflections have been detected for SiO_2 -coated samples apart from a rougher background reflecting the presence of amorphous SiO_2 , as compared to the XRD of the bare $Tm,Yb:GdVO_4$ annealed NPs, included in Figure 1(a) for comparison.

Figure 1(b) shows a characteristic TEM image of an annealed sample of $Tm,Yb:GdVO_4$ NPs, which present polygonal forms, mainly of square or rectangular sections, and lengths of 25–40 nm. Figures 1(c) and 1(d) display HRTEM images of $Tm,Yb:GdVO_4@SiO_2$ NPs, with darker and lighter parts being the $Tm,Yb:GdVO_4$ core and the amorphous silica coating, respectively. We determined that the coating layer had an average thickness of ~ 7 nm around NPs. Also, HRTEM images of discrete nanoparticles reveal a well-defined crystalline structure in the core, with the observed lattice fringe distances in Figure 1(d), 0.267 nm, matching the (112) interplanar spacing of $GdVO_4$, according to the JCPDS File 86-0996.

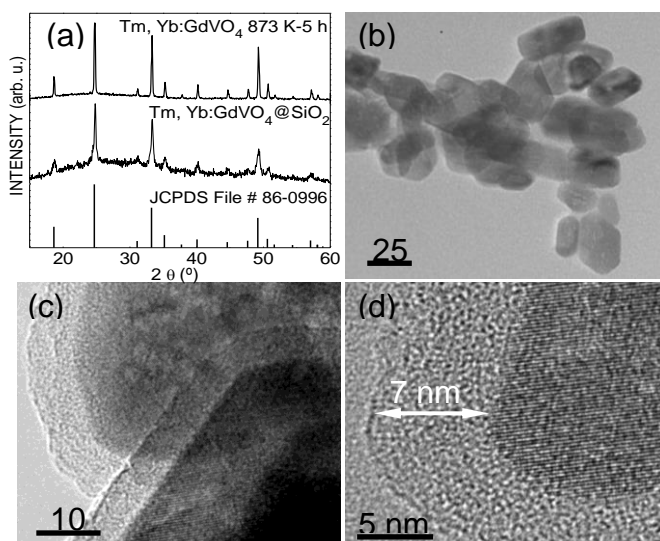


Figure 1. Structural and morphological characterization of $Tm,Yb:GdVO_4$ nanoparticles. (a) X-ray diffraction patterns of the $Gd_{0.84}Yb_{0.15}Tm_{0.01}VO_4$ sample annealed at 873 K for 5 h, and after the coating with a SiO_2 layer of 7 nm. For comparison the XRD pattern scheme of tetragonal $I4_1/amd$ $GdVO_4$, JCPDS File 86-0996 has been also included. (b) TEM image of annealed $Tm,Yb:GdVO_4$ NPs. (c) and (d) HRTEM images of core-shell $Tm,Yb:GdVO_4@SiO_2$ NPs,

showing the lattice fringes of the crystalline core (darker areas) and the amorphous silica shell (lighter areas around the core).

Figure 2(a) shows the upconversion emission spectra of 1% Tm^{3+} , 15% $\text{Yb}^{3+}:\text{GdVO}_4@\text{SiO}_2$ core-shell nanoparticles under 980 nm excitation at room temperature and 333 K. In the figure we indicated the spectral range corresponding to the I-BW in yellow. As can be seen, when the temperature increased, all emission bands drop in intensity, with the exception of the band at 700 nm that slightly increases its intensity. In order to explain why this is happening, first it is necessary to identify the energy levels assigned to each radiative transitions. Figure 2(b) shows the energy level diagram of the Tm^{3+} and Yb^{3+} ions, indicating the pathways for 980 nm excited upconversion and the transitions involved in the generation of such spectra. In a first step, the excitation at 980 nm is absorbed by Yb^{3+} promoting its electrons from the $^2\text{F}_{7/2}$ fundamental state to the $^2\text{F}_{5/2}$ excited state, and transfer part of its energy to the $^3\text{H}_5$ energy level of Tm^{3+} , from which electrons relax very fast to the $^3\text{F}_4$ energy level. Then, a second energy transfer from Yb^{3+} promotes Tm^{3+} electrons to the $^3\text{F}_2$ energy level which relaxes populating the $^3\text{F}_3$ and $^3\text{H}_4$ energy levels. Finally, a third electronic transfer promotes Tm^{3+} electrons in $^3\text{H}_4$ to the $^1\text{G}_4$ energy level, from where the blue and red emissions centered at 475 and 650 nm arise through the radiative $^1\text{G}_4 \rightarrow ^3\text{H}_6$ and $^1\text{G}_4 \rightarrow ^3\text{F}_4$ transitions, respectively. The 700 nm and 800 nm arise from the $^3\text{F}_3 \rightarrow ^3\text{H}_6$ and $^3\text{H}_4 \rightarrow ^3\text{H}_6$ radiative transitions. The initial energy levels of these radiative transitions can be populated both, from the second energy transfer process detailed above or from the non-radiative relaxation of electrons from the $^1\text{G}_4$ level.

The energy gap between the $^3\text{F}_3$ and $^3\text{H}_4$ energy levels is 2046 cm^{-1} .^[21] This relative low energy difference between these two electronic levels allows the existence of a thermal equilibrium between their electronic populations governed by the Boltzmann law. Thus, we can consider that the $^3\text{F}_{2,3}$ and $^3\text{H}_4$ energy levels are thermally coupled and can be used for temperature determination using the fluorescence intensity ratio (FIR) technique.^[22] In fact, in Figure 2(a) it can be seen that the intensity of the peak at 700 nm, arising from the $^3\text{F}_3 \rightarrow ^3\text{H}_6$ transition, increases as the temperature increases, while the intensity of the peak at 800 nm, arising from the $^3\text{H}_4 \rightarrow ^3\text{H}_6$ transition, decreases as the temperature increases, proving the thermal coupling between the $^3\text{F}_3$ and $^3\text{H}_4$ energy levels.

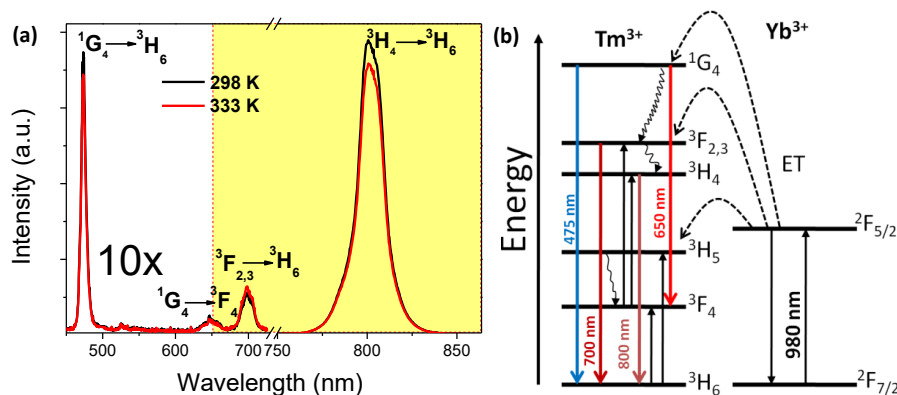


Figure 2. (a) Upconversion emission spectra of the Tm,Yb:GdVO₄@SiO₂ core-shell nanoparticles at room temperature and at 333 K. (b) Energy level diagram of the Tm³⁺ and Yb³⁺ in GdVO₄, indicating the absorption, energy transfer and emission pathways.

Since the upconversion luminescence is a non-linear process, the intensity of the emission bands depends on the dopant concentrations, as well as on temperature. In order to optimize the intensity ratio of the emission lines at 700 and 800 nm, and obtain the maximum thermal sensitivity, we studied the evolution of the FIR with temperature of Tm,Yb:GdVO₄@SiO₂ core-shell nanoparticles with different concentrations of Tm³⁺. In a previous study we optimized the concentration of Yb³⁺ (~15 mol%) to maximize the intensity of the Tm³⁺ emissions in these core-shell nanoparticles,^[23] thus in the present work the concentration of Yb³⁺ was kept constant at 15 mol%. The normalized FIR of the emission lines at 700 and 800 nm of the Tm,Yb:GdVO₄@SiO₂ core-shell nanoparticles for different concentrations of Tm³⁺ is shown in Figure 3(a). The experimental points were fitted to a Boltzmann distribution equation with an additional offset that takes into account the overlapping of the emission lines, according to the equation:^[22]

$$FIR = A \exp \frac{\Delta E}{kT} + C \quad (1)$$

where ΔE is the energy gap between the two thermally coupled levels, k is the Boltzmann constant and T is the absolute temperature, and A and C are fitting constants.

The value of the energy gap between the two thermally coupled energy levels ³F_{2,3} and ³H₄ was set to 2046 cm⁻¹, as reported in the literature for the Tm:GdVO₄ single crystal.^[21] The core-shell nanoparticles with a 1 mol% Tm³⁺ showed the highest slope. The absolute thermal sensitivity can be calculated from the first derivative of the FIR fittings with respect to the temperature,^[22] as:

$$S_{abs} = FIR \frac{\Delta E}{kT^2} \quad (2)$$

The thermal sensitivities calculated for the $\text{Tm,Yb:GdVO}_4\text{@SiO}_2$ core-shell nanoparticles are presented in Figure 3(b). As can be seen, and as expected from the slopes of FIR in Figure 3(a), the nanoparticles with 1 mol% Tm^{3+} have the highest absolute thermal sensitivity with a maximum of $2.26\% \text{ K}^{-1}$ at 333 K.

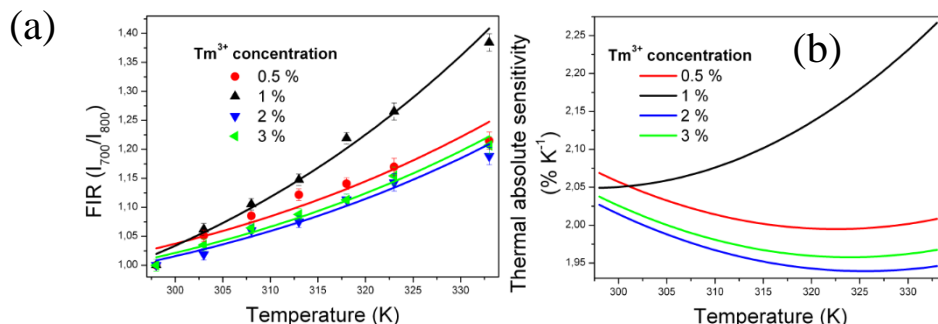


Figure 3. (a) Normalized FIR as a function of temperature of the $\text{Tm,Yb:GdVO}_4\text{@SiO}_2$ core-shell nanoparticles with different concentration of Tm^{3+} ; (b) Absolute thermal sensitivity of the (0.5-3 %) $\text{Tm,Yb:GdVO}_4\text{@SiO}_2$ core-shell nanoparticles

The comparison with other Tm^{3+} -doped systems is presented in Table 1. As can be seen, the thermal sensitivity of $\text{Tm,Yb:GdVO}_4\text{@SiO}_2$ core-shell nanoparticles is the highest among Tm^{3+} , Yb^{3+} co-doped systems.^[16,24-27] Xing *et al.*^[25] and Xu *et al.*^[27] reported the same temperature dependent properties of the thermally coupled $^3\text{F}_{2,3}$ and $^3\text{H}_4$ energy levels in Tm,Yb:LiNbO_3 single crystal,^[25] but in that case, the thermal sensitivity was one order of magnitude lower, and the maximum thermal sensitivity was achieved at much higher temperatures. The same FIR was explored in Tm,Yb co-doped oxyfluoride glasses,^[27] but again, the thermal sensitivity was one order of magnitude smaller. Zhou *et al.* take advantage of the thermal population of the $^3\text{F}_{2,3}$ from the lower $^3\text{H}_4$ energy level to calculate the intensity ratio with the emission line located at 650 nm arising from the $^1\text{G}_4 \rightarrow ^3\text{F}_4$ radiative transition.^[26] In that case the thermal sensitivity increased, and takes a value closer to the one obtained in the present paper, but still lower.

Table 1. Comparison of Tm^{3+} -doped systems used in luminescence nanothermometry.

Material	Temperature range (K)	Excitation wavelength (nm)	Wavelength ratio	Maximum thermal sensitivity ($\% \text{ K}^{-1}$), Temperature (K)	Ref.
$\text{Tm,Yb:GdVO}_4\text{@SiO}_2$	298 – 333	980	I_{700}/I_{800}	2.26 (333)	This work
$\text{Tm,Yb:Y}_2\text{O}_3$	303 – 753	976	I_{476}/I_{488}	0.35 (303)	24
Tm,Yb:LiNbO_3	323 – 723	980	I_{700}/I_{800}	0.24 (773)	25

Tm,Yb:NaYF ₄ @Pr:NaYF ₄	350 – 510	980	I ₆₄₆ /I ₆₉₆	1.53* (417)	26
Tm,Yb:CaF ₂	299 – 323	920	I ₇₉₀ /I ₈₀₀	0.24* (299)	16
Tm,Yb:oxyfluoride glass	293 – 703	980	I ₇₀₀ /I ₈₀₀	0.3 (703)	27
Tm,Yb:Ba ₅ Gd ₈ Zn ₄ O ₂₁	300 – 510	980	I ₄₈₉ /I ₄₈₄	0.6 (300)	28

* Estimated from the data reported in the publications.

Motivated by the good results obtained for thermal sensitivity, we studied the potentiality of using Tm,Yb:GdVO₄@SiO₂ core-shell nanoparticles in biological systems. To analyze how the fluorescence intensities of the Tm³⁺ luminescence bands are attenuated by the biological tissue, we used a phantom tissue of variable thickness. A drop of the core-shell nanoparticles dispersed in phosphate-buffered saline (PBS) was placed in a microscope slide and was optically excited by a continuous fiber-coupled diode laser at 980 nm. The laser beam was focused on the core-shell nanoparticles using a 20X microscope objective (N.A. = 0.4). The same objective was used to collect the Tm³⁺ emission and after passing a dichroic mirror to eliminate the excitation radiation, it was analyzed by using a high sensitivity Si CCD camera (Synapse, Horiba) attached to a high-resolution monochromator (iHR320, Horiba). 2 % of intralipid solution in water was used as phantom tissue as it has similar scattering properties than biological tissues.^[19]

Figure 4 shows the collected emission intensity from the Tm³⁺ emission bands as a function of the tissue thickness. As can be seen, a monotonous decrease of the collected signal with the tissue thickness is observed, indicating that the emission band of Tm³⁺ is attenuated within the phantom tissue either by absorption or scattering processes (or by a combination of them).^[29] We have obtained a penetration depth of 1.6 mm. The results are similar to those obtained in Tm,Yb:CaF₂ nanoparticles (maximum penetration depth of 2 mm).^[16] This penetration depth might be increased by improving the detection of the emission and/or by increasing the power of the excitation radiation.

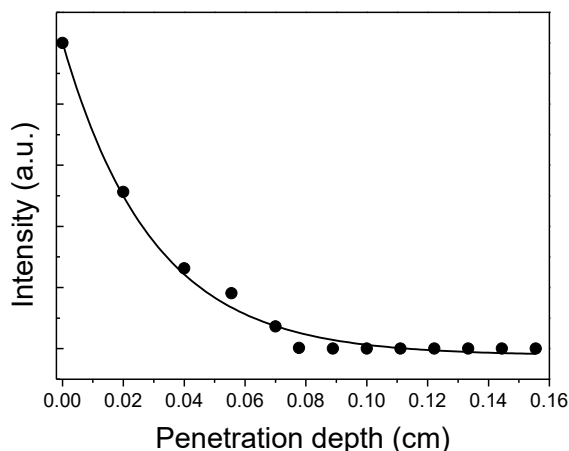


Figure 4. Penetration depth of the upconversion emission at 800 nm generated by Tm,Yb:GdVO₄@SiO₂ core-shell nanoparticles in a 2 % intralipid aqueous solution (continuous line was done for the eyes guiding).

For *in vitro* experiment, we incubated HeLa cancer cells with Tm,Yb:GdVO₄@SiO₂ core-shell nanoparticles, as described in the Experimental Section. After incubation, the HeLa cells were examined in a confocal microscope illuminated with a continuous fiber-coupled diode laser at 980 nm as the pump source and the fluorescence was detected by the same system described before. Figure 5(a) shows an optical transmission microscope image of the HeLa cells after incubation, the arrow indicate the position of the nanoparticles when the excitation laser is off. Figure 5(b) shows an optical transmission microscope image of the same region when the excitation laser is on. The blue emission arising from the Tm,Yb:GdVO₄@SiO₂ core-shell nanoparticles can be seen and it suggests that the nanoparticles are incorporated into vesicles. An enlarged image of the area in which the nanoparticle is located is shown also in this figure. In the enlarged image some tiny signs of autofluorescence arising from the cell seem to be present, however, they no hamper the observation of the emission arising from the luminescent nanoparticle. An intensity scan of the blue emission along the line indicated in Figure 5(c) was performed to corroborate that the blue emission is only arising from the luminescent nanoparticles. The results show an increase of the intensity in the area where the nanoparticles are located, but not in the rest of the cell. The red dashed line in the graph indicates the level of noise. At this point we should note that we performed a number of different toxicity assays. We have found that incubation of HeLa cells with medium solutions containing Tm,Yb:GdVO₄@SiO₂ core-shell nanoparticles caused a reduce toxicity, as it is shown in Figure

5(d), for the different concentrations analyzed. The toxicity increased as the concentration of core-shell nanoparticles increased.

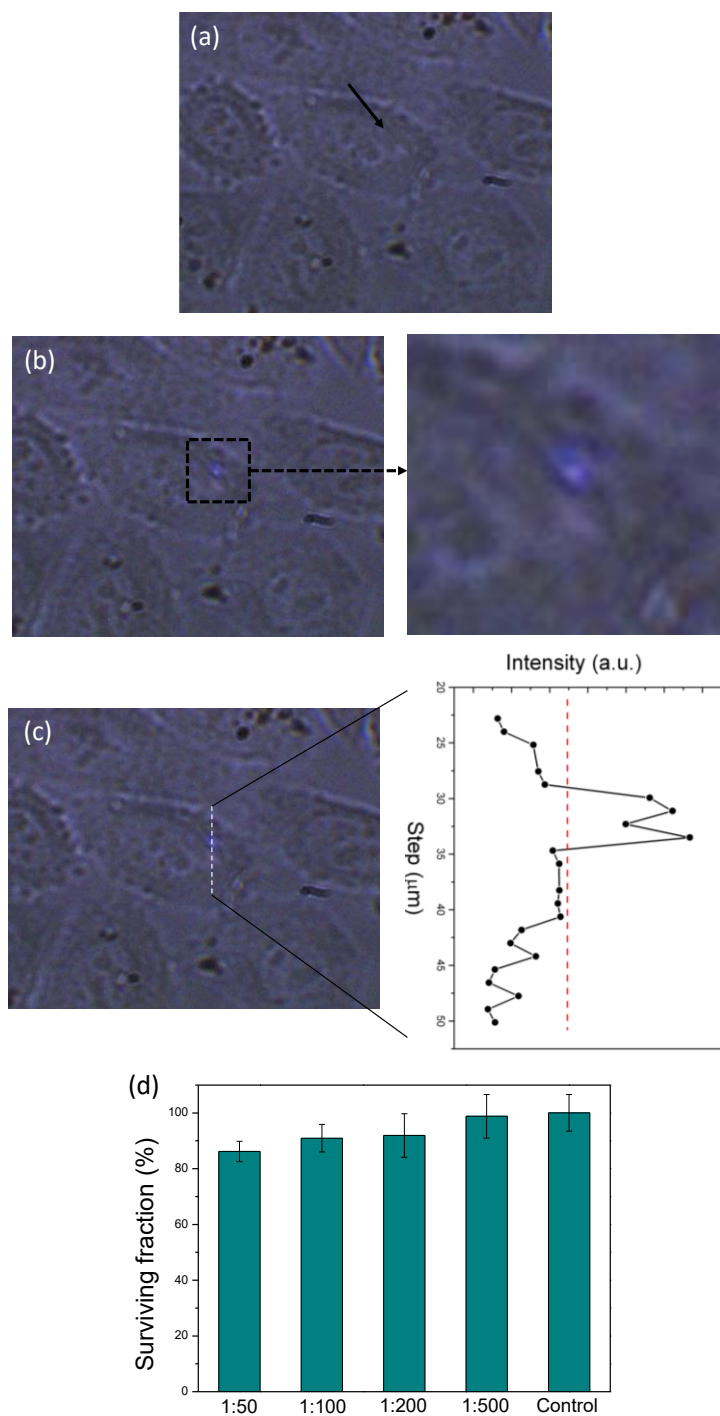


Figure 5. Microscope optical transmission image of the HeLa cells incubated with Tm,Yb:GdVO₄@SiO₂ core-shell nanoparticles when the excitation laser is (a) off, and (b) on. The arrow indicate the position were the core-shell nanoparticles are located, as can be seen when the laser is on in (b), together with an enlarged image of the square indicated in the image. (c) Intensity scan of the blue emission along the dashed line indicated in the figure with a scan step of 2 μm . (d) Percent survival of HeLa cell line incubated with different concentrations of Tm³⁺, Yb³⁺:GdVO₄@SiO₂ core-shell nanoparticles. Each point corresponds to the mean value \pm SD from five different experiments.

4. Conclusions

In summary, we investigated the upconversion emissions generated by Tm,Yb:GdVO₄@SiO₂ core-shell nanoparticles in the physiological range of temperatures containing different concentrations of Tm³⁺ after pumping at 980 nm. The two emission lines located at 700 and 800 nm, that lye in the I-BW, and arising from the thermally coupled ³F_{2,3} and ³H₄ energy levels of Tm³⁺, respectively, were identified to have potential to develop a luminescent thermometer operating by the FIR technique. The nanoparticles containing 1% Tm³⁺ were found to have the highest thermal sensitivity for this purpose with a maximum of 2.26 % K⁻¹ at 333 K, which is the highest value reported for Tm³⁺, Yb³⁺ co-doped systems to the best of our knowledge. A penetration depth of 1.6 mm in biological tissues could be achieved for the 800 nm emission arising from these core-shell nanoparticles. Furthermore, the inert silica shell surrounding the luminescent active core allowed dispersing them in biological compatible fluids like PBS, which facilitated internalizing the core-shell nanoparticles in HeLa cells, proving their potentiality for biolabelling applications.

Acknowledgements

This work was supported by the Spanish Government under Projects No. MAT2013-47395-C4-1-4-R, TEC2014-55948-R and MAT2014-56607-R, and by Catalan Authority under Project No. 2014SGR1358. The ICTS CNME at the University Complutense of Madrid is acknowledged for making TEM and HRTEM facilities available. Ol. A. Savchuk is supported by Catalan Government through the fellowship 2015FI B2 00136. P.H.G. thanks the Spanish Ministerio de Economia y competitividad (MINECO) for Juan de la Cierva program. F.D. acknowledges additional support through the ICREA Academia award 2010ICREA-02 for excellence in research.

References

1. L. D. Carlos, F. Palacio, *Thermometry at the Nanoscale: Techniques and Selected Applications* (Ed: P. R. N. Childs), RSC Nanoscience & Nanotechnology, Cambridge, United Kingdom **2016**, Ch. 1.
2. D. Jaque, B. del Rosal, E. M. Rodriguez, L. M. Maestro, P. Haro-Gonzalez and J. G. Sole, *Nanomedicine* **2014**, *9*, 1047.
3. D. Jaque, F. Vetrone, *Nanoscale* **2012**, *4*, 4301.
4. C. D. S. Brites, P. P. Lima, N. J. O. Silva, A. Millan, V. S. Amaral, F. Palacio and L. D. Carlos, *Nanoscale* **2013**, *5*, 7572.
5. E. Carrasco, B. del Rosal, F. Sanz-Rodríguez, A. J. de la Fuente, P. Haro-Gonzalez, U. Rocha, K. U. Kumar, C. Jacinto, J. G. Solé, and D. Jaque, *Adv. Funct. Mater.* **2015**, *25*, 615.
6. D. Jaque, L. Martinez Maestro, B. del Rosal, P. Haro-Gonzalez, A. Benayas, J. L. Plaza, E. Martin Rodriguez and J. G. Sole, *Nanoscale* **2014**, *6*, 9494.
7. O. S. Wolfbeis, *Chem. Soc. Rev.* **2015**, *44*, 4743.
8. A. Benayas, F. Ren, E. Carrasco, V. Marzal, B. del Rosal, B. A. Gonfa, A. Juarranz, F. Sanz-Rodríguez, D. Jaque, J. Garcia-Sole, D. Ma, and F. Vetrone, *Adv. Funct. Mater.* **2015**, *25*, 6650.
9. Q. Ju, X. Chen, A. Fujin, D. Peng, X. Lin, W. Kong, P. Shi, G. Zhub and F. Wang, *J. Mater. Chem. B* **2015**, *3*, 3548.
10. U. Rocha, C. J. da Silva, W. F. Silva, I. Guedes, A. Benayas, M. L. M. Maestro, E. Boverovan, F. C. J. M. Veggel, J. A. G. S. Sole, D. Jaque, *ACS Nano* **2013**, *7*, 1188.
11. F. Helmchen and W. Denk, *Nat. Methods* **2005**, *2*, 932.
12. M. Haase and H. Schäfer, *Angew. Chem. Int. Ed.* **2011**, *50*, 5808.
13. Q. Q. Dou, H. C. Guo, E. Ye, *Mater. Sci. Eng. C* **2014**, *45*, 635.
14. H. S. Mader, P. Kele, S. M. Saleh and O. S. Wolfbeis, *Curr. Opin. Chem. Biol.* **2010**, *14*, 582.
15. M. Nyk, R. Kumar, T. Y. Ohulchansky, E. J. Begey, and P. N. Prasad, *Nano Lett.* **2008**, *8*, 3834.
16. N.-N. Dong, M. Pedroni, F. Piccinelli, G. Conti, A. Sbarbati, J. E. Ramirez-Hernandez, L. M. Maestro, M. C. I. de la Cruz, F. Sanz-Rodríguez, A. Juarranz, F. Chen, F. Vetrone, J. A. Capobianco, J. G. Sole, M. Bettinelli, D. Jaque, and A. Speghini, *ACS Nano* **2011**, *5*, 8665.

17. S. Han, R. Deng, X. Xie, and X. Liu, *Angew. Chem. Int. Ed.* **2014**, *53*, 11702.
18. X.-D. Wang, O. S. Wolfbeis and R. J. Meier, *Chem. Soc. Rev.* **2013**, *42*, 7834.
19. H. J. van Staveren, C. J. M. Moes, J. van Marie, S. A. Prah, M. J. C. van Gemert, *Appl. Opt.* **1991**, *30*, 4507.
20. T. Mosmann, *J. Immunol. Methods* **1983**, *65*, 55.
21. R. Lisiecki, P. Solarz, G. Dominial-Dzik, W. Ryba-Romanowski, M. Sobczyk, P. Cerny, J. Sulc, H. Jelinkova, Y. Urata, and M. Higuchi, *Phys. Rev. B* **2006**, *74*, 035103.
22. S. A. Wade, S. F. Collins, G. W. Baxter, *J. Appl. Phys.* **2003**, *94*, 4743.
23. R. Calderon-Villajos, C. Zaldo and C. Cascales. *Nanotechnol.* **2012**, *23*, 505205.
24. D. Li, Y. Wang, X. Zhang, K. Yang, L. Liu, Y. Song, *Opt. Commun.* **2012**, 285, 1925.
25. L. Xing, Y. Xu, R. Wang, W. Xu, and Z. Zhang, *Opt. Lett.* **2014**, *39*, 454.
26. S. Zhou, G. Jiang, X. Li, S. Jiang, X. Wei, Y. Chen, M. Yin, and C. Duanm, *Opt. Lett.* **2014**, *39*, 6687.
27. W. Xu, X. Y. Gao, L. J. Zheng, Z. G. Zhang, and W. W. Cao, *Sens. Actuators B* **2012**, *173*, 250.
28. H. Suo, C. Guo, Z. Yang, S. Zhou, C. Duan and M. Yin, *J. Mater. Chem. C* **2015**, *3*, 7379.
29. U. Rocha, K. U Kumar, C. Jacinto, I. Villa, F. Sanz-Rodriguez, M. C. I. De la Cruz, A. Jauranz, E. Carrasco, F. C. J. M. Van Veggel, E. Bovero, J. G. Sole, D. Jaque, *Small* **2014**, *10*, 1141.

Paper XI

De la Cruz, L.G.; Savchuk, Ol.; Carvajal, J. J.; Haro-González, P.; Aguiló, M.; Díaz, F. *Luminescence thermometry and imaging in the second biological window with Nd:KGd(WO₄)₂ nanoparticles* (2016) Submitted to Chemistry of materials.

Luminescence thermometry and imaging in the second biological window at high penetration depth with Nd:KGd(WO₄)₂ nanoparticles.

Ol. Savchuk,^a J.J. Carvajal,^{a,*} L.G. De la Cruz,^a P. Haro-González,^b M. Aguiló,^a F. Díaz^a

^aPhysics and Crystallography of Materials and Nanomaterials (FiCMA-FiCNA) and EMaS, Universitat Rovira i Virgili (URV), Marcel·lí Domingo, 1, E-43007 Tarragona, Spain.

^bFluorescence Imaging Group, Departamento de Física de Materiales, Facultad de Ciencias, Universidad Autónoma de Madrid, C/ Francisco Tomás y Valiente, 7, E-28049 Madrid, Spain.

Abstract: Neodymium-doped monoclinic KGd(WO₄)₂ nanoparticles were synthesized by the Pechini sol-gel method. Under excitation at 808 nm, the 3 at. % Nd:KGd(WO₄)₂ nanoparticles exhibited strong emission bands at 883 nm and 1067 nm in the near infrared region range, corresponding to the ⁴F_{3/2} → ⁴I_{9/2} and ⁴F_{3/2} → ⁴I_{11/2} transitions of Nd³⁺, and lying in the first and second biological windows, respectively. Both emissions show promising properties for thermal sensing in this range of wavelengths. In fact, the thermal analysis of these nanoparticles indicated a linear ascent behavior of the fluorescence intensity ratio. The surface of these nanoparticles was functionalized by silanization using 3-aminopropyltriethoxysilane as the coupling agent, allowing deagglomerating with sizes around 16 nm, which allowed dispersing them in water. In this form they were used for NIR imaging in the second biological windows, achieving a depth penetration of 1 cm, the deepest ever reported in this spectral range. Hence these nanoparticles are promising for nanothermometry and imaging applications in the second biological windows.

1. INTRODUCTION

The variation of the luminescent properties of luminescent nanoparticles (LNPs) with temperature have attracted attention in last years, and play a crucial role in thermal image applications, used at the same time in biophotonics, forthcoming diagnosis and therapy procedures.^[1-3]

Aside from this important interest, thermal sensing of biosystems is a key part for the simultaneous monitoring of their temperature to found the origin of behavior and therefore early detection and treatment of many diseases, since one of the first signals of any given illness (such

as inflammation, hyperthermia, cancer or cardiac problems) is the appearance of thermal singularities.^[4] However, traditional temperature sensors (thermocouples, thermistors and infrared thermometers) could not fulfill the measure requirements in living cells,^[5] principally because they determine the temperature by contact (thermocouples and thermistors), measure only temperature at the surface, and have a low spatial resolution.^[6]

Because of these limitations, the use of temperature sensors based on the fluorescence properties of nanoparticles have shown great potential due to their operation in non-contact mode and can find applications both, in cellular imaging and in temperature sensing at the nanoscale,^[1,7,8] after a suitable chemical functionalization of the surface of these nanoparticles that allow their dispersion in biological compatible fluids.^[9-12] However, most of these systems operate in the visible range of wavelengths,^[8,13] which limits their penetration depth into a biological tissue to a few millimeters.^[14,15]

Therefore, finding an appropriate alternative, which has sufficient emission of signal but also allows for a deeper penetration during in-vivo imaging experiments, is important. Fortunately, two regions have been identified in the near infrared region (NIR) of the electromagnetic spectrum where the absorption of light by the different component of the biological tissue is reduced, the so-called biological windows. Initially, the focus on research was centered at the first biological window (I-BW), that extends from 700 nm to 950 nm.^[16,17] At present, focus has shifted to the second biological window (II-BW),^[18-19] that extends from 1,000 nm to 1,400 nm. Two water absorption bands at 980 nm and 1500 nm limit this spectral range. Since longer wavelengths are used in the II BW, there is a reduction of the optical scattering if compared to the I-BW. This reduction is considered to lead to an improvement in the resolution of sub-tissue images, and a longer penetration depth.^[19]

Among the most promising material candidates to work in these biological windows we encounter carbon nanotubes (CNTs) and lanthanide (Ln^{3+})-doped LNPs. Despite CNTs have a unique fluorescence emission band that spans up to the whole spectral range of the II-BW, and make them useful for a deep-tissue imaging,^[18] they can generate unwanted thermal loading during the emission process,^[20] that might mask temperature measurements. Ln^{3+} -doped nanocrystals, from their side, have attracted great interest due to their large Stokes shifts, narrow emission band widths, long luminescence lifetimes, biocompatibility, and nontoxicity, giving rise to potential applications in diverse fields such as bio-imaging.^[21-27] To date, multifunctional Ln^{3+} -doped LNPs that exhibit two or more different properties are highly desirable for many technological applications such as multifunctional imaging, and simultaneous diagnosis and therapy.^[24,28] The Nd^{3+} ion with an absorption around 800 nm is considered a good candidate to

achieve efficient emissions in the I- and II-BWs, based on the three main emission channels of Nd^{3+} ions: ${}^4\text{F}_{3/2} \rightarrow {}^4\text{I}_{9/2}$, ${}^4\text{F}_{3/2} \rightarrow {}^4\text{I}_{11/2}$ and ${}^4\text{F}_{3/2} \rightarrow {}^4\text{I}_{13/2}$ that lead to emissions at around 910 nm, 1050 nm, and 1330 nm, respectively,^[18] and significantly improve the penetration depth for deep-tissue imaging.^[29,30] LNPs doped with neodymium can be used to work in both the I-BW and II-BW. Furthermore, Nd^{3+} ion shows several advantages such as a small thermal loading due to a single de-excitation channel, no excited state absorption, a large transparency over the visible range, a weaker cross-relaxation process, and a long (ms) radiative lifetime.^[31,32] However, the sensitivities of state-of-the-art Nd^{3+} -based luminescence thermometers are relatively low,^[33] and the penetration depths demonstrated up to now did not exceed 5 mm.^[19,34] Thus, it is necessary to explore the possibilities of new hosts in which Nd^{3+} can be embedded, to improve both, thermal sensitivity and penetration depth.

In this context, $\text{KGd}(\text{WO}_4)_2$, that crystallizes in the monoclinic system with space group C2/c, is reported as an excellent host for lanthanide ions due to its highly thermal and chemical stability.^[35,36] It also provides a strong physical anisotropy with weaker concentration quenching effects, and activated by Ln^{3+} ions shows high efficiency for stimulated emission at low pumping energies with laser diode excitation,^[37,38] due to the high absorption cross-section that lanthanide ions show in this material.^[39] Based on all these properties, $\text{KGd}(\text{WO}_4)_2$ seems to be a potential candidate to improve the properties of Nd^{3+} -based systems for luminescence thermometry.

In this work, we synthesized and optimized the doping concentration of Nd^{3+} in $\text{KGd}(\text{WO}_4)_2$, and analyzed its spectroscopic properties. The nanoparticles showing the highest emission efficiency were functionalized by silanization to disperse them in biological compatible fluids, and their thermometric response in the I and II-BW, as well as their penetration depth in the II-BW were analyzed.

2. EXPERIMENTAL TECHNIQUES

2.1 Synthesis of $\text{Nd}^{3+}:\text{KGd}(\text{WO}_4)_2$ nanoparticles by the Pechini sol-gel method.

We followed the procedures developed by Galceran et al.^[40] to produce $\text{KGd}(\text{WO}_4)_2$ nanoparticles by the Pechini method. Briefly, powders of K_2CO_3 (Alfa Aesar, 99.0%), Gd_2O_3 and Nd_2O_3 (Aldrich, 99.9%) were used as starting materials to synthesize 1 to 5 at. % $\text{Nd}^{3+}:\text{KGd}(\text{WO}_4)_2$ nanoparticles. Stoichiometric amounts of these compounds were dissolved in HNO_3 (Labkem, 65%). The solution was maintained at 100 °C until the liquid was completely evaporated. After that, powders of $(\text{NH}_4)_2\text{WO}_4$ (Aldrich, 99.99%) and EDTA (Alfa Aesar,

99.0%) were dissolved in water during at room temperature. This solution was mixed with the nitrates generated and was kept for 2 hours at 50 °C to allow the complexation reaction to take place. The esterification reaction took place when adding polyethyleneglycol (Aldrich, m.w. 400) at this solution. When mixed together, EDTA and PEG create a rigid net able to reduce the segregation of metals which could take place at high temperatures during the process of polymer decomposition. The following step was a pre-calcination at 300 °C during three hours to start decomposing the organic resin. Finally, the precursor powder, was calcined at 1000 °C for 8 min and then cooled down to RT.

2.2 Chemical functionalization of the surface of Nd:KGd(WO₄)₂ nanoparticles.

The surface of 5 at. % Nd:KGd(WO₄)₂ nanoparticles was chemically functionalized by silanization to disperse them in water. Different amounts of nanoparticles were mixed in a vial with 2.5 ml of 3-aminopropyltriethoxysilane (APTES) (Aldrich, 99%) and different volumes of water, as listed in Table 1. This solution was left under sonication for 5 hours at room temperature, using a 5 mm micro-tip in a high-power ultrasonic processor. Different conditions of amplification and pulse duration were used in the experiments, summarized in Table 1. The vial was submerged in a water-ice bath in order to minimize the polymerization of APTES due to the increase of temperature during the sonication process. After that the excess of APTES not linked to the surface of the nanoparticles was removed by adding 2.5 ml of ethanol and/or acetone (Pure Merck), depending on the experiment (see Table 1) and ultrasonicated additionally during 5 minutes. This step was repeated several times until the supernatants became colorless indicating that the excess of APTES that was not linked to the surface of the nanoparticles was removed. The resulting mixture was centrifuged during 6 min at 800 rpm in order to separate the functionalized nanoparticles. Finally, the chemically functionalized nanoparticles were dispersed in 2.5 ml of water using the high-power ultrasonic processor to study their deposition time that will allow us estimating their stability in water compatible fluids.

Table 1. Parameters used in the functionalization of nanoparticles.

Sample Name	Ultrasound amplification (%)	Ultrasound pulse duration on (s) /off (s)	% vol. Silane - Water	Weight of NPs (mg)	Agglomeration
Exp 1	20	1/1	100-0	50	Yes
Exp 2	40	1/1	100-0	50	Yes
Exp 3	40	1/1	50-50	50	Yes
Exp 4	40	1/1	25-75	50	Yes
Exp 5	35	1/1	25-75	50	Yes
Exp 6	35	2/1	25-75	50	Yes
Exp 7	35	3/1	25-75	50	Yes
Exp 8	35	3/1	25-75	12	No

2.3 Characterization techniques

X-ray powder diffraction patterns were recorded from the nanoparticles obtained with different dopant concentrations using Cu K α radiation in a Bruker-AXS D8-Discover diffractometer equipped with a parallel incident beam (Göbel mirror), a vertical θ - θ goniometer, an XYZ motorized stage, and a point detector. The X-ray diffractometer was operated at 40 kV and 40 mA. Identification of the crystalline phases was achieved by comparing the recorded XRD pattern with the JCPDS database.

The particle morphology, and size distribution of the NPs were analyzed using transmission electron microscopy (TEM) analysis, performed with a JEOL JEM-1011 microscope. The preparation of the samples consisted in placing a drop of the nanopowders, previously mixed in a volatile solvent such as ethanol (Merck, pro analysis 99.8%) or distilled water, on a copper grid covered by a holey carbon film (HD200 Copper Form-var/carbon).

The optical reflectance of the Nd³⁺:KGd(WO₄)₂ nanocrystals was recorded at room temperature using a Varian Cary 500 spectrophotometer to analyze the position of the Nd³⁺ absorption bands in the material. The spectra were recorded from 600 nm to 1000 nm, taking measurements with a data interval of 0.1 nm and 20 seconds of integration time.

The Nd³⁺ photoluminescence measurements to determine the efficiency of Nd³⁺-doped materials were carried out at room temperature by a homemade set-up using an 808 nm diode laser (Ostech) as the excitation light source with a power of 1.1 W coupled to an optical fiber and a collimator lens that focuses the light onto an integrating sphere. The sample was located in a hole of the sphere at 180° of the pumping source and at 90° of the detector, a Yokogawa AQ6373 optical spectrum

analyzer (OSA). The spectra were recorded from 850 nm to 1400 nm.

To determine the variation of the luminescence properties of the 5 at. % $\text{Nd}^{3+}:\text{KGd}(\text{WO}_4)_2$ nanoparticles with temperature, they were introduced in a heating stage (LinkamTHMS 600), and their emission was collected in a 90° geometry to minimize the influence of the laser pump on the collected spectra. The pumping source was collimated, as well as the emission generated by the sample by a lens or a microscope objective, respectively. The spectra were recorded from 850 nm to 1400 nm with the high sensitive mode of the Yokogawa AQ6373 OSA.

3 RESULTS AND DISCUSSION

3.1 Structural and morphological characterization

The synthesized nanocrystals were structurally characterized by X-ray powder diffraction. Figure 1(a) shows the X-ray powder diffraction pattern of the $\text{Nd}^{3+}:\text{KGd}(\text{WO}_4)_2$ nanocrystals, which crystallizes in the monoclinic system with space group C2/c, since all the peaks observed in the experimental pattern could be indexed according to the reference JCPDS 89-8489 pattern^[41], also shown in Figure 1(a).

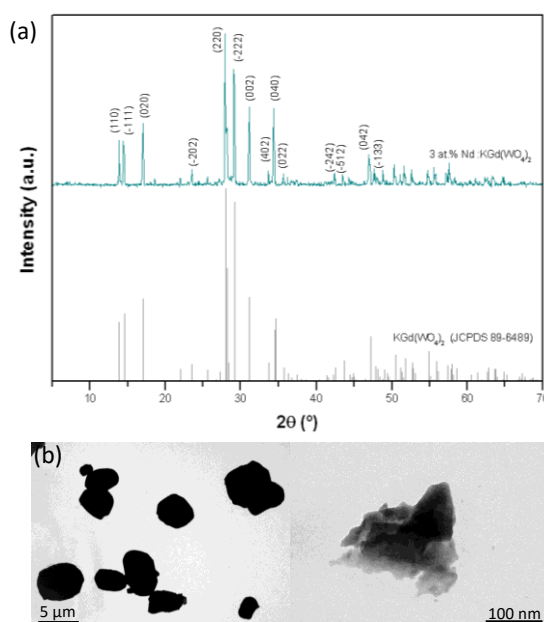


Figure 1. (a) X-ray powder diffraction patterns of monoclinic $\text{KGd}(\text{WO}_4)_2$ nanocrystals. (b) TEM images of 3 at. % $\text{Nd}^{3+}:\text{KGd}(\text{WO}_4)_2$ nanoparticles.

To determine the particle size of the nanocrystals obtained, we used the X-ray diffraction data and the Scherrer's equation,^[42] which correlates the broadening of the diffraction peaks with the crystallite size.^[43] We calculated the crystallite sizes using the full width at half maximum (FWHM) of the (220), ($\bar{2}22$), (002) and (040) peaks of the diffraction pattern of 3 at. % Nd³⁺:KGd(WO₄)₂ nanoparticles, determining a crystallite size of 63.22 nm.

TEM images of these nanoparticles give information about the size distribution and morphology of the Nd³⁺ doped nanoparticles obtained. Figure 1(b) shows typical TEM pictures of these nanoparticles recorded at different magnifications. The particles were agglomerated with a non-defined shape and with a high variety of sizes ranging from 2 μm to 6 μm . It was possible to observe the smaller particles, which were forming those big aggregates, with sizes between 70-150 nm, in agreement with the particle size determined from the Scherrer's equation.

3.2 Spectroscopic characterization

We recorded the reflectance of 3 at. % Nd³⁺:KGd(WO₄)₂ nanoparticles. As can be seen in Figure 2(a), the presence of the characteristic bands of Nd³⁺ ions at around 750 and 900 nm (corresponding to the $^4F_{3/2} \rightarrow ^4I_{9/2}$ and $^4F_{3/2} \rightarrow ^4I_{11/2}$ transitions, respectively) is evidenced, confirming the doping of the nanoparticles with Nd³⁺.

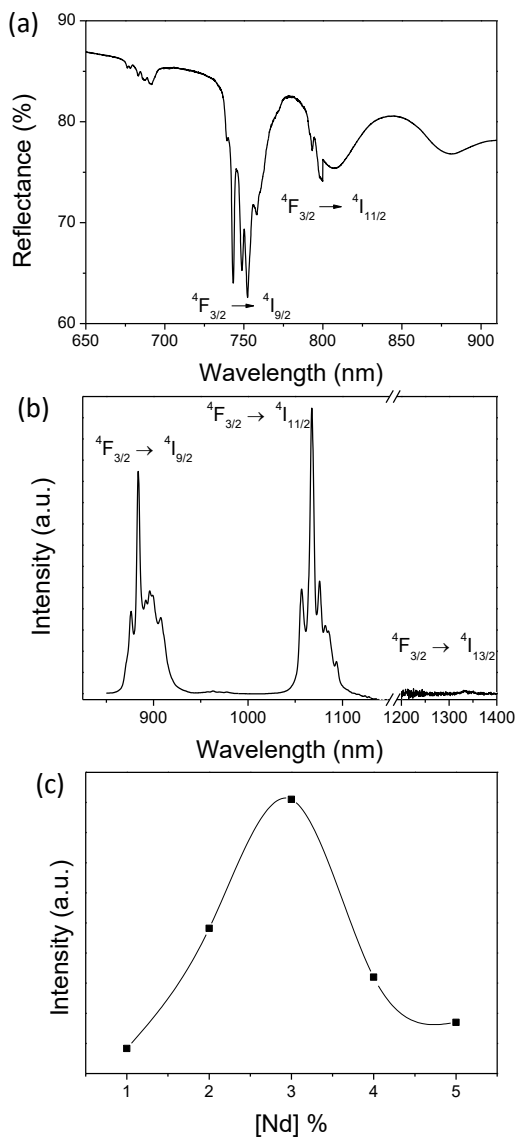


Figure 2. (a) Reflectance spectra of 5 at. % $\text{Nd}^{3+}:\text{KGd}(\text{WO}_4)_2$ nanoparticles. b) Emission spectra of 3 at. % $\text{Nd}^{3+}:\text{KGd}(\text{WO}_4)_2$ nanoparticles. c) Evolution of the emission intensity of the ${}^4F_{3/2} \rightarrow {}^4I_{11/2}$ transition in $\text{Nd}^{3+}:\text{KGd}(\text{WO}_4)_2$ nanoparticles as a function of the concentration of Nd^{3+} .

In this study, we optimized the percentage of Nd^{3+} , ranged between 1 at. % and 5 at. % that gives the maximum emission intensity, analyzing it with an integrating sphere. It was possible to observe the two multiplets corresponding to the ${}^4F_{3/2} \rightarrow {}^4I_{9/2}$ (~850 nm), and ${}^4F_{3/2} \rightarrow {}^4I_{11/2}$ (~1075 nm) transitions, as shown in Figure 2(b). The first transition is located in the I-BW and the second transition lies in the II-

BW. Among the transitions of Nd^{3+} we expected to obtain the emission corresponding to the ${}^4\text{F}_{3/2} \rightarrow {}^4\text{I}_{13/2}$ transition, located at around 1300 nm, lying again in the II-BW. However, as shown in Figure 2(b), it was barely seen, since it is very weak. The 3 at. % $\text{Nd}^{3+}:\text{KGd}(\text{WO}_4)_2$ nanocrystals showed the highest intensity in the NIR range, as can be seen in Figure 2(c), and those are the particles we have chosen for further characterizations as nanothermometers, and for imaging purposes.

3.3 Thermometric characterization

To know the potential use of 3 at. % $\text{Nd}^{3+}:\text{KGd}(\text{WO}_4)_2$ nanoparticles for thermal sensing, it requires an adequate knowledge of the thermal response of the intensity of the luminescence bands. Figure 3(a) shows the emission spectra obtained for the 3 at. % $\text{Nd}^{3+}:\text{KGd}(\text{WO}_4)_2$ nanoparticles at two different temperatures (25 and 60 °C) within the physiological range. The change in the intensity of emission induced by temperature is observed in the two most intense peaks, at around 883 nm and 1067 nm, as can be seen in detail in the insets.

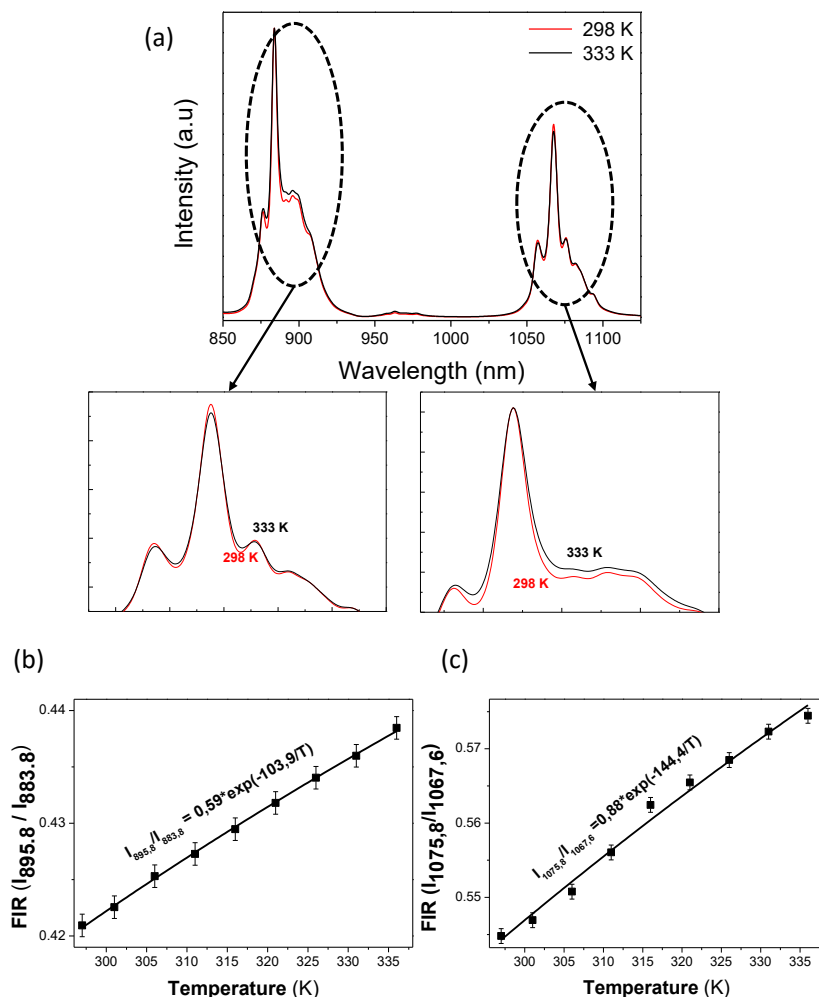


Figure 3. a) Normalized emission spectra of 3 at. % $\text{Nd}^{3+}:\text{KGd}(\text{WO}_4)_2$ nanoparticles at two different temperatures (25 and 60 °C). b) Temperature variation of the ratio between the emitted intensities at 895.8 nm and 883.8 nm in the ${}^4\text{F}_{3/2} \rightarrow {}^4\text{I}_{9/2}$ transition. c) Temperature variation of the ratio between the emitted intensities at 1075.8 nm and 1067.6 nm in the ${}^4\text{F}_{3/2} \rightarrow {}^4\text{I}_{11/2}$ transition.

This allowed us to calculate two different intensity ratios, corresponding to the two emission bands recorded for Nd^{3+} , one lying in the I-BW, and the second one lying in the II-BW. For the ${}^4\text{F}_{3/2} \rightarrow {}^4\text{I}_{9/2}$ transition, we used the ratio between the emission peaks located at 883.8 nm and 895.8 nm (see Figure 3(b)), while for the ${}^4\text{F}_{3/2} \rightarrow {}^4\text{I}_{11/2}$ transition, the ratio used was between the emission peaks located at 1067.6 nm and 1075.8 nm (see Figure 3(c)). The intensity ratios in both cases presented an almost linear behavior in the intensity change in the biological range of temperatures. Also, we calculated the thermal sensitivity (S), defined as the rate of change of the

FIR with temperature, achieving maxima of 0.12 % K⁻¹ and 0.165 % K⁻¹ at 25 °C for the I- and II-BWs, respectively.

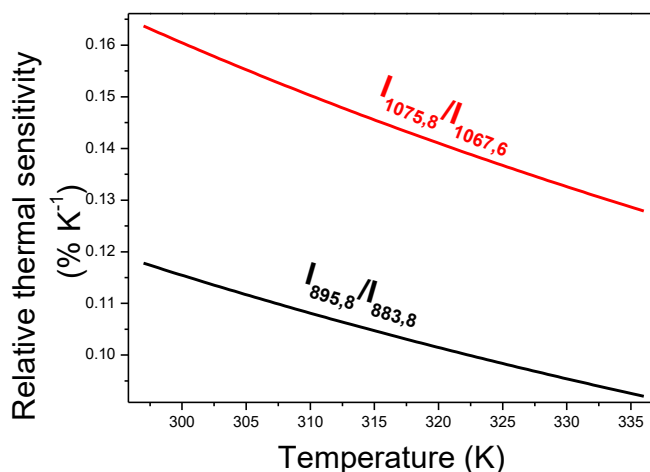


Figure 4. Relative thermal sensitivity calculated for the FIR($I_{895.8}/I_{883.8}$) and the FIR($I_{1075.8}/I_{1067.6}$) intensity ratios corresponding to the ${}^4F_{3/2} \rightarrow {}^4I_{9/2}$ and ${}^4F_{3/2} \rightarrow {}^4I_{11/2}$ Nd^{3+} transitions, respectively in $Nd^{3+}:KGd(WO_4)_2$ nanoparticles.

The sensitivity obtained in the I-BW is similar to the thermal sensitivities reported for other luminescent nanothermometers operating in this spectral region such as $Nd^{3+}:NaYF_4$ ^[44] (0.12 % K⁻¹), and slightly smaller than that reported for $Nd^{3+}:YAG$ ^[34] (0.15 % K⁻¹), $Nd^{3+}:LaF_3$ ^[19] (0.25 % K⁻¹), $Nd^{3+}:NaLa_3$ ^[45] (0.26 % K⁻¹) and $Yb^{3+}, Nd^{3+}:LiLaP_4O_{12}$ ^[33] (0.3 % K⁻¹). In the case of the sensitivity achieved in the II-BW, although it is not as high as the one reported for $Nd^{3+}:NaGdF_4 + CdS/PbS/ZnS$ @ PLGA hybrid nanoparticles,^[46] which have a thermal sensitivity of 2.5 % K⁻¹ at 30 °C, it is the first one described in this biological window for a nanothermometer constituted only by a single type of nanoparticles, and being of the order of those reported for nanothermometers based on Nd^{3+} operating in the I-BW.

3.4 Surface functionalization of the $Nd^{3+}:KGd(WO_4)_2$ nanoparticles and sedimentation analysis

As mentioned above it is very important to make the nanoparticles dispersible in a biocompatible fluid like water. To do that, we explored the silanization reaction. The results of the experiments are indicated in Table 1. We

observed that despite we modified different parameters, such as the ultrasound amplification, the pulse duration, and the contents of silane and water, the most effective change was generated when reducing the concentration of luminescent nanoparticles. Figure 4 shows TEM images of the 3 at. % $\text{Nd}^{3+}:\text{KGd}(\text{WO}_4)_2$ nanoparticles illustrating the evolution of the deagglomeration of the nanoparticles in the most significant experiments. As we can see in Figure 4(a), corresponding to conditions of Exp. 1 in Table 1, the nanoparticles form big aggregates, with sizes between 80-300 nm, and the functionalization with silane did not permit a correct dispersion. In Exp. 7, in which we increased the amplification of the ultrasound wave and the duration of the pulse, we could not still avoid the formation of aggregates with sizes around 200-700 nm (see Figure 4(b)), and although the nanoparticles start to be deagglomerated, they are embedded in the polymer matrix formed by the silane molecules. However, by using the same conditions, but reducing the amount of nanoparticle to a quarter part of the initial amount used, corresponding to the conditions of Exp.8 as listed in Table 1, we obtained nanoparticles fully dispersed with a mean size of 16 nm, as can be seen in Figure 4(c).

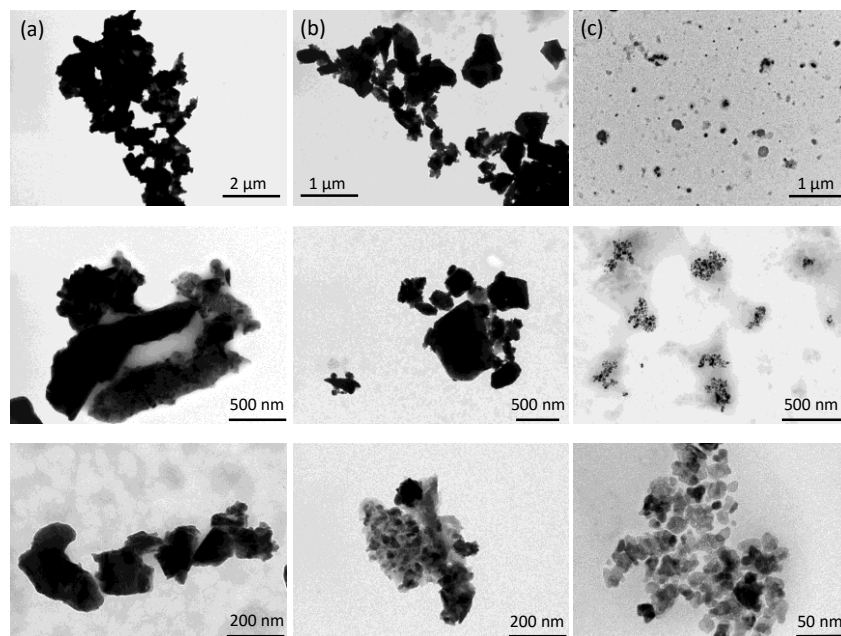


Figure 4. TEM images of the 3 at. % $\text{Nd}^{3+}:\text{KGd}(\text{WO}_4)_2$ nanoparticles with their surfaces functionalized by silanization using different conditions as listed in Table 1. a) Exp.1 (20% ultrasound amplification, 1 s pulse duration, 100% silane, 50 mg nanoparticles), b) Exp.7 (35% ultrasound amplification, 3 s pulse duration, 25% silane/75% water, 50 mg nanoparticles) and c) Exp.8 (35%

ultrasound amplification, 3 s pulse duration, 25% silane/75% water, 12 mg nanoparticles).

The sedimentation time is a very important characteristic to take into account in the dispersion of the nanoparticles, since dispersions are unstable from a thermodynamic point of view; however, they can be kinetically stable over a large period of time, which determines their shelf life.^[47]

To analyze the sedimentation of our functionalized nanoparticles, different photographs of the vials containing the 3 at. % $\text{Nd}^{3+}:\text{KGd}(\text{WO}_4)_2$ nanoparticles dispersed in water were recorded immediately after sonication and later on after 20 min., 30 min. and 40 min. Results are shown in Figure 5.

Figure 5(a) shows the photographs of 3 at. % $\text{Nd}^{3+}:\text{KGd}(\text{WO}_4)_2$ nanoparticles functionalized with silane molecules under the conditions of Exp. 1 in Table 1. Here we can observe that the nanoparticles tend to sediment at the bottom of the vial, and the water of the top part of the vial become clearer as the time increased.

As we observed in TEM images, the reduction of the nanoparticles concentration helped to achieve a larger degree of deagglomeration of the nanoparticles, thus a greater dispersion was obtained in the same period of time, as can be observed in Figure 5(b), corresponding to Exp. 8. In that case we can observe that despite the initial sedimentation, also present in the previous experiments, the turbulence of water in the top part of the vial almost did not change with time, indicating the stability of this dispersion for times longer than 40 min.

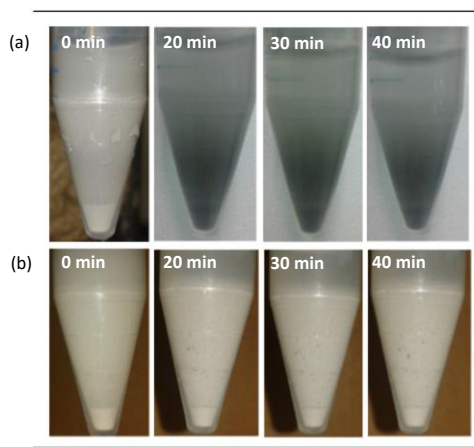


Figure 5. Sedimentation evolution with time of 3 at. % $\text{Nd}^{3+}:\text{KGd}(\text{WO}_4)_2$ nanoparticles functionalized by silanization. a) Exp. 1 (20% ultrasound amplification, 1 s pulse duration, 100% silane, 50 mg nanoparticles), and b) Exp.10(35% ultrasound amplification, 3 s pulse duration, 25% silane/75% water, 12 mg nanoparticles) as listed in Table 1.

3.5 NIR imaging of biological tissues

To explore the possibilities of using these nanoparticles as optical bioprobes for imaging in the NIR, in the II-BW, a drop of the dispersed nanoparticles in water with concentration of 0.5 mg ml^{-1} was placed between two microscopic slides. A continuous wave diode laser emitting at 808 nm with a power of 5 W was used as the excitation source, placed at a distance of 5 cm of the nanoparticles, producing an spot of $\sim 3.5 \text{ cm}$ on the sample. A piece of chicken breast, as a tissue comparable to human tissue [48] with different thicknesses ranging from 0.5 to 1 cm, was located on the top of the 3 at. % $\text{Nd}^{3+}:\text{KGd}(\text{WO}_4)_2$ nanoparticles, in between the sample and the excitation source. The signal arising from the luminescent nanoparticles was collected by a Peltier cooled InGaAs infrared camera (Xenics) with an attached filters wheel that allows collecting emissions of a particular wavelength range of interest, above 900 nm, 1000 nm and 1100 nm, respectively, and eliminate excitation laser. The first filter allows recording the images generated by the emissions at 1067 nm and 1300 nm of Nd^{3+} , and partially the emission centered at 883 nm. The second filter allows recording the images generated by the 1067 and 1300 nm of Nd^{3+} , while the third one allows only recording the images generated by the 1300 nm emission of Nd^{3+} .

Figure 6 shows the spectral NIR images collected using different filters. As can be seen up to a penetration depth of at least 1 cm can be achieved with the 900 and 1000 nm long pass filters that allow passing the NIR emission of Nd^{3+} centered at 1067 nm. Such deep penetration of the NIR emission into the biological tissue can be attributed to the fact that 1067 nm is located at the II-BW, that presents less absorption and scattering of the light.

In the case of the 1100 nm longpass filter, we could not observe the fluorescence at 1 cm. This can be explained by the fact that the $1.3 \mu\text{m}$ Nd^{3+} emission is less efficient than those at 883 and 1067 nm. However, a penetration depth of 0.5 cm could still be easily observed in that case.

To the best of our knowledge, this is the first time that the penetration depth in biological tissue is tested using Nd^{3+} -doped nanoparticles operating in the II-BW, achieving a record penetration depth of 1 cm, much larger than that reported for Nd^{3+} -doped nanoparticles operating in the I-BW (0.5 cm).^[19,34] A possible reason to explain such a high penetration depth might be the high absorption cross-section of Nd^{3+} in $\text{KGd}(\text{WO}_4)_2$,^[39] much higher than that reported for YAG,^[49] or GdVO_4 ,^[50] for

instance. In fact, the intensity of the emissions at 883 and 1067 nm of Nd^{3+} in $\text{KGd}(\text{WO}_4)_2$ is two orders of magnitude higher than that obtained in NaGdF_4 (see Figure S1 in Supplementary Material).

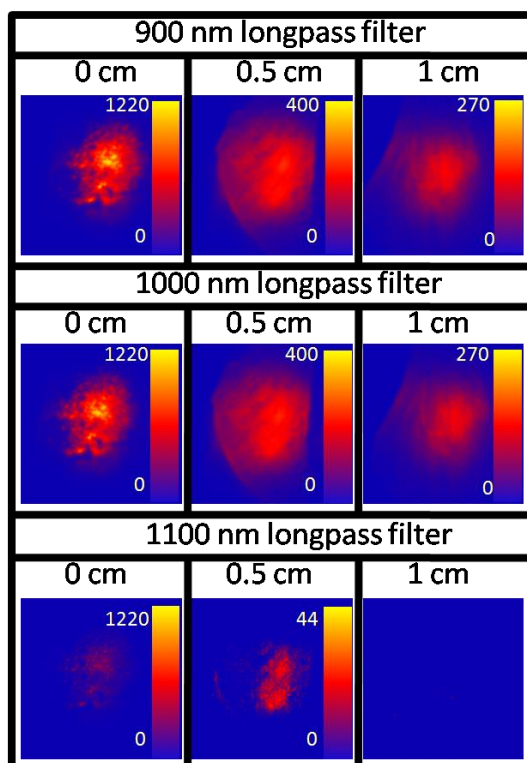


Figure 6. NIR emission images of $\text{Nd}^{3+}:\text{KGd}(\text{WO}_4)_2$ nanoparticles at different thickness of chicken breast.

4. CONCLUSIONS

In summary, we performed an investigation of the luminescence properties of Nd^{3+} -doped $\text{KGd}(\text{WO}_4)_2$ nanoparticles, showing intense emissions bands at around 883 nm and 1067 nm corresponding to the ${}^4\text{F}_{3/2} \rightarrow {}^4\text{I}_{9/2}$ and ${}^4\text{F}_{3/2} \rightarrow {}^4\text{I}_{11/2}$ transitions, lying in the I- and II-BW, respectively, under infrared (808 nm) optical excitation. The optimum doping conditions were 3 at. % of Nd^{3+} , which showed the highest emission intensity. The thermal characterization of the luminescence properties of these nanoparticles indicate that they can be used as luminescent nanothermometers in the I- and II-BW. When working in the I-BW, the thermal sensitivity of our nanoparticles is similar to the previously reported for other materials. Added to this, the dispersion of the nanoparticles we achieved when functionalized with silane molecules, indicate that these nanoparticles can be potentially used in in-vivo tests, due to their sizes of

~16 nm, which would prevent their sedimentation in blood vessels. We also performed NIR imaging in biological tissue with these nanoparticles, achieving at least a penetration depth 1 cm when operating in the II-BW, the maximum ever achieved with Nd³⁺-doped nanoparticles operating in this spectral region. Thus, these Nd³⁺:KGd(WO₄)₂ luminescent nanoparticles seems to be promising materials for nanothermometry and imaging applications in the second biological windows. Furthermore, since one of the great interests for the use of nanoparticles in the biomedical field is their potential multifunctionality, these particles containing Gd³⁺ might, in the future, be investigated for their contrasting capabilities for MRI, compacting different tools in a single theranostic nanoparticle.

ACKNOWLEDGEMENTS

This work was supported financially by the Spanish Government under Projects No. MAT2013-47395-C4-4-R and TEC2014-55948-R, and by Catalan Authority under Project No. 2014SGR1358. Ol. A. Savchuk is supported by Catalan Government through the fellowship 2015FI-B2 00136. F.D. acknowledges additional support through the ICREA Academia awards 2010ICREA-02 for excellence in research.

REFERENCES

1. Jaque, D.; Vetrone, F. Luminescence Nanothermometry. *Nanoscale* **2012**, *4*, 4301-4326.
2. Brites, C. D. S.; Lima, P. P.; Sila, N. J. O.; Millan, A.; Palacio, F.; Carlos, L. D. Thermometry at the Nanoscale. *Nanoscale* **2012**, *4*, 4799-4829.
3. Ang, L. Y.; Lim, M. E.; Ong, L. C.; Zhang, Y. Applications of Upconversion Nanoparticles in Imaging, Detection and Therapy. *Nanomedicine* **2011**, *6*, 1273-1288.
4. Stark, A. M.; Way, S. The Use of Thermovision in the Detection of Early Breast Cancer. *Cancer* **1974**, *33*, 1664-1670.
5. Lee, J.; Kotov, N. A. Thermometer Design at the Nanoscale. *Nano Today* **2007**, *2*, 48-53.
6. Ring, E. The Historical Development of Temperature Measurement in Medicine. *J. Infrared Phys. Technol.* **2007**, *49*, 297-301.
7. Wolfbeis, O. S. Springer series on fluorescence 7. *Lanthanide luminescence: photophysical, analytical and biological aspects*; Hänninen, P., Härmä, H., Eds.; Springer-verlag: Berlin, 2011; pp. 183-184.

8. Vetrone, F.; Naccache, R.; Zamarron, A.; de la Fuente A. J.; Sanz-Rodriguez F.; Maestro, L. M.; Rodriguez E. M.; Jaque, D.; Sole, G. J.; Capobianco, J. A. Temperature Sensing Using Fluorescent Nanothermometers. *ACS Nano* **2010**, *4*, 3254-3258.
9. Chen, X.; Liu, Y.; Tu, D. Lanthanide-Doped Luminescent Nanomaterials: From Fundamental to Bioapplications; Springer: Berlin, 2014; pp. 59-60.
10. Attanayake, G. K. Development of Highly Luminescent and Water-Dispersible Lanthanide Based Nanomaterials for Potential Bio-Medical Imaging, Western Carolina University, Master thesis (2013).
11. Méndez, M. Synthesis and Characterization of Downshifting Ln³⁺ Doped Lanthanum-Based Nanoparticles for Photovoltaic Applications, Universitat Rovira i Virgili, Doctoral thesis (2013).
12. Diamente, P. R.; van Veggel F. C. J. Water-soluble Ln³⁺-doped LaF₃ nanoparticles: Retention of Strong Luminescence and Potential as Biolabels, *J. Fluorescence* **2015**, *15*, 543-551.
13. Dong *et al.* NIR-to-NIR Two-Photon Excited CaF₂:Tm³⁺, Yb³⁺ Nanoparticles: Multifunctional Nanoprobes for Highly Penetrating Fluorescence Bio-Imaging. *ACS Nano* **2011**, *5*, 8665-8671.
14. Frangioni, J. V. In Vivo Near-Infrared Fluorescence Imaging. *Curr. Opin. Chem. Biol.* **2003**, *7*, 626-634.
15. Marquez, G.; Wang, L. V.; Lin, S. P.; Scharz, J. A.; Thomsen, S. L. Anisotropic Absorption and Reduced Scattering Spectra of Chicken Breast Tissue Measured Using Oblique Incidence Reflectometry. *Applied Optics* **1998**, *37*, 798-804.
16. Smith, A. M.; Mancini, M. C.; Nie, S. Bioimaging: Second Window for in Vivo Imaging. *Nat. Nanotechnol.* **2009**, *4*, 710-711.
17. Weissleder, R. A Clearer Vision for in Vivo Imaging. *Nat. Biotechnol.* **2001**, *19*, 316-317.
18. Rocha, U.; Kumar, K. U.; Jacinto, C.; Villa, I.; Sanz-Rodriguez, F.; Iglesias de la Cruz, M. C.; Juarranz, A.; Carrasco, E.; van Veggel, F. C. J. M.; Bovero, E.; Sole, J. G.; Jaque, D. Neodymium-Doped LaF₃ Nanoparticles for Fluorescence Bioimaging in the Second Biological Window. *Small* **2014**, *10*, 1141-1154.
19. Rocha, U.; da Silva, C. J.; Silva, W. F.; Guedes, I.; Benayas, A.; Maestro, L. M.; Elias, M. A.; Bovero, E.; van Veggel, F. C. J. M.; Sole, J. A. G.; Jaque, D. Subtissue

- Thermal Sensing Based on Neodymium-Doped LaF₃ Nanoparticles. *ACS Nano* **2013**, *7*, 1188-1199.
20. Welsher, K.; Sherlock, S. P.; Dai, H. Deep-Tissue Anatomical Imaging of Mice Using Carbon Nanotube Fluorophores in the Second Near-Infrared Window. *Proc. Natl. Acad. Sci.* **2011**, *108*, 8943-8948.
21. Naccache, R.; Rodriguez, E. M.; Bogdan, N.; Sanz-Rodriguez, F.; de la Cruz, M. C. I.; de la Fuente, A. J.; Vetrone, F.; Jaque, D.; Sole, J. G.; Capobianco, J. A. High-Resolution Fluorescence Imaging of Cancers Using Lanthanide Ion-Doped Upconverting Nanocrystals. *Cancers* **2012**, *4*, 1067-1105.
22. Chatterjee, D. K.; Rufaihah, A. J.; Zhang, Y. Upconversion Fluorescence Imaging of Cells and Small Animals Using Lanthanide Doped Nanocrystals. *Biomaterials* **2008**, *29*, 937-943.
23. Wang, F.; Liu, X. Recent Advances in the Chemistry of Lanthanide-Doped Upconversion Nanocrystals. *Chem. Soc. Rev.* **2009**, *38*, 976-989.
24. An, M.; Cui, J.; He, Q.; Wang, L. Down-/Up-Conversion luminescence Nanocomposites for Dual-Modal Cell Imaging. *J. Mater. Chem.* **2013**, *1*, 1333-1339.
25. Liu, Y.; Tu, d.; Zhu, H.; Li, R.; Luo, W.; Chen, X. A Strategy to Achieve Efficient Dual-Mode Luminescence of Eu³⁺ in Lanthanides Doped Multifunctional NaGdF₄ Nanocrystals. *Adv. Mater.* **2010**, *22*, 3266-3271.
26. Kumar, R.; Nyk, M.; Ohulchanskyy, T. Y.; Flask, C. A.; Prasad, P. N. Combined Optical and MR Bioimaging Using Rare Earth Ion Doped NaYF₄ Nanocrystals. *Adv. Funct. Mater.* **2009**, *19*, 853-859.
27. Chen, J.; Zhao, J. X. Upconversion Nanomaterials: Synthesis, Mechanism, and Applications in Sensing. *Sensors* **2012**, *12*, 2414-2435.
28. Liu, K.; Liu, X.; Zeng, Q.; Zhang, Y.; Tu, L.; Liu, T.; Kong, X.; Wang, Y.; Cao, F.; Lambrechts, S. A. G.; Aalders, M. C. G.; Zhang, H. Covalently Assembled NIR NanoplatforM for Simultaneous Fluorescence Imaging and Photodynamic Therapy of Cancer Cells. *ACS Nano* **2012**, *6*, 4054-4062.
29. Pokhrel, M.; Mimun, L. C.; Yust, B.; Kumar, G. A.; Dhanale, A.; Tang, L.; Sardar, D. K. Stokes Emission in GdF₃:Nd³⁺ Nanoparticles for Bioimaging Probes. *Nanoscale* **2014**, *6*, 1667-1674.
30. Li, X.; Wang, R.; Zhang, F.; Zhou, L.; Shen, D.; Yao, C.; Zhao, D. Nd³⁺ Sensitized Up/Down Converting Dual-Mode Nanomaterials for Efficient *In-vitro* and *In-vivo* Bioimaging Excited at 800 nm. *Sci. Rep.* **2013**, *3*, 1-7.

31. Deloachet al., Evaluation of absorption and emission properties of Yb³⁺ doped crystals for laser applications, *Quantum Electron.* **29**, No. 4, 1179-1191 (1993).
32. Krupke, W. F. Ytterbium Solid-State Lasers. *Quantum Electron.* **2000**, *6*, 1287–1296.
33. Marciniak, L.; Bernarkiewicz, A.; Stefanski, M.; Tomala, R.; Hreniak, D.; Strek, W. Near Infrared Absorbing Near Infrared Emitting Highly-Sensitive Luminescent Nanothermometer Based on Nd³⁺ to Yb³⁺ Energy Transfer. *Phys. Chem. Chem. Phys.* **2015**, *7*, 24315-24321.
34. Benayas, A.; del Rosal, B.; Pérez-Delgado, A.; Santacruz-Gómez, K.; Jaque, D.; Hirata, G. A.; Vetrone, F. Nd:YAG Near-Infrared Luminescent Nanothermometers *Adv. Opt. Mater.* **2015**, DOI: 10.1002/adom.201400484.
35. Pujol, M. C.; Sole, R.; Massons, J.; Gavalda, Jna.; Solans, X.; Zaldo, C.; Diaz, F.; Aguilo, M. Structural Study of Monoclinic KGd(WO₄)₂ and Effects of Lanthanide Substitutions. *J. Appl. Cryst.* **2001**, *34*, 1-6.
36. Wang, Z.; Li, Y.; Jiang, Q.; Zeng, H.; Ci, Z.; Sun, L. Pure Near-Infrared to Near-Infrared Upconversion of Multifunctional Tm³⁺ and Yb³⁺ co-doped NaGd(WO₄)₂ Nanoparticles. *J. Mater. Chem. C.* **2014**, *2*, 4495-4501.
37. Chen, J.; Zhao, J. X. Spectroscopic Properties of KGd(WO₄)₂ and KGd(WO₄)₂:Ho³⁺ Single Crystals Studied by Brillouin and Raman Scattering Methods. *Sensors* **2012**, *12*, 2414-2435.
38. Petrov, V.; Güell, F.; Massons, J.; Gavalda, J.; Sole, R. M.; Aguilo, M.; Diaz, F.; Griebner, U. Efficient Tunable Laser Operation of Tm:KGd(WO₄)₂ in the Continuous-Wave Regime at Room Temperature. *Quantum Electron.* **2004**, *40*, 1244-1251.
39. Mateos, X.; Pujol, M. C.; Güell, F.; Galán, M.; Solé, R. M.; Gavalda, J.; Aguiló, M.; Massons, J.; and Díaz F. Erbium Spectroscopy and 1.5 μm Emission in KGd(WO₄)₂:Er, Yb Single Crystals. *Quantum Electron.* **2004**, *40*, 759-770.
40. Galceran, M.; Pujol, M. C.; Aguiló, M.; Díaz, F. Sol-Gel Modified Pechini Method for Obtaining Nanocrystalline KRE(WO₄)₂ (RE = Gd and Yb). *J. Sol-gel Sci. Technol.* **2007**, *42*, 79-88.
41. Thangaraju, D.; Durairajan, A.; Balaji, D.; Moorthy Babu, S. Synthesis and Characterization of Monoclinic KGd(WO₄)₂ Particles for Non-Cubic Transparent Ceramics. *Opt. Mater.* **2013**, *35*, 753–756.
42. Monshi, A.; Reza, M. Modified Scherrer Equation to Estimate More Accurately Nano-Crystallite Size Using XRD. *J. Nano Sci Eng.* **2012**, *2*, 154-160.

43. Leroy, A.; Klug, H. Determination of Crystallite Size with the X-Ray Spectrometer. *J. Appl. Phys.* **1950**, *21*, 137- 143.
44. Wawrzynczyk, D.; Bednarkiewicz, A.; Nyk, M.; Strek, W.; Samoc, M. Neodymium(III) Doped Fluoride Nanoparticles as Non-Contact Optical Temperature Sensors. *Nanoscale* **2012**, *4*, 6959–6961.
45. Carrasco, E.; del Rosal, B.; Sanz-Rodriguez, F.; de la Fuente, A. J.; Haro Gonzalez, P.; Rocha, U.; Kumar, K. U.; Jacinto, C.; Garcia-Sole, J.; Jaque, D. Intratumoral Thermal Reading During Photo-Thermal Therapy by Multifunctional Fluorescent Nanoparticles. *Adv. Funct. Mater.* **2015**, *4*, 615-626.
46. Ceron, E. N.; Ortgiesm D. H.; del Rosal, B.; Ren, F.; Benayas, A.; Vetronwe, F.; Ma, D.; Sanz-Rodriguez, F.; Sole, J. G.; Jaque, D.; Rodriguez, E. M. Hybrid Nanostructures for High-Sensitivity Luminescence Nanothermometry in the Second Biological Window. *Adv. Mater.* **2015**, *27*, 4781–4787.
47. Kissa E. Dispersions: Characterization, Testing, and Measurement. *Marcel Dekker*: New York, 1999; pp. 6-7.
48. Marquez, G.; Wang, L.V.; Lin, S. P.; Schwartz, J. A.; Thomsen, S. L. Anisotropy in the Absorption and Scattering Spectra of Chicken Breast Tissue. *Appl. Opt.* **1998**, *37*, 798-804.
49. Aull, B.F.; Janssen, H.P. Vibronic Interactions in Nd:YAG Resulting in Nonreciprocity of Absorption and Stimulated Emission Cross Sections. *IEEE J Quantum Electron.* **1982**, *18*, 925-930.
50. Jensen, T.; Ostroumov, V.G.; Meyn, J.P.; Huber, G.; Zagumennyi, A.I.; Shcherbakiv, I.A. Spectroscopic Characterization and Laser Performance of Diode-Laser-Pumped Nd:GdVO₄. *Appl. Phys. B* **1994**, *58*, 373-379.

Paper XII

Savchuk, Ol. A.; Carvajal, J. J.; Haro-González, P.; Aguiló, M.; Díaz, F. *Luminescent nanothermometry using short-wavelength infrared light* (2016) To be submitted in Chem. Phys. Phys. Chem.

Luminescent nanothermometry using short-wavelength infrared light

Ol. A. Savchuk,¹ J. J. Carvajal,^{,1} P. Haro-Gonzalez,² M. Aguiló,¹ F. Díaz¹*

¹Physics and Crystallography of Materials and Nanomaterials (FiCMA-FiCNA) and EMaS, Universitat Rovira I Virgili (URV), Marcel·lí Domingo 1, Tarragona, 43007, Spain

²Fluorescence Imaging Group, Departamento de Física de Materiales, Facultad de Ciencias, Universidad Autónoma de Madrid, 28049 Madrid, Spain

*Corresponding author: joanjosep.carvajal@urv.cat

Keywords: luminescence, nanothermometry, nanosensors, biological windows.

ABSTRACT

We analyzed the potentiality of the short-wavelength infrared (SWIR) emissions of different lanthanide ions (Er^{3+} , Tm^{3+} and Ho^{3+}) embedded in different hosts for luminescence thermometry. The 1.55 μm emission band generated by Er^{3+} has different Stark sub-levels that can be used in temperature sensing purposes. However, the thermal sensitivity that can be achieved with this emission is relatively low. In the case of Tm^{3+} containing nanoparticles, the emissions arising from the $^3\text{F}_4$ and $^3\text{H}_4$ energy levels, that are electronically coupled, useful for luminescence thermometry, with a linear evolution for the intensity ratio as the temperature increases that simplifies the calibration procedure for thermometers based on this parameter. Tm,Yb:NaYF_4 nanoparticles were found to have the highest relative sensitivity among the $\text{Tm}^{3+}, \text{Yb}^{3+}$ co-doped nanoparticles analyzed. Adding Ho^{3+} to the system generate an efficient energy transfer between the Tm^{3+} and Ho^{3+} ions, that results in a new emission line centered at 1.96 μm that can be used also for luminescence thermometry purposes. Pumping at 808 nm in these systems increases their thermal sensitivity. The thermal sensitivities achieved for SWIR luminescence thermometry are comparable to those reported previously in the visible, and are higher than those reported for most of the systems operating in the I- and II-BWs.

We demonstrated the potentiality of these emissions in the SWIR region for luminescence thermometry and imaging in ex vivo experiments by monitoring the heat generated by hot air in chicken meat, with a penetration depth of at least 0.5 cm

in this kind of biological tissue.

1. Introduction

Hyperthermia in the treatment of cancer requires monitoring the body temperature to ensure patient safety [1, 2]. In addition, temperature must be measured to confirm that heat has been adequately applied to the affected tissues and to prevent damages in the surrounding health tissue. Moreover, any temperature increment in the body is usually a sign of the presence of a disease or infection [3]. Thus, temperature monitoring techniques are called to play a major role in assuring safe and effective medical treatments.

Usually, contact type thermometers are used to measure the body temperature of patients in cavities such as the mouth, armpit or rectum, but they provide only a measurement of the surface temperature. If local temperature measurements are required apart from these areas, contact thermometers must be put in contact with internal tissues producing pain and risk of infection [4]. One of the most promising alternatives to avoid these problems is the use of noncontact thermometry methods, which provide fast, accurate and non invasive techniques for monitoring the temperature inside the body [4]. Among the different noncontact thermometry techniques, luminescence thermometry offers a high spatial and thermal resolution [5, 6]. Among luminescent nanothermometers, the use of lanthanide (Ln^{3+}) doped materials has some advantages among other luminescent systems, including: reduced or non-existing toxicity, non photobleaching effect, and excitation with low cost near infrared diode lasers [7].

Among Ln^{3+} -based luminescence nanothermometers, those using upconversion mechanisms that convert efficiently near infrared (NIR) radiation to visible light have been extensively studied, especially those based on Er^{3+} , Yb^{3+} co-doped systems [8-10]. However, biological tissues show strong extinction coefficients in the visible range of the electromagnetic spectrum, restricting the use of this kind of light for biomedical applications. A reduced absorption and scattering in biological tissues can be achieved by using specific wavelengths lying in the NIR, in the so called biological or therapeutic windows [11, 12] localized between 650-950 nm (first biological window, I-BW) and 1000-1350 nm (second biological window, II-BW). Recently, the benefits of using luminescent nanoparticles emitting in these biological windows for in vivo temperature controlled photothermal therapy of tumors have been

demonstrated [13]. In this sense, Nd^{3+} ions have become the most promising lanthanide ion because of its efficient emissions lying in these spectral ranges after pumping at ~ 800 nm with highly efficient and low cost diode lasers [14-19]. However, still the quest for an outstanding host matrix for Nd^{3+} that maximizes the quantum efficiency of this ion, allowing for high penetration depths in the body is a matter of special interest. For instance, using $\text{KGd}(\text{WO}_4)_2$ as the host matrix, in which lanthanide ions exhibit high absorption and emission cross sections [20], a penetration depth higher than 1 cm has been achieved [21].

Despite all this work, no studies have been devoted to explore the possibilities of longer emission wavelengths in luminescence thermometry. Naczynski et al. [22] reported that longer wavelengths than those considered in the II-BW, lying in the so called short-wavelength infrared (SWIR) that extends from 1.35 to 2.3 μm , transmit more effectively through specific biological tissues than those used in the visible, I- and II-BWs. For instance, they demonstrated that SWIR light at 1.5 μm transmits three- and two-times more effectively in oxygenated blood and melanin-containing tumors, respectively, than 550 nm light. They also showed that the majority of biological tissue samples exhibit markedly low attenuation between 1 – 1.35 μm as well as between 1.5 – 1.65 μm , effectively extending the wavelength region of lowered attenuation within the II-BW. However, when comparing the penetration depth in biological tissues of light in both regions, while $<0.4\%$ light in the I- and II-BW penetrated through 5 mm of pigmented tumor tissue, $\sim 80\%$ of the transmittance was achieved by SWIR light, being detectable through 1 cm of phantom tissue, suggesting that light in the I- and II-BWs has a limited use for detecting optical probes in tissues containing melanin. The authors attributed these advantages to the reduced tissue absorbance and scattering within the SWIR region. In fact, in a real scenario in which light would need to penetrate through multiple tissue layers, the refractive index changes experimented by light would lead to greater scattering conditions. Thus, in this situation, emissions in the SWIR region would show higher signal-to-background ratios than visible or NIR light.

Here, we study the emissions in the SWIR region generated by Er^{3+} , Tm^{3+} and Ho^{3+} ions, in most cases in combination with Yb^{3+} , used as sensitizer, in different host matrices, including fluorides (NaYF_4), oxyfluorides ($\text{NaY}_2\text{F}_5\text{O}$), simple oxides (Lu_2O_3) and complex oxides ($\text{KGd}(\text{WO}_4)_2$ and $\text{KLu}(\text{WO}_4)_2$), excited with diode lasers emitting 808 and 980 nm radiation. We analyzed the possibilities of these emissions

for temperature sensing purposes, determining also which hosts would be more suitable. The thermometric responses of these particles are compared with those shown by other Ln^{3+} -doped nanoparticles operating in the visible, and in the I- and II-BWs, showing the potential of SWIR emitting nanoparticles for temperature measurements in biomedical applications.

2. Experimental section

2.1 Nanoparticles synthesis

Hexagonal 1 % Er, 20 % Yb: NaYF_4 , 1 % Tm, 20 % Yb: NaYF_4 and 1 % Er, 20 % Yb: $\text{NaY}_2\text{F}_5\text{O}$ nanoparticles were provided by Boston Applied Technology.

Monoclinic potassium rare-earth double tungstates $\text{KRE}(\text{WO}_4)_2$ (RE=Lu, Gd) single doped with 1 % Tm; co-doped with 1 % Tm, 10 % Yb; 1 % Tm, 1.5 % Ho or 3 % Er, 10 % Yb and triply doped with 1 % Tm, 10 % Yb, 1.5 % Ho were synthesized by the modified Pechini sol-gel method. Analytic grade purity reagents of Ho_2O_3 (99.9999%), Tm_2O_3 (99.9%), Yb_2O_3 , Lu_2O_3 (99.9999%) and Gd_2O_3 (99.9999%) were dissolved in hot nitric acid in stoichiometric proportions to form the nitrate precursors. Citric acid (CA), as the chelating agent, and ethylenglycol (EG), as the esterification agent, were used also in this reaction. The nitrate precursors were dissolved in distilled water with citric acid in a molar ratio of CA to metal cations $C_M = [\text{CA}]/[\text{METAL}] = 1$. Ammonium tungstate $(\text{NH}_4)_2\text{WO}_4$ (99.99%) and potassium carbonate K_2CO_3 (99.99%) were added to the aqueous solution that was heated at 353 K under magnetic stirring during 24 h until complete dissolution. Then, EG was added to the mixture in a molar ratio $C_E = [\text{EG}]/[\text{CA}] = 2$. The solution was heated at 373 K to evaporate water and generate the polymeric gel. After that, the polymeric gel was calcined at 573 K for 3 h to obtain the precursor powders that were then calcined at 1023 K for 2 h to eliminate the organic compounds and crystallize the desired nanoparticles.

4 % Er, 20 % Yb doped Lu_2O_3 nanoparticles were synthesized also by the modified Pechini sol-gel method. Lu_2O_3 , Er_2O_3 and Yb_2O_3 were dissolved in hot nitric acid to form the nitrate salts. In this case we used ethylenediaminetetraacetic acid (EDTA) as the complexation agent. The nitrate salts were dissolved in an aqueous solution with an EDTA molar ratio to metal cations $C_M = [\text{EDTA}]/[\text{METAL}] = 1$. Further, EG was added to the mixture in a molar ratio $C_E = [\text{EDTA}]/[\text{EG}] = 2$, and the solution was heated on a hot plate under constant stirring to form a transparent solution. Then, the

solution was dehydrated on the hot plate at 363 K to form a polymeric viscous white gel. After, the gel was calcined at 573 K to eliminate the organic compounds. A brown foam was formed when the organic compounds were calcined, resulting in a fragile brown mass that constitutes the precursor powders. Finally, these precursor powders were calcined at 1073 K for 2 h to obtain the nanocrystalline powder.

2.2 Comparative intensity photoluminescence measurements

Nanoparticles were placed in a borosilicate bottom flat vial and compacted to ensure that they fully fill the bottom of the vial. The vial was inserted in a sample holder that was placed inside a Labsphere 4GPS-020-SL integrating sphere. Samples were excited with a 200 μm core diameter fiber-coupled laser diode from Apollo Instruments, Inc. emitting at 808 or 980 nm. The laser was collimated with a spot size of 3 mm on the sample, and a power of 100 mW. The emission arising from the nanoparticles was collected using a Yokogawa AQ6375 optical spectrum analyzer (OSA).

2.3 Temperature dependent photoluminescence measurements

For the temperature-dependent photoluminescence experiments, the nanoparticles were introduced into a modified Linkam THMS 600 heating stage, with a thermocouple connected to the heating stage for temperature control, and with a boron nitride disk that homogenizes the temperature distribution inside the chamber and along the sample. The heating stage was placed in a homemade microscope setup in which the same diode lasers with emission at 808 and 980 nm described before were used to excite the sample using a microscope objective with 40X magnification and N.A. of 0.6 that produced a laser spot of ~ 10 μm on the sample. The emission was collected by the same microscope objective, and after passing a dichroic filter for elimination of the excitation wavelength, was sent to the Yokogawa AQ6375 OSA.

3. Results and Discussion

3.1. Er³⁺ emissions in the SWIR

Er³⁺, Tm³⁺ and Ho³⁺ ions show several SWIR emission lines that can be used in nanothermometry. Spectra of Er³⁺, Yb³⁺ co-doped nanoparticles excited at 980 nm are shown in Figure 1a. The emission spectra consist of a broad band located at around 1.55 μm . The mechanism of production of this emission band is the following (see

Figure 1b): after the absorption of a photon at 980 nm by Yb^{3+} the electrons of Yb^{3+} are promoted to the excited $^2\text{F}_{5/2}$ energy level. Then, an energy transfer from the excited $^5\text{F}_{5/2}$ energy level of Yb^{3+} to Er^{3+} ions occurs, populating the $^4\text{I}_{11/2}$ energy level of this ion. After, a multiphonon relaxation from the $^4\text{I}_{11/2}$ to the $^4\text{I}_{13/2}$ energy level allows generating the radiative $^4\text{I}_{13/2} \rightarrow ^4\text{I}_{15/2}$ transition, whose emission is centered at $1.55 \mu\text{m}$ [20].

As can be seen in Figure 1a, Er,Yb:NaYF₄ nanoparticles show the most intense emission among the materials analyzed. This material already received an important attention for bioimaging applications and nanothermometry in the visible region because of its efficient upconversion emissions [23, 24]. Er,Yb:NaY₂F₅O and Er,Yb:KGd(WO₄)₂ nanoparticles show emissions with a similar intensity. Finally, with less intensity we encounter the sesquioxide Er,Yb:Lu₂O₃ nanoparticles. Thus, according to these results, fluorides, and in particular NaYF₄, are the most efficient materials to generate emissions from Er^{3+} in the SWIR region.

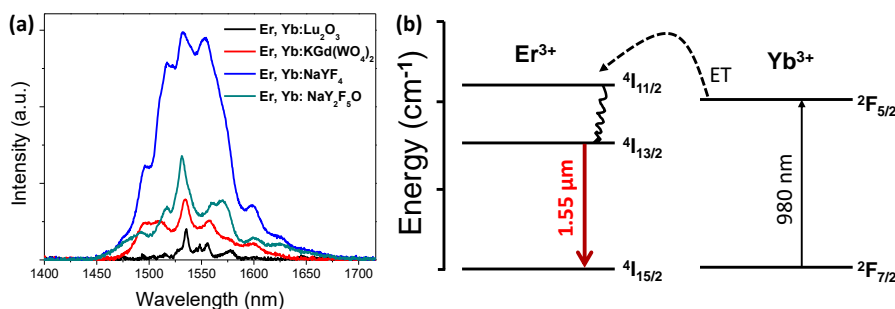


Figure 1. (a) Absolute intensity of the different hosts co-doped with Er^{3+} and Yb^{3+} ions excited at 980 nm. (b) Mechanism of generation of SWIR emission lines for the samples doped with Er^{3+} and Yb^{3+} .

We studied the temperature induced changes in the intensity of the emission line centered at $1.55 \mu\text{m}$, produced by Er^{3+} in the different nanoparticles analyzed in this work. The results are presented in Figure 2a. In general, we observed that when the temperature increases, the intensity of the emission band decreases, and this effect is more accentuated for Er^{3+} ,Yb:NaYF₄ nanoparticles.

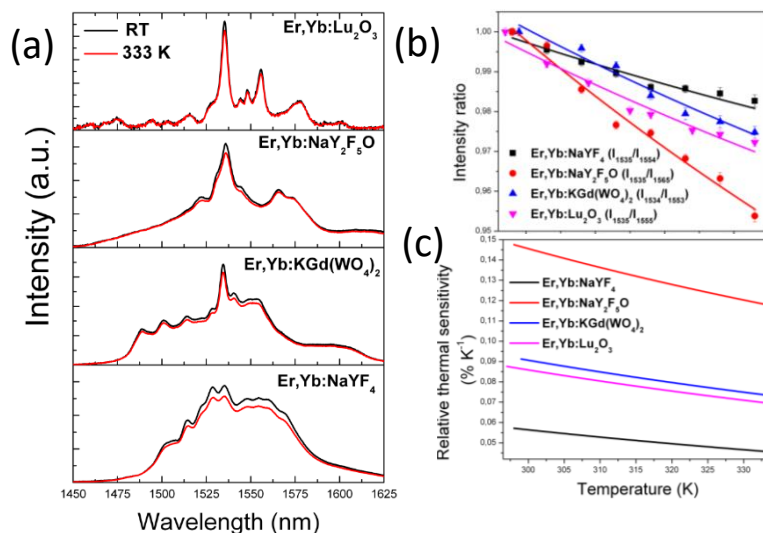


Figure 2. (a) Near infrared emission of Er³⁺, Yb³⁺ co-doped samples recorded at room temperature and 333 K; (b) intensity ratio of the emission lines as a function of temperature; (c) relative thermal sensitivity of Er³⁺, Yb³⁺ co-doped samples.

The fluorescence intensity ratio (FIR) between the emission lines generated from the Er³⁺, Yb³⁺ co-doped systems as a function of temperature are presented in Figure 2b. The FIR is defined as:

$$FIR = \frac{I_1}{I_2} = \frac{g_1 v_1 \sigma_1}{g_2 v_2 \sigma_2} = B \exp\left(-\frac{\Delta E}{k_B T}\right) \quad (1)$$

where g_i , v_i , and σ_i , are the degeneracy of levels, the spontaneous emission, and the absorption rates, respectively, k_B is the Boltzmann constant, T is the absolute temperature, and ΔE is the energy difference between the two energy states considered and can be used when the emission lines considered arise from thermally coupled levels, i.e. when their energy separation is low, of the order of 200 – 2000 cm⁻¹ [25]. In this case, the emission lines considered arise from different Stark sublevels of the same manifold, thus they can be considered to be thermally coupled. In each case we considered the emission lines that show the highest slope for FIR. The FIR follows an almost linear tendency in all cases and can be fitted to the Boltzmann distribution described in eq. 1 [25]. The FIR is higher for the Er,Yb:NaY₂F₅O nanoparticles, despite the highest intensity emission and the maximum temperature intensity change was observed for Er,Yb:NaYF₄ nanoparticles

(see Figures 1a and 2a). This is a consequence of the activation of phonon-assisted processes and multi-phonon decays caused by temperature increase when oxygen is incorporated in the nanoparticles. The two oxides considered in this work showed almost the same slope (the FIR lines are almost parallel), while in that case the fluoride nanoparticles show the smallest slope. This is due to the fact that the intensity of almost all the emission lines in the emission spectra of the Er,Yb:NaYF₄ nanoparticles decreased the same amount when the temperature increased.

Another important parameter that allows to compare the performance of luminescent thermometers is the thermal sensitivity, that considers the maximum change of the parameter considered, the FIR in this case, for each temperature degree. Here, we used the relative thermal sensitivity, which was calculated using the following equation [5]:

$$S_{rel} = \frac{\partial R / \partial T}{R} \quad (2)$$

where R is the luminescent parameter that changes with temperature (FIR in the present case). The relative thermal sensitivities for the Er³⁺ emissions in the SWIR considered in this article are presented in Figure 2c. All the studied nanoparticles show a relative thermal sensitivity with their maxima at room temperature. Er,Yb:NaY₂F₅O nanoparticles show the highest relative sensitivity (0.15 % K⁻¹), almost 3 times higher than that of Er,Yb:NaYF₄ nanoparticles. We showed previously the potentiality of Er,Yb:NaY₂F₅O nanoparticles in luminescence nanothermometry using the lifetime thermometry technique in the visible, showing curiously that the thermal sensitivity in that case was also three times higher than for Er,Yb:NaYF₄ nanoparticles [26].

A part from the potential biological applications of this line for temperature determination, it can also be used to determine the temperature in telecommunication systems in order to prevent optical damages by the pumping lasers, since the 1.55 μm line falls in the S-band region of optical telecommunications and Er³⁺-doped fibers are commercially used for amplifying this signal [27, 28]. However, when comparing the relative thermal sensitivities of Er³⁺, Yb³⁺ co-doping systems operating in the visible, with those achieved here, Er³⁺ emissions in the SWIR show smaller thermal sensitivities, indicating that Er³⁺ probably is not the best ion to be used for luminescence thermometry in the SWIR.

3.2. Tm^{3+} and Ho^{3+} emissions in the SWIR after pumping at 980 nm

The photoluminescence spectra in the SWIR region of different nanoparticles co-doped with Tm^{3+} and Yb^{3+} ions excited with a 980 nm cw diode laser are shown in Figure 3a. The spectra consist of two emission bands located at $\sim 1.45 \mu m$ and $\sim 1.8 \mu m$. The mechanism for the generation of these emission lines starts when Yb^{3+} absorbs a photon at 980 nm and promotes its electrons to the $^2F_{5/2}$ excited state. Then, an energy transfer process occurs due to the energy match between the $Yb^{3+} \ ^2F_{5/2}$ and $Tm^{3+} \ ^3H_5$ levels. From this 3H_5 energy level, electrons can relax non-radiatively to the 3F_4 energy level. From here, the energy of a second excited electron of Yb^{3+} is transferred to Tm^{3+} while its electrons are in the 3F_4 excited state, promoting them to the 3F_3 state. From here, a second non-radiative relaxation takes place towards the 3H_4 energy level, from which an emission band located at $\sim 1.45 \mu m$ arises, resulting from the $^3H_4 \rightarrow ^3F_4$ transition. When the electrons in the 3F_4 state relax radiatively to the 3H_6 ground state, a second emission line is generated, located at $1.8 \mu m$ (see Figure 3b).

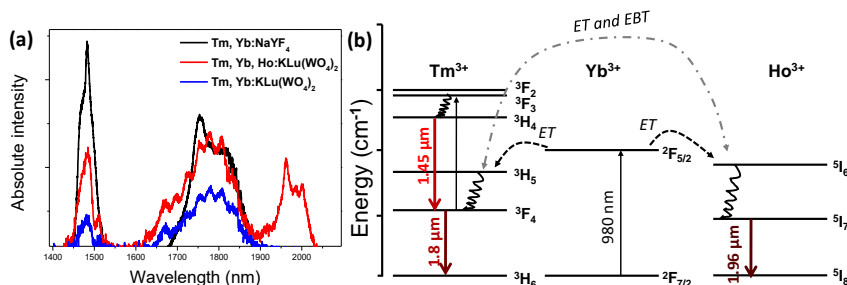


Figure 3. (a) Absolute intensity of the different hosts co-doped with Tm^{3+} , Yb^{3+} and Ho^{3+} ions excited at 980 nm. (b) Mechanisms of generation SWIR emission lines for the samples doped with Tm^{3+} , Yb^{3+} and Ho^{3+} ions.

When the nanoparticles include also Ho^{3+} , an additional line can be observed at $1.96 \mu m$, assigned to the $^5I_7 \rightarrow ^5I_8$ transition of Ho^{3+} . This emission can be generated by the energy transfer from Yb^{3+} to Ho^{3+} . After Yb^{3+} absorbed a photon at 980 nm and promoted its electrons to the $^2F_{5/2}$ excited state, it can transfer this energy to the resonant 5I_6 level of Ho^{3+} . From here, and after a non-radiative relaxation towards the 5I_7 level, the transition that generates the $1.96 \mu m$ emission takes place, from this excited level to the ground state of Ho^{3+} [29]. Another possibility for the generation of this emission is a direct energy transfer process from the 3H_5 level of Tm^{3+} to the

resonant 5I_6 level of Ho^{3+} , followed by the non-radiative relaxation towards the 5I_7 level, from which the $^5I_7 \rightarrow ^5I_8$ transition takes place [30], however, since the concentration of Yb^{3+} is ten times higher than that of Tm^{3+} in the nanoparticles, the first mechanism seems to be the more realistic to occur.

The highest intensity is observed again for the Tm,Yb:NaYF_4 nanoparticles, followed by the $\text{Tm,Yb:KLu(WO}_4)_2$ nanoparticles, followed by the $\text{Tm,Yb,Ho:KLu(WO}_4)_2$ nanoparticles, with a similar intensity at $\sim 1.8 \mu\text{m}$, and with the additional emission band at $\sim 1.96 \mu\text{m}$. $\text{Tm,Yb:KLu(WO}_4)_2$ nanoparticles show the smallest intensity, indicating the importance of the incorporation of Ho^{3+} in this material to enhance the emission intensity at these wavelengths.

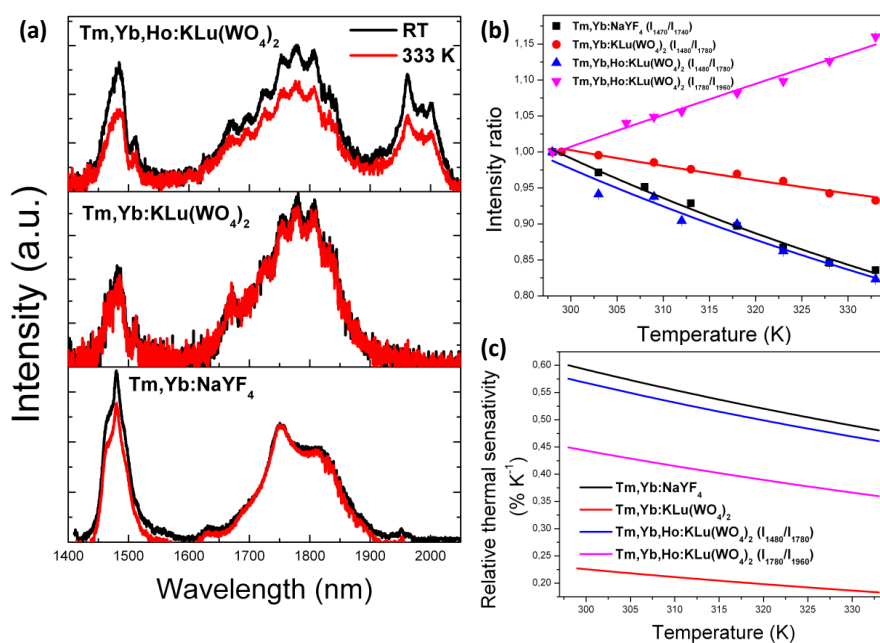


Figure 4. (a) Near infrared emission of Tm^{3+} , Yb^{3+} co-doped and Tm^{3+} , Yb^{3+} , Ho^{3+} triply doped samples recorded at room temperature and 333 K. (b) Intensity ratio of the emission lines located at (1470–1480) nm and (1770–1780) nm as a function of temperature for the different nanoparticles analyzed. (c) Relative thermal sensitivity calculated for the Tm^{3+} , Yb^{3+} co-doped and Tm^{3+} , Yb^{3+} , Ho^{3+} triply doped nanoparticles.

We also analyzed the evolution of the intensity of the spectra for Tm^{3+} , Yb^{3+} co-doped and Tm^{3+} , Yb^{3+} , Ho^{3+} triply doped nanoparticles as the temperature increased, when excited at 980 nm. Figure 4a presents the emission spectra of Tm,Yb:NaYF_4 , $\text{Tm,Yb:KLu(WO}_4)_2$, $\text{Tm,Yb,Ho:KLu(WO}_4)_2$ nanoparticles at room temperature and 333 K. As can be seen at high temperatures the emission intensity decreases in all samples. However, the intensity of the emission bands centered at 1.45 and 1.8 μm

decreased at different rates as the temperature increased. Furthermore, since the 3F_4 energy level of Tm^{3+} is populated by the radiative relaxation from the 3H_4 level, we can consider that the emission lines centered at around 1.45 and 1.8 μm produced by these levels are electronically coupled [31, 32]. Thus, although we cannot consider that these systems are in thermal equilibrium, governed by a Boltzmann distribution, we can observe how the intensity ratio between these two emission bands evolves with temperature, and use it to determine the temperature by luminescence means. Figure 4b shows the evolution of the intensity ratio between some selected peaks of these nanoparticles showing the highest slope as the temperature increased. These intensity ratios were calculated by deconvoluting the peaks that can be distinguished in the different bands, and using the areas determined under each peak. As can be seen the intensity ratio between the emission lines located at 1780 and 1960 nm of and $Tm,Yb,Ho:KLu(WO_4)_2$ nanoparticles increases with temperature, while the rest of the intensity ratios considered, involving peaks in the 1.45 and 1.8 μm bands decreases. Among these, the slope for the intensity ratio for $Tm,Yb:NaYF_4$ and $Tm,Yb,Ho:KLu(WO_4)_2$ nanoparticles are almost identical, while that corresponding to the $Tm,Yb:KLu(WO_4)_2$ nanoparticles is the smallest among the materials considered.

To compare the performance of these nanoparticles with other luminescent radiometric nanothermometers we calculated their relative thermal sensitivity using eq. 2. The results are shown in Figure 4c. $Tm,Yb:NaYF_4$ and $Tm,Yb,Ho:KLu(WO_4)_2$ nanoparticles show the highest relative sensitivity, with a maximum of about 0.6 % K^{-1} at room temperature. This thermal sensitivity is higher than that of Er^{3+} -doped systems operating in this spectral region. When compared to the thermal sensitivity of other Tm^{3+} -doped systems, it is higher than that reported for $Tm,Yb:Y_2O_3$ phosphors operating in the visible (0.34 % K^{-1}) [33] and for $Tm,Yb:CaF_2$ nanoparticles (~0.16 % K^{-1} , estimated from the data provided in the publication) [34], Tm,Yb co-doped oxyfluoride glass ceramics (0.3 % K^{-1}) [35] and $Tm,Yb:LiNbO_3$ single crystal (0.024 % K^{-1}) [36] operating in the I-BW.

3.3 Tm^{3+} and Ho^{3+} emissions in the SWIR after pumping at 808 nm.

Tm^{3+} can also be excited at 808 nm which allows exploring new possibilities to develop luminescent nanothermometers in the SWIR. The luminescence spectra in the SWIR for Tm -doped, Tm, Yb and Tm, Ho co-doped $KLu(WO_4)_2$ nanoparticles are

presented in Figure 5. In the case of Tm-doped and Tm, Yb co-doped nanoparticles, the spectra consist of two broad bands centered at 1.45 and 1.8 μm , as expected. Pumping at 808 nm excites electrons from the fundamental $^3\text{H}_6$ to the excited $^3\text{H}_4$ energy level of Tm^{3+} , from which they decay radiatively to the $^3\text{F}_4$ level, generating the emission at 1.45 μm , followed by the $^3\text{F}_4 \rightarrow ^3\text{H}_6$ transition that generates the emission at 1.8 μm .

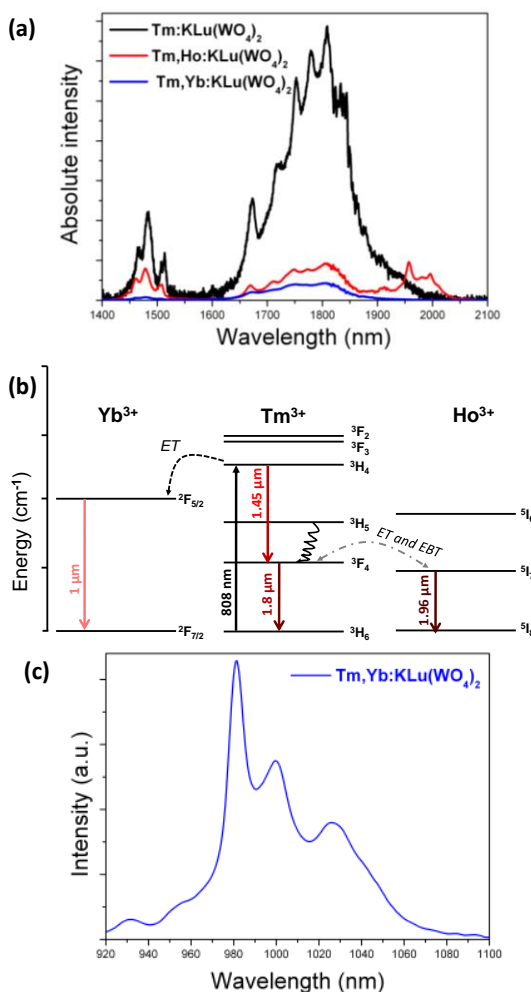


Figure 5. (a) Absolute intensity and (b) mechanism of generation of emission bands in the SWIR region of KLu(WO₄)₂ nanoparticles doped with Tm³⁺; Tm³⁺, Yb³⁺ and Tm³⁺, Ho³⁺ ions excited at 808 nm. (c) Emission at around 1 μm generated by the Tm, Yb:KLu(WO₄)₂ nanoparticles excited at 808 nm.

In the case of Tm,Ho:KLu(WO₄)₂ nanoparticles, an energy transfer process between Tm³⁺ and Ho³⁺ is produced, as explained before, that generates the additional emission band at 1.96 μm . The emission intensity generated from the Tm:KLu(WO₄)₂

nanoparticles is much higher than that obtained for the Tm, Ho co-doped $\text{KLu}(\text{WO}_4)_2$ and Tm,Yb:KLu(WO₄)₂ nanoparticles. In the case of Tm, Yb co-doped nanoparticles, we observed that the Yb³⁺ emission at ~1μm is observed. This can be explained by the energy transfer process from the ³H₄ excited state of Tm³⁺ to the ²F_{5/2} excited state of Yb³⁺, from where it can relax radiatively emitting at around 1 μm through the ²F_{5/2} → ²F_{7/2} transition. This energy transfer process between Tm³⁺ and Yb³⁺, that seems to be very efficient, would be the responsible for the reduced intensity of the Tm³⁺ emissions in Tm,Yb:KLu(WO₄)₂ nanoparticles. The reduced intensity for the Tm,Ho:KLu(WO₄)₂ nanoparticles compared to that of Tm:KLu(WO₄)₂ nanoparticles compared to that of Tm:KLu(WO₄)₂ nanoparticles would be explained by the energy transfer between Tm³⁺ and Ho³⁺.

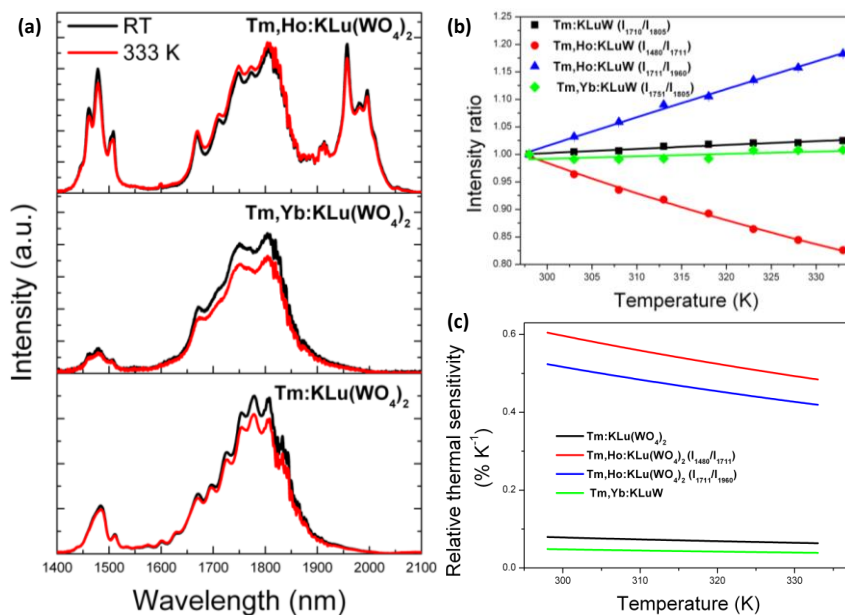


Figure 6. (a) Temperature dependence of the SWIR emissions for the KLu(WO₄)₂ nanoparticles doped with Tm³⁺; Tm³⁺, Yb³⁺ and Tm³⁺, Ho³⁺ ions. (b) Intensity ratio between selected SWIR emission lines in Tm:KLu(WO₄)₂, Tm,Yb:KLu(WO₄)₂ and Tm,Ho:KLu(WO₄)₂ nanoparticles. (c) Relative thermal sensitivity of the intensity ratios considered in (b) as a function of temperature.

For these Tm³⁺ doped nanoparticles pumped at 808 nm we also analyzed the possibilities to use them as luminescent thermometers. The evolution of the intensity of the SWIR emissions arising from these nanoparticles when the temperature increased is presented in Figure 6a. Again, we observe that the evolution of the intensity of the different emission bands is different as the temperature increases. For

Tm³⁺ doped and for Tm³⁺, Yb³⁺ co-doped nanoparticles we observed that while the intensity of the 1.45 μm band is almost insensitive to temperature changes, the intensity of the 1.8 μm band decreases as the temperature increased. The case of the Tm³⁺, Ho³⁺ co-doped nanoparticles is different. In that case, we can observe that while the intensity of the bands at 1.45 and 1.96 μm decreases slightly with temperature, the intensity of the 1.8 μm band increases slightly as the temperature increases. This would indicate the possibility of an energy backtransfer from Ho³⁺ to Tm³⁺, as indicated in Figure 5b, that is more efficient as the temperature increases. This gives an additional mechanism to use the intensity of these emission bands to determine the temperature by luminescence thermometry.

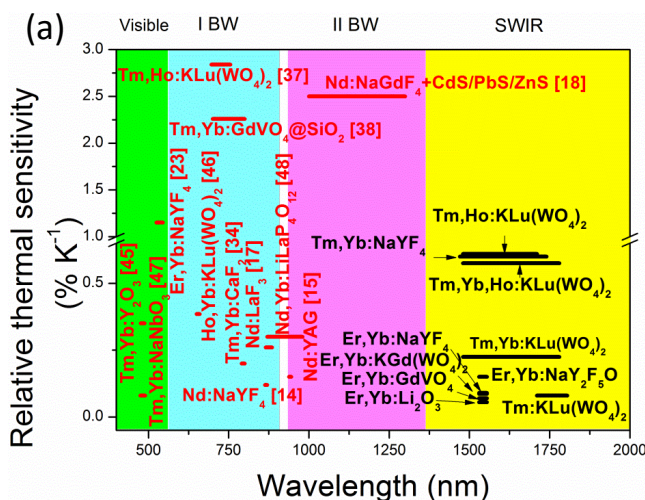
In the case of the Tm³⁺-doped sample, when we analyzed the intensity ratio between the peaks located at 1.45 and 1.8 μm we observed a reduced slope (see Figure S1) compared to that obtained in Tm,Yb:KLu(WO₄)₂ and Tm,Yb,Ho:KLu(WO₄)₂ excited at 980 nm. However, in this case we observed a linear evolution with a higher slope for the intensity ratio between the two peaks located at 1710 and 1805 nm for the Tm³⁺-doped nanoparticles. These transitions arise from two Stark sublevels of the ³F₄ energy level of Tm³⁺. Thus, we can consider that they are thermally coupled. However, the maximum relative thermal sensitivity for this FIR was found to be around 0.1 % K⁻¹.

In the case of Tm,Yb:KLu(WO₄)₂, the intensity ratio, if we consider emission lines lying also in the 1700-1800 nm range, is almost constant with temperature, as can be seen in Figure 6b, exhibiting also the smallest thermal sensitivity among the intensity ratios considered.

For the Tm³⁺, Ho³⁺ co-doped nanoparticles we observed a linear dependence with a significant slope for the intensity ratio between the peaks located at 1480 and 1780 nm and 1780 and 1960 nm, respectively, as we observed before for the Tm³⁺-doped nanoparticles excited at 980 nm, when the temperature increased. Additionally, the relative thermal sensitivity calculated in this case is a little higher than when excited at 980 nm, 0.61 % K⁻¹ for the I₁₄₈₀/I₁₇₈₀ and 0.52 % K⁻¹ for the I₁₇₈₀/I₁₉₆₀, which would indicate a better performance for the Tm³⁺, Ho³⁺ co-doped nanoparticles excited at 808 nm.

The comparison among relative thermal sensitivities for all the samples analyzed in this work and other ratiometric systems based on Ln-doped nanoparticles extracted from the literature in the spectral range from the visible to the SWIR is presented in

Figure 7a. In this graph, the spectral range in which the different nanoparticles can be used is also included. As can be seen in Figure 7a, the relative thermal sensitivity achieved by our nanoparticles in the SWIR region, especially those doped with Tm^{3+} , is higher than the one that can be achieved with most of the luminescent nanoparticles that have been used operating in the I- and II-BWs. Their thermal sensitivities are only surpassed by Er,Yb:NaYF₄ nanoparticles operating in the visible [23], Ho,Tm:KLu(WO₄)₂ [37] and Tm,Yb:GdVO₄@SiO₂ core-shell nanoparticles [38] operating in the I-BW and Nd:NaGdF₄ + CdS/PbS/ZnS composite structures operating in the II-BW [18]. Thus, we consider that the emissions in the SWIR of these nanoparticles can be used as efficient luminescent nanothermometers. Figure 7b presents the data reported in the literature on the penetration depth of biological systems in different spectral regions. As can be seen the penetration depth in the SWIR region achieved by Er,Yb:NaYF₄ nanoparticles [22] and Er-doped complex structures [39] is higher than the one that can be achieved in the I-BW region with Tm,Yb:CaF₂ [34] and in the II-BW region with Nd:LaF₃ [40], single-walled carbon nanotubes [41] and CdS/PbS/ZnS quantum dots [42]. This penetration depth is only surpassed by the one achieved in the I-BW by α -Tm:NaYF₄@CaF₂ core-shell nanoparticles, for which a penetration depth of 32 mm in pork meat was achieved due to the high quantum yield, ~ 0.6 %, exhibited by these core-shell nanoparticles [43].



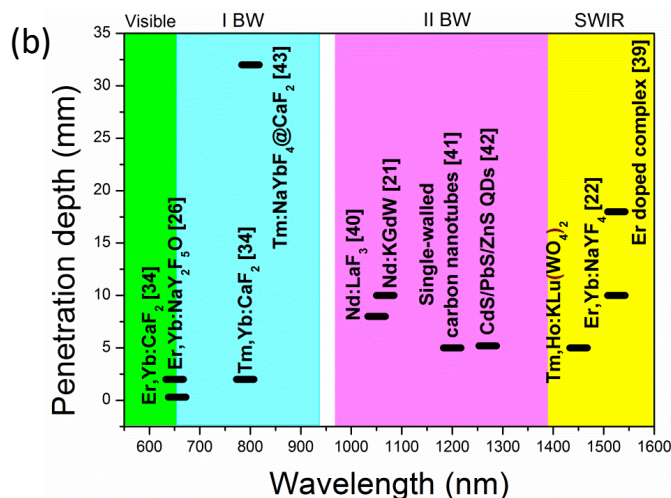


Figure 7. (a) Comparison of the relative thermal sensitivities of Ln-doped luminescent thermometers operating in the different spectral regions. (b) Penetration depth reported in biological systems in the different spectral regions.

3.4 Ex-vivo luminescence thermometry in the SWIR

In order to prove the potentiality of these nanoparticles for temperature sensing purposes in biological tissues, we performed a temperature sensing experiment inside a piece of chicken breast. Tm,Ho:KLu(WO₄)₂ nanoparticles were chosen for this experiment since as they show the highest thermal sensitivity when pumping at 808 nm. Also, by using this excitation wavelength we avoid the heating of water contained in the biological tissues that would happen if pumping at 980 nm. Chicken breast was used since its characteristics are comparable to those of human tissues [44]. Tm,Ho:KLu(WO₄)₂ nanoparticles were deposited on a microscope glass slide on top of which a slice of chicken breast ~2 mm in thickness was placed. Due to the restrictions in optical setup used in the experiment, we were not able to place a thicker slice of the chicken breast to heat investigate thicker depths. A heating gun with a fixed power of 1 W was used to heat the chicken breast. A horizontal moving stage was fixed to the heating gun for controlling its movement. The heating gun was displaced away from the chicken sample to generate a decrease of temperature in the biological tissue. Also, the maximum temperature that was achieved in the chicken breast was controlled not to overpass 318 K (45 °C). A fiber-coupled diode laser with emission at 808 nm and a power of 200 mW was focused on the nanoparticles by means of a microscope objective with 40X magnification and N.A. = 0.6. The

emission arising from the nanoparticles through the chicken breast was collected by the same objective, and after passing a dichroic filter for elimination of the excitation wavelength, was sent to the Yokogawa AQ6375 OSA to record the spectra. After the analysis of the emission spectrum and comparing the obtained data with the calibration curve in Figure 6b, the temperature was deduced. Moreover, in order to verify the data, temperature was also recorded by a digital multimeter connected to a small Pt-100 thermo-resistor located inside the chicken breast slide, very close to the nanoparticles. The scheme of the setup is shown in Figure 8a.

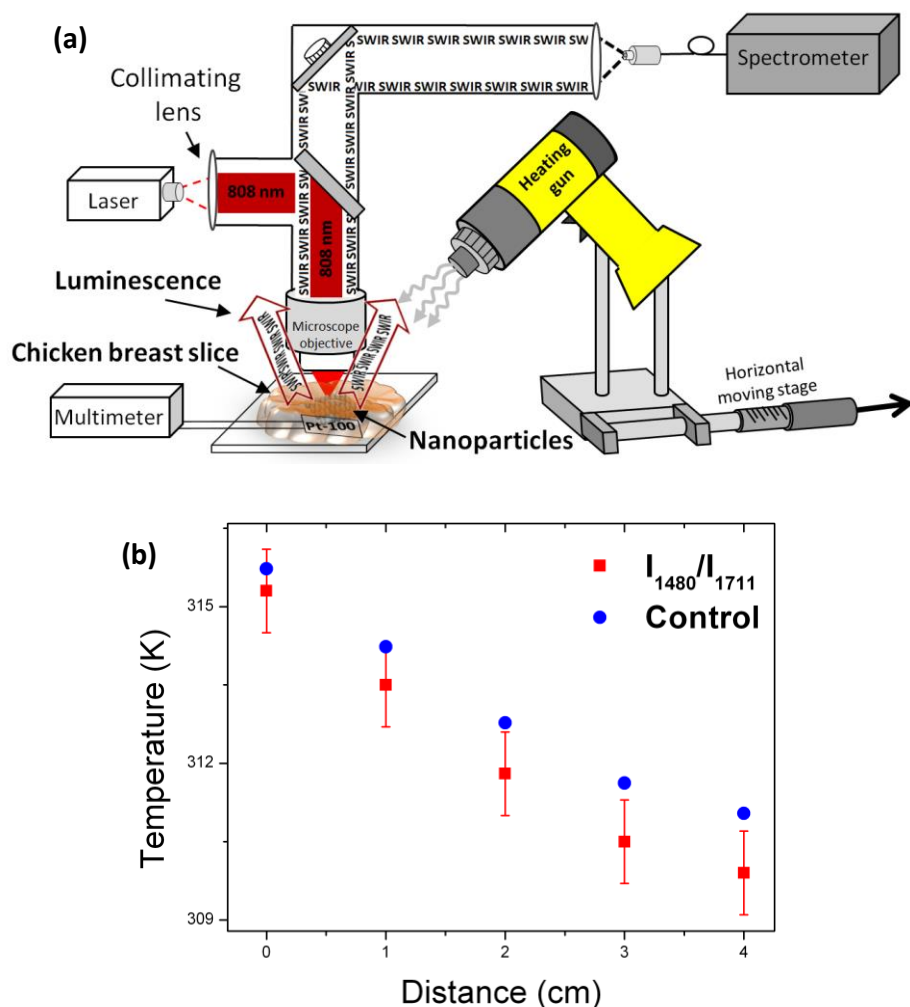


Figure 8. (a) Scheme of the setup used in the temperature sensing experiment inside the chicken breast. (b) Temperature data recorded by luminescent nanoparticles and thermo-resistor (control) during the heating process.

The temperature profile of the heating process determined from the emission of the luminescent nanoparticles and the Pt-100 thermo-resistor are shown in Figure 8b. In this graph it can be observed that by moving away the heating gun from the chicken sample, a temperature drop of ~ 1.5 K/cm was generated. The temperature dropping could be monitored both with the Pt-100 thermo-resistor and the intensity ratio determined from the intensity of the 1480 and 1711 nm emission lines of Ho,Tm:KLu(WO₄)₂ nanoparticles. The intensity ratio showed a difference of 0.8 K to respect the thermo-resistor that might be due to the different thermal conductivity of the two materials, or also to the different location of the thermal probes (the thermo-resistor was located inside the chicken breast, while the luminescent nanoparticles were located below it). The experiment demonstrates the potentiality of using luminescent nanoparticles generating SWIR emission lines for temperature determination purposes in biomedical applications.

3.5. *Ex-vivo SWIR imaging experiment.*

To prove the potentiality of the luminescent nanoparticles with emissions in the SWIR for bioimaging applications, we used again a piece of chicken breast. An scheme of the setup is shown in Figure 9a. In this case, a drop of the Ho,Tm:KLu(WO₄)₂ nanoparticles dispersed in water, with a concentration of 0.5 mg ml⁻¹, was placed between two microscope slides, and a piece of chicken breast with a thickness of 0.5 cm was placed over them. A continuous wave diode laser emitting at 808 nm wavelength with a power of 7.5 W, located at a distance of 5 cm from the sample, producing a spot of ~ 3.5 cm on it, and thus an excitation density of 0.78 W/cm², was used for exciting the luminescent nanoparticles. The signal was collected by a Peltier cooled InGaAs infrared Xenics camera with an attached filters wheel that allowed collecting the emission arising from particular wavelength ranges of interest and eliminate the excitation laser. Figure 9b shows the images recorded in the SWIR range. As can be seen, in the signal recorded using a 1300 nm longpass filter allows identifying the shape of the chicken breast sample. This image would correspond only to the ~ 1.45 μ m emission arising from the Ho,Tm:KLu(WO₄)₂ nanoparticles, since the spectral sensitivity of the InGaAs detector does not go beyond 1.7 μ m. Thus, we believe that with a detector that allows detecting beyond this limit, the bioimaging in the SWIR region can still be improved. What is also important to remember is that this image corresponds to the emission generated 0.5 cm below the surface of the

chicken sample, thus indicating that at least a penetration depth of 0.5 cm can be achieved using these nanoparticles.

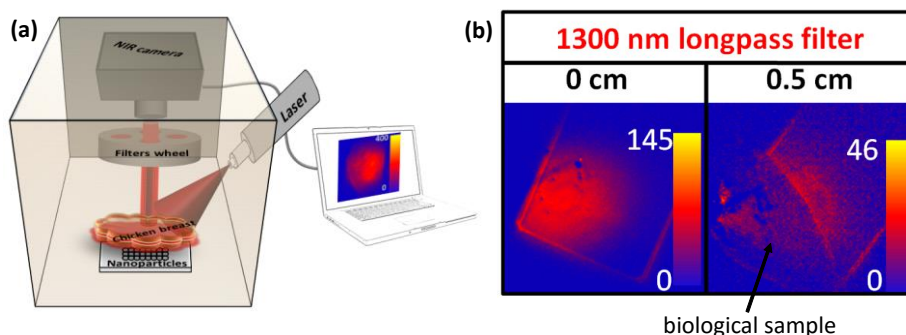


Figure 9. (a) Scheme of the setup used for the *ex-vivo* SWIR imaging experiment. (b) SWIR images achieved using the light emitted by the $\text{Ho,Tm:KLu(WO}_4)_2$ nanoparticles covered or not with a piece of chicken breast 0.5 cm thick.

Conclusions

In summary, we analyzed the SWIR emissions of Er^{3+} , Tm^{3+} and Ho^{3+} in different hosts and their potentiality for luminescence thermometry in this spectral region. The $1.55 \mu\text{m}$ emission line generated by the Er^{3+} ion have two Stark sub-levels that are thermally coupled and can be used in the temperature sensing purposes in biological tissues or also for telecommunications system. However, the thermal sensitivity of this emission is relatively low. In the case of Tm^{3+} containing systems, the emissions arising from the $^3\text{F}_4$ and $^3\text{H}_4$ energy levels, that are electronically coupled, provide a channel that allows determining temperature by luminescence means, and in particular the intensity ratio between selected lines corresponding to the $\sim 1.45 \mu\text{m}$ and $\sim 1.8 \mu\text{m}$ emission bands shows a linear tendency as the temperature increased that simplifies the calibration procedure for thermometers based on this parameter. Tm,Yb:NaYF_4 nanoparticles were found to have the highest relative sensitivity among other $\text{Tm}^{3+}, \text{Yb}^{3+}$ co-doped systems.

Adding Ho^{3+} to the system generate an efficient energy transfer between the Tm^{3+} and Ho^{3+} ions, that results in a new emission line centered at $1.96 \mu\text{m}$ that can be used also for luminescence thermometry purposes. The intensity ratio between the peak at $\sim 1.45 \mu\text{m}$, corresponding to Tm^{3+} , and the peak at $\sim 1.96 \mu\text{m}$, corresponding to Ho^{3+} , follows a linear evolution as temperature increases with a high thermal sensitivity. Moreover, excitation at 808 nm of Tm^{3+} and Ho^{3+} co-doped samples increases the

thermal sensitivity and introduces advantages in the possibility to use this system for biological applications, since the 808 nm excitation wavelength lie in the I-BW and avoids the heating of water contained in biological tissues when those are illuminated with a 980 nm laser. The thermal sensitivities achieved under these conditions are comparable to those that have been reported previously in luminescence thermometry in the visible, and are higher than the one reported for most of the systems operating in the I- and II-BWs.

We demonstrated the potentiality of these emissions in the SWIR region for luminescence thermometry and imaging in *ex vivo* experiments by monitoring the heat generated by hot air in chicken meat, with a penetration depth of at least 0.5 cm in this kind of biological tissue.

We believe that the results presented here open the door to a new spectral biological window in which luminescence thermometry can be used, especially in some specific biological tissues, like those containing melanine, that have not been considered yet in luminescence thermometry.

Acknowledgements

This work was supported by the Spanish Government under Projects No. MAT2013-47395-C4-R, and TEC2014-55948-R, and by Catalan Authority under Project No. 2014SGR1358. OI. A. Savchuk is supported by Catalan Government through the fellowship 2015FI_B2 00136. F. D. acknowledges additional support through the ICREA Academia awards 2010ICREA-02 for excellence in research. P.H.G. thanks the ministerio de Economía y Competitividad for Juan de la Cierva program (JCI-2012-12885).

References

1. R. B. Roemer, *Annu. Rev. Biomed. Eng.*, 1989, **1**, 347.
2. A. Y. Cheung, A. Neyzari, *Cancer Res.*, 1984, **44**, 4736.
3. N. P. O'Grady, P. S. Barie, J. G. Bartlett, T. Bleck, G. Garvey, J. Jacobi, P. Linden, D. G. Maki, M. Nam and W. Pasculle, *Clin. Infect. Dis.*, 1998, **26**, 1042.
4. M. Miyakawa, J. Ch. Bolomey, *Non invasive thermometry of a human body*, CRC press, New York, 1995.
5. C. D. S. Brites, P. P. Lima, N. J. O. Silva, A. Millán, V. S. Amaral, F. Palacio, L. D.Carlos, *Nanoscale*, 2012, **4**, 4799.

6. D. Jaque, F. Vetrone, *Nanoscale* 2012, **4**, 4301.
7. M. Haase and H. Schäfer, *Angew. Chem. Int. Ed.*, 2011, **50**, 5808.
8. M. L. Debasu, D. Ananias, I. Pastoriza-Santos, L. M. Liz-Marzán, J. Rocha, L. D. Carlos, *Adv. Mater.*, 2013, **25**, 4868.
9. F. Vetrone, R. Naccache, A. Zamarron, A. J. de la Fuente, F. Sanz-Rodríguez, L. M. Maestro, E. M. Rodriguez, D. Jaque, J. G. Sole, J. A. Capobianco, *ACS Nano*, 2010, **4**, 3254.
10. S. P. Wang, S. Westcott, W. Chen, *J. Phys. Chem. B*, 2002, **106**, 11203.
11. L. A. Sordillo, Y. Pu, S. Pratavieira, Yu. Budansky, and R. R. Alfanoa, *J. Biomed. Opt.*, 2014, **19**, 056004.
12. R. Weissleder, *Nat. Biotechnol.*, 2001, **19**, 316.
13. E. Carrasco, B. del Rosal, F. Sanz-Rodríguez, A. Juarranz de la Fuente, P. Haro-Gonzalez, U. Rocha, K. U. Kumar, C. Jacinto, J. G. Sole, D. Jaque, *Adv. Func. Mater.*, 2015, **25**, 615.
14. D. Wawrzynczyk, A. Bednarkiewicz, M. Nyk, W. Strek and M. Samoc, *Nanoscale*, 2012, **4**, 6959.
15. A. Benayas, B. del Rosal, A. Perez-Delgado, K. Santacruz-Gomez, D. Jaque, G. A. Hirata and F. Vetrone, *Adv. Opt. Mater.* 2015, **3**, 687.
16. E. Carrasco, B. del Rosal, F. Sanz-Rodríguez, A. Juarranz de la Fuente, P. Haro-Gonzalez, U. Rocha, K. U. Kumar, C. Jacinto, J. G. Sole, D. Jaque, *Adv. Func. Mater.* 2015, **25**, 615.
17. U. Rocha, C. J. da Silva, W. F. Silva, I. Guedes. A. Benayas, L. M. Maestro, M. A. Elias, E. bovero, F. C. J. M. van Veggel, J. A. G. Sole, and D. Jaque, *ACS Nano*, 2013, **7**, 1188.
18. E. N. Ceron, D. H. Orgies, B del Rosal, F. Ren, A. Benayas, F. Vetrone, D. Ma, F. Sanz-Rodríguez, J. G. Sole, D. Jaque and E. M. Rodriguez, *Adv. Mater.* 2015, **27**, 4781.
19. I. Villa, A. Vedda, I. X. Cantarelli, M. Pedroni, F. Piccinelli, M. Bettinelli, A. Speghini, M. Quintanilla, F. Vetrone, U. Rocha, C. Jacinto, E. Carrasco, F. S. Rodríguez, A. Juarranz, B. del Rosal, D. H. Orgies, P. H. Gonzalez, J. G. Sole, and D. G. Jaque, *Nano Res.*, 2015, **8**, 649.
20. X. Mateos, M. C. Pujol, F. Güell, M. Galan, R. M. Sole, J. Gavalda, M. Aguilo, J. Massons and F. Diaz, *IEEE J. Quant. Electron.*, 2004, **40**, 759.
21. Nd doped KGdW submitted

22. D. J. Naczynski, M. C. Tan, M. Zevon, B. Wall, J. Kohl, A. Kulesa, S. Chen, C. M. Roth, R. E. Riman and P. V. Moghe, *Nat. Commun.*, 2013, **4**, 2199.
23. F. Vetrone, R. Naccache, A. Zamarron, A. Juarranz de la Fuente, F. Sanz-Rodriguez, L. M. Maestro, E. M. Rodriguez, D. Jaque, J. G. Sole and J. A. Capobianco, *ACS Nano*, 2010, **4**, 3254.
24. L. H. Fischer, G. S. Harms and O. S. Wolbeis, *Angew. Chem. Int. Ed.*, 2011, **50**, 4546.
25. S. A. Wade, S. F. Collins, G. W. Baxter, *J. Appl. Phys.*, 2003, **94**, 4743.
26. Ol. A. Savchuk, P. Haro-Gonzalez, J. J. Carvajal, D. Jaque, J. Massons, M. Aguiló, F. Diaz, *Nanoscale*, 2014, **6**, 9727.
27. Chi-Hung Huang, Leon McCaughan, *IEEE J. of selected topics in quantum electronics* 1996, **2**, 367-372.
28. Y. He, Q. Han, J. Ning and H. Xiao, *Rec. Adv. Electr. Eng.*, 2012, **5**, 96.
29. L. Tao, Y. H. Tsang, B. Zhou, B. Richards, A. Jha, *J. Non-Cryst. Solids*, 2012, **358**, 1644.
30. M. Faleonieri, A. Lanzi, G. Salvetti, *Appl. Phys. B*, 1996, **62**, 537.
31. N. Ishiwada, S. Fujioka, T. Ueda, T. Yokomori, *Opt. Lett.*, 2011, **36**, 760.
32. E. J. McLaurin, L. R. Bradshaw, D. R. Gamelin, *Chem. Mater.* 2013, **25**, 1283.
33. D. Li, Y. Wang, X. Zhang, K. Yang, L. Liu, Y. Song, *Opt. Commun.*, 2012, **285**, 1925.
34. N. N. Dong, M. Pedroni, F. Piccinelli, G. Conti, A. Sbarbati, J. E. Ramírez-Hernández, L. M. Maestro, M. C. Iglesias-de la Cruz, F. Sanz-Rodriguez, A. Juarranz, F. Chen, F. Vetrone, J. A. Capobianco, J. G. Sole, M. Bettinelli, D. Jaque, A. Speghini, *ACS Nano*, 2011, **5**, 665.
35. W. Xu, X. Y. Gao, L. J. Zheng, Z. G. Zhang, and W. W. Cao, *Sens. Actuat. B*, 2012, **173**, 250.
36. L. Xing, Y. Xu, R. Wang, W. Xu and Z. Zhang, *Opt. Lett.*, 2014, **39**, 454.
37. Tm,Ho:KLuW to be submitted
38. Tm,Yb:GdVO₄@SiO₂ to be submitted
39. R. Wang, X. Li, L. Zhou, F. Zhang, *Angew. Chem.*, 2014, **126**, 12282.
40. U. Rocha, K. U. Kumar, C. Jacinto, I. Villa, F. Sanz-Rodriguez, M. C. I. de la Cruz, A. Juarranz, E. Carrasco, F. C. J. M. van Veggel, E. Bovero, J. G. Sole, D. Jaque, *Small*, 2014, **10**, 1141.
41. K. Welscher, S. P. Sherlock, H. Dai, *PNAS*, 2011, **108**, 8943.

42. A. Benayas, F. Ren, E. Carrasco, V. Marzal, B. del Rosal, B. A. Gonfa, A. Juarranz, F. Sanz-Rodriguez, D. Jaue, J. Garcia-Sole, D. Ma, F. Vetrone, *Adv. Func. Mater.*, 2015, **25**, 6650.
43. G. Chen, J. Shen, T. Y. Ohulchanskyy, N. J. Patel, A. Kutikov, Z. Li, J. Song, R. K. Pandey, H. Agren, P. N. Prasad and G. Han, *ACS Nano*, 2012, **6**, 8280.
44. G. Marquez, L. V. Wang, S. -P. Lin, J. A. Schwartz and S. L. Thomsen, *Appl. Opt.*, 1998, **37**, 4.
45. D. Li, Y. Wang, X. Zhang, K. Yang, L. Liu, Y. Song, *Opt. Commun.*, 2012, **285**, 1925.
46. O. A. Savchuk, J. J. Carvajal, M. C. Pujol, E. W. Barrera, J. Massons, M. Aguilo, and F. Diaz, *J. Phys. Chem. C*, 2015, **119**, 18546.
47. A.F. Pereira, U. K. Kumar, W. F. Silva, W. Q. Santos, D. Jaque, C. Jacinto, *Sens. Actuat. B*, 2015, **213**, 65.
48. Ł. Marciniak, A. Bednarkiewicz, M. Stefanski, R. Tomala, D. Hreniak and W. Strek, *Phys. Chem. Chem. Phys.*, 2015, **17**, 24315.

CHAPTER 6

Photothermal converter materials

The heat generated by a material, if controlled, can be used as an instrument in many applications, for instance in biomedicine for cancer treatment. Materials which are able to absorb light and efficiently convert it into thermal energy are called photothermal converters. If those materials have to be used in biomedicine, one has to take into account that human tissues show a strong extinction coefficient in the visible range of the electromagnetic spectrum. Thus, the photothermal agents used for these purposes should be especially designed to absorb light in the range of wavelengths lying in the biological windows, opening the possibilities to treat internal tumors. Graphene-based materials have emerged as promising photothermal agents for photothermal therapy since they present high absorption cross-sections in these regions of the electromagnetic spectrum. In the following chapter, we analyzed the photothermal efficiency of graphene-based materials. Also, we developed a new fast and useful method for determining the photothermal efficiency based on the use of an integrating sphere. We validated it by comparing the photothermal efficiency of gold nanorods measured by using our method and the time constant method, well established in the literature. Finally, we applied this method to determine the photothermal efficiency of graphene (G) and graphene oxide (GO), and analyzed the dependence of their heat converting capacity on the material concentration in the solvent, the laser power irradiation and the wavelength of the laser with which those photothermal agents were illuminated.

Moreover, if the photothermal agent is a multifunctional material, from which information, like local temperature production can be extracted or they can be used for bioimaging in real time, would facilitate the application of this material for therapeutical treatment and prevent serious damages in healthy surrounding tissues, when the system generates an overheat. Here, we are presenting also the multifunctional Ho^{3+} , Tm^{3+} co-doped

$\text{KLu}(\text{WO}_4)_2$ nanoparticles. These nanoparticles have the ability to generate heat when illuminated at 808 nm as an increased probability of non-radiative processes to occur between Ho^{3+} and Tm^{3+} ions. Additionally, the emission lines, generated by these nanoparticles and located at 696 and 750 nm, which lie in the first biological window, possess temperature-dependent properties with a high thermal sensitivity.

Paper XIII

Savchuk, Ol. A.; Carvajal, J. J.; Massons, J.; Aguiló, M.; Díaz, F.
Determination of photothermal conversion efficiency of graphene and graphene oxide through an integrating sphere method (2016) Carbon 103, 134-141.

Determination of photothermal conversion efficiency of graphene and graphene oxide through an integrating sphere method

*Ol. S. Savchuk, J.J. Carvajal, * J. Massons, M. Aguiló, F. Díaz*

Physics and Crystallography of Materials and Nanomaterials (FiCMA-FiCNA) and EMaS, Universitat Rovira i Virgili (URV), Marcel·lí Domingo 1, E-43007 Tarragona, Spain

Abstract: We report a new method for the determination of photothermal conversion efficiency of photothermal agents, based on the use of an integrating sphere. We validated this method by comparing the photothermal conversion efficiency of Au nanorods calculated by this method and by the more conventional time constant method. Then, we applied this method to determine the photothermal conversion efficiency of graphene and graphene oxide nanosheets dispersions in dimethylformamide and water, respectively, finding out that they are excellent photothermal agents with photothermal conversion efficiencies among the highest reported up to now. We also analyzed the influence of the concentration of the materials, and the wavelength and power of irradiation in the temperature increase that can be achieved with them, finding out that they can be used, for instance, in cancer treatment through hyperthermia procedures with reduced costs when compared to other photothermal agents.

1. Introduction

Heat can be used as an instrument to increase death rate in cells, useful to treat diseases as cancer, for instance [1]. Increasing the temperature of biological molecules above the limit of 39 °C induces chemical reactions leading to unwanted products that damage cells and tissues (denaturation) in performing their functions, and finally at a temperature above 48 °C necrosis is induced. Thus, if controlled, heat may be used to treat abnormal cells, such cancer cells, through hyperthermia treatment. However, heat also affects negatively to health tissues. Thus, predicting and controlling the temperature distribution in a body region during hyperthermia treatment is mandatory [2].

Conventional methods of temperature promotion in abnormal cells can be classified by: (i) external heating mainly used for superficial tumors, induced by radiofrequency [3], microwave [4] or ultrasounds [5]; and (ii) internal heating for non-superficial tumors using electrodes or antennas located very close to the tumor [6, 7]. However, these methods face great difficulties deriving mainly from the complex nature of organs and tissues, and undesirable hyperthermia effects induced in surrounding tissues.

To avoid the non-specific heating of surrounding tissues, especially in the case of non-superficial tumor treatments, laser irradiation at near-infrared (NIR) frequencies has been explored [8]. This radiation is less absorbed by biological tissues, thus, penetration depths of several centimeters in biological tissues can be achieved using this radiation [9-11]. To use this kind of radiation in an effective way, the use of photothermal agents that can convert the NIR light energy into thermal energy is indispensable. Photothermal agents mainly include: (i) metal plasmonic nanostructures (Au nanostructures [12], Pd-based nanosheets [13] and Ge nanoparticles [14]); (ii) organic compounds (polyaniline [15], polypyrrole [16], dopamine-melanin [17], polymers [18]); (iii) nanoparticles with ferromagnetic properties alone, or combined with good absorbers in the NIR region (FePt [19], ZnFe₂O₄-reduced graphene oxide [20], Fe₃O₄@polylactic acid coated with graphene oxide [21], WO₃nanorods [22]); and (iv) semiconductor nanoparticles (Cu_{2-x}Se [23], CuS [24]).

Among these photothermal agents, Au nanostructures have the ability to accumulate within a solid tumor in the body [12], and since their surface plasmon resonance can be tuned within a broad range of wavelengths from the visible to the NIR [12], Au nanostructures can be tailored for particular hyperthermia treatments. However, despite the excellent photothermal conversion efficiency and great physical properties, Au nanostructures have bad photostability after a long period of laser irradiation [25], and new photothermal agents have been developed to overcome these problems. However, their photothermal conversion efficiency is low [23-25], which implies the necessity of using a higher concentration of nanoparticles or a higher power density of the laser irradiation to generate hyperthermia. Another problem is that the size of these photothermal agents is considerably big, which reduces the time of blood stream circulation before their deposition in blood vessels [26]. From another side, although the use of magnetic nanoparticles allows having contrast agents for tomography and magnetic resonance imaging [19-22], the powerful femtosecond laser irradiation needed to excite them and increase the temperature of biological tissues, generates microbubbles that cause irreversible damages [19].

Thus, an ideal photothermal agent should meet several requirements, as suitable nanosize and uniform shape, good dispersability in aqueous solution or biological compatible fluids, large NIR absorption cross-section, high photostability and low cytotoxicity in living systems.

Graphene-based materials have emerged as promising photothermal agents for photothermal therapy especially due to their high absorption cross-sections in the NIR that can be combined with the ability to modify chemically those materials to use them also as drug

loaders [27]. Photothermal therapy based on graphene materials has been extensively investigated for cancer therapy [28-33], and antibacterial treatment [27]. Also, magnetic nanoparticles that acted as good contrast agents for magnetic resonance have been used together with graphene-based materials [21], in which the photothermal effect could be enhanced by applying an external magnetic field [34]. On the other hand graphene (G) can be functionalized with fluorescent dyes or up-conversion nanoparticles that can serve as imaging probes for photothermal therapy [35]. Moreover, graphene-based magneto-plasmonic nanocomposites have been developed for simultaneous enhancement of the NIR absorption and multimodal imaging guided cancer therapy [34]. This is especially important when operating in the so-called biological windows [36] corresponding to the 650-950 and 1000-1350 nm spectral ranges, where tissue scattering and absorption are minimized, and where graphene-based materials can operate efficiently [37].

Despite the large number of studies about the use of graphene-based materials on photothermal therapy, there are no reports on determining the photothermal efficiency of these graphene-based materials with the objective of predicting and controlling the temperatures that can be generated with them.

In the present work we developed a fast and effective method for determining the efficiency of the heat production after laser illumination based on the use of an integrating sphere. We validated it by comparing the photothermal efficiency of gold nanorods measured by using the integrating sphere and the time constant method [38], well established in the literature. Finally, we applied this method to determine the photothermal efficiency of graphene (G) and graphene oxide (GO), and analyzed the dependence of their heat converting capacity on the material concentration in the solvent, the laser power irradiation and the wavelength of the laser with which those photothermal agents are illuminated.

2. Experimental Section

2.1 Photothermal agents

A GO colloidal suspension dispersed in distilled water, with flake sizes between 300 and 700 nm and 60% of the sample with a thickness of 1 atomic layer, provided by Graphene Market and a G colloidal suspension dispersed in dimethylformamide (DMF), with flake sizes between 150 and 3000 nm and 60% of the sample with a thickness of 1 atomic layer, provided by Graph Nanotech, were used as photothermal agents. DMF, although not being a biological compatible fluid, was used since it has a surface tension similar to the surface energy of G, and

thus prevent G nanosheets from aggregation. The colloids were diluted for obtaining different concentrations, from 0.5 to 5 g/l in the case of GO and from 0.05 to 1 g/l in the case of G. Since G has a larger absorption cross-section in the NIR, we reduced its concentration to obtain comparable results with those obtained when using GO.

Citrate-capped gold nanorods with an axial diameter of 25 nm, a length of 50 nm, and a concentration of 150 $\mu\text{g/ml}$ were provided by Strem Chemicals.

2.2 Absorption measurements

The optical absorption measurements of the GO, G and Au nanorods in solutions, with a concentration of 1 g/l, 1 g/l and 150 $\mu\text{g/ml}$, respectively, were recorded using a Varian Cary 500 Scan spectrometer. This spectrometer has two monochromators with a 1200 lines/mm grating for the UV/VIS region and a 300 lines/mm grating in the NIR region. The optical sources used were a deuterium lamp and a quartz halogen lamp in the zone of visible and infrared. The detectors were a photomultiplier tube in UV/VIS region (175 – 850 nm) and a lead sulfide diode in the IR region (850 – 3300 nm).

2.3 Photothermal conversion efficiency determined from the time constant

For photothermal conversion measurements, 0.3 ml of samples were introduced in a glass cuvette (Helma Analytics) with dimensions 2×1 cm. Solutions were irradiated with a Lumics fiber-coupled diode laser emitting at 808 and 980 nm in order to study the wavelength dependent photothermal conversion. In the case of Au nanorods, they were irradiated with a 650 nm diode laser. The laser beam was focused on the cuvette with a collimating lens, allowing a beam diameter of 5 mm on the sample. The temperature evolution was recorded by a digital multimeter connected to a small Pt-100 thermo-resistor located inside of the cuvette. After around 10 min of irradiation, the sample reached the thermal equilibrium, and thus the maximum temperature for a particular laser power irradiation. After that, laser irradiation was switched off for allowing the sample to cool down to the room temperature while data were recorded in the cooling cycle.

2.4 Photothermal conversion efficiency using an integrating sphere

For photothermal conversion efficiency using an integrating sphere the glass cuvette containing the sample (GO in water with a concentration 1 g/l or G in DMF with a concentration 1 g/l) was placed inside the integrating sphere, perpendicular to the laser irradiation provided by the fiber-coupled diode laser emitting at 808 and 980 nm, with a power of 200 mW. The laser

from the fiber tip was collimated with a spot size of 5 mm in diameter on the sample. A baffle was introduced in the integrating sphere, between the sample and the detector, in order to prevent the direct reflections from the sample to the detector. The signal was collected using a powermeter Ophir Nova II. An scheme of the experimental setup used for these measurements is provided in Figure 1.

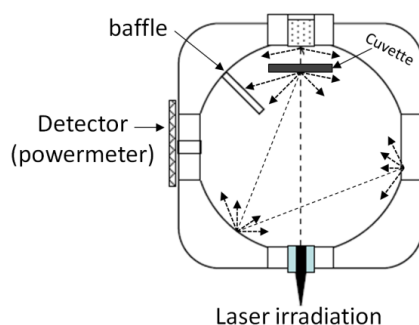


Figure 1. (a) Scheme of the setup for photothermal conversion efficiency measurements.

3. Results and Discussion

Figure 2(a) shows the room temperature visible-NIR absorbance spectra of 1 g/l GO and 1g/l G nanosheets colloidal suspensions in water and dimethylformamide (DMF), respectively. In the case of GO, the absorbance falls almost exponentially from the UV region to the NIR region. Instead, G shows an almost constant absorbance all over the visible and NIR regions, higher than the theoretical one that would be expected for monolayer graphene [39], but similar to that reported for other graphene samples [40]. The inset in the figure shows the absorption of GO and G in the so-called first biological window (650-1000 nm) [36] and we can observe that the absorption of GO decrease slightly in this range of wavelengths, while that of G is almost constant.

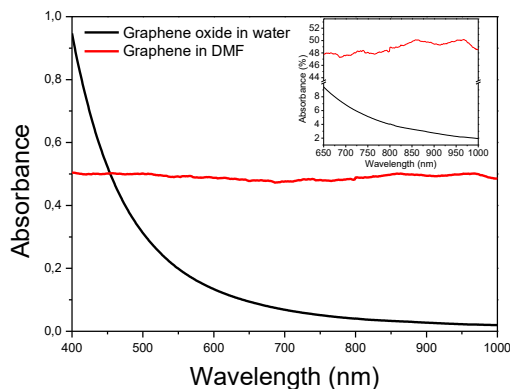


Figure 2. Absorption spectra of GO in water and G in DMF in the visible and NIR ranges. Inset shows a magnification of the curves in the 650-1000 nm range, coinciding with one of the biological windows.

We focused our attention on two particular wavelengths that are often used to illuminate photothermal agents, 808 and 980 nm, since they also constitute two consolidated laser wavelength technologies. GO shows an absorbance of 4% at 808 nm that is reduced to 2%, at 980 nm. Instead, G shows an absorbance one order the magnitude higher at 808 nm (48%), and it is maintained at 980 nm (49%).

We compared the temperature increase of the GO and G dispersions in water and DMF, respectively, at two different irradiation wavelengths. Figure 3(a) shows the results of the irradiation with 980 nm. It should be noted that after approximately 10 minutes of irradiation time, the system reached the steady state (see Figure 3(a)), when the heat produced by the material is compensated by the heat irradiated to the environment. The temperature increase for GO in water is about 3 °C, however for G in DMF the temperature increase is 4 times higher, around 12 °C. At 808 nm, the temperature increase for GO in water is about 4 °C, higher than that obtained at 980 nm due to the higher absorption of GO at this wavelength, while that of G in DMF is 15 °C, as can be seen in Figure 3(b).

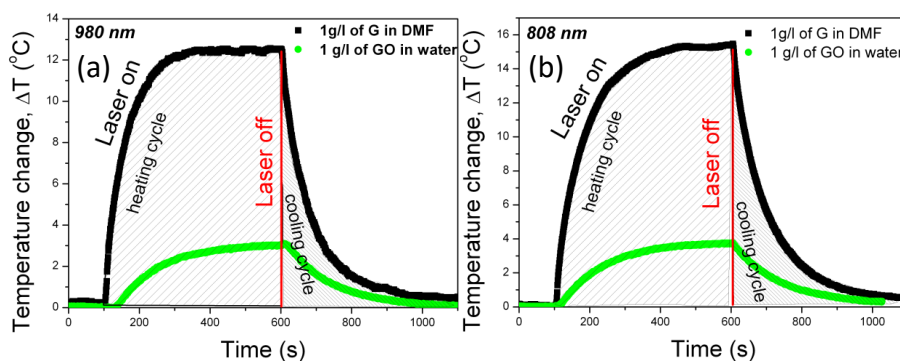


Figure 3. (a) Temperature profile of the G and GO under the same conditions with 980 nm irradiation wavelength; (b) Temperature profile of G and GO at 808 nm irradiation wavelength.

We also investigated the influence of the GO and G concentrations and the power of the laser irradiation on the temperature that can be achieved in the liquid dispersions. The results of these analysis for GO in water are shown in Figure 4(a). As can be seen, the temperature increases almost linearly as the power of the laser increases. When illuminated at 980 nm, the temperature increase ranged from 4 °C at an irradiation power of 200 mW to 14 °C at the highest irradiation power (800 mW) for a concentration of 5 g/l of GO in water. If we focus our attention of the GO concentration on water, the temperature increase varied from 2 °C for a concentration of 0.5 g/l to 7.5 °C for a concentration of 5 g/l, while keeping the irradiation power at 400 mW. When illuminated at 808 nm, the temperature increase that can be achieved was higher, as expected from the higher absorption of GO at this wavelength. It ranged from 3 °C for an irradiation power of 100 mW to 22 °C for an irradiation power of 800 mW for a concentration of 5 g/l. The increase of temperature depending on the concentration of GO in water also changed, achieving 2.5 °C for a concentration of 0.5 g/l and 12 °C for a concentration of 5 g/l, while keeping the irradiation power at 400 mW in both cases.

In the case of G nanosheets dispersed in DMF, the results are shown in Figure 4(b). The results are similar for both wavelengths, although higher at 808 nm, changing from around 6-9 °C at an irradiation power of 100 mW to 45-54 °C at 800 mW. The concentration dependence of the heat produced, changed from 3-4 °C for a concentration of 0.1 g/l to 13-15 °C for a concentration of 1 g/l, at an irradiation power of 200 mW. Note, however, that the concentration and power of the laser in the case of G in DMF had to be reduced in order to maintain the range of temperature variation achieved previously on GO.

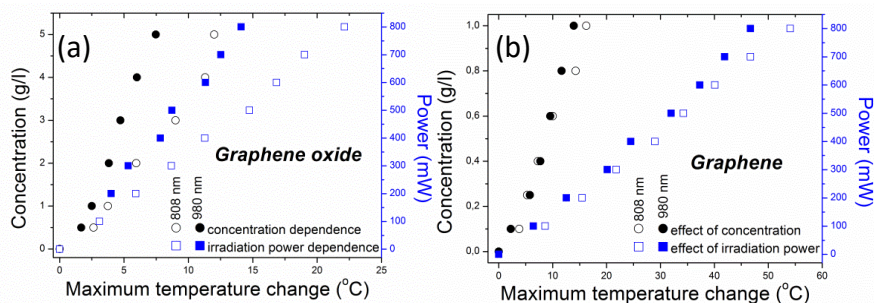


Figure 4. Temperature change under 980 and 808 nm laser irradiation at different concentrations and different irradiation powers of (a) GONanosheets dispersed in water, and (b) G nanosheets dispersed in DMF.

For the G dispersion in DMF, the temperature change values that can be achieved under these conditions are more or less double of those that can be achieved when using GO in water,

using much less quantity of material in the solvent. This can be explained by the higher absorption of G. These results show that just by changing the wavelength of irradiation, the applied irradiation power or the concentration of the photothermal agent, we can vary the heat produced by G or GO, achieving an appropriate value for a particular application. For instance, it has been shown that cancer cells can be killed after maintenance at 42 °C for 15 – 60 min or over 50 °C for 4 – 6 min [41]. These conditions can be achieved by using a concentration of GO of 5 g/l in water, illuminated at 808 nm with a power of 800 mW, or a concentration G of 1 g/l in DMF, illuminated at 808 nm with a power of 400 mW.

We determined the photothermal efficiency of G and GO by using an integrating sphere. In the scheme presented in Figure 5, we show the basic processes of interaction of light with a photothermal agent. The incident light (0) can be: (1) absorbed by the material; (2) absorbed by the cuvette and the solvent; (3) scattered and reflected from the wall of the cuvette or the surface of material; (4) the non-reflected and non-absorbed light can be transmitted.

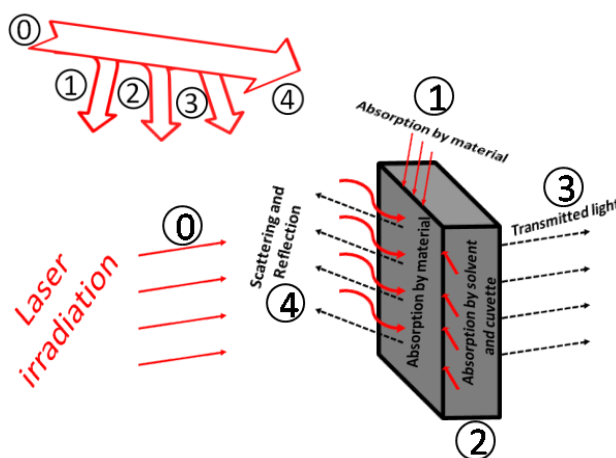


Figure 5. Scheme showing the interaction of the light with the material (G and GO in this case) when using an integrating sphere.

In our calculations we have assumed that all the light absorbed by the photothermal agent is transformed to heat. Taking into account that with the integrating sphere we are able to measure reflected, scattered and transmitted light, the photothermal conversion efficiency can be calculated by the following equation:

$$\eta = \frac{P_{heat}}{P_{inc}} = \frac{P_{blank} - P_{sample}}{P_{empty} - P_{sample}} \quad (1)$$

where P_{empty} define the power that was measured in the integrating sphere without sample, P_{sample} is the power that was measured when the sample was inside of the sphere, P_{blank} is the

power measured when only the solvent was present in the cuvette inside of the integrating sphere.

The photothermal efficiencies calculated by this method for G and GO after illumination at 808 and 980 nm are listed in Table 1, together with the parameters used to determine them. The results show that the photothermal efficiency of G in DMF is around 63-67 (± 5) %, and quite similar at the two wavelengths analyzed. However, the photothermal efficiency of GO in water depends on the wavelength used to irradiate the sample, being higher at 808 nm, as expected, since the optical absorption of GO is higher at this wavelength.

Table 1. Data of calculated photothermal efficiency using the integrating sphere.

Material	Wavelength of irradiation (nm)	Incident power (mW)	P _{empty} (mW)	P _{blank} (mW)	P _{sample} (mW)	Efficiency (%)
G	808	200	6,2	4,37	0,58	67 \pm 5
GO	808	200	6,2	4,38	1,9	58 \pm 5
G	980	200	7,82	5,32	1	63 \pm 5
GO	980	200	7,82	4,07	2,02	35 \pm 5

Table 2. Photothermal conversion efficiency of G and GO compared with other photothermal materials reported in the literature.

Material	Irradiation wavelength (nm)	Incident power (W)	Method	Efficiency (%)	Ref.
Hollow Au-Ag alloy nanourchins	808	1	Time constant	80.4	[12]
Au nanorods	815	0.151	Time constant	61	[42]
Au/AuS nanoshells	815	0.161	Time constant	59	[42]
Cu ₇ 2S ₄ nanoparticles	980	0.29	Time constant	56.7	[43]
Au nanorods	808	2	Time constant	50	[44]
Dopamine-melanin colloidal nanospheres	808	2	Time constant	40	[17]
Biodegradable Au nanovesicles	808	1	Time constant	37	[45]
Au/SiO ₂ nanoshells	815	0.163	Time constant	34	[42]
FePt nanoparticles	800	1 μ J per pulse	$\frac{P_{converted\ to\ heat}}{P_{excitation}}$	30	[19]
Cu ₆ S ₅ nanoparticles	980	0.51	Time constant	25.7	[23]
Au nanoshell	808	2	Time constant	25	[44]
Cu _{2-x} Se nanoparticles	800	2	Time constant	22	[24]
Au nanorods	808	1	Time constant	22	[45]
Au nanoshells	808	1	Time constant	18	[45]

The high values of photothermal efficiencies we determined for G and GO are among the highest reported for photothermal agents, as can be seen in Table 2 where we included data of photothermal efficiencies of other photothermal materials reported in the literature. Especially when illuminated at 808 nm, they are higher than those reported for Au nanostructures [7, 10, 46], semiconductors materials [47, 16, 17]; polymer nanostructures [45, 48], or nanoparticles with ferromagnetic properties [13]. Only Au-Ag alloy urchin shaped nanostructures show a higher efficiency of ~80 % [12], but G and GO can be produced at a more competitive price when compared to this alloy. When irradiated with a laser beam with emission at 980 nm, while G is still the most efficient photothermal agent, other materials like $\text{Cu}_{7.2}\text{S}_4$ nanocrystals show a higher photothermal conversion efficiency [43] than GO. Still, however, GO is one of the materials with the highest photothermal conversion efficiency at that wavelength.

This higher photothermal conversion efficiency of G and GO as photothermal agents is important, since they can be used to combat cancerous cells but using a lower concentration of material, a shorter irradiation time and a lower irradiation power, which apart from being more cost effective, is safer for the healthy tissues of the body. If we compare the results obtained for G and GO, despite the photothermal efficiency determined for G is higher, it is not dispersible in water, or any other suitable solvents for biological applications, unless a chemical functionalization process is developed that, of course, will affect to its light absorption properties, and thus, will modify its photothermal conversion efficiency. From another side, GO although having lower photothermal efficiency than G, since it can form hydrogen bonds between the polar functional groups present on its surface and the water molecules surrounding, it and can form a stable colloidal suspension, thus, having advantages for potential biomedical applications. In this context, it is worth to mention that the attachment of polyethylene glycol (PEG) to graphene derivatives increased substantially the optical absorption of these materials, increasing substantially their photothermal conversion efficiency [28, 30, 31, 33]. In front of other photothermal agents, such as Au nanostructures, a part from the higher photothermal efficiency, G and GO have an additional advantage, since Au nanoparticles tend to change their shape when illuminated with a high laser power, thus modifying their plasmonic resonances [49] which will decrease significantly their photothermal efficiency at that particular wavelength.

Table 3. Comparison of the photothermal conversion data reported in the literature for different graphene-based materials for an irradiation wavelength of 808 nm

Material	Concentration (g l ⁻¹)	Power density (W cm ⁻²)	Absorbance	ΔT _{max} (°C)	Time (s)	Reference
PEGylated nano G	0.5	2	0.5	35	180	[28]
Nano reduced GO	0.02	0.6	19	27	480	[29]
Nano GO	0.02	0.6	2	12	420	[29]
PEGylated nano reduced GO	0.01	1	0.2	29	300	[30]
PEGylated reduced GO	0.01	1	0.22	29	300	[30]
PEGylated nano GO	0.01	1	0.07	15	300	[30]
PEGylated GO nanoribbons	0.001	7.5	0.55*	34	600	[31]
PEGylated reduced GO	0.001	7.5	0.22*	20	600	[31]
GO nanoribbons	0.001	7.5	0.05*	5	600	[31]
Glucose reduced GO + Fe catalyst	0.1	7.5	0.32 [#]	38	120	[32]
Hydrazine reduced GO	0.1	7.5	0.32 [#]	45	120	[32]
GO	0.1	7.5	0.02 [#]	10	120	[32]
PEGylated GO nanomesh	0.01	0.1	1.1	30	460	[33]
PEGylated reduced GO nanoplates	0.01	0.1	0.39	16	460	[33]
PEGylated reduced GO	0.01	0.1	0.42	15	460	[33]
GO nanomesh	0.01	0.1	0.03	5	460	[33]
GO	1	1	0.05	4	400	This work
G	1	1	0.48	15	400	This work

* The absorbance has been determined with a concentration of 1 g l⁻¹.

[#] The absorbance has been determined with a concentration of 0.5 g l⁻¹.

When comparing the photothermal conversion efficiency of graphene-based materials reported in the literature with the results presented in this manuscript, what we observed is that in general the photothermal conversion efficiency reported in the literature is presented just as a temperature evolution profile, similar to that shown here in Figure 3. This makes difficult the task of comparing our results with those previously reported. However, we listed the available data in the literature with the idea to establish some comparisons between the results reported previously and those achieved in the present paper. Table 3 shows this comparison.

As can be seen in the table, materials were excited at different laser power densities, different concentrations were used, and even absorbances are plotted in different scales without indicating if they are in a 1 scale or in %. This adds some difficulties to establish these comparisons. However, some generalizations can be extracted from these data. First, GO is the

graphene derivative showing a smaller photothermal conversion, with temperature increments of the order of 4-5 °C, even in the form of nanomeshes or nanoribbons. From another side, it is clear that reduced GO shows a higher photothermal conversion that can multiply by 9 the temperature increment achieved by GO. Finally, another important tendency is that the materials tending to show the maximum photothermal conversion are those that are linked to polyethylene glycol (PEG) that also show the highest absorbance, indicating a synergistic effect between the graphene derivative and PEG. It should also be noted that the same material in different sizes, PEGylated nano reduced GO vs. PEGylated reduced GO for instance, tend to show the same photothermal conversion, indicating that the lateral size of the graphene-derivative flakes does not have an influence on the photothermal properties of the material. Thus, apparently from the data reported, it seems that the photothermal conversion is linked to the absorbance of a particular material: the higher the absorbance, the higher the photothermal conversion. Note also, that in this comparison we did not include the composite materials of graphene or graphene derivatives with other inorganic and organic materials developed also for photothermal treatments, since it would be difficult even more the task of establishing general tendencies.

To validate this new method for the determination of the photothermal efficiency of G and GO, we calculated the photothermal efficiency of Au nanorods by using the integrating sphere, and compared the photothermal efficiency obtained by this method with that obtained using the time constant method [44], a method well established for this purpose. Figure 6 (a) shows the absorption spectra of these Au nanorods, with 2 absorption bands located at 525 and 650 nm, corresponding to the transversal and longitudinal plasmonic resonances. We used this last wavelength, with a power of 200 mW, to illuminate the Au nanorods and determine their photothermal efficiency.

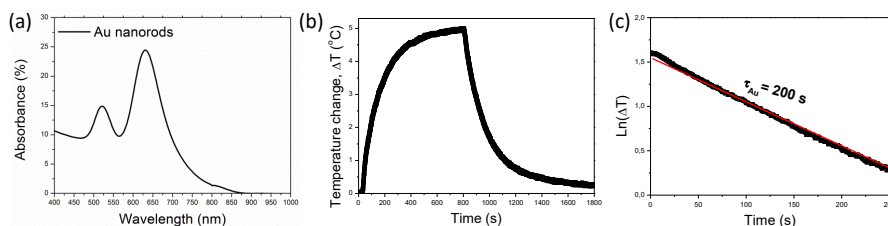


Figure 6. (a) Absorption spectrum of Au nanorods, 25 nm in diameter and 50 nm in length. (b) Temperature profile generated by Au nanorods being excited at 650 nm with a diode laser. (c) Time constant for heat transfer of the Au nanorods by applying the natural logarithm of temperature change versus time data, which is obtained from the cooling cycle shown in panel (b).

To apply the time constant method, we take into account that the time evolution of the temperature after the laser was switched off can be described by equation (cooling cycle in Fig. 6b):

$$\Delta T = (T_{max} - T_{amb}) \exp\left(-\frac{t}{\tau}\right) \quad (2)$$

where ΔT is the change of temperature; T_{max} is the maximum temperature reached by the sample, T_{amb} is the ambient temperature of the surroundings; t is time; and τ is the thermal time constant. This thermal time constant can be calculated by:

$$\tau = \frac{\sum_i m_i c_{pi}}{hA} \quad (3)$$

Here, h is the convective heat transfer coefficient, A is the external area of the cuvette and m_i and c_{pi} are the mass and specific heat of each element of the system, respectively (glass cuvette, solvent, heating material). The fitting of the temperature evolution data as a function of time to equation (2) allows determining τ from which we can determine the heat transfer coefficient h in equation (3). Finally, the thermal conversion efficiency was calculated using the equation proposed by Roper as following [38]:

$$\eta = \frac{hA(T_{max}-T_{amb})-Q_0}{I(1-10^{-A_\lambda})} \quad (4)$$

where Q_0 is the heat dissipated from the light absorbed by the glass cuvette and the solvent - that was determined independently, by using a glass cuvette filled with the solvent- I is the laser incident power, and A_λ is the absorbance of the material.

The photothermal efficiency calculated for Au nanorods using the integrating sphere or the time constant methods are listed in Table 4.

Table 4. Photothermal efficiency for Au nanorods calculated by two methods.

Material	Wavelength of irradiation (nm)	Incident power (mW)	Method of calculation	Efficiency (%)
Au nanorods	650	200	Integrating sphere	56 ± 5
Au nanorods	650	200	Time constant method	52 ± 5

As can be seen from the table, the values obtained by both methods are similar. Thus, the method of determining the photothermal conversion efficiency using an integrating sphere proved its expectations and can be used as another technique with more advantages than the time constant method. Also, the value of the photothermal conversion efficiency calculated by the time constant method is in a good agreement with those previously reported for Au nanorods [38].

Finally, and to show the compatibility of both methods for determining this parameter in graphene-based materials, we compared the photothermal conversion efficiency values for G and GO determined by the integrating sphere method and the time constant method. For that, we determined the time constant from the cooling cycles of the evolution of temperature with time for G and GO illuminated at 980 and 808 nm presented in Figure 3. The time constants for G and GO are shown in Figure 7. Figure 8 shows the comparison of the photoluminescence conversion efficiencies for G, GO and Au nanorods determined by both methods. As we can see in the figure, the photothermal conversion efficiencies for all the materials considered is similar, or even the same when the uncertainties are considered, independently of the determination method used. This validates the method we developed using the integrating sphere for determination of the photothermal conversion efficiency, that simplifies the procedures required for the determination of this parameter.

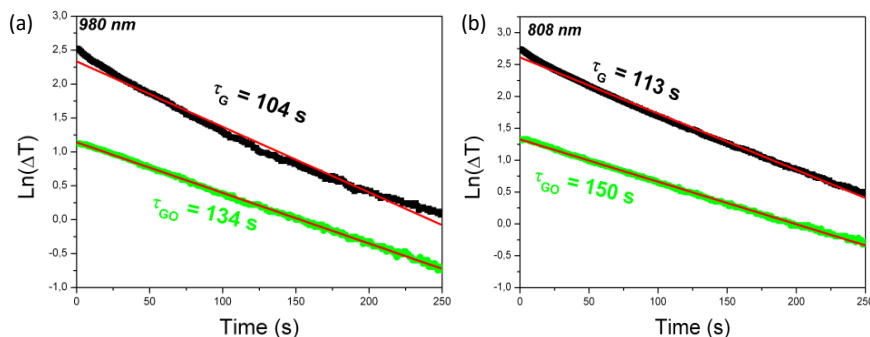


Figure 7. Time constants for heat transfer of graphene and graphene oxide by applying the natural logarithm of temperature change versus time data, which is obtained from the cooling cycles shown in Figure 3 after illumination at (a) 980 nm and (b) 808 nm.

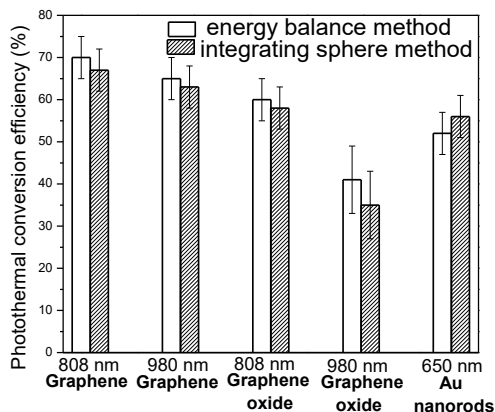


Figure 8. Comparison of the photothermal conversion efficiencies of graphene, graphene oxide and Au nanorods determined by the time constant and the integrating sphere methods.

4. Conclusion

In conclusion we developed and validated a new method for determining the photothermal efficiency of G and GO using an integrating sphere. Compared to the time constant method for determining the same parameter, the integrating sphere presents the advantage of simplicity. By applying this method we found that the photothermal efficiency of G and GO are among the highest reported for photothermal agents, which identify them as important photothermal agents for biological purposes, such as eliminating cancer cells by hyperthermia treatments. Even, from the data reported in the literature for other graphene derivatives, if those materials are functionalized with PEG or are produced in the form of nanoribbons or nanomeshes, their photothermal conversion efficiencies might be higher. This method is not exclusive for graphene-based materials, but can also be used for any photothermal material, and will allow detecting differences in photothermal conversion efficiency when the absorbance properties of the materials are different, since the method is sensible to these changes, with the additional advantage that it is not necessary to know the optical absorbance of the material to be analyzed in advance. We also analyzed the influence of the concentration of G and GO, and the wavelength and power of irradiation in the temperature increase that can be achieved with them. The results indicate that by using a concentration of GO of 5 g/l in water illuminated at 808 nm with a power of 800 mW, or a concentration of G of 1 g/l in DMF illuminated at the same wavelength with a power of 400 mW, we can obtain the temperature increase required for cancer treatment by hyperthermia.

Acknowledgements

This work was supported by the Spanish Government under Projects No. MAT2013-47395-C4-4-R and TEC2014-55948-R, and by Catalan Authority under Project No. 2014SGR1358.OI. A. Savchuk is supported by Catalan Government through the fellowship 2015FI_B2 00136. F. D. acknowledges additional support through the ICREA Academia awards 2010ICREA-02 for excellence in research.

References

- [1] Pustovalov VK, Astafyeva LG and Fritzsche W. Selection of thermo-optical parameter of nanoparticles for achievement of their maximal thermal energy under optical irradiation. *Nano Energy* 2013;2:1137–1141.
- [2] Lepock JR, Frey HE, Rodahl AM and Kruuv J. Thermal analysis of CHL V79 cells using differential scanning calorimetry: implications for hyperthermic cell killing and the heat shock response. *J Cell Physiol* 1988;137:14–24.
- [3] Wust P, Hildebrandt B, Sreenivasa G, Rau B, Gellermann J, Riess H, Felix R and Schlag PM. Hyperthermia in combined treatment of cancer. *Lancet Oncol* 2002;3: 487–497.
- [4] Jones E L, Oleson JR, Prosnitz LR, Samulski TV, Vujaskovic Z, Yu D, Sanders LL and Dewhirst MW. Randomized trial of hyperthermia and radiation for superficial tumors. *J Clin Oncol* 2005;23:3079–3085.
- [5] Marmor JB, Pounds D, Postic TB and Hahn GM. Treatment of superficial human neoplasms by local hyperthermia induced ultrasound. *Cancer* 1979;43:188–197.
- [6] Mulier PMJ and Hoey MF. Method and apparatus for RF ablation and hyperthermia. US patent 5807395A, 1998.
- [7] Sogawa A, Inokuchi K, Sugimachi K, Kai H, Hotta T and Kawai Y. Endotract antenna device for hyperthermia. US patent 4662383A, 1987.
- [8] Carrasco E, Rosal B, Sanz-Rodríguez F, de la Fuente ÁJ., Haro-Gonzalez P, Rocha U, Kumar KU, Jacinto C, Solé JG, and Jaque D. Intratumoral thermal reading during photothermal therapy by multifunctional fluorescent nanoparticles. *Adv Funct Mater* 2015;25:615–626.
- [9] Chen, ZG, Zhang LS, Sun YG, Hu JQ, Wang DY. 980 nm laser-driven photovoltaic cells based on rare-earth up-converting phosphors for biomedical applications. *Adv Funct Mater* 2009;19:3815–3820.
- [10] Chen WR, Adams RL, Carubelli R, Nordquist RE. Laser-photosensitizer assisted immunotherapy: a novel modality for cancer treatment. *Cancer Lett* 1997;115: 25–30.
- [11] Chen WR, Adams RL, Higgins AK, Bartels KE, Nordquist RE. Photothermal effects on murine mammar tumors using indocyanine green and an 808-nm diode laser: an in vivo efficacy study. *Cancer Lett* 1996;98:169–173.
- [12] Liu Z, Cheng L, Zhang L, Yang Z, Liu Z, Fang J. Sub-100 nm hollow Au-Ag alloy urchin-shaped nanostructure with ultrahigh density of nanotips for photothermal cancer therapy. *Biomaterials* 2014;35:4099-4107.

- [13] Tang S, Chen M, and Zheng N. Sub-10-nm Pd nanosheets with renal clearance for efficient near-infrared photothermal cancer therapy. *Small* 2014;10(15):3139–3144.
- [14] Yin HB, Cai HH, Cai JY, Teng JW, Yang PH. Facile solution for the syntheses of water-dispersible germanium nanoparticles and their biological applications. *Materials Lett* 2013;109:108-111.
- [15] Zhou J, Lu Z, Zhu X, Wang X, Liao Y, Ma Z, Li F. NIR photothermal therapy using polyaniline nanoparticles. *Biomaterials* 2013;34:9584-9592.
- [16] Zha Z, Yue X, Ren Q, and Dai Z. Uniform polypyrrole nanoparticles with high photothermal conversion efficiency for photothermal ablation of cancer cells. *Adv Mater* 2013;25:777–782.
- [17] Liu Y, Ai K, Liu J, Deng M, He Y, and Lu L. Dopamine-melanin colloidal nanospheres: an efficient near-infrared photothermal therapeutic agent for in vivo cancer therapy. *Adv Mater* 2013;25:1353–1359.
- [18] Xu L, Cheng L, Wang C, Peng R and Liu Z. Conjugated polymers for photothermal therapy of cancer. *Polym Chem* 2014;5:1573-1580.
- [19] Chen CL, Kuo LR, Lee SY, Hwu YK, Chou SW, Chen CC, Chang FH, Lin KH, Tsai DH, Chen YY. Photothermal cancer therapy via femtosecond-laser-excited FePt nanoparticles. *Biomaterials* 2013;34:1128-1134.
- [20] Akhavan O, Meidanchi A, Ghaderid E and Khoei S. Zinc ferrite spinel-graphene in magneto photothermal therapy of cancer. *J Mater Chem B* 2014;2:3306-3314.
- [21] Li XD, Liang XL, Yue XL, Wang JR, Li CH, Deng ZJ, Jing LJ, Lin L, Qu EZ, Wang SM, Wu CL, Wu HX and Dai ZF. Imaging guided photothermal therapy using iron oxide loaded poly(lactic acid) microcapsules coated with graphene oxide. *J Mater Chem B* 2014;2:217.
- [22] Zhou Z, Kong B, Yu C, Shi X, Wang M, Liu W, Sun Y, Zhang Y, Yang H, Yang S. Tungsten oxide nanorods: an efficient nanoplatform for tumor CT imaging and photothermal therapy. *Sci Rep* 2014;4:3653-3663.
- [23] Tian Q, Jiang F, Zou R, Liu Q, Chen Z, Zhu M, Yang S, Wang J, Wang J and Hu J. Hydrophilic Cu₉S₅ nanocrystals: a photothermal agent with a 25.7% heat conversion efficiency for photothermal ablation of cancer cells in vivo. *ACS Nano* 2011;5(12):9761–9771,.
- [24] Hessel CM, Pattani VP, Rasch M, Panthani MG, Koo B, Tunnell JW and Korgel BA. Copper selenide nanocrystals for photothermal therapy. *Nano Lett* 2011;11:2560–2566.

- [25] Tian Q, Hu J, Zhu Y, Zou R, Chen Z, Yang S, Li R, Su Q, Han Y and Liu X. Sub-10 nm Fe₃O₄@Cu_{2-x}S core-shell nanoparticles for dual-modal imaging and photothermal therapy. *J Am Chem Soc* 2013;135:8571–8577.
- [26] Choi HS, Liu W, Misra P, Tanaka E, Zimmer JP, Ipe BI, Bawendi MG, Frangioni JV. Renal clearance of quantum dots. *Nat Biotechnol* 2007;25(10):1165-1170.
- [27] Wu MC, Deokar AR, Liao JH, Shih PY, and Ling YC. Graphene-based photothermal agent for rapid and effective killing of bacteria. *ACS Nano* 2013;7(2):1281–1290.
- [28] Yang K, Zhang S, Zhang G, Sun X, Lee ST, and Liu Z. Graphene in mice: ultrahigh in vivo tumor uptake and efficient photothermal therapy. *Nano Lett* 2010;10:3318–3323.
- [29] Robinson JT, Tabakman SM, Liang Y, Wang H, Sanchez Casalongue H, Vinh D and Dai H. Ultrasmall reduced graphene oxide with high near-infrared absorbance for photothermal therapy. *J. Am. Chem. Soc.* 2011;133:6825-6831.
- [30] Yang K, Wan J, Zhang S, Tian B, Zhang Y and Liu Z. The influence of surface chemistry and size of nanoscale graphene oxide on photothermal therapy of cancer using ultra-low laser power. *Biomater.* 2012;33:2206-2214.
- [31] Akhavan O, Ghaderi E and Emamy H. Nontoxic concentrations of PEGylated graphene nanoribbons for selective cancer cell imaging and photothermal therapy. *J. Mater. Chem.* 2012;22:20626-20633.
- [32] Akhavan O, Ghaderi E, Aghayee S, Fereydooni Y and Talebi A. The use of a glucose-reduced graphene oxide suspension for photothermal cancer therapy. *J. Mater. Chem.* 2012;22:13773-13781.
- [33] Akhavan O and Ghaderi E. Graphene nanomesh promises extremely efficient in vivo photothermal therapy. *Small* 2013;9:3593-3601.
- [34] Shi X, Gong H, Li Y, Wang C, Cheng L, Liu Z. Graphene-based magnetic plasmonicnanocomposite for dual bioimaging and photothermal therapy. *Biomaterials* 2013;34:4786-4793.
- [35] Wang Y, Wang H, Liu D, Song S, Wang X, Zhang H. Graphene oxide covalently grafted upconversion nanoparticles for combined NIR mediated imaging and photothermal/photodynamic cancer therapy. *Biomaterials* 2013;34:7715-7724.
- [36] Smith AM, Mancini MC, Nie S. Bioimaging: second window for in vivo imaging. *Nat Nanotechnol* 2009;4:710-711.
- [37] Li JL, Tang B, Yuan B, Sun L, Wang XG. A review of optical imaging and therapy using nanosized graphene and graphene oxide. *Biomaterials* 2013;34:9519-9534.

- [38] Roper DK, Ahn W. and Hoepfner M. Microscale heat transfer transduced by surface plasmon resonant gold nanoparticles. *J Phys Chem C Nanomater Interfaces* 2007;111(9):3636–3641.
- [39] Hsu PC, Lin TA, Tsai IS. Numerous single-layer graphene sheets prepared from natural graphite by non-chemical liquid-phase exfoliation. *Micro Nano Lett* 2014;9(12):922-926.
- [40] Rybin M, Pereyaslavtsev A, Vasilieva T, Myasnikov V, Sokolov I, Pavlova A, Obratsova E, Khomich A, Ralchenko V and Obratsova E. Efficient nitrogen doping of graphene by plasma treatment. *Carbon* 2016;96:196-202.
- [41] Habash RWY, Bansal R, Krewski D, Alhafid HT. Thermal therapy, part 1: an introduction to thermal therapy. *Crit Rev Biomed Eng* 2006;34(6):459-489.
- [42] Cole JR, Mirin NA, Knight MW, Goodrich GP and Halas NJ. Photothermal efficiencies of nanoshells and nanorods for clinical therapeutic applications. *J. Phys. Chem. C* 2009;113:12090–12094.
- [43] Li B, Wang Q, Zou R, Liu X, Xu K, Lia W and Hu J. Cu₇2S₄ nanocrystals: a novel photothermal agent with a 56.7% photothermal conversion efficiency for photothermal therapy of cancer cells. *Nanoscale* 2014; 6, 3274.
- [44] Pattani VP and Tunnell JW. Nanoparticle-mediated photothermal therapy: a comparative study of heating for different particle types. *Lasers Surg Med* 2012;44:675–684.
- [45] Huang P, Lin J, Li W, Rong P, Wang Z, Wang S, Wang X, Sun X, Aronova M, Niu G, Leapman RD, Nie Z and Chen X, Biodegradable gold nanovesicles with an ultrastrong plasmonic coupling effect for photoacoustic imaging and photothermal therapy. *Angew. Chem. Int. Ed.* 2013;52:13958 –13964.
- [46] Cheng FY, Chen CT and Yeh CS. Comparative efficiencies of photothermal destruction of malignant cells using antibody-coated silica@Au nanoshells, hollow Au/Ag nanospheres and Au nanorods, *Nanotechnology* 2009;20:425104-425113.
- [47] Choi J, Yang J, Jang E, Suh JS, Huh YM, Lee K and Haam S. Gold nanostructures as photothermal therapy agent for cancer. *Anticancer Agents Med Chem* 2011;11:953-964.
- [48] Huff TB, Tong L, Zhao Y, Hansen MN, Cheng JX, Wei A. Hyperthermic effects of gold nanorods on tumor cells. *Nanomedicine* 2007;2(1):125–132.
- [49] Link S, El-Sayed MA. Shape and size dependence of radiative, non-radiative and photothermal properties of gold nanocrystals. *Int Rev Phys Chem* 2000;19:409–453.

Paper XIV

Savchuk, Ol. A.; Carvajal, J. J.; Brites, C. D. S.; Carlos, L. D.; Aguiló, M.; and Díaz, F. *Multifunctional Ho,Tm:KLuW nanoparticles for temperature sensing applications* (2016) To be submitted to Nanoscale.

Multifunctional Ho,Tm:KLuW nanoparticles for temperature sensing applications

Ol. A. Savchuk,¹ J. J. Carvajal,^{1} C. D. S. Brites,² L. D. Carlos,² M. Aguiló,¹ and F. Diaz¹*

¹Física i Cristal·lografia de Materials i Nanomaterials (FiCMA-FiCNA) – EMaS, Universitat Rovira i Virgili (URV), Campus Sescelades, Marcel·li Domingo 1, E-43007 Tarragona, Spain.

²Department of Physics, CICECO – Aveiro Institute of Materials, University of Aveiro, Campus Universitario de Santiago, 3810-193 Aveiro, Portugal.

*Corresponding Author: joanjosep.carvajal@urv.cat.

1. Abstract

The unique properties of luminescent nanoparticles have the potential to impact the photothermal therapy as they may conglomerate both heating and temperature measurement valences. Here, we report the temperature dependence of upconversion emission of Ho,Tm:KLu(WO₄)₂ nanoparticles for application in luminescence nanothermometry, operating in the first biological window with the highest thermal sensitivity ever reported for luminescent systems operating in this spectral region, 2.8 % K⁻¹ at 300 K. Moreover, besides upconversion the excitation beam can induce simultaneous heat release by the judicious proportion of Ho³⁺ and Tm³⁺ ions in the nanoparticles. The particles display a maximum photothermal conversion efficiency, of 34±2 % highlighting their potential to be used in photothermal therapy.

2. Introduction

Temperature is one of the basic and important variables in science. Many industrial and scientific processes as well as different processes in everyday life depend on the temperature.^{1,2} In medicine, for instance, an elevated body temperature or fever is one of the basic diagnostic signs of a viral or bacterial infection. Thus, an accurate determination and appropriate monitoring of temperature can detect early stage diseases in the primordial phase of development.³ Non-contact thermometry techniques are slowly replacing the classical contact temperature measurement techniques in remote applications, or in those in which these contact with the thermal probe might distort the measurements or affect the body of analysis, offering great advantages and a diverse field of applications^{2, 4-6}. Among the different non-contact thermometry techniques, luminescence thermometry in which the temperature is inferred from the luminescent properties of the sensor is one of the most promising ones, combining higher spatial (10^{-1} μm), temporal (10 μs), and thermal (10^{-2} K) resolutions, in comparison with other noncontact thermometric techniques, such as infrared thermometry^{2, 4-7}.

Among the different luminescence thermometry techniques, those based on the comparison of the emission intensities arising from thermally coupled energy levels in trivalent lanthanide ions (Ln^{3+}) doped systems are the most popular, maybe because they present a temperature determination that is not affected by fluctuations in the concentration of the luminescence centers and/or excitation source.⁷⁻¹⁰ Nonetheless, those systems still suffer from lower thermal sensitivities, *i.e.* the ability of translate a small temperature change into a measurable change in the luminescent properties, it can be increased by the proper choice of the energy levels to be analyzed. If the energetic separation between the levels is small the thermal sensitivity is reduced, on the other hand, if these levels are far apart, thermalization is no longer observed and the rationalization of the response of the system is far more complicated. As the energy difference becomes wider, the electronic population (and hence the concomitant luminescence

intensity arising from the upper thermally coupled level) will be abridged, which may introduce problems from the instrumental point of view to detecting it.¹¹

To overcome the aforementioned disadvantages, luminescent ratiometric thermometers have been developed based on two emission bands arising from different trivalent lanthanide ions, rather than a single one.¹²⁻¹⁶ Such systems are excellent candidates for noncontact temperature measurements with very high sensitivities and have potentiality for different applications at the nanoscale, including the detection of ‘hot-spots’ in electronic microchips,¹³ the detection of activation energies in catalytic reactions and melting point transitions from lipid membranes in nanofluidic devices¹⁵ and even for cryogenic temperature sensing applications in space exploration.¹⁶ Some of ratiometric luminescent thermometers use downshifting mechanisms, where an incident high energy photon is transformed by the material into lower-energy photons. The high thermal sensitivity of such systems was demonstrated by some of us, using the emission from distinct emission (Tb^{3+} and Eu^{3+}), located in the visible range of the electromagnetic spectrum, at 545 and 612 nm, respectively.¹³ The spatial resolution achieved (limited only by the experimental apparatus implemented) is within the 1-10 μm with a maximum relative thermal sensitivity (S_r) of 4.9 % K^{-1} and temporal resolution in the order of the integration time used, 100 ms. This S_r value compares favorably with the highest value reported for multi-center thermometers,^{12, 14, 15, 17-19} but also for single-center Ln^{3+} -doped systems.⁷⁻¹⁰ The Tb^{3+} and Eu^{3+} pair is the most used for multi-center luminescence downshifting thermometers,^{14-16, 19} but other pair of ions, such as $\text{Tm}^{3+}/\text{Tb}^{3+}$,¹² $\text{Nd}^{3+}/\text{Yb}^{3+}$,¹⁷ or $\text{Tm}^{3+}/\text{Ho}^{3+}$,¹⁸ have also been used for the same purpose. Ishiwada and co-workers developed a phosphor thermometer based on Tb^{3+} , $\text{Tm}^{3+}:\text{Y}_2\text{O}_3$ particles that operated in a wide temperature range from 323 – 1123 K. Under 355 nm excitation, the ratio between the emission intensities of the Tm^{3+} (at 466 nm) and the Tb^{3+} (540 nm) is strongly temperature dependent.¹³ Although, the authors did not compute the thermal sensitivity of the system, we are able to compute $S_r=0.8$ % K^{-1} (at 1023 K) from the published data. Marciniak *et. al.* have found that $\text{Nd}^{3+}, \text{Yb}^{3+}:\text{LiLaP}_4\text{O}_{12}$

nanocrystals possess a temperature-dependent luminescence intensity ratio between Nd^{3+} (870 nm) and Yb^{3+} (980 nm) emissions, under 800 nm excitation. Moreover, the thermal sensitivity of such system was found to be Yb^{3+} concentration dependent and the best performance was obtained for the 0.5% of Yb^{3+} ion ($0.3 \% \text{ K}^{-1}$)¹². The upconverting thermometer of Pandey and Rai is based on the temperature dependent of the blue upconversion emission generated from the Ho^{3+} , Yb^{3+} , $\text{Tm}^{3+}:\text{Y}_2\text{O}_3$ phosphors, upon 980 nm excitation.¹⁸ Intensity ratio of the two emission lines at 477 and 488 nm, arising from the radiative transition $^1\text{G}_4 \rightarrow ^3\text{H}_6$ of the Tm^{3+} ion and $^5\text{F}_3 \rightarrow ^5\text{I}_8$ of Ho^{3+} ion showed a linear tendency in 303–703 K temperature range, with a relative thermal sensitivity was found to be $0.7 \% \text{ K}^{-1}$.¹⁸ The use of the near infrared region of the electromagnetic spectrum is due to the strong extinction coefficient of the biological tissues in the visible range of the spectrum, resulting in a lower penetration depth of the light, in comparison with that in the near infrared region. Luminescent materials for biological applications should be especially designed to avoid the strong absorption of biological tissues, presenting emission lines within the so called biological windows, spectral regions where these effects are strongly mitigated.^{20, 21} Other common issue is related to their excitation at 980 nm, strongly absorbed by the water, that may cause an significant increment of the temperature of the biological tissues.^{22, 23}

The current trend in luminescence thermometry is multifunctionality. When the luminescent thermometric materials can combine different functionalities, like photothermal heating and thermometric functions, they present a crucial advantage of being able to control the thermal dose delivered in a heat treatment, minimizing the use of invasive treatments and facilitating chirurgical procedures. An example of implementation of these multifunctional systems was reported by Carrasco *et al.* that controlled photothermal therapy *in-vivo* in a cancer tumor²³ using $\text{Nd}^{3+}:\text{LaF}_3$ nanoparticles, which acted at the same time as nanoheaters and luminescent thermal nanosensors.

Here, we report $\text{Ho}^{3+}, \text{Tm}^{3+}$ co-doped $\text{KLu}(\text{WO}_4)_2$ nanoparticles as new multifunctional heater-thermometer nanoplatfoms. We show that the emission lines at 696 and 750 nm, within the first biological window (I-BW), can be used for luminescence nanothermometry, presenting the highest relative thermal sensitivity ever reported for luminescent thermometers operating in this spectral region. Moreover, the heat dissipation in the nanoparticles (ascribed to the increase of the probability of non-radiative processes between Ho^{3+} and Tm^{3+} ions) is fine-tuned by adjusting the relative $\text{Ho}^{3+}/\text{Tm}^{3+}$ content demonstrating that the nanoparticles have the potential to be used in photothermal therapy (real time heating and temperature monitoring can be made simultaneously in a single nanoparticle).

3. Experimental Section

Synthesis of Ho,Tm:KLu(WO₄)₂ nanoparticles

Ho^{3+} and Tm^{3+} doped $\text{KLu}(\text{WO}_4)_2$ nanocrystals were synthesized by the modified Pechini sol-gel method.²⁴ Ho_2O_3 (99.9999%), Tm_2O_3 (99.9%) and Lu_2O_3 (99.9999%), were used as starting reagents. They were dissolved in hot nitric acid in stoichiometric proportions to form the nitrate precursors. Concentrations of Tm^{3+} between 5 and 15 % and Ho^{3+} between 1 and 5 %, substituting Lu^{3+} , were investigated. Citric acid (CA), as the chelating agent and ethylenglycol (EG), as the esterification agent, were also used in this reaction. The nitrate precursors were dissolved in distilled water with citric acid in a molar ratio of CA to metal cations $\text{CM} = [\text{CA}]/[\text{METAL}] = 1$. Ammonium tungstate $(\text{NH}_4)_2\text{WO}_4$ (99.99%) and potassium carbonate K_2CO_3 (99.99%) were added to the aqueous solution that was heated at 353K under magnetic stirring during 24 h until the complete dissolution of the reagents. Then, EG was added to the mixture in a molar ratio $\text{CE} = [\text{EG}]/[\text{CA}] = 2$. The solution was heated at 373K in order to evaporate water and generate the polymeric gel. After that, the polymeric gel was calcinated at

573 K for 3 h to obtain the precursor powders that were then calcinated at 1023K for 2 h to eliminate the organic compounds and crystallize the desired nanoparticles.

Structural and morphological characterization

The crystalline structure of the obtained Ho,Tm:KLu(WO₄)₂ nanoparticles was investigated by means of X-ray powder diffraction analysis using a Bruker-AXS D8-Discover diffractometer using Cu K_α radiation.

The morphology of the Ho,Tm:KLu(WO₄)₂ nanoparticles obtained by the modified Pechini sol-gel method was investigated by using a transmission electron microscope transmission electron microscope (TEM) JEOL 1011.

Elemental Analysis

Elemental analysis for Ho, Tm and Lu were performed by inductively coupled plasma optical emission spectroscopy (ICP-OES) analysis on a Jobin Yvon Activa-M instrument with a glass concentric nebulizer. The samples were digested under microwaves with 0.5 mL of hydrochloric acid (HCl) and 1 mL of nitric acid (HNO₃). After being digested under microwaves, the samples were recovered in 50 mL of ultrapure water. The method is accurate within 10%.

Photoluminescence Emission

To compare the emission intensities of the different nanoparticles synthesized, the samples were placed in a borosilicate vial with bottom flat and compacted to ensure that they fully fill the bottom of the vial. This vial was introduced in a sample holder that was placed inside a Labsphere 4GPS-020-SL integrating sphere, where the samples were excited with a 200 μm core diameter fiber-coupled laser diode from Apollo Instruments, Inc. emitting at 808 nm with a power of 100 mW. The laser was collimated to a spot size of 3 mm on the sample. The emission

arising from the nanoparticles was collected using an OSA Yokogawa AQ6373 spectrum analyzer.

For the temperature-dependent experiments, the Ho,Tm:KLu(WO₄)₂ nanoparticles were placed in a Linkam THMS 600 heating stage equipped with a BN disk that allowed an improved temperature distribution in the chamber. The nanoparticles were excited by a fiber-coupled diode laser at 808 nm with a power of 100 mW. The laser beam was focused on the sample by a 40 X microscope objective with N.A.=0.6 providing a spot size of around 20 μm on the sample. The emission was collected by the same microscope objective, and after passing a dichroic filter to eliminate the scattered excitation radiation, was measured by a Yokogawa AQ63753 optical spectrum analyzer.

4. Results and Discussion

¡Error! No se encuentra el origen de la referencia.(a) shows the X-ray diffraction (XRD) patterns recorded for the Ho,Tm:KLu(WO₄)₂ nanoparticles containing different concentrations of Ho³⁺ and Tm³⁺ ions. These nanoparticles crystallize in the monoclinic system with the C2/c spatial group. The reference XRD pattern, corresponding to KLu(WO₄)₂ (JCPDS file 54-1204), was included for comparison. The Scherrer equation was used to calculate the crystallite size of these luminescent nanoparticles. In all cases a mean size of 155±10 nm was obtained, indicating that different dopant concentrations produce non-measurable changes on the crystallite size, within the error of the technique.

Transmission electron microscope (TEM) images of the 1% Ho, 5% Tm:KLu(WO₄)₂ and 1% Ho, 15% Tm:KLu(WO₄)₂ nanoparticles are shown in **¡Error! No se encuentra el origen de la referencia.** (b) and **¡Error! No se encuentra el origen de la referencia.** (c), respectively. The nanoparticles have an irregular shape with the presence of agglomerates with sizes up to 2 μm, a characteristic observation for nanoparticles synthesized by this method. In these agglomerates

are discernible smaller nanoparticles, some of them showing rod-like structures with sizes around 150 ± 10 nm in diameter and 1000 ± 30 nm in length.

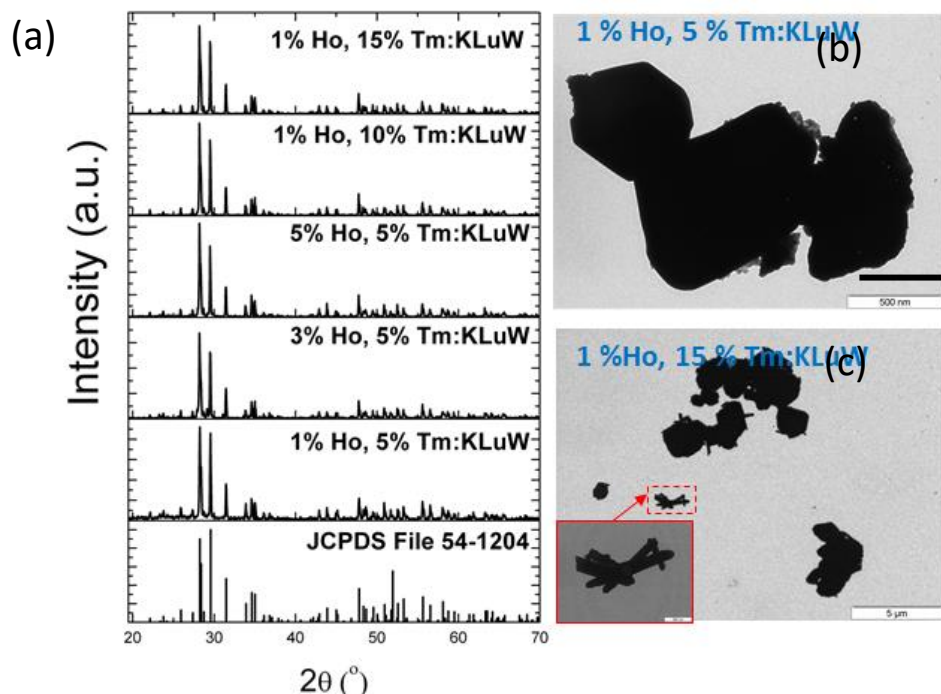


Figure 1. (a) XRD pattern of the Ho,Tm:KLu(WO₄)₂ nanoparticles synthesized by the Pechini method containing different dopant concentrations. TEM images of (b) 1% Ho, 15% Tm:KLu(WO₄)₂ and (c) 1% Ho, 5% Tm:KLu(WO₄)₂ nanoparticles. Inset in (c) shows the presence of nanorods.

The up-conversion emission spectra of Ho,Tm:KLu(WO₄)₂ nanoparticles with different concentrations of Ho³⁺ and Tm³⁺, excited at 808 nm and recorded using an integrating sphere are shown in Figure 1a. The spectra consist of three separated emission bands located in the blue, green and the red regions of the visible spectrum. These bands are generated by Tm³⁺-to-Ho³⁺ energy transfer, as previously reported for other host materials.²⁵⁻²⁷ To better understand this process, we include a simplified energy level diagram of Ho³⁺ and Tm³⁺ ions in Figure 2(c), together with possible absorption, emission and energy transfer processes involved in the upconversion mechanism. First, the 808 nm radiation excites electrons of Tm³⁺ to the ³H₄ energy level from where they non-radiatively relax to the ³F₄ level. From here, the absorption of a

Figure 1. Comparison of the emission intensity of Ho,Tm:KLu(WO₄)₂ nanoparticles excited at 808 nm with (a) the same concentration of Ho³⁺ and different concentrations of Tm³⁺ and (b) different concentrations of Ho³⁺ and the same concentration of Tm³⁺. (c) Energy level diagram depicting the upconversion mechanism for the generation of the emission spectra shown in (a).

When the concentration of Ho³⁺ was kept constant at 1% w/w, the intensity of all bands decreased as the concentration of Tm³⁺ increased, as can be seen in Figure 1(a). On the other hand, as the concentration of Ho³⁺ increased (and keeping the Tm³⁺ concentration constant at 5% w/w), the intensity of all bands increases for a concentration up to 3 % Ho³⁺, and later decreases, Figure 1 (b). The concentration of dopants in the nanoparticles was measured by ICP, Table 1. As the nominal concentration of Ho³⁺ and Tm³⁺ in the precursor powders increased, the concentration in the synthesized nanoparticles also increase: Keeping the Tm³⁺ concentration constant at 5% w/w show that an optimal concentration of Ho³⁺ at around 3 % maximizes the intensity of the emission intensity, at the same experimental conditions.

Table 1. ICP analysis of the dopant concentration of Ho,Tm:KLu(WO₄)₂ nanoparticles synthesized by the Pechini method.

Material	Ho (%)	Tm (%)	Lu (%)
1% Ho, 5% Tm:KLu(WO ₄) ₂	0.93	4.9	94.17
3% Ho, 5% Tm:KLu(WO ₄) ₂	2.2	3.57	94.22
5% Ho, 5% Tm:KLu(WO ₄) ₂	5.08	5.16	89.75
1% Ho, 15% Tm:KLu(WO ₄) ₂	0.98	11.57	87.44

We studied the evolution of the intensity of the emission bands which lies in the I-BW,^{28, 29} generated from Ho,Tm:KLu(WO₄)₂ nanoparticles. Since the energy transfer process in Ho³⁺, Tm³⁺ co-doped systems is strongly temperature dependent,^{30, 31} the ratio between the integrated areas of the ³F_{2,3}→³H₆ (Tm³⁺, at 696 nm) and ⁵S₂,⁵F₄→⁵I₇ (Ho³⁺, 755 nm) transitions can be used for this purpose. We claim this observation based on the energy transfer and backtransfer processes that may affect the emission intensities of the Tm³⁺ and Ho³⁺ transitions. The intensity

ratio of the emission lines located at 696 and 755 nm for the Ho,Tm:KLu(WO₄)₂ nanoparticles containing different concentration of dopants are shown in Figure 2(a) for the physiological range of temperatures. As can be seen, and as expected, the intensity ratio is strongly temperature dependent. In the absence of a complete physical model based on the rate equations of the levels depicted in Figure 1c (involved in the energy transfer processes), the experimental points were tentatively fitted to an empirical exponential equation of the form:

$$\Delta = \frac{I_1}{I_2} = \Delta_0 + A \exp(\alpha T) \quad (1)$$

where Δ_0 , A and α are constants to be determined by fitting for each particle composition. The calibration curves for the different nanoparticles are included in Figure 2(a).

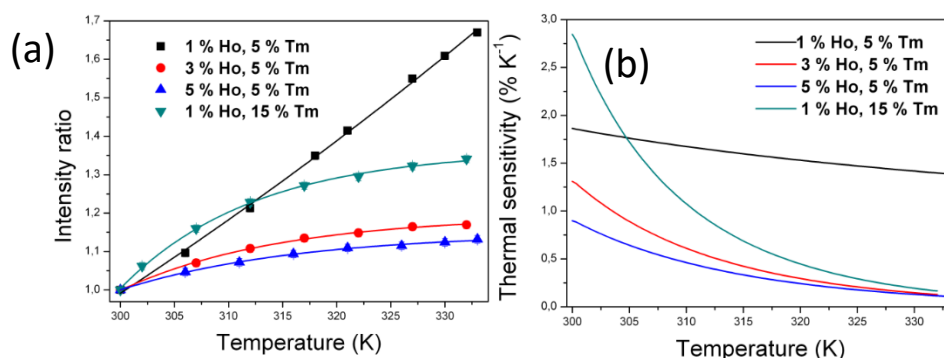


Figure 2 (a) Intensity ratio of the emission bands located at 696 and 755 nm of Ho,Tm:KLu(WO₄)₂ nanoparticles containing different dopant concentrations as a function of temperature in the biological range of temperatures. (b) Thermal sensitivity as a function of temperature in the biological range for the Ho,Tm:KLu(WO₄)₂ nanoparticles.

The intensity ratio corresponding to the 1 % Ho, 5 % Tm:KLu(WO₄)₂ nanoparticles show the highest slope. The relative thermal sensitivity S_r determines the material performance being usefull for comparison purposes and is determined using:³²

$$S_r = \frac{1}{\Delta} \left| \frac{\partial \Delta}{\partial T} \right| = \frac{A \alpha \exp(\alpha T)}{\Delta_0 + A \exp(\alpha T)} \quad (2)$$

where $\Delta = I_{696}/I_{755}$ is the experimentally measured thermometric parameter. The temperature uncertainty is estimated from Eq. 2 as:

$$\delta T = \frac{1}{S_r} \frac{\delta \Delta}{\Delta} = \frac{\Delta_0 + A \exp(\alpha T)}{A \alpha \exp(\alpha T)} \frac{\delta \Delta}{\Delta_0 + A \exp(\alpha T)} = \frac{\delta \Delta}{A \alpha \exp(\alpha T)} \quad (3)$$

where $\delta \Delta / \Delta$ is the relative error in the determination of the thermometry parameter ($\delta \Delta$ is, defined by the experimental setup).

The thermal sensitivity for the different Ho,Tm:KLu(WO₄)₂ nanoparticles is compared in Figure 2(b). The highest thermal sensitivity was found for the 1 % Ho, 15 % Tm:KLu(WO₄)₂ nanoparticles, reaching a value of 2.8 % K⁻¹ at 300 K that exponentially decreases as the temperature increases, reaching 0.3 % K⁻¹ at 333 K. The 1 % Ho, 5 % Tm:KLu(WO₄)₂ nanoparticles exhibit a smaller relative thermal sensitivity over the 300-333 K range varying from 1.9 to 0.3 % K⁻¹. The comparison of the maximum relative thermal sensitivities achieved with Ho,Tm:KLu(WO₄)₂ nanoparticles with those reported for other Ln³⁺-doped nanoparticles with emissions in the I-BW is presented in Table 2. It is worth to mention, that up to now, only single –center Ln³⁺-doped nanoparticles, mainly Nd³⁺-doped,³³⁻³⁶ and Tm³⁺, Yb³⁺ co-doped nanoparticles (in which only the emissions of Tm³⁺ were considered),³⁷⁻⁴⁰ were used for luminescence nanothermometry in the I-BW. As can be seen, the maximum relative thermal sensitivity of Ho,Tm:KLuW nanoparticles is one order of magnitude higher than those of the Ln³⁺-doped systems operating within the I-BW reported up to now. The temperature uncertainty was determined to be equal to 0.2 K, at 303 K.

Table 2. Comparison of Ln³⁺-doped systems used in luminescence nanothermometry operating in the I BW. The temperature range (ΔT), the excitation wavelength (λ_{exc}) the emission wavelenghts used to define the thermometric parameter (Δ) and the reported the relative thermal sensitivity (S_r) are presented for comparison.

Material	ΔT (K)	λ_{exc} (nm)	Δ	S_r (% K ⁻¹)	Ref.
Ho ³⁺ ,Tm ³⁺ :KLu(WO ₄) ₂	300 – 333	808	I ₆₉₆ /I ₇₅₅	2.84	This work
Tm ³⁺ ,Yb ³⁺ :GdVO ₄ @SiO ₂	298 – 333	980	I ₇₀₀ /I ₈₀₀	2.00	40
Nd ³⁺ :Gd ₂ O ₃	288 – 323	580	I ₈₂₄ /I ₈₉₂	1.75	36
Tm ³⁺ ,Yb ³⁺ :oxyfluoride glass	293 – 703	980	I ₇₀₀ /I ₈₀₀	0.3	39
Nd ³⁺ :LaF ₃	283 – 333	808	I ₈₆₅ /I ₈₈₅	0.26	33
Tm ³⁺ ,Yb ³⁺ :LiNbO ₃	323 – 723	980	I ₇₀₀ /I ₈₀₀	0.24	37

$\text{Tm}^{3+}, \text{Yb}^{3+}:\text{CaF}_2$	299 – 323	920	I_{790}/I_{800}	0.24	38
$\text{Nd}^{3+}:\text{YAG}$	283 – 343	808	I_{938}/I_{945}	0.15	34
$\text{Nd}^{3+}:\text{NaYF}_4$	273 – 423	830	I_{863}/I_{870}	0.12	35

Another important parameter for a nanothermometer is the response time. In order to evaluate this parameter for $\text{Ho}, \text{Tm}:\text{KLu}(\text{WO}_4)_2$ nanoparticles we used a portable spectrometer (MAYA Pro, Ocean Optics) controlled by a homebuilt MathLab© GUI to read the emission lines at 696 and 755 nm from the upconversion emission spectra recorded by the spectrometer, and calculate Δ , in real time. Figure 3 shows the intensity ratio between the 696 and 755 emission bands generated by the 1 % Ho, 5 % $\text{Tm}:\text{KLu}(\text{WO}_4)_2$ nanoparticles as a function of time. From this plot the value of the response time was estimated to be 250 μs , (the integration time of the spectrometer), meaning that, probably, the real response time of our system is still shorter. From this graph we can also estimate the thermal inertia of the system, corresponding to the time when the value of the intensity ratio reaches a steady state value. The thermal inertia measurement indicates that reliable measurements can be taken every 1.5 s for an induced increment of temperature of 10 K.

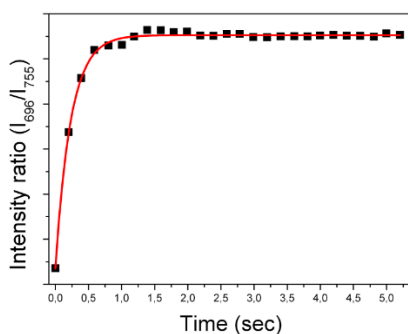
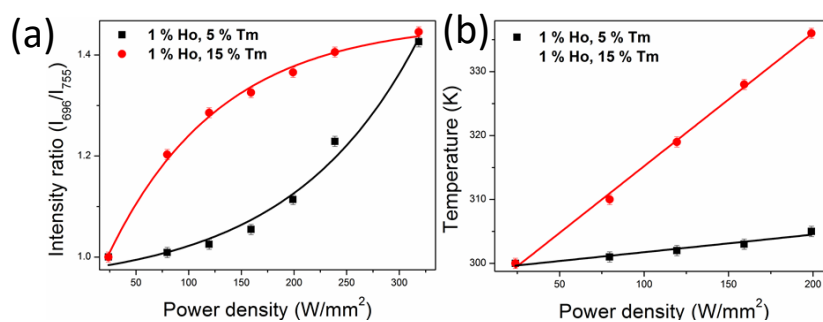


Figure 3. Intensity ratio of the emission bands located at 696 and 755 nm of the 1 % Ho, 5 % $\text{Tm}:\text{KLu}(\text{WO}_4)_2$ nanoparticles as a function of time (solid red line for eyes guiding).

Also, we find out that Δ varies with the excitation power density. Figure 4(a) shows this dependence in the case of 1 % Ho, 5 % Tm and 1 % Ho, 15 % Tm co-doped $\text{KLu}(\text{WO}_4)_2$ nanoparticles. In both cases, as the power density increases Δ increases. However, the changes

in the intensity ratio are higher for the 1 % Ho, 15 % Tm:KLu(WO₄)₂ nanoparticles than for the 1 % Ho, 5 % Tm:KLu(WO₄)₂ nanoparticles. An increase in Δ means that the temperature also increases and thus, this change in temperature can be correlated with the excitation power density. In Figure 4b the temperature deduced from the calibration curve plotted in Figure 2a is represented against the power density. As can be seen in the graph for the sample with a lower concentration of Tm³⁺ the temperature increased less than that for the sample with a higher Tm³⁺ concentration, this would mean that the first sample is generating less heat. This increase of temperature can be correlated to the heat produced by the nanoparticles as a consequence of the increased probability of non-radiative processes between Ho³⁺ and Tm³⁺ ions as the Tm³⁺ concentration increases. As a result, the sample containing more Tm³⁺ is converting the absorbed energy into heat much efficiently than the sample containing less Tm³⁺, and as the excitation power density increases, the more heat they produce. Thus, these results indicate that these nanoparticles can be used simultaneously as luminescent nanothermometers and photothermal nanoheaters. This would result beneficial, for instance, in hyperthermia applications for tumor treatments, since the same nanoparticles can be used to generate heat and thermometric response by a single laser beam paving the road to real-time temperature monitoring and heat dose control, avoiding eventual damages in the healthy surrounding tissues that result from excess of heating.



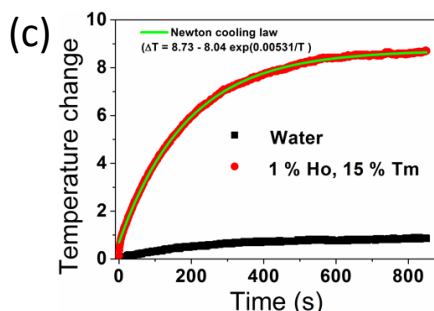


Figure 4 (a) Evolution of the intensity ratio with the excitation power density (solid lines for eyes guiding) for Ho,Tm:KLu(WO₄)₂ nanoparticles. (b) Evolution of the temperature deduced from the calibration curve presented in Figure 3(a) versus the power density. Solid lines are the linear fitting with $r^2 > 0.999$ in both cases. (c) Temperature increment that can be achieved with a dispersion of 1 % Ho, 15 % Tm:KLu(WO₄)₂ nanoparticles in water with a concentration of 1.0 g L⁻¹ at an excitation power of 1 W.

The heat produced by the nanoparticles was evaluated with another experiment. 1 % Ho, 15 % Tm:KLu(WO₄)₂ nanoparticles were dispersed in water with a concentration of 1 g·L⁻¹ and placed in a glass cuvette. A fiber-coupled diode laser with emission at 808 nm (1 W) was focused on the cuvette by means of collimating lenses producing a spot of diameter around 5 mm, giving a power density of 0.005 W cm⁻², lower than the laser safety limit for biological tissues (0.726 W cm⁻²)⁴¹. A thermo-resistor, was immersed in the cuvette to produce a temperature readout for the solution temperature, Figure 4(c) to have an independent temperature readout apart from the one that can be determined from the luminescence arising from the sample. A temperature increase of about 8 K was achieved in the cuvette containing the Ho,Tm:KLu(WO₄)₂ nanoparticles after 600 s of irradiation. For comparison, the same experiment was performed in water only, and the heating was less than 1 K.

In order to compare the heating efficiency of these nanoparticles with others nanoheater systems, we calculated the photothermal conversion efficiency using integrating sphere that was validated with the time constant method,⁴² and in details described elsewhere.⁴³ Powder nanoparticles in the form of pallet was placed inside the integrating sphere, perpendicular to the laser irradiation provided by the fiber-coupled diode laser emitting at 808 nm, with power

ranging from 0.030–0.500 W. The laser from the fiber tip was collimated with a spot size of 5 mm in diameter on the sample. A baffle was introduced in the integrating sphere, between the sample and the detector, in order to prevent the direct reflections from the sample to the detector. The signal was collected using a powermeter from Thorlabs (model Thorlabs S302C). The photothermal conversion efficiency was calculated using equation:

$$\eta = \frac{P_{empty} - P_{sample}}{P_{sample}} \times 100\% \quad (4)$$

where P_{empty} the power that was measured in the integrating sphere without sample, and P_{sample} is the power that was measured when the sample was inside the integrating sphere. The calculated photothermal conversion efficiency is $34 \pm 2\%$.

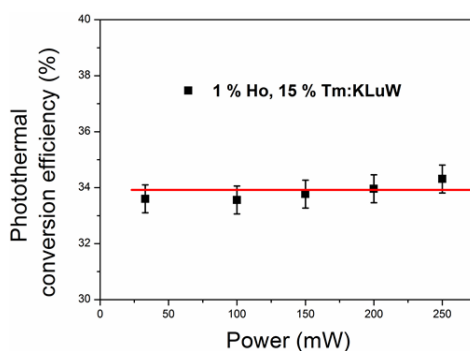


Figure 5. Photothermal conversion efficiency of the 1 % Ho, 15 % Tm:KLuW nanoparticles as a function of excitation power. Solid line represents the mean value of the photothermal conversion efficiency.

Moreover, the heating efficiency show negligible dependence on the excitation power, within the range studied, as it shown in the Figure 5. In the Table 3, the list of the photothermal conversion efficiency of different nanoheaters materials are presented for comparison. The heating efficiency of the 1 % Ho, 15 % Tm:KLuW nanoparticles is in the middle range, higher than for the metallic nanoparticles,⁴⁴ semiconductors,^{45, 46} and also some Au nanostructures,^{47 48, 49} but lower than the graphene and graphene oxide,⁴³ Au nanostructures,^{47, 49} organic materials (Table 3).⁵⁰ However, the main advantage of our luminescent nanoheater system among listed in

the table is the multifunctionality, combining imaging, photothermal therapy and temperature control using one single type of nanoparticles.

Table 3 The photothermal conversion efficiency of Ho,Tm:KLuW nanoparticles compared with others systems. The wavelength (λ) and the power (P) of the laser together with the photothermal efficiency (η)

Material	λ (nm)	P (W)	η (%)	Ref.
Graphene in DMF	808	0.2	67	43
Au nanorods	815	0.151	61	47
Au/AuS nanoshells	815	0.161	59	47
Graphene oxide in water	808	0.2	58	43
Au nanorods	808	2	50	48
Dopamine-melanin	808	2	40	50
biodegradable Au nanovesicles	808	1	37	49
1 % Ho,15 % Tm:KLuW	808	0.2	34	This work
Au/SiO ₂ nanoshells	815	0.163	34	47
FePt nanoparticles	800	-	30	41
Cu ₉ S ₅	980	0.51	25,7	45
Au nanoshell	808	2	25	48
Cu _{2-x} Se nanoparticles	800	2	22	46
Au nanorods	808	1	22	49
Au nanoshells	808	1	18	49

5. Conclusion

In summary, we demonstrated that Ho³⁺, Tm³⁺ co-doped KLu(WO₄)₂ nanoparticles are a multifunctional material. These nanoparticles have the ability to generate heat when illuminated at 808 nm due to the increased probabilities of non-radiative processes to occur between Ho³⁺ and Tm³⁺ ions as the Tm³⁺ concentration in the nanoparticles increases. Additionally, the emission lines generated by upconversion processes in these nanoparticles and located at 696 and 755 nm, which lie in the I-BW, can be used for luminescence thermometry purposes, with thermal sensitivity of 2.8 % K⁻¹ at 300 K, temperature uncertainty of 0.2 K. Regarding the performance as nanoheater, the photothermal conversion efficiency was determined to be

34±2 %, a value higher than that of semiconductor and metallic nanoparticles and which would allow controlling the temperature achieved by the heating process generated by the same nanoparticles in hyperthermia treatments, for instance.

6. Acknowledgements

This work was developed in the scope of the project CICECO – Aveiro Institute of Materials (Ref. FCT UID /CTM /50011/2013), financed by national funds through the FCT/MEC and when applicable co-financed by FEDER under the PT2020 Partnership Agreement. CDSB (SFRH/BPD/89003/2012) thanks Fundação para a Ciência e Tecnologia (Portugal) for the post-doctoral grant.

References

1. L. Michalski, K. Eckersdorf, J. Kucharski and J. McGhee, *Temperature measurement*, . . . , John Wiley & Sons Ltd, West Sussex, England, 2nd edn., 2001.
2. L. D. Carlos and F. Palacio, *Thermometry at the Nanoscale*, Cambridge: Royal Society of Chemistry, UK, 2016.
3. W. Huang, S. Ghosh, S. Velusamy, K. Sankaranarayanan, K. Skadron and M. R. Stan, *Very Large Scale Integration (VLSI) Systems, IEEE Transactions on*, 2006, **14**, 501-513.
4. C. D. S. Brites, P. P. Lima, N. J. O. Silva, A. Millán, V. S. Amaral, F. Palacio and L. D. Carlos, *Nanoscale*, 2012, **4**, 4799-4829.
5. D. Jaque and F. Vetrone, *Nanoscale*, 2012, **4**, 4301–4326.
6. X. D. Wang, O. S. Wolfbeis and R. J. Meier, *Chem. Soc. Rev.*, 2013, **42**, 7834-7869.
7. F. Vetrone, R. Naccache, A. Zamarron, A. J. de la Fuente, F. Sanz-Rodriguez, L. M. Maestro, E. M. Rodriguez, D. Jaque, J. G. Solé and J. A. Capobianco, *ACS nano*, 2010, **4**, 3254-3258.
8. L. H. Fischer, G. S. Harms and O. S. Wolfbeis, *Angewandte Chemie International Edition*, 2011, **50**, 4546-4551.
9. L. Aigouy, G. Tessier, M. Mortier and B. Charlot, *Appl Phys Lett*, 2005, **87**, 184105.
10. E. Saïdi, B. Samson, L. Aigouy, S. Volz, P. Löw, C. Bergaud and M. Mortier, *Nanotechnology*, 2009, **20**, 115703-115711.
11. S. A. Wade, S. F. Collins and G. W. Baxter, *J Appl Phys*, 2003, **94**, 4743.
12. N. Ishiwada, S. Fujioka, T. Ueda and T. Yokomori, *Opt. Lett.*, 2011, **36**, 760-762.
13. C. D. S. Brites, P. P. Lima, N. J. O. Silva, A. Millán, V. S. Amaral, F. Palacio and L. D. Carlos, *Advanced Materials*, 2010, **22**, 4499-4504.
14. A. Cadiou, C. D. S. Brites, P. M. F. J. Costa, R. A. S. Ferreira, J. Rocha and L. D. Carlos, *ACS nano*, 2013, **7**, 7213-7218.
15. C. D. S. Brites, P. P. Lima, N. J. O. Silva, A. Millán, V. S. Amaral, F. Palacio and L. D. Carlos, *Nanoscale*, 2013, **5**, 7572-7580.

16. Z. Wang, D. Ananias, A. Carné-Sánchez, C. D. S. Brites, I. Inhar, D. MasPOCH, J. Rocha and L. D. Carlos, *Advanced Functional Materials*, 2015, **25**, 2824-2830.
17. Ł. Marciniak, A. Bednarkiewicz, M. Stefanski, R. Tomala, D. Hreniak and W. Strek, *Phys. Chem. Chem. Phys.*, 2015, **17**, 24315-24321.
18. A. Pandey and V. K. Rai, *Applied Physics B*, 2013, **113**, 221-225.
19. S. Zheng, W. Chen, D. Tan, J. Zhou, Q. Guo, W. Jiang, C. Xu, X. Liu and J. Qiu, *Nanoscale*, 2014, **6**, 5675-5679.
20. L. A. Sordillo, Y. Pu, S. Pratavieira, Y. Budansky and R. R. Alfano, *J Biomed Opt*, 2014, **19**, 056004-056004.
21. R. Weissleder, *Nat. Biotechnol.*, 2001, **19**, 316-317.
22. D. T. Klier and M. Kumke, *RSC Advances*, 2015, **5**, 67149-67156.
23. G. Kucsko, P. C. Maurer, N. Y. Yao, M. Kubo, H. J. Noh, P. K. Lo, H. Park and M. D. Lukin, *Nature*, 2013, **500**, 54-58.
24. M. Galceran, M. Pujol, M. Aguiló and F. Díaz, *Journal of sol-gel science and technology*, 2007, **42**, 79-88.
25. S. A. Payne, L. K. Smith, W. L. Kway, J. B. Tassano and W. F. Krupke, *Journal of Physics: Condensed Matter*, 1992, **4**, 8525.
26. M. Guan, H. Zheng, L. Mei, Z. Huang, T. Yang, M. Fang and Y. Liu, *Infrared Phys Techn*, 2014, **67**, 107-110.
27. Y. Li, Y. Wang, B. Yao and Y. Liu, *Laser Physics Letters*, 2008, **5**, 597.
28. F. Helmchen and W. Denk, *Nature methods*, 2005, **2**, 932-940.
29. D. Jaque, L. M. Maestro, B. Del Rosal, P. Haro-Gonzalez, A. Benayas, J. Plaza, E. M. Rodríguez and J. G. Solé, *Nanoscale*, 2014, **6**, 9494-9530.
30. A. Brenier, J. Rubin, R. Moncorge and C. Pedrini, *Journal de Physique*, 1989, **50**, 1463-1482.
31. B. M. Walsh, N. P. Barnes and B. Di Bartolo, *J. Lumin.*, 2000, **90**, 39-48.
32. M. A. R. C. Alencar, G. S. Maciel, C. B. de Araujo and A. Patra, *Appl Phys Lett*, 2004, **84**, 4753-4755.
33. E. Carrasco, B. del Rosal, F. Sanz-Rodríguez, Á. J. de la Fuente, P. H. Gonzalez, U. Rocha, K. U. Kumar, C. Jacinto, J. G. Solé and D. Jaque, *Advanced Functional Materials*, 2015, **25**, 615-626.
34. A. Benayas, B. del Rosal, A. Perez-Delgado, K. Santacruz-Gomez, D. Jaque, G. A. Hirata and F. Vetrone, *Advanced Optical Materials*, 2015, **3**, 687-694.
35. D. Wawrzynczyk, A. Bednarkiewicz, M. Nyk, W. Strek and M. Samoc, *Nanoscale*, 2012, **4**, 6959-6961.
36. S. Balabhadra, M. L. Debasu, C. D. S. Brites, L. A. O. Nunes, O. L. Malta, J. Rocha, M. Bettinelli and L. D. Carlos, *Nanoscale*, 2015, **7**, 17261-17267.
37. S. Zhou, G. Jiang, X. Li, S. Jiang, X. Wei, Y. Chen, M. Yin and C. Duan, *Opt. Lett.*, 2014, **39**, 6687-6690.
38. N. N. Dong, M. Pedroni, F. Piccinelli, G. Conti, A. Sbarbati, J. E. Ramírez-Hernández, L. M. Maestro, M. C. Iglesias-de la Cruz, F. Sanz-Rodríguez, A. Juarranz, F. Chen, F. Vetrone, J. A. Capobianco, J. G. Solé, M. Bettinelli, D. Jaque and A. Speghini, *ACS nano*, 2011, **5**, 8665-8671.
39. W. Xu, X. Gao, L. Zheng, Z. Zhang and W. Cao, *Sensor Actuat B-Chem*, 2012, **173**, 250-253.
40. O. A. Savchuk, J. J. Carvajal, C. Cascales, M. Aguiló and F. Diaz, *ACS applied materials & interfaces*, 2016, **8**, 7266-7273.
41. Z. Chen, W. Sun, H. J. Butt and S. Wu, *Chemistry—A European Journal*, 2015, **21**, 9165-9170.
42. D. K. Roper, W. Ahn and M. Hoepfner, *The Journal of Physical Chemistry C*, 2007, **111**, 3636-3641.

43. O. A. Savchuk, J. Carvajal, J. Massons, M. Aguiló and F. Díaz, *Carbon*, 2016, **103**, 134-141.
44. C.-L. Chen, L.-R. Kuo, S.-Y. Lee, Y.-K. Hwu, S.-W. Chou, C.-C. Chen, F.-H. Chang, K.-H. Lin, D.-H. Tsai and Y.-Y. Chen, *Biomaterials*, 2013, **34**, 1128-1134.
45. Q. Tian, F. Jiang, R. Zou, Q. Liu, Z. Chen, M. Zhu, S. Yang, J. Wang, J. Wang and J. Hu, *ACS nano*, 2011, **5**, 9761-9771.
46. C. M. Hessel, V. P. Pattani, M. Rasch, M. G. Panthani, B. Koo, J. W. Tunnell and B. A. Korgel, *Nano letters*, 2011, **11**, 2560-2566.
47. J. R. Cole, N. A. Mirin, M. W. Knight, G. P. Goodrich and N. J. Halas, *The Journal of Physical Chemistry C*, 2009, **113**, 12090-12094.
48. V. P. Pattani and J. W. Tunnell, *Laser Surg Med*, 2012, **44**, 675-684.
49. P. Huang, J. Lin, W. Li, P. Rong, Z. Wang, S. Wang, X. Wang, X. Sun, M. Aronova and G. Niu, *Angewandte Chemie International Edition*, 2013, **52**, 13958-13964.
50. Y. Liu, K. Ai, J. Liu, M. Deng, Y. He and L. Lu, *Advanced Materials*, 2013, **25**, 1353-1359.

Conclusions

We developed novel contributions to the field of luminescent nanothermometry in terms of new materials, combination of ions and new detection techniques never tested before for this purpose. In this context, we studied the temperature dependence of the luminescence properties of luminescent nanoparticles by conventional and upconversion mechanism, in the range of the electromagnetic spectrum from the visible to the NIR.

Concerning the visible range of the electromagnetic spectrum:

- We provided a new possibility of temperature determination in biological systems with Er^{3+} and Yb^{3+} doped $\text{NaY}_2\text{F}_5\text{O}$ nanoparticles by using fluorescence lifetime nanothermometry
- We also demonstrated that $\text{Tm}^{3+}, \text{Yb}^{3+}:\text{GdVO}_4@\text{SiO}_2$ core-shell nanoparticles can be used as visual thermochromic thermometers in the 300 – 673 K temperature range, with high spatial resolution and high temporal resolution. We used these core-shell nanoparticles to monitor the heating process of a Pt wire with a small diameter decorated with our nanoparticles, generated by the Joule effect when circulating an electrical current through it, indicating that they might be used to detect hot spots in microelectronic chips.
- In $\text{Er}^{3+}, \text{Yb}^{3+}:\text{GdVO}_4@\text{SiO}_2$ core-shell nanoparticles we have shown the benefits of the SiO_2 coating on the thermometric properties of these nanoparticles, achieving an enhancement of the thermal sensitivity by a factor of 2 compared to bare $\text{Er}^{3+}, \text{Yb}^{3+}:\text{GdVO}_4$ nanoparticles. Moreover, the SiO_2 shell protects the nanoparticles from overheating during the excitation process. These core-shell nanoparticles show a high thermal resolution (0.4 K) and the spatial resolution that can be achieved with them is estimated to be of the order of their sizes. Furthermore, a good stability in different solvents, like water, methanol and DMSO, make possible to use them in biological applications as we proved by monitoring the increase of temperature of a piece of chicken breast externally by hot air.

- We introduced Ho^{3+} , Yb^{3+} :KLuW upconversion nanoparticles as a versatile material for luminescence nanothermometry and in which different thermometric techniques such as FIR of two thermally coupled Stark sublevels of the $^5\text{F}_5$ manifold, with emissions at 650 and 660 nm, the intensity ratio between the red and green bands, the fluorescence lifetime and the change of the color perception of the emitted light have been tested, showing in all cases similar results. One of the thermometric techniques used in Ho^{3+} , Yb^{3+} :KLuW nanoparticles is the. Thus, we demonstrated that we can use a single material to determine temperature by different luminescence nanothermometry techniques. Additionally, an alternative way of the excitation at 808 nm was shown by adding the Tm^{3+} ion in Ho^{3+} , Yb^{3+} :KLuW nanoparticles. We studied their upconversion emission dependence with temperature for two different excitation wavelengths. In both cases system generates an emission bands that can be used in the ratiometric technique of luminescence thermometry. In the case of excitation at 808 nm, the nanoparticles exhibited a higher thermal sensitivity in the biological range of the temperatures.
- We developed a novel non-contact and non-invasive setup for luminescence thermometry by using a digital color sensor that allows collecting signals simultaneously in the blue, green and red channels, coupled to an excitation and optical focusing systems, together with luminescent up-conversion nanoparticles with emission in at least two of these channels. We demonstrated the potentiality of this setup for temperature sensing in the biological range by using Er^{3+} , Yb^{3+} :NaYF₄ nanoparticles emitting in the green and the red and in the larger temperature interval (up to 673 K) with potential interest in microelectronics by using Tm^{3+} , Yb^{3+} :GdVO₄ nanoparticles emitting in the blue and in the red. Furthermore, we have shown that by embedding Er^{3+} , Yb^{3+} :NaYF₄ nanoparticles in PDMS, we can generate transparent composites that might allow the fabrication of thermometric microfluidic chips, in which the same chip can act as a luminescent thermometer.
- We developed a greener synthesis method for Er^{3+} , Yb^{3+} :NaYF₄ nanoparticles through a microwave-assisted solvothermal method that allows producing these nanoparticles at lower temperatures and reaction times. Furthermore, this synthesis method allowed producing α and β phases for Er^{3+} , Yb^{3+} :NaYF₄ separately. The analysis of the temperature dependent upconversion emission of these nanoparticles for luminescence nanothermometry allowed us to conclude that nanoparticles with bigger sizes in the nanoscale posses a higher thermal sensitivity. We used these nanoparticles

to visualize the temperature distribution generated by a graphene layer deposited on a microscope slide cover glass when illuminated with a laser emitting at 808 nm, with a thermal resolution of 0.1 K.

Concerning the NIR region of electromagnetic spectrum where biological systems show less absorption and scattering:

- We have investigated the upconversion emissions generated by $\text{Tm}^{3+}, \text{Yb}^{3+}:\text{GdVO}_4@\text{SiO}_2$ core-shell nanoparticles located at 700 and 800 nm, that lie in the first biological window, arising from the thermally coupled ${}^3\text{F}_{2,3}$ and ${}^3\text{H}_4$ energy levels of Tm^{3+} , respectively. We obtained a thermal sensitivity of $2.26\% \text{ K}^{-1}$, which is the highest ever reported for $\text{Tm}^{3+}, \text{Yb}^{3+}$ co-doped systems. We were also able to internalize these core-shell nanoparticles in HeLa cells for biolabelling purposes.
- We analyzed the emission bands of Nd^{3+} -doped $\text{KGd}(\text{WO}_4)_2$ nanoparticles lying in the first and second biological windows, located at 883 and 1067 nm and arising from the ${}^4\text{F}_{3/2} \rightarrow {}^4\text{I}_{9/2}$ and ${}^4\text{F}_{3/2} \rightarrow {}^4\text{I}_{11/2}$ transitions, respectively. The thermal characterization of their luminescence properties indicate that they can be used as luminescent nanothermometers in both spectral regions. The disaggregation and dispersion of the nanoparticles we achieved when functionalized with silane molecules indicate that these nanoparticles can be potentially used in biological systems, due to their sizes of ~ 16 nm, which would prevent their sedimentation in blood vessels. We also performed NIR imaging in biological tissues with these nanoparticles, achieving a penetration depth of at least 1 cm in the first and second biological windows.
- We analyzed the temperature dependent properties of the infrared emissions lying in the SWIR region of $\text{Er}^{3+}, \text{Yb}^{3+}$ and $\text{Tm}^{3+}, \text{Yb}^{3+}$ co-doped nanoparticles. The $1.55 \mu\text{m}$ emission band generated by Er^{3+} presents different Stark sub-levels that are thermally coupled and that can be used for temperature sensing purposes. However, the thermal sensitivity achieved with this emission is quite low ($0.15\% \text{ K}^{-1}$). In the case of Tm^{3+} containing nanoparticles, we observed that the intensity ratio between the emission bands located at 1.45 and $1.8 \mu\text{m}$, and arising from the ${}^3\text{F}_4$ and ${}^3\text{H}_4$ energy levels that are electronically coupled, shows a linear evolution as the temperature increases that can be used for thermometric applications. $\text{Tm}^{3+}, \text{Yb}^{3+}:\text{NaYF}_4$ nanoparticles show the highest thermal sensitivity among other $\text{Tm}^{3+}, \text{Yb}^{3+}$ co-doped systems. Adding Ho^{3+} to the system generates an efficient energy transfer between Tm^{3+} and Ho^{3+} , resulting in the generation of a new emission band centered at $1.96 \mu\text{m}$. The intensity ratio between the Tm^{3+} peak at around $1.45 \mu\text{m}$ and the Ho^{3+} emission at

1.96 μm provides a new channel for luminescence thermometry with high thermal sensitivity. Also these emissions can be used for bioimaging, achieving a penetration depth of at least 5 mm in this spectral region.

From another side, we observed that some of the nanoparticles analyzed can also be used as photothermal agents. We extended this study to other materials that can be used for the same purpose, as graphene-based materials and developed a new method to determine their thermal efficiencies that simplifies precedent procedures. Thus, concerning the photothermal converter materials:

- We demonstrated that Ho^{3+} , Tm^{3+} co-doped $\text{KLu}(\text{WO}_4)_2$ nanoparticles act as multifunctional materials. They have the ability to generate heat when illuminated at 808 nm due to the increase of non-radiative processes to occurring between Ho^{3+} and Tm^{3+} ions. Additionally, the emission lines generated by upconversion processes in these nanoparticles and located at 696 and 755 nm, which lie in the I-BW, can be used for luminescence thermometry purposes, with thermal sensitivity of $2.8\% \text{ K}^{-1}$ at 300 K, temperature uncertainty of 0.2 K. Regarding the performance as nanoheater, the photothermal conversion efficiency was determined to be $34 \pm 2\%$, a value higher than that of semiconductor and metallic nanoparticles and which would allow controlling the temperature achieved by the heating process generated by the same nanoparticles in hyperthermia treatments, for instance.
- We developed a new method for determining the photothermal conversion efficiency of photothermal agents using an integrating sphere. Compared to the time constant method for determining the same parameter, the integrating sphere present the advantage of simplicity, since we only need to perform a power balance of the system. We applied this method to determine the photothermal efficiency of graphene and graphene oxide flakes, and we found that is among the highest reported for photothermal agents, which identify them as important photothermal agents for biological purposes, such as killing cancer cells by hyperthermia treatments.